Modélisation de l'accélération d'électrons par des impulsions lasers relativistes de quelques cycles optiques sur des plasmas surdenses

Neïl Zaim

To cite this version:

Neïl Zaim. Modélisation de l'accélération d'électrons par des impulsions lasers relativistes de quelques cycles optiques sur des plasmas surdenses. Plasma Physics [physics.plasm-ph]. Université Paris Saclay (COmUE), 2019. English. NNT : 2019SACLX089 . tel-02489458

HAL Id: tel-02489458
https://theses.hal.science/tel-02489458
Submitted on 24 Feb 2020

université
PARIS-SACLAY

NNT : 2019SACLX089

Modeling electron acceleration driven by relativistic intensity few-cycle laser pulses on overdense plasmas

Thèse de doctorat de l'Université Paris-Saclay
préparée à l'École Polytechnique

École doctorale n°572 Ondes et Matières (EDOM)
Spécialité de doctorat : Physique des plasmas

Thèse présentée et soutenue à Palaiseau, le 3 décembre 2019, par

Neïl Zaïm

Composition du Jury :

Sophie Kazamias Professeur des Universités, Université Paris-Sud (LAL)	Présidente
Luis Silva Professeur, Instituto Superior Técnico (Lisbonne)	Rapporteur
Emmanuel d'Humières Professeur des Universités, Université de Bordeaux (CELIA)	Rapporteur
Guy Bonnaud Professeur, CEA (INSTN)	Examinateur
Victor Malka Professeur, Weizmann Institute of Science (Rehovot)	Examinateur
Jean-Marcel Rax PRCE, École Polytechnique (LOA)	Directeur de thèse
Jérôme Faure Directeur de Recherche, CNRS (LOA)	Co-directeur de thèse

Thèse de doctorat

Remerciements

Ce manuscrit est le fruit de trois années de travail qui se sont déroulées dans d'excellentes conditions. Je profite donc de ces quelques lignes pour remercier l'ensemble des personnes qui sont impliquées dans cette thèse.

Mes premiers remerciements vont à mes directeurs de thèse, les professeurs Jean-Marcel Rax et Jérôme Faure, pour m'avoir accueilli au LOA et permis de réaliser ce doctorat. Je remercie tout particulièrement Jérôme, mon encadrant, qui tout en me laissant une grande liberté de travail, est resté très disponible pour répondre à mes questions et me prodiguer de précieux conseils. Ses compétences scientifiques et humaines font du groupe APPLI un espace de travail agréable et propice à la production de recherche de haut niveau. Cela a été un véritable plaisir de travailler avec lui et il restera un modèle pour moi pour la suite de ma carrière.

Je suis également très reconnaissant envers l'ensemble des membres qui ont accepté de faire partie de mon jury : les rapporteurs Luis Silva et Emmanuel d'Humières qui ont méticuleusement relu ce manuscrit en un temps limité ainsi que la présidente du jury Sophie Kazamias et les examinateurs Guy Bonnaud et Victor Malka. Je leur exprime toute ma gratitude pour leur lecture très approfondie de ma thèse et pour leurs commentaires pertinents et leurs retours positifs.

Je remercie également tous les membres du CEA avec qui j'ai eu la chance de collaborer. Merci tout d'abord à Henri Vincenti pour sa bonne humeur et pour le temps qu'il a consacré à me conseiller et à me dépanner sur le code et les simulations. Merci aussi à Fabien Quéré et aux membres de son groupe qui m'ont aidé pendant la thèse (Adrien, Guillaume B, Guillaume B, Haithem et Ludovic). J'espère que cette collaboration se poursuivra aussi bien qu'elle a commencé pendant mon postdoc au CEA Saclay ! Merci finalement à Xavier Davoine et Laurent Videau du CEA Bruyères pour leur assistance sur les simus hydros.

Je remercie bien évidemment l'ensemble du LOA pour la très bonne ambiance qui règne au labo. Je remercie en particulier mes supers collègues de bureau Aline et Isabel et mon professeur d'échecs Jean-Baptiste. Je remercie aussi tous les membres du labo avec qui j'ai pu interagir pour les bons souvenirs qu'il va me rester et pour avoir rendu cette thèse très agréable : Agustin, Zhao, Benoit, Davide, Dan, Diego, Domenico, Dominykas, Fred, Geoffrey, Sylvain, Stefan, Siyi, Raj, Rick, Rodrigo, Rostyslav, Pablo, Pascal, Pierre, Jaismeen, Julius, Kosta, Lena, Lucas, Louis, Maxence, Magali, Maïmouna, Marco, Marie et ceux que j'oublie. Mention spéciale au secrétariat (Catherine, Carole, Sandrine et Patricia) qui a fonctionné de manière absolument impeccable pendant ces trois ans !

D'un point de vue plus personnel, je ne pourrais jamais assez remercier ma famille (les parents, Miloud, Magali, Chloé, Camille, Sami, Adeline, Amé, Nour et aussi tous les cousins, oncles et tantes des deux côtés de la Méditerranée) pour tout ce qu'ils m'ont apporté et pour tous les bons moments passés ensemble depuis déjà 27 ans. Je n'aurais pas pu arriver jusque ici sans eux. Un grand merci aussi à la famille Corbineau ainsi qu'à Adrien pour avoir assisté à la double thèse.

Je finis par remercier Marie-Caroline pour vivre à mes côtés.

Résumé en français

Cette thèse de doctorat est consacrée à l'accélération d'électrons par des lasers femtosecondes ultraintenses. Les faisceaux d'électrons ainsi générés sont ultracourts et intrinsèquement synchronisés avec l'impulsion laser accélératrice, ce qui les rend particulièrement attractifs pour l'amélioration de la résolution temporelle dans des expériences pompe-sonde telles que la diffraction d'électrons ultrarapide. Si l'accélération par sillage laser, se produisant dans les plasmas sous-denses (transparents), est la méthode la plus souvent considérée pour atteindre cet objectif, des électrons peuvent également être accélérés lors de l'interaction entre un laser ultraintense et un plasma sur-dense (opaque). L'émission d'électrons dans le cadre de cette interaction a été relativement peu étudiée dans le passé car (i) les faisceaux d'électrons obtenus sont généralement de moins bonne qualité que ceux générés par sillage laser et (ii) l'interaction est extrêmement sensible à la forme du gradient de densité à la surface du plasma, qui est particulièrement difficile à contrôler expérimentalement. Pour des interfaces plasma-vide très abruptes, les mécanismes menant à l'éjection d'électrons sont bien compris. En particulier, il a été récemment montré que les électrons gagnent dans ce cas une grande quantité d'énergie lors de leur interaction dans le vide avec l'impulsion laser réfléchie, ce qui ouvre de nouvelles possibilités (e.g. contrôler l'interaction dans le vide en modifiant la structure du laser). A l'opposé, pour des gradients de densité plasma plus étendus, l'interaction n'est pas aussi bien comprise et de nouvelles expériences sont donc nécessaires dans ce régime. D'une manière plus générale, le potentiel réel des plasmas sur-denses en tant que source d'électrons demeure inconnu, ce qui motive de nouveaux travaux de recherche dans cette direction.

Dans cette thèse, l'accélération d'électrons lors de l'interaction entre un laser d'intensité relativiste et un plasma sur-dense a été étudiée dans deux cas précédemment inexplorés. Premièrement, nous avons considéré le cas où l'impulsion laser n'est composée que de quelques cycles optiques. Cette étude est motivée par des expériences récentes réalisées au Laboratoire d'Optique Appliquée. L'objectif principal est de déterminer s'il y a des changements fondamentaux dans la physique de l'interaction lorsque l'on utilise des impulsions de durées extrêmement courtes. Deuxièmement, nous avons examiné le cas où le laser incident a une polarisation radiale. Les lasers polarisés radialement sont intéressants car leur champ électrique possède une forte composante longitudinale, capable en principe d'accélérer des électrons dans le vide dans la direction de propagation du laser. Si cet état de polarisation a été largement étudié théoriquement et numériquement dans le passé, les résultats expérimentaux sont restés jusqu'à cette thèse peu probants, principalement parce qu'il n'y avait pas de méthode connue pour injecter efficacement des électrons dans le champ laser. Or, nous avons précisément vu que les électrons éjectés de la surface d'un plasma sur-dense pouvaient être accélérés dans le vide par l'impulsion laser réfléchie. Nous avons donc étudié dans cette thèse l'accélération d'électrons injectés par un plasma sur-dense dans un laser polarisé radialement. Les objectifs de cette étude sont d'établir précisément les conditions menant à une accélération efficace dans le vide, de déterminer si la polarisation radiale permet d'améliorer l'accélération par rapport à la polarisation linéaire et finalement de quantifier les propriétés des faisceaux d'électrons qui peuvent être obtenus de cette manière. Le travail effectué au cours de cette thèse est essentiellement théorique et numérique, mais dans chaque cas les études effectuées sont confrontées à de nouveaux résultats expérimentaux.

Ce manuscrit est structuré comme suit :

Nous donnons dans le premier chapitre une vue d'ensemble de l'accélération d'électrons avec des lasers ultraintenses. Nous commençons par décrire l'accélération par sillage laser dans les plasmas sous-dense, puis nous présentons l'état de l'art de l'accélération d'électrons dans les plasmas sur-denses. Nous détaillons ensuite les résultats obtenus dans le passé concernant l'accélération par laser dans le vide, à la fois en polarisation linéaire et radiale. Dans chaque cas, nous décrivons le mécanisme d'accélération de manière théorique et nous présentons les principaux résultats expérimentaux.

Dans le second chapitre, nous introduisons les méthodes numériques utilisées pour modéliser l'accélération d'électrons par laser. Les simulations particule-test sont particulièrement peu couteuses et permettent de résoudre les équations du mouvement d'électrons individuels se trouvant au sein d'une impulsion laser. La prise en compte d'effets plasmas se fait à travers la méthode PIC (Particle-In-Cell) dont nous présentons d'abord l'algorithme standard. Les simulations PIC de l'interaction d'un laser avec un plasma sur-dense sont extrêmement couteuses en trois dimensions. Nous décrivons donc par la suite deux techniques permettant de réduire le cout des simulations par rapport à la méthode PIC standard : l'utilisation de coordonnées cylindriques en incidence normale et l'utilisation de solveurs de Maxwell pseudo-spectraux en incidence oblique. Finalement, nous décrivons une méthode pouvant être utilisée pour modéliser analytiquement les impulsions très focalisées de quelques cycles optiques, qui peut être utile pour les simulations particule-test.

Le troisième chapitre est consacré à l'analyse de résultats expérimentaux récents obtenus avec le laser de la Salle Noire du Laboratoire d'Optique Appliquée, qui délivre des impulsions de quelques cycles optiques d'intensité relativiste. Dans un premier temps, nous nous concentrons sur l'estimation de la longueur de gradient pendant l'interaction. Nous décrivons ensuite les résultats expérimentaux obtenus. A court gradient, ces résultats sont conformes à la théorie présentée dans le premier chapitre. L'émission simultanée d'électrons et d'harmoniques du laser y est en particulier observée. A plus long gradient, les résultats sont plus inattendus : l'émission d'électrons ne se produit que pour des impulsions lasers de quelques cycles optiques. Des simulations PIC 2D permettent d'expliquer l'origine de ces électrons : ils sont accélérés par des ondes plasmas formées dans le sillage du laser dans la zone de densité quasi-critique du preplasma. Ce nouveau régime d'accélération par sillage laser est caractérisé par la rotation des ondes plasmas induite par le gradient de densité. L'émission d'électrons ne se produit que pour des impulsions de quelques cycles optiques en vertu de la condition de résonance qui stipule que des durées d'impulsions laser extrêmement courtes sont nécessaires pour former des ondes plasmas pour ces hautes densités.

Dans le quatrième chapitre, nous étudions numériquement l'accélération d'électrons injectés par un plasma sur-dense dans une impulsion polarisée radialement en incidence normale. L'incidence normale est choisie car les électrons sont dans ce cas injectés par le champ longitudinal proche de l'axe optique, ce qui est idéal pour l'accélération dans le vide par le champ laser réfléchi. Nous commençons par détailler les conditions menant à une accélération efficace par un laser polarisé radialement puis nous montrons, grâce à des simulations PIC, que ces conditions sont vérifiées lorsque l'on utilise un plasma sur-dense pour injecter les électrons. Nous étudions ensuite, à l'aide de simulations particule-test, les conditions pouvant mener à des faisceaux d'électrons bien collimatés. En particulier, augmenter l'énergie des impulsions laser semble être une approche prometteuse, ce que nous confirmons par des simulations PIC montrant que des faisceaux d'électrons de très bonne qualité peuvent être obtenus avec des lasers polarisés radialement.

Les premiers résultats expérimentaux en polarisation radiale sont présentés dans le cinquième et dernier chapitre. Contrairement à l'étude numérique précédente, ces résultats ont été obtenus en incidence oblique, pour des raisons essentiellement pratiques. La possibilité d'accélérer des électrons à des énergies relativistes est démontrée pour la première fois dans ces expériences. Comme attendu, les électrons sont émis dans la direction de propagation du laser, ce qui peut mener à une diminution de la divergence angulaire du faisceau d'électrons. L'étude de l'émission d'harmoniques ainsi que l'analyse de simulations PIC 3D des expériences révèlent des changements intéressants dans la physique de l'interaction. En particulier, nous observons que les électrons sont éjectés du plasma uniquement aux positions où le laser est localement polarisé p. Ceci n'est pas optimal pour l'accélération dans le vide car les électrons sont injectés loin de l'axe optique, où le champ longitudinal est maximal. Par ailleurs, le laser perd partiellement sa structure spatiale lors de la réflexion sur le plasma, ce qui mène en particulier à l'apparition de champs transverses importants sur l'axe optique, qui peuvent dévier les électrons accélérés par le champ longitudinal et à terme mener à un élargissement de la divergence angulaire du faisceau d'électrons. Ces défauts (électrons injectés loin de l'axe optique, perte de structure spatiale du laser réfléchi) peuvent être évités en incidence normale et nous anticipons donc que ces résultats expérimentaux peuvent encore être largement améliorés.

Finalement, des perspectives plus générales sur le domaine de l'interaction laser-plasma sur-dense sont données dans les conclusions.

Contents

Introduction

Since their first observation by Plücker and Hittorf in the mid-19th century [1], electron beams have been extensively used for many practical purposes. Most famously, they have been the main components of televisions for nearly a century until the advent of LCD screens. Electron beams are also routinely employed in industry for heating or treating materials, welding, 3D printing, machining and lithography. In hospitals, electron beam therapy is used in the treatment of superficial tumors and electrons are also useful to generate X-rays for radiography and radiotherapy. At much higher energies (up to ≈ 100 GeV), electron beams have allowed us to unravel the fundamental interactions between subatomic particles in colliders, such as the Large Electron-Positron Collider at CERN.

Beams of accelerated electrons also serve as remarkable tools for imaging matter with unmatched precision. Owing to significant progress in aberration-correcting electron optics, sub-angström resolutions are now achievable in the most advanced electron microscopes. For instance, figure 1 shows an image of individual atoms from a monolayer of MoS_2 obtained with a record 39 pm resolution using a scanning transmission electron microscope. Electron microscopes are also able to take advantage of electron diffraction to explore the crystal structure of solids in reciprocal space.

At the same time, the development of mode-locking techniques in the 1980s has permitted the generation of light pulses with femtosecond duration [3]. This has led to the rise of ultrafast science, a new branch of physics which describes phenomena occuring on extremely short timescales (attoseconds to picoseconds). Since then, significant efforts were made to combine the ultrahigh spatial resolution of electron microscopy with ultrahigh temporal resolution. Such temporal information can be obtained in **pump-probe experiments**, where a pump pulse is used to excite a sample out of its equilibrium state and a separate probe pulse (which would be a pulsed electron beam in the case of electron imaging) measures the state of the sample at a precise delay after the pump. By repeating the experiment at various delays between the two pulses, it is then possible to reconstruct the ultrafast evolution of the sample relaxation towards equilibrium. The achievable temporal resolution in such experiments is of course limited by the duration of both the pump and probe pulses.

The prospects of observing new ultrafast phenomena (the collective motion of atoms in a solid, the

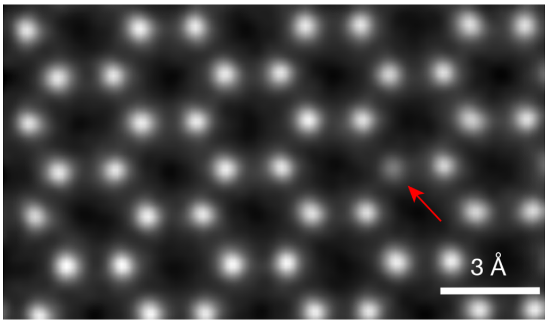

Figure 1: Scanning transmission electron microscope image of a monolayer of MoS_2 acquired with a ptychographic reconstruction technique. The dimmer spot indicated by the red arrow reveals the presence of a sulfur mono-vacancy (i.e. a sulfur atom is missing). Image taken from [2].

intermediate steps of a chemical reaction, etc.) has therefore driven the development of electron beams with femtosecond durations. Such beams can then directly be used as a probe in time-resolved experiments. There has been for example significant advances in ultrafast transmission electron microscopy (UTEM) [4]. In this case however, it is challenging to obtain at the same time high spatial *and* high temporal resolution. This is more easily achieved in diffraction mode, via ultrafast electron diffraction (UED) experiments which are less sensitive to the spatial quality of the electron beam. UED typically employs 100 keV to few-MeV electrons pulses to uncover the ultrafast dynamics of phase transitions in solids and of transient structures in chemical reactions [5]. Femtosecond electron beams are also useful for the generation of ultrashort X-ray bursts in free-electron lasers, that can in turn also be used in pump-probe experiments.

Obtaining such short electron beams requires using a femtosecond laser pulse and a method for transfering the ultrashort nature of the laser to the electrons. In today's conventional accelerators, the femtosecond laser is struck on a photocathode and thereby triggers the emission of electrons which are then accelerated by an external RF or DC field. Using state-of-the-art RF bunching cavities, few-MeV electron beams with sub 10-fs durations are now achievable [6]. However, such low temporal resolutions have still not been attained in UED experiments. This is because the resolution in pump-probe experiments is limited not only by the duration of the pulses, but also by the *synchronization* between the pump and probe pulses. When RF fields are used for electron acceleration or compression, perfect synchronization of the generated electron beam with the pump pulse cannot be obtained, which has de facto limited the temporal resolution of UED experiments to values exceeding 100 fs [7].

Yet, many physical processes, including the fastest phonon modes in solids and the vibration or breaking of molecular bonds, have a characteristic timescale in the 10-100 fs range. Directly observing these processes requires attaining even better temporal resolutions. Consequently, several groups around the world are currently exploring various routes to achieve this breakthrough. For example, substantial progress has recently been made in laser-RF synchronization methods [8] and in timestamping techniques [9]. Alternately, many researchers are looking for other ways to generate and control ultrashort few-MeV electron beams that would ensure that they remain inherently synchronized with a laser field. This can explain for example the recent attract for THz pulses, which can be generated by optical rectification [10] in perfect synchronization with a laser pulse and have the potential to accelerate [11] and manipulate [12] relativistic electrons.

Another promising possibility is to directly use the laser field to accelerate the electrons. Obtaining femtosecond electron beams in this manner requires using ultrashort laser pulses with extreme intensities, which was made possible by the development in 1985 of the chirped pulse amplification technique [13]. When such an intense laser interacts with matter, the latter is instantly ionized and forms a plasma. If the conditions are adequate, electron bunches can be efficiently accelerated from the ensuing laser-plasma interaction. Since plasmas can support much higher electric fields than the dielectric structures of conventional accelerators, this method offers the possibility of accelerating electrons to large energies over very short distances. The standard scheme for accelerating electrons with lasers is laser wakefield acceleration [14, 15]. It takes place in underdense plasmas, which typically come from the ionization of a gas target, and is now very well understood. It has lead to the generation of high quality electron beams [16, 17, 18] with energies up to 8 GeV [19] and durations lower than 2 fs [20], and is a rising candidate for achieving UED experiments with unprecedented time resolution [21, 22].

Electrons can also be accelerated when an ultraintense laser pulse is focused onto an opaque overdense plasma, which typically originates from the ionization of a solid target. The mechanisms leading to electron emission in this case have been less studied, which is partly because laser wakefield acceleration has demonstrated better beam quality. Another important reason is that the interaction is extremely sensitive to the density profile at the plasma front surface, which is a parameter that is particularly challenging to control in experiments. The recent development of ultraintense lasers with an extremely high temporal contrast has enabled the completion of experiments with a fine monitoring of the gradient scale length and the identification of some of the processes leading to the ejection of electrons from the plasma [23, 24]. In particular, it was noted that, if the gradient scale length is appropriate (of the order of $\lambda/10$, where λ is the laser wavelength), the ejected electrons can receive large energy gains in vacuum directly from the reflected laser field. This opens up new possibilities as this process, labeled vacuum laser acceleration (VLA), had beed extensively studied theoretically but never clearly observed experimentally. For instance, we can now consider tailoring the structure of the laser pulse in order to control the interaction in vacuum. Furthermore, the different electron acceleration mechanisms are still not fully established, which is especially true for longer gradient scale lengths, that exceed the laser wavelength. Overall, the full potential of overdense plasmas as a source of ultrashort electron beams remains unknown and more work, both theoretical and experimental, is therefore required in this direction.

It is in this context and in the continuity of these recent results that I have carried out my PhD thesis. I have studied the acceleration of electrons from the interaction of a relativistic intensity ($> 10^{18}\,\mathrm{W/cm^2}$) ultrashort ($< 50$ fs) laser pulse with an overdense plasma which has a density gradient on its front surface. I have more specifically focused on two unexplored interaction scenarios:

- I have considered the case where the laser pulse is so short that it only consists of a few optical oscillations. This corresponds to the so-called **few-cycle regime**. This study is motivated by the recent upgrade of the Salle Noire laser, developed by the PCO group at LOA, which can now deliver 3.5 fs (less than 1.5 optical cycles) pulses with a relativistic intensity (exceeding $10^{19}\,\mathrm{W/cm^2}$) at a kHz repetition rate. In particular, the first experiments on solid targets with these laser parameters were performed in the course of my PhD. Working with few-cycle pulses has several advantages. First, it leads to lower pulse energies for a given intensity, which means that the repetition rate, which is a crucial parameter for applications, can be increased. Secondly, few-cycle pulses can in principle result in shorter electron beam durations, which is also beneficial for applications in ultrafast science. The main objectives of this study are to determine whether there are substantial changes in the physics of the interaction with extremely short pulse durations and to evaluate the effect of the carrier-envelope phase (CEP) which is a new relevant parameter.

- I have also examined the case where the incident laser pulse is **radially polarized**. Such beams are particularly attractive for vacuum laser acceleration (VLA) as they possess a strong longitudinal electric field that can directly accelerate electron in the laser propagation direction. They have been widely studied numerically and theoretically and promising results have been obtained. However, until this work, there had been no experimental observation of electron acceleration to relativistic energies with radially polarized beams, which is because no practical way to efficiently inject the electrons into the laser was found. We have precisely seen in the previous paragraphs that VLA could be achieved by focusing a laser pulse onto an overdense plasma. This therefore provides a great opportunity to test the effectiveness of VLA with radial polarization as an electron acceleration scheme. The objectives of this study are to accurately establish the conditions under which acceleration by a radially polarized beam is efficient, to determine whether it can lead to improved results (lower angular spread, high energies, etc.) compared to linear polarization and if so, to quantify the electron beam parameters achievable with this acceleration method.

The work presented in this manuscript is above all theoretical and numerical. I have tried to develop simple analytical models whenever possible, and relied on the Particle-In-Cell (PIC) method otherwise. However, I have also closely collaborated throughout my thesis with the experimental teams working with two state-of-the-art laser facilities: the Salle Noire laser at LOA, that we have previously mentioned, and the UHI100 laser at CEA Saclay. The UHI100 laser delivers 24 fs pulses with a peak power of ~ 20 TW on target and has been used in many seminal experiments concerning the interaction of ultrahigh intensity pulses with overdense plasmas [25, 26, 27, 24]. We will present in particular new experimental results obtained with each of these laser systems, which will be confronted to my numerical studies. The purpose of the simulations shown in this present work are therefore not only to provide general results regarding the interaction of the plasma with a few-cycle or a radially polarized pulse, but also to serve as a tool for explaining or predicting novel experimental results.

More generally, this thesis aims at providing a better understanding of the pathways and mechanisms of energy transfer to the plasma electrons in laser-solid target interactions. This is indeed a complex and fundamental question that has implications for ion acceleration [28], high harmonic generation [29] and inertial confinement fusion [30].

This manuscript is organized as follows.

Chapter 1 is a background chapter in which we review different schemes used to accelerate electrons with an ultraintense laser pulse. After depicting laser-wakefield accelerators, we focus on electron emission from overdense plasmas and on the vacuum laser acceleration process that can subsequently occur. We provide in particular a summary of previous results obtained with radially polarized lasers. In each case, the acceleration mechanism is described theoretically and the principal experimental results are presented.

In chapter 2, we describe the numerical methods that I have used to study laser-plasma interaction. We present in particular the standard Particle-In-Cell (PIC) algorithm as well as two useful techniques for substantially reducing the cost of 3D simulations: the use of cylindrical coordinates at normal incidence and the use of pseudo-spectral Maxwell solvers at oblique incidence. We also present at the end of this chapter a method to obtain exact solutions to Maxwell's equations that can be used to model few-cycle pulses in simulations.

We show in chapter 3 results from recent experiments performed with relativistic intensity few-cycle pulses with the Salle Noire laser. We find that, if the gradient scale length is large enough (larger than the laser wavelength), such extremely short pulses can drive laser wakefield acceleration in the near-critical density part of the plasma. This regime is characterized by the rotation of the plasma waves induced by the density gradient. Few-cycle pulses are required to trigger this mechanism because of the resonance condition at these high densities. We place a strong emphasis in this chapter on the estimation of the plasma density profile during interaction and on the uncertainties associated with this estimation.

We examine in chapter 4 the acceleration of electrons injected by an overdense plasma into a radially polarized beam. We establish the initial conditions leading to efficient acceleration and show that these conditions can be fulfilled by focusing a radially polarized laser onto an overdense plasma. This results in an acceleration to higher energies than with other existing injection methods. We focus in this chapter on the interaction at normal incidence and demonstrate that, under appropriate conditions, narrow divergences can be obtained.

Finally, we study in chapter 5 the interaction at oblique incidence by presenting recent experimental results obtained with the UHI100 laser, in which the possibility of accelerating electrons to relativistic energies in the longitudinal direction is demonstrated for the first time. These experiments are analyzed by making use of full-3D PIC simulations.

CHAPTER 1

Overview of laser-driven electron acceleration

Contents

We survey in this chapter existing methods for accelerating electrons to relativistic energies using lasers. We provide in each case a brief theoretical description of the acceleration mechanisms as well as the main experimental results.

We start by defining in section 1.1 the parameters characterizing a laser pulse and we give typical values considered in this manuscript. In particular, we look at very intense lasers that rapidly turn any matter they interact with into a plasma. We therefore succinctly describe the basic principles of plasma physics and laser-plasma interaction in section 1.2. Two distinct regimes exist, depending on whether the plasma frequency is lower (underdense plasmas) or higher (overdense plasmas) than the laser frequency. Laser pulses can propagate in an underdense plasma and, if the conditions are appropriate, they may generate plasma waves that can in turn accelerate electrons over very short distances. This is the principle of laser wakefield acceleration (LWFA), which is the standard method for accelerating electrons with lasers and is overviewed in section 1.3.

We place important emphasis on overdense plasmas, which reflect incident light. Relativistic electron beams can also be generated when a high-intensity laser is focused on such target. We present in section 1.4 the different theoretical and experimental results regarding the ejection of electrons from overdense plasmas. We highlight in particular the crucial importance of the plasma gradient scale length during the interaction, which is often overlooked, thereby complicating the interpretation of many experimental results. In some cases, the ejected electron beam can interact with the reflected laser pulse and even gain energy from it. The process by which an electron can gain large amount of energy in vacuum directly from the laser field is known as vacuum laser acceleration (VLA) and is reviewed in section 1.5. We focus in particular on the case of radially polarized beams, which have an attractive structure for accelerating electrons in vacuum.

More generally, this chapter aims at providing a theoretical and physical background that will be used in the remainder of this manuscript.

1.1 Laser parameters

A laser pulse is entirely determined by its electromagnetic fields $\boldsymbol{E}$ and $\boldsymbol{B}$. In most cases, a linearly polarized laser can be approximately described by a Gaussian beam, which is characterized by a Gaussian decrease of its electromagnetic field amplitude in the transverse direction. The $\boldsymbol{E}$ and $\boldsymbol{B}$ fields of a

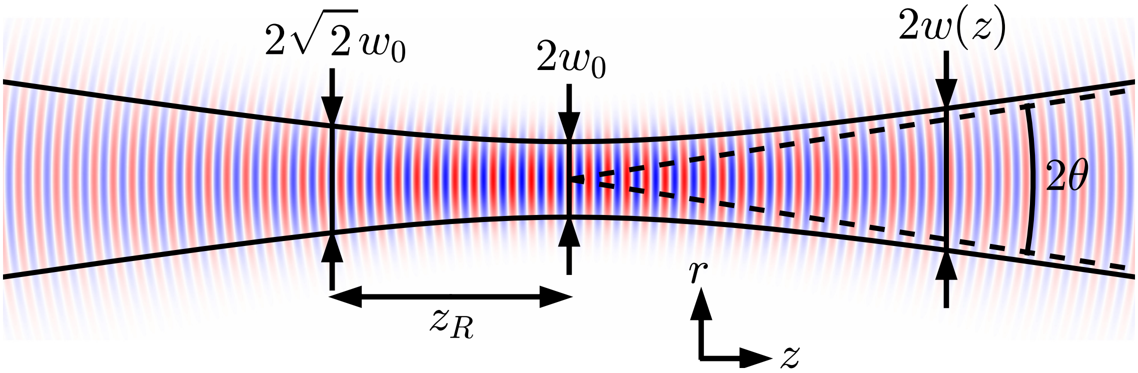

Figure 1.1: The electric field of a Gaussian beam with $w_0 = 2\lambda$, $\phi_{CEP} = 0$ and $g(t) = 1$ (infinitely long duration) shown at time $t = 0$.

Gaussian beam propagating along the z-direction and polarized along the x-direction are [31]:

$$\boldsymbol{E}(\boldsymbol{r},t) = E_0 \frac{w_0}{w(z)} \exp\left(-\frac{r^2}{w(z)^2}\right) \cos\left(kz - \omega t + k\frac{r^2}{2R(z)} - \arctan\left(\frac{z}{z_R}\right) + \phi_{CEP}\right) g\left(t - \frac{z}{c}\right) \boldsymbol{e}_x \quad (1.1)$$

$$\boldsymbol{B}(\boldsymbol{r},t) = \frac{E_0}{c} \frac{w_0}{w(z)} \exp\left(-\frac{r^2}{w(z)^2}\right) \cos\left(kz - \omega t + k\frac{r^2}{2R(z)} - \arctan\left(\frac{z}{z_R}\right) + \phi_{CEP}\right) g\left(t - \frac{z}{c}\right) \boldsymbol{e}_y \quad (1.2)$$

Where $r = \sqrt{x^2 + y^2}$ is the radial coordinate in cylindrical coordinates and $\boldsymbol{e}_i$ is a unit vector directed along the i axis. These equations are valid within the paraxial approximation (more details can be found in section 2.3.1). An example of field calculated using equation 1.1 is plotted in figure 1.1. We define the following quantities related to Gaussian beam, but which can usually be extended to other beam profiles:

- ω is the frequency of the pulse and $k = \frac{\omega}{c} = \frac{2\pi}{\lambda}$ is its wavevector. Here, c is the speed of light in vacuum.

- w_0 is the beam radius at focus, usually known as the **beam waist**. It is a typical transverse size of the beam at focus and is defined as the radius above which the electric field amplitude is less than $1/e$ of its on-axis value.

- z_R is the **Rayleigh length** defined as $z_R = \pi w_0^2/\lambda = k w_0^2/2$. It is a characteristic propagation distance during which the beam expands due to diffraction. At $z = z_R$, the beam cross-section has doubled compared to $z = 0$.

- $w(z) = w_0\sqrt{1 + \left(\frac{z}{z_R}\right)^2}$ is the $1/e$ beam radius (in amplitude) at position z.

- Far from focus, the beam is emitted in a cone whose opening angle is 2θ where $\theta = \arctan\frac{\lambda}{\pi w_0}$. We have in all practical cases $\theta \approx \frac{\lambda}{\pi w_0}$. Therefore, the tighter the focusing, the more rapidly the laser diffracts.

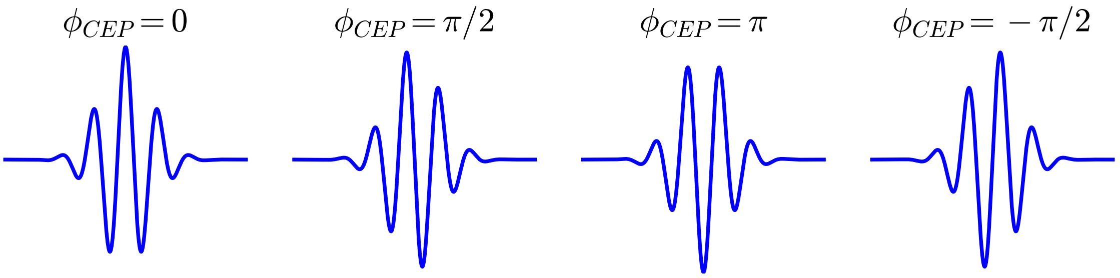

Figure 1.2: Electric field on the axis at $t = 0$ of a 3.5-fs, $\lambda = 800$ nm laser pulse for different values of the CEP.

- $R(z) = z + \frac{z_R^2}{z}$ is the radius of curvature of the wavefronts at position z.
- The term $\arctan\left(\frac{z}{z_R}\right)$ is known as the **Gouy phase**. It causes the beam to acquire an extra phase of π while passing through focus, which results in a superluminal phase velocity on the axis at focus.
- g is a temporal envelope which is often assumed to be Gaussian:

  $$g(t) = \exp\left(-2\ln(2)\frac{t^2}{\tau^2}\right) \tag{1.3}$$

  Where τ is the pulse duration in full width at half maximum (FWHM) of intensity. It is a good time to mention that, unless specified otherwise, the pulse durations are always given in FWHM of intensity in this manuscript.
- ϕ_{CEP} is the phase at which the temporal envelope is maximum at $z = 0$. This parameter is known as the **carrier-envelope phase (CEP)**. It is irrelevant for many-cycle pulses but has a significant impact on the temporal shape of the electric field for few-cycle pulses, as illustrated in figure 1.2.
- E_0 is the peak amplitude of the electric field (which is attained only if ϕ_{CEP} is an integer multiple of π). Rather than directly dealing with E_0 in, say, TV/m, it is more common to use either the **peak intensity** $I_0 = \dfrac{c\varepsilon_0 E_0^2}{2}$ in W/cm^2 or the **normalized field amplitude** $a_0 = \dfrac{eE_0}{m_e c\omega}$. Here, ε_0 is the vacuum permittivity and e and m_e are respectively the electron charge and mass. I_0 and a_0 are linked by the following relation, in practical units:

  $$a_0 = 8.5 \times 10^{-10} \lambda[\mu\mathrm{m}] I_0^{1/2}[\mathrm{W/cm^2}] \tag{1.4}$$

  It can be noted that a nonrelativistic electron in a plane wave oscillates with a velocity amplitude of $a_0 c$. Therefore, the motion of electrons interacting with lasers such that $a_0 \ll 1$ is nonrelativistic while the motion of electrons interacting with lasers such that $a_0 > 1$ is strongly relativistic. For a wavelength of 800 nm, $a_0 = 1$ corresponds to $I_0 = 2.14 \times 10^{18}\,\mathrm{W/cm^2}$ and $E_0 = 4.02$ TV/m.
- The **peak power** of the laser is given by $P = \dfrac{\pi w_0^2 I_0}{2}$.

Laser system	**Salle Noire**	**UHI100**
Central wavelength	800 nm	800 nm
Repetition rate	1 kHz	10 Hz (single shot in practice)
Pulse energy	≈ 2.5 mJ	≈ 460 mJ
Pulse duration	3.5 fs	24 fs
Peak power	≈ 670 GW	≈ 18 TW
w_0	$1.5\,\mu\mathrm{m}$	$3.2\,\mu\mathrm{m}$
Peak intensity	$\approx 1.6\times10^{19}\,\mathrm{W/cm^2}$	$\approx 5.8\times10^{19}\,\mathrm{W/cm^2}$
a_0	≈ 2.7	≈ 5.2
Peak electric field	$\approx 11\,\mathrm{TV/m}$	$\approx 21\,\mathrm{TV/m}$

Table 1.1: Typical on-target parameters of the Salle Noire and UHI100 laser systems for the experiments that are studied in this thesis.

- The **pulse energy** is $U = \dfrac{P\tau}{2\sqrt{\frac{\ln 2}{\pi}}} \approx P\tau$.

We mainly consider in this manuscript relativistic ($a_0 > 1$), tightly focused ($w_0 = 1-5\,\mu\mathrm{m}$) and ultrashort ($\tau = 3-30$ fs) laser pulses with 800-nm wavelength. In particular, much of the work performed in this thesis is based on experimental results obtained with the **Salle Noire** and the **UHI100** laser systems. Both lasers use the chirped pulse amplification technique to generate 24-fs pulses with a central wavelength of 800 nm.

The Salle Noire system, which has been developed at the Laboratoire d'Optique Appliquée (LOA), additionally uses a helium-filled hollow core fiber to post-compress the laser pulses [32, 33, 34, 35]. By changing the pressure in the fiber, the final pulse duration can be continuously varied from 24 fs to 3.5 fs, thus reaching the so-called few-cycle regime. The laser functions at a kHz repetition rate, which makes the generated electron beams more easily transferable to applications. Even though this limits the on-target pulse energy to 2.5 mJ, a tight focusing (down to $w_0 = 1.5\,\mu\mathrm{m}$) can be used to reach relativistic intensities (up to a_0 = 2.7 for 3.5-fs pulses).

The UHI100 laser system is located at CEA Saclay. It delivers more energetic pulses, typically around 500 mJ on target. The 24-fs pulses can be focused down to $w_0 = 3.2\,\mu\mathrm{m}$, which results in $a_0 = 5.2$.

The parameters of the two lasers are summed up in table 1.1 and a graphic representation of the electric field of the pulses is shown in figure 1.3. Even though the total energy is 200 times higher in a UHI100 pulse, the intensity is only 4 times higher because a Salle Noire pulse occupies a much smaller volume.

1.2 The plasma state

Ultrahigh intensity laser pulses can ionize any atom they interact with, as will be described in section 1.2.1. One consequence is that when such a pulse impinges on a solid or gas target, it will de facto interact with a plasma. We therefore present in sections 1.2.2 and 1.2.3 basic results regarding plasmas and their interaction with electromagnetic waves.

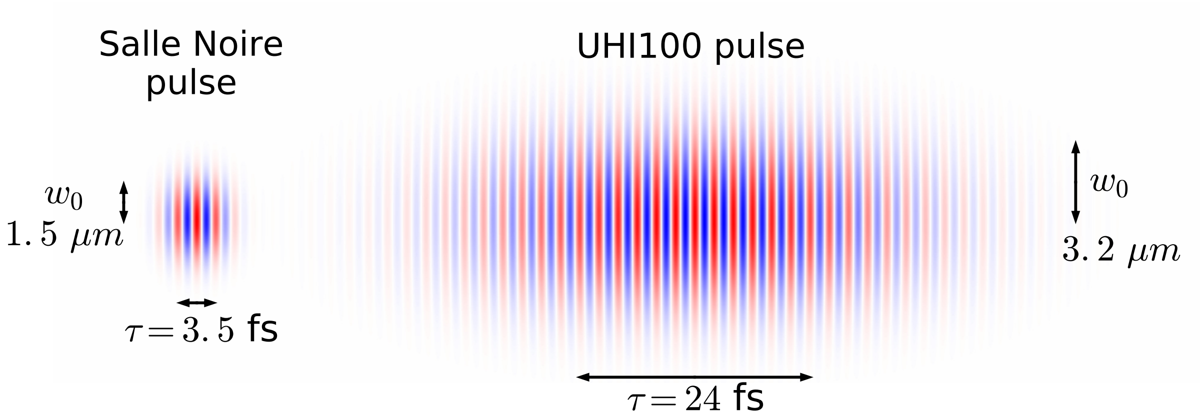

Figure 1.3: Electric field at $t = 0$ of Gaussian beams with parameters corresponding to the Salle Noire and the UHI100 lasers. A Gaussian temporal envelope is used.

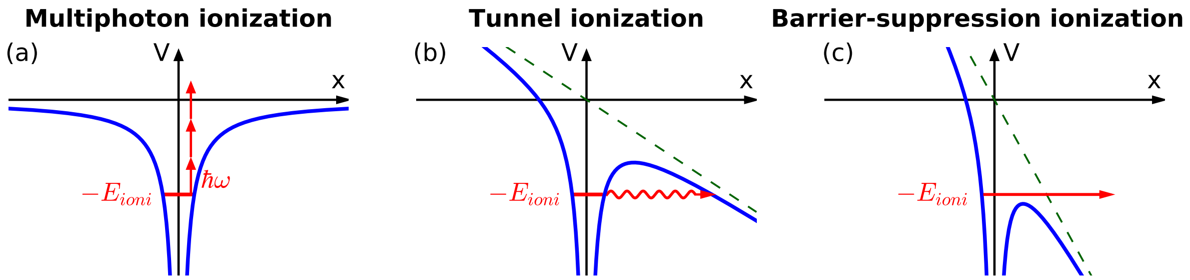

Figure 1.4: Field ionization mechanisms. (a) The binding potential of the electron is undisturbed by the laser field. The electron may be ionized by absorbing multiple photons so that the total absorbed energy exceeds the ionization energy E_{ioni}. (b) The field is intense enough to disturb the nucleus Coulomb potential. The electron may be freed by tunnelling through the resulting potential barrier. (c) If the field is high enough to suppress the potential barrier, the electron is ejected from its parent atom or ion. The dashed green line represents the potential created by the external field.

1.2.1 Field ionization

Field ionization is the process by which an electromagnetic wave, the laser field in our case, can strip a bound electron from its nucleus. At the considered wavelength (800 nm), the energy of a single photon is $\approx$ 1.5 eV, which is smaller than the ionization energy of any atom or ion. An electron may therefore be freed by absorbing several photons at the same time, a process known as multiphoton ionization, which becomes significant for intensities exceeding $10^{10}\,\mathrm{W/cm^2}$ [36]. For even higher intensities, the binding Coulomb field felt by the electron becomes perturbated by the applied electric field. The dominant ionization mechanisms in this case are **tunnel ionization**, in which the electron is ejected by quantum tunnelling and **barrier-suppression ionization**, where the potential perturbation is strong enough for the electron to classicaly escape from the nucleus. These three mechanisms are summed up in figure 1.4.

The intensity I_{BSI} at which barrier-suppression ionization occurs can be simply estimated by assuming

Element	**Z**	E_{ioni} **(first ionization)**	I_{BSI} **(first ionization)**	E_{ioni} **(last ionization)**	I_{BSI} **(last ionization)**
Hydrogen	1	13.6 eV	$1.37 \times 10^{14}\,\mathrm{W/cm^2}$	13.6 eV	$1.37 \times 10^{14}\,\mathrm{W/cm^2}$
Helium	2	24.6 eV	$1.46 \times 10^{15}\,\mathrm{W/cm^2}$	54.4 eV	$8.76 \times 10^{15}\,\mathrm{W/cm^2}$
Carbon	6	11.3 eV	$6.52 \times 10^{13}\,\mathrm{W/cm^2}$	490 eV	$6.41 \times 10^{18}\,\mathrm{W/cm^2}$
Nitrogen	7	14.5 eV	$1.77 \times 10^{14}\,\mathrm{W/cm^2}$	667 eV	$1.62 \times 10^{19}\,\mathrm{W/cm^2}$
Oxygen	8	13.6 eV	$1.37 \times 10^{14}\,\mathrm{W/cm^2}$	871 eV	$3.60 \times 10^{19}\,\mathrm{W/cm^2}$
Aluminium	13	5.99 eV	$5.15 \times 10^{12}\,\mathrm{W/cm^2}$	2 304 eV	$6.67 \times 10^{20}\,\mathrm{W/cm^2}$
Silicon	14	8.15 eV	$1.76 \times 10^{13}\,\mathrm{W/cm^2}$	2 673 eV	$1.04 \times 10^{21}\,\mathrm{W/cm^2}$
Argon	18	15.8 eV	$2.49 \times 10^{14}\,\mathrm{W/cm^2}$	4 426 eV	$4.74 \times 10^{21}\,\mathrm{W/cm^2}$
Cesium	55	5.99 eV	$9.15 \times 10^{11}\,\mathrm{W/cm^2}$	42 913 eV	$4.48 \times 10^{24}\,\mathrm{W/cm^2}$

Table 1.2: First and last ionization energy of usual or representative chemical elements, with the corresponding barrier-suppresion ionization intensites. Cesium is the element with the lowest first ionization energy and helium with the highest. The ionization energies have been obtained from the NIST Atomic Spectra Database.

that the potential felt by the electron is the sum of the Coulomb nucleus potential and the potential due to a homogeneous external electric field $\boldsymbol{E} = E\boldsymbol{e}_x$ [36]. The total potential on the x-axis is thus:

$$V = -\frac{Z^* e^2}{4\pi\varepsilon_0 x} - eEx \tag{1.5}$$

Here, Z^* corresponds to the degree of ionization (i.e. $Z^* = 1$ for a first ionization, $Z^* = 2$ for a second ionization, etc.) Above the barrier-suppression intensity, we have the relation $V < -E_{ioni}$ for $x > 0$, where E_{ioni} is the ionization energy of the electron. This translates to:

$$I_{BSI} = \frac{\pi^2 c \varepsilon_0^3 E_{ioni}^4}{2e^6 Z^{*2}} \tag{1.6}$$

Which becomes in practical units:

$$I_{BSI}[\mathrm{W/cm^2}] = 4 \times 10^9 \frac{E_{ioni}^4[eV]}{Z^{*2}} \tag{1.7}$$

Barrier-supression intensities provide a simple way to estimate the degree of field ionization of a laser-generated plasma as a function of the electric field amplitude. Numerical values of I_{BSI} obtained with equation 1.7 for the first and last ionization energies of some usual or representative elements are shown in table 1.2. We note in particular that the intensitiy for first ionization is at most $\sim 10^{15}\,\mathrm{W/cm^2}$. Consequently, when a laser pulse is focused to relativistic intensities ($> 10^{18}\,\mathrm{W/cm^2}$) on a target, the latter is always ionized well before the temporal center of the pulse reaches it. The main conclusion is therefore that relativistic intensity lasers inevitably interact with plasmas.

On the other hand, last ionization intensities can be extremely high. Thus, depending on the elements composing the target, it is entirely possible that the plasma is not entirely ionized during the interaction and that the high-intensity part of the laser pulse induces additional ionization.

1.2.2 Mathematical descriptions of plasmas

Plasma is a state of matter in which long range electromagnetic interactions coming from ions and unbound electrons play a significant role. There is a large variety in the plasma conditions (density and temperature can both span over several orders of magnitude) which can give rise to complex and interesting phenomena [37, 38, 39]. Plasmas are usually modeled either with a kinetic or a fluid description.

In **kinetic models**, each species s of the plasma is entirely described through its distribution function $f_s(\boldsymbol{r},\boldsymbol{p},t)$, which corresponds to its density in phase-space. At time t, the number of particles in an infinitesimal 6-dimensional volume $d^3\boldsymbol{r}d^3\boldsymbol{p}$ centered around $(\boldsymbol{r},\boldsymbol{p})$ is given by: $dN = f_s(\boldsymbol{r},\boldsymbol{p},t)d^3\boldsymbol{r}d^3\boldsymbol{p}$. Measurable macroscopic quantities can then be obtained by integration of the distribution function. For example, the density of species s is given by:

$$n_s(\boldsymbol{r},t) = \int_{\mathbb{R}^3} f_s(\boldsymbol{r},\boldsymbol{p},t)d^3\boldsymbol{p} \tag{1.8}$$

Similarly, the average velocity at position $\boldsymbol{r}$ is:

$$\boldsymbol{v}_s(\boldsymbol{r},t) = \frac{1}{n_s(\boldsymbol{r},t)}\int_{\mathbb{R}^3} \boldsymbol{v}(\boldsymbol{p})f_s(\boldsymbol{r},\boldsymbol{p},t)d^3\boldsymbol{p} \tag{1.9}$$

Where $\boldsymbol{v}(\boldsymbol{p}) = \dfrac{\boldsymbol{p}}{\sqrt{1+|\boldsymbol{p}/(m_s c)|^2}}$ and m_s is the mass of a particle.

In **fluid models**, the species are directly described through these macroscopic averaged fields. Sometimes, different fluids are used for different species (e.g. in two-fluid models where one fluid describes the electrons and the other the ions) and sometimes a single fluid is used to model the whole plasma (e.g. in magnetohydrodynamics). A fluid approach leads to simplified equations, which can even be solved analytically in some cases.

During relativistic laser-plasma interactions, strongly out-of-equilibrium phenomena that can involve trajectory crossings, which cannot be described with an average velocity, are frequent and a fluid approach is usually not sufficient. Moreover, the electrons move at such high velocities (close to c) that collisions are entirely negligible within the timescale of the interaction (30 fs at most for the pulses considered in this thesis). The corresponding kinetic equation that governs the evolution of the distribution functions of noncollisional plasmas is the **Vlasov equation**. It should be used to accurately describe high-intensity laser-plasma interactions and reads:

$$\frac{\partial f_s}{\partial t} + \boldsymbol{v}(\boldsymbol{p}).\frac{\partial f_s}{\partial \boldsymbol{r}} + q_s\left(\boldsymbol{E}+\boldsymbol{v}(\boldsymbol{p})\times\boldsymbol{B}\right).\frac{\partial f_s}{\partial \boldsymbol{p}} = 0 \tag{1.10}$$

q_s is here the charge of the particle. Long range electromagnetic interactions between charged particles in the plasma are taken into account by the Lorentz force term in the Vlasov equation. The $\boldsymbol{E}$ and $\boldsymbol{B}$ fields can be obtained via Maxwell's equations:

$$\boldsymbol{\nabla}.\boldsymbol{E} = \frac{\rho}{\varepsilon_0} \qquad \text{Gauss's law} \tag{1.11}$$

$$\boldsymbol{\nabla}.\boldsymbol{B} = 0 \qquad \text{Gauss's law for magnetism} \tag{1.12}$$

$$\boldsymbol{\nabla}\times\boldsymbol{E} = -\frac{\partial \boldsymbol{B}}{\partial t} \qquad \text{Maxwell-Faraday} \tag{1.13}$$

$$\boldsymbol{\nabla}\times\boldsymbol{B} = \mu_0\left(\boldsymbol{J}+\varepsilon_0\frac{\partial \boldsymbol{E}}{\partial t}\right) \qquad \text{Ampère's law} \tag{1.14}$$

The resulting **Vlasov-Maxwell system** 1.10-1.14 is a complete set of equations describing the evolution of the plasma. Vlasov and Maxwell's equations are coupled because the source terms in equations 1.11 and 1.14 are obtained by integrating the distribution functions of the plasma species:

$$\rho(\boldsymbol{r},t) = \sum_s q_s \int_{\mathbb{R}^3} f_s(\boldsymbol{r},\boldsymbol{p},t) d^3\boldsymbol{p} \tag{1.15}$$

$$\boldsymbol{J}(\boldsymbol{r},t) = \sum_s q_s \int_{\mathbb{R}^3} \boldsymbol{v}(\boldsymbol{p}) f_s(\boldsymbol{r},\boldsymbol{p},t) d^3\boldsymbol{p} \tag{1.16}$$

Physically this means that the motion of the particles generates electromagnetic fields which in turn affect in a self-consistent manner the motion of the particles. The Vlasov-Maxwell system is a nonlinear set of equations for which analytical solutions cannot in general be found. A numerical approach is therefore prefered in most cases. The Particle-In-Cell (PIC) algorithm, presented in chapter 2, is the standard method to model kinetic plasmas when collisions are negligible and is widely used in the field of laser-plasma interactions.

1.2.3 Electromagnetic waves in a plasma

Let us consider in this section the propagation of a nonrelativistic ($a_0 \ll 1$) electromagnetic monochromatic plane wave of the form $\boldsymbol{E} = \boldsymbol{E}_0 e^{i(\omega t - kz)}$ in a homogeneous plasma of density n_e. We use a fluid model to describe the plasma. We assume that the plasma is cold (negligible temperature compared to the electron motion in the electromagnetic field), noncollisionnal and that the ions are immobile. With these hypotheses, the fluid equation of motion is:

$$\frac{\partial \boldsymbol{v}_e}{\partial t} + (\boldsymbol{v}_e.\boldsymbol{\nabla})\boldsymbol{v}_e = -\frac{e}{m_e}(\boldsymbol{E} + \boldsymbol{v}_e \times \boldsymbol{B}) \tag{1.17}$$

$\boldsymbol{v}_e$ is here the fluid electron velocity. For a small perturbation from equilibrium, which can be assumed since the wave is nonrelativistic, this equation can be linearized and becomes:

$$\frac{\partial \boldsymbol{v}_e}{\partial t} = -\frac{e}{m_e}\boldsymbol{E} \tag{1.18}$$

The principal impact of the electromagnetic wave is thus to induce an electron oscillation at the frequency ω. We can rewrite this equation for the current density $\boldsymbol{J} = -en_e\boldsymbol{v}_e$:

$$\frac{\partial \boldsymbol{J}}{\partial t} = \varepsilon_0 \omega_p^2 \boldsymbol{E} \tag{1.19}$$

We have defined here the **plasma frequency** ω_p as:

$$\omega_p \equiv \sqrt{\frac{n_e e^2}{m_e \varepsilon_0}} \tag{1.20}$$

The plasma frequency is a fundamental characteristic of plasmas. It corresponds to the timescale for which collective phenomena arise in plasmas. In particular, ω_p is the frequency of electron **plasma waves** (or Langmuir waves), which are collective electron oscillations around their equilibrium position in response to an initial charge separation. We note that the plasma frequency only depends on the plasma density ($\omega_p \propto \sqrt{n_e}$). High-density plasmas thus respond more quickly to an external perturbation than low-density plasmas.

By inserting equation 1.19 into the derivative of Ampère's law 1.14 with respect to time and by combining the result with Maxwell-Faraday equation 1.13, we can obtain the wave equation in a cold noncollisional plasma:

$$\boldsymbol{\nabla}^2 \boldsymbol{E} - \frac{1}{c^2}\left(\frac{\partial^2 \boldsymbol{E}}{\partial t^2} + \omega_p^2 \boldsymbol{E}\right) = 0 \tag{1.21}$$

Note that to obtain this equation we have used the relation $\boldsymbol{\nabla}.\boldsymbol{E} = 0$, which is valid since there is, to first order, no charge separation induced by the plane wave. Equation 1.21 admits solutions of the form $e^{i(\omega t - kz)}$ provided that k and ω satisfy the dispersion relation:

$$k = \frac{\omega}{c}\sqrt{1 - \frac{\omega_p^2}{\omega^2}} = \frac{\sqrt{\omega^2 - \omega_p^2}}{c} \tag{1.22}$$

We see that there are two very distinct cases, depending on whether $\omega < \omega_p$ or $\omega > \omega_p$. The transition between the two cases occurs at the **critical density** n_c, which is the plasma density for which $\omega = \omega_p$. The critical density reads mathematically:

$$n_c = \frac{m_e \varepsilon_0 \omega^2}{e^2} \tag{1.23}$$

For a wavelength of 800 nm, we have $n_c = 1.74 \times 10^{21}\,\mathrm{cm}^{-3}$

Overdense plasmas

We first consider the case $\omega < \omega_p$, or equivalently $n_e > n_c$. Such plasmas are known as overdense plasmas. In this case, k is imaginary in equation 1.22. This means that the wave is evanescent with a skin depth given by $1/|k|$. In other words, light with a frequency smaller than the plasma frequency cannot propagate in a plasma.

Physically, the condition $\omega < \omega_p$ means that the collective plasma behaviour is faster than the electromagnetic wave oscillation. The response of the plasma to the electromagnetic field is to generate currents and charge separations in such a way that they cancel the incoming radiation, i.e. that the total field inside the plasma is 0. Overdense plasmas thus behave in a similar manner as metals or perfect conductors. In particular, they are opaque and reflect incident light. At a wavelength of $\lambda = 800$ nm, overdense plasmas are typically generated by the ionization of a solid or liquid target.

Underdense plasmas

We now consider the case $\omega > \omega_p$, or equivalently $n_e < n_c$. Such plasmas are known as underdense plasmas. In this case, k is real in equation 1.22. This means that the electromagnetic wave can propagate in the plasma. In other words, plasmas are transparent to light with a frequency higher than the plasma frequency. At a wavelength of $\lambda = 800$ nm, underdense plasmas are typically generated by the ionization of a gas target.

Physically, the condition $\omega > \omega_p$ means that the electromagnetic wave oscillation is faster than the collective plasma behaviour. In this case, the plasma response is too slow to cancel out the electromagnetic field, which can propagate. The plasma nonetheless affects the propagation of light, as can be seen by the fact that the dispersion relation 1.22 is different than the vacuum dispersion relation $\omega = kc$. We note in particular that underdense plasmas are dispersive. The electromagnetic wave phase velocity can be calculated by the formula $v_\phi = \omega/k$, which yields:

$$v_\phi = \frac{c}{\sqrt{1 - \frac{\omega_p^2}{\omega^2}}} \tag{1.24}$$

The phase velocity is superluminal. It is close to c in the strongly underdense limit $\omega \gg \omega_p$ but can be significantly greater than c if ω approaches ω_p. We can deduce from the previous formula the refractive index of plasmas:

$$N = \sqrt{1 - \frac{\omega_p^2}{\omega^2}} \tag{1.25}$$

For plasmas, we note that we have $N < 1$. The group velocity can also be calculated using the formula $v_g = \frac{d\omega}{dk}$, which yields:

$$v_g = c\sqrt{1 - \frac{\omega_p^2}{\omega^2}} \tag{1.26}$$

Unlike the phase velocity, the group velocity in plasmas in smaller than c. This means that the plasma tends to slow down the pulses. We can again note that we have $v_g \approx c$ in the strongly underdense limit $\omega \gg \omega_p$.

We conclude this section by mentioning that the critical density is increased when relativistic intensity electromagnetic waves are considered. This means that pulses with $a_0 \gg 1$ can propagate in denser plasmas than pulses with $a_0 \ll 1$, a process known as relativistic transparency [40, 41]. Physically, it can be understood by the relativistic increase in the inertia of the electrons as they oscillate in the field, which reduces the effective plasma frequency.

1.3 Laser wakefield acceleration

Laser wakefield acceleration (LWFA) [15], also known as laser-plasma acceleration, is the most common method for accelerating electrons to relativistic energies with lasers. In this scheme, the driving laser pulse propagates in an underdense plasma and generates plasma waves in its wake. The electrostatic fields associated to the plasma waves propagate with a phase velocity that is equal to the group velocity of the laser pulse and can be used to accelerate an electron bunch. This method has led to the generation of high quality electron beams with energies up to 8 GeV [19] and measured durations lower than 2 fs [20].

1.3.1 Plasma wave generation in the linear regime

We start by explaining, using a fluid model, how a linearly polarized laser pulse can generate plasma waves in a homogenous plasma. This process can be studied analytically in three dimensions with the following assumptions:

- As in section 1.2.3, the plasma is cold and noncollisional and the ions are immobile.

- We consider a nonrelativistic intensity ($a_0^2 \ll 1$) laser driver. This is known as the linear regime.
- We assume that the driving laser pulse remains the same throughout its propagation. We thus neglect the laser diffraction as well as any change in the laser field induced by the plasma.
- We assume that the pulse duration is much longer than the laser period: $\tau \gg 2\pi/\omega$ where τ is the pulse duration and ω is the laser frequency.
- We assume that the plasma is strongly underdense: $\omega_p \ll \omega$.

The main difference with the model of section 1.2.3 is that we consider here a laser pulse with a finite volume rather than a plane wave. As we will see, the spatial variations in the intensity of the laser pulse result in the emergence of charge separations, via the ponderomotive force, which are at the origin of plasma waves.

We use in this section the electric potential V and the magnetic vector potential $\boldsymbol{A}$, which are such that:

$$\boldsymbol{E}(\boldsymbol{r},t) = -\boldsymbol{\nabla} V(\boldsymbol{r},t) - \frac{\partial \boldsymbol{A}}{\partial t}(\boldsymbol{r},t) \tag{1.27}$$

$$\boldsymbol{B}(\boldsymbol{r},t) = \boldsymbol{\nabla} \times \boldsymbol{A}(\boldsymbol{r},t) \tag{1.28}$$

We choose the Coulomb gauge ($\boldsymbol{\nabla}.\boldsymbol{A} = 0$) since it conveniently separates the plasma and laser fields: in this case V represents the electrostatic potential due to charge separations while $\boldsymbol{A}$ represents the laser pulse. Since we assumed that the laser pulse does not evolve during the interaction, this means that the magnetic vector potential is of the form:

$$\boldsymbol{A}(\boldsymbol{r},t) = A_0 \widehat{a}(x,y,z-v_g t)\cos(kz-\omega t)\boldsymbol{e}_x \tag{1.29}$$

Where $A_0 = m_e c a_0/e$ is the peak amplitude of the magnetic vector potential and $\widehat{a}$ is a positive function representing the pulse envelope which is normalized so that its maximal absolute value is 1. We have also assumed without loss of generality that the laser field is polarized in the x direction. The laser electric and magnetic fields are then given by $\boldsymbol{E}_L = -\frac{\partial \boldsymbol{A}}{\partial t}$ and $\boldsymbol{B}_L = \boldsymbol{\nabla} \times \boldsymbol{A}$ while the plasma electrostatic field is $-\boldsymbol{\nabla} V$.

With these notations, the fluid momentum conservation equation reads:

$$\frac{\partial \boldsymbol{v}_e}{\partial t} + (\boldsymbol{v}_e.\boldsymbol{\nabla})\boldsymbol{v}_e = -\frac{e}{m_e}(\boldsymbol{E}_L + \boldsymbol{v}_e \times \boldsymbol{B}_L - \boldsymbol{\nabla} V) \tag{1.30}$$

Since we consider the linear regime, we write the electron velocity in a perturbative manner as $\boldsymbol{v}_e = \boldsymbol{v}_{e1} + \boldsymbol{v}_{e2}$ where $\boldsymbol{v}_{e1}$ is its first-order linear component and $\boldsymbol{v}_{e2}$ its second order component. With these notations, the first order of equation 1.30 is:

$$\frac{\partial \boldsymbol{v}_{e1}}{\partial t} = -\frac{e}{m_e}\boldsymbol{E}_L \tag{1.31}$$

$$\boldsymbol{v}_{e1} = \frac{e}{m_e}\boldsymbol{A} \tag{1.32}$$

Thus, as previously, the main electron motion is an oscillation at the laser frequency. The curl of this expression gives: $\boldsymbol{B}_L = m_e/e\boldsymbol{\nabla}\times\boldsymbol{v}_{e1}$. We can then use this relation in the second order of equation 1.30, which reads:

$$\frac{\partial \boldsymbol{v}_{e2}}{\partial t} + (\boldsymbol{v}_{e1}.\boldsymbol{\nabla})\boldsymbol{v}_{e1} = -\boldsymbol{v}_{e1}\times\boldsymbol{\nabla}\times\boldsymbol{v}_{e1} - \frac{e}{m_e}\boldsymbol{\nabla}V \tag{1.33}$$

$$\frac{\partial \boldsymbol{v}_{e2}}{\partial t} = -\frac{e^2}{2m_e^2}\boldsymbol{\nabla}|\boldsymbol{A}|^2 - \frac{e}{m_e}\boldsymbol{\nabla}V \tag{1.34}$$

We have used here the vector identity $\boldsymbol{\nabla}(|\boldsymbol{v}_{e1}|^2/2) = \boldsymbol{v}_{e1}\times\boldsymbol{\nabla}\times\boldsymbol{v}_{e1} + (\boldsymbol{v}_{e1}.\boldsymbol{\nabla})\boldsymbol{v}_{e1}$. Overall, the equation of motion up to order 2 is:

$$\frac{\partial \boldsymbol{v}_e}{\partial t} = -\frac{e}{m_e}\boldsymbol{E}_L - \frac{e^2}{2m_e^2}\boldsymbol{\nabla}|\boldsymbol{A}|^2 - \frac{e}{m_e}\boldsymbol{\nabla}V \tag{1.35}$$

Next, we use the fact that the laser oscillations are much faster than the other timescales of the system, namely the temporal variations of the pulse envelope ($\omega \gg 2\pi/\tau$) and the plasma response ($\omega \gg \omega_p$). This allows us to average the equation of motion 1.35 over the fast oscillations, which yields:

$$\frac{\partial \widehat{\boldsymbol{v}}_e}{\partial t} = -\frac{A_0^2e^2}{4m_e^2}\boldsymbol{\nabla}\widehat{a}^2 - \frac{e}{m_e}\boldsymbol{\nabla}V \tag{1.36}$$

$$\frac{\partial \widehat{\boldsymbol{v}}_e}{\partial t} = -\frac{a_0^2c^2}{4}\boldsymbol{\nabla}\widehat{a}^2 - \frac{e}{m_e}\boldsymbol{\nabla}V \tag{1.37}$$

Where $\widehat{\boldsymbol{v}}_e$ is the averaged electron velocity. We see here that the average effect of the laser field on the electrons is a force, known as the **ponderomotive force**, which is proportional to the gradient of $\widehat{a}^2$ and pushes the electrons towards the regions of low laser intensity. The ponderomotive force causes charge separations that can be self-consistently studied by adding the Poisson equation and the continuity equation to the averaged equation of motion 1.37. In the Coulomb gauge, the Poisson equation is:

$$\boldsymbol{\nabla}^2 V = \frac{e}{\varepsilon_0}(n_e - n_0) = \frac{e}{\varepsilon_0}\delta n_e \tag{1.38}$$

Where n_e and n_0 are respectively the local and equilibrium electron density and $\delta n_e \equiv n_e - n_0$. The averaged linearized continuity equation is:

$$\frac{\partial \delta n_e}{\partial t} + n_0\boldsymbol{\nabla}.\widehat{\boldsymbol{v}}_e = 0 \tag{1.39}$$

The three equations 1.37-1.38-1.39 together with the choice of the laser field $\boldsymbol{A}(\boldsymbol{r},t)$ entirely determine the evolution of the three unknown variables δn_e, $\widehat{\boldsymbol{v}}_e$ and $\boldsymbol{V}$. By combining these three relations, we can obtain the equation verified by a single variable. For example, this yields after some algebra for the density pertubation δn_e:

$$\left(\frac{\partial^2}{\partial t^2} + \omega_p^2\right)\frac{\delta n_e}{n_0} = \frac{a_0^2c^2}{4}\boldsymbol{\nabla}^2\widehat{a}^2 \tag{1.40}$$

The plasma density perturbation δn_e thus behaves as an harmonic oscillator at the frequency ω_p which is driven by the ponderomotive force of the laser. In other words, the laser pulse triggers plasma waves.

These laser generated plasma waves are often called **wakefields**, hence the term laser wakefield acceleration.

The plasma equations are more easily solved when expressed with respect to the normalized potential $\phi = eV/m_e c^2$, which results in:

$$\left(\frac{\partial^2}{\partial t^2} + \omega_p^2\right)\phi(\boldsymbol{r},t) = \frac{a_0^2\omega_p^2}{4}\widehat{a}^2(x,y,z-v_g t) \tag{1.41}$$

Since the laser pulse, and thus the potential ϕ it creates, propagate without evolving with a velocity v_g, the relevant longitudinal variable is $\zeta = z - v_g t$. We thus perform the change of variable $(z,t) \to (\zeta, t^*)$ and we have in particular $\frac{\partial}{\partial t^*} = 0$. This relation directly comes from the fact that the laser driver is nonevolving[1]. With these new variables, equation 1.41 becomes:

$$\left(\frac{\partial^2}{\partial \zeta^2} + k_p^2\right)\phi(x,y,\zeta) = \frac{a_0^2 k_p^2}{4}\widehat{a}^2(x,y,\zeta) \tag{1.42}$$

Where $k_p = \omega_p / v_g$ is the plasma wavenumber. For an infinitely short (and infinitely wide) driver pulse such that $\widehat{a}^2(x,y,\zeta) = \delta(\zeta)/k_p$, where δ is the Dirac function, the resulting potential is:

$$\phi = -\frac{a_0^2}{4}\sin(k_p\zeta)H(-\zeta) = \frac{a_0^2}{4}\sin(\omega_p t - k_p z)H(-\zeta) \tag{1.43}$$

Where H is the Heaviside step function. For an arbitrary function $\widehat{a}^2(x,y,\zeta)$, we can use the linearity of equation 1.42 to obtain its general solution:

$$\phi(x,y,\zeta) = -\frac{a_0^2 k_p}{4}\int_{\zeta}^{+\infty}\widehat{a}^2(x,y,\zeta')\sin(k_p(\zeta-\zeta'))d\zeta' \tag{1.44}$$

Far behind the laser pulse ($\zeta \approx -\infty$), this integral can be expressed as a function of the Fourier transform of $\widehat{a}^2$ with respect to ζ, noted $\widetilde{a}^2$:

$$\phi(x,y,\zeta) = -\frac{a_0^2 k_p}{4}|\widetilde{a}^2(x,y,k_p)|\sin\left(k_p\zeta + arg\left(\widetilde{a}^2(x,y,k_p)\right)\right) \tag{1.45}$$

As we can see from this equation, in the linear regime the laser pulse triggers a sinusoidal response from the plasma. The resulting plasma waves have a wavelength $\lambda_p = 2\pi/k_p$ and a phase velocity that is equal to the group velocity of the laser pulse. If the temporal envelope $\widehat{a}^2(x,y,\zeta)$ is real and symmetric with respect to ζ, which can usually be assumed, then we have $arg\left(\widetilde{a}^2(x,y,k_p)\right) = 0$ and the previous equation reduces to:

$$\phi(x,y,\zeta) = -\frac{a_0^2 k_p}{4}|\widetilde{a}^2(x,y,k_p)|\sin(k_p\zeta) \tag{1.46}$$

---

[1] More generally, equation 1.42 can be obtained with the quasi-static approximation, which corresponds to $\frac{\partial}{\partial t^*} \ll v_g \frac{\partial}{\partial \zeta}$ and physically means that the changes in the driving laser along its propagation occur on timescales much larger than the pulse duration and the plasma period. Here, we have assumed that the driving laser does not evolve at all, which is an even stronger approximation.

The electric field and the density perturbation δn_e of the resulting accelerating structure can then be obtained by taking respectively the gradient and the Laplacian of the potential. This yields in particular for the longitudinal electric field E_z:

$$E_z(x,y,\zeta) = \frac{e a_0^2 k_p^2}{4 m_e c^2} |\widetilde{a}^2(x,y,k_p)| \cos\left(k_p \zeta\right) \tag{1.47}$$

Thus, the accelerating field behind the laser is important when the longitudinal Fourier transform of the pulse envelope has a significant value at the wavenumber k_p. This occurs when:

- The pulse duration is smaller than the plasma period $2\pi/\omega_p$, in conformity with the uncertainty principle.
- The laser envelope is spatially modulated (in the longitudinal direction) at the plasma wavelength $\lambda_p = 2\pi/k_p$. This is for instance the case in self-modulated laser wakefield acceleration [42].

In particular, for a given laser pulse, there is a plasma density for which $k_p^2 |\widetilde{a}^2(x=0, y=0, k_p)|$, and thus the on-axis accelerating field E_z is maximum. This is known as the **resonance condition** and the corresponding density for which plasma wave excitation is optimal is the resonant density.

Let us consider as an example the usual case of a cylindrically symmetric pulse which is Gaussian in the longitudinal and transverse coordinates, $\widehat{a} = \exp\left(-2\ln(2)\frac{\zeta^2}{v_g^2 \tau^2}\right)\exp\left(-\frac{r^2}{w_0^2}\right)$. We have far behind such a laser driver:

$$\phi(r,\zeta) = -\sqrt{\frac{\pi}{\ln(2)}} a_0^2 \frac{\omega_p \tau}{8} \exp\left(-\frac{\omega_p^2 \tau^2}{16 \ln(2)}\right) \exp\left(-\frac{2r^2}{w_0^2}\right) \sin(k_p \zeta) \tag{1.48}$$

$$E_z(r,\zeta) = E_0 \sqrt{\frac{\pi}{\ln(2)}} a_0^2 \frac{\omega_p \tau}{8} \exp\left(-\frac{\omega_p^2 \tau^2}{16 \ln(2)}\right) \exp\left(-\frac{2r^2}{w_0^2}\right) \cos(k_p \zeta) \tag{1.49}$$

$$E_r(r,\zeta) = -E_0 \sqrt{\frac{\pi}{\ln(2)}} a_0^2 \frac{v_g \tau}{2 w_0} \exp\left(-\frac{\omega_p^2 \tau^2}{16 \ln(2)}\right) \frac{r}{w_0} \exp\left(-\frac{2r^2}{w_0^2}\right) \sin(k_p \zeta) \tag{1.50}$$

$$\delta n(r,\zeta) = n_0 \sqrt{\frac{\pi}{\ln(2)}} a_0^2 \frac{\omega_p \tau}{8} \exp\left(-\frac{\omega_p^2 \tau^2}{16 \ln(2)}\right) \exp\left(-\frac{2r^2}{w_0^2}\right) \sin(k_p \zeta) \left[1 + \frac{2}{w_0^2 k_p^2}\left(1 - \frac{2r^2}{w_0^2}\right)\right] \tag{1.51}$$

Where r is the transverse cylindrical coordinate and $E_0 = m_e c \omega_p / e$. The electrostatic accelerating structure resulting from the propagation of a Gaussian beam in an underdense plasma possesses a longitudinal component E_z that can accelerate electrons and a radial component E_r that can confine the electrons on the $r = 0$ axis. The field is both accelerating and focusing for a quarter of the plasma period, which can result in high-quality accelerated electron beams.

The amplitude of the accelerating field is plotted in figure 1.5 in the case of (a) constant laser parameters, (b) constant density and laser amplitude or (c) constant density and laser pulse energy. As expected, for given laser parameters, there is a density for which wakefield generation is optimal. The resonance condition reads mathematically for such a Gaussian pulse:

$$\omega_p \tau = 4\sqrt{\ln(2)} \approx 3.33 \tag{1.52}$$

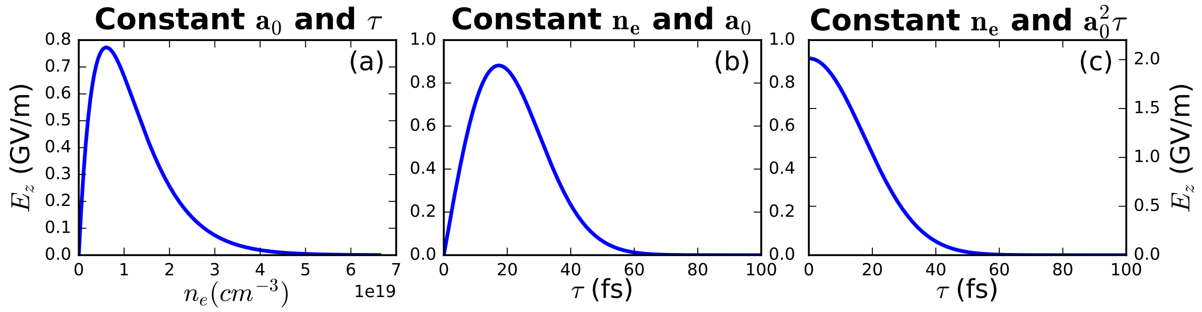

Figure 1.5: (a) Amplitude of the longitudinal electric field E_z of the plasma waves in the linear regime as a function of plasma density for a 24-fs pulse with Gaussian envelope and $a_0 = 0.1$. The resonant density in this case is $n_e = n_{eres} = 6 \times 10^{18}\,\mathrm{cm}^{-3}$, which corresponds to $n_c/300$ for a wavelength of 800 nm. In (b), E_z is plotted at the density n_{eres} as a function of pulse duration for a constant laser amplitude of a_0 = 0.1. The resonant duration is here 17.3 fs. In (c), E_z is plotted at the density n_{eres} as a function of pulse duration for a constant laser pulse energy ($a_0^2\tau$ is kept constant). The constant is chosen so that $a_0 = 0.1$ at 24 fs.

Similarly, for given values of a_0 and n_e, there is a pulse duration for which the E_z field is maximum. The resonance condition in this case is[2]:

$$\omega_p \tau = 2\sqrt{2\ln(2)} \approx 2.35 \tag{1.53}$$

In both cases, the resonance condition signifies that plasma wave formation is optimal when the pulse duration is approximately half a plasma period. Long pulses efficiently excite wakefields in low-density plasmas while short pulses are better suited to high-density plasmas. For instance, for a wavelength of 800 nm, the resonant density is $\approx n_c/300$ for 24-fs pulses and $\approx n_c/12.5$ for 5-fs pulses[3]. We can also point out that the resonance is rather broad and thus that wakefields can still be formed outside of these specific densities.

In experiments, the pulse duration is usually varied at a constant pulse energy. In this case there is no longer a resonance since decreasing the pulse duration always result in a stronger wakefield, as can be seen in figure 1.5(c). This is of course because the laser amplitude a_0 increases as the pulse duration is reduced[4]. In any case, an important result is that a laser pulse cannot efficiently drive wakefields in a plasma whose density is much greater than the resonant density. This means in particular that few-cycle pulses are required to excite plasma waves in near-critical density plasmas.

---

[2] Sometimes, the resonance is defined as the maximum of E_z/E_0 rather than E_z. This leads to a single resonance condition, given by equation 1.53, instead of two different resonance conditions (equations 1.52 and 1.53) here. The difference comes from the fact that E_0 depends on ω_p.

[3] Of course this last value is not perfectly accurate because the assumption $\omega \gg 2\pi/\tau$ used in the derivation of the ponderomotive force is not verified for few-cycle pulses. This model nonetheless provides a good estimation of the resonant density.

[4] Once again the model breaks for very short pulses. This is even more true in this case because the linear assumption $a_0^2 \ll 1$ is no longer valid as the pulse duration approaches 0.

1.3.2 The nonlinear regime

In the linear regime ($a_0^2 \ll 1$), the plasma is only slightly perturbated by the driving laser, which has allowed us to linearize the fluid equations and results in a sinusoidal response of the plasma. This is no longer the case in the nonlinear regime ($a_0 > 1$). The nonlinear regime can still be studied analytically using a cold fluid model neglecting the ion motion but this time in one dimension only. In this model, which is not detailed in this manuscript, a nonevolving laser pulse is assumed (the quasistatic approximation) to obtain the differential equation[5] verified by the normalized electric potential ϕ [43, 44]:

$$\frac{\partial^2\Phi}{\partial\zeta^2} = k_{\mathrm{p}}^2\gamma_{\mathrm{p}}^2\left(\beta_{\mathrm{p}}\left(1-\frac{1+(a_0\widehat{a})^2/2}{\gamma_{\mathrm{p}}^2(1+\phi)^2}\right)^{-1/2}-1\right) \tag{1.54}$$

Where $\beta_p = v_g/c$ and $\gamma_p = 1/\sqrt{1-\beta_p^2}$. Equation 1.54 is usually solved numerically. This is done in figure 1.6, which shows the normalized potential, longitudinal electric field and density perturbation generated by a 5-fs pulse near the resonant density in the linear ($a_0 = 0.25$) and the nonlinear regimes ($a_0 = 2.3$, corresponding to the Salle Noire laser). As expected, in the linear regime these quantities evolve sinusoidally and the density perturbation remains small ($\delta_n \ll n_0$). On the other hand, the fields become distorted in the nonlinear regime and we observe the formation of sharp density peaks whose value can reach several times the initial density. We also note that the effective plasma period tends to increase in the nonlinear regime. There is still a resonance, as is illustrated in figure 1.7. Even though the resonant values may slightly change, the main trends found in the previous section still hold in the nonlinear regime, even for few-cycle pulses with relativistic intensities which can in principle not be described by the 3D linear model.

There is no general analytical model to study the formation of plasma waves in 3 dimensions in the nonlinear regime. PIC simulations are thus generally used to study this process. When transverse effects are included, the formation of plasma cavities entirely void of electrons (meaning that $\delta_n = -n_0$) is observed. This is known as the blowout or **bubble regime**, because the cavity usually has an approximately spherical shape. A typical density perturbation map in the blowout regime is shown in figure 1.8(b). The bubble provides an ideal structure for accelerating electrons, with fields that are both accelerating and focusing over nearly half a plasma wavelength. It has led to the first demonstration of laser wakefield acceleration of a high-quality electron beam with a narrow divergence and energy spread [16, 17, 18]. The formation of the ion cavities occurs when the intensity of the laser is high enough to expel all the electrons from the optical axis ($a_0 \geq 2$ is commonly required) and when both the pulse transverse and longitudinal sizes are matched to the plasma wavelength [45]:

$$c\tau \approx \frac{w_0}{\sqrt{2}} \approx \lambda_p/2 \tag{1.55}$$

1.3.3 Injection methods

In the previous sections, we have presented how a laser pulse can generate a plasma-based accelerating structure. We have however not described how electrons can be trapped by the structure and accelerated

---

[5] Note that equation 1.54 is also valid without averaging the laser normalized magnetic potential over the fast oscillations, i.e. using $\widehat{a}^2\cos^2(k\zeta)$ instead of $\widehat{a}^2/2$. However, we have used the averaged potential in the images presented in this manuscript.

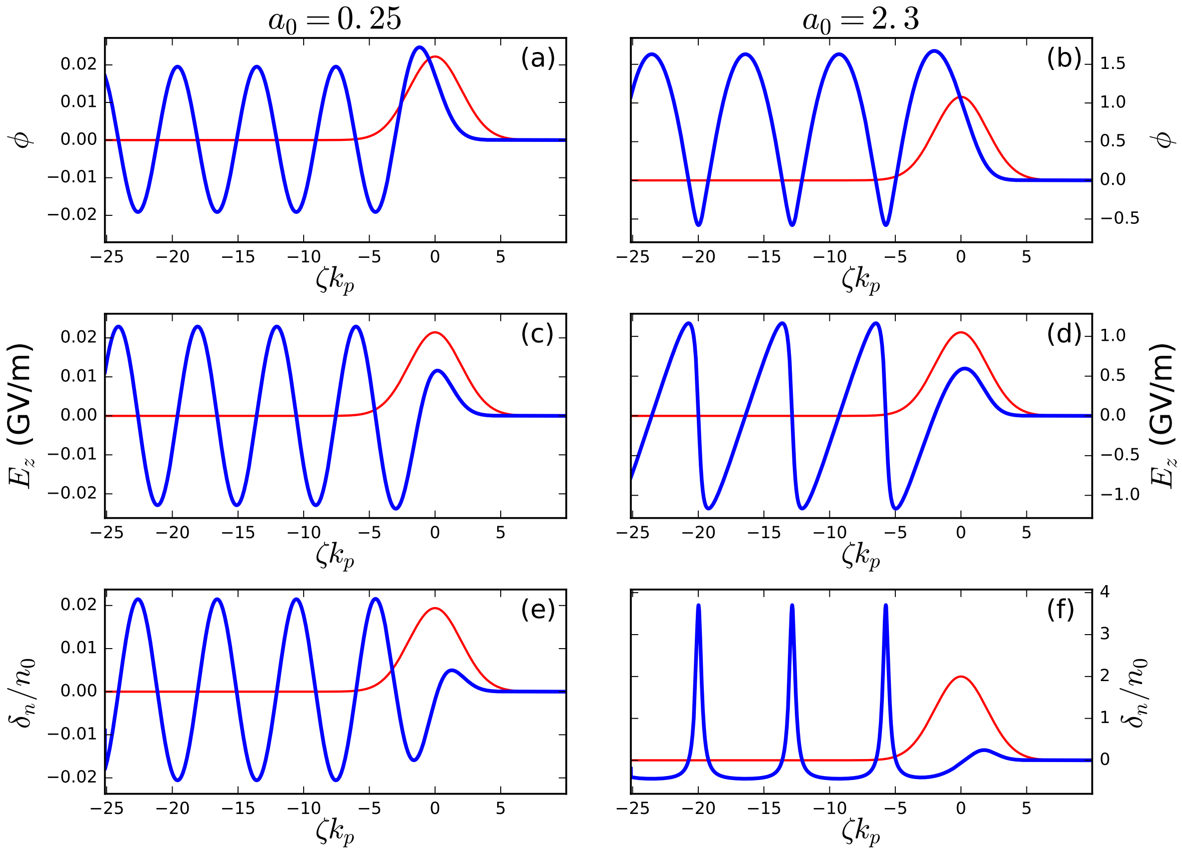

Figure 1.6: (a)-(b) Normalized potential, (c)-(d) longitudinal electric field and (e)-(f) density perturbation of the plasma waves driven by a 5-fs pulse with (a),(c),(e) $a_0 = 0.25$ or (b),(d),(f) $a_0 = 2.3$ in a plasma with density $n_e = 1.4 \times 10^{20}\,\mathrm{cm}^{-3}$ ($n_c/12.5$ for $\lambda = 800$ nm) according to the 1D nonlinear theory of wakefield generation (eq. 1.54). The red curve shows for reference the electric field envelope $\widehat{a}(\zeta)$ in arbitrary units.

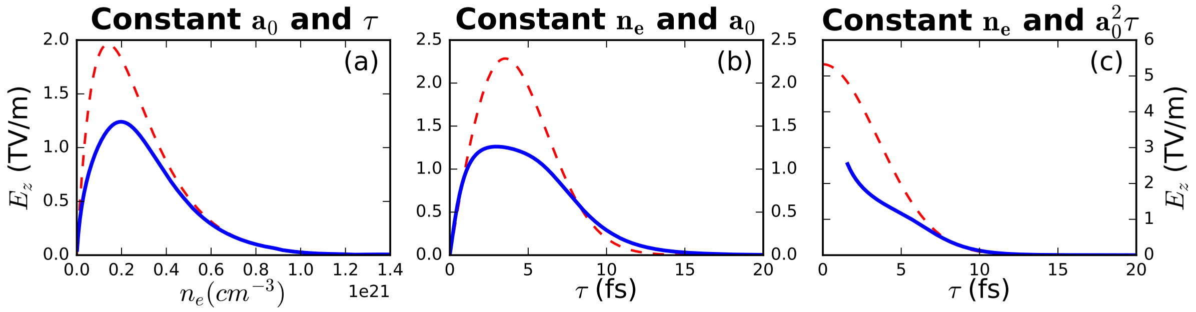

Figure 1.7: (a) Amplitude of the longitudinal electric field E_z of the plasma waves in the nonlinear regime as a function of plasma density for a 5-fs pulse with Gaussian envelope and $a_0 = 2.3$. The resonant density in this case is $2 \times 10^{20}\,\mathrm{cm}^{-3}$, which corresponds to $n_c/8.7$ for a wavelength of 800 nm. In (b), E_z is plotted at a density of $1.4 \times 10^{20}\,\mathrm{cm}^{-3}$ as a function of pulse duration for a constant laser amplitude of a_0 = 2.3. The resonant duration is here 3 fs. In (c), E_z is plotted at a density of $1.4 \times 10^{20}\,\mathrm{cm}^{-3}$ as a function of pulse duration for a constant laser pulse energy ($a_0^2\tau$ is kept constant). The constant is chosen so that $a_0 = 2.3$ at 5 fs. The red dashed lines show the corresponding curves obtained with the linear model. The difference between the red and blue curves is due to assumptions made in the linear model ($a_0^2 \ll 1$ and $\omega_p \ll \omega$) which are not verified here. In (c) the value of the electric field is not given for very short pulse durations because of numerical difficulties when integrating equation 1.54 near the density peaks.

to high energies. The injection of electrons into the wakefields usually cannot be studied with a fluid model because the accelerated electrons follow a significantly different trajectory from the fluid electrons making up the plasma waves.

An electron can gain energy if it remains for a long time in an accelerating phase of the wakefield. Since the accelerating structure propagates at a speed close to c, an electron can only be trapped in an accelerating phase if it rapidly acquires a relativistic velocity in the direction of propagation of the laser. This may happen spontaneously (self-injection of the hot plasma electrons or by wavebreaking) but a dedicated technique is often employed to trap electrons [47]. We can cite in particular the use of a second laser pulse [48] or of an externally produced electron beam [49]. We focus in this section on two specific injection methods, ionization injection and injection in density gradients, because they will be useful later on in this manuscript.

1.3.3.1 Ionization injection

In this method [50, 51], the trapped electrons are generated by field ionization (see section 1.2.1) by the strong electric fields at the center of the laser pulse. These electrons therefore originate from ions with high ionization energies. The idea of this technique is that some electrons are generated at the right phase of the wakefield (the optimal phase corresponds to electrons starting with an accelerating half-cycle) and are thus more likely to be trapped than electrons created early in front of the laser. A mathematical description of ionization injection can be found in [52].

This method can be achieved in practice by adding an adequate chemical element into the gas

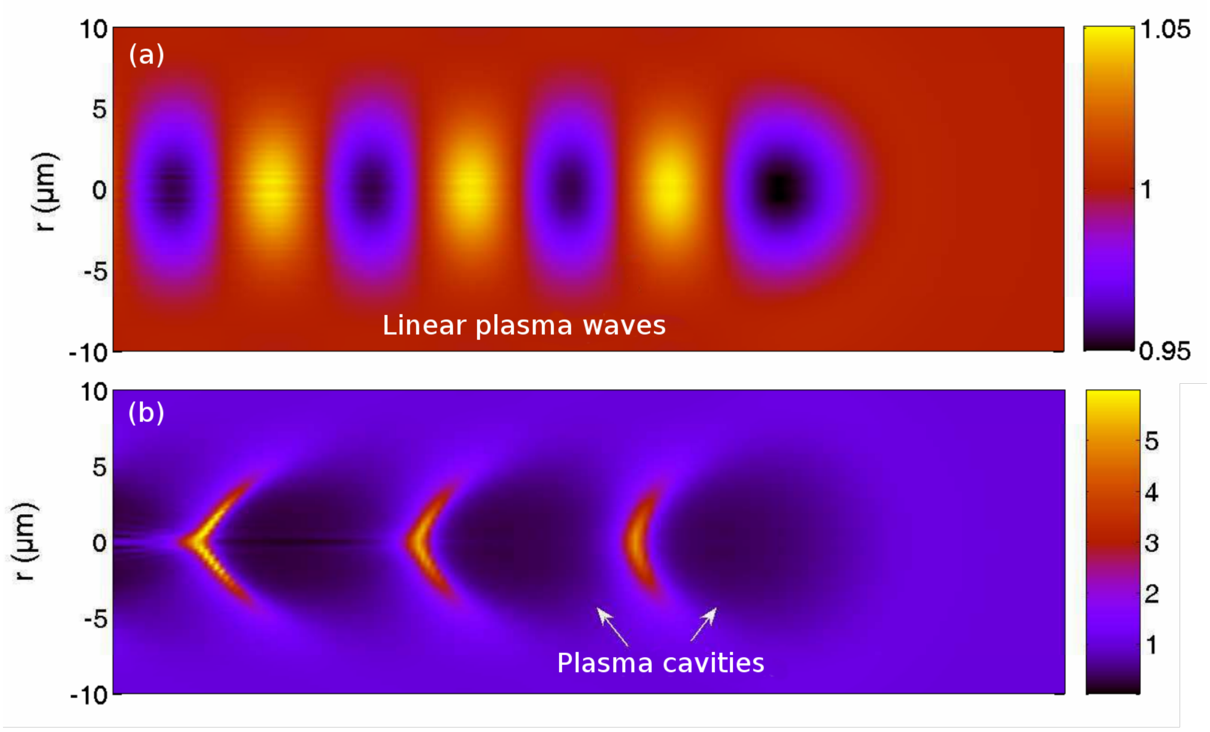

Figure 1.8: Illustration of the normalized density perturbation δ_n/n_0 *in (a) the linear regime and (b) the bubble regime. Images taken from [46].*

Initial ion state	**Ionization energy**	**Barrier suppression intensity**
N	14.5 eV	$1.77 \times 10^{14}\,\mathrm{W/cm^2}$
N^{+}	29.6 eV	$7.68 \times 10^{14}\,\mathrm{W/cm^2}$
N^{2+}	47.7 eV	$2.30 \times 10^{15}\,\mathrm{W/cm^2}$
N^{3+}	77.4 eV	$8.97 \times 10^{15}\,\mathrm{W/cm^2}$
N^{4+}	97.9 eV	$1.47 \times 10^{16}\,\mathrm{W/cm^2}$
N^{5+}	552 eV	$1.03 \times 10^{19}\,\mathrm{W/cm^2}$
N^{6+}	667 eV	$1.62 \times 10^{19}\,\mathrm{W/cm^2}$

Table 1.3: Ionization energies of nitrogen and corresponding barrier-suppresion ionization intensites. The ionization energies have been obtained from the NIST Atomic Spectra Database.

target. Let us consider as an example the case of nitrogen, which is commonly used for this purpose. The ionization energies of nitrogen and the corresponding barrier suppression intensities are given in table 1.3. For a relativistic laser driver ($I > 10^{18}\,\mathrm{W/cm^2}$), the electrons generated from N to N^{4+} will be ionized at the very front of the laser. Most of them will be part of the fluid electrons forming the plasma waves. On the other hand, the N^{5+} and N^{6+} ions have a high ionization energy and can therefore only be ionized at the temporal center of the laser pulse. Some of their electrons will be created at the appropriate phase of the wakefield and will become trapped. In experiments, the total accelerated charge can be controled by adjusting the percentage of nitrogen (or any other appropriate element) in the gas target.

1.3.3.2 Injection in density gradients

In this method [53], the target density profile is tailored in order to locally reduce the phase velocity of the plasma waves and thus facilite the injection of plasma electrons into the wakefields. We briefly describe in this section the standard theory of plasma wave formation in a density gradient. We work in the linear regime and assume that the plasma density n_0 only depends on the longitudinal coordinate z. Additionally, we use the fact that $\omega \gg \omega_p$ in the linear model to neglect the longitudinal variation of the group velocity: $v_g \approx c$ everywhere. In this case, only the dependence of k_p on z must be taken into account in the equation 1.42 verified by the normalized potential ϕ within the quasistatic approximation:

$$\left(\frac{\partial^2}{\partial \zeta^2} + k_p^2(z)\right)\phi = \frac{a_0^2 k_p^2(z)}{4}\widehat{a}^2 \tag{1.56}$$

In the case of a homogeneous plasma, k_p is constant and we have seen that solutions to this equation are of the form $\phi_0 \sin(k_p(z - v_g t))$ behind the laser driver (see equation 1.46). Thus, we can assume as a first approximation that solutions to equation 1.56 are of the form:

$$\phi = \phi_0(z)\sin(k_p(z)(z - v_g t)) \tag{1.57}$$

Such an approximation is reasonable if the plasma density gradient scalelength L is much larger than the plasma wavelength: $k_p(z)L \gg 1$. In this case, the phase of the plasma wave can be defined as

$\varphi = k_p(z)(z - v_g t)$. The effective frequency ω_{eff} and wavenumber k_{eff} of such a wave are:

$$\omega_{eff} = -\frac{\partial \phi}{\partial t} = k_p(z) v_g = \omega_p(z) \tag{1.58}$$

$$k_{eff} = \frac{\partial \phi}{\partial z} = k_p(z) + \frac{\partial k_p}{\partial z}(z - v_g t) \tag{1.59}$$

The density gradient leaves the frequency unchanged but adds an additional time-varying term to the plasma wavenumber. The phase velocity of the wakefield is given by ω_{eff}/k_{eff} and reads:

$$v_\varphi = \frac{v_g}{1 + \frac{z - v_g t}{k_p} \frac{\partial k_p}{\partial z}} \tag{1.60}$$

Behind the laser pulse, we have $z - v_g t < 0$. In a density downramp such that $\frac{\partial k_p}{\partial z} < 0$, the effect of the density gradient is a decrease in the local phase velocity. This decrease is time-dependent: the further away from the laser, the slower is the phase velocity. A negative density gradient can thus greatly facilitate electron injection, which occurs whenever the wakefield is slow enough to trap the hot plasma electrons.

1.3.4 LWFA in experiments

Laser wakefield accelerators have been operating successfully in the past decades and accelerating gradients exceeding 100 GV/m - more than 3 orders of magnitude higher than those achievable with conventional accelerators - have been attained, thus enabling relativistic acceleration over very short distances. Nevertheless, plasma-based accelerators are still not routinely used for scientific, industrial or medical applications. This is largely due to the fact that relativistic laser plasma interactions rely on many competing and complex nonlinear phenomena, which can limit the stability, tunability and quality of the generated electron beam. For instance, we have assumed in the previous sections that the driving laser pulse does not evolve during its propagation in the plasma. This is not the case in practice and many effects coming from the retroaction of the plasma on the laser (dispersion, self-modulation, relativistic self-focusing, ionization induced defocusing, etc.) must be taken into account in experiments. Still, significant progress have been made over the past 25 years, owing to the development of laser technology, the better understanding of the interaction and the development of adequate diagnostics [54].

Significant efforts are made to increase the accelerated electron energies, with the ultimate objectives of using the electron beam in free-electron lasers or in particle colliders. High energies are usually attained in the linear regime in low density plasmas. Low-densities are required so that the group velocity of the laser (and thus the phase velocity of the plasma waves) remains very close to c, which prevents the electrons from overtaking the wakefield. The diffraction of the laser pulse can be compensated by using preformed plasma channels, which can guide the laser over tens of centimeters and large laser energies (tens of joules) are required to sustain the accelerating structure over such long distances. As of today, the highest published electron energy is 8 GeV [19], which has been achieved using 30 J, 35 fs laser pulses over an acceleration distance of 20 cm. Higher electron energies can be expected in the future from further progress in laser technology and from the sought-after use of multiple acceleration stages.

Laser-plasma accelerators are also attractive for their potential use in ultrafast science, since they can generate femtosecond-duration electron beams and secondary radiations which are inherently synchronized with the driving laser. We can cite in particular the betatron radiation emitted as the trapped

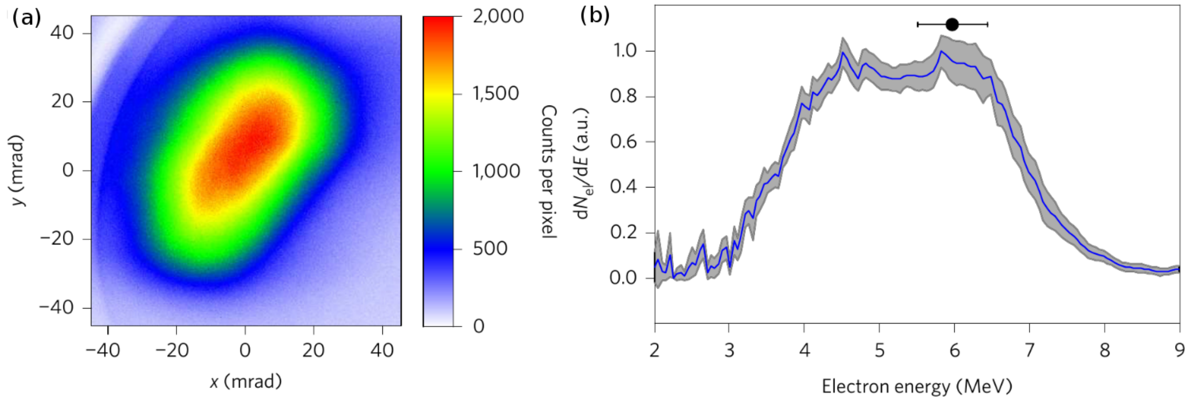

Figure 1.9: Images taken from [56]. (a) Angular distribution and (b) energy spectrum of electron beams accelerated in the bubble regime in Salle Noire. The charge in this case is ∼100 fC, but electron bunches containing up to ∼10 pC have also been obtained [57], albeit with lower energies.

electrons oscillate in the wakefield [55] which could provide a compact and inexpensive source of ultrashort X-ray pulses.

Directly using the wakefield accelerated electron beams for ultrafast imaging (for instance as a probe in ultrafast electron diffraction) would require electrons with few-MeV energy, which is lower than what is commonly obtained. The scaling laws for the bubble regime [45] show that high-quality electron bunches with few-MeV energy can be obtained in high-density plasmas ($\sim n_c/10$ at 800 nm) with tightly focused, few-mJ and few-cycle drivers, i.e. with parameters corresponding to the Salle Noire laser. Pioneering results have indeed recently been obtained in Salle Noire [56, 57] in which the acceleration of few-MeV, few-degrees wide, pC electron beams over very short distances (tens of microns) are demonstrated. An example of beam angular distribution and energy spectrum is shown in figure 1.9. The duration of the electron bunch immediatly after the interaction is estimated from PIC simulations to be approximately 1 fs. Such an electron beam has great potential for ultrafast science, especially because the experiments are performed at a kHz repetition rate thanks to the use of a limited laser driver energy (few-mJ). Using high repetition rates is indeed desirable in many applications since it improves the data collection statistics. Research regarding the development and optimization of both the laser system and the gas targets is still ongoing in order to improve the stability and quality of the electron beam, with the final objective of performing ultrafast electron diffraction experiments with sub 10-fs resolution.

1.4 Electron acceleration from overdense plasmas

High-energy electron bunches are also generated when a laser pulse is focused to relativistic intensities on a solid-density target. However, the physics of electron acceleration has been less studied for overdense plasmas than for underdense plasmas. This is partly due to the fact that laser wakefield acceleration in underdense plasmas has demonstrated better electron beam quality than what has been achieved from solid targets, thus sparking more interest. Another reason is that the interaction between a laser and an overdense plasma strongly varies depending on the density profile at the interface between the plasma and vacuum. The density gradient scalelength L is in particular a key parameter of the interaction. It is however very challenging to control experimentally, since it requires extremely high temporal contrast, which has hampered the interpretation and understanding of many experiments. For a very sharp plasma-vacuum interface ($L \ll \lambda$), the physics of electron emission from the plasma is now fairly well understood and will be described in section 1.4.2.1. The ejection of electron in this case is closely related to the emission of high-harmonics, which will be briefly reviewed in section 1.4.3. On the contrary, there is no unified theory describing the acceleration of electrons when the gradient scalelength exceeds the laser wavelength and there is therefore a need for a better understanding of the interaction in this regime.

1.4.1 Basics of laser-overdense plasma interaction

1.4.1.1 Laser reflection on an overdense plasma

As we have seen in section 1.2.3, when a laser pulse impinges on an overdense plasma, the collective electron response results in a cancellation of the electromagnetic fields inside the plasma and in a specular reflection of the laser. In practice the vacuum-plasma boundary is not entirely abrupt and the plasma usually has a density gradient on its front surface. This density gradient, sometimes referred to as a **preplasma**, is either due to the rising edge of the laser or created on purpose using a separate pulse, called a **prepulse**. In the presence of a preplasma, the main laser pulse can propagate up to a point where it is reflected. The density n_{ref} at which reflection occurs can be obtained from the total internal reflection condition:

$$N(n_{ref}) = \sin\theta_i \tag{1.61}$$

Where $N(n_{ref})$ is the refractive index at the density n_{ref} and θ_i is the incidence angle of the laser on the target, as defined in figure 1.10. The refractive index in a plasma is given by equation 1.25 and reads:

$$N(n_{ref}) = \sqrt{1 - \frac{n_{ref}}{n_c}} \tag{1.62}$$

We deduce from the two previous equations the plasma density at reflection:

$$n_{ref} = n_c \cos^2\theta_i \tag{1.63}$$

The interaction heavily depends on the polarization state of the laser pulse. In the case of linear polarization and oblique incidence, we say that the laser is **p-polarized** if its electric field is in the incidence plane while its magnetic field is oriented in the y direction and that the laser is **s-polarized** if its magnetic field is in the incidence plane while its electric field is in the y direction. P-polarization usually results in a stronger coupling between the laser and the plasma because part of the electric field is directed towards the density gradient, which can easily cause charge separations. Unless specified otherwise, we will consider p-polarized pulses throughout this manuscript.

Using the coordinate system defined in fig 1.10, we also introduce the following common geometric directions:

- The normal direction is the direction of the density gradient. It is parallel to the x-axis.

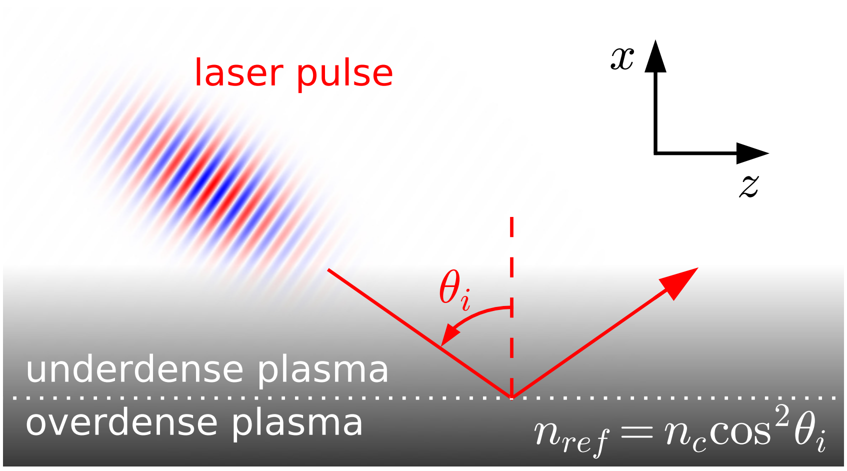

Figure 1.10: Illustration of the interaction between a laser pulse and an overdense plasma with a density gradient on its front surface. The laser propagates in an underdense plasma until it is reflected at the density $n_{ref} = n_c \cos^2\theta_i$, where θ_i is the incidence angle of the laser.

- The specular direction is the direction of propagation of the reflected laser pulse. It is parallel to the line $z = x \tan\theta_i$.
- The grazing direction is the positive z-direction. It is perpendicular to the density gradient.

1.4.1.2 Importance of the gradient scale length

It is almost always assumed that the density in the preplasma only depends on the x-coordinate, although this 1D hypothesis might not always be valid, especially when the plasma is created by the rising front of the laser pulse itself. Most commonly, an exponential density profile is chosen:

$$n_e(x) = \begin{cases} n_{MAX} \exp\left(-x/L\right) & \text{if } x > 0 \\ n_{MAX} & \text{if } x < 0 \end{cases} \tag{1.64}$$

Where x is the coordinate in the direction of the density gradient defined in fig 1.10, n_{MAX} is the maximum plasma density, which is usually in the range $100n_c - 400n_c$ for solid targets and $L = \left(\frac{|\nabla n_e|}{n_e}\right)^{-1}$ is the **gradient scale length**. The exponential density profile, plotted in figure 1.11, comes from a simple isothermal model of preplasma expansion that will be described in section 3.1.1. As it turns out, the gradient scale length L is a key parameter that can drastically change the interaction. It has a critical impact on laser absorption by the plasma [58, 24], electron acceleration [24, 59], high-harmonic generation [24, 26, 59] and ion acceleration [60]. The effect of the gradient scale length on the shape of the reflected pulse in 2D PIC simulations is shown in figure 1.12. When no preplasma is present ($L = 0$), the laser is simply reflected specularly and its shape remains unaffected. In this case, the plasma behaves as a perfect conductor and is often called a **plasma mirror**. When a sharp density gradient with $L = \lambda/7$ is introduced, the laser pulse is still specularly reflected and mainly unaltered by the plasma, although significant high-harmonic generation is observed. The term plasma mirror is still commonly used in this

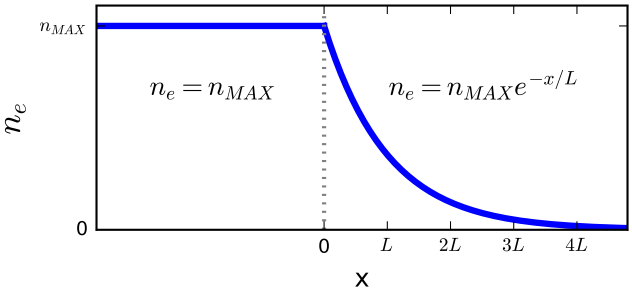

Figure 1.11: Preplasma exponential density profile given by equation 1.64

regime. On the other hand, when a large preplasma with $L = 2\lambda$ is present, the reflected pulse is strongly distorted. A temporal chirp is observed since lower frequencies are reflected earlier ($n_c \propto \omega^2$). The term plasma mirror is not appropriate in this case. Consequently, we only use the term plasma mirror in this manuscript to refer to overdense plasmas with very sharp ($L \ll \lambda$) density gradients on their front surface.

Since the gradient scale length is a crucial parameter, it must be controlled in experiments. However, this can only be achieved using laser pulses with extremely high temporal contrast. If the contrast is not high enough, the target is ionized very early in front of the laser pulse which initiates an uncontrolled plasma expansion. Multiphoton ionization typically starts when the intensity exceeds $10^{10} - 10^{11}\,\mathrm{W/cm^2}$ which means that for a relativistic intensity laser driver ($I > 10^{18}\,\mathrm{W/cm^2}$), a temporal contrast higher than 10^{10} is usually required to supress unwanted preplasma expansion caused by the main pulse. This value is particularly difficult to attain experimentally. As a result, many experiments have been performed without precisely knowing the gradient scale length during interaction, which makes their interpretations difficult. This has made the literature somewhat unclear, with a wide variety of experimental results [61], and has considerably hindered the understanding of the physics involved.

Once the laser contrast is high enough, the standard way to adjust the gradient scale length in experiments is to add a spatially overlapped prepulse which is responsible for ionizing the target and triggering the preplasma expansion. The prepulse must precede and be perfectly synchronized with the main pulse. Then, the gradient scale length during the interaction can be varied by changing the delay between the two pulses. A short delay leads to a sharp plasma-vacuum interface while a larger value for the delay results in longer preplasma expansion. The relation between the prepulse lead and the gradient scale length can be obtained by performing interferometric measurements [62, 63]. The prepulse usually has a weaker intensity than the main pulse, on the order of $10^{14} - 10^{15}\,\mathrm{W/cm^2}$, and is focused to a much larger spot size, so that the plasma during the interaction is transversely homogeneous. The expansion of the plasma during the experiments carried out in Salle Noire and the corresponding estimated density profiles during interaction will be studied in more details in section 3.1.

1.4.1.3 Electron heating mechanisms

In this section, we introduce 3 laser absorption mechanisms that are frequently mentioned in the literature.

Brunel absorption / Vacuum heating

This mechanism [64] occurs for p-polarized pulses at oblique incidence when the gradient scale length is

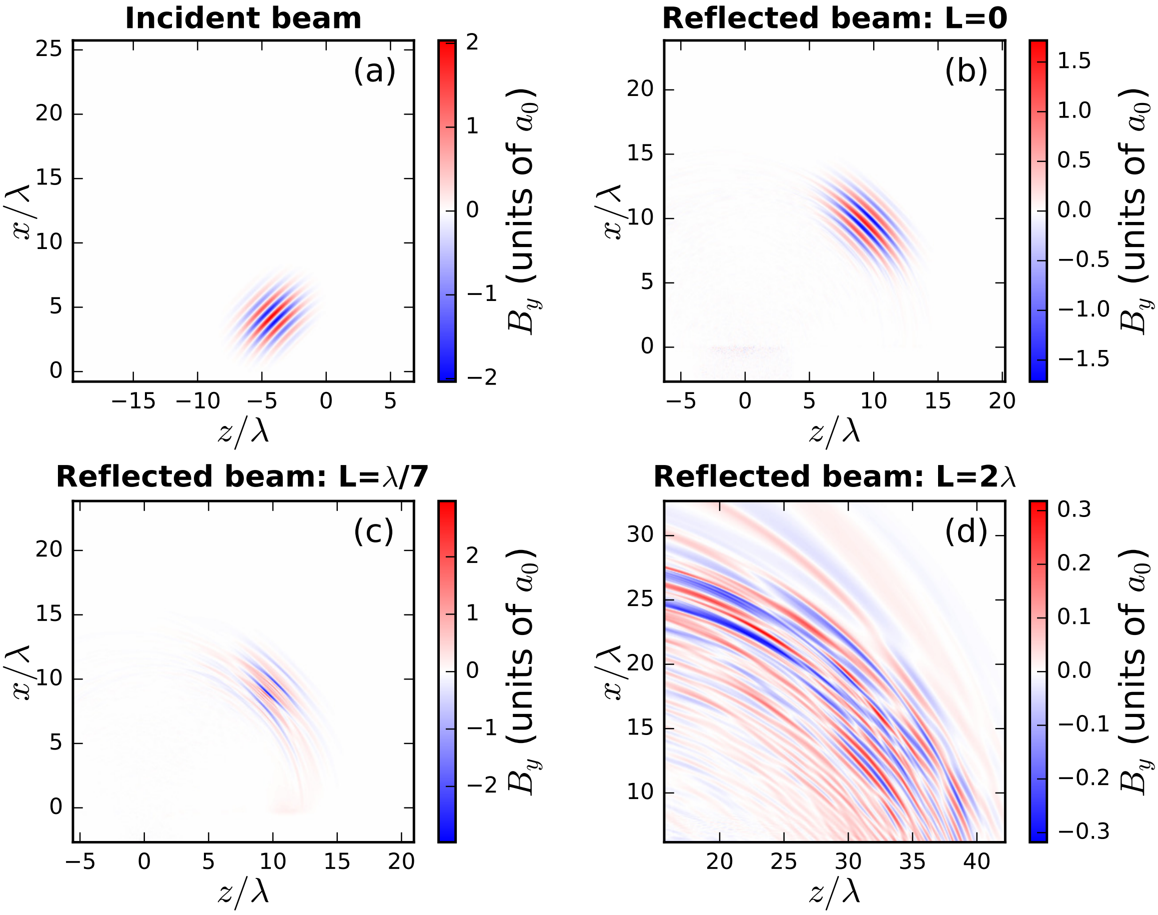

Figure 1.12: Results from 2D PIC simulations. (a) Magnetic field of a 5-fs laser pulse with $\lambda = 800$ *nm,* $w_0 = 1.5\,\mu\mathrm{m}$ *and* $a_0 = 2.15$ *impinging on an overdense plasma with a* 45° *incidence angle. (b)-(d) Magnetic field of the reflected pulse for* $L = 0$ *(b),* $L = \lambda/7$ *(c) and* $L = 2\lambda$ *(d). The position* $x = 0$ *corresponds here to the point where the plasma starts in the simulations, with a density of* $n_c/20$*. Detailed simulation parameters are provided in appendix B.*

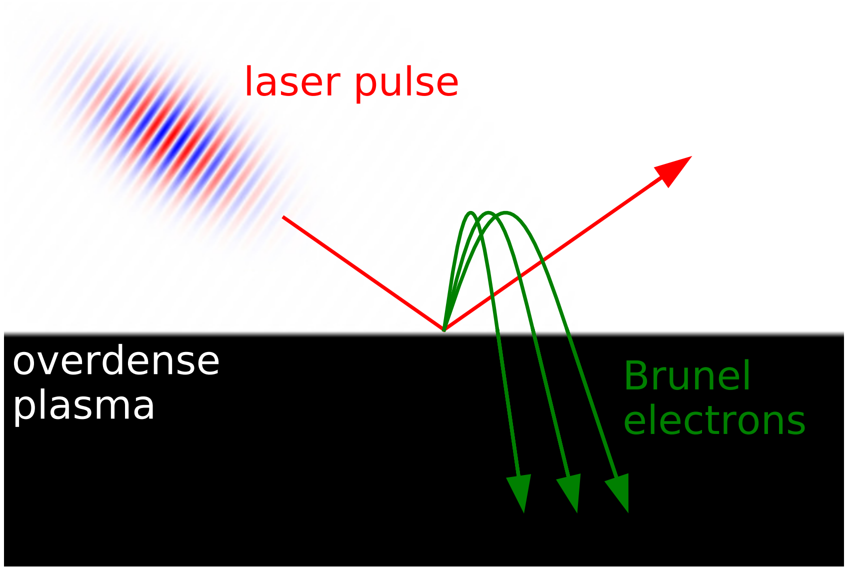

Figure 1.13: Schematic illustration of vacuum heating. Brunel electrons (in green) originating from the plasma surface are pushed in vacuum during half a laser cycle by the laser. They then penetrate the plasma bulk where there is no laser field and they deposit their energy to the plasma through collisions.

much shorter than the quivering amplitude of the electrons oscillating in the laser field. Brunel absorption is thus relevant for high laser intensities and sharp density gradients. In this case, the electrons on the surface of the plasma are pulled out into vacuum at every optical cycle by the normal component of the laser electric field (E_x). When the sign of the laser Lorentz force changes, the electrons are pushed back into the plasma bulk where the laser field is screened. They can then propagate ballistically inside the target and deposit their kinetic energy (acquired from the laser field) to the plasma via collisions. These hot electrons travelling into the plasma after spending half a laser cycle in vacuum are known as **Brunel electrons**. Vacuum heating is illustrated in figure 1.13.

$\boldsymbol{J} \times \boldsymbol{B}$ heating

At normal incidence, Brunel absorption can no longer occur because the electric field has no component direct towards the density gradient. However, for relativistic lasers, the $\boldsymbol{v} \times \boldsymbol{B}$ term in the Lorentz force can push the electrons into the bulk of the plasma where they escape the laser field. Then, as in the previous case, this population of hot electrons deposit their energy in a collisional manner. This process is known as $\boldsymbol{J} \times \boldsymbol{B}$ heating [65].

Resonant absorption

Resonant absorption [66] corresponds to the resonant excitation of plasma waves when the laser frequency matches the plasma frequency ($\omega = \omega_p$, or equivalently n_e=n_c). Resonant absorption requires a normal electric field component to generate the charge separation that will trigger the plasma waves and can thus only occur for oblique incidence and p-polarization. Since the laser is reflected in this case at $n_c \cos^2 \theta_i$, before reaching the critical density, it is the evanescent laser field inside the plasma that causes resonant absorption.

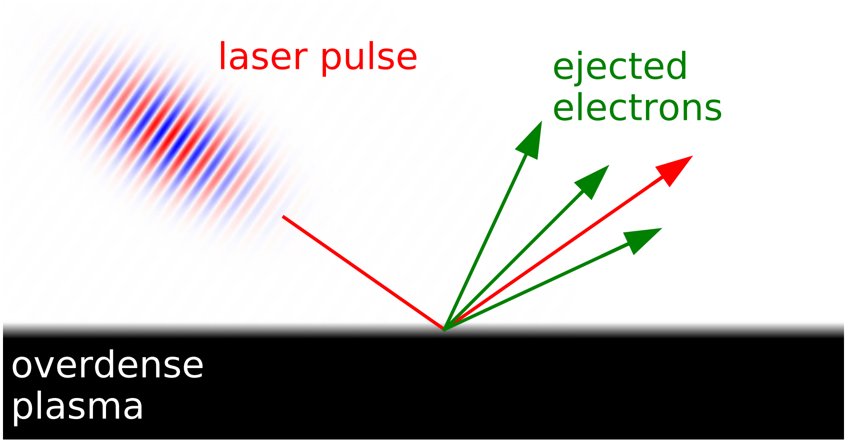

Figure 1.14: Schematic illustration of the acceleration of electrons (in green) from an overdense plasma in the backward direction.

1.4.2 Electron acceleration in the backward direction

We consider in this section the acceleration of electrons in the backward direction of an overdense target, as illustrated in figure 1.14. Electrons may also be accelerated in the forward direction when thin targets are used (this is in fact essential for most ion acceleration experiments), but we will only consider in this manuscript electron acceleration in the backward direction from thick targets. Even though electron acceleration experiments on thick solid targets with sub-100-fs relativistic intensity pulses have been performed more than 15 years ago [67], the mechanisms responsible for accelerating the electrons are well understood only in the case of very sharp gradients ($L \ll \lambda$). This is largely due to the lack of control on the preplasma in many experiments.

1.4.2.1 Electron acceleration at short gradients

We first consider the case of short gradient scale lengths ($L \ll \lambda$). The ejection of energetic electrons from the plasma in this regime has been fully described in [23, 61] using theory and PIC simulations in a 1D geometry (i.e. for an infinitely wide laser driver). We summarize this process in the following paragraphs.

When no density gradient is present on the front surface ($L = 0$), it is found that electrons are only ejected from the plasma if $a_0 > n_{MAX}/n_c$. For plasmas originating from solid targets, we usually have $n_{MAX} > 100n_c$. This means that, for present-day laser drivers with $a_0 < 100$, electrons cannot be ejected from a solid-density plasma with a step-like density profile. In this case, the electrons at the surface of the plasma have Brunel-like trajectories (see fig. 1.13). This is mainly due to the gyromagnetic effect [68]: when electrons are pulled out of the plasma by the laser electric field, the magnetic force tends to rotate these electrons back into the plasma.

The gyromagnetic effect can be overcome if strong electrostatic fields at the plasma surface help electron ejection. Such electrostatic fields become significant when decreasing the plasma density (hence the condition $a_0 > n_{MAX}/n_c$) or when adding a density gradient in front of the plasma. We will focus on the latter case since a plasma with a density gradient is easier to produce experimentally than a plasma

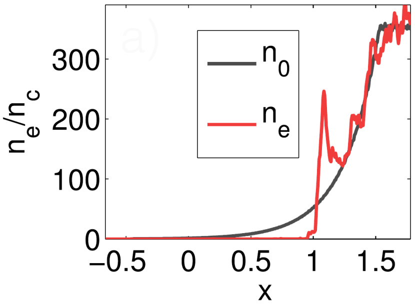

Figure 1.15: Image taken from [23]. Snapshot from a 1D PIC simulation showing the ion (grey) and electron (red) density profile during the interaction of a laser with $a_0 = 8$ and a plasma with an exponential density profile and $L = \lambda/16$ at $45°$ incidence.

with a step-like density profile and a density of a few n_c. Figure 1.15 shows a snapshot from a 1D PIC simulation of the interaction between a laser with $a_0 = 8$ and a plasma with an exponential density profile and $L = \lambda/16$. An important result is that, while the ions remain immobile, the surface electrons tend to regroup into a sharp **density peak** which oscillates following the sign of the laser field. The electrostatic field resulting from this charge separation is of great importance in the electron ejection process.

With these elements in mind, electron ejection from the plasma can be described with a two step **push-pull mechanism**, which is illustrated in figure 1.16. In the first step (the push phase), the normal component of the electric field of the laser E_z pushes electrons inside the plasma, creating a sharp density peak. As the electron density peak is pushed deeper into the density gradient, the immobile ions create a large restoring static field, resembling a plasma capacitor. The second step (the pull phase) starts when the sign of the electric field switches. Both the laser and the static field then work together to pull the electrons out of the plasma. If most electrons eventually return to the plasma, a small fraction of the electrons inside the density peak ($< 1\%$) gain enough energy from the plasma capacitor to escape from the plasma.

This process is in principle repeated for every cycle of the laser with a strong enough electric field in the density gradient direction. This results in a train of attosecond electron bunches at the exit of the plasma. It should be noted however that the ejected charge can significantly change between two consecutive cycles, meaning that electron ejection in one period can impact following periods in a non trivial way. In particular, with $\sim$25 fs pulses, it is not uncommon that most electrons are ejected before the temporal center of the pulse where the electric field is the strongest. This particular case can be explained by the fact that the charge separation induced by the ejection of electrons tends to prevent further electrons from escaping from the plasma.

An important feature of this mechanism is that electrons are ejected with a high velocity at a zero of the laser field. As will be seen in section 1.5, these are ideal conditions for the electrons to gain energy from their interaction in vacuum with the reflected laser field [27].

The push-pull mechanism requires a density gradient so that the plasma electrostatic field become substantial. However, if the gradient scale length is too large, the electrons no longer form a sharp density peak and the mechanism breaks. Electron acceleration at short density gradients is optimal when L is on the order of $\lambda/10$ for a $45°$ incidence angle. In this regime, the electrons are emitted around the specular

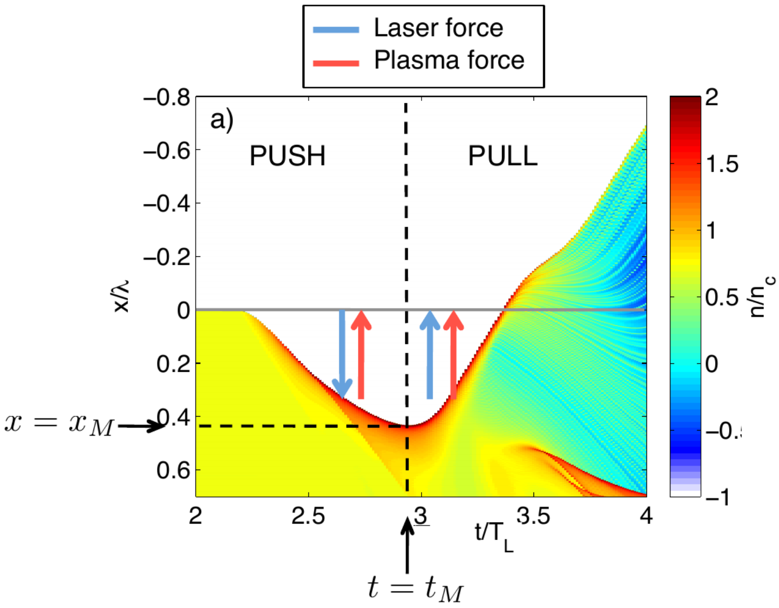

Figure 1.16: Illustration of the push-pull mechanism. In the push phase, the laser force pushes electrons inside the plasma while the immobile ions create a restoring plasma force. This results in an electron density peak. In the subsequent pull phase, both the laser and plasma force pull the electrons towards vacuum. Some of the electrons in the density peak are ejected in the process. Image taken from [61].

direction, with an angular distribution that is strongly impacted by the interaction of the electrons with the reflected laser pulse (see section 1.5.1.5).

1.4.2.2 Electron acceleration at long gradients

For longer gradient scale lengths, the mechanisms responsible for electron ejection are not that well understood. In recent experiments carried out at CEA Saclay [24] with a precise control of the preplasma, a transition from the push-pull mechanism to stochastic heating by the interference pattern formed between the incident and reflected pulse is found to occur when the gradient scale length exceeds $\lambda/4$ at 45° incidence. The gradient scale length at the transition decreases when the incidence angle increases.

Numerous experiments have been performed with a contrast such that the gradient scale length during the interaction is even larger ($L \sim \lambda$ or greater). Many have reported on the emission of relativistic electrons bunches, meaning that there are probably other electron acceleration mechanisms at play in this regime. However, due to the lack of precise control and knowledge of the preplasma density profile, there is a wide disparity of experimental results and if many mechanisms have been proposed (including resonant absorption [69, 70], ponderomotive acceleration [67], acceleration by surface quasistatic fields [71], laser wakefield acceleration [70, 72] or direct laser acceleration[6] [74, 75, 76]), it is still unclear which ones actually arise in experiments and the precise experimental conditions under which they

---

[6] Note that direct laser acceleration corresponds here to the acceleration of electrons oscillating in a plasma channel under the combined action of laser and plasma fields, as initially described in [73]. It is different from the acceleration of electrons by a laser pulse in vacuum, which will be described in section 1.5.

appear are not known. There is therefore a need for a better understanding of the interaction at long gradients, which requires experiments with a better control of the preplasma density profile.

1.4.3 High-harmonic generation

We give in this section a quick introduction to the two main mechanisms responsible for the emission of high-harmonics from overdense plasmas. Even though this is not the main topic of this thesis, high-harmonic generation is closely linked to electron acceleration in the short gradient regime and can provide a useful probe of the interaction. Unlike electrons, high-harmonics are only emitted at short gradients [24] ($L \ll \lambda$). Both the Coherent Wake Emission (**CWE**) and the Relativistic Oscillating Mirror (**ROM**) mechanisms will be briefly discussed in the following. For more details, a tutorial review on high-harmonic generation from plasma mirrors can be found in [29].

1.4.3.1 Coherent Wake Emission (CWE)

Coherent Wake Emission is the dominant high-harmonic generation mechanism at nonrelativistic intensities ($a_0 < 1$). It is caused by hot Brunel electrons (see section 1.4.1.3) propagating towards the plasma bulk. Brunel electrons returning earlier to the plasma tend to have a lower velocity than electrons reaching the plasma surface at a later time. As a result, the different electron trajectories will cross which results in the formation of an electron density peak. This density peak then triggers plasma waves which radiate coherently at the local plasma frequency. Since the whole process is repeated at every laser period, it leads to high-harmonics in the frequency domain. The maximum emitted frequency corresponds to the maximum plasma frequency and reads:

$$\omega_{CWEMAX} = \omega_{laser}\sqrt{\frac{n_{MAX}}{n_c}} \tag{1.65}$$

This frequency typically corresponds to a maximum harmonic order $\omega_{CWE}/\omega_{laser}$ ranging between 15 and 20.

The CWE mechanism is significant for gradient scale lengths ranging between approximately $\lambda/100$ and $\lambda/15$. This is lower than the gradient scale length required for electron ejection ($L \sim \lambda/10$). This means that electron and high-harmonic emission cannot occur simultaneously in the nonrelativistic regime, as was observed experimentally in [59].

1.4.3.2 Relativistic Oscillating Mirror (ROM)

The Relativistic Oscillating Mirror mechanism is the domimant high-harmonic generation mechanism in the relativistic regime. As we have seen in section 1.4.2.1 when a high-intensity laser is focused on an overdense plasma with an abrupt density gradient, a sharp electron density peak is formed while the ions remain mostly immobile. This density peak oscillates driven by the normal component of the laser electric field. If the laser has a relativistic intensity ($a_0 > 1$), these oscillations are strongly nonlinear and the electrons in the density peak radiate at high frequencies. Once again, since this process is repeated periodically, it leads to the generation of high-harmonics of the laser pulse in the frequency domain.

This mechanism is called the Relativistic Oscillating Mirror. Its name comes from the fact that the oscillating electron density peak can be seen as a mirror reflecting the incident pulse. At the times

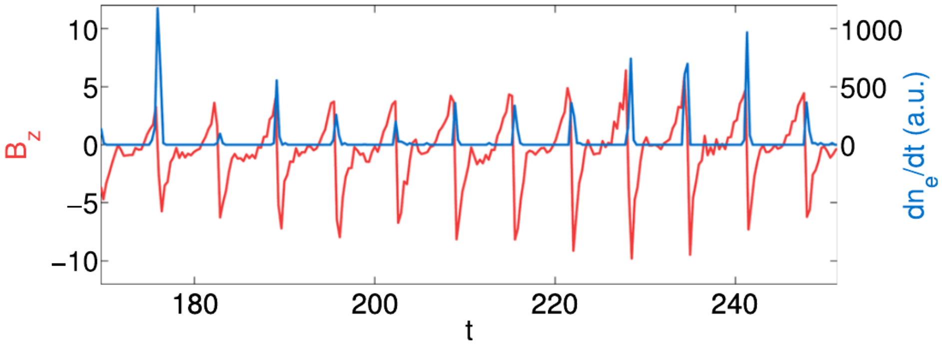

Figure 1.17: Snapshot from a 1D PIC simulation showing the reflected magnetic field (red) and ejected electron density (blue) at the plasma edge after the interaction of a laser with $a_0 = 5$ and $\tau = 24$ fs and a plasma with an exponential density profile and $L = \lambda/8$ at 45° incidence. We observe the simultaneous emission of high-harmonics via the ROM mechanism and attosecond electron bunches through the push-pull mechanism. It can be observed that the charge contained in each electron peak significantly varies from one cycle to the next. Image taken from [23].

when the mirror moves with a relativistic velocity towards vacuum, the frequency of the reflected pulse is strongly Doppler upshifted, thus leading to high frequencies.

We note that the process leading to electron ejection via the push-pull mechanism and high-harmonic generation through the ROM mechanism is essentially the same. In both cases, the emission comes from the nonlinear oscillation of the electron density peak. At every laser period, when the sign of the electric field switches, the density peak is pulled by both the laser field and the plasma static field towards vacuum and quickly reaches a relativistic speed. The electrons in the peak then radiate, forming an attosecond electromagnetic pulse, and a small part of them will be ejected from the plasma, forming an attosecond electron bunch. This means in particular that the ROM mechanism is efficient for the same gradient scale lengths as electron acceleration, typically around $\lambda/10$. Thus, unlike in the nonrelativistic regime, electrons and harmonics can be emitted simultaneously when $a_0 > 1$. This was confirmed experimentally [24] and is illustrated in figure 1.17, which has been obtained from a 1D PIC simulation.

1.5 Vacuum Laser Acceleration

When electrons are ejected from a plasma mirror by the push-pull mechanism presented in the previous section, they later interact with the reflected laser pulse and can even gain energy from it. The possibility of accelerating electrons directly from the laser fields has attracted considerable attention in the past decades. Indeed, many theoretical [77, 78, 79, 80, 81, 82] and numerical [83, 84, 85, 86] studies have been carried out with the prospects of understanding this fundamental interaction and profiting from the immense accelerating fields involved, that can exceed 10 TV/m - 2 orders of magnitude higher than what is commonly achieved in laser wakefield accelerators. However, if directly using the laser fields is conceptually the simplest method to accelerate electrons with lasers, it is not the easiest to achieve experimentally. This is because electrons are only efficiently accelerated when they remain for a long time in an accelerating phase of the laser pulse, which is challenging to accomplish.

We present in section 1.5.1 the main theoretical and experimental results regarding the acceleration of electrons by a linearly polarized laser field. In particular, we expose the conditions leading to an efficient accelerations and we show that plasma mirrors naturally fulfill these conditions and can thus serve as ideal injectors to achieve electron acceleration in the reflected laser pulse. In section 1.5.2, we present previous theoretical, numerical and experimental results concerning radially polarized beams, which possess an ideal structure for accelerating electrons in vacuum. The acceleration of electrons injected by a plasma mirror into a laser pulse with radial polarization will eventually be the main subject of chapters 4 and 5.

1.5.1 Vacuum Laser Acceleration with linear polarization

1.5.1.1 Acceleration principle

Let us consider a laser propagating along the z direction which is linearly polarized such that the electric field oscillates in the x-direction ($\boldsymbol{E} = E\boldsymbol{e}_x$) while the magnetic field oscillates in the y-direction ($\boldsymbol{B} = E/c\boldsymbol{e}_y$). It might seem conterintuitive that such a laser can accelerate electrons in vacuum along the longitudinal direction z, given that the accelerating $\boldsymbol{E}$ field is directed towards the transverse direction x. Indeed, in the nonrelativistic regime ($\beta_e \ll 1$, where $\beta_e = |\boldsymbol{v}_e|/c$ is the electron velocity relative to the speed of light), the laser will only make electrons oscillate in the polarization direction at the laser frequency, but cannot induce an acceleration in the longitudinal direction. On the other hand, in the relativistic regime the magnetic force must be taken into account and can lead to an acceleration in the longitudinal direction. To illustrate this acceleration principle, let us consider an electron moving with relativistic speed mainly along the direction of propagation of the laser pulse. This electron is subject to the electric force $\boldsymbol{F}_E = -e\boldsymbol{E}$ and to the magnetic force $\boldsymbol{F}_B = -e\boldsymbol{v_e} \times \boldsymbol{B}$. Three cases can be considered.

The first case, illustrated in figure 1.18(a), corresponds to an electron moving exactly along the z-axis. In this case, the electric and magnetic forces have opposite directions but the magnetic force is weaker by a factor β_e, which results in a total force with magnitude $(1-\beta_e)|e\boldsymbol{E}|$ oriented towards $-\boldsymbol{E}$. The electric force dominates in the nonrelativistic regime while the magnetic force virtually compensates the electric force in the ultrarelativistic regime. The net effect of the laser in this case is a deflection of the electron in the transverse direction.

The second case, illustrated in figure 1.18(b), corresponds to an electron moving with an angle θ_x with respect to the z-axis in the direction of the electric force. Compared to the previous case, the electric force is still oriented along the x-axis but the magnetic force is rotated so that it remains perpendicular to the velocity. The resulting total force induced by the laser tends to increase the electron momentum both in the z-direction and the x-direction: the electron gains energy. Such an electron is said to be in an **accelerating phase** of the laser. Several points can be noted:

- Only the electric force does work, while only the magnetic force has a component in the longitudinal direction. The acceleration process can thus be seen as the laser electric field providing kinetic energy to the electron in the transverse direction while the laser magnetic field rotates the electron towards the longitudinal direction.

- An electron gaining energy will always see an increase in its transverse momentum. This means that electrons accelerated by a linearly polarized laser will tend to be pushed to the side of the beam.

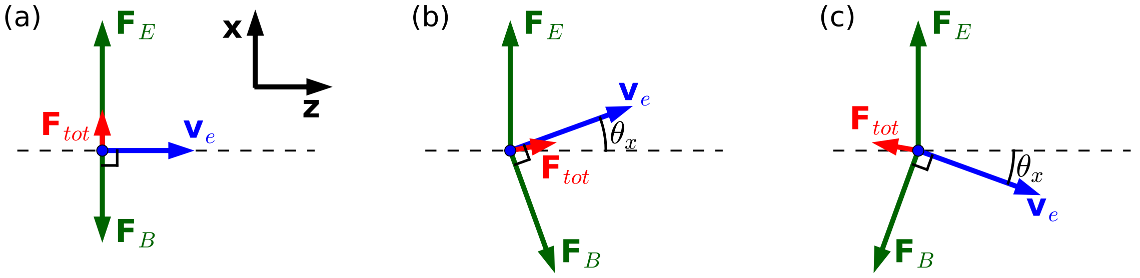

Figure 1.18: Schematic illustration of the forces acting on a relativistic electron interacting with a linearly polarized laser. The blue dot represents an electron moving with a velocity $\boldsymbol{v}_e$ in the direction indicated by the blue arrow. The green arrows represent either the electric force $\boldsymbol{F}_E$ or the magnetic force $\boldsymbol{F}_B$ acting on the electron while the red arrows represent the total force $\boldsymbol{F}_{tot}$ acting on the electron. The dashed black lines show the z-axis. In (a), the electron is moving along the z direction and is deflected by the laser field. In (b), the electron is moving with an angle θ_x with respect to the z-axis such that it is accelerated by the laser field. In (c), the electron is moving with an angle θ_x with respect to the z-axis such that it is decelerated by the laser field. Note that in (a) the electron is mildly relativistic ($\beta_e = 0.7$) so that the total force remains appreciable while in (b) and (c) the electron is ultrarelativistic ($\beta_e \approx 1$).

- The total force acting on the electron is not zero, even in the ultrarelativistic limit for which the force has a magnitude of $\sqrt{2(1-\cos\theta_x)}|e\boldsymbol{E}|$.

- For $\beta_e < \cos\theta_x$, the total force makes an angle greater than θ_x with respect to the z-axis and the laser is decollimating. On the other hand, if the electron is fast enough so that $\beta_e > \cos\theta_x$, the total force makes an angle smaller than θ_x with respect to the z-axis and the laser is collimating. In the ultrarelativistic limit ($\beta_e \approx 1$), the angle made by the force with respect to the z-axis is minimal at a value of $\theta_x/2$ and the laser is collimating.

The third case, illustrated in figure 1.18(c), corresponds to an electron moving with an angle θ_x with respect to the z-axis in the direction opposite to the electric force. This case is essentially the opposite of the previous case and can be obtained by simply changing the sign of the electromagnetic fields, which correspond to shifting the laser phase by π. The resulting total force induced by the laser tends to decrease the electron momentum both in the z-direction and the x-direction: the electron loses energy. Such an electron is said to be in an **decelerating phase** of the laser. We note in particular that an electron which sees a decrease in its transverse momentum will also see a decrease in its longitudinal momentum and lose energy.

In reality, an electron can oscillate between these three situations during its interaction with a linearly polarized pulse. It will gain a significant amount of energy if it remains in an accelerating phase of the laser for a long enough time.

It is worth noting that we have considered here an electron with no velocity $v_{e,y}$ in the transverse y direction. Since the laser force has no component in this direction, $v_{e,y}$ is indeed 0 at all times provided that $v_{e,y} = 0$ initially. Our previous study is valid in this scenario. If $v_{e,y}$ is different from 0, two main changes occur:

- The electron will drift in the y direction with a constant momentum $p_{e,y}$.
- The magnetic force is reduced, which leads to weaker accelerating fields in the longitudinal direction and thus to less efficient acceleration. The ideal case therefore corresponds to $v_{e,y} = 0$, which we have studied before and which results in a two-dimensional electron motion in the $z-x$ plane.

We finally mention that we have not considered the case of electrons contrapropagating with the laser, which is of lesser interest as electrons are not efficiently accelerated in this situation.

1.5.1.2 1D conservation laws

We make the assumption in this section that the laser field is one-dimensional: it only depends on the variable $t-z/c$. It is entirely characterized by its magnetic vector potential $\boldsymbol{A}$, which reads, in the Coulomb gauge ($\boldsymbol{\nabla}.\boldsymbol{A} = 0$) :

$$\boldsymbol{A} = A(t-z/c)\boldsymbol{e}_x \tag{1.66}$$

The resulting electric and magnetic fields are then given by:

$$\boldsymbol{E} = E(t-z/c)\boldsymbol{e}_x \tag{1.67}$$

$$\boldsymbol{B} = \frac{E(t-z/c)}{c}\boldsymbol{e}_y \tag{1.68}$$

Where $E = -\partial_t A$. We define $a = \frac{eA}{m_e c}$ as the normalized vector potential and $\boldsymbol{u}_e = \frac{\boldsymbol{p}_e}{m_e c}$ as the normalized electron momentum. We will see that in one dimension, there are three constants of motion which determine the evolution of the three components of $\boldsymbol{u}_e$.

The first two constants of motion are obtained from the conservation of canonical momentum, which comes from the assumed invariance along the x and y directions. Along the x direction the constant of motion is given by $u_{e,x} - a$. We can then obtain the normalized momentum in the x direction $u_{e,x}$ as a function of the laser field a and the initial conditions:

$$u_{e,x} = u_{e,xi} + a - a_i \tag{1.69}$$

Where $u_{e,xi}$ denotes the initial normalized momentum in the x direction and a_i the laser normalized magnetic potential at the initial position of the electron. Along the y direction, there is no vector potential and we thus simply obtain the conservation of the electron momentum:

$$u_{e,y} = u_{e,yi} \tag{1.70}$$

The third constant can be obtained from the equation of motion projected along the z direction and the equation stating the conservation of energy:

$$\frac{du_{e,z}}{dt} = -\frac{e}{m_e c}\beta_{e,x}E \tag{1.71}$$

$$\frac{d\gamma_e}{dt} = -\frac{e}{m_e c^2}v_{e,x}E = -\frac{e}{m_e c}\beta_{e,x}E \tag{1.72}$$

We note that the right hand side is the same in the two equations, which means that the quantity $u_{e,z} - \gamma_e$, where γ_e is the electron Lorentz factor, is the desired third constant of motion. After some algebra and using the relation $\gamma_e^2 = u_{e,x}^2 + u_{e,y}^2 + u_{e,z}^2$ we can express either $u_{e,z}$ or γ_e as a function of $u_{e,x}$ and the initial conditions. The result is:

$$u_{e,z} = \frac{1 + u_{e,x}^2 + u_{e,yi}^2 - (\gamma_{e,i} - u_{e,zi})^2}{2\,(\gamma_{e,i} - u_{e,zi})} \tag{1.73}$$

$$\gamma_e = \frac{1 + u_{e,x}^2 + u_{e,yi}^2 + (\gamma_{e,i} - u_{e,zi})^2}{2\,(\gamma_{e,i} - u_{e,zi})} \tag{1.74}$$

In one dimension, the sole knowledge of the laser fields allow us to determine consecutively $u_{e,x}$ and $u_{e,z}$ as a function of the initial conditions. We once again remark here, consistently with the previous section, that an increase in the longitudinal momentum or the energy of the electron always comes with an increase in its transverse momentum.

Sometimes these equations can be integrated to obtain the electron trajectory $x_e(a)$, $y_e(a)$ and $z_e(a)$ as we will see in the next section in the case of a plane wave. Even when this is not possible, useful information can be obtained from these conservation laws.

Let us for example examine the common case of a pulse, so that $a \to 0$ when either $t - z/c \to -\infty$ (early in front of the pulse) or $t - z/c \to +\infty$ (far behind the pulse). In particular, the normalized potential is always 0 at the end of the interaction ($t \to +\infty$) after the electron has overtaken the laser. We consider two distinct cases:

1. The initial vector potential is zero: $a_i = 0$. This corresponds to an electron initially in front of the pulse or, for an approximately sinusoidal laser potential, inside the pulse around a maximum of the electric field (the latter could correspond for example to an electron generated by field ionization). Since a is the same at the beginning and at the end of the interaction and the momentum only depends on a and the initial conditions, we conclude that there is zero net momentum change from the interaction. In this case, the electron oscillates in the laser field but the accelerating phases exactly compensate the decelerating phases and the electron eventually does not gain energy.

2. The initial vector potential different from zero: $a_i \neq 0$. The variation of the transverse momentum in this case is given by $\Delta u_{e,x} = \Delta a$, where Δa is the difference between the final and the initial normalized vector potential. Then, the variation of the longitudinal momentum and of the Lorentz factor is given by $\Delta u_{e,z} = \Delta\gamma_e = \dfrac{\Delta(u_{e,x}^2)}{2\,(\gamma_{e,i} - u_{e,zi})}$. In this case, there is a net energy change and the electron can be effectively accelerated by the laser pulse. The energy gain is maximum when the initial vector potential is either minimum (if $u_{e,xi}$ is positive) or maximum (if $u_{e,xi}$ is negative), thus leading to the highest $\Delta(u_{e,x}^2)$. **This ideal scenario corresponds to an electron initially inside the pulse at a zero of the electric field.** Physically, it means that the electron starts with a whole accelerating half-cycle that will not be entirely compensated by the subsequent decelerating phases.

Overall, this means that an electron can gain energy from a laser pulse either because it begins its interaction inside the pulse, which allows it to convert initial magnetic potential into momentum, or because of transverse variations in the laser field.

1.5.1.3 Electron motion in a plane wave

We now consider the particular case of a plane wave, for which the trajectories can be obtained analytically. In this case, the normalized magnetic vector potential is given by:

$$\boldsymbol{a} = a_0 \cos(\omega(t - z/c))\boldsymbol{e}_x = a_0 \cos\phi\, \boldsymbol{e}_x \tag{1.75}$$

Where ω is the plane wave frequency and $\phi \equiv \omega(t - z/c)$ denotes its phase. The resulting electric and magnetic fields are:

$$\boldsymbol{E} = E_0 \sin\phi\, \boldsymbol{e}_x \tag{1.76}$$

$$\boldsymbol{B} = \frac{E_0}{c} \sin\phi\, \boldsymbol{e}_y \tag{1.77}$$

With $E_0 = m_e c \omega a_0 / e$. To simplify the equations, we will consider an electron with no initial transverse momentum $\boldsymbol{u}_{e,i} = u_{e,zi}\boldsymbol{e}_z$ which starts its interaction at the optimal initial phase. This optimal phase corresponds to a zero of the electric field and we choose $\phi_i = 0$, resulting in $a_i = a_0$. As an illustration, we plot in figure 1.19 electron trajectories corresponding to 3 different choices for a_0 and $\gamma_{e,i}$.

The conservation laws for the transverse momentum can be written very simply:

$$u_{e,y} = 0 \tag{1.78}$$

$$u_{e,x}(\phi) = a_0 (\cos\phi - 1) \tag{1.79}$$

The motion is two-dimensional in the $x - z$ plane because the electron has no initial velocity in the y direction. In this case, the electron oscillates in the x direction with a negative average momentum that is equal to the conserved canonical momentum. With our choice of initial conditions, this result in a drift of the electron towards negative x positions. The only case with no transverse drift thus corresponds to zero canonical momentum, which is the worst scenario in terms of maximum reached energy. We thus see another reason why electrons tend to be pushed to the side of the beam as they are accelerated with linear polarization: not only are the accelerating fields transverse, but the most favorable initial conditions result in a transverse drift of the electrons.

After some algebra (a more detailed derivation can be found in [77]), we can also express the longitudinal momentum and Lorentz factor as a function of ϕ:

$$u_{e,z}(\phi) = \gamma_{e,i}\left(\beta_{e,zi} + \frac{a_0^2}{2}(\cos\phi - 1)^2 (1 + \beta_{e,zi})\right) \tag{1.80}$$

$$\gamma_e(\phi) = \gamma_{e,i}\left(1 + \frac{a_0^2}{2}(\cos\phi - 1)^2 (1 + \beta_{e,zi})\right) \tag{1.81}$$

Where $\beta_{e,zi} = u_{e,zi}/\gamma_{e,i}$ is the initial electron velocity along the z direction. Several points can be noted:

- If $u_{e,zi} \geq 0$, then $u_{e,z} \geq 0$ at all times. In other words, if the electron initially moves in the direction of laser propagation, it will never be contrapropagating with the laser. This is always true in the absence of initial transverse momentum. In this case, the electron will therefore drift both towards the positive z direction and the negative x direction, as can be seen in figures 1.19(j) to (l).

- The laser is accelerating for $0 < \phi < \pi$ and decelerating for $\pi < \phi < 2\pi$.

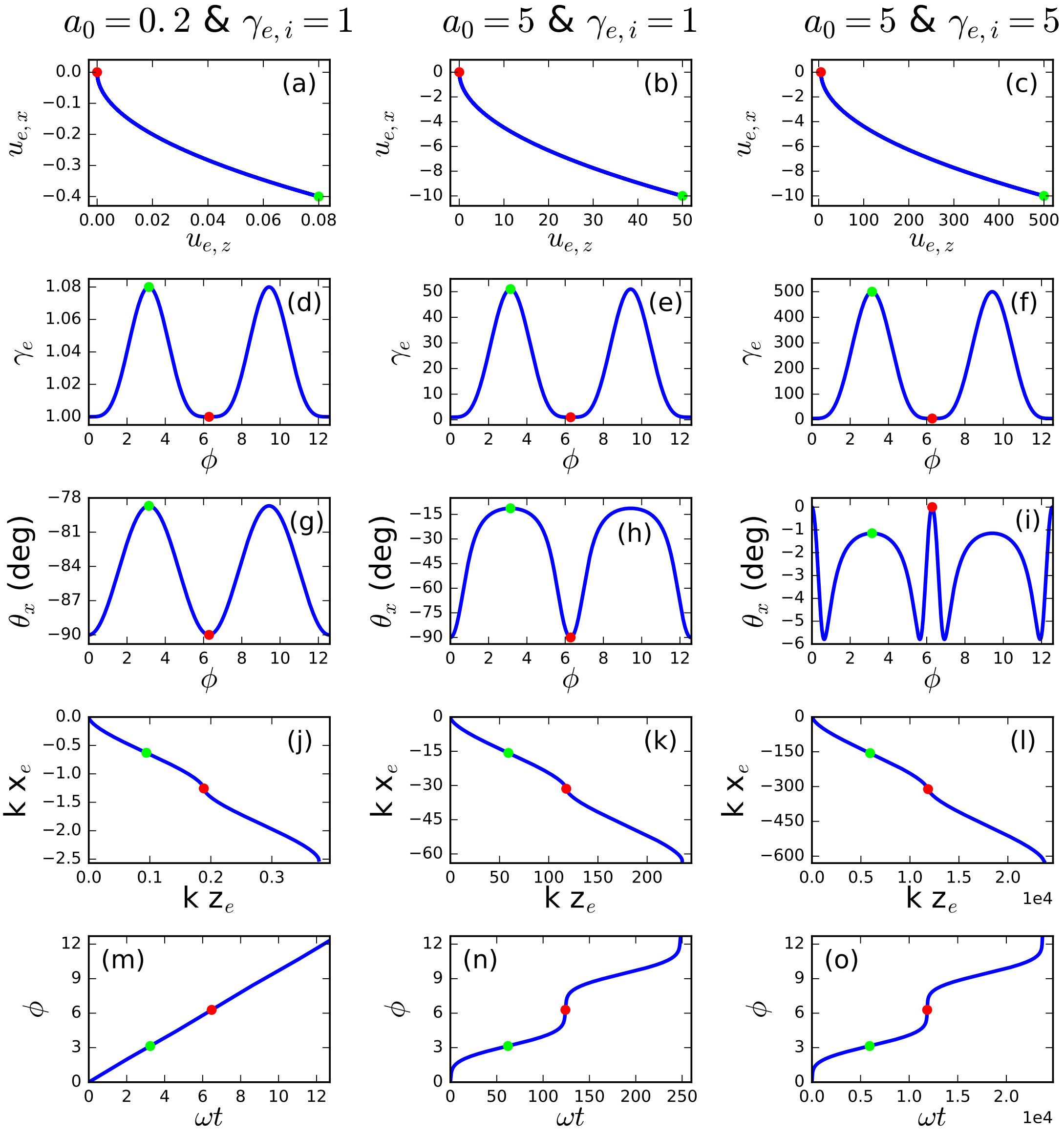

Figure 1.19: Electron trajectories in a plane wave. In the left panels, the plane wave is nonrelativistic ($a_0 = 0.2$) and the electron has no initial velocity. In the middle panels, the plane wave is relativistic ($a_0 = 5$) and the electron has no initial velocity. In the right panels, the plane wave is relativistic ($a_0 = 5$) and the electron has a significant initial velocity, corresponding to a kinetic energy of ≈ 2 MeV, in the longitudinal direction. In all cases, the electron has no transverse momentum at the initial phase $\phi = 0$. (a)-(c) Trajectories in momentum space. (d)-(f) Lorentz factor as a function of the phase seen by the electron. (g)-(i) Angle θ_x with respect to the z-axis as a function of the phase seen by the electron. (j)-(l) Trajectories in real space. (m)-(o) Phase seen by the electron as a function of time. In all images, the green dot shows a point where the electron energy is maximum while the red dot shows a point where the electron energy is minimum.

- The highest reached energy gain is proportional to $\Delta\gamma_e = 2\gamma_{e,i}a_0^2(1+\beta_{e,zi})$. Unsurprisingly, the energy gain grows when increasing either the laser normalized amplitude, which results in stronger accelerating fields, or the initial electron velocity, which results in a longer time spent in an accelerating phase. The possible energy gain in a given plane wave is unbounded: any value can be reached provided that the initial velocity is chosen high enough.

- As stated previously, an accelerated electron sees an increase in both its transverse and longitudinal momentum. However, the maximum change in the transverse momentum is simply proportional to a_0, while the maximum change in the longitudinal momentum is proportional to a_0^2 and also increases with the initial energy. Thus, electrons reaching high energy (high $\gamma_{e,i}$ and a_0) tend to be mainly accelerated in the longitudinal direction, while electrons with a lower energy have a motion which is mainly in the transverse direction, as is illustrated by the different scales in figures 1.19(a) to (c) and (j) to (l). This can be quantified by the angle θ_x that the electron momentum makes with respect to the z axis, which is such that $\tan\theta_x = u_{e,x}/u_{e,z}$. At the position where the energy is maximum, this angle is:

  $$\tan\theta_x = \frac{2a_0}{\gamma_{e,i}\left(\beta_{e,zi}+2a_0^2(1+\beta_{e,zi})\right)} \tag{1.82}$$

  In the limit where $a_0^2 \gg 1$, this expression becomes:

  $$\tan\theta_x = \frac{1}{\gamma_{e,i}a_0(1+\beta_{e,zi})} \tag{1.83}$$

  These expressions are useful to estimate the emission angle of electrons accelerated by a linearly polarized pulse. Low energy electrons tend to be accelerated with large angles while high energy electrons are accelerated closer to the optical axis, as can be seen in figure 1.19(g) to (i).

The transverse position $x(\phi)$ can be obtained by integrating $\frac{dx}{d\phi} = \frac{dx(\phi)}{dt}\frac{dt}{d\phi}$. Indeed, both $\frac{dx(\phi)}{dt} = \frac{cu_{e,x}(\phi)}{\gamma_e(\phi)}$ and $\frac{dt}{d\phi} = \left(\frac{d\phi}{dt}\right)^{-1} = \left(\omega\left(1-\frac{u_{e,x}(\phi)}{\gamma_e(\phi)}\right)\right)^{-1}$ are known. The longitudinal position $z(\phi)$ can be obtained in a similar manner. In the case of a plane wave, the integration can be performed analytically and the result is, with our choice of initial conditions (see [77] for more details):

$$kx(\phi) = a_0\gamma_{e,i}(1+\beta_{e,zi})(\sin\phi-\phi) \tag{1.84}$$

$$kz(\phi) = \frac{1}{2(1-\beta_{e,zi})}\left[\left(2\beta_{e,zi}+\frac{3}{2}a_0^2(1+\beta_{e,zi})\right)\phi - 2a_0^2(1+\beta_{e,zi})\sin\phi + \frac{a_0^2}{4}(1+\beta_{e,zi})\sin 2\phi\right] \tag{1.85}$$

Where we have assumed that the electron is initially at $x=z=0$. In the transverse direction, the electron motion is the combination of an oscillation with a quivering amplitude x_{quiv} of $a_0\gamma_{e,i}(1+\beta_{e,zi})\frac{\lambda}{2\pi}$ and of a drift of $a_0\gamma_{e,i}(1+\beta_{e,zi})\lambda$ per cycle. In the longitudinal direction, the laser advances by $\frac{2\beta_{e,zi}+\frac{3}{2}a_0^2(1+\beta_{e,zi})}{2(1-\beta_{e,zi})}\lambda$ per cycle. It is common to define the dephasing length Z_{deph} as the distance traveled by the electron during an accelerating phase, which is in this case:

$$Z_{deph} = z(\phi=\pi) = \frac{2\beta_{e,zi}+\frac{3}{2}a_0^2(1+\beta_{e,zi})}{4(1-\beta_{e,zi})}\lambda \tag{1.86}$$

Finally, we plot in figures 1.19(m) to (o) the plane wave phase ϕ seen by the electron as a function of time. As expected, the electron spends a longer time in phases for which it has a relativistic energy since it dephases more slowly with respect to the laser in this case.

1.5.1.4 Electron motion in a laser pulse

The previous 1D calculations are useful as they provide an intuition as well as orders of magnitudes regarding the interaction between an electron and a laser in vacuum. In reality, a laser pulse has a finite transverse extent and thus diffracts, which results in several important changes:

- An electron can exit the laser pulse if its transverse excursion exceeds the beam radius $w(z)$, thus effectively ending the interaction.
- The interaction can also end if the electron remains in the pulse long enough so that the laser fields have become negligible due to diffraction.
- Another effect of diffraction is the Gouy phase shift, which induces an extra phase of π as the laser beam passes through focus. **This leads to a superluminal phase velocity on the axis at focus that makes the electron dephase more rapidly with respect to the laser.** The Gouy phase has a negative effect on electron acceleration as it reduces the time an electron can spend in an accelerating cycle at the positions where the laser is most intense.
- Unlike in a plane wave, the laser intensity depends on the transverse position. One consequence is that an electron oscillating through multiple laser cycles will be pushed by the ponderomotive force to regions of lower intensities. The derivation of the relativistic ponderomotive force $\boldsymbol{F}_{pond}$ experienced by an electron in a laser beam is given in reference [80] and relies on averaging the electron motion over the fast oscillations, as was done in the case of plasma wave formation in the linear regime (see section 1.3.1). The result is:

  $$\boldsymbol{F}_{pond} = -\frac{e^2}{2m_e\overline{\gamma_e^2}}\boldsymbol{\nabla}\overline{\boldsymbol{A}_{perp}^2} \tag{1.87}$$

  Where $\overline{q}$ denotes the average of quantity q over the laser oscillations and $\boldsymbol{A}_{perp}$ is the transverse magnetic vector potential in the Coulomb gauge. This expression is valid provided that the electron velocity is not too fast in the longitudinal z direction so that an averaging over the fast oscillations can be performed. In the case of a Gaussian beam, it will result in a force that is independent in the direction of polarization and that pushes the electrons isotropically towards the side of the beam.
- We have stated in the previous section that the possible energy gain in a plane wave is unbounded. This is no longer the case for a beam with a finite transverse extent. This is because the accelerating field is transverse and therefore an energy gain necessarily results from a displacement in the transverse direction. An upper bound for the energy gain can be obtained by considering an electron traveling from $x=-\infty$ to $x=+\infty$ while remaining at the phase corresponding to the maximum accelerating field [79]:

  $$\Delta W_{MAX} = e\int_{-\infty}^{+\infty} E_x(t)v_{e,x}dt \tag{1.88}$$

  $$\Delta W_{MAX} = e\int_{-\infty}^{+\infty} E_x(x)dx \tag{1.89}$$

For a Gaussian laser, we have at most $E_x(x) = E_0 \exp(-(x/w_0)^2)$, where E_0 is the peak electric field and w_0 is the beam waist. The result of the integral is then:

$$\Delta W_{MAX} = eE_0 w_0 \sqrt{\pi} \tag{1.90}$$

Noting that $E_0 w_0$ is proportional to the square root of the laser peak power (see section 1.1), we can rewrite this expression as:

$$\Delta W_{MAX} = \frac{2e}{\sqrt{c\varepsilon_0}} \sqrt{P} \tag{1.91}$$

In practical units, this result becomes:

$$\Delta W_{MAX}[\mathrm{MeV}] \approx 39\sqrt{P[\mathrm{TW}]} \tag{1.92}$$

Two important points should be noted:

1. This value has been obtained by assuming that the electron remains at the optimal phase throughout its trajectory *and* that diffraction is negligible during the interaction (i.e. the electron travels much less than a Rayleigh length in the longitudinal direction as it passes through the beam). Satisfying both conditions is most likely impossible, which means that the maximum energy gain given by equation 1.92 cannot even be approached in practice.
2. This scaling law means that accelerating electrons in vacuum is not adapted for reaching high energy gains. For instance, with a 10 PW laser, the energy gain cannot exceed 4 GeV. For comparison, 8 GeV electron beams have been obtained from laser wakefield acceleration using a PW-class laser [19]. On the other hand, this method could be well-suited for producing MeV electron beams, which could be useful for applications such as ultrafast electron diffration, and can in principle be obtained from sub-TW laser systems.

Unlike in a plane wave, there is no analytical expression for the trajectories of electrons in a realistic laser pulse and one has to resort to test-particle simulations, whose principle will be presented in section 2.1, to study quantitatively this process. In simulations, two typical electron trajectories, corresponding to two extreme cases, can be found [61]:

- First, electrons that see many laser oscillations tend to be mainly affected by the ponderomotive force. The succession of accelerating and decelerating phases leads in this case to low energy gains. Electrons are isotropically scattered in the transverse direction which leads to axisymmetric angular distributions which are characterized by the presence of a hole in the direction of laser propagation. The intrinsic isotropy of the ponderomotive force means that the interaction of a laser with an electron bunch is inherently a 3D process, which cannot be properly reproduced in 2D simulations. The fastest electrons tend to be accelerated closer to the laser propagation direction than the slowest ones. This regime of acceleration is called the **ponderomotive** regime[7]. A typical electron trajectory and electron angular distribution in this regime is shown in figure 1.20.
- At the other end, electrons remaining for a long time in an accelerating phase of the laser can reach considerably higher energies. In order to obtain a net energy gain, the electron must not

---

[7] The term *ponderomotive scattering* is also often used.

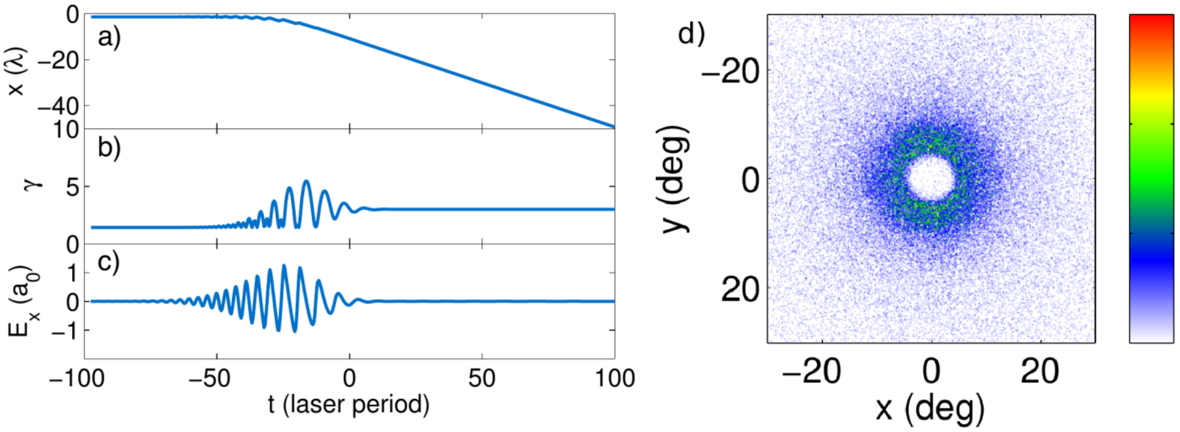

Figure 1.20: Ponderomotive electron dynamics in a linearly polarized (in the x direction) laser with $a_0 = 4$, $w_0 = 5\,\mu\mathrm{m}$ and $\tau = 30$ fs obtained from test-particle simulations. Panels (a) to (c) show the trajectory of an electron beginning its interaction in front of the laser with an initial momentum $u_{e,zi} = 1$ (corresponding to $\gamma_{e,i} \approx 1.4$ and $\beta_{e,zi} \approx 0.71$) and transverse initial positions $x_{e,i} = -1.5\ \lambda$ and $y_{e,i} = 1.1\ \lambda$. The electron sees many laser oscillations and is eventually scattered towards the side of the beam with a low energy gain ($\gamma_e = 3$ at the end). (d) Final angular distribution of a bunch of electrons initially on the optical axis in front of the laser pulse with an average initial momentum $u_{e,zi} = 1$. The initial electron distribution is Gaussian both in real space and momentum space, with $\sigma_x = \sigma_y = 3.1\lambda$, $\sigma_z = 0.1\lambda$, $\sigma_{ux} = \sigma_{uy} = 0.1$ and $\sigma_{uz} = 1$. The electron bunch and the laser overlap around focus. The angular distribution after interaction is isotropic with a hole in the laser propagation direction. Images taken from [61].

lose this energy in the following decelerating cycles. This can occur if the electron exits the pulse transversally after being accelerated ($x_{quiv} \sim w_0$) or if it remains in an accelerating cycle long enough so that the next decelerating cycle is diminished due to diffraction ($Z_{deph} > z_R$). In this case, electrons are emitted in the direction of polarization of the laser, which leads to nonisotropic angular distributions. It is once again observed that faster electrons are directed closer to the optical axis. This more efficient regime of acceleration is known as **Vacuum Laser Acceleration (VLA)**[8], and is usually aimed for in experiments. A typical electron trajectory and electron angular distribution in this regime is shown in figure 1.21.

The conditions leading to an efficient acceleration and to high energy gains are the following:

- The electron should start its interaction **inside the laser pulse**, near the beam spatial and temporal

---

[8] We can note that the use of the term *Vacuum Laser Acceleration (VLA)* is not standardized. In some articles, this term is used to refer both to the regime where electrons remain for a long time at a given phase of the laser (sometimes labeled the *subcycle* regime) and to the ponderomotive regime [87, 76]. Sometimes, a different term may be used. In particular, use of the word *direct* is frequent, especially in the case of radially polarized lasers (e.g. *direct electron acceleration* [88], *direct laser acceleration* [89], *direct-field electron acceleration* [90] or simply *direct acceleration* [91]). However, this may be confused with the direct laser acceleration mechanism occuring in plasma channels initially described in [73]. Finally, some authors do not use a specific term and use instead unambiguous but longer expressions such as *electron acceleration by laser fields in vacuum* [78]. In this manuscript, we will only use the term *Vacuum Laser Acceleration (VLA)* to describe the regime where electrons remain for a long time at a given phase of the laser (subcycle regime) and we will not use a specific term which emcompasses both the VLA and ponderomotive regimes.

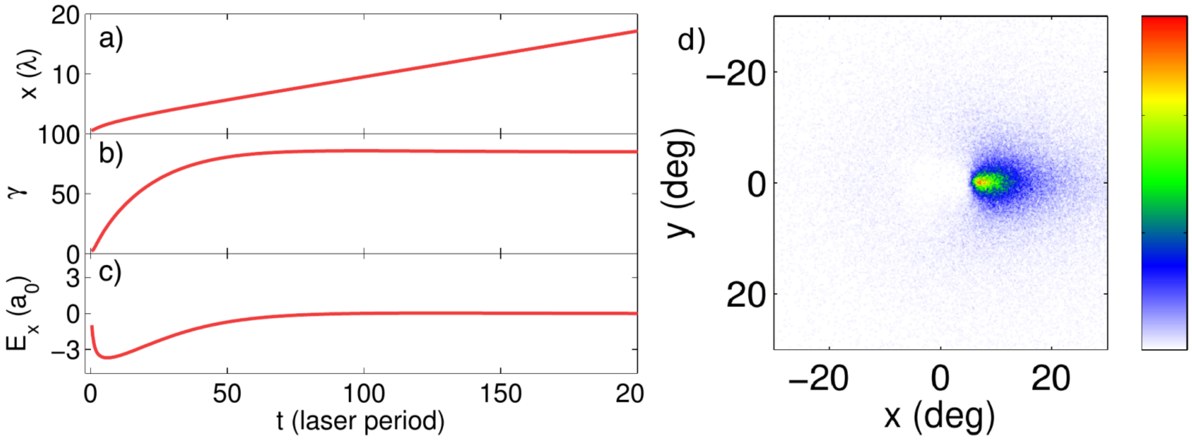

Figure 1.21: VLA electron dynamics in a linearly polarized (in the x direction) laser with $a_0 = 4$, $w_0 = 5\ \mu\mathrm{m}$ and $\tau = 30$ fs obtained from test-particle simulations. Panels (a) to (c) show the trajectory of an electron beginning its interaction inside the laser at focus, close to a zero of the electric field ($\phi_i/2\pi = -0.1$, with $E_x \propto \sin\phi$), with an initial momentum $u_{e,zi} = 1$ (corresponding to $\gamma_{e,i} \approx 1.4$ and $\beta_{e,zi} \approx 0.71$) and transverse initial positions $x_{e,i} = 0.6\ \lambda$ and $y_{e,i} = 0$. The electron remains for a long time in an accelerating cycle, which results in a high energy gain ($\gamma_e = 100$ at the end). (d) Final angular distribution of a bunch of electrons initially on the optical axis inside the laser pulse at focus, around a zero of the electric field, with an average initial momentum $u_{e,zi} = 1$. The initial electron distribution is Gaussian both in real space and momentum space, with $\sigma_x = \sigma_y = 3.1\lambda$, $\sigma_z = 0.1\lambda$, $\sigma_{ux} = \sigma_{uy} = 0.1$ and $\sigma_{uz} = 1$. The angular distribution after interaction is characterized by a bright spot in the polarization direction. Images taken from [61].

intensity maxima and **close to a zero of the electric field**. This is similar to the 1D case where the electron benefits from the ensuing initial canonical momentum. It means that the electron begins its interaction with an accelerating half-cycle and is thus more likely to be trapped for a long time in this accelerating phase.

- The electron should have a **relativistic initial velocity** in the direction of propagation of the laser beam. This reduces the dephasing between the electron and the laser and allows to electron to spend more time in the accelerating cycle[9].

Electrons that satisfy these conditions tend to have VLA trajectories while electron that do not satisfy these requirements tend to have ponderomotive trajectories. As an example, the only difference between figure 1.20, which illustrates ponderomotive behavior, and 1.21, which illustrates VLA behavior, is that the electrons are initially in front of the laser pulse in the former case, while they are inside the laser pulse around the optimal phase in the latter case.

1.5.1.5 Experiments with linear polarization

If VLA has been studied theoretically and numerically for the past 25 years, it has proved difficult to observe experimentally. This is because it is extremely challenging to inject an electron bunch with a relativistic velocity at a precise phase inside a laser pulse. Historically, two methods have been used to inject an electron into an intense laser field.

The first one is the **ionization of a low density gas** target by the laser pulse itself [92, 93]. In this case, the density must be chosen low enough to ensure that no plasma effects occur during the interaction. While the first ionized electrons are created early in front of the pulse, this method offers the possibility of generating electrons deep inside the laser pulse if at least one the barrier suppression intensity thresholds of the elements making up the gas target is matched to the laser peak intensity. However, the electrons are created in this case near the maxima of the electric field, where the transverse canonical momentum is small, and without initial velocity. These conditions are far from optimal and lead to low energy gains. For instance, in reference [93], 300 keV electrons have been detected in the polarization plane using a 400-fs laser with $a_0 = 1.5$ ($I_0 = 3 \times 10^{18}\,\mathrm{W/cm^2}$ with $\lambda = 1\,\mu\mathrm{m}$). The fact that electrons are detected in the polarization plane even though the VLA regime is not attained might seem inconsistent with the isotropic nature of the ponderomotive regime. However, in this case the electrons have a nonzero initial transverse canonical momentum if they are not ionized exactly at a maximum of the electric field, which will result in a drift of the electron in the polarization diretion. The electron feels the ponderomotive force, but this initial momentum in the polarization plane still affects the final angular distribution.

The second method for electron injection is the use of a **pre-existing electron beam** that is copropagating with the laser pulse. In reference [94], this was done by focusing a 750-ps long prepulse onto a thin plastic target, which creates electrons with an initial energy of a few tens of keV. Then, using a

---

[9] However, it should be noted that if the initial momentum in the z direction is too high, the electron will barely be deflected by the laser, which will result in a low energy gain (since energy gains arise from a transverse displacement of the electron in linear polarization). The initial conditions leading to an efficient acceleration of an initially ultrarelativistic ($\gamma_e \gg 1$) electron are more complex and can involve the electron having an initial transverse momentum or starting the interaction far from focus. It can even sometimes be beneficial for the electron to lose part of its initial energy at the beginning of the interaction so that it can regain more energy later on.

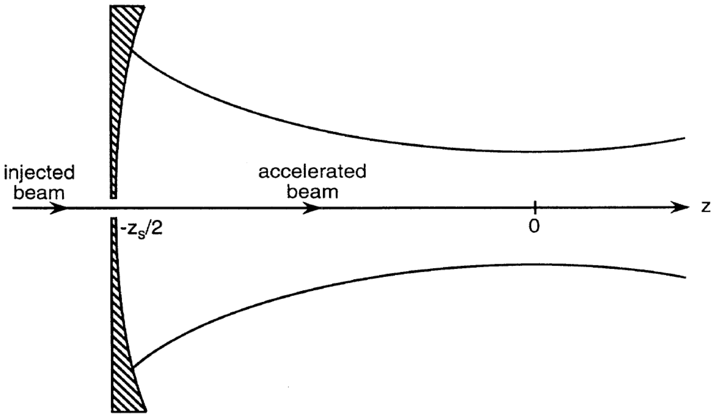

Figure 1.22: Setup for accelerating a pre-accelerated electron bunch with a laser pulse in vacuum. The electrons pass through a hole in the focusing parabolic mirrord. The laser pulse and the electron beam can then meet at focus. Image taken from [78].

main pulse with $\tau = 400$ fs, $w_0 = 10\,\mu\mathrm{m}$ and $a_0 = 3$, the authors observed electrons with an energy up to 1 MeV in the polarization plane, making an angle $\theta_x \sim 45^\circ$ with respect to the laser propagation direction. However, these results still remain controversial [95, 96] since in this regime the ponderomotive force is supposed to be dominant and result in an isotropic electron angular distribution [80]. Indeed, the fact that electron were detected in the polarization plane is more consistent with an ionization injection scenario than with an pre-existing electron beam in front of the laser pulse.

A more common possibility to generate the pre-accelerated electron beam is to use a conventional accelerator such as a DC gun or a linac. In this case, a parabolic mirror with a hole in its center can be used to let the electron bunch pass while focusing the laser beam. This setup, initially proposed in [78], is illustrated in figure 1.22. The main drawback of this scheme resides in the fact that the electron beam is initially in front of the laser pulse, which is not a favorable scenario. Injecting the electron beam close to the laser spatial intensity maximum would require placing an optical element around focus, which would thus be damaged by the high intensities involved during experiments. Even if this was not an issue, injecting the electrons at a precise phase of the laser would necessitate an electron beam with attosecond duration in synchronization with the laser, which is beyond the reach of current technology. In practice, the electron beam will span over multiple laser wavelengths. This means that some electrons will be accelerated while other will be decelerated by the laser, which eventually results in an increase of the electron beam energy spread. For example, an experiment was performed in 2012 using the method presented in figure 1.22 at the Brookhaven National Laboratory [87]. In the experiments, a 20-MeV electron beam is generated with a linear accelerator. When a copropagating $\mathrm{CO_2}$ laser pulse with $a_0 \sim 1$ is focused onto the electrons, an slight increase in the electron beam energy spread is observed, thereby illustrating the difficulties associated with this injection method.

More recently, it was demonstrated that plasma mirrors could also be used to inject electrons into a laser beam. We have indeed seen in section 1.4.2.1 that focusing a relativistic intensity laser onto an overdense plasma with a sharp density gradient on its front surface leads to the periodic emission of electrons, via the push-pull mechanism, that can then interact with the reflected pulse. Moreover, these electrons are injected at a precise phase of the laser, near a zero of the electric field, with a relativistic velocity in the direction of the reflected pulse. These are precisely the optimal injection conditions that we have identified in the previous section. We can thus expect to observe the VLA regime if the laser pulse has a sufficient intensity.

This was indeed confirmed by an experiment performed with the UHI100 laser at CEA Saclay [27]. In the experiments, 25-fs pulses with $\lambda = 800$ nm, $w_0 = 5.5\,\mu\mathrm{m}$ and $a_0 \approx 3.1$ impinge on an overdense plasma with a controllable density gradient. A typical experimental angular distribution obtained at the optimal gradient scale length for electron emission in the short gradient regime ($L \sim \lambda/15$) is displayed in figure 1.23(a). This distribution is characterized by a hole in the specular direction surrounded by an isotropic halo of electrons and a bright spot located in the polarization plane, between the specular and normal directions. The intuitive interpretation of this result is that the isotropic halo correspond to electrons having ponderomotive trajectories, while the bright spot in the incident plane correspond to electrons having VLA trajectories. This explanation is supported by the fact that electrons in the bright spot have a higher energy (~ 10 MeV) than electrons in the isotropic halo (~ 5 MeV), as can be seen in figure 1.23(b).

In order to confirm this physical interpretation, test-particle simulations of the interaction between an electron beam initially close to a zero of the electric field and the reflected laser pulse (neglecting its high-harmonic content) were carried out. By adjusting the initial electron beam parameters, an excellent agreement with the experiments could be found, as is visible in figures 1.23(c) and (d). The test-particle simulations can then be used to extract information regarding the electron trajectories. In figure 1.24, the electrons are sorted depending on the number of laser optical cycles N_{oc} that they see during their interaction with the reflected laser. As expected, the isotropic halo corresponds to electrons that experience many oscillations and are scattered by the ponderomotive force, while the bright spot in the polarization plane corresponds to electrons who undergo Vacuum Laser Acceleration. This experiment constituted the first clear experimental observation of electrons accelerated in the VLA regime and confirmed that **plasma mirrors can be used as ideal injectors for accelerating electrons in vacuum**.

1.5.1.6 Ponderomotive regime for few-cycle pulses

The expression of the ponderomotive force has been obtained by averaging the electron motion over the laser oscillations. One might wonder whether this concept is still relevant for pulses only consisting of a few optical oscillations. I have briefly examined this matter by performing test-particle simulations of the interaction of an electron bunch with a laser pulse in the ponderomotive regime.

In the simulations, the electrons all have the same initial longitudinal momentum $u_{e,zi} = 1$ (corresponding to $\gamma_{e,i} \approx 1.4$ and $\beta_{e,zi} \approx 0.71$) and have no transverse momentum. The electron bunch has a Gaussian distribution in real space with $\sigma_x = \sigma_y = 3.1\lambda$ and $\sigma_z = 0.1\lambda$, where $\lambda = 800$ nm is the laser wavelength. The electrons interact with a laser pulse with $w_0 = 5\,\mu\mathrm{m}$, $a_0 = 4$ and either $\tau = 30$ fs or $\tau = 3.5$ fs. The electron bunch is initially in front of the pulse, which should lead to a ponderomotive scattering of the electrons. The laser meets the electrons around $t = 0$ and $z = 0$, which corresponds to its envelope temporal and spatial maxima.

The final angular distributions in the simulations are displayed in figure 1.25. We observe in both cases an isotropic scattering of the electron bunch, which is a signature of the ponderomotive regime. Even though further studies could probably be done on the subject, these simulations show that the concept of the ponderomotive force is still relevant for few-cycle pulses.

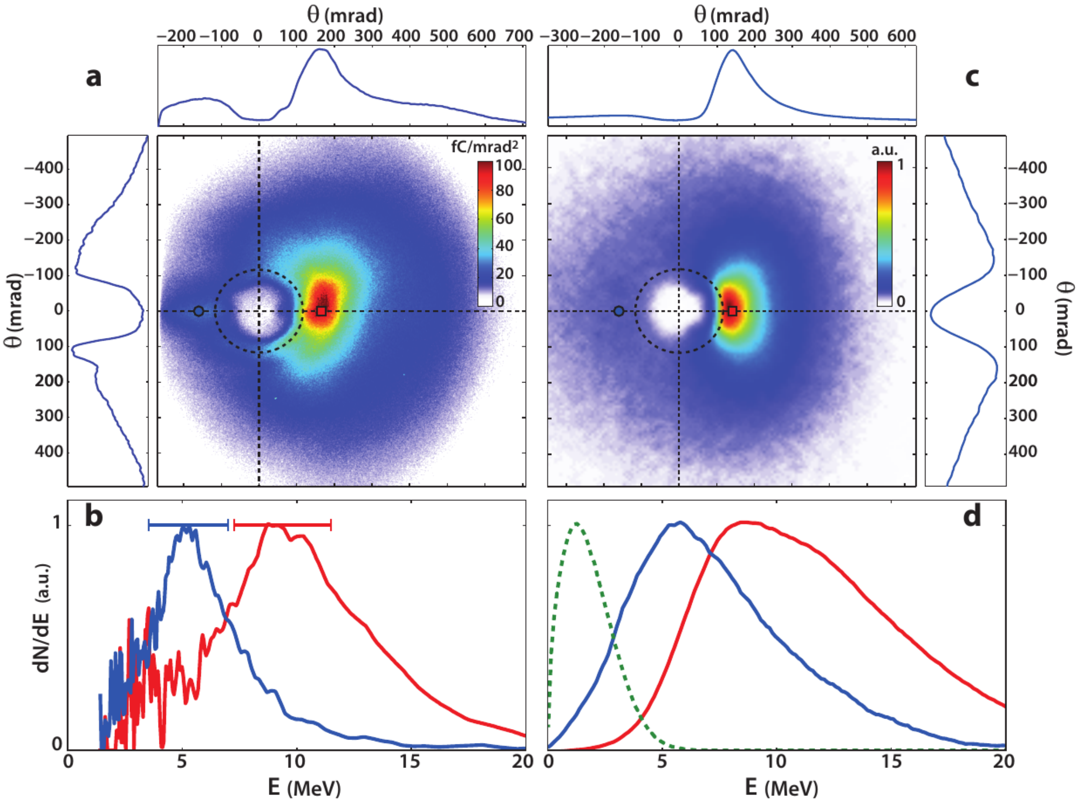

Figure 1.23: (a) Typical experimental angular distribution of electrons emitted from a plasma mirror obtained with the UHI100 laser. The side panels show the values of the distribution along the dashed line, while the dashed circle shows the angular extent of the reflected beam. (b) Electron energy spectra measured at the position of the red square and the blue circle in (a). Panel (c) and (d) show the same quantities but obtained from a test-particle simulation. The green dashed curve in (d) shows the initial energy spectrum in the simulation, which indicates that electrons have been accelerated in vacuum from ~ 1.5 *MeV to* ~ 10 *MeV in experiments. Image taken from [61].*

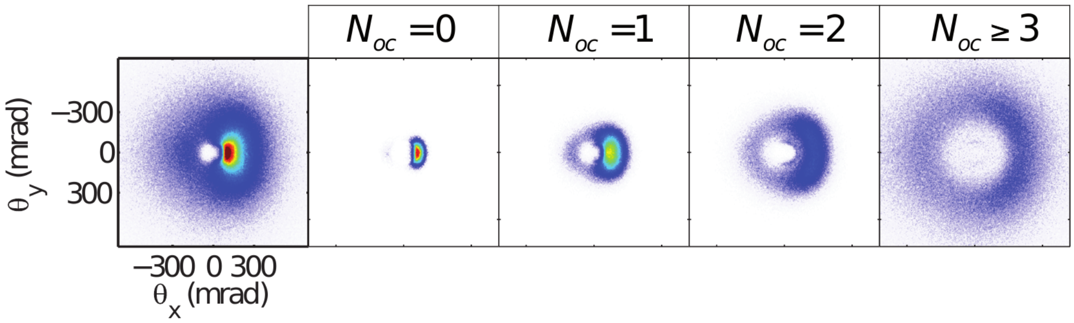

Figure 1.24: Angular distributions of several electron populations which are separated depending on the number of laser optical cycles N_{oc} that they experience in the test-particle simulation. Image taken from [61].

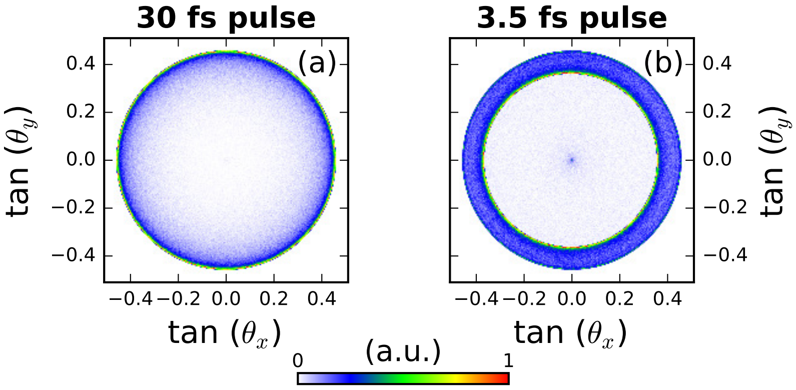

Figure 1.25: Results from test-particle simulations. Final angular distributions of an electron bunch initially in front of a (a) 30 fs or a (b) 3.5 fs laser pulse with $a_0 = 4$.

1.5.2 Vacuum Laser Acceleration with radial polarization

1.5.2.1 Introduction to radial polarization

When VLA is carried out with linearly polarized pulses, the accelerating fields are transverse. This means that the electrons are pushed off the optical axis as they are accelerated, which tends to widen the resulting angular distributions. For this reason, the possibility of accelerating electrons with longitudinal (i.e. in the direction of propagation of the laser) fields has frequently been studied [78, 97, 98, 99, 100, 101, 102, 90, 91, 88, 89, 103, 104, 105, 106, 107]. The existence of longitudinal electromagnetic field components is a consequence of Gauss's law in vacuum ($\boldsymbol{\nabla}.\boldsymbol{E} = 0$) when there is a variation of the transverse fields in the polarization direction. As an example, let us consider a beam which is linearly polarized in the x direction so that we can assume that $E_y = 0$. In this case, Gauss's law reads:

$$\frac{\partial E_x}{\partial x} + \frac{\partial E_z}{\partial z} = 0 \tag{1.93}$$

We can see that whenever there is a transverse variation of the E_x field, a nonzero longitudinal field must also be present. In fact, taking longitudinal fields into account is crucial in the description of the ponderomotive force presented in the previous section [80]. Equation 1.93 also tells us that large variations in the transverse field lead to large E_z field amplitudes. Therefore, tight focusings result in a more important contribution from the longitudinal field. We can estimate the transverse and longitudinal variations of the fields as $\left|\frac{\partial E_x}{\partial x}\right| \sim \frac{|E_x|}{w_0}$ and $\left|\frac{\partial E_z}{\partial z}\right| \sim k|E_z|$. This allows us to roughly evaluate the amplitude of the longitudinal field in a linearly polarized beam:

$$|E_z| \sim \frac{|E_x|}{kw_0} \sim \frac{\lambda}{2\pi w_0}|E_x| \tag{1.94}$$

We note that the longitudinal field becomes significant only when the beam waist is on the order of the laser wavelength. More precisely, the amplitude at focus of the longitudinal field in a linearly polarized Gaussian beam can be calculated to first order with respect to the small parameter $1/(kw_0)$, resulting in [80]:

$$|E_z| = \frac{2E_0}{kw_0}\frac{x}{w_0}\exp\left(\frac{-r^2}{w_0^2}\right) \tag{1.95}$$

Where E_0 is the peak amplitude of the transverse field. The amplitude of the E_x and E_z fields on the x-axis at the focus of a linearly polarized Gaussian beam is shown in figures 1.26(a) and (b). As expected, the longitudinal field only acquires significant values at positions where the E_x field varies rapidly. In particular, the E_z field amplitude is 0 on the plane $x = 0$ and maximum for $x = \pm w_0/\sqrt{2}$. We also note that the longitudinal field is much weaker than the transverse field, even for an extreme focusing ($w_0 = \lambda$), consistently with the previous scaling $E_z \sim \frac{\lambda}{2\pi w_0}|E_x|$.

Directly using the E_z field of a linearly polarized pulse for accelerating electrons in the longitudinal direction would not be very effective because:

- As we have just seen, the E_z field has a weak amplitude for linear polarization.
- The longitudinal field is maximum in a region with strong transverse fields. This means that even if electrons were to gain energy from the E_z field, they would still be deflected by the E_x field.

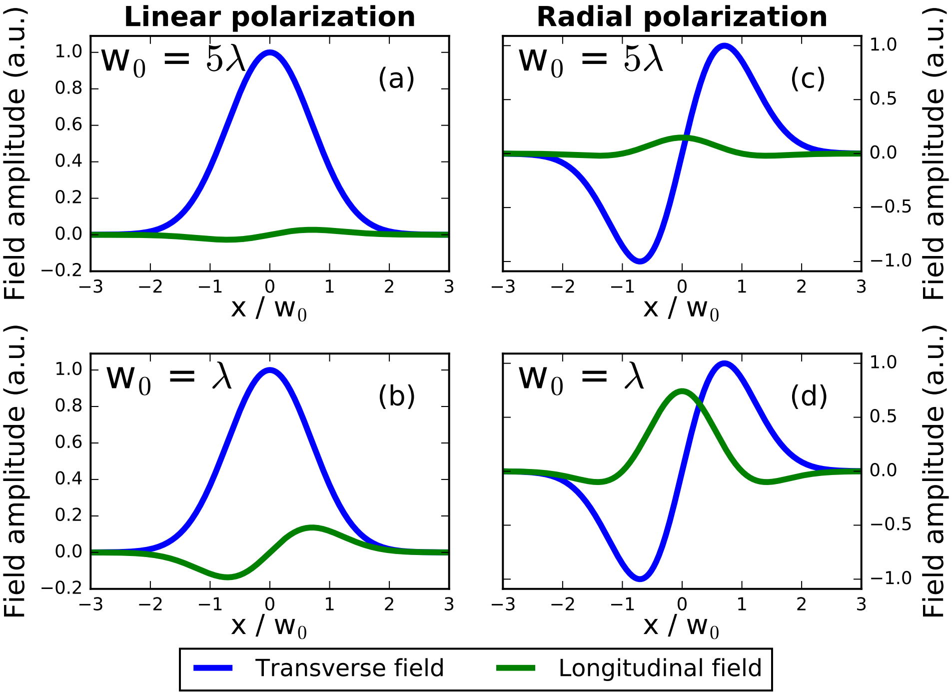

Figure 1.26: Amplitude at focus on the x-axis of the transverse (blue curve) and longitudinal (green curve) electric field in the case of a linearly polarized beam with $w_0 = 5\lambda$ (a), a linearly polarized beam with $w_0 = \lambda$ (b), a radially polarized beam with $w_0 = 5\lambda$ (c) and a radially polarized beam with $w_0 = \lambda$ (d).

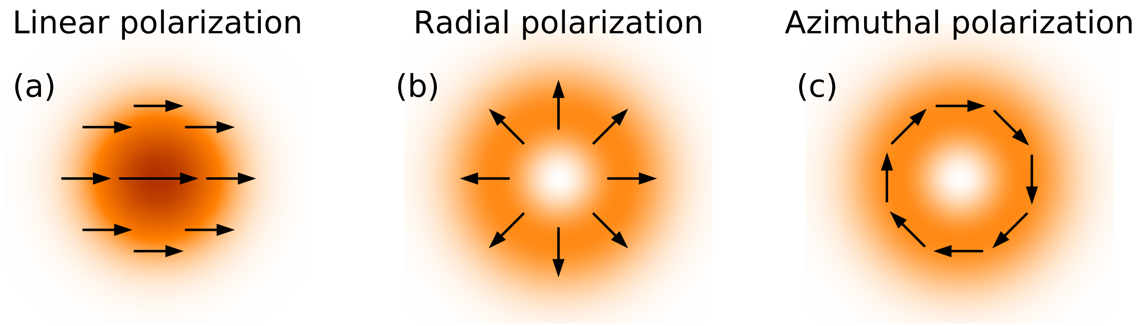

Figure 1.27: Typical intensity distribution at focus of (a) a linearly polarized beam, (b) a radially polarized beam and (c) an azimuthally polarized beam. The arrows show the local direction of the electric field.

Both issues can be solved if **radially polarized pulses** are used instead of linearly polarized pulses. A laser is radially polarized if at every position the polarization points towards its center, as is illustrated in figure 1.27(b). Such beams have a rotational symmetry and are consequently described using cylindrical coordinates (r, θ, z). The radial electric field E_r vanishes on the optical axis (otherwise there would be a singularity at $r = 0$), which results in intensity profiles with a characteristic doughnut-shape. The magnetic field of a radially polarized beam only has an azimuthal component B_θ.

At focus on the optical axis, there is a strong variation of the radial E_r field in the polarization direction, which results in a strong longitudinal electric field E_z, as can be seen in figures 1.26(c) and (d). The ratio between the peak amplitude of the longitudinal field and the peak amplitude of the radial field is $\approx 0.742\dfrac{\lambda}{w_0}$ for radial polarization, compared to $\approx 0.137\dfrac{\lambda}{w_0}$ for linear polarization. For extreme focusings $(w_0 \sim \lambda)$, the longitudinal field even becomes comparable to the radial field, as is apparent in figure 1.26(d). Moreover, the E_z is maximum in a region where the transverse fields vanish. This is particularly attractive for vacuum laser acceleration as it means that, unlike in the case of linear polarization, an electron located close to the optical axis can be accelerated by the strong longitudinal field of a radially polarized beam without being deflected. The prospects of obtaining more collimated and more energetic electron beams from VLA in this different acceleration scenario explain why radially polarized beams have attracted considerable attention in the past two decades [78, 97, 98, 99, 100, 101, 102, 90, 91, 88, 89, 103, 104, 105, 106, 107].

Figure 1.28 illustrates another common explanation for the emergence of a strong longitudinal field with radial polarization. Far from focus, the beam is either converging or diverging and its electric field possesses both a longitudinal (in the z direction) and a transverse component. For a linearly polarized beam, the longitudinal components interfere destructively on the axis at focus while the transverse components interfere constructively. On the other hand, for a radially polarized beam, the transverse components interfere destructively while the longitudinal components interfere constructively, which results in a strong E_z field in a region with no transverse field.

Altough there are other methods for producing radially polarized beams [108, 109, 110, 111, 112], a phase mask consisting of four or eight half-wave plates with different optical axes, as shown in figure 1.29, is usually used to convert the laser polarization from linear to radial. This method has been used to obtain

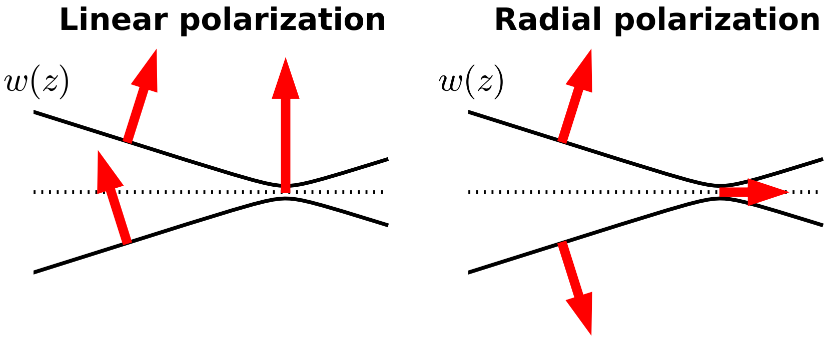

Figure 1.28: Schematic illustration explaining the presence of a strong longitudinal field for radially polarized beams. On the optical axis at focus, the longitudinal fields interfere destructively for linear polarization, resulting in a pure transverse field, but interfere constructively for radial polarization, resulting in a strong longitudinal field.

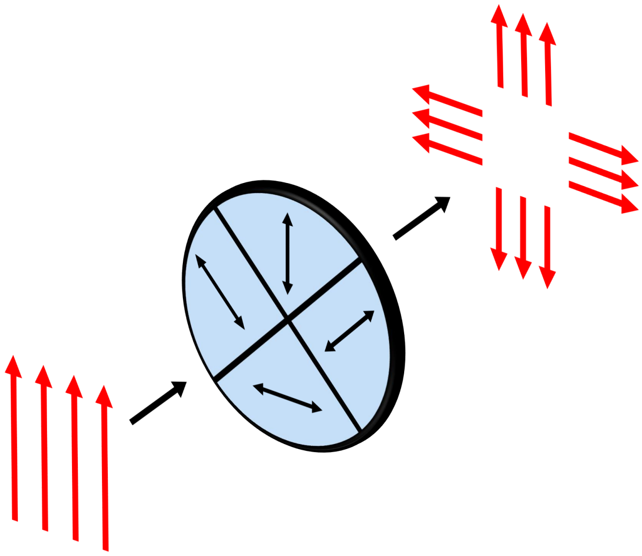

Figure 1.29: Schematic illustration of the conversion from linear to radial polarization using a segmented waveplate consisting of 4 half-wave plates. The red arrows represent the laser polarization while the black arrows show the half-wave plates fast optical axis.

radial polarization in all previous experiments with high-intensity laser pulses [113, 114, 115].

We conclude this section by introducing azimuthally polarized lasers, for which the electric field E_θ is in the azimuthal direction, as illustrated in figure 1.27(c). Azimuthally polarized beams are similar to radially polarized beams but have the electric and magnetic fields "exchanged", meaning that the main components of such pulses are E_θ, B_r and B_z. They do not exhibit an E_z field and therefore cannot directly accelerate electrons in the longitudinal direction. This polarization state is often studied concurrently with radial polarization in experiments since it can be generated in the same manner simply by turning the waveplate (or the laser initial polarization) by $\pi/2$.

We will present in the following sections the principal previous results that have been obtained regarding electron acceleration with radially polarized lasers.

1.5.2.2 Fields of a radially polarized pulse

To lowest order, the nonzero components of a radially polarized pulse within the paraxial approximation are given by the following expressions, in cylindrical coordinates [100]:

$$E_r(\boldsymbol{r},t) = E_{0,z}\left(\frac{w_0}{w(z)}\right)^2 \frac{kr}{2}\exp\left(-\frac{r^2}{w(z)^2}\right)\cos\phi\, g\left(t-\frac{z}{c}\right) \tag{1.96}$$

$$B_\theta(\boldsymbol{r},t) = \frac{E_r(\boldsymbol{r},t)}{c} \tag{1.97}$$

$$E_z(\boldsymbol{r},t) = E_{0,z}\left(\frac{w_0}{w(z)}\right)^2 \exp\left(-\frac{r^2}{w(z)^2}\right)\left[-\left(1-\frac{r^2}{w(z)^2}\right)\sin\phi - \frac{kr^2}{2R(z)}\cos\phi\right] g\left(t-\frac{z}{c}\right) \tag{1.98}$$

Where $E_{0,z}$ is the peak amplitude of the longitudinal field and $\phi = kz - \omega t + k\frac{r^2}{2R(z)} - 2\arctan\left(\frac{z}{z_R}\right) + \phi_{CEP}$ is the phase of the beam. The other quantities are the same as for linearly polarized Gaussian beams: w_0 is the beam waist, $z_R = \pi w_0^2/\lambda$ is the Rayleigh length, $w(z) = w_0\sqrt{1+z^2/z_R^2}$ is the beam radius at position z, $R(z) = z + z_R^2/z$ is the radius of curvature and g is a temporal envelope. Several important comments can be made simply from these expressions:

- The radial field is maximum at the transverse position $r = w(z)/\sqrt{2}$. At focus, the peak amplitude of this field is given by $E_{0,r} = \dfrac{kw_0}{2\exp(1/2)\sqrt{2}}E_{0,z}$. It is common to define the normalized peak amplitude of the radial and longitudinal field as $a_{0,r} = eE_{0,r}/(m_e c\omega)$ and $a_{0,z} = eE_{0,z}/(m_e c\omega)$. We obviously still have $a_{0,r} = \dfrac{kw_0}{2\exp(1/2)\sqrt{2}}a_{0,z}$, which becomes in practical units the relation $a_{0,z} \approx 0.742\dfrac{\lambda}{w_0}a_{0,r}$ that we have given in the previous section. The longitudinal field is therefore substantial only in the case of very tight focusing. We could even in principle have $a_{0,z} > a_{0,r}$, but this would require $w_0 < 0.742\lambda$ which is challenging to achieve in practice (this corresponds to $w_0 < 600$ nm for $\lambda = 800$ nm).
- Out of focus, the peak amplitude of the radial field varies as $E_{r,0}\dfrac{w_0}{w(z)}$ while the peak amplitude of the longitudinal field varies as $E_{z,0}\left(\dfrac{w_0}{w(z)}\right)^2$. Thus, the longitudinal field decreases more rapidly than the radial field as the beam diffracts. This is consistent with the fact that the longitudinal field is associated with a transverse radiation of the radial field, which is most important at focus[10].

---

[10] Strictly speaking, the maximum of the E_z field as given by equation 1.98 very far from focus ($|z| \gg z_R$) is obtained at position $r = w(z)$ and corresponds to the term in $\cos\phi$, which varies as $\dfrac{w_0}{w(z)}$. At this transverse position ($r = w(z)$), the E_z and E_r fields are in phase and the total electric field is perpendicular to the curve $w(z)$ ($E_z/E_r = -dw(z)/dz$). This means that the term

Laser system	**Salle Noire**	**UHI100**
Central wavelength	800 nm	800 nm
Pulse energy	$\approx$ 2.5 mJ	$\approx$ 460 mJ
Pulse duration	3.5 fs	24 fs
Peak power	$\approx$ 670 GW	$\approx$ 18 TW
w_0	$1.5\,\mu\mathrm{m}$	$3.2\,\mu\mathrm{m}$
a_0 (linear polarization)	≈ 2.7	≈ 5.2
$a_{0,r}$ (radial polarization)	≈ 1.7	≈ 3.2
$a_{0,z}$ (radial polarization)	≈ 0.67	≈ 0.59
ΔW_{MAX} (eq. 1.121)	≈ 25 MeV	≈ 130 MeV

Table 1.4: Typical on-target parameters of the Salle Noire and UHI100 laser systems. The last three lines show the normalized field amplitudes as well as the maximum energy gain that could be expected with radial polarization.

- The peak power of a radially polarized pulse is given by [88]:

$$P = \varepsilon_0 c \frac{\pi w_0^2}{4} \exp(1) E_{0,r}^2 \tag{1.99}$$

This relation allows us to compare the normalized amplitudes $a_{0,z}$ and $a_{0,r}$ of a radially polarized beam to the normalized amplitude a_0 of a linearly polarized Gaussian beam with the same peak power and beam waist:

$$a_{0,z} = \frac{\sqrt{2}}{\pi}\frac{\lambda_0}{w_0} a_0 \approx 0.45 \frac{\lambda_0}{w_0} a_0 \tag{1.100}$$

$$a_{0,r} = \exp\left(-\frac{1}{2}\right) a_0 \approx 0.61 a_0 \tag{1.101}$$

We note in particular that the peak electric field of a radially polarized pulse is smaller than the peak electric field of a linearly polarized pulse with similar laser parameters. As an example, we show in table 1.4 the field amplitudes that could be expected from radially polarized pulses generated from either the Salle Noire or UHI100 laser system. We note that we can expect in both cases longitudinal electric field values on the order of $a_{0,z} \sim 0.6$. Even though they are not relativistic, these values remain high enough to make these lasers potentially suitable to study longitudinal electron acceleration in vacuum.

- On the optical axis $r = 0$, only the longitudinal electric field E_z is nonzero. This means that an electron initially on the optical axis with no transverse momentum will remain on the optical axis throughout the interaction. As a result, many of the previous results regarding electron acceleration with radially polarized beam have been obtained for on-axis electrons, since it greatly simplifies the

---

proportional to $\cos\phi$ in the expression of E_z is in fact a part of the transverse field which acquires a nonzero component in the z direction because of the beam curvature (the component in the z direction far from focus in figure 1.28). The truly longitudinal component thus corresponds to the term in $\sin\phi$ in equation 1.98 and varies as $\left(\frac{w_0}{w(z)}\right)^2$, as noted in the main text.

study of the interaction. In particular, all theoretical studies on the subject consider an electron on the optical axis, while transverse effects are taken into account via numerical simulations. A review of the theory of on-axis electron acceleration by a radially polarized beam will be presented in the next section.

- Electrons can also have plane trajectories. This happens for example for an electron initially in the plane $y = 0$ with no initial velocity along the y direction. This may be used the simplify the study of the transverse dynamics of an electron accelerated by a radially polarized beam, as will be done for instance in chapter 4.

- We notice that the Gouy phase shift for a radially polarized laser is twice as important as for a linearly polarized laser. This is essentially because radial polarization, as given by equations 1.96-1.98, is a first-order mode, which can for instance be obtained by combining two Laguerre-Gauss modes with radial index $p = 0$ and azimuthal index $l = 1$ which are perpendicular to each other [116]. The Gouy phase shift leads to an extra phase of 2π as the laser passes through focus. This means that an on-axis electron interacting with the beam from $z = -\infty$ to $z = \infty$ will experience at least one full accelerating half-cycle and one full decelerating half-cycle. This unavoidable dephasing between the electron and the laser constitutes in fact one of the principal limitations (along with the field amplitude decrease due to diffraction) to the energy that an electron can gain from a radially polarized pulse, as will be seen in the next section. The Gouy phase shift results in a superluminal phase velocity on the axis at focus that is even higher than for linear polarization. On the axis $r = 0$, the phase velocity reads [88]:

$$v_\phi = \frac{c}{1 - \dfrac{(\lambda/w_0)^2}{\pi^2\left(1 + (z/z_R)^2\right)}} \tag{1.102}$$

$$\tag{1.103}$$

The phase velocity is maximum at focus ($z = 0$), where its value is:

$$v_{\phi,MAX} = \frac{c}{1 - \dfrac{\lambda}{\pi z_R}} \tag{1.104}$$

$$\tag{1.105}$$

For instance, the maximum phase velocity in the case of the Salle Noire laser ($w_0 = 1.5\,\mu\mathrm{m}$) is approximately 1.03 c.

- We can see from equation 1.97 that, in the paraxial approximation, the E_r and B_θ fields have the same amplitude everywhere. This means that the accelerating principle for linear polarization, in which the electric field accelerates the electron in the transverse direction while the magnetic field rotates the electron towards the optical axis also applies to the E_r and B_θ fields. Therefore, in a radially polarized pulse, the electrons can be accelerated by the E_z field if they remain close to the optical axis, but can also be accelerated by the E_r/B_θ fields in the same way that electrons can be accelerated by the E_x/B_y fields in linearly polarized beams. For electrons with a relativistic velocity in the laser propagation direction, the E_r and $\boldsymbol{v} \times B_\theta$ forces virtually cancel each other and

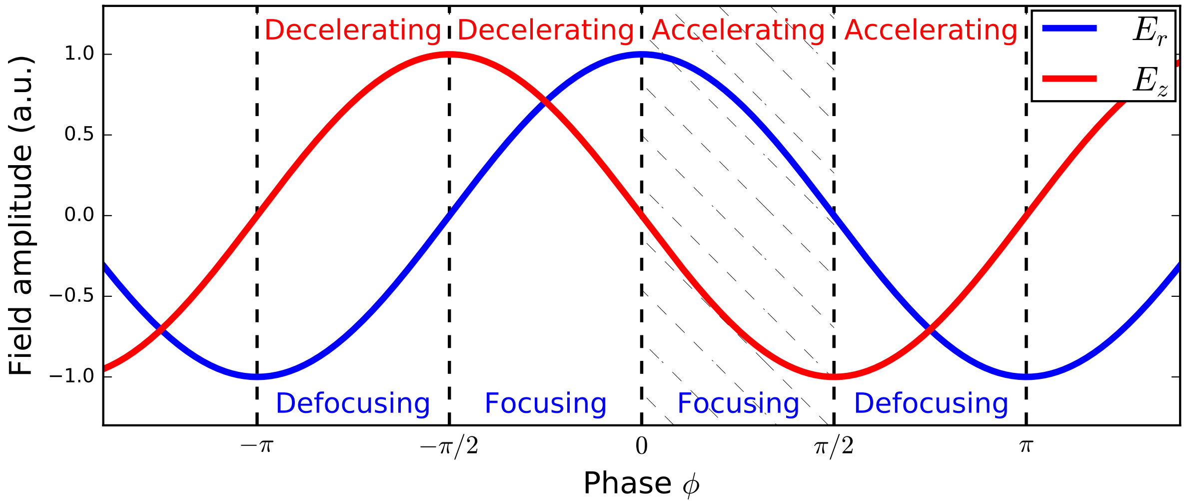

Figure 1.30: Illustration of the accelerating/decelerating and focusing/defocusing phases in a radially polarized beam. The hatched region corresponds to the quarter of the optical cycle where the fields are both accelerating and focusing.

the electrons mainly feel the effect of the E_z field. This is an ideal scenario as the electron beam remains collimated in this case (we will see in chapter 4 that, with nonparaxial field expressions, the E_r and B_θ fields do not have the same amplitude everywhere, which can make things more complicated). On the other hand, an electron with a significant transverse momentum will feel the effect of both the longitudinal and transverse fields.

- There is a $\pi/2$ phase shift between the E_z and E_r fields. Assuming that electrons are mainly accelerated by the longitudinal field, this means that radially polarized beams are both accelerating and focusing for only a quarter of the optical cycle. The different accelerating and decelerating phases as well as focusing and defocusing phases are represented in figure 1.30. Here, the words focusing and defocusing correspond to the sign of the force induced by the E_r field. Once again, outside of the paraxial approximation, the magnetic force can exceed the transverse electric force, which means that the transverse fields are in fact not always focusing when $E_r > 0$. This point will be discussed in more details in chapter 4.

- We finally conclude this section by remarking that the fields of a radially polarized beam have a similar structure as the fields of other common accelerating methods. For instance, it can be argued that the accelerating field structure is similar to that in the linear regime of laser wakefield acceleration (see equations 1.49-1.50). Indeed, in both cases the fields have a longitudinal E_z component proportional to $\exp(-r^2/w_0^2)$ and a radial E_r component proportional to $r\exp(-r^2/w_0^2)$, which is dephased by $\pi/2$ with respect to the longitudinal component. However, a significant difference is that the laser wakefield accelerating fields do not contain a strong B_θ component, as they are of electrostatic origin (they come from a charge separation). This means that the radial fields have a much stronger impact on the focusing of the electron beam in laser plasma accelerators, since the E_r force will not be compensated by the $v \times B_\theta$ force in this case. The fields of a radially polarized beam are in fact even more similar to those of the propagating TM$_{01}$ mode in circular waveguides that is very commonly used in RF linear accelerators [117]. For this reason, radially polarized beams are often refered to as TM$_{01}$ beams (see e.g. [88])[11]. In that sense, it can be said that radially polarized pulses have an ideal structure for accelerating electrons in vacuum with lasers. Nevertheless, it should be kept in mind that acceleration with radially polarized lasers suffers from important defects compared to RF cavities, which are inherent to VLA. First, the accelerating structure is small, typically less than a micron, which means that it is difficult to inject electrons at a precise phase of the laser. Secondly, the phase velocity of the accelerating field cannot be controlled and is greater than c on the axis at focus, which means that electrons will always be dephased with respect to the laser.

1.5.2.3 Theory of on-axis longitudinal acceleration

We consider in this section an electron on the optical axis ($r = 0$) which interacts with the longitudinal electric field E_z of a radially polarized laser. We additionally assume in this section that the laser in infinitely long ($g = 1$, where g is the temporal envelope). The value of the longitudinal electric field in this case is given by:

$$E_z(z,t) = -E_{0,z}\left(\frac{w_0}{w(z)}\right)^2 \sin\phi \tag{1.106}$$

With $\phi = kz - \omega t - 2\arctan\left(\frac{z}{z_R}\right) + \phi_{CEP}$. It is first important to note that this longitudinal field originates from a transverse variation of the radial field. This means that transverse effects are intrinsically included in this on-axis study of the electron motion, even if the resulting trajectories are monodimensional. In particular, the 1D conservation laws that we have derived for linearly polarized pulses in section 1.5.1.2 do not apply here.

Analytical model without diffraction

In the case of linearly polarized beams, the study of electron oscillations in a plane wave could be carried out analytically and has resulted in useful physical considerations regarding the interaction. We may thus be tempted to do the same in the case of radial polarization and study the on-axis trajectories of an electron in a field of the form:

$$E_z = -E_{0,z}\sin\phi \tag{1.107}$$

Where $\phi = kz - \omega t$. This corresponds to neglecting diffraction in the expression of E_z, which is somewhat inconsistent with the fact that the longitudinal field comes from a finite transverse extent of the laser. I have found that the relativistic motion of an electron in such a field can be studied analytically, which has to my knowledge not been published anywhere. We start by writing the equations of conservation of momentum and energy for the electron, which read respectively:

$$\frac{d\gamma_e\beta_{e,z}}{dt} = \frac{eE_{0,z}}{m_e c}\sin\phi \tag{1.108}$$

$$\frac{d\gamma_e}{dt} = \frac{eE_{0,z}}{m_e c}\beta_{e,z}\sin\phi \tag{1.109}$$

---

[11] As in waveguides, higher order radially polarized modes labeled TM$_{np}$ also exist in vacuum [118].

By combining these two equations, we can eliminate γ_e and find the equation determining the evolution of $\beta_{e,z}$:

$$\frac{d\beta_{e,z}}{dt} = \frac{eE_{0,z}}{m_e c}\sin\phi\left[1-\beta_{e,z}^2\right]^{\frac{3}{2}} \tag{1.110}$$

As in the case of the linearly polarized plane wave, we perform the change of variable $t \to \phi$. By noting that $\frac{d\phi}{dt} = -\omega(1-\beta_{e,z})$, the previous equation then becomes:

$$\frac{d\beta_{e,z}}{d\phi} = -a_{0,z}\sin\phi\frac{\left[1-\beta_{e,z}^2\right]^{\frac{3}{2}}}{1-\beta_{e,z}} \tag{1.111}$$

This equation can be integrated by separation of variables, which results in:

$$\beta_{e,z}(\phi) = \frac{1-\left(\sqrt{\frac{1-\beta_{e,zi}}{1+\beta_{e,zi}}} - a_{0,z}\left(\cos\phi - \cos\phi_i\right)\right)^2}{1+\left(\sqrt{\frac{1-\beta_{e,zi}}{1+\beta_{e,zi}}} - a_{0,z}\left(\cos\phi - \cos\phi_i\right)\right)^2} \tag{1.112}$$

Here, ϕ_i is the initial phase, for which the electron normalized longitudinal velocity is $\beta_{e,zi}$. We first note that in some cases, there is a value of the phase, noted ϕ_c, such that $\beta_{e,z}(\phi_c) = 1$. Such a value for $\beta_{e,z}$ is of course impossible to attain. The interpretation in this case is that the electron actually approaches but never reaches the phase ϕ_c: it no longer oscillates in the field but instead becomes "locked" at this accelerating phase of the laser where it can gain an infinite amount of energy. This can be confirmed by integrating $\beta_{e,z}(\phi)$ to obtain the position $z_e(\phi)$. We indeed find in this case that z_e diverges as ϕ approaches ϕ_c. This phase-locking of the electron occurs for:

$$a_{0,z} \geq a_{0,zc} = \frac{1}{1-\cos\phi_i}\sqrt{\frac{1-\beta_{e,zi}}{1+\beta_{e,zi}}} \tag{1.113}$$

We thus find that there exist in this model two radically different scenarios:

1. For $a_{0,z} < a_{0,zc}$, the electron indefinitely oscillates in the field. This can roughly correspond to the ponderomotive regime discussed in the case of linear polarization.

2. For $a_{0,z} \geq a_{0,zc}$, the electron is indefinitely accelerated. This can roughly correspond to the VLA regime discussed in the case of linear polarization.

Of course, this second scenario cannot exist in reality as the electron will always dephase with respect to the laser due to the Gouy phase shift. However, this model remains useful as it provides an estimation of the electric field at which the transition between the ponderomotive and VLA regimes occur. We will see in chapter 4 that this estimation is in good agreement with simulations. We can remark that the worst initial phase corresponds to an electron which initially starts with a decelerating half-cycle ($\phi_i = 0$). In this case, the electron will always oscillate in the field regardless of $a_{0,z}$. On the opposite, the optimal initial phase, for which the electron is most likely to be phased-locked, corresponds to beginning with an accelerating half-cycle ($\phi_i = \pm\pi$). Phase-locking is also facilitated by a significant initial velocity. In the particular case where the electron begins its interaction at $\phi_i = \pm\pi$ with no initial velocity, it becomes trapped for $a_{0,z} > 0.5$, which is a moderately low value. Finally, if the electron begins its interaction at rest at a maximum of the electric field, the threshold value for attaining the VLA regime is given by $a_{0,zc} = 1$. This would correspond to the case of an electron created by ionization inside the laser pulse.

Maximum theoretical energy gain

The equation of motion can no longer be solved analytically if diffraction is included in the field. However, for an ultrarelativistic electron such that $z \approx ct$, the energy gain can be calculated analytically [78]. In this case, we have the relation $kz - \omega t = 0$ along the electron trajectory and the phase seen by the electron is given by $\phi = -2\arctan\left(\frac{z}{z_R}\right) + \phi_{CEP}$. We note that for an ultrarelativistic electron the Gouy phase shift is the only source of dephasing with the laser. The energy gained by the electron is given by:

$$\Delta W = -e\int_{t_i}^{t_f} E_z(t)c\,dt \tag{1.114}$$

$$\Delta W = -e\int_{z_i}^{z_f} E_z(z)dz \tag{1.115}$$

$$\Delta W = e\int_{z_i}^{z_f} E_{0,z}\frac{\sin\left(-2\arctan\left(\frac{z}{z_R}\right)+\phi_{CEP}\right)}{1+\frac{z^2}{z_R^2}}dz \tag{1.116}$$

Where t_i (resp. z_i) is the time (position) at which the interaction starts and t_f (z_f) is the time (position) at which the interaction ends. This integration can be carried out analytically and results in:

$$\Delta W = \frac{eE_{0,z}z_R}{2}\left[\cos\left(-2\arctan\left(\frac{z}{z_R}\right)+\phi_{CEP}\right)\right]_{z_i}^{z_f} \tag{1.117}$$

$$\Delta W = \frac{eE_{0,z}z_R}{2}\left(\cos\phi_f - \cos\phi_i\right) \tag{1.118}$$

Where ϕ_i and ϕ_f are respectively the initial and final phase seen by the electron during the interaction. We first note that for an interaction between $z = -\infty$ and $z = +\infty$, the Gouy phase shift is 2π and we thus have $\phi_f = \phi_i$ which results in zero energy gain. The electron sees in this case a full accelerating half-cycle and a full decelerating half-cycle which exactly compensate each other. This is a particular case of the Lawson-Woodward theorem, which will be seen in section 1.5.3, and which states that the net energy gain is zero for an ultrarelativistic electron interacting with a pure electromagnetic wave in vacuum from $z = -\infty$ to $z = +\infty$. For an ultrarelativistic electron, an energy gain can therefore only be obtained if the interaction is spatially limited. The energy gain is maximum for an electron that only sees an accelerating half-cycle, regardless of its initial position. This can occur for example for an interaction between $z = -\infty$ and $z = 0$, between $z = -z_R$ and $z = +z_R$ or between $z = 0$ and $z = +\infty$. The latter case is interesting because it could correspond to the case of an electron injected by a plasma mirror into a reflected radially polarized pulse. In any case, the energy gained by an ultrarelativistic electron that experiences a full accelerating half-cycle is given by:

$$\Delta W_{MAX} = eE_{0,z}z_R \tag{1.119}$$

This can be rewritten as a function of the laser power:

$$\Delta W_{MAX} = 2e\sqrt{\frac{2}{\pi c\varepsilon_0}}\sqrt{P} \tag{1.120}$$

In practical units, this result becomes:

$$\Delta W_{MAX}[\mathrm{MeV}] \approx 31\sqrt{P[\mathrm{TW}]} \tag{1.121}$$

In reality, an electron evolves at a velocity which is smaller than c and will thus dephase more quickly with respect to the laser. This means that an electron accelerated by a radially polarized beam will always receive a smaller energy gain than that given by equation 1.121. We remark that, even though they have been obtained in a very different manner, the maximum energy gain in a radially polarized pulse is very similar to that for linear polarization (see equation 1.92). In particular, the energy gain scales in both cases as the square root of the laser power. This once again means that VLA is not well-suited for generating extremely high energy electron beams.

We also remark that, unlike the case of linear polarization, this maximum energy gain has been obtained with a practical scenario (an on-axis ultrarelativistic electron whose interaction is limited to a single accelerating half-cycle, for instance between $z = 0$ and $+\infty$) which takes dephasing and diffraction into account. This means that the maximum energy gain given by equation 1.121 can be approached in practice (provided that an adequate injection method is found). Consequently, the energy gain that can be attained with a radially polarized pulse is probably higher than with a similar linearly polarized pulse (although the maximum energy gain that can be achieved *in practice* with linear polarization is not well quantified).

Equation 1.121 indicates that the energy gain is at most ≈ 25 MeV with the Salle Noire laser ($\approx 670GW$) and ≈ 130 MeV with the UHI100 laser ($\approx 18TW$). These values are somewhat high but it should be kept in mind that attaining these maximum energy gains would require using an initially ultrarelativistic electron beam.

1.5.2.4 Previous simulation results

The trajectories of electrons interacting with radially polarized pulses can only be obtained numerically, usually through test-particle or PIC simulations. We sum up in this section the principal numerical results that have obtained obtained on the subject over the past two decades.

Historically, the first test-particle simulations have been carried out for infinitely long pulse durations [97, 100, 101]. In this situation, the electons de facto begin their interaction inside the laser. In [100], it is shown that the optimal initial phase in this case corresponds to an electron starting its interaction with an accelerating half-cycle. We will see in chapter 4 that this condition still holds when finite duration pulses are used. In [101], Salamin notes that, using a 1 PW or 10 PW laser with $w_0 = 0.53\lambda$ ($a_{0,z}$ between $\approx$ 350 and $\approx$ 1000), electrons initially at rest at $z = 0$ at the optimal phase and close to the optical axis ($r < 0.25\lambda$) are accelerated to energies in the GeV range with a final angle $< 1^\circ$ with respect to the optical axis. These results are promising but have been obtained with an extremely high laser power and an extremely tight focusing.

Next, simulations of electrons initially at rest at $z = 0$ in front of a finite duration pulse have been performed [98, 99, 90]. Experimentally, this would correspond to the ionization of elements with low ionization energies, since in this case the electrons are generated early in front of the pulse. In reference [90], it was observed that when $a_{0,z} < 1$, the electrons tend to experience many laser oscillations, which results in a low energy gain. On the opposite, when $a_{0,z} > 1$, electrons can remain for a long time in an accelerating phase of the laser and gain large amounts of energy. This corresponds to a transition between the ponderomotive regime and the VLA regime. We note in particular that the value of the electric field at the transition is consistent with that obtained in the diffractionless model of the previous section in the case of injection by ionization ($\cos\phi_i = 0$ and $\beta_{e,zi} = 0$).

In the same publication, the authors find that, for a given peak power, there exists an optimal beam waist w_0 which is such that $a_{0,z}$ is slightly higher than 1. For larger beam waists, we have $a_{0,z} < 1$ and the acceleration is ponderomotive and inefficient. For smaller beam waists, the interaction distance is reduced without significantly increasing the electric field seen by the electron. Indeed, even though this case potentialy corresponds to $a_{0,z} \gg 1$, the electron will spend a long time in the first cycle for which the normalized longitudinal field is greater than 1 and will consequently never penetrate in the temporal center of the pulse where $a_{0,z} \gg 1$. However, it was found in [91] that when the initial electron longitudinal position $z_{e,i}$ is an adjustable parameter, the best focusing is in fact the tightest. For very small beam waists, the electron should initially be located well before the laser focus $z_{e,i} < 0$ and its trajectory should be such that it reaches the temporal center of the pulse at $z = 0$ where it can be efficiently accelerated.

Then, the acceleration of electrons injected by ionization into a radially polarized beam has been studied more accurately using PIC simulations [102, 89, 105, 106]. In [102], it is shown that high quality GeV electron beams can be obtained using a laser with $w_0 = 3\lambda$ and a peak power ranging between 2 PW and 100 PW ($a_{0,z}$ between $\approx$ 15 and $\approx$ 100). They note that electrons ionized inside the laser reach higher energies than electrons ionized early in front of the pulse. They additionally observe that, for identical laser parameters, radial polarization leads to more energetic and more collimated electron beams in this scenario. However, it should be noted that, on top of the extremely high peak powers involved, the target in the simulations is a low-density nanosphere with a radius of $\lambda/4$ that is exactly at focus on the optical axis.

The ionization injection method has been studied in a very different regime in [89]. Using a 6-fs, 300-GW laser focused on a low-density hydrogen target, they obtain a 1-fC, 240-keV electron beam with good emittance and energy spread. However, it should be noted that to obtain these results, the authors have used a very tight focusing $w_0 \approx \lambda$ so that the longitudinal field reaches $a_{0,z} \approx 1.6$. Slightly higher energies are in principle achievable if targets with higher-Z elements are used, but the authors find that this leads to an unwanted increase in the energy spread, as electrons originating from different ionization states will follow different trajectories [105]. In [106], these results are extended to few-TW laser powers and they show in particular that few-MeV electron beams are achievable in this case. Nevertheless, the same extreme focusing is used.

More recently, the acceleration of pre-accelerated electron beams which are initially in front of the laser pulse has been studied [91, 103, 107]. Unsurprisingly, it is observed that an electron can gain more energy from the laser if it initially has a velocity in the longitudinal direction. In [107], it is found that the threshold $a_{0,z} > 1$ for reaching the VLA regime that was previously obtained for electrons initially at rest can be extended to electrons that have an initial velocity. To do that, the authors consider the frame where the electrons are initially at rest, inside which the threshold $a_{0,z} > 1$ is in principle valid. In this frame, the longitudinal field seen by the electron is increased due to the relativistic Doppler downshift of the laser frequency. Because of that, the threshold in the laboratory frame is lowered to:

$$a_{0,z} > \sqrt{\frac{1-\beta_{e,zi}}{1+\beta_{e,zi}}} \tag{1.122}$$

This threshold was found to be in good agreement with simulations. Interestingly, this threshold exactly corresponds to the one obtained analytically in my model without diffraction that was presented in the previous section, for an electron initially at a maximum of the electric field (see equation 1.113 for $\cos\phi_i = 0$). According to the analytical model, we could thus expect the threshold to be lowered by a factor 2 for an electron initially inside the laser that starts its interaction with an accelerating half-cycle. Finally, in the same paper [107], the authors point out that the laser pulse tends to reduce the pre-accelerated electron bunch duration, as electrons at the rear of the bunch are accelerated earlier that electron in front of the bunch.

1.5.2.5 Previous experimental attempts

There have been in the past only two experimental attempts at electron acceleration in vacuum with radially polarized pulses. Each of the experiments have used one of the injection methods that were previously employed in the case of linear polarization: the ionization of a low density gas target and the use of pre-accelerated electron beams.

The first experiment [113] has been performed at the Advanced Laser Light Source in Canada and corresponds to the ionization of a gas target. A 15-fs infrared ($\lambda = 1.8\,\mu\mathrm{m}$) with an on-target energy of $550\ \mu$J interacts inside a chamber filled with a low-density oxygen gas. The pulse is focused using an on-axis parabola with a numerical aperture of 0.7. The resulting beam waist is expected to be $w_0 \approx 0.6\lambda$, but has not been measured and is therefore possibly underestimated. Such a tight focusing would result in $a_{0,z} \approx 1.4$, which should be sufficient to accelerate electron to relativistic energies. However, an energy gain of only ≈ 20 keV was obtained, which suggests that such high longitudinal fields were not achieved. The authors nonetheless observe that the electron signal disappears when the polarization is switched to azimuthal or linear, which indicates a significant effect of the polarization.

The second experiment [119] was carried out using an electron beam which was pre-accelerated with a DC gun. A $\lambda = 800$ nm, 8-fs laser pulse with an on-target energy of $600\ \mu$J is focused to a beam waist $w_0 = 1.2\,\mu\mathrm{m}$ onto the electron beam. The peak longitudinal field is not provided but these parameters correspond to $a_{0,z} \approx 0.4$. The electron beam has an initial energy of 40 keV and is approximately 1-mm long. Therefore, depending on their position in the bunch, some electrons will be accelerated, some will be decelerated and most will not feel the laser at all. This effectively resulted in an increase of the beam energy spread, as in similar experiments performed with linear polarization (see section 1.5.1.5). The maximum detected energy is 50 keV, which corresponds to a 10 keV energy gain.

We have seen that both previous experiments have resulted in inefficient acceleration. This is due to the modest laser energies used, the possible difficulty of generating high quality radially polarized beams and the fact that nonoptimal injection methods were used. We will show both numerically and experimentally in chapters 4 and 5 that using a plasma mirror injector can solve the last issue, resulting in the demonstration of electron acceleration to relativistic energies.

1.5.3 Lawson-Woodward theorem

We conclude our study of VLA by presenting an important result regarding the acceleration of electrons in vacuum, known as the **Lawson-Woodward theorem** [120, 78]. The theorem states that under some conditions, described below, the interaction between an electron and an electromagnetic wave results in zero net energy gain for the electron. The conditions under which the theorem can be applied are the following:

1. We neglect the power radiated by the electron.

2. The electron has an ultrarelativistic velocity ($\gamma_e \gg 1$) *in the same direction* throughout the interaction. This means that, with an appropriate choice of coordinates, the electron trajectory can be written as $z \approx ct$, $x = y = 0$. This assumption implies in particular that the transverse fields are not strong enough to significantly deflect the electron.

3. The electron only interacts with a pure propagating electromagnetic wave (no static component and no imaginary wavevectors) in vacuum from $z = -\infty$ to $z = +\infty$.

With these assumptions, the electron only moves in the z direction and therefore only the E_z component of the electric field can work. The total energy gain is thus given by:

$$\Delta W = -e \int_{-\infty}^{\infty} E_z(x(t), y(t), z(t), t) c dt \tag{1.123}$$

$$\Delta W = -ec \int_{-\infty}^{\infty} E_z(0, 0, ct, t) c dt \tag{1.124}$$

Since the electron trajectory is known in advance, we can sum over the contribution of each plane wave constituting the electromagnetic field to calculate the energy gain. We therefore write the Fourier transform of E_z:

$$E_z(x, y, z, t) = \int d\boldsymbol{k} \widetilde{E}_z(k_x, k_y, k_z) e^{i(k_x x + k_y y + k_z z - \omega t)} \tag{1.125}$$

Here, $\widetilde{E}_z$ is the Fourier transform of E_z at $t = 0$ and $\omega = \sqrt{k_x^2 + k_y^2 + k_z^2}$. Along the electron trajectory, we have in particular:

$$E_z(0, 0, ct, t) = \int d\boldsymbol{k} \widetilde{E}_z(k_x, k_y, k_z) e^{i(k_z c - \omega)t} \tag{1.126}$$

Injecting this expression into equation 1.124, we obtain:

$$\Delta W = -ec \int d\boldsymbol{k} \left[\widetilde{E}_z(k_x, k_y, k_z) \int_{-\infty}^{\infty} e^{i(k_z c - \omega)t} dt \right] \tag{1.127}$$

$$\Delta W = -ec \int d\boldsymbol{k} \widetilde{E}_z(k_x, k_y, k_z) \delta(k_z c - \omega) \tag{1.128}$$

Where δ is the Dirac delta function. Thus, only wavevectors such that $\omega = k_z c$ can contribute to the energy gain. In the absence of static field and of imaginary wavevectors, this can only be satisfied by a vector $\boldsymbol{k}$ of the form $(0, 0, k_z)$, where k_z is a strictly positive real number. This corresponds to a plane wave copropagating with the electron. However, in such a case the electric field is purely transverse and we have $\widetilde{E}_z(0, 0, k_z) = 0$. This eventually means that $\Delta W = 0$, which proves the theorem.

This theorem is useful as it applies to every laser polarization and can rule out many scenarios in which one wants to post-accelerate an initially ultrarelativistic beam using a laser pulse in vacuum. However, it should be kept in mind that its domain of applicability is limited and, as we will see in the following, somewhat vague. Condition 1 is verified in virtually all cases that we consider here and is therefore not the principal concern. Condition 3 is more restrictive and is not verified in the case of injection by a plasma mirror or by ionization of a low-density gas, because the interaction in vacuum does not occur from $z = -\infty$ to $z = +\infty$. This means that the Lawson-Woodward theorem is of no importance in these situations. The theorem is in fact of interest only when pre-accelerated electron beams are used.

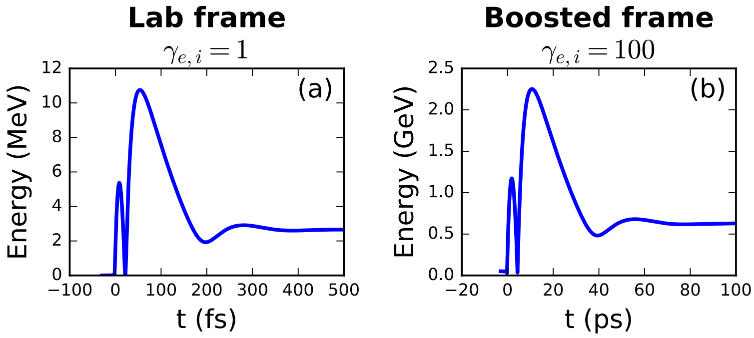

Figure 1.31: Electron trajectories obtained from single particle simulations. (a) The electron is initially at rest at $z = 0$ on the optical axis in front of a radially polarized pulse with $\lambda = 800$ nm, $\tau = 3.5$ fs, $w_0 = 1.5\,\mu\mathrm{m}$ and $a_{0,z} = 1.5$. (b) Same interaction seen in the inertial frame where the electron has an initial Lorentz factor $\gamma_{e,i} = 100$. (c) Same simulation as in (b) except that the electron has this time an initial Lorentz factor $\gamma_{e,i} = 100\ 000$. We have used in these simulations exact expressions for the electromagnetic field as presented in section 2.3.

Condition 2 is also very restrictive and can moreover be quite tricky. First of all it should be noted that the theorem cannot be applied whenever the laser significantly deflects or slows down the electron, because in this case the trajectory cannot be approximated by $z = ct$. For example, an initially relativistic electron can very well start its interaction by losing most of its energy, so that it is at one point non-relativistic, and be even more accelerated later on, resulting in a net energy gain [97, 91, 107]. Another possibility is that the electron remains ultrarelativistic throughout the interaction but gains energy by being deflected, for example by the transverse fields in linear polarization [12]. Overall, it cannot be concluded from the theorem that an initially relativistic electron cannot be accelerated from VLA.

More fundamentally, an electron always has a velocity which is smaller than c and it is therefore not entirely clear at what point the second condition can be considered true. In particular the fact that an electron is relativistic or not depends on the choice of the inertial frame. For every electron that remains ultrarelativistic throughout the interaction in a given frame, there exist another frame in which the electron is initially at rest. Conversely, for every electron that gains energy from VLA (and is therefore not subject to the Lawson-Woodward theorem), there exist an infinite number of frames in which the electron remains relativistic throughout the interaction, which seems to contradict the theorem.

As an example, let us consider an electron initially at rest on the optical axis and at $z = 0$ in front of a radially polarized pulse with $\lambda = 800$ nm, $\tau = 3.5$ fs, $w_0 = 1.5\,\mu\mathrm{m}$ and $a_{0,z} = 1.5$. The kinetic energy of this electron as a function of time is plotted in figure 1.31(a). Since the laser field is intense enough ($a_{0,z} > 1$), the electron remains for a long time in an accelerating half-cycle and eventually gains ≈ 2.66 MeV from the interaction.

Let us now look at the same interaction in the inertial frame where the electron has an initial Lorentz factor $\gamma_{e,i} = 100$ and moves in the positive z direction. In this frame, the laser pulse is strongly Doppler upshifted: its wavelength is ≈ 4 nm, its duration is ≈ 17.5 as, its beam waist is unchanged, its longitudinal

---

[12] More generally, the VLA scenario with transverse fields, where the electron gains energy by being deflected by the $\boldsymbol{E}$ field and is rotated back in the z direction by the $\boldsymbol{B}$ field, violates by essence condition 2, and is therefore not subject to the theorem.

electric field amplitude is unchanged (but $a_{0,z}$ is decreased to $\approx$ 0.0075 due to the frequency increase), its Rayleigh length is increased from $8.84\,\mu\mathrm{m}$ to ≈ 1.77 mm and its peak power is increased from ≈ 3 TW to ≈ 120 PW. The electron energy as a function of time in this frame is shown in figure 1.31(b). It increases from ≈ 51 MeV, to ≈ 629 MeV, which corresponds to a ≈ 578 MeV energy gain. We note that this trajectory has been obtained from a test-particle simulation and that the final electron energy matches that theoretically expected from the Lorentz transformation. Its minimum energy during the interaction is ≈ 29 MeV, which can be considered to be relativistic (this value can be raised to an arbitrarily high number if $\gamma_{e,i}$ is chosen large enough). Therefore, its trajectory can be well approximated by $z = ct$, and the electron appears to verify all the conditions of the Lawson-Woodward theorem. Yet, it receives a net energy gain.

We show in figure 1.31(c) the same simulation as in figure 1.31(b) except that the electron has an initial Lorentz factor $\gamma_{e,i} = 100\,000$ instead of $\gamma_{e,i} = 100$ (this corresponds to choosing $\gamma_{e,i} \approx 500$ ($\approx$ 255 MeV) in the initial frame of figure 1.31(a)). In this case the electron initially loses approximately 20% of its energy, but regains it later on in the following accelerating half-cycle, resulting in a negligible net energy change. This corresponds to a typical Lawson-Woodward trajectory. This suggests that condition 2 can be understood in the following way: for given laser parameters (and thus in a given frame), the energy gain tends towards 0 as the trajectory approaches $z = ct$. How close must the trajectory be to $z = ct$ for the energy gain to be negligible is not specified by the theorem and depends on the given laser parameters. In particular, the fact that we can always change the inertial frame shows that from every real number $\beta < 1$, there exist trajectories such that $\beta_{e,z} > \beta$ at all time for which the Lawson-Woodward theorem does not apply. However, it should be noted that the laser power becomes increasingly large as β approaches 1 in this scenario.

We heuristically notice that the theorem can be applied whenever the initial electron energy is relativistic and higher than the maximum theoretical energy gain given by the laser pulse peak power (equation 1.121). This could provide a clearer criterion for condition 2 (even though this hypothesis has not been tested thoroughly and we consequently do not exclude that counterexamples can be found) and shows that the theorem still has relevance in many practical cases. Nevertheless, its implications should not be overestimated because:

- The theorem does not apply to injection methods where the interaction is spatially limited (as is the case with plasma mirrors).
- The theorem only applies to highly energetic electron beams. However, we have previously seen that VLA is anyway not well-suited to accelerate electrons to high-energies. This means that the theorem does not apply to scenarios where VLA would be the most appealing (e.g. for generating few-MeV electron beams).

In particular, this theorem should not be used to dismiss the mere possibility of accelerating electrons with lasers in vacuum.

1.6 Conclusion

We have presented in this chapter different techniques for generating relativistic electrons using ultra-high intensity laser pulses. Laser wakefield acceleration in underdense plasmas remains the standard method for obtaining high-quality electron beams, and multiple GeV energy gains as well as few-fs bunch durations have been obtained. Electrons can also be accelerated from the interaction between a laser pulse and an overdense plasma with a density gradient on its front surface. For large preplasmas, the interaction is not well understood and there is a need for more experiments in this regime. As will be seen in chapter 3, we indeed observe experimentally electrons at long gradients in Salle Noire, which we attribute to laser wakefield acceleration taking place in the underdense part of the preplasma. On the opposite, the interaction is well understood for sharp density gradients. In this case, the electrons are ideally injected into the reflected laser pulse where they can gain large amounts of energy from VLA, as has been demonstrated experimentally with linearly polarized pulses. Plasma mirrors thus provide a simple method for studying this fundamental acceleration process. It has often been proposed that radial polarization be used instead of linear polarization in order to improve the quality of the VLA generated electron beams. We will therefore study in chapters 4 and 5 the acceleration of electrons injected by a plasma mirror into a radially polarized beam.

CHAPTER 2

Numerical methods

Contents

The relativistic motion of an electron accelerated in vacuum by a monochromatic plane wave can be solved analytically, as was shown in chapter 1. However, an analytical approach is no longer possible when more realistic multi-dimensional laser pulse profiles are used. Numerical simulations are therefore necessary to study the acceleration of electrons in vacuum more quantitatively. The simplest method is to perform test particle simulations, in which the motion of a set of electrons inside a known electromagnetic field is computed. These inexpensive simulations, described in section 2.1, are particularly useful when the initial conditions for the electrons are known.

When modeling the injection of electrons by an overdense plasma into a laser pulse, plasma effects must be included in the simulations. The method of choice to simulate the interaction of an ultrahigh intensity laser pulse with a plasma is the Particle-In-Cell (PIC) method, where the motion of a collection of charged particles is solved self-consistently with Maxwell's equations. The standard PIC loop is presented in section 2.2.2. PIC simulations can be very computationally demanding and full-3D simulations of the interaction between a relativistic intensity laser pulse and an overdense plasma are not tractable with the standard PIC method. We present in sections 2.2.3 and 2.2.4 two solutions enabling 3D simulations: the use of cylindrical coordinates at normal incidence and the use of pseudo-spectral Maxwell solvers for any laser incidence.

Finally, in Section 2.3, we present a method that can be used to model ultrashort and tightly focused laser pulses in simulations.

2.1 Test-particle simulations

Test particle simulations, also known as **single particle** simulations, solve the relativistic equation of motion of a set of charged particles in a known electromagnetic field:

$$\frac{d\boldsymbol{p}_p(t)}{dt} = q_p\left(\boldsymbol{E}\left(\boldsymbol{r}_p(t),t\right) + \boldsymbol{v}_p \times \boldsymbol{B}\left(\boldsymbol{r}_p(t),t\right)\right) \tag{2.1}$$

$$\frac{d\boldsymbol{r}_p(t)}{dt} = \boldsymbol{v}_p(t) \tag{2.2}$$

Here, $\boldsymbol{r}_p(t)$, $\boldsymbol{v}_p(t)$, $\boldsymbol{p}_p(t)$ and q_p are respectively the position, velocity, momentum and charge of particle p at time t and $\boldsymbol{E}(\boldsymbol{r},t)$ and $\boldsymbol{B}(\boldsymbol{r},t)$ are the electromagnetic fields (the laser fields in the case of VLA). Since the $\boldsymbol{E}$ and $\boldsymbol{B}$ fields are known in advance, the particles have no influence on the fields and do not interact with each other. For a given electromagnetic field, a particle trajectory is therefore entirely determined by its initial position in phase space $(\boldsymbol{r}_p(0),\boldsymbol{p}_p(0))$. This means in particular that single particle simulations become inaccurate when the charge of the simulated electron beam becomes too high.

There are different methods for integrating equations 2.1-2.2, but the **Boris pusher** [121] is the most common choice as it is fast, accurate and easy to implement. A leapfrog integration is used in the Boris pusher, meaning that positions and velocities are calculated at interleaved time points. More specifically, after a time step Δt is chosen, positions are computed at times $n\Delta t$ while velocities are computed at times $(n+1/2)\Delta t$, where n is an integer. This is done so that the time derivatives are centered, which increases the stability and accuracy of the integration. In the Boris scheme, the following equations are used to update a particle's position and momentum:

$$\boldsymbol{p}_p^{n+1/2} = \boldsymbol{p}_p^{n-1/2} + \Delta t q_p\left(\boldsymbol{E}_p^n + \bar{\boldsymbol{v}}_p^n \times \boldsymbol{B}_p^n\right) \tag{2.3}$$

$$\boldsymbol{r}_p^{n+1} = \boldsymbol{r}_p^n + \Delta t \boldsymbol{v}_p^{n+1/2} \tag{2.4}$$

We have used the notation $\boldsymbol{a}_p^n \equiv \boldsymbol{a}_p(n\Delta_t)$ for the particle position, velocity and momentum and the notation $\boldsymbol{A}_p^n \equiv \boldsymbol{A}(\boldsymbol{r}_p^n,n\Delta_t)$ for the fields. The Boris pusher is characterized by the use of an average velocity $\bar{\boldsymbol{v}}_p^n$ in the calculation of the magnetic force, thereby increasing the accuracy of the method. It is defined by [122]:

$$\bar{\boldsymbol{v}}_p^n \equiv \frac{\boldsymbol{p}_p^{n+1/2} + \boldsymbol{p}_p^{n-1/2}}{2\bar{\gamma}_p^n} \tag{2.5}$$

Where $\bar{\gamma}_p^n$ is an average Lorentz factor equal to:

$$\bar{\gamma}_p^n \equiv \sqrt{1 + \left(\frac{\boldsymbol{p}_p^{n+1/2} + \boldsymbol{p}_p^{n-1/2}}{2m_p c}\right)^2} \tag{2.6}$$

Equation 2.3 is implicit since $\bar{\boldsymbol{v}}_p^n$ depends on $\boldsymbol{p}_p^{n+1/2}$ so an algorithm must be used to obtain $\boldsymbol{p}_p^{n+1/2}$ from $\boldsymbol{p}_p^{n-1/2}$. This is done in practice using a three step method first described in [121]. First, half of the electric field is applied, then the magnetic rotation is calculated and finally the other half of the electric force is applied.

Test particle simulations are particularly inexpensive compared to PIC simulations. Moreover, since the trajectories of different particles are independent from one another, single particle simulations can be easily parallelized by having different processors compute the motion of different particles. These simulations are useful when the initial conditions of the particles are well known. For instance, they yield the same results as PIC simulations when studying the acceleration of electrons in vacuum after ionization of a low density hydrogen gas [89], because the electrons are all generated early in front of the laser pulse in this case (this only works of course if the density of the gas is low enough to make plasma and space charge effects negligible).

However, when plasma mirrors are used as an injection method, test particle simulations provide no information regarding the initial conditions for the electrons. They can therefore not be used as a tool to predict final electron distributions for given laser and plasma parameters. Nevertheless, after an experimental result is obtained, it is possible to retrieve the experimental electron spectrum and angular distribution by tuning the initial conditions in the single particle simulations, as was done in reference [27]. Then, these simulations are used to extract useful information regarding the electron trajectories without having to perform expensive 3D PIC simulations.

It should also be noted that test particle simulations are very sensitive to the choice of the laser electromagnetic fields, as was shown in reference [104]. Since in principle any arbitrary function of space and time can be chosen as the $\boldsymbol{E}$ and $\boldsymbol{B}$ fields in the simulations, incorrect results may be obtained if the fields are unphysical. For instance, using laser fields described by the paraxial approximation leads to severely flawed electron angular distributions [80, 123]. Extra care must therefore be taken when choosing the electromagnetic fields. A possible way of modeling ultrashort and tightly focused pulses will be discussed in section 2.3.

The test particle simulations presented in this thesis have been carried out using a code initially developed in `C++` by Olle Lundh for which I have made further developments (parallelization with the OpenMP library, implementation of the pulse profiles described in section 2.3 and of more exotic initial particle distributions).

2.2 Particle-In-Cell simulations

When simulating the interaction between an overdense plasma and an ultraintense laser pulse, plasma and space charge effects must be included and test particle simulations are no longer appropriate. As we have seen in chapter 1, kinetic phenomena are prevalent during the interaction, which means that fluid (hydrodynamic or magnetohydrodynamic) simulations are not suitable either. Since collisions can be neglected, the Vlasov-Maxwell system (see section 1.2.2) provides the relevant equations to solve in order to describe the plasma response. The Particle-In-Cell (PIC) algorithm is the standard method for solving this system and thus for modeling collisionless kinetic plasmas.

PIC simulations are widely used in the field of high-intensity laser-plasma interaction to gain additional insight from experiments, mainly by accessing quantities that are not directly measurable (plasma density maps with subwavelength resolution, electromagnetic field values). They are also used to predict experimental results and to validate analytical models of the interaction. The PIC method relies on very little assumptions, which can lead to very good agreement with experiments, provided that the laser and plasma are modeled accurately.

2.2.1 Principle of the PIC method

One possible approach to simulate the laser-plasma interaction would be to directly solve the Vlasov-Maxwell system, using for instance finite difference methods. Such schemes exist indeed [124], but are not frequently used because of the high dimensionalities involved. For example, solving for the distribution functions f_s in a 3D geometry requires a 6D grid (3 dimensions for real space and 3 dimensions for momentum space), which can be prohibitively expensive.

Rather than being described through the distribution functions f_s of its constituent species, the plasma is usually modeled by a collection of charged particles (electrons and ions) interacting with each other. In the PIC method, the particles interact through Maxwell's equations. Accelerated particles emit electromagnetic radiations via the source terms in Maxwell's equations. These generated field will then retroact on the particles' motion through the Lorentz force. A PIC code therefore consists in the resolution of the equation of motion of charged particles coupled with Maxwell's equations. In practice, the particles evolve freely in space while the fields (electromagnetic fields, charge density and current density) are calculated on a grid. The main steps of the PIC loop are described in section 2.2.2.

Ideally, each PIC particle would represent a single physical electron. This can however not be realistically done in practice, as the number of simulated particles would be too high. For instance, assuming $\lambda_0 = 800$ nm, the number of electrons in a volume of λ_0^3 at 200 times the critical density is already 1.7×10^{11}. For this reason, each particle in a simulation represents many physical particles which are close to each other in phase space and is therefore called a **macroparticle**. Macroparticles have a finite spatial extent, characterized by a **shape function** $S(\boldsymbol{r})$ such that the charge density associated to particle p is:

$$\rho_p(\boldsymbol{r}) = q_p w_p S(\boldsymbol{r} - \boldsymbol{r}_p) \tag{2.7}$$

Here, $\boldsymbol{r}_p$ is the central position of macroparticle p, w_p is its weight, which corresponds to the number of physical particles it represents and q_p is the charge of a single *physical* particle. The shape function is normalized: $\int_{\mathbb{R}^3} S(\boldsymbol{r}) d^3\boldsymbol{r} = 1$ so that the total charge of the particle is $q_p w_p$. The distribution function associated to the macroparticle is:

$$f_p(\boldsymbol{r},\boldsymbol{p}) = w_p S(\boldsymbol{r} - \boldsymbol{r}_p)\delta(\boldsymbol{p} - \boldsymbol{p}_p) \tag{2.8}$$

Where δ is the Dirac function and p_p the momentum of the particle. It can be noted that, even though macroparticles do not have a well-defined position, they have a well-defined momentum. Using such distribution functions, PIC simulations solve the Vlasov-Maxwell system, with the minor approximation that the particle shape functions remain constant in the simulations.

The shape functions are used to make the connections between the particles and the grid. For instance, the charge density deposited by particle p on a grid point located at position $\boldsymbol{r}_{grid}$ is:

$$\rho_{grid,p} = q_p w_p S(\boldsymbol{r}_{grid} - \boldsymbol{r}_p) \tag{2.9}$$

Similarly, the electric field $\boldsymbol{E}_p$ acting on the particle is obtained from the electric field $\boldsymbol{E}_{grid}$ on the neighboring grid points and from the shape function $S(\boldsymbol{r})$:

$$\boldsymbol{E}_p = \sum_{grid} S(\boldsymbol{r}_{grid} - \boldsymbol{r}_p)\boldsymbol{E}_{grid} \tag{2.10}$$

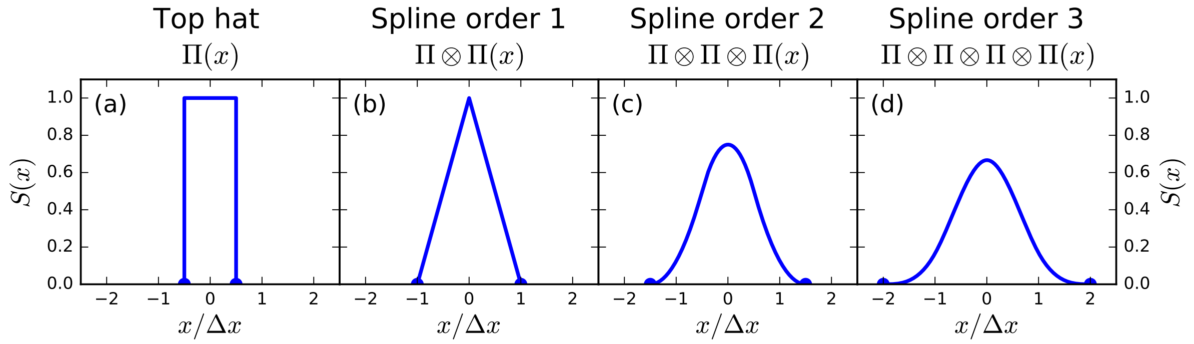

Figure 2.1: Standard 1D macroparticle shape functions of order (a) 0, (b) 1, (c) 2 and (d) 3. Δx is the grid spatial step.

Usually, the shape functions described in [125] are used. They are obtained by consecutively performing the convolution of a top-hat function with itself, as shown in figure 2.1. The shape function of order n is made of piecewise polynomials of order n and its first $(n-1)$ derivatives are continuous. These functions are chosen for their advantageous numerical properties (low noise and error in the force calculations, the total deposited charge is always the macroparticle charge). Increasing the spline order broadens the macroparticle spatially, which reduces the numerical noise but increases the number of computer operations, as the macroparticle deposits charge and current on more grid points. A spline of order 3 is used in all the PIC simulations presented in this manuscript. In this case, and in a 3D geometry, the particle has a volume of $4\Delta x \times 4\Delta y \times 4\Delta z$, which means that it interacts with 64 adjacent grid points.

2.2.2 The standard PIC loop

PIC simulations make extensive use of leapfrog methods. Typically, the electric field and the particle positions are calculated at integer times (multiples of the timestep Δt) while the magnetic field and the particle momenta are calculated are half-integer times. Let us assume that the particles' momenta are known at time $(n-1/2)\Delta t$ and are noted $\boldsymbol{p}_p^{n-1/2}$ and that their positions are known at time $n\Delta t$ and are noted $\boldsymbol{r}_p^n$. Furthermore, we assume that the electric field is known on the grid at time $n\Delta t$ (noted $\boldsymbol{E}_{grid}^n$) and that the magnetic field is known at time $(n+1/2)\Delta t$ (noted $\boldsymbol{B}_{grid}^{n+1/2}$). We hereafter briefly summarize the different steps occuring in the course of one PIC iteration, during which these quantities are updated to $\boldsymbol{p}_p^{n+1/2}$, $\boldsymbol{r}_p^{n+1}$, $\boldsymbol{E}_{grid}^{n+1}$ and $\boldsymbol{B}_{grid}^{n+3/2}$. These different steps are represented in figure 2.2. A PIC simulation consists in performing this loop for a desired number of timesteps. A more comprehensive description of the standard PIC algorithm is given in [125] and [126].

Interpolation

In order to update the particles momenta from $\boldsymbol{p}_p^{n-1/2}$ to $\boldsymbol{p}_p^{n+1/2}$ using the Lorentz force, the electromagnetic fields must be interpolated from the grid to the positions of the particles. This is done through the shape function, as described in equation 2.10. The same shape function must be used for the interpolation and for the current deposition, so that no self-forces are applied by a particle on itself [125].

We note that the Lorentz force requires the magnetic field to be calculated at time $n\Delta t$. In practice, $\boldsymbol{B}_{grid}^n$ is obtained by computing the average between $\boldsymbol{B}_{grid}^{n-1/2}$ and $\boldsymbol{B}_{grid}^{n+1/2}$. This method may lead to an

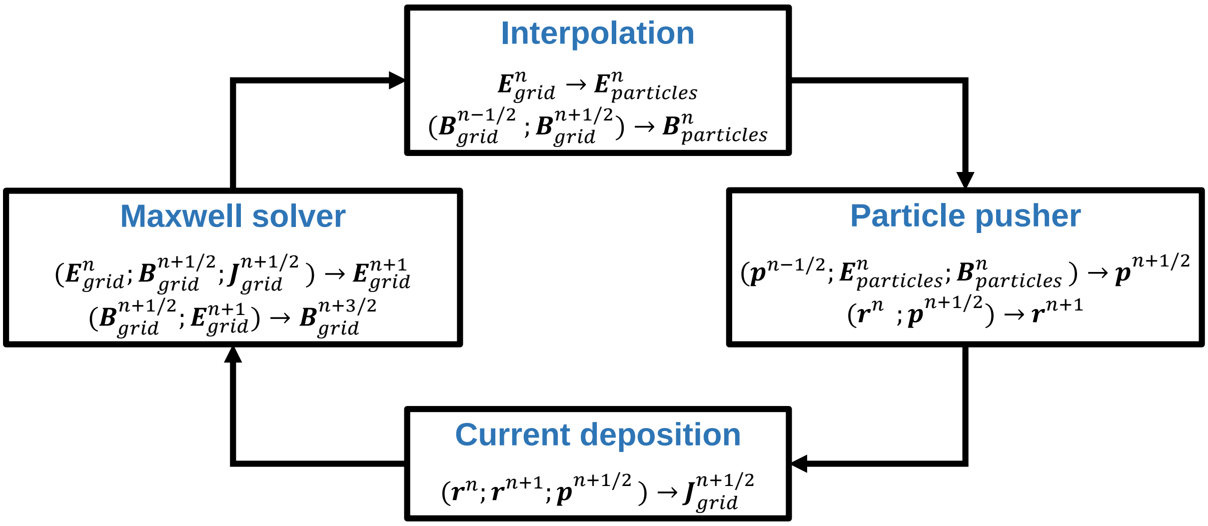

Figure 2.2: Diagram showing the four main steps of the standard PIC loop.

substantial overestimation of the force when the $\boldsymbol{E}$ and $\boldsymbol{v} \times \boldsymbol{B}$ terms should practically cancel each other, as is the case for example when an ultrarelativistic electron copropagates with a laser beam. In such a case, a higher precision is required when estimating $\boldsymbol{B}^{n}_{grid}$, so that an accurate cancellation of the $\boldsymbol{E}$ and $\boldsymbol{v} \times \boldsymbol{B}$ forces is obtained. This can be achieved for example with a third-order time interpolation [127].

Particle pusher

Once the electromagnetic fields are known at the positions of the particles, the relativistic equations of motion are integrated to obtain $\boldsymbol{p}_p^{n+1/2}$ and $\boldsymbol{r}_p^{n+1}$. This is usually done using the Boris pusher which was described in section 2.1.

Current deposition

In this step, the source terms are calculated on the grid in order to update the electromagnetic fields from Maxwell's equations 2.11-2.14:

$$\nabla . \boldsymbol{E} = \frac{\rho}{\varepsilon_0} \qquad \text{Gauss's law} \tag{2.11}$$

$$\nabla . \boldsymbol{B} = 0 \qquad \text{Gauss's law for magnetism} \tag{2.12}$$

$$\nabla \times \boldsymbol{E} = -\frac{\partial \boldsymbol{B}}{\partial t} \qquad \text{Maxwell-Faraday} \tag{2.13}$$

$$\nabla \times \boldsymbol{B} = \mu_0 \left(\boldsymbol{J} + \varepsilon_0 \frac{\partial \boldsymbol{E}}{\partial t} \right) \qquad \text{Ampère's law} \tag{2.14}$$

Only two of Maxwell's equations (Maxwell-Faraday and Ampère's law) are time-dependent. These are therefore the equations that will be used to update the $\boldsymbol{E}$ and $\boldsymbol{B}$ fields. Consequently, only the current needs to be deposited on the grid in order to update the electromagnetic fields. Additionally, we require that the algorithms used for the current deposition and Maxwell solver ensure that Gauss's law and Gauss's law for magnetism are satisfied throughout the simulation. In the case of the Yee Maxwell

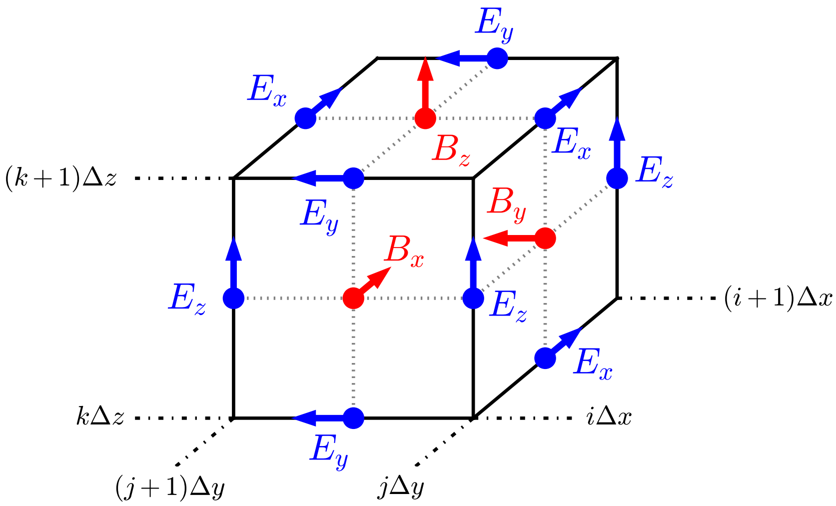

Figure 2.3: Diagram showing one grid cell of the Yee lattice. Different components of the electromagnetic fields are calculated at different positions in the cell.

solver, which will be described below, Gauss's law for magnetism is satisfied over the simulation provided that it is satisfied in the first iteration and Gauss's law is satisfied during the whole of the simulation if it is satisfied in the first iteration and if the continuity equation 2.15 is always verified.

$$\frac{\partial \rho}{\partial t} + \boldsymbol{\nabla}.\boldsymbol{J} = 0 \tag{2.15}$$

The current deposition should therefore be done in such a way that the charge conservation equation 2.15 is satisfied on the grid. If the current is deposited in the same manner as the charge (see equation 2.9) then the continuity equation is not verified. For this reason, a current deposition algorithm which satisfies equation 2.15 for any shape function was developed by Esirkepov [128]. Esirkepov's method is used in most present-day PIC codes.

Yee Maxwell solver

The most commonly used Maxwell solver in PIC simulations is the Yee solver [129], which is based on the finite-difference method. The Yee solver uses a staggered grid, which means that the different compoments of the electromagnetic fields are computed at different points in space. The Yee lattice grid cell is shown in figure 2.3. The positions are chosen so that the space derivatives in Maxwell-Faraday (2.13) and Ampère's law (2.14) are centered, which makes the discretized spatial derivates second-order accurate. The components of the current are calculated on the same positions as those of the electric field.

The electric field is updated to $\boldsymbol{E}_{grid}^{n+1}$ by discretizing Ampère's law. For example, using the notation $\boldsymbol{A}_{i,j,k}^{n} = \boldsymbol{A}(i\Delta x, j\Delta y, k\Delta z, n\Delta t)$, the x-component of the electric field $E_{x grid}$ is updated via the following formula:

$$E_{x\,i+\frac{1}{2},j,k}^{\,n+1} = E_{x\,i+\frac{1}{2},j,k}^{\,n} + c^2\Delta t \left[\frac{B_{z\,i+\frac{1}{2},j+\frac{1}{2},k}^{\,n+1/2} - B_{z\,i+\frac{1}{2},j-\frac{1}{2},k}^{\,n+1/2}}{\Delta y} - \frac{B_{y\,i+\frac{1}{2},j,k+\frac{1}{2}}^{\,n+1/2} - B_{y\,i+\frac{1}{2},j,k-\frac{1}{2}}^{\,n+1/2}}{\Delta z} - \mu_0 J_{x\,i+\frac{1}{2},j,k}^{\,n+1/2} \right] \tag{2.16}$$

Similar equations are used for updating $E_{y_{grid}}$ and $E_{z_{grid}}$. Then the magnetic field is updated to $\boldsymbol{B}_{grid}^{n+3/2}$ through the discretization of Maxwell-Faraday, which reads for the x-component:

$$B_{x\,i,j+\frac{1}{2},k+\frac{1}{2}}^{\,n+3/2} = B_{x\,i,j+\frac{1}{2},k+\frac{1}{2}}^{\,n+1/2} + \Delta t \left[-\frac{E_{z\,i,j+1,k+\frac{1}{2}}^{\,n+1} - E_{z\,i,j,k+\frac{1}{2}}^{\,n+1}}{\Delta y} + \frac{E_{y\,i,j+\frac{1}{2},k+1}^{\,n+1} - E_{y\,i,j+\frac{1}{2},k}^{\,n+1}}{\Delta z} \right] \tag{2.17}$$

Again, similar equations are used for updating $B_{y_{grid}}$ and $B_{z_{grid}}$. The fields $\boldsymbol{E}_{grid}^{n+1}$ and $\boldsymbol{B}_{grid}^{n+3/2}$ will then be used in the next iteration to update the particles' momenta via the Lorentz force.

Additional modules in the PIC loop

The 4 steps presented above (interpolation, particle pusher, current deposition and Maxwell solver) are the fundamental constituents of the PIC loop. Other modules may also be added to take new physics into account in the simulations, such as collisions, ionization or quantum electrodynamics effects [130].

Among these, only field ionization was included in some of the simulations presented in this manuscript. It is incorporated into the PIC loop by calculating at every time step the ionization probability of every atom or ion with a bound electron. This probability depends on the electric field interpolated at the position of the macroparticle and the ionization energy of the bound electron. It is usually calculated using the ADK model for tunnel ionization, developed by Ammosov, Delone and Krainov [131].

Typical parameters for plasma mirror simulations

Here, we present common parameters that are used when simulating the interaction of an ultraintense laser pulse with a plasma mirror. We also give the typical number of computation hours that is required to run these simulations.

The plasma is usually modeled using the density profile shown in figure 2.4. At the beginning of the simulation, each cell with a non-zero density is filled with a given number of particles (typically 10 particles per cell per specie in 3D and 100 particles per cell per specie in 2D, but this number can vary depending on the simulation). The density in each cell is adjusted by appropriately choosing the weight of the macroparticles. The exponential density profile is artificially cut at a finite density n_{MIN}, typically around $n_c/20$-$n_c/10$, in order to reduce the number of particles in the simulation. The maximum density n_{MAX} is usually around $100n_c$-$250n_c$. For high laser intensities, the choice of the initial plasma temperature only has a weak effect on the simulation results [61].

Plasma mirror simulations require very fine grid cells. Acceptable orders of magnitude regarding the charge and energy of ejected electrons can be obtained for spatial resolution on the order of $\Delta x \sim \lambda/50$. However, with the standard PIC algorithm presented above, full convergence of the high-harmonic generation efficiency and of the electron angular distribution requires spatial steps of approximately $\Delta x \sim \lambda/300$ [132, 133]. This makes the simulations computationally very expensive. Converged 2D simulations typically cost $\sim$ 10 000-20 000 hours while 3D simulations require billions of hours [132, 133].

Given the high number of computation hours involved, these simulations have to be carried out on parallel supercomputers. Efficient parallelization of the code is achieved, using the Message Passing

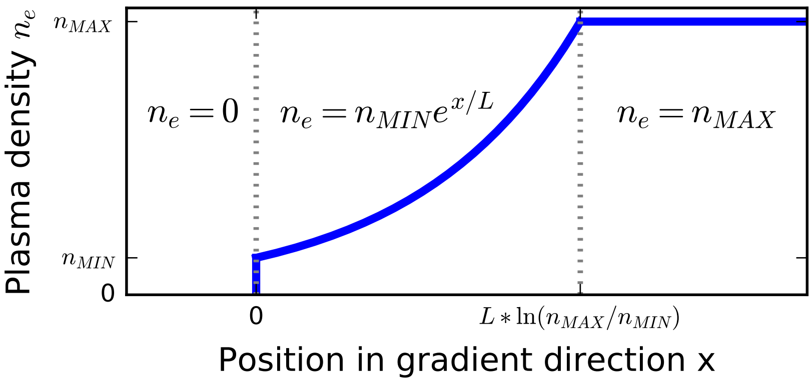

Figure 2.4: Initial plasma density profile in the plasma mirror simulations. The density profile is made of 3 parts: in the first part there is no plasma, in the second part the plasma density increases exponentially in the gradient direction and in the third part the plasma density is constant.

Interface (MPI) and OpenMP standards, through a domain-decomposition technique. The simulation box is divided into several subdomains and each MPI process is assigned one domain. The PIC loop is then performed locally in each subdomain. At every timestep, the MPI processes exchange information with their nearest neighboors regarding particles passing through different subdomains and the resolution of Maxwell's equations on the domain borders. With this method, converged 2D simulations are achievable on all present-day supercomputers but 3D plasma mirror simulations with the standard PIC algorithm remain out of reach, even with the largest existing supercomputing facilities.

The 2D simulations presented in this thesis use the standard PIC loop and have been performed using the code Warp, developed in Berkeley, on supercomputer Occigen, located at the CINES in Montpellier, France.

2.2.3 PIC simulations in cylindrical geometry

As we have seen in the previous section, converged 3D simulations of plasma mirror interaction with an ultraintense laser pulse are not tractable with the standard PIC loop. However, such simulations are desirable in some cases to obtain more realistic and quantitative results. In particular, the electron angular distributions resulting from VLA after the laser-plasma interaction possess intrinsically 3D features that cannot be retrieved from 2D PIC simulations.

When the laser impinges on the plasma at normal incidence, 3D simulations can be achieved by taking advantage of the approximate axial symmetry of the problem to strongly reduce the computational cost of the simulations. This is done by calculating the fields in cylindrical coordinates (r,θ,z) and by performing a Fourier series expansion in the azimuthal coordinate θ. This reads, for a given field A:

$$A(r,\theta,z) = \mathrm{Re}\left(\sum_{m=0}^{\infty} \widehat{A}^m(r,z)\exp(-im\theta)\right) \tag{2.18}$$

$$\begin{aligned} A(r,\theta,z) = \widehat{A}^0(r,z) &+ \mathrm{Re}\left(\widehat{A}^1(r,z)\right)\cos(\theta) + \mathrm{Im}\left(\widehat{A}^1(r,z)\right)\sin(\theta) \\ &+ \mathrm{Re}\left(\widehat{A}^2(r,z)\right)\cos(2\theta) + \mathrm{Im}\left(\widehat{A}^2(r,z)\right)\sin(2\theta) + \ldots \end{aligned} \tag{2.19}$$

The idea of this method is that only the first few modes are necessary to describe the interaction if the problem has an approximate cylindrical symmetry. For instance, a radially polarized pulse with a cylindrical envelope propagating in the z-direction is entirely described by the $m = 0$ mode. If the pulse has instead a linear polarization, it is then entirely described by the $m = 1$ mode. Therefore, in the simulations, the Fourier expansion is truncated at a chosen maximum order l for all the considered fields (charge and current densities and electromagnetic fields). The resulting simulation is performed on l 2D (r,z) grids. This means that its computational cost is that of l 2D simulations, which is considerably reduced compared to a single 3D simulation.

This method was developed and implemented into the code CALDER-CIRC by Agustin Lifschitz at LOA [134]. The interpolation, current deposition and Yee solver are adapted to the cylindrical geometry and a dedicated technique is used to deal with the singularity on the $r = 0$ axis. The code CALDER-CIRC was used in this thesis to simulate the interaction between a radially polarized pulse and a plasma mirror at normal incidence, as is presented in Chapter 4.

2.2.4 Pseudo-spectral Maxwell solvers

The code CALDER-CIRC is a very useful tool to perform 3D simulations at a very reasonable cost when the laser has a normal incidence. However electron acceleration and high-harmonic generation experiments with solid targets are rarely performed at normal incidence. This is because:

- From a theoretical point of view, in linear polarization there is virtually no electric field component directed towards the plasma at normal incidence, which hampers the ejection of electrons and emission of harmonics at short gradients.

- From an experimental point of view, after interaction at normal incidence, the laser pulse is reflected back into the laser system, which may cause damage to optics and amplifying media.

3D simulations are therefore also desirable to accurately explain and predict experimental results in geometries that differ from normal incidence. They are not tractable with the standard PIC method because convergence of the simulations occurs for very small spatial steps ($\Delta x \sim \lambda/300$). One possibility to make these simulations feasible is therefore to reduce the numerical errors induced by the different steps of the PIC loop so that the simulations can converge for larger spatial steps. One of such errors is **numerical dispersion**, which comes from the Maxwell solver. Numerical dispersion is commonly used to quantify the errors introduced by the discretization of Maxwell's equations. In particular, numerical dispersion causes an electromagnetic wave to propagate at a nonphysical velocity, which can depend on its wavelength and on its direction with respect to the simulation grid. As we will see in the following section, the Yee solver induces numerical dispersion.

2.2.4.1 Numerical dispersion in the Yee solver

Numerical dispersion is studied through the vacuum **numerical dispersion relation** of a given solver. In the case of the Yee solver, it can be obtained by assuming field expressions of the form $\boldsymbol{E} = \boldsymbol{E_0} e^{i(k_x x + k_y y + k_z z - \omega t)}$ and $\boldsymbol{B} = \boldsymbol{B_0} e^{i(k_x x + k_y y + k_z z - \omega t)}$ and by inserting these expressions into the discretized time-dependent Maxwell's equations 2.16- 2.17. The resulting Yee vacuum dispersion relation is:

$$\frac{\sin^2\left(\frac{\omega \Delta t}{2}\right)}{c^2 \Delta t^2} = \frac{\sin^2\left(\frac{k_x \Delta x}{2}\right)}{\Delta x^2} + \frac{\sin^2\left(\frac{k_y \Delta y}{2}\right)}{\Delta y^2} + \frac{\sin^2\left(\frac{k_z \Delta z}{2}\right)}{\Delta z^2} \tag{2.20}$$

This equation is different from the physical dispersion relation $\omega = kc$ (even though equation 2.20 reduces to $\omega = kc$ when $k_x \Delta x$, $k_y \Delta y$, $k_z \Delta z$ and $\omega \Delta t$ approach zero), as can be seen in figures 2.5(a) and 2.5(b) in the 2D case. This means that the discretization of Maxwell's equations introduces numerical dispersion. One consequence is that solutions that are exponentially growing in time may appear if the timestep Δt is too large. This happens when Δx, Δy, Δz, Δt, k_x, k_y and k_z are such that the right hand side of equation 2.20 is greater than $1/(c\Delta t)^2$, which can only be fulfilled if the frequency ω is imaginary. In order to avoid such numerical instability, a condition called the **CFL condition** (named after Courant, Friedrich and Lewy, also known as the **Courant condition**) must be respected. The CFL condition is:

$$\frac{1}{c^2 \Delta t^2} \geq \frac{1}{\Delta x^2} + \frac{1}{\Delta y^2} + \frac{1}{\Delta z^2} \tag{2.21}$$

When the spatial steps are the same in all directions, the Courant condition reduces to its usual form: $\Delta t \leq \frac{\Delta x}{c\sqrt{3}}$. In 2D this inequality becomes $\Delta t \leq \frac{\Delta x}{c\sqrt{2}}$ and in 1D $\Delta t \leq \frac{\Delta x}{c}$.

Another consequence of numerical dispersion is that the group and phase velocities of electromagnetic waves are not always equal to c. The phase velocity $v_{\phi_{Yee}}$ can be obtained by calculating $\omega / |\boldsymbol{k}|$, which yields:

$$v_{\phi_{Yee}} = \frac{2}{\Delta t |\boldsymbol{k}|} \arcsin\left(\frac{c\Delta t}{\Delta x}\sqrt{\sin^2\left(\frac{k_x \Delta x}{2}\right) + \sin^2\left(\frac{k_y \Delta y}{2}\right) + \sin^2\left(\frac{k_z \Delta z}{2}\right)}\right) \tag{2.22}$$

Similarly, the group velocity can be calculated using the formula $v_{g_{Yee}} = |\boldsymbol{\nabla_k} \omega|$, which yields, after assuming for simplicity that $\Delta x = \Delta y = \Delta z$:

$$v_{g_{Yee}} = \frac{c\sqrt{\sin^2\left(\frac{k_x \Delta x}{2}\right)\cos^2\left(\frac{k_x \Delta x}{2}\right) + \sin^2\left(\frac{k_y \Delta x}{2}\right)\cos^2\left(\frac{k_y \Delta x}{2}\right) + \sin^2\left(\frac{k_z \Delta x}{2}\right)\cos^2\left(\frac{k_z \Delta x}{2}\right)}}{\sqrt{\left(\sin^2\left(\frac{k_x \Delta x}{2}\right) + \sin^2\left(\frac{k_y \Delta x}{2}\right) + \sin^2\left(\frac{k_z \Delta x}{2}\right)\right)\left(1 - \frac{c^2 \Delta t^2}{\Delta x^2}\left(\sin^2\left(\frac{k_x \Delta x}{2}\right) + \sin^2\left(\frac{k_y \Delta x}{2}\right) + \sin^2\left(\frac{k_z \Delta x}{2}\right)\right)\right)}} \tag{2.23}$$

The 2D Yee phase and group velocities are plotted in figures 2.5(c)-(d) as a function of $k_x \Delta x$ and $k_y \Delta y$. We first note that we always have $v_{\phi_{Yee}} \leq c$ and $v_{g_{Yee}} \leq c$, which means that the Yee solver tends to underestimate the velocity of electromagnetic pulses. In the particular case where $k_x = k_y$, then $v_{\phi_{Yee}} = v_{g_{Yee}} = c$. The Yee solver is thus not dispersive when the electromagnetic waves are propagating along the grid diagonal. On the other hand, when either $k_x = 0$ or $k_y = 0$, $v_{\phi_{Yee}}$ and $v_{g_{Yee}}$ can strongly

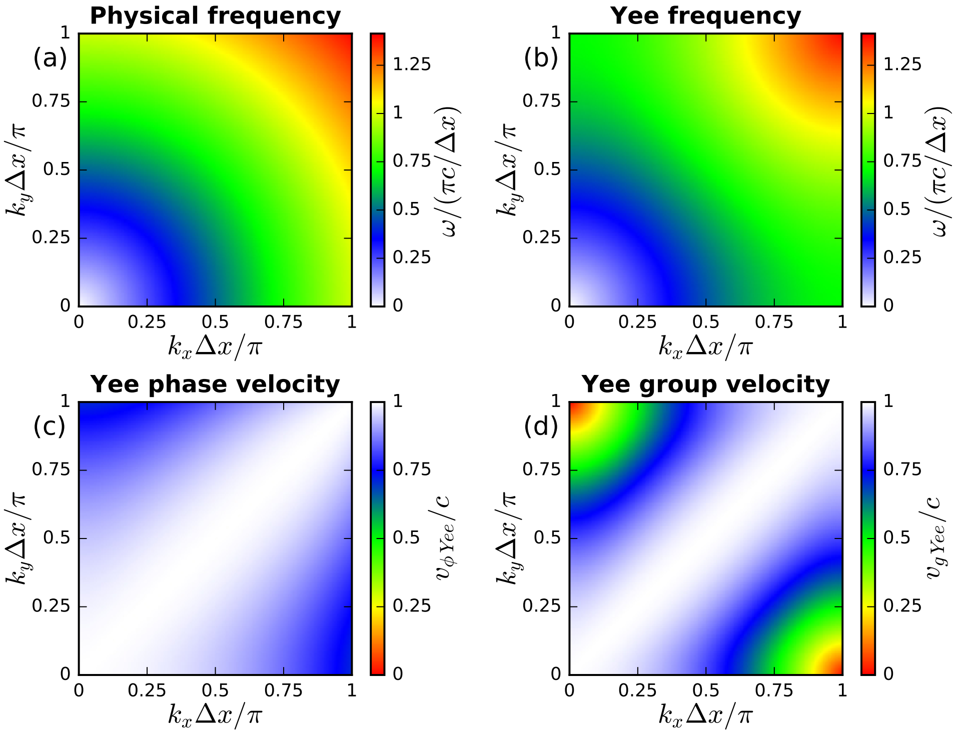

Figure 2.5: (a) 2D Physical dispersion relation in vacuum as a function of k_x and k_y. (b) 2D Yee dispersion relation in vacuum and corresponding (c) phase velocity and (d) group velocity as a function of k_x and k_y. We assume here that $\Delta x = \Delta y$ and we have chosen $\Delta t = \frac{\Delta x}{c\sqrt{2}}$.

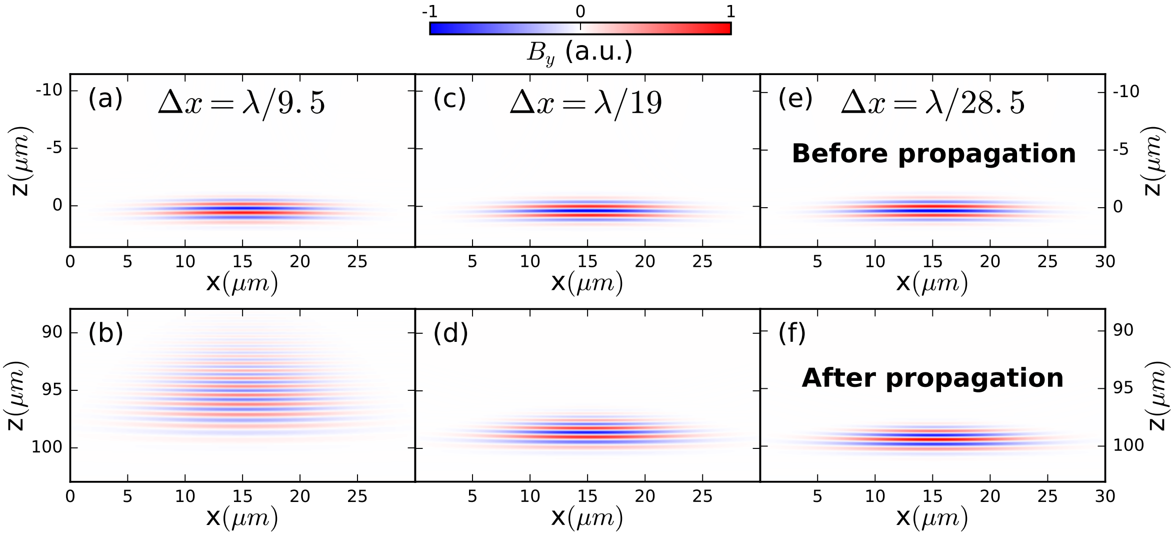

Figure 2.6: Snapshots from 2D simulations. Magnetic field of a 3.14 fs laser pulse (in FWHM of intensity) with central wavelength $\lambda = 800$ nm (a),(c),(e) before or (b),(d),(f) after a 100 $\mathrm{\mu m}$ propagation with the Yee solver. The spatial step is the same in both direction and is either (a)-(b) $\Delta x = \lambda/9.5$, (c)-(d) $\Delta x = \lambda/19$ or (e)-(f) $\Delta x = \lambda/28.5$. The laser pulse propagates towards the bottom direction and has a Rayleigh length of 141 $\mathrm{\mu m}$. Detailed simulation parameters are provided in appendix B.

differ from c, especially in the high-frequency limit where $|\boldsymbol{k}|$ approaches $\pi/\Delta x$. This means that the Yee solver is highly dispersive for electromagnetic pulses propagating along one of the grid directions. This is illustrated in figure 2.6, which shows the vacuum propagation with the Yee solver of a few-cycle pulse for a distance of 125 wavelengths along one of the grid directions. When a large spatial step is used ($\Delta x = \lambda/9.5$), strong numerical dispersion is observed: the laser pulse becomes chirped as its high frequency components lag behind, which results in an artificial increase of the laser pulse duration. As expected, numerical dispersion becomes less significant when the spatial step is reduced. For $\Delta x = \lambda/19$, the increase in pulse duration is small but still visible and it becomes imperceptible for $\Delta x = \lambda/28.5$. The "numerical vacuum" therefore behaves as a dispersive material, with an anisotropic frequency-dependent refractive index. In plasma mirror simulations, this causes the harmonic emission to be emitted at a frequency-dependent angle, following Snell-Descartes law [132].

2.2.4.2 Principle of pseudo-spectral solvers

The example of figure 2.6 illustrates the fact that the grid cells must be fine enough not only to resolve the relevant physical phenomena (e.g. resolve the laser and plasma wavelengths for a given problem) but also to reduce the numerical errors induced by the discretization of Maxwell's equations to an acceptable level. If the accuracy of the Maxwell solver is improved, the spatial step Δx may therefore be chosen larger, which can reduce the computational cost of the simulation.

The spatial derivatives in the Yee solver are estimated from centered finite difference. For instance, if a is a 1D function sampled at equally spaced grid points $a_j = a(j\Delta x)$, then the derivative of a sampled on the same gridpoints is calculated by:

$$\left(\frac{da}{dx}\right)_j = \frac{a_{j+1} - a_{j-1}}{2\Delta x} \tag{2.24}$$

This method is second-order accurate, which means that the errors coming from the discretization of the spatial derivative scale as Δx^2 [135]. The accuracy of the finite difference spatial derivative can be raised by taking into consideration more adjacent grid points in the calculation. For example, a fourth-order accuracy can be obtained with the following formula, which takes into account the two nearest grid points in each direction:

$$\left(\frac{da}{dx}\right)_j = \frac{-a_{j+2} + 8a_{j+1} - 8a_{j-1} + a_{j-2}}{12\Delta x} \tag{2.25}$$

More generally, finite difference with an arbitrary order p accuracy can be achieved by including the $p/2$ (p is assumed to be even) nearest grid points in each direction in the calculation [136]:

$$\left(\frac{da}{dx}\right)_j = \sum_{l=1}^{p/2} \alpha_{p,l} \frac{a_{j+l} - a_{j-l}}{2l\Delta x} \tag{2.26}$$

Where $\alpha_{p,l} = (-1)^{l+1} \dfrac{2((p/2)!)^2}{(p/2-l)!(p/2+l)!}$ [137]. Of course, the computational load of the finite difference method increases with the accuracy order.

Alternatively, the spatial derivatives can be calculated through a discrete Fourier transform:

$$\left(\frac{da}{dx}\right)_j = \left(\mathscr{F}^{-1}\left[ik_x \mathscr{F}(a)\right]\right)_j \tag{2.27}$$

Here, $\mathscr{F}$ is the *discrete* Fourier transform, $\mathscr{F}^{-1}$ is the inverse discrete fourier transform, k_x is the Fourier transform variable of x and i is the unit imaginary number. According to the Nyquist-Shannon sampling theorem, equation 2.27 is *exact* with the assumptions that the function a is periodic and that it contains no frequency component such that $|k_x| > \pi/\Delta x$ [135]. In fact, equation 2.27 is the limit of equation 2.26 as the accuracy order p approaches infinity. With this method, all the spatial derivates $\left(\frac{da}{dx}\right)_j$ can be calculated in one step with infinite precision and at a reasonable computational cost thanks to the fast Fourier transform (FFT) algorithm, which scales as $O(n\ln(n))$, where n is the data size.

This idea is the basis of pseudospectral methods. Among these, the best known is the pseudospectral time domain (**PSTD**) Maxwell solver [138]. In the PSTD method, the spatial derivatives are calculated in Fourier space, but the fields are still advanced in time through finite differences in a leapfrog arrangement. The following equations are used to advance the fields in time in the PSTD solver:

$$\widetilde{\boldsymbol{E}}^{n+1} = \widetilde{\boldsymbol{E}}^{n} + ic^2\Delta t \boldsymbol{k} \times \widetilde{\boldsymbol{B}}^{n+1/2} - \frac{\Delta t}{\varepsilon_0}\widetilde{\boldsymbol{J}}^{n+1/2} \tag{2.28}$$

$$\widetilde{\boldsymbol{B}}^{n+3/2} = \widetilde{\boldsymbol{B}}^{n+1/2} - i\Delta t \boldsymbol{k} \times \widetilde{\boldsymbol{E}}^{n+1} \tag{2.29}$$

Here, we use the notation $\widetilde{\boldsymbol{A}}^n \equiv \mathscr{F}(\boldsymbol{A}(t = n\Delta t))$. Even though the PSTD solver is more accurate than the Yee solver, it still introduces numerical dispersion and still has a Courant condition because of the errors coming from the time integration. In this case, the dispersion is isotropic and the electromagnetic waves propagate at slightly superluminal velocities.

Instead of using finite differences, the time integration can also be performed analytically under the weak assumption that the current density is constant during one timestep (an assumption which is already implicitly made in the PSTD or Yee solvers). This idea is implemented in the pseudospectral *analytical* time domain (**PSATD**) Maxwell solver [139, 140]. Because the time derivatives are calculated analytically and the spatial derivatives are computed with infinite precision in Fourier space, the PSATD is free of numerical dispersion: its vacuum dispersion relation is $\omega = |\boldsymbol{k}|c$, there is no Courant condition and the electromagnetic waves travel at c regardless of their direction or frequency.

Pseudospectral solvers naturally calculate all the electromagnetic fields components at the same position on the unit grid cell, but they can be easily recast on the Yee staggered grid of figure 2.3 [141]. Similarly, the $\boldsymbol{E}$ and $\boldsymbol{B}$ fields in the PSATD solver can either be calculated at the same times or in a leapfrog arrangement as in the Yee solver. In the latter case, the following equations are used for the Maxwell solver [140]:

$$\widetilde{\boldsymbol{E}}^{n+1} = \widetilde{\boldsymbol{E}}^{n} + 2iSc\widehat{\boldsymbol{k}} \times \widetilde{\boldsymbol{B}}^{n+1/2} - \frac{2S}{|\boldsymbol{k}|c\varepsilon_0}\widetilde{\boldsymbol{J}}^{n+1/2} + \frac{\widehat{\boldsymbol{k}}}{\varepsilon_0}\left(\widehat{\boldsymbol{k}}.\widetilde{\boldsymbol{J}}^{n+1/2}\right)\left(\frac{2S}{|\boldsymbol{k}|c} - \Delta t\right) \tag{2.30}$$

$$\widetilde{\boldsymbol{B}}^{n+3/2} = \widetilde{\boldsymbol{B}}^{n+1/2} - \frac{2iS}{c}\widehat{\boldsymbol{k}} \times \widetilde{\boldsymbol{E}}^{n+1} + i\mu_0\frac{1-C}{|\boldsymbol{k}|}\widehat{\boldsymbol{k}} \times \left(\widetilde{\boldsymbol{J}}^{n+3/2} - \widetilde{\boldsymbol{J}}^{n+1/2}\right) \tag{2.31}$$

Here, $\widehat{\boldsymbol{k}} = \boldsymbol{k}/|\boldsymbol{k}|$, $S = \sin(|\boldsymbol{k}|c\Delta t/2)$ and $C = \cos(|\boldsymbol{k}|c\Delta t/2)$. If a first-order Taylor expansion is performed on the parameters S and C, i.e. $S \simeq |\boldsymbol{k}|c\Delta t/2$ and $C \simeq 1$, then the PSATD equations 2.30-2.31 reduce to the PSTD equations 2.28-2.29. Equivalently, the PSTD solver tends towards the PSATD solver as Δt approach zero.

When pseudospectral solvers are used in PIC codes, the electromagnetic fields are updated in Fourier space but an inverse discrete Fourier transform has to be performed at every time step so that the fields can be interpolated at the position of the particles.

2.2.4.3 Finite order pseudo-spectral solvers

The PSTD and PSATD solvers calculate the spatial derivatives with infinite precision. For this reason, it is often said that pseudospectral solvers are infinite order methods.

It is also possible to define pseudo-spectral solvers with *finite* accuracy order. In this case, the spatial derivatives are calculated in Fourier space with the following formula:

$$\left(\frac{da}{dx}\right)_j = \left(\mathscr{F}^{-1}\left[ik_x^*\mathscr{F}(a)\right]\right)_j \tag{2.32}$$

Where k_x^* is a modified wavenumber which can be obtained by converting equation 2.26 into Fourier space [142]. For an accuracy of order p, k_x^* reads:

$$k_x^* = \sum_{l=1}^{p/2}\alpha_{p,l}\frac{\exp(ilk_x\Delta x) - \exp(-ilk_x\Delta x)}{2il\Delta x} = \sum_{l=1}^{p/2}\alpha_{p,l}\frac{\sin(lk_x\Delta x)}{l\Delta x} \tag{2.33}$$

The order-p PSTD and the order-p PSATD are simply obtained by replacing $\boldsymbol{k}$ with $\boldsymbol{k}^*$ in equations 2.28-2.29 and 2.30-2.31 respectively. Thus, the computational load of a finite order pseudo-spectral solver does not depend on the choice of the order p and is similar to that of the infinite order case. It might seem peculiar to lower the accuracy of a solver without decreasing its computational cost but as we will

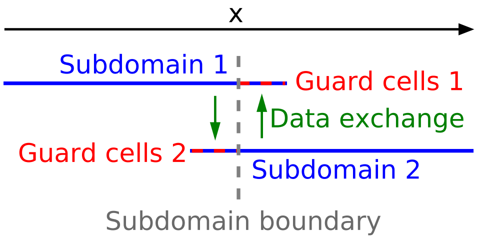

Figure 2.7: Principle of the domain decomposition for pseudospectral solvers in 1D. At every timestep, the fields are advanced in Fourier space by performing local FFTs in each subdomain, including the guard cells. Then, after a local inverse FFT, the fields in the guard cells are replaced by the fields in the adjacent subdomains.

see in the following section, finite order pseudo-spectral solvers are very useful for massively parallel simulations.

It is worth mentioning that the derivatives calculated using equation 2.32 are the same as those calculated using equation 2.26. This means that the order-p PSTD solver is mathematically equivalent to an order-p finite difference solver, the only difference being that the derivatives are calculated in the Fourier domain, which is more efficient for very high orders. It follows in particular that the infinite order PSTD solver is the limit of finite difference solvers as the accuracy order p approaches infinity [143].

2.2.4.4 Domain decomposition method for pseudo-spectral solvers

Even though the PSATD solver has been known since 1973 [139] and is much more precise than the Yee solver, it had not, until recently, been widely used in large-scale PIC simulations. This is because of its inefficient parallel scalability coming from the use of global FFTs, which require many global inter-processor communications. This has limited the number of cores that could be used with pseudospectral solvers, thereby rendering them impractical for demanding 3D simulations that can require up to hundreds of thousands of cores.

In order to overcome this issue, a domain decomposition technique for pseudospectral solvers was recently proposed [140]. In this method, the simulation box is divided into subdomains and each MPI process is assigned one domain, together with guard cells along the subdomain border, as illustrated in figure 2.7. The FFTs are then performed locally and information is exchanged between neighboring MPI processes concerning the fields in the guard cell regions. This decomposition technique, which enables efficient parallelization of pseudospectral solvers up to 800 000 cores [133], is identical to that of the standard PIC algorithm but usually mandates more guard cells.

Indeed, in the case of the Yee solver, because the spatial derivatives are performed locally (only taking into account the nearest grid point in each direction), only one guard cell surrounding each subdomain is necessary. Similarly, for a solver of accuracy order p, $p/2$ guard cells are in principle required for the calculation of the spatial derivatives on the domain borders. Using less than $p/2$ guard cells in this case would introduce **truncation errors**. Such errors are unavoidable with infinite order pseudospectral solvers since in this case $p/2 = +\infty$ (this is essentially because the FFT is a global operation).

Truncation errors have been characterized analytically and numerically in reference [144] for the PSTD solver of arbitrary order. The main results from this study are that:

- For a given number of guard cells, increasing the accuracy of the solver increases the truncation errors. This is because high-order solvers have a reduced locality (more distant grid points are taken into account in the spatial derivative calculation).

- For a given accuracy order, increasing the number of guard cells decreases the truncation errors but increases the computional load of the simulations by increasing the number of grid points in each process as well as the number of inter-processor communications.

- The best compromise is found when ultrahigh order (e.g. order $p = 100$) solvers are used with a limited number of guard cells (typically around 10). Compared to infinite order, using ultrahigh order solvers reduces the truncation errors while maintaining an excellent precision on the spatial derivatives. Using ~10 guard cells is then enough to ensure that the truncation errors remain acceptable while limiting the increase in the computional cost associated to the guard regions.

In practice, the PSATD solver with ultrahigh order is used in massively parallel simulations. Using finite order has the effect of increasing the locality of the PSATD solver and can thus mitigate the truncation errors arising from the domain decomposition method. Unlike in the infinite order case, the finite order PSATD is subject to numerical dispersion. However, numerical dispersion can be rendered arbitrarily small if the accuracy order is high enough. The dispersion relation of the order-p PSATD is [132]:

$$\omega(\boldsymbol{k}) = |\boldsymbol{k}^*|c = \frac{c}{\Delta x}\sqrt{\left(\sum_{l=1}^{p/2}\alpha_{p,l}\frac{\sin(lk_x\Delta x)}{l}\right)^2 + \left(\sum_{l=1}^{p/2}\alpha_{p,l}\frac{\sin(lk_y\Delta x)}{l}\right)^2 + \left(\sum_{l=1}^{p/2}\alpha_{p,l}\frac{\sin(lk_z\Delta x)}{l}\right)^2} \tag{2.34}$$

Where we have assumed for simplicity that $\Delta x = \Delta y = \Delta z$. There is no Courant condition in vacuum associated to this dispersion relation. The phase velocity can be immediatly obtained by dividing the previous expression by $|\boldsymbol{k}|$ and the group velocity can be calculated as previously using the formula $v_{g_{PSATDp}} = |\boldsymbol{\nabla}_{\boldsymbol{k}}\omega|$, which yields:

$$\begin{aligned} v_{g_{PSATDp}} = \frac{c^2}{\Delta x\omega(\boldsymbol{k})}\Bigg[&\left(\left(\sum_{l=1}^{p/2}\alpha_{p,l}\cos(lk_x\Delta x)\right)\left(\sum_{l=1}^{p/2}\alpha_{p,l}\frac{\sin(lk_x\Delta x)}{l}\right)\right)^2 + \\ &\left(\left(\sum_{l=1}^{p/2}\alpha_{p,l}\cos(lk_y\Delta x)\right)\left(\sum_{l=1}^{p/2}\alpha_{p,l}\frac{\sin(lk_y\Delta x)}{l}\right)\right)^2 + \left(\left(\sum_{l=1}^{p/2}\alpha_{p,l}\cos(lk_z\Delta x)\right)\left(\sum_{l=1}^{p/2}\alpha_{p,l}\frac{\sin(lk_z\Delta x)}{l}\right)\right)^2\Bigg]^{1/2} \end{aligned} \tag{2.35}$$

The dispersion relation, phase velocity and group velocity of the PSATD solver of order 100 in the 2D case are plotted in figure 2.8. We see in particular that numerical dispersion is negligible outside of the high-frequency limit where either k_x or k_y approach $\pi/\Delta x$. This can be confirmed by looking at the same example as with the Yee solver: the propagation of a few-cycle laser pulse, which is shown in figure 2.9. In the case of the Yee solver, the pulse was strongly chirped after 100 $\mu\mathrm{m}$ of propagation for $\Delta x = \lambda/9.5$. On the opposite, with the PSATD solver of order 100, no significant dispersion of the pulse is observed,

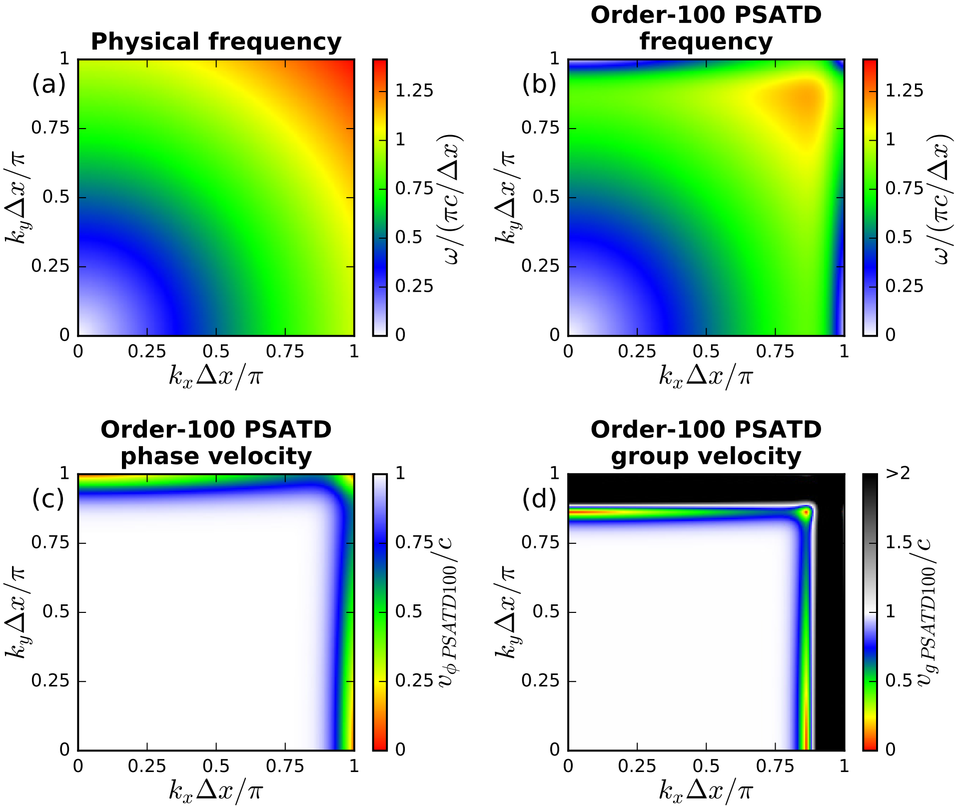

Figure 2.8: (a) 2D Physical dispersion relation in vacuum as a function of k_x and k_y. (b) 2D PSATD of order 100 dispersion relation in vacuum and corresponding (c) phase velocity and (d) group velocity as a function of k_x and k_y.

even for spatial steps as large as $\Delta x = \lambda/3.2$, for which the description of the laser pulse itself (and more particularly of its interaction with particles) would be very doubtful. This example confirms that improving the precision of the Maxwell solver is a way to obtain acceptable solutions to a given problem with larger spatial and time steps and thus to reduce the computational load of the simulations.

In the case of plasma mirror simulations, it was shown in reference [133] that convergence of the ejected electron angular distribution is achieved for $\Delta x \sim \lambda/70$ with the order-100 PSATD solver. For comparison, a spatial resolution of $\Delta x \sim \lambda/300$ is necessary to attain convergence in 2D simulations with the Yee solver. Even though at a given resolution simulations with pseudospectral solvers are approximately twice as slow as simulations with the Yee solver (because of the FFT calculations) [132], the possibility of using larger spatial steps with the PSATD solver reduces the time to solution by more than two orders of magnitude in 3D simulations. This method make 3D PIC simulations of electron acceleration from plasma mirrors achievable with existing supercomputing facilities. A single 3D simulation remains nevertheless extremely expensive, with a numerical cost of several million computation hours, which prohibits the exploration of large parameter spaces. It can be noted that an even finer spatial resolution is required to attain convergence of the high-harmonic generation efficiency, which can make the simulations even more costly [145]. It is worth mentioning that the PSATD solver has also been

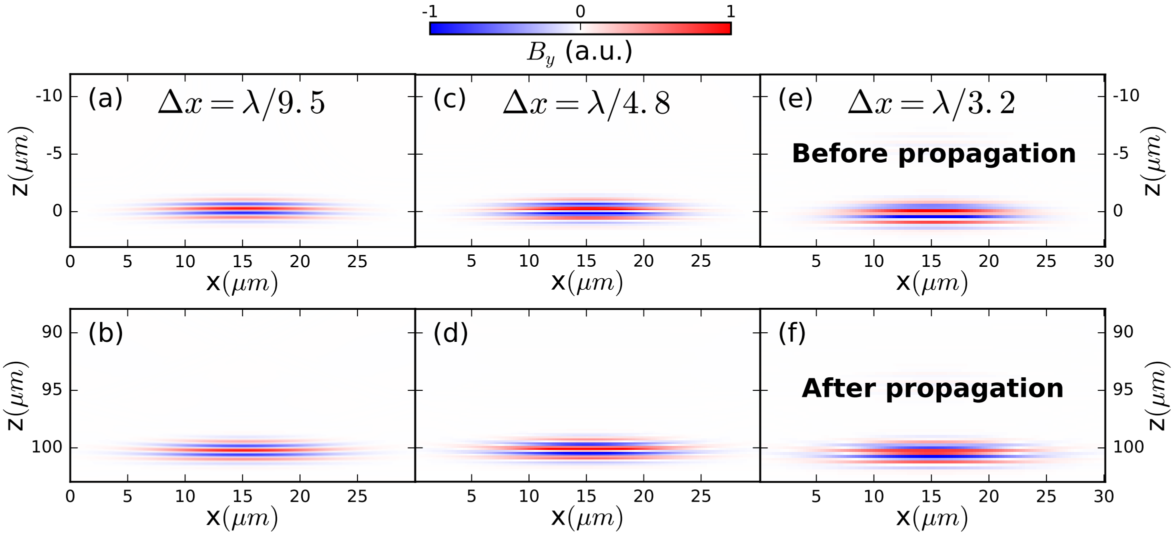

Figure 2.9: Snapshots from 2D simulations. Magnetic field of a 3.14 fs laser pulse (in FWHM of intensity) with central wavelength $\lambda = 800$ nm (a),(c),(e) before or (b),(d),(f) after a 100 μm propagation with the order-100 PSATD solver. The spatial step is the same in both direction and is either (a)-(b) $\Delta x = \lambda/9.5$, (c)-(d) $\Delta x = \lambda/4.8$ or (e)-(f) $\Delta x = \lambda/3.2$. The laser pulse propagates towards the bottom direction and has a Rayleigh length of 141 μm. Detailed simulation parameters are provided in appendix B.

used to improve the accuracy and stability of laser wakefield acceleration simulations, notably through the reduction of numerical Cherenkov radiation [146, 147, 148, 136].

In this thesis, the PSATD solver of order 100 was used to perform 3D simulations of electron acceleration from plasma mirrors using the code Warp [149] coupled with the high-performance PICSAR library [150], which is developed by the group of Henri Vincenti at CEA Saclay.

2.3 Modeling tightly focused few-cycle laser pulses

We describe in this section how laser pulses can be described in simulations. The most common approach is to use Gaussian beams with a temporal envelope. This method is usually suitable for PIC simulations, in which Maxwell's equations are solved, but is inappropriate for test particle simulations. We therefore present, following the work of April [151, 152], closed-form expressions of linearly or radially polarized pulses that are exact solutions of Maxwell equations and that can be used in either PIC or test particle simulations. It should be noted that only ideal laser pulses, containing no aberrations or imperfections, are considered in this thesis.

2.3.1 Gaussian beams

We briefly explain here how the expression of the Gaussian beam can be obtained as well as the approximations upon which it relies.

It can be shown using Maxwell's equations that the electric and magnetic fields in vacuum must satisfy the electromagnetic wave equation:

$$\nabla^2 \boldsymbol{E}(\boldsymbol{r},t) - \frac{1}{c^2}\frac{\partial^2 \boldsymbol{E}}{\partial t^2}(\boldsymbol{r},t) = 0 \tag{2.36}$$

$$\nabla^2 \boldsymbol{B}(\boldsymbol{r},t) - \frac{1}{c^2}\frac{\partial^2 \boldsymbol{B}}{\partial t^2}(\boldsymbol{r},t) = 0 \tag{2.37}$$

This means that each cartesian component φ of the electromagnetic fields must satisfy the *scalar* wave equation:

$$\nabla^2 \varphi(\boldsymbol{r},t) - \frac{1}{c^2}\frac{\partial^2 \varphi}{\partial t^2}(\boldsymbol{r},t) = 0 \tag{2.38}$$

By performing a Fourier transform with respect to time (or equivalently by assuming a monochromatic temporal dependence of the form $\varphi(\boldsymbol{r},t) = \widetilde{\varphi}(\boldsymbol{r},\omega)e^{i\omega t}$), the wave equation becomes the Helmholtz equation:

$$\nabla^2 \widetilde{\varphi}(\boldsymbol{r},\omega) + k^2 \widetilde{\varphi}(\boldsymbol{r},\omega) = 0 \tag{2.39}$$

Where $k = \omega/c$. Simple solutions to the Helmholtz equation are plane waves of the form e^{-ikz} (here propagating along the positive z-direction) and spherical waves of the form $e^{-ik|\boldsymbol{r}|}/|\boldsymbol{r}|$ (in this case originating from a source point at $\boldsymbol{r} = 0$).

Next, we consider a beam propagating along the z direction, so that its principal spatial dependence is e^{-ikz}. This term can be factored out of the Helmholtz equation by writing $\widetilde{\varphi}(\boldsymbol{r},\omega) = \widetilde{u}(\boldsymbol{r},\omega)e^{-ikz}$ and by inserting this expression into equation 2.39, which yields:

$$\frac{\partial^2 \widetilde{u}}{\partial x^2} + \frac{\partial^2 \widetilde{u}}{\partial y^2} + \frac{\partial^2 \widetilde{u}}{\partial z^2} - 2ik\frac{\partial \widetilde{u}}{\partial z} = 0 \tag{2.40}$$

The **paraxial approximation** consists in neglecting the term $\frac{\partial^2 \widetilde{u}}{\partial z^2}$ in the previous equation. This means that the longitudinal variation of the laser pulse, excluding the oscillating term e^{-ikz}, is small compared to one wavelength and compared to the transverse variation of the laser pulse. It is valid if the wavevectors $\boldsymbol{k}$ that make up the laser pulse are directed close to the optical axis, which corresponds experimentally to a weak focusing. With this approximation, the paraxial Helmholtz equation, or paraxial wave equation is:

$$\frac{\partial^2 \widetilde{u}}{\partial x^2} + \frac{\partial^2 \widetilde{u}}{\partial y^2} - 2ik\frac{\partial \widetilde{u}}{\partial z} = 0 \tag{2.41}$$

Spherical waves of the form $\widetilde{\varphi} = e^{-ik|\boldsymbol{r}|}/|\boldsymbol{r}|$ are not anymore solutions to the paraxial wave equation. However, a solution to equation 2.41 can be obtained by assuming $z^2 \gg x^2 + y^2$ and making the substitutions $|\boldsymbol{r}| \approx z + (x^2 + y^2)/(2z)$ in the phase term and $|\boldsymbol{r}| \approx z$ in the amplitude term of the spherical wave. The resulting function, sometimes refered to as a "paraxial spherical wave" [31], is an exact solution to equation 2.41 and reads:

$$\widetilde{u} \propto \frac{1}{z}\exp\left(-ik\frac{r^2}{2z}\right) \tag{2.42}$$

Here $r = \sqrt{x^2 + y^2}$ is the radial coordinate in cylindrical coordinates.

The expression of the Gaussian beam can be obtained by assuming that a source point located at the complex position $(0,0,-iz_R)$, where z_R is the Rayleigh length as defined in chapter 1, generates a paraxial spherical wave [31, 153]. This technique, known as the **complex source point** method, leads to the following expressions:

$$\widetilde{u}(\boldsymbol{r},\omega) = F(\omega)\varphi_0 \frac{iz_R}{\widetilde{q}(z)} \exp\left(-ik\frac{r^2}{2\widetilde{q}(z)}\right) \tag{2.43}$$

$$\widetilde{\varphi}(\boldsymbol{r},\omega) = F(\omega)\varphi_0 \frac{iz_R}{\widetilde{q}(z)} \exp\left(-ik\frac{r^2}{2\widetilde{q}(z)}\right)\exp(-ikz) \tag{2.44}$$

Here, φ_0 is a parameter related to the amplitude of $\widetilde{\varphi}$, F is a function that takes into account the possible dependence of the amplitude on ω and $\widetilde{q}(z) = z + iz_R$. The linearly polarized (along x) monochromatic (with frequency ω) Gaussian beam is obtained by taking the real part of $\widetilde{\varphi}(\boldsymbol{r},\omega)e^{i\omega t}$, where $\widetilde{\varphi}(\boldsymbol{r},\omega)$ is given by equation 2.44, for the E_x and B_y components and by assuming that all the other components are zero. After some algebra, this yields:

$$\boldsymbol{E}(\boldsymbol{r},t) = E_0\frac{w_0}{w(z)}\exp\left(-\frac{r^2}{w(z)^2}\right)\cos\left(kz - \omega t + k\frac{r^2}{2R(z)} - \arctan\left(\frac{z}{z_R}\right)\right)\boldsymbol{e}_x \tag{2.45}$$

$$\boldsymbol{B}(\boldsymbol{r},t) = \frac{E_0}{c}\frac{w_0}{w(z)}\exp\left(-\frac{r^2}{w(z)^2}\right)\cos\left(kz - \omega t + k\frac{r^2}{2R(z)} - \arctan\left(\frac{z}{z_R}\right)\right)\boldsymbol{e}_y \tag{2.46}$$

The parameters are the same as defined in chapter 1: $w_0 = \sqrt{2z_R/k}$ is the beam waist radius, $w(z) = w_0\sqrt{1+z^2/z_R^2}$ is the beam radius at position z, $R(z) = z + z_R^2/z$ is the radius of curvature, ω_0 is the frequency of the beam and E_0 its electric field amplitude. When modeling a pulsed laser beam, it is very common to multiply the previous expression by a temporal envelope $g(t - z/c)$, which is often chosen to be a Gaussian:

$$\boldsymbol{E}(\boldsymbol{r},t) = E_0\frac{w_0}{w(z)}\exp\left(-\frac{r^2}{w(z)^2}\right)\cos\left(kz - \omega t + k\frac{r^2}{2R(z)} - \arctan\left(\frac{z}{z_R}\right)\right)g\left(t-\frac{z}{c}\right)\boldsymbol{e}_x \tag{2.47}$$

$$\boldsymbol{B}(\boldsymbol{r},t) = \frac{E_0}{c}\frac{w_0}{w(z)}\exp\left(-\frac{r^2}{w(z)^2}\right)\cos\left(kz - \omega t + k\frac{r^2}{2R(z)} - \arctan\left(\frac{z}{z_R}\right)\right)g\left(t-\frac{z}{c}\right)\boldsymbol{e}_y \tag{2.48}$$

Equations 2.47- 2.48 are not exact solutions to Maxwell's equations. They indeed rely on three main approximations:

- The paraxial Helmholtz equation was solved rather than the exact Helmholtz equation. This becomes inaccurate when the beam waist w_0 approaches one laser wavelength.
- The wave equation was solved independently for every cartesian component of the electromagnetic field. Even without the paraxial approximation, this is not a sufficient condition to obtain a solution to Maxwell's equations. In particular, the longitudinal field E_z which is necessarily present if the beam as a finite transverse extent is not included in equations 2.47- 2.48.
- Using a temporal envelope g is only valid if the different frequency components have the same spatial shape. This is a reasonable approximation for long pulses with narrow spectra. However, this is no longer the case for few-cycle pulses as the different frequency components will not diffract in the same way. For instance, it is not possible for two different frequency components to simultaneously have the same beam waist w_0 and the same Rayleigh length z_R.

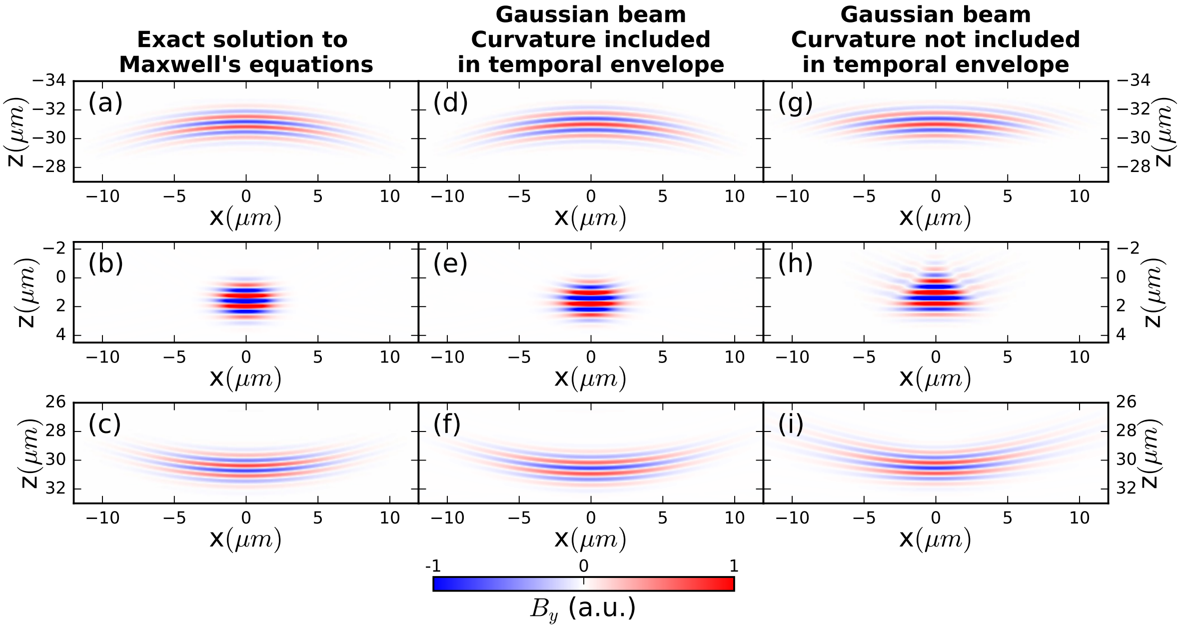

Figure 2.10: Snapshots from 3D PIC simulations of the propagation of an 800-nm, 3.5-fs laser pulse with $w_0 = 1.5\ \mu\mathrm{m}$. The pulse is introduced at the plane $z = -35\ \mu\mathrm{m}$ either using an exact solution to Maxwell's equations (equations 2.82-2.87) (a)-(c), a Gaussian beam with its curvature included in the envelope g (d)-(f) or a Gaussian beam without the curvature included in g (equations 2.47-2.48) (g)-(i). The curvature is taken into account by the transformation $g\left(t - \frac{z}{c}\right) \to g\left(t - \frac{z}{c} - \frac{r^2}{2cR(z)}\right)$. The pulse is shown before focus (a),(d),(g), at focus (b),(e),(h) and after focus (c),(f),(i). The propagation of the pulse is acceptable when the exact solution to Maxwell's equation or the Gaussian beam with the curvature included are used. On the other hand, the shape of the pulse at focus is unsatisfactory when the curvature is not taken into account in the envelope. Detailed simulation parameters are provided in appendix B.

In the case of PIC simulations, the electromagnetic field is introduced at a given plane, either through boundary conditions or by way of an antenna made of ficticious macroparticles that oscillate in a controlled way so as to generate the desired field. Outside of this plane, the laser pulse is propagated by the Maxwell solver. The fields in the PIC simulations are therefore always a solution to Maxwell's equations (neglecting numerical errors) even if the expressions used to produce them are not. In practice, equations 2.47- 2.48 are suitable to introduce a linearly polarized pulse even with parameters that correspond to the Salle Noire laser ($w_0 = 1.5\,\mu\mathrm{m}$, 3.5-fs pulse duration), provided that the curvature of the beam is taken into account in the temporal envelope, as illustrated in figure 2.10. Higher-order terms, such as the longitudinal electric field E_z, will naturally appear in the simulation.

On the other hand, in test-particle simulations, the electromagnetic fields can be chosen everywhere without restriction. Using field expressions that are not solution to Maxwell's equations can be troublesome. For example, it was noted in [80] that using equations 2.47-2.48 tends to confine electrons in the polarization plane, which leads to an anisotropic ponderomotive force. Similarly, in the case of radial polarization, using the paraxial approximation results in an excessive confinement of the electrons on the optical axis [123]. These nonphysical effects can lead to severe faults in the prediction or interpretation of experimental results, which can be avoided by using expressions that are exact solutions to Maxwell's equations. Yet, it should be kept in mind that there are many different ways to model an ideal laser pulse in a manner that suppresses the nonphysical effects described above, the choice of which can still have a significant impact on VLA in test-particle simulations [104].

2.3.2 Modeling ultrashort pulses: the Poisson spectrum

We start by presenting how ultrashort pulse durations can be dealt with. One possibility is to add corrections to $g(t-z/c)$ in a perturbative manner [80, 98]. Another possibility is to perform an inverse Fourier transform of the field component $\widetilde{\varphi}(\boldsymbol{r},\omega)$ calculated in the previous section. This means that we sum up the contribution of monochromatic Gaussian beams of different frequencies, which reads mathematically:

$$\begin{aligned}
\varphi(\boldsymbol{r},t) &= \int_{-\infty}^{\infty} \widetilde{\varphi}(\boldsymbol{r},\omega)\exp(i\omega t)d\omega && (2.49)\\
&= \varphi_0 \int_{-\infty}^{\infty} F(\omega)\frac{iz_R}{\widetilde{q}(z)}\exp\left(i\left(\omega t - kz - k\frac{r^2}{2\widetilde{q}(z)}\right)\right)d\omega && (2.50)\\
&= \varphi_0 \int_{-\infty}^{\infty} F(\omega)\frac{iz_R}{\widetilde{q}(z)}\exp\left(i\omega\left(t-\frac{z}{c}-\frac{r^2}{2c\widetilde{q}(z)}\right)\right)d\omega && (2.51)
\end{aligned}$$

We have used in the last line the fact that $\omega = kc$. We also note that the function $F(\omega)$ corresponds here to the spectrum of the pulse. The calculation of this integral is greatly simplified if we assume that the pulse is **isodiffracting**, which means that the Rayleigh length is the same for all frequency components. This assumption is not always true in experiments. For example, in the case of the Salle Noire laser, a wide spectrum is obtained through self-phase modulation in a hollow-core fiber [34]. At the fiber output, all the frequency components have the same waist, which is fixed by the fiber radius. This means that the Rayleigh length is proportional to the frequency and thus that Salle Noire few-cycle pulses are not isodiffracting. However, assuming that w_0 is the same for all frequency components makes the integral 2.51 impractical to carry out analytically [154], because z_R and $\widetilde{q}(z)$ both depend on ω in this case. For this reason, we only consider in the following isodiffracting pulses for which the previous integral simply corresponds to an inverse Fourier transform of $F(\omega)$. Thus, by denoting $f(t)$ the inverse Fourier transform of $F(\omega)$, the result of the integral for isodiffracting pulses is:

$$\varphi(\boldsymbol{r},t) = \varphi_0\frac{iz_R}{\widetilde{q}(z)}f\left(t-\frac{z}{c}-\frac{r^2}{2c\widetilde{q}(z)}\right) \tag{2.52}$$

We observe in particular that the value of component φ on the optical axis at the waist ($r = z = 0$) is given by $\varphi_0 f(t)$. The temporal shape of the pulse is therefore directly given by the real part of the inverse Fourier transform of the spectrum $F(\omega)$. This method is useful because it easily provides a closed-form expression of a Gaussian beam with any spectrum whose Fourier transform can be calculated analytically. We may be tempted to use a Gaussian spectrum of the form:

$$F(\omega) = e^{i\phi_0}\frac{\tau}{2\sqrt{2\pi\ln(2)}}\exp\left(\frac{\tau^2(\omega-\omega_0)^2}{8\ln(2)}\right) \tag{2.53}$$

Where ϕ_0 is an absolute phase that correspond to the CEP of the laser pulse, ω_0 is the central frequency and τ is the pulse duration in FWHM of intensity. In this case we simply have:

$$f(t) = e^{i\phi_0} \exp\left(-2\ln(2)\frac{t^2}{\tau^2}\right) \exp(i\omega_0 t) \tag{2.54}$$

And we finally have from equation 2.52:

$$\varphi(\boldsymbol{r},t) = \varphi_0 e^{i\phi_0} \frac{iz_R}{\widetilde{q}(z)} \exp\left(-2\ln(2)\frac{\left(t-\frac{z}{c}-\frac{r^2}{2c\widetilde{q}(z)}\right)^2}{\tau^2}\right) \exp\left(i\omega_0\left(t-\frac{z}{c}-\frac{r^2}{2c\widetilde{q}(z)}\right)\right) \tag{2.55}$$

However, such an expression has two important drawbacks. First, it diverges exponentially as r approaches infinity. This can be clearly seen in the case $t = z = 0$, for which equation 2.55 becomes:

$$\varphi(\boldsymbol{r},t=0) = \varphi_0 e^{i\phi_0} \exp\left(\ln(2)\frac{r^4}{2(\tau c z_R)^2}\right) \exp\left(-\frac{\omega_0 r^2}{2cz_R}\right) \tag{2.56}$$

This spurious exponential growth of the fields comes from the fact that the Gaussian spectrum contains negative frequency components ($\omega < 0$) which diverge in equation 2.43. Secondly, because the Gaussian spectrum contains a non-zero static component ($F(\omega = 0) \neq 0$), the resulting fields do not verify the condition $\int_{-\infty}^{+\infty} \boldsymbol{E}(\boldsymbol{r},t)dt = 0$, which should be verified by laser pulses. Using fields that do not satisfy this condition in test-particle simulations results in an additional unphysical acceleration (which is essentially the acceleration by a static field) that can lead to erroneous conclusions (see e.g. [155]). Both issues can be solved by cutting the spectrum at an arbitrary positive frequency ω_{cut}:

$$F(\omega) = e^{i\phi_0} \frac{\tau}{2\sqrt{2\pi\ln(2)}} \exp\left(\frac{\tau^2(\omega-\omega_0)^2}{8\ln(2)}\right) H(\omega-\omega_{cut}) \tag{2.57}$$

Where H is the Heaviside step function. This was previously done in references [156, 157] with $\omega_{cut} = 0$. The inverse Fourier transform of this spectrum reads:

$$f(t) = \frac{e^{i\phi_0}}{2} \exp\left(-2\ln(2)\frac{t^2}{\tau^2}\right) \exp(i\omega_0 t) \left(1 + i\,\mathrm{erfi}\left(\sqrt{2\ln(2)}\frac{t}{\tau} - i\frac{(\omega_0-\omega_{cut})\tau}{2\sqrt{2\ln(2)}}\right)\right) \tag{2.58}$$

Where erfi is the imaginary error function. The spectrum $F(\omega)$ and the pulse temporal shape in this case are shown in figure 2.11. The main disadvantage of this method is that it leads to rather complicated pulse expressions involving the error functions.

Rather than a Gaussian spectrum, we use in this thesis a Poisson-like spectrum, as initially done in [158], which is defined as:

$$F(\omega) = e^{i\phi_0} \left(\frac{s}{\omega_0}\right)^{s+1} \frac{\omega^s e^{-s\frac{\omega}{\omega_0}}}{\Gamma(s+1)} H(\omega) \tag{2.59}$$

Here, Γ is the gamma function, ω_0 is the frequency for which $F(\omega)$ is maximum and s is a parameter related to the pulse duration in FWHM of intensity τ by the relation [158]:

$$\omega_0\tau = s\sqrt{2\left(4^{1/(s+1)}-1\right)} \tag{2.60}$$

This spectrum is chosen because:

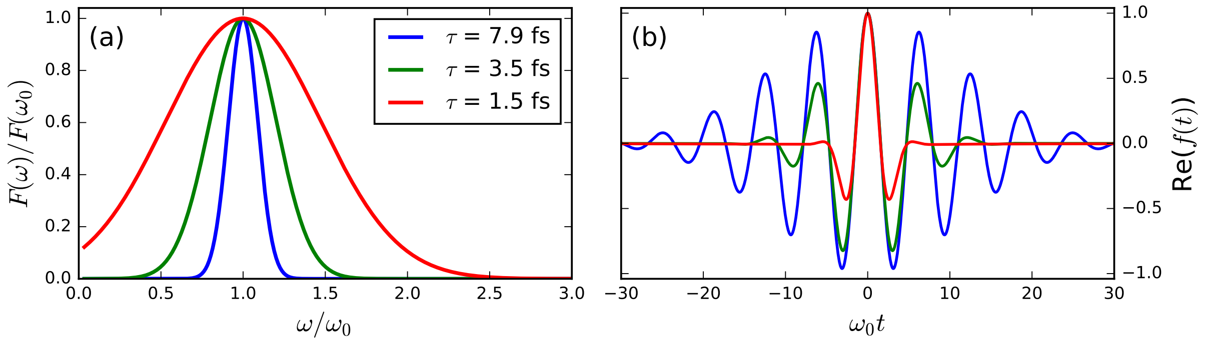

Figure 2.11: (a) Normalized Gaussian spectrum cut at the frequency $\omega_{cut} = \omega_0/30$, where ω_0 is the central frequency, for pulse durations of 7.9 fs, 3.5 fs and 1.5 fs in FWHM of intensity for an 800-nm laser pulse. (b) Corresponding temporal shape of the laser pulses at position $\boldsymbol{r} = 0$. We have assumed that $\phi_0 = 0$

- It tends towards a Gaussian spectrum for long pulse durations ($s \to \infty$). It is therefore one of the possible extensions of the gaussian temporal envelope for few-cycle pulses.
- There are no static or negative frequency components, as insured by the Heaviside function. Consequently, the obtained fields are not diverging when r approaches $+\infty$ and the condition $\int_{-\infty}^{+\infty} \boldsymbol{E}(\boldsymbol{r},t)dt = 0$ is satisfied.
- The function $F(\omega)$ has a simple inverse Fourier transform:

$$f(t) = e^{i\phi_0}\left(1 - \frac{i\omega_0 t}{s}\right)^{-(s+1)} \tag{2.61}$$

The Poisson spectrum and the real part of its inverse Fourier transform are shown in figure 2.12 for different pulse durations. The Gaussian beam with a Poisson-like spectrum can be obtained by inserting equation 2.61 into equation 2.52 for the E_x and B_y fields and by assuming that the other components are zero. The final result is the real part of the following expression:

$$\boldsymbol{E}(\boldsymbol{r},t) = E_0 e^{i\phi_0}\frac{iz_R}{\tilde{q}(z)}\left(1 - \frac{i}{s}\left(\omega_0 t - k_0 z - \frac{k_0 r^2}{2\tilde{q}(z)}\right)\right)^{-(s+1)} \boldsymbol{e}_x \tag{2.62}$$

$$\boldsymbol{B}(\boldsymbol{r},t) = \frac{E_0}{c} e^{i\phi_0}\frac{iz_R}{\tilde{q}(z)}\left(1 - \frac{i}{s}\left(\omega_0 t - k_0 z - \frac{k_0 r^2}{2\tilde{q}(z)}\right)\right)^{-(s+1)} \boldsymbol{e}_y \tag{2.63}$$

Where k_0 is defined as ω_0/c.

These fields can be easily generalized from 3 to 2 dimensions (x,z). In this case the solution 2.43 of the paraxial wave equation becomes:

$$\tilde{u}(\boldsymbol{r},\omega) = F(\omega)\varphi_0\sqrt{\frac{iz_R}{\tilde{q}(z)}}\exp\left(-ik\frac{x^2}{2\tilde{q}(z)}\right) \tag{2.64}$$

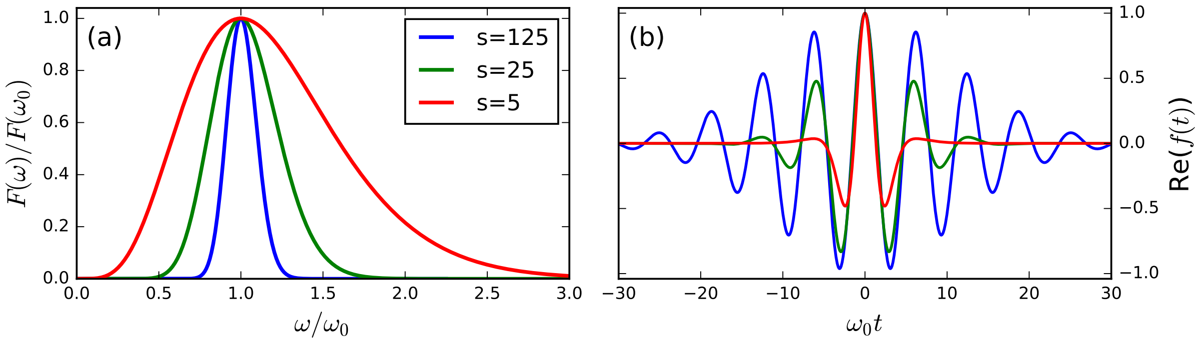

Figure 2.12: (a) Normalized Poisson-like spectrum for s *= 125, 25 or 5. This corresponds respectively to pulse durations of 7.9 fs, 3.5 fs and 1.5 fs in FWHM of intensity for an 800-nm laser pulse. (b) Corresponding temporal shape of the laser pulses at position* $\boldsymbol{r} = 0$*. We have assumed that* $\phi_0 = 0$

Then, the same steps as in the three-dimensional case can be performed. This provides the expression of the electromagnetic fields of the 2D Gaussian beam with a Poisson-like spectrum:

$$\boldsymbol{E}(\boldsymbol{r},t) = E_0 e^{i\phi_0}\sqrt{\frac{iz_R}{\widetilde{q}(z)}}\left(1-\frac{i}{s}\left(\omega_0 t - k_0 z - \frac{k_0 x^2}{2\widetilde{q}(z)}\right)\right)^{-(s+1)}\boldsymbol{e}_x \tag{2.65}$$

$$\boldsymbol{B}(\boldsymbol{r},t) = \frac{E_0}{c} e^{i\phi_0}\sqrt{\frac{iz_R}{\widetilde{q}(z)}}\left(1-\frac{i}{s}\left(\omega_0 t - k_0 z - \frac{k_0 x^2}{2\widetilde{q}(z)}\right)\right)^{-(s+1)}\boldsymbol{e}_y \tag{2.66}$$

These fields were used in the 2D PIC simulations carried out during this thesis.

Of course, the field expressions presented here are still unsuitable for test-particle simulations, in particular because they are obtained with the paraxial approximation and have no longitudinal component.

2.3.3 Nonparaxial pulses

There are various possibilities to obtain nonparaxial field expressions. We can cite in particular:

- The Lax expansion method [159] in which the fields calculated in a power series of the small parameter $\varepsilon = 1/k_0 w_0$ whose leading term is the paraxial Gaussian beam 2.45-2.46.

- The angular representation method [160] which uses plane wave decomposition to obtain field expressions in the form of integrals that have to be either evaluated numerically or developped in a power series of ε (see e.g. [80]).

Both methods are very common but they do not provide closed form solutions to Maxwell's equations. Yet, such analytical solutions are desirable since they are not limited by a validity range, they can be implemented at a low computational cost in test particle simulations and the laser parameters can be varied easily. We describe in this section one way to obtain closed-form solutions to Maxwell's equations that reduce to Gaussian beams in the paraxial limit ($k_0 w_0 \gg 1$) [151, 152].

A possible approach would be to use the electromagnetic potentials $V(\boldsymbol{r},t)$ and $\boldsymbol{A}(\boldsymbol{r},t)$, which are such that:

$$\boldsymbol{E}(\boldsymbol{r},t) = -\boldsymbol{\nabla} V(\boldsymbol{r},t) - \frac{\partial \boldsymbol{A}}{\partial t}(\boldsymbol{r},t) \tag{2.67}$$

$$\boldsymbol{B}(\boldsymbol{r},t) = \boldsymbol{\nabla} \times \boldsymbol{A}(\boldsymbol{r},t) \tag{2.68}$$

The idea here is that, in the Lorenz gauge ($\boldsymbol{\nabla}.\boldsymbol{A} + \frac{1}{c^2}\frac{\partial V}{\partial t} = 0$), if the $\boldsymbol{A}$ and V fields are solution to the (nonparaxial) wave equation then the electromagnetic fields obtained through equations 2.67-2.68 satisfy Maxwell's equations. Therefore, with an appropriate choice for the magnetic potential $\boldsymbol{A}$, the $\boldsymbol{E}$ and $\boldsymbol{B}$ fields can be obtained by simple differentiations. This method was used by Davis to obtain the expression of a linearly polarized beam from a magnetic potential oriented in the direction of polarization ($\boldsymbol{A} = (A_x, 0, 0)$) [161] and the expression of a radially polarized beam from a magnetic potential oriented in the direction of propagation ($\boldsymbol{A} = (0, 0, A_z)$) [162]. However, these fields were obtained within the paraxial approximation (with calculations up to the third order in ε in the case of linear polarization), even though this method can be extended to the nonparaxial case.

A formally equivalent but more convenient method consists in using the **Hertz vectors** (also known as polarization potentials) rather than the magnetic potential. The electric Hertz vector $\boldsymbol{\Pi}_e$ and the magnetic Hertz vector $\boldsymbol{\Pi}_m$ are two vector fields that can be seen as potentials of the usual potentials $\boldsymbol{A}$ and V. Indeed, if the $\boldsymbol{\Pi}_e$ and $\boldsymbol{\Pi}_m$ fields are known, then the $\boldsymbol{A}$ and V fields are given by [163]:

$$\boldsymbol{A}(\boldsymbol{r},t) = \frac{1}{c^2}\frac{\partial \boldsymbol{\Pi}_e}{\partial t}(\boldsymbol{r},t) + \mu_0 \boldsymbol{\nabla} \times \boldsymbol{\Pi}_m(\boldsymbol{r},t) \tag{2.69}$$

$$V(\boldsymbol{r},t) = -\boldsymbol{\nabla}.\boldsymbol{\Pi}_e(\boldsymbol{r},t) \tag{2.70}$$

The Hertz vectors are designed so that potentials obtained using equations 2.69-2.70 automatically satisfy the Lorenz condition. The $\boldsymbol{E}$ and $\boldsymbol{B}$ fields can be obtained from $\boldsymbol{\Pi}_e$ and $\boldsymbol{\Pi}_m$ using equations 2.67 to 2.70, which yields [164]:

$$\boldsymbol{E}(\boldsymbol{r},t) = \boldsymbol{\nabla}\left(\boldsymbol{\nabla}.\boldsymbol{\Pi}_e(\boldsymbol{r},t)\right) - \frac{1}{c^2}\frac{\partial^2 \boldsymbol{\Pi}_e}{\partial t^2}(\boldsymbol{r},t) - \mu_0 \boldsymbol{\nabla} \times \frac{\partial \boldsymbol{\Pi}_m}{\partial t}(\boldsymbol{r},t) \tag{2.71}$$

$$\boldsymbol{B}(\boldsymbol{r},t) = \frac{1}{c^2}\boldsymbol{\nabla} \times \frac{\partial \boldsymbol{\Pi}_e}{\partial t}(\boldsymbol{r},t) + \mu_0 \boldsymbol{\nabla} \times \boldsymbol{\nabla} \times \boldsymbol{\Pi}_m(\boldsymbol{r},t) \tag{2.72}$$

Electromagnetic fields obtained in this manner are solutions to Maxwell's equations in vacuum provided that the Hertz vectors verify the wave equation:

$$\boldsymbol{\nabla}^2 \boldsymbol{\Pi}_e(\boldsymbol{r},t) - \frac{1}{c^2}\frac{\partial^2 \boldsymbol{\Pi}_e}{\partial t^2} = 0 \tag{2.73}$$

$$\boldsymbol{\nabla}^2 \boldsymbol{\Pi}_m(\boldsymbol{r},t) - \frac{1}{c^2}\frac{\partial^2 \boldsymbol{\Pi}_m}{\partial t^2} = 0 \tag{2.74}$$

The next step is therefore to find adequate solutions $\boldsymbol{\Pi}_e$ and $\boldsymbol{\Pi}_m$ to the wave equations such that the resulting E and B fields can satisfactorily model a laser pulse. We work in the frequency domain $(\boldsymbol{r}, \omega)$ and subsequently look for solutions to the scalar Helmholtz equation 2.39.

We can start by extending the complex source point method to the nonparaxial case and consider a spherical wave emitted by a point source located at the complex position $(0, 0, -ia)$, where a is a distance called the confocal parameter. However, the resulting field $e^{-ik\widetilde{R}}/\widetilde{R}$, where $\widetilde{R}=\sqrt{r^2+(z+ia)^2}$ is nonphysical since it diverges when $z=0$ and $r^2=a^2$ ($\widetilde{R}=0$) [153]. This issue can be overcome by adding a point sink term $e^{+ik\widetilde{R}}/\widetilde{R}$, which corresponds to a spherical wave converging towards the complex point $(0,0,-ia)$ [165]. The resulting complex source-sink method gets rid of the singularity at $z=0$ and $r=a$ and provides a usable solution to the Helmholtz equation:

$$\widetilde{\varphi}(\boldsymbol{r},\omega)=iF(\omega)\varphi_0 e^{-ka}a\frac{e^{-ik\widetilde{R}}-e^{ik\widetilde{R}}}{\widetilde{R}} \tag{2.75}$$

$$=2F(\omega)\varphi_0 e^{-ka}a\frac{\sin(k\widetilde{R})}{\widetilde{R}} \tag{2.76}$$

The constants are chosen such that, in the paraxial limit $ka\gg 1$, this expression reduces to equation 2.44 with a corresponding to the Rayleigh length z_R [152]. It is instructive to look at the field $\widetilde{\varphi}$ on the optical axis $r=0$:

$$\widetilde{\varphi}(r=0,z,\omega)=F(\omega)\varphi_0\frac{ia}{z+ia}\left(e^{-ikz}-e^{-2ka}e^{ikz}\right) \tag{2.77}$$

The term e^{-ikz} comes from the point source while the term e^{ikz} comes from the point sink. Therefore, on the optical axis, the effect of adding a sink is to add a counterpropagating wave, which is in principle not desired. However the amplitude of this wave is reduced by a factor e^{-2ka}, which makes the counterpropagating wave negligible in practical cases. For instance, in the Salle Noire laser for which $w_0=1.5\,\mu\text{m}$, we have $ka\sim k_0 z_R\approx 70$ and thus $e^{-2ka}\sim 10^{-60}$. We see that the sink term is completely negligible on axis (but is nevertheless essential to remove the singularity at $\widetilde{R}=0$).

As previously, this solution can be converted to the temporal domain with an inverse Fourier transform:

$$\varphi(\boldsymbol{r},t)=\int_{-\infty}^{\infty}\widetilde{\varphi}(\boldsymbol{r},\omega)e^{i\omega t}d\omega \tag{2.78}$$

$$=i\varphi_0\int_{-\infty}^{\infty}F(\omega)ae^{-ka}\frac{e^{-ik\widetilde{R}}-e^{ik\widetilde{R}}}{\widetilde{R}}e^{i\omega t}d\omega \tag{2.79}$$

$$=i\varphi_0\int_{-\infty}^{\infty}\frac{a}{\widetilde{R}}F(\omega)\left(e^{i\omega t_-}-e^{i\omega t_+}\right)d\omega \tag{2.80}$$

With $t_+\equiv t+\frac{\widetilde{R}}{c}+\frac{ia}{c}$ and $t_-\equiv t-\frac{\widetilde{R}}{c}+\frac{ia}{c}$. Once again, the calculation is greatly simplified if we assume that the pulse is isodiffracting, which means in this case that a is independent of ω. With this assumption, the integral is simply an inverse Fourier transform of the spectrum $F(\omega)$, whose result is:

$$\varphi(\boldsymbol{r},t)=\frac{i\varphi_0 a}{\widetilde{R}}\left(f(t_-)-f(t_+)\right) \tag{2.81}$$

Finally, the electromagnetic fields can be obtained by plugging this function into the Hertz vectors. To obtain a pulse linearly polarized in the x direction, we use $\Pi_e(\boldsymbol{r},t)=\varphi(\boldsymbol{r},t)e_x$ and $\Pi_m(\boldsymbol{r},t)=\varepsilon_0 c\varphi(\boldsymbol{r},t)e_y$. Then, the $\boldsymbol{E}$ and $\boldsymbol{B}$ fields are obtained from equations 2.71-2.72:

$$E_x(\boldsymbol{r},t)=\frac{A_0}{\widetilde{R}}\left[\left(\frac{x^2}{\widetilde{R}^2}-1\right)\frac{G_-^{(2)}}{c^2}-\left(\frac{3x^2}{\widetilde{R}^2}-1\right)\left(\frac{G_+^{(1)}}{c\widetilde{R}}-\frac{G_-^{(0)}}{\widetilde{R}^2}\right)+\frac{\cos\widetilde{\theta}}{c}\left(\frac{G_+^{(2)}}{c}-\frac{G_-^{(1)}}{\widetilde{R}}\right)\right] \tag{2.82}$$

$$E_y(\boldsymbol{r},t)=\frac{A_0xy}{\widetilde{R^3}}\left[\frac{G_-^{(2)}}{c^2}-\frac{3G_+^{(1)}}{c\widetilde{R}}+\frac{3G_-^{(0)}}{\widetilde{R}^2}\right] \tag{2.83}$$

$$E_z(\boldsymbol{r},t)=\frac{A_0x}{\widetilde{R^2}}\left[\cos\widetilde{\theta}\left(\frac{G_-^{(2)}}{c^2}-\frac{3G_+^{(1)}}{c\widetilde{R}}+\frac{3G_-^{(0)}}{\widetilde{R}^2}\right)-\left(\frac{G_+^{(2)}}{c^2}-\frac{G_-^{(1)}}{c\widetilde{R}}\right)\right] \tag{2.84}$$

$$B_x(\boldsymbol{r},t)=\frac{A_0xy}{\widetilde{cR^3}}\left[\frac{G_-^{(2)}}{c^2}-\frac{3G_+^{(1)}}{c\widetilde{R}}+\frac{3G_-^{(0)}}{\widetilde{R}^2}\right]=\frac{E_y}{c}(\boldsymbol{r},t) \tag{2.85}$$

$$B_y(\boldsymbol{r},t)=\frac{A_0}{c\widetilde{R}}\left[\left(\frac{y^2}{\widetilde{R}^2}-1\right)\frac{G_-^{(2)}}{c^2}-\left(\frac{3y^2}{\widetilde{R}^2}-1\right)\left(\frac{G_+^{(1)}}{c\widetilde{R}}-\frac{G_-^{(0)}}{\widetilde{R}^2}\right)+\frac{\cos\widetilde{\theta}}{c}\left(\frac{G_+^{(2)}}{c}-\frac{G_-^{(1)}}{\widetilde{R}}\right)\right] \tag{2.86}$$

$$B_z(\boldsymbol{r},t)=\frac{A_0y}{\widetilde{cR^2}}\left[\cos\widetilde{\theta}\left(\frac{G_-^{(2)}}{c^2}-\frac{3G_+^{(1)}}{c\widetilde{R}}+\frac{3G_-^{(0)}}{\widetilde{R}^2}\right)-\left(\frac{G_+^{(2)}}{c^2}-\frac{G_-^{(1)}}{c\widetilde{R}}\right)\right] \tag{2.87}$$

The physical fields are the real parts of the previous expressions where A_0 is proportional to the amplitude of the field, $\cos\widetilde{\theta}=(z+ia)/\widetilde{R}$ and $G_\pm^{(n)}\equiv f^{(n)}(t_+)\pm f^{(n)}(t_-)$, where $f^{(n)}$ is the nth derivative of f. If a Poisson spectrum (equation 2.59) is used, as is the case in this thesis, then we have:

$$f^{(n)}(t)=e^{i\phi_0}\frac{\Gamma(s+n+1)}{\Gamma(s+1)}\left(\frac{i\omega_0}{s}\right)^n\left(1-\frac{i\omega_0t}{s}\right)^{-(s+n+1)} \tag{2.88}$$

Because we have used a solution of the wave equation in the Hertz vectors, the fields given by equations 2.82-2.87 are an exact solution to Maxwell's equations in vacuum. We notice that the $\boldsymbol{E}$ and $\boldsymbol{B}$ fields play a symmetric role and that one can be obtained from the other by performing the exchange $x\leftrightarrow y$. The 6 components of the electromagnetic field are nonzero in this expression. However, we have in all practical cases $E_x\gg E_z\gg E_y$ (for a laser polarized in the x direction). The 3 components of the electric field are shown at $t=0$ in figure 2.13 with parameters corresponding to the Salle Noire laser. In principle, the tighter the focusing, the more significant the E_z and E_y are. However, even in the case of the Salle Noire laser ($w_0=1.5\,\mu\mathrm{m}$), we have $|E_z|_{MAX}\approx 0.065|E_x|_{MAX}$ and $|E_y|_{MAX}\approx 0.0024|E_x|_{MAX}$. It may also be noted that there is no simple expression to obtain the peak amplitude of a given component, which generally depends on A_0, a, ϕ_0 and s (for a Poisson spectrum). If A_0 is real and positive and $\phi_0=-\pi/2$, the E_x and B_y fields are maximum at $t=0$ and $\boldsymbol{r}=0$.

Radially polarized fields can be obtained in a similar manner by choosing $\Pi_e(\boldsymbol{r},t)=\varphi(\boldsymbol{r},t)e_z$ and $\Pi_m=0$. In this case and in cylindrical coordinates, only the E_r, E_z and B_θ fields are nonzero. They read:

$$E_r(\mathbf{r},t)=\frac{3A_0\sin(2\widetilde{\theta})}{2\widetilde{R}}\left(\frac{G_-^{(0)}}{\widetilde{R}^2}-\frac{G_+^{(1)}}{c\widetilde{R}}+\frac{G_-^{(2)}}{3c^2}\right) \tag{2.89}$$

$$E_z(\mathbf{r},t)=\frac{A_0}{\widetilde{R}}\left[\frac{3\cos^2\widetilde{\theta}-1}{\widetilde{R}}\left(\frac{G_-^{(0)}}{\widetilde{R}}-\frac{G_+^{(1)}}{c}\right)-\frac{\sin^2\widetilde{\theta}}{c^2}G_-^{(2)}\right] \tag{2.90}$$

$$B_\theta(\mathbf{r},t)=\frac{A_0\sin\widetilde{\theta}}{c\widetilde{R}}\left(\frac{G_-^{(1)}}{c\widetilde{R}}-\frac{G_+^{(2)}}{c^2}\right) \tag{2.91}$$

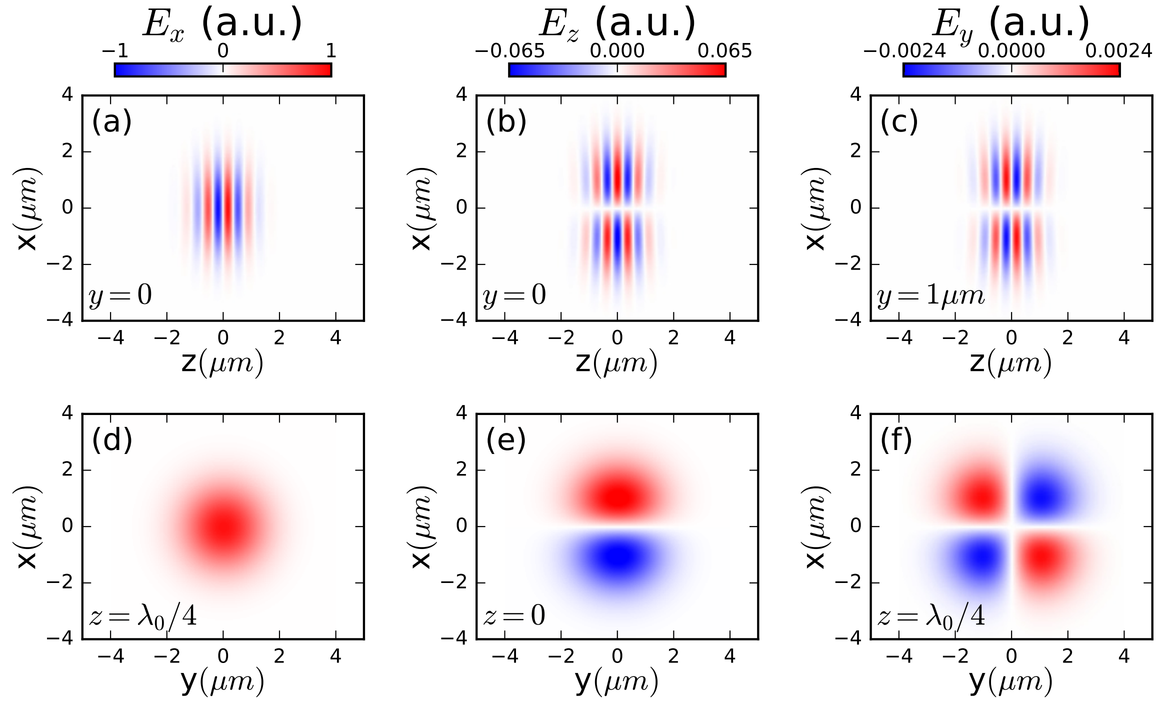

Figure 2.13: Exact expression of a pulse linearly polarized in the x direction. E_x (a),(d), E_z (b),(e) and E_y (c),(f) fields obtained from equations 2.82-2.84 with a Poisson spectrum in a plane of constant y (a)-(c) or constant z (d)-(f). The fields are obtained at focus ($t = 0$) with A_0 real and positive, $\phi_0 = 0$ and Salle Noire parameters ($s = 25$ and $a = 8.84\,\mu\mathrm{m}$, which correspond to 3.5 fs and $w_0 = 1.5\,\mu\mathrm{m}$). The fields are normalized so that the peak amplitude of the E_x field is 1.

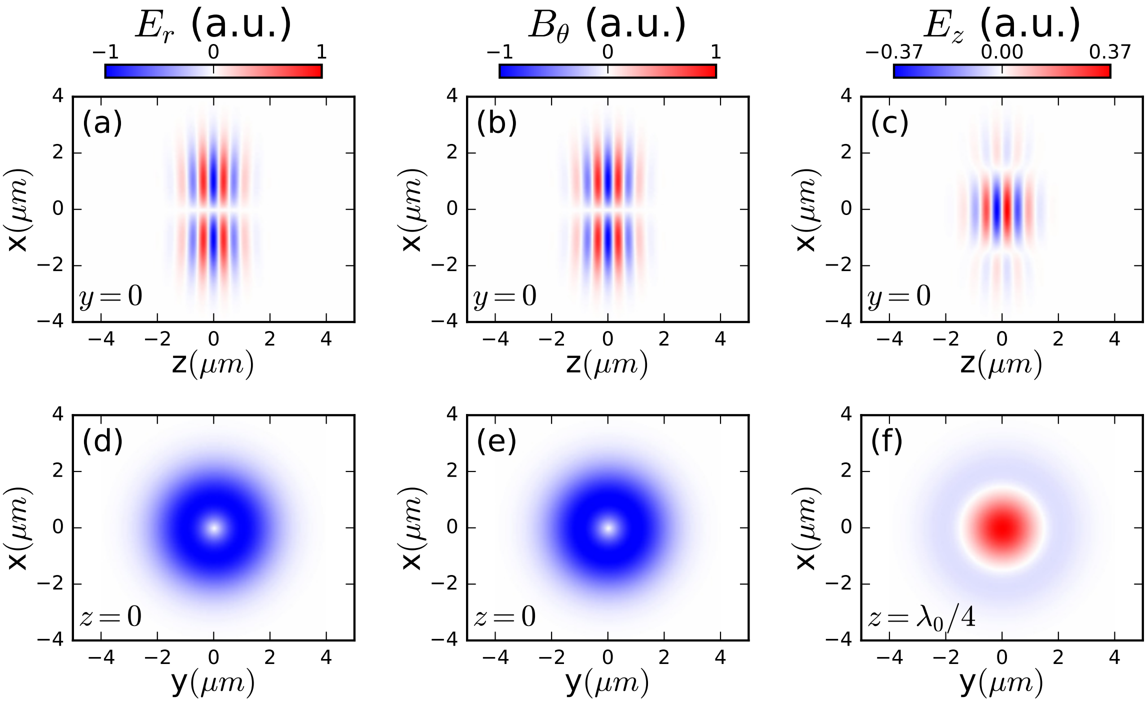

Figure 2.14: Exact expression of a radially polarized pulse. E_r (a),(d), B_θ (b),(e) and E_z (c),(f) fields obtained from equations 2.89-2.91 with a Poisson spectrum in a plane of constant y (a)-(c) or constant z (d)-(f). The fields are obtained at focus ($t=0$) with A_0 real and positive, $\phi_0=0$ and Salle Noire parameters ($s=25$ and $a=8.84\,\mu\text{m}$, which correspond to 3.5 fs and $w_0=1.5\,\mu\text{m}$). The fields are normalized so that the peak amplitude of the E_r field is 1.

We have here $\sin\widetilde{\theta}=r/\widetilde{R}$ and $\sin(2\widetilde{\theta})=2\sin\widetilde{\theta}\cos\widetilde{\theta}$. These fields are plotted in figure 2.14 with Salle Noire parameters. We have in this case $|E_z|_{MAX}\approx 0.37|E_r|_{MAX}$. Once again, there is no simple expression to obtain the peak amplitude of a given component. If A_0 is real and positive and $\phi_0=-\pi/2$, the E_z field is maximum at $t=0$ and $\boldsymbol{r}=0$.

Finally, fields with azimuthal polarization can be straightforwardly obtained from fields with radial polarization by exchanging the $\boldsymbol{E}$ and $\boldsymbol{B}$ fields: $(\boldsymbol{E},\boldsymbol{B})\to(\boldsymbol{B}\boldsymbol{c},-\boldsymbol{E}/\boldsymbol{c})$.

Unless specified otherwise, these fields have been used in the test-particle simulations presented in this manuscript.

CHAPTER 3

Few-cycle laser wakefield acceleration on solid targets with long gradient scale lengths

Contents

Thanks to a recent upgrade, the Salle Noire laser can deliver few-cycle pulses (duration as low as 3.5 fs) with relativistic intensity (up to $a_0 = 2.7$) at a kHz repetition rate. The first experiments on solid targets with few-cycle pulses were performed during the course of my thesis and I contributed to their analysis. The results at short density gradients ($L \ll \lambda$) are fully consistent with the theory presented in section 1.4.2.1. For longer gradient scale lengths ($L > \lambda$), it is observed that electron emission only occurs when ultrashort pulses with sub-10 fs duration are used. PIC Simulations indicate that in this regime the electrons are accelerated by a laser wakefield formed in the near-critical density part of the plasma.

We discuss in section 3.1 the preplasma expansion and the estimation of the plasma density profile during interaction. The experimental results are then presented in section 3.2. We briefly present in section 3.3 PIC simulations of the interaction at short gradients. Finally, the electron acceleration mechanism at long gradients is studied in section 3.4 using PIC simulations.

3.1 Preplasma Expansion

During the experiments in Salle Noire, a prepulse with ~ 30 fs duration and $\sim 10^{14} - 10^{15}\,\mathrm{W/cm^2}$ intensity is used to ionize and heat the target, thereby creating a plasma with a temperature of a few tens of eV. The plasma then expands into vacuum. At a precise delay after the prepulse, the main pulse is focused on the expanded plasma and the relativistic interaction takes place. The plasma density profile during the interaction, which is a critical parameter, is thus determined by the preplasma expansion, which must therefore be studied thoroughly.

We start by presenting in section 3.1.1 the isothermal model of plasma expansion, which leads to the exponential density profile. We then present in section 3.1.2 an interferometry experiment aimed at measuring the expansion velocity during the experiments in Salle Noire [63]. We put in particular a strong emphasis on the uncertainties associated with this measurements. Finally, we show in section 3.1.3 results from 1D hydrodynamic simulations of the preplasma expansion, which are compared to the interferometry experiment.

3.1.1 Isothermal model of preplasma expansion

Here, we present the model leading to the usual exponential density profile, which can be found in references [166, 167]. A 1D two-fluid model is used with the following assumptions:

- The plasma is made of ions with charge Ze and electrons with charge $-e$.
- There are no collisions.
- There are no external fields. The only field is the electric field $\boldsymbol{E} = -\frac{\partial V}{\partial x}$ due to charge separation in the plasma.
- The ion fluid is cold (zero temperature).
- The electron fluid is isothermal with temperature T_e.

- At $t = 0$, the ion density is constant $n_i = n_{i0}$ for $x < 0$ and zero for $x > 0$. At $t > 0$, the plasma expands towards the positive x direction due to the charge separation generated by the nonzero electron temperature.

With these assumptions, the equations of conservation of mass and momentum for the ions respectively read:

$$\frac{\partial n_i}{\partial t} + v_i \frac{\partial n_i}{\partial x} + n_i \frac{\partial v_i}{\partial x} = 0 \tag{3.1}$$

$$\frac{\partial v_i}{\partial t} + v_i \frac{\partial v_i}{\partial x} = -\frac{Ze}{m_i}\frac{\partial V}{\partial x} \tag{3.2}$$

Where v_i is the fluid ion velocity and m_i is the ion mass.

Additionally, we use the fact that the timescale of electron motion is much shorter than the timescale of ion motion. Since the plasma expansion occurs through the ion motion, we can assume that the electron fluid is at thermal equilibrium at all times and thus follows a Boltzmann distribution[1] and that the plasma is quasi-neutral almost everywhere. This reads mathematically:

$$n_e = n_{e0} \exp\left(\frac{eV}{k_B T_e}\right) \tag{3.3}$$

$$n_e = Z n_i \tag{3.4}$$

Where $n_{e0} = Z n_{i0}$ is the electron density in the unperturbed region of the plasma ($x \to -\infty$) and k_B is the Boltzmann constant. Equations 3.1 to 3.4 form a complete set of equations for the 4 unknown variables n_e, n_i, v_i and V. A solution to this set of equation for $t > 0$ is given by:

$$n_e = Z n_i = \begin{cases} n_{e0} \exp\left(-\frac{x}{c_s t} - 1\right) & \text{if } x > -c_s t \\ n_{e0} & \text{if } x < -c_s t \end{cases} \tag{3.5}$$

$$v_i = \begin{cases} c_s + \frac{x}{t} & \text{if } x > -c_s t \\ 0 & \text{if } x < -c_s t \end{cases} \tag{3.6}$$

$$E = -\frac{\partial V}{\partial x} = \begin{cases} \frac{k_B T_e}{e c_s t} & \text{if } x > -c_s t \\ 0 & \text{if } x < -c_s t \end{cases} \tag{3.7}$$

Where $c_s = \sqrt{\frac{Z k_B T_e}{m_i}}$ is the ion sound velocity. The plasma thus expands with an exponential density profile and a gradient scale length that increases linearly with time at the speed of sound: $L = c_s t$. As one would expect, the higher the electron temperature, the faster the plasma expansion. The plasma is unperturbed for $x < -c_s t$ and the electron density at the initial plasma-vacuum boundary is always $n_e(x = 0) = n_{e0} \exp(-1)$ for $t > 0$. The electric field is homogeneous inside the density gradient and decreases with time as $\propto 1/t$. As illustrated by the red lines in figure 3.1, this electric field E corresponds to the presence of a positive surface charge $\varepsilon_0 E$ at $x = -c_s t$ and a negative surface charge $\varepsilon_0 E$ at $x = +\infty$.

---

[1] The Boltzmann distribution equation may sometimes (this is done in [167] for instance) be replaced by the assumption that at equilibrium the electric field due to charge separation compensates the electron pressure: $n_e e E = -\nabla p_e = -k_B T_e \nabla n_e$. This equation, which can be obtained by neglecting the electron mass in the electron fluid equation of motion, leads to the same exponential density gradient.

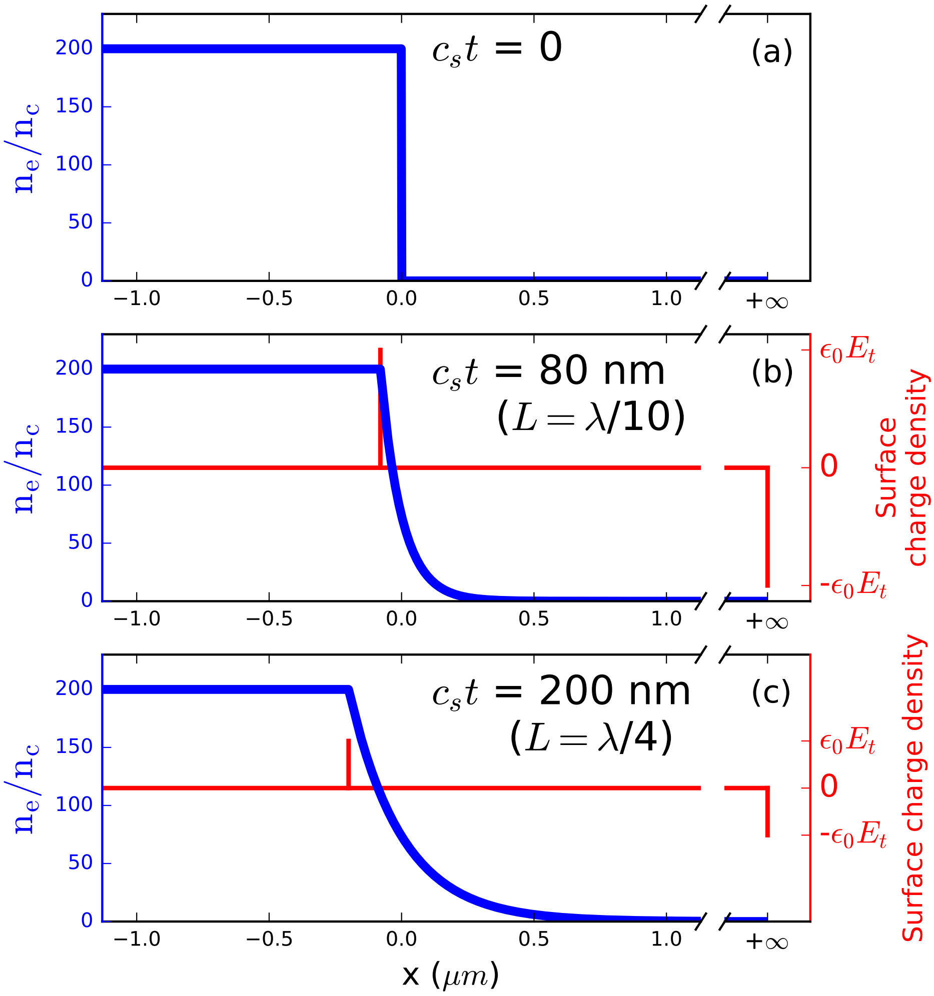

Figure 3.1: *1D isothermal expansion of a plasma with initial density* $n_{e0} = 200 n_c$. *The blue curves show the exponential density profile (equation 3.5) for a gradient scale length of 0 (a), 80 nm (b) and 200 nm (c). The red curves show the corresponding surface charge density, where* $E_t = \frac{k_B T_e}{e c_s t}$.

This solution is not well-behaved, as can be seen from the fact that the ion fluid velocity diverges when $t \to 0$ or $x \to +\infty$. Physically, this comes from the fact that the quasi-neutral hypothesis $n_e = Zn_i$, which may at a first glance seem inconsistent with the presence of an electrostatic field, is only reasonable when the gradient scale length is larger than the local Debye length $L > \lambda_D$. The Debye length $\lambda_D = \sqrt{\frac{\varepsilon_0 k_B T_e}{n_e e^2}}$ is indeed precisely the scale length below which the quasi-neutral hypothesis cannot be made in plasmas [37]. The condition $L > \lambda_D$ is violated either at short times t (because then $L = c_s t$ can be arbitrarily small) or at large positions x (because then the Debye length becomes arbitrarily large due to the decrease in plasma density), which is precisely when the solution becomes ill-behaved.

A more rigorous approach to obtain the 1D isothermal plasma expansion is thus to replace the quasi-neutral hypothesis by the Poisson equation $\varepsilon \frac{\partial^2 V}{\partial x^2} = e(n_e - Zn_i)$ and to solve the resulting set of equations numerically, as is done in [166]. This leads to a few notable modifications which make the solution well-behaved[2] but the exponential density profile (eq. 3.5) remains a very good approximation of the solution in this case.

Still, it should be kept in mind that this model is based on two strong assumptions that are not accurate:

- The isothermal hypothesis has two principal flaws. First, the temperature is assumed to be homogeneous inside the plasma. In practice, the prepulse only heats the target within the skin depth of the plasma, which is much shorter than the laser wavelength for strongly overdense plasmas. The energy is then transfered to the bulk of the plasma by collisional processes (including collisional ionization) which can lead to significant inhomogeneities in the electron temperature. Secondly, the electron temperature also tends to decrease with time due to thermal losses as well as the fact that electrons lose energy when accelerating the ions. Adiabatic, rather than isothermal, models of plasma expansion also exist [168] and a decrease in the electron temperature with time is indeed observed in this case.

- The 1D hypothesis is motivated by the fact that the transverse size of the prepulse creating the plasma is usually much larger than that of the main pulse, meaning that the plasma is transversely homogeneous during interaction. However, this assumption is no longer valid when the gradient scale length approaches the transverse size of the prepulse, because the plasma then expands both in the longitudinal (x) and transverse directions.

3.1.2 Spatial Domain Interferometry experiments in Salle Noire

With the assumptions of the previous model, the gradient scale length during the experiments in Salle Noire is given by $c_s \Delta t$, where $c_s = \sqrt{\frac{Z k_B T_e}{m_i}}$ is the plasma ion speed of sound and Δt is the delay between the prepulse and the main pulse. Δt is known accurately in experiments, but precisely evaluating c_s is

---

[2] The main differences are the following:

- There is, at a given time, a finite maximum fluid ion velocity. Consequently, there exists an ion front after which the ion density is rigorously 0.
- The surface charge densities shown in figure 3.1 become volume charge densities with a finite width.
- The negative charge density is located at the ion front rather than at $x = +\infty$

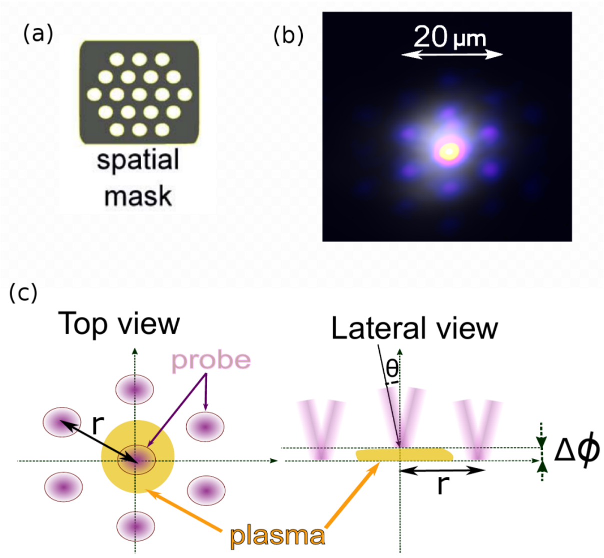

Figure 3.2: Images taken from [63]. (a) Schematic drawing of the honeycomb transmission mask placed in the path of the probe pulse. (b) On-target intensity profile of the pump (greyscale) and probe (colorscale) pulses. (c) Principle of the Spatial Domain Interferometry measurement.

more challenging. We note that the expansion velocity depends on both the ionization state of the plasma ions Z and the electron temperature T_e, which cannot easily be directly measured. To overcome these difficulties, an interferometry experiment, detailed in [63] has been carried out in Salle Noire in order to directly measure c_s.

3.1.2.1 Interferometry measurements

The preplasma expansion velocity is evaluated experimentally from an interferometric pump-probe measurement labeled **Spatial Domain Interferometry (SDI)**. The pump pulse is the prepulse that iniates the expansion. The probe pulse is the main pulse which has been modified by adding a periodic transmission mask, illustrated in figure 3.2(a), before the focusing parabola. The resulting on-target intensity distribution is shown in the colorscale of figure 3.2(b). It consists of a central spot (the **0th order spot**) surrounded by 6 weaker spots (the **1st order spots**).

The principle of the pump-probe measurement is illustrated in figure 3.2(c). In the ideal case, only the 0th-order spot is reflected by an expanded plasma while the first order spots are reflected at a position where the prepulse has not generated a plasma. As a result, the optical path length seen by the central spot is shorter, which produces a phase difference $\Delta\phi$ between the 0th order and 1st order spots. This phase difference grows as the delay between the pump and probe pulses is increased, due to the plasma expansion. Everytime, $\Delta\phi$ is increased by π, there is an inversion in the interference pattern formed by the reflected central and side spots far from the target, which can be detected experimentally.

In the experiments in Salle Noire, the pump pulse, whose on-target intensity profile can be seen in the greyscale of figure 3.2(b), spatially overlaps both the 0th order and 1st order spots. As a result, the side spots are also reflected on an expanding plasma. Nevertheless, because the prepulse intensity is

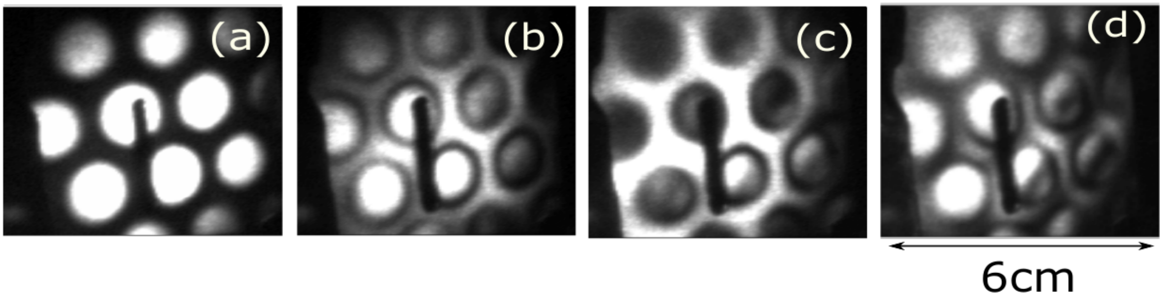

Figure 3.3: Images taken from [169]. Experimental reflected probe intensity profile in the far-field for a delay of 0 ps (a), 6 ps (b), 12 ps (c) and 20 ps (d) between the pump and probe pulses. The inversions in the interference pattern observed in (c) and (d) correspond respectively to $\Delta\phi = \pi$ and $\Delta\phi = 2\pi$.

weaker at the position of the side spots, the electron temperature is smaller and the plasma expansion is slower. Consequently, a phase difference $\Delta\phi$ is still created between the 0th order spot and the 1st order spots. The resulting inversion in the reflected probe intensity profile have been observed experimentally, as shown in figure 3.3.

Then, after making some assumptions regarding the preplasma expansion that will be detailed in the following section, it is possible to retrieve the expansion velocity from the delays at which the inversions occur. A velocity of $c_s = 10.8$ nm/ps was obtained in this case [63]. However, as pointed out in [169], there are large uncertainties on this value.

3.1.2.2 Analysis of the measurements

The purpose of this section is to detail how the expansion velocity can be estimated from the measurement presented in the previous section. This is useful to clearly understand the assumptions underlying the estimation of the preplasma density profile, which will then be compared to hydrodynamic simulations in section 3.1.3. The relevant experimental data is the following:

- The inversions in the reflected probe intensity profiles have been observed at delays of 12 ps, 20 ps and 30 ps. The corresponding phase differences $\Delta\phi$ are respectively π, 2π and 3π.
- The prepulse intensity at the position of the 0th order spot is $I_0 = 3.5 \times 10^{14}\,\mathrm{W/cm^2}$
- The average prepulse intensity at the position of the 1st order spots is $I_1 = 8.7 \times 10^{13}\,\mathrm{W/cm^2}$
- The incidence angle of the probe pulse is $49.3°$
- The duration of the pump and probe pulses is 30 fs.
- The intensity of the probe central spot is $\sim 10^{16}\,\mathrm{W/cm^2}$
- The intensity of the probe side spots is on the order of $\sim 10^{15}\,\mathrm{W/cm^2}$

The dephasing $\Delta\phi$ between the 0th and 1st order spots of the probe pulse has two sources:

1. During its reflection, the probe propagates in a underdense plasma whose refractive index is smaller than 1, thus effectively reducing the optical path length of the pulse. In the following, this process is referred to as the propagation dephasing.

2. Because of the plasma expansion, the probe reaches critical density and is thus reflected before the initial solid target surface, as is illustrated in figure 3.2. This also reduces the pulse optical path length. In the following, this process is referred to as the expansion dephasing.

The expansion dephasing is usually much larger than the propagation dephasing, but we evaluate both processes in the following paragraphs.

Propagation dephasing

The change in the reflected probe phase due to the propagation in an underdense plasma is given by:

$$\Delta\phi_{prop} = k\int (N(s)-1)\,ds \tag{3.8}$$

$$\Delta\phi_{prop} = k\int \left(\sqrt{1-\frac{n_e(s)}{n_c}}-1\right) ds \tag{3.9}$$

Where the integral is performed along the whole laser path and $k = 2\pi/\lambda$ is the laser wavenumber. Let us evaluate this integral for a pulse impinging on an overdense plasma with a 1D exponential density profile at oblique incidence. We assume without loss of generality that $n_e = n_c$ at $x = 0$ and we write in this case $n_e = n_c \exp(-x/L)$. The integral 3.9 then becomes:

$$\Delta\phi_{prop} = 2k\int_{s_{ref}}^{+\infty} \left(\sqrt{1-\exp\left(-\frac{x(s)}{L}\right)}-1\right) ds \tag{3.10}$$

Here, s_{ref} is the position at which the laser is reflected. The integral corresponds to the path of the reflected pulse and the factor 2 ensures that the path of the incident pulse is also taken into account in the calculation. We chose s such that $s = 0$ when $x = 0$ and we thus have $s = x/\cos\theta_i$, where θ_i is the laser incident angle. We then perform the change of variable $s \to x$ in the previous integral:

$$\Delta\phi_{prop} = \frac{2k}{\cos\theta_i}\int_{x_{ref}}^{+\infty} \left(\sqrt{1-\exp\left(-\frac{x}{L}\right)}-1\right) dx \tag{3.11}$$

The laser is reflected at the density $n_c\cos^2\theta_i$, which corresponds to the position $x_{ref} = -2L\ln(\cos\theta_i)$. The integral 3.11 can be evaluated analytically. The result is, after some algebra:

$$\Delta\phi_{prop} = -\frac{4kL}{\cos\theta_i}\left(1-\sin\theta_i+\ln\left(\frac{1+\sin\theta_i}{2}\right)\right) \tag{3.12}$$

This result is valid for $0 \leq \theta_i < \pi/2$.

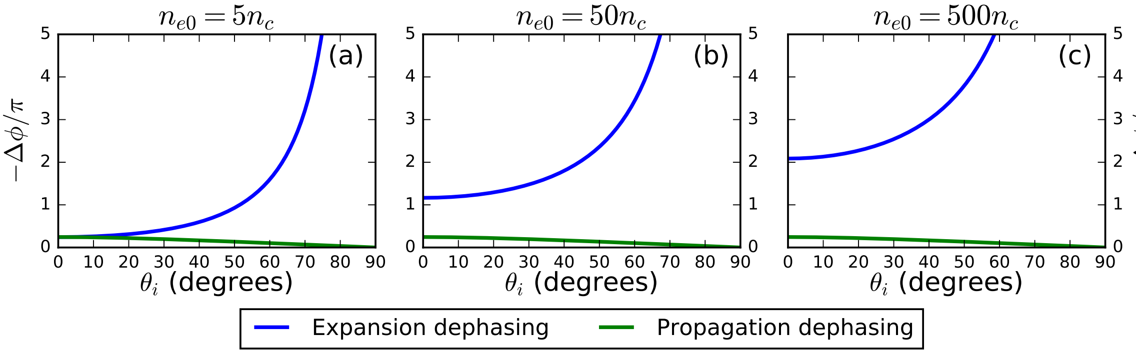

Figure 3.4: Expansion (blue curve) and propagation (red curve) dephasings as a function of the probe incidence angle for a gradient scale length $L = \lambda/10$ and maximum plasma densities of 5 n_c (a), 50 n_c (b) and 500 n_c (c). The dephasings are plotted using equations 3.12 and 3.15.

Expansion dephasing

As stated previously, the probe pulse is reflected at the density $n_c \cos^2\theta_i$. If we assume that the density profile is given by equation 3.5, the position at which the laser is reflected is given by:

$$x_{ref} = L \ln\left(\frac{n_{e0}}{\exp(1) n_c \cos^2\theta_i}\right) \tag{3.13}$$

This result assumes in particular that the density at the initial vacuum-solid target boundary $x = 0$ is $n_{e0}\exp(-1)$, in agreement with the isothermal model of plasma expansion presented in section 3.1.1. The phase difference due to the reflection at $x = x_{ref}$ rather than at $x = 0$ is given by:

$$\Delta\phi_{exp} = -\frac{2kx_{ref}}{\cos\theta_i} \tag{3.14}$$

$$\Delta\phi_{exp} = -\frac{2kL}{\cos\theta_i} \ln\left(\frac{n_{e0}}{\exp(1) n_c \cos^2\theta_i}\right) \tag{3.15}$$

Comparison between propagation and expansion dephasing

For an exponential density profile, both dephasings depend linearly on the gradient scale length L. On the other hand, they depend nontrivially on the incidence angle θ_i and the expansion dephasing additionally depends on the maximum plasma density n_{e0}. The propagation and expansion dephasings are plotted as a function of the incidence angle for 3 different plasma densities in figure 3.4.

The propagation dephasing decreases when the incidence angle is increased due to the fact that the laser does not penetrate in the highest plasma density region where the optical index is significantly smaller than 1. On the other hand, the expansion dephasing increases for rising incidence angles and diverges when θ_i approaches π. This is both because the reflection position x_{ref} becomes increasingly large and because of the geometric factor $1/\cos\theta_i$, which comes from the fact that at grazing incidence the total laser propagation distance is much greater than its propagation distance in the gradient direction x.

At normal incidence, the two dephasings are comparable in amplitude when $n_{e0} \sim 5\ n_c$. However, much higher bulk plasma densities that usually exceed $100\ n_c$ are used in most solid target experiments.

In such a case, the expansion dephasing is dominant. This effect is amplified at oblique incidence for which the propagation dephasing rapidly becomes negligible.

Estimation of the expansion velocity in the interferometry measurement

The measurements in Salle Noire were carried out with a 49.3° incidence angle. We find in this case that the expansion dephasing is ≈ 17 times higher than the propagation dephasing for $n_{e0} = 50 n_c$ and ≈ 27 times higher than the propagation dephasing for $n_{e0} = 500 n_c$. We thus neglect the propagation dephasing and only consider the expansion dephasing in the estimation of the expansion velocity in the SDI measurements.

The phase $\Delta\phi$ measured experimentally then corresponds to the difference between the expansion dephasing $\Delta\phi_{exp,1}$ seen by the probe 1st order spots and the expansion dephasing $\Delta\phi_{exp,0}$ seen by the probe 0th order spot:

$$\Delta\phi = \Delta\phi_{exp,1} - \Delta\phi_{exp,0} \tag{3.16}$$

$$\Delta\phi = \frac{2k}{\cos\theta_i}\left(L_0 \ln\left(\frac{n_{e0,0}}{\exp(1) n_c \cos^2\theta_i}\right) - L_1 \ln\left(\frac{n_{e0,1}}{\exp(1) n_c \cos^2\theta_i}\right)\right) \tag{3.17}$$

Where $L_n = c_{s,n}\Delta t$ and $n_{e0,n}$ respectively correspond to the gradient scale length and maximum plasma density at the position of the probe nth order spot. We can immediatly see that the sole measurement of the ratio $\Delta\phi/\Delta t$ is not sufficient to determine the four unknown variables $c_{s,0}$, $c_{s,1}$, $n_{e0,0}$ and $n_{e0,1}$. Other hypotheses must therefore be made in order the estimate the expansion velocity.

The first one that we make is to assume that the expansion velocity is at every position proportional to the square root of the local prepulse intensity. This approximation is motivated by the fact that the expansion velocity is proportional to the square root of the temperature in the 1D isothermal expansion model. If we assume that the prepulse absorption coefficient is the same everywhere, the temperature will be proportional to the local prepulse fluence[3], and thus to the local prepulse intensity (at least in the absence of spatiotemporal couplings). This approximation reads mathematically $c_s \propto \sqrt{T} \propto \sqrt{I}$. When considering the position of the probe 0th and 1st order spots, this becomes:

$$c_{s,1} = \sqrt{\frac{I_1}{I_0}} c_{s,0} \tag{3.18}$$

We then insert this expression into equation 3.17 to obtain:

$$\Delta\phi = \frac{2kc_{s,0}\Delta t}{\cos\theta_i}\left(\ln\left(\frac{n_{e0,0}}{\exp(1) n_c \cos^2\theta_i}\right) - \sqrt{\frac{I_1}{I_0}} \ln\left(\frac{n_{e0,1}}{\exp(1) n_c \cos^2\theta_i}\right)\right) \tag{3.19}$$

If we make the additionnal approximation that the maximum plasma density is the same everywhere, the previous equation is simplified to:

$$\Delta\phi = \frac{2kc_{s,0}\Delta t}{\cos\theta_i}\left(1 - \sqrt{\frac{I_1}{I_0}}\right) \ln\left(\frac{n_{e0}}{\exp(1) n_c \cos^2\theta_i}\right) \tag{3.20}$$

Or equivalently:

$$c_{s,0} = \frac{\Delta\phi}{\Delta t}\frac{\cos\theta_i}{2k}\left[\left(1 - \sqrt{\frac{I_1}{I_0}}\right) \ln\left(\frac{n_{e0}}{\exp(1) n_c \cos^2\theta_i}\right)\right]^{-1} \tag{3.21}$$

---

[3] The fluence is the incident energy per unit area, commonly expressed in $\mathrm{J/cm^2}$. It is proportional to the intensity and the pulse duration.

With this expression, the expansion velocity can be directly estimated from the experimental measurement of the ratio $\Delta\phi/\Delta t$ (approximately $\pi/10$ ps^{-1}) provided that a maximum plasma density n_{e0} is chosen.

However, choosing n_{e0} is not obvious. It can be estimated from the molecular density of the target ($2.2 \times 10^{22}\,\mathrm{cm}^{-3}$ for fused silica) and the ionization state of the plasma, but choosing the ionization state is in turn not obvious. For a fully ionized target (Si^{14+} and O^{8+}), we have 30 electrons per molecule which results in an electronic density of 380 n_c. This provides an upper bound for n_{e0}. The plasma ionization state may be estimated using the intensity of the prepulse and the barrier suppression ionization threshold for silicon and oxygen, which are given in table 3.1. For a prepulse intensity of $3.5 \times 10^{14}\,\mathrm{W/cm}^2$, this would lead to Si^{2+} and O^{+} and $n_{e0} = 50n_c$. However, this evaluation is based on the assumption that field ionization is the dominant ionization mechanism, which may not be true. Indeed, once the target is ionized, the prepulse only interacts inside the plasma skin depth, which is much shorter than a wavelength for a strongly overdense plasma. Then, collisional processes are responsible for causing additional ionization in the plasma bulk, and possibly ionization to higher states than those induced by field ionization. This renders the estimation of the plasma ionization state (which may very well be inhomogeneous and time-dependent) not straightforward.

The choice of n_{e0} alone leads to significant uncertainties regarding the plasma expansion velocity. Choosing $n_{e0} = 50n_c$ results in c_s = 6.9 nm/ps whereas choosing $n_{e0} = 380n_c$ results in c_s = 4.5 nm/ps. Other sources of uncertainties in equation 3.21 include:

- The assumption that the plasma density profile is exponential.
- The assumption that the prepulse absorption coefficient is the same everywhere, which leads to $c_s \propto \sqrt{I}$. The ratio of absorbed energy may indeed depend on the local prepulse intensity.
- The assumption that the maximum plasma density n_{e0} is the same everywhere. We could indeed expect a lower value of the ionization state at the position of the probe 1st order, since the prepulse intensity is lower at that point.
- The fact that the probe pulse, which was more intense than the pump pulse in the interferometry measurement, can induce further ionization as it travels in the preplasma, thus influencing its own propagation. PIC simulations performed at long gradients that will be shown in section 3.4 indeed show that the ionization induced by a pulse can affect the position at which it is reflected (see figure 3.22). This effect, which could be different for the probe 0th and 1st orders, is difficult to evaluate because the plasma ionization state during the expansion is not precisely known.
- The experimental uncertainties in the estimation of the prepulse intensities.

Overall, the uncertainty on the expansion velocity measurement probably exceeds 50%.

In the following we heuristically choose a maximum density of $n_{e0} = 100n_c$, which corresponds to 8 ionized electrons per molecule and results in an expansion velocity of c_s = 5.8 nm/ps. This value differs from the value of c_s = 10.8 nm/ps obtained in the publication presenting the measurements [63]. This is because of the following differences:

- The maximum plasma density was chosen as $n_{e0} = 300n_c$, rather than $n_{e0} = 100n_c$ here.
- It was assumed that the laser reflects at n_c rather than $n_c \cos^2\theta_i$. This corresponds to dropping the term $\cos^2\theta_i$ in the logarithm of equation 3.21.

Initial ion state	**Ionization energy**	**Barrier suppression intensity**
Si	8.15 eV	$1.76 \times 10^{13}\,\mathrm{W/cm^2}$
$\mathrm{Si^{+}}$	16.3 eV	$7.06 \times 10^{13}\,\mathrm{W/cm^2}$
$\mathrm{Si^{2+}}$	33.5 eV	$5.60 \times 10^{14}\,\mathrm{W/cm^2}$
$\mathrm{Si^{3+}}$	45.1 eV	$1.03 \times 10^{15}\,\mathrm{W/cm^2}$
$\mathrm{Si^{4+}}$	167 eV	$1.24 \times 10^{17}\,\mathrm{W/cm^2}$
$\mathrm{Si^{5+}}$	205 eV	$1.96 \times 10^{17}\,\mathrm{W/cm^2}$
$\mathrm{Si^{6+}}$	247 eV	$3.04 \times 10^{17}\,\mathrm{W/cm^2}$
$\mathrm{Si^{7+}}$	304 eV	$5.34 \times 10^{17}\,\mathrm{W/cm^2}$
$\mathrm{Si^{8+}}$	351 eV	$7.50 \times 10^{17}\,\mathrm{W/cm^2}$
$\mathrm{Si^{9+}}$	401 eV	$1.03 \times 10^{18}\,\mathrm{W/cm^2}$
$\mathrm{Si^{10+}}$	476 eV	$1.70 \times 10^{18}\,\mathrm{W/cm^2}$
$\mathrm{Si^{11+}}$	523 eV	$2.08 \times 10^{18}\,\mathrm{W/cm^2}$
$\mathrm{Si^{12+}}$	2440 eV	$8.39 \times 10^{20}\,\mathrm{W/cm^2}$
$\mathrm{Si^{13+}}$	2670 eV	$1.04 \times 10^{21}\,\mathrm{W/cm^2}$
O	13.6 eV	$1.37 \times 10^{14}\,\mathrm{W/cm^2}$
$\mathrm{O^{+}}$	35.1 eV	$1.52 \times 10^{15}\,\mathrm{W/cm^2}$
$\mathrm{O^{2+}}$	54.9 eV	$4.04 \times 10^{15}\,\mathrm{W/cm^2}$
$\mathrm{O^{3+}}$	77.4 eV	$8.97 \times 10^{15}\,\mathrm{W/cm^2}$
$\mathrm{O^{4+}}$	114 eV	$2.70 \times 10^{16}\,\mathrm{W/cm^2}$
$\mathrm{O^{5+}}$	138 eV	$4.03 \times 10^{16}\,\mathrm{W/cm^2}$
$\mathrm{O^{6+}}$	739 eV	$2.43 \times 10^{19}\,\mathrm{W/cm^2}$
$\mathrm{O^{7+}}$	871 eV	$3.60 \times 10^{19}\,\mathrm{W/cm^2}$

Table 3.1: Ionization energies of silicon and oxygen and corresponding barrier-suppresion ionization intensites. The ionization energies have been obtained from the NIST Atomic Spectra Database.

- It was assumed that the density at $x = 0$ is always n_{e0}, rather than $n_{e0}\exp(-1)$ here. This corresponds to dropping the term $\exp(1)$ in the logarithm of equation 3.21.
- A calculation error was made in equation (9) of [63]. It essentially corresponds to multiplying rather than dividing by $\cos\theta_i$ in equation 3.14 and eventually to dividing rather than multiplying by $\cos\theta_i$ in equation 3.21. Without this error, the estimated velocity would have been c_s = 4.6 nm/ps.

Estimation of the expansion velocity in the new experimental campaign

In the experiments that will be presented in section 3.2, a more energetic prepulse was used, with a peak fluence of $\approx 50\,\mathrm{J/cm^2}$ (compared to $\approx 10\,\mathrm{J/cm^2}$ in the interferometry measurement). This corresponds to a peak intensity of $\approx 1.8\times10^{15}\,\mathrm{W/cm^2}$ for a 25-fs pulse duration. No spatial domain interferometry measurement were made with this prepulse. Thus, to estimate the expansion velocity in this case, we have used the previously described assumption that the expansion velocity is proportional to the square root of the fluence. This leads to an expansion that is approximately $\sqrt{5}$ times faster than during the interferometry measurement. We obtain in this manner a value of c_s = 12.9 nm/ps, which is used in the analysis of the experiments.

We can also point out that in the recent experiments, the main pulse duration was varied between 3.5 fs and 24 fs. The prepulse initially had the same duration, since it is created by picking up a small part of the main pulse, but propagates through dispersive optic elements, which increases its on-target duration. This means that experiments performed with the shortest main pulse durations have the longest prepulse duration. For instance, we estimated that the experiments performed with a 5-fs main pulse duration have a prepulse duration on the order of 100 fs. However, it is observed that the delay for which electron emission is optimal in the short gradient regime is similar regardless of pulse duration (see figure 3.12 that will be presented later), indicating that the plasma expansion is the same for every prepulse duration. This was also observed in the hydrodynamic simulations presented in the next paragraph (simulations with different prepulse duration but identical fluence lead to almost indistinguishable results). This tends to confirm that the prepulse fluence is the main parameter driving the preplasma expansion.

3.1.3 1D hydrodynamic simulations of preplasma expansion

The spatial domain interferometry method presented in the previous section essentially provides a measurement of the position x_{ref} at which the probe pulse is reflected (or more precisely of the difference between the position $x_{ref,0}$ at which the probe 0th is reflected and the position $x_{ref,1}$ at which the probe 1st order is reflected), where the density is $n_c\cos^2\theta_i$. Then, the expansion velocity is estimated by assuming an isothermal plasma expansion and choosing a maximum plasma density.

In order obtain more insight on the preplasma expansion, 1D hydrodynamic simulations of plasma expansion using the code ESTHER have been carried out by Laurent Videau, at the CEA-DAM-DIF center in Bruyères-le-Châtel. These simulations are useful to test the validity of the isothermal expansion model, upon which our previous estimation of c_s relies, and can be directly compared with the interferometry measurements.

3.1.3.1 The ESTHER code

ESTHER is a 1D Lagrangian hydrodynamic code developed at the CEA DAM [170]. In the simulations, the prepulse impinges with p-polarization and 45° incidence on a solid fused silica target with a step-like density profile and an initial temperature of 300 K. Field ionization is not included in the simulations. However, in the absence of ionization, the laser pulse would cross the target without depositing energy since fused silica is transparent in its solid state. In order to avoid this, an imaginary part is artificially added to the optical index of the target to model the initial laser absorption and creation of the plasma. This means that the very beginning of the interaction is probably poorly modeled. However, once the target is in plasma state, the imaginary index becomes irrelevant. We accordingly observe that the results are independent on the choice of the imaginary index provided that it is high enough so that a plasma is created during the first laser optical cycles, as is the case in experiments. This suggests that artificialy adding an imaginary optical index is a cost-effective way to model the initial ionization.

Once the prepulse has deposited part of its energy into the target, the plasma expansion is calculated using an equation of state that is valid from the solid phase to the plasma phase [171]. In the case of silica, only a single temperature model is available. This means that the electron and ion temperatures are the same, even at the beginning of the plasma expansion. This is probably not the case in reality and is a possible source of uncertainty in the simulations.

The mass density, fluid velocity and temperature as a function of time are then given as outputs. An estimation of the ionization state is also given, but its validity is unclear and we have consequently not used it.

3.1.3.2 Simulation results

Simulations have been carried out with laser parameters corresponding to either the prepulse in the interferometry measurement or the more energetic prepulse in the recent experimental campaign. In the former case, we use a pulse duration of 30 fs with a peak intensity of 3.5 $\times 10^{14}\,\mathrm{W/cm^2}$, resulting in a fluence of $\approx 11\,\mathrm{J/cm^2}$. In the latter case, we use a pulse duration of 100 fs with a peak intensity of 5 $\times 10^{14}\,\mathrm{W/cm^2}$, resulting in a higher fluence of $\approx 53\,\mathrm{J/cm^2}$. The pulse duration is chosen to model the chirped prepulse used in the experiments, as explained in the last paragraph of section 3.1.2.2. Choosing a pulse duration of 50 fs and an intensity of $10^{15}\,\mathrm{W/cm^2}$ (same fluence) leads to identical results, meaning that the exact choice of the pulse duration is not significant.

The expansion of the plasma mass density is displayed for both simulations in figure 3.5. As expected, a higher fluence leads to a faster plasma expansion. We notice that the density profiles have a very similar shape in the two cases. In particular, we observe that for short delays Δt after the prepulse, the density profile is close to an exponential (a pure exponential would be a straight line in this logarithmic scale). This confirms that choosing an exponential density profile in the simulations is a reasonable approximation at short gradients.

On the other hand, the density profile significantly deviates from an exponential for longer delays. This is an indication that the isothermal assumption is violated in the simulations. This can be confirmed by plotting the expanding plasma temperature, which is done in figure 3.6(a) in the case of the high fluence simulation. We indeed observe that not only the temperature is not homogeneous, with the highest values located towards the expansion direction, but it also decreases with time during the expansion.

The fluid velocity during expansion is plotted for the same simulation in figure 3.6(b). The linear relation between position and velocity that is predicted from the isothermal model is well reproduced. Nonetheless, unlike in the model, the maximum velocity remains finite in simulations because the plasma is bounded in space.

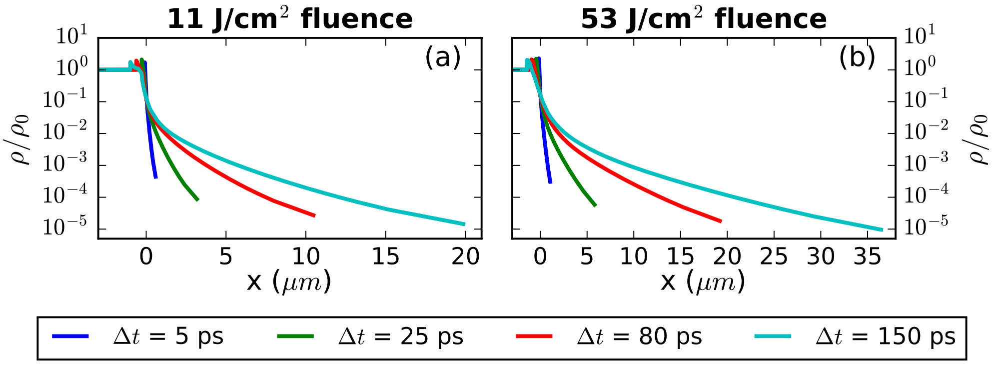

Figure 3.5: Results from 1D hydrodynamic simulations. Mass density of a fused silica target at four different delays after irradiation at $\Delta t = 0$ *by a 30-fs, 3.5* $\times 10^{14}\,\mathrm{W/cm^2}$ *prepulse (a) or a 100-fs, 5* $\times 10^{14}\,\mathrm{W/cm^2}$ *prepulse.* ρ_0 *is the mass density of fused silica in its solid state.*

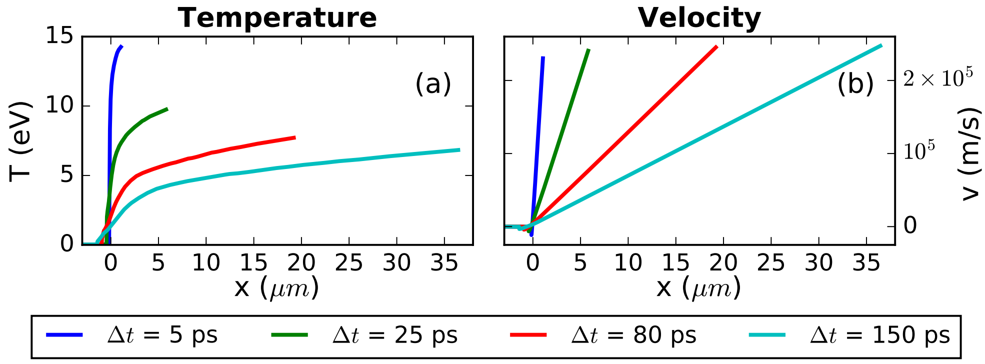

Figure 3.6: Results from 1D hydrodynamic simulations. Temperature (a) and velocity (b) of a fused silica target at four different delays after irradiation at $\Delta t = 0$ *by a 100-fs, 5* $\times 10^{14}\,\mathrm{W/cm^2}$ *prepulse.*

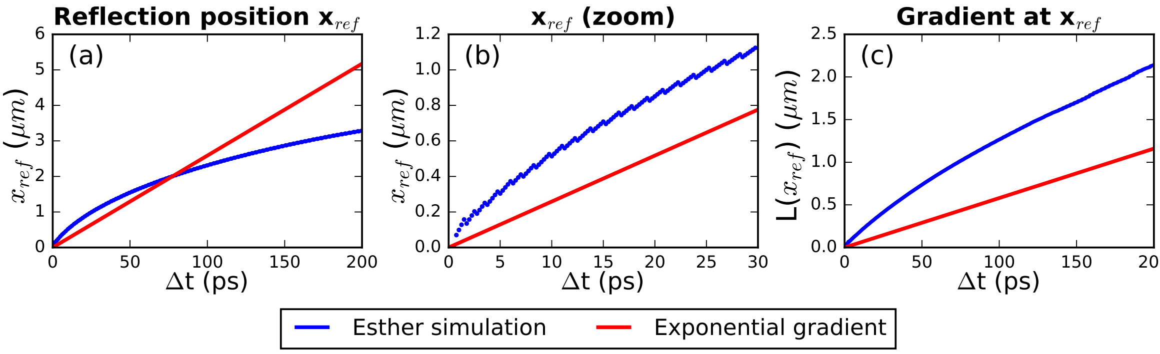

Figure 3.7: (a) Reflection position x_{ref} of the probe pulse 0th order in the interferometric measurement estimated from hydrodynamic simulation (blue curve) or from an exponential density profile with the previously evaluated expansion velocity (red curve). (b) Same plot but zoomed on the first 30 ps of the expansion. (c) Gradient scale length at position x_{ref}. The apparent discontinuities in the blue curve in (b) occur when the reflection position jumps from one grid cell to the next.

The density profiles shown in figure 3.5(b) have been used in the simulations with a long gradient scale length that will be presented in section 3.4.

3.1.3.3 Comparison between simulations and interferometry measurements

The purpose of this section is to test the consistency between the hydrodynamic simulations and the expansion velocity obtained with spatial domain interferometry. The main difficulty arises from the fact that ESTHER simulations provide mass density profiles while it is the electron density which has an effect on the interaction. This is essentially because the ionization state is not precisely known.

One possible test is to compare the position of reflection x_{ref} given by either the hydrodynamic simulations or an exponential density profile with the measured expansion velocity. We first consider the case of the interferometry measurement (simulation with the lowest prepulse fluence). We use the previously estimated values of $c_s = 5.8$ nm/ps and $n_{e0} = 100\ n_c$. The latter corresponds to an ionization state of 8 electrons per molecule that we use to evaluate the electron density n_e from the mass density ρ in the ESTHER simulation. The reflection position x_{ref} in the simulations is then obtained by finding the position such that $n_e(x_{ref}) = n_c \cos^2\theta_i$. In the case of the experimental density profile, x_{ref} is estimated with equation 3.13.

The result is shown in figure 3.7(a) and a close-up of the beginning of the expansion in shown in figure 3.7(b). If similar orders of magnitude are obtained, we find a faster initial expansion of the reflection position in the hydrodynamic simulations, especially in the first 30 ps which correspond to delays where the interferometry measurement is performed. A better agreement can be obtained in the first 30 ps by choosing 4 electrons per molecule, resulting in $n_{e0} = 50\ n_c$ and $c_s = 6.9$ nm/ps.

The gradient scale length $L(x_{ref})$ at the reflection position is plotted in figure 3.7(c). We once again observe a faster expansion in the simulation. We can also remark that, if both x_{ref} and $L(x_{ref})$ evolve linearly with Δt for an exponential gradient, the plasma expansion appears to be more "concave" in simulations.

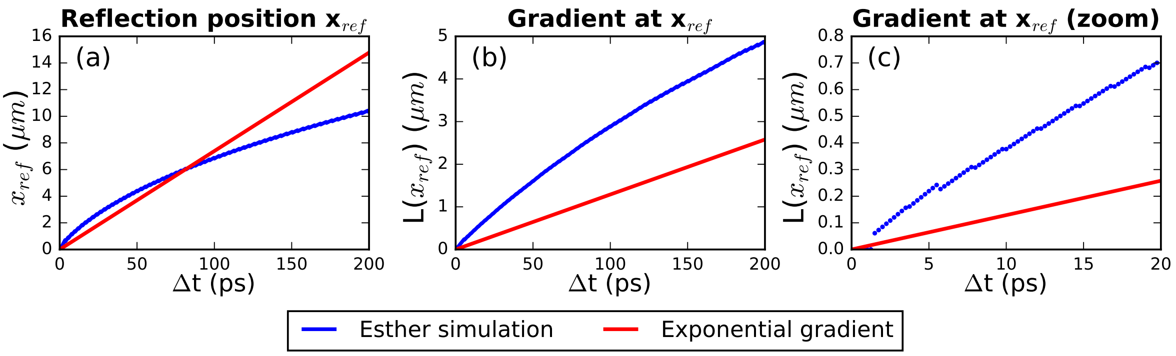

Figure 3.8: (a) Reflection position x_{ref} of the main pulse in the recent experimental campaign estimated from hydrodynamic simulation (blue curve) or from an exponential density profile with the previously evaluated expansion velocity (red curve). (b) Gradient scale length at position x_{ref}. (c) Same plot but zoomed on the first 20 ps of the expansion. The apparent discontinuities in the blue curve in (c) occur when the reflection position jumps from one grid cell to the next.

The same test has been performed for the highest fluence simulation ($\approx 53\,\mathrm{J/cm^2}$), which corresponds to the recent experimental campaign. We assume in this case that the plasma has an ionization state of 8 electrons per molecule during expansion and correspondigly use $n_{e0} = 100\ n_c$ and $c_s = 12.9$ nm/ps to estimate the electron density in the exponential gradient. However, we also make the hypothesis that the main pulse, with its peak intensity on the order of $10^{18} - 10^{19}\,\mathrm{W/cm^2}$ depending on the duration, causes further ionization as it propagates in the preplasma, resulting in a final ionization state estimated from the barrier-suppression ionization thresholds of 22 electrons per molecule (Si^{10+} and O^{6+}). Consequently, we assume that the main pulse is reflected at a density $n_e(x_{ref}) = 8/22 \times n_c \cos^2\theta_i$, where 8 and 22 correspond to the initial (during expansion) and final (after reflection) ionization states and $n_e(x)$ is the density profile immediatly before interaction with the main pulse. Results are displayed in figure 3.8. We once again find a faster expansion of the gradient scale length L in simulation.

In both cases, we remark that the difference between the simulations and the exponential density profile are more pronounced for the gradient scale length at the position of reflection $L(x_{ref})$ than for the reflection position itself. This is because the density profiles are not exponential in simulations and is a reminder that the SDI method is a measurement of the reflection position but not directly of the density gradient at reflection, which is the more relevant parameter in experiments.

The previous tests had the disadvantage of relying not only on the choice of the ionization state, but also on the choice of the maximum plasma density n_{e0} (although both were chosen self-consistently). One way to test the agreement between simulations and measurements without have to choose n_{e0} is to simulate the interferometry experiment using the ESTHER density profile. For this purpose we have performed a new ESTHER simulation with an intensity corresponding to the prepulse intensity at the position of the probe 1st order spots (I = $8.7 \times 10^{13}\,\mathrm{W/cm^2}$). This allows us to estimate the density profile seen by the probe side spots. After choosing an ionization state, we can calculate numerically both the propagation and expansion dephasing seen by the 0th and 1st order spots and eventually evaluate $\Delta\phi$. We have done this for 3 different choices of ionization state:

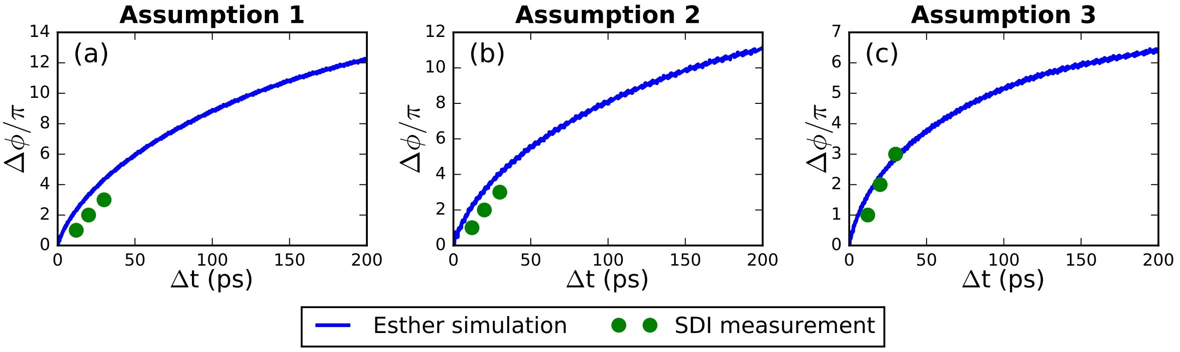

Figure 3.9: Dephasing $\Delta\phi$ between the probe 1st order and 0th order spots evaluated using (a) 6 electrons per molecule for the 0th order spot and 4 electrons per molecule for the first order spots, (b) 8 electrons per molecule for both the 0th and 1st order spots and (c) 4 electrons per molecule for both the 0th and 1st order spots. The green dots show for comparison the experimental measurements.

- Assumption 1: we only take the ionization levels whose barrier-suppresion intensity thresholds are much lower (at least one order of magnitude) than the probe pulse intensity. We obtain in this manner 6 electrons per molecule (Si^{4+} and O^{+}) for the central spot and 4 electrons per molecule (Si^{2+} and O^{+}) for the side spots.

- Assumption 2: we take 8 electrons per molecule for both the central and side spots. This is consistent with the previous assumptions that $n_{e0} = 100\ n_c$ everywhere.

- Assumption 3: we take 4 electrons per molecule for both the central and side spots. This assumption is chosen because we have found retrospectively that it leads to the best agreement with the interferometry measurement.

Results from these tests are shown in figure 3.9. $\Delta\phi = 3\pi$ was measured for a delay $\Delta t = 30$ ps. In simulations, we find for the same delay $\Delta\phi = 4.3\pi$ with assumption 1, $\Delta\phi = 4\pi$ with assumption 2 and $\Delta\phi = 2.8\pi$ with assumption 3. Similar orders of magnitude for the dephasing are obtained, with values up to $\approx 50\%$ higher in simulations. As previously, we observe a concave plasma expansion in the hydrodynamic simulations.

Overall, the comparisons performed in this section are useful as they illustrate the significant uncertainties associated with the estimation of the preplasma density profile, and in particular those arising from the fact that the ionization states are not known. Nevertheless, similar orders of magnitude are found in both measurements and simulations, which confirms that the spatial domain interferometry method can provide a reasonable estimation of the expansion velocity. We consistently find a somewhat faster plasma expansion in simulations. This difference can be explained by the uncertainties associated with the measurements, but could also mean that these 1D hydrodynamic simulations with a single temperature model tend to overestimate the expansion.

3.1.4 Conclusion on the preplasma expansion

Both the spatial domain interferometry measurement and the 1D hydrodynamic simulations allow us to have a reasonable estimation of the preplasma density profile during experiments. It should be kept in mind that there are significant uncertainties associated with this estimation. This might sound concerning given that the gradient scale length is a key parameter of the interaction. However:

- The delay between the prepulse and the main pulse can be continuously varied in experiments. Performing such a gradient scan makes it possible to identify the different electron acceleration regimes relevant to a given set of laser parameters, which can then be understood using PIC simulations. The uncertainties on the density profile will result in uncertainties on the gradient scale length for which a given mechanism occurs/is optimal, but do not prevent us from studying the physics of the interaction.

- The experiments are reproducible since using the same prepulse parameters will lead to the same plasma expansion. This means that if a better estimation of the plasma density profile is obtained, the experiments can still be retrospectively analyzed more accurately.

It should also be noted that we have only considered in this section a one-dimensional expansion. When the longitudinal extension of the preplasma is of the same order of magnitude as the prepulse spot size ($\approx 13\,\mu\mathrm{m}$ in Salle Noire), transverse effects likely come into play in the plasma expansion. This effect could be significant in the electron acceleration mechanism at long gradients identified in section 3.4. A detailed study of the multi-dimensional expansion of the preplasma in Salle Noire using 2D or 3D hydrodynamic simulations could be the subject of future work.

3.2 Experimental Results

We present in this section results from the first experiments in Salle Noire where relativistic intensity few-cycle pulses have been used on solid targets, which have been carried out by Maïmouna Bocoum and Frederik Böhle [34]. We focus primarily on the emission of fast electrons but we also mention results regarding high-harmonic generation in section 3.2.3.

3.2.1 Experimental setup

The Salle Noire laser delivers 2.6-mJ pulses at 1-kHz repetition rate with an extremely high temporal contrast ($> 10^{10}$) [32]. The 800 nm, 24 fs laser pulses are post-compressed in a helium-filled stretched hollow-core fiber [33, 35]. The pulse duration can be tuned by changing the pressure in the fiber, thereby providing near Fourier transform limited pulses from 3.5 fs to 24 fs. The laser beam is focused down to $w_0 = 1.5\,\mu\mathrm{m}$ resulting in peak intensities ranging from $2.3 \times 10^{18}\,\mathrm{W/cm}^2$ ($a_0 \simeq 1$) for 24 fs pulses to $1.6 \times 10^{19}\,\mathrm{W/cm}^2$ ($a_0 \simeq 2.7$) for 3.5 fs pulses.

In the experiment, represented in Fig. 3.10, p-polarized pulses impinge on an optically flat fused silica (SiO_2) target with an incidence angle $\theta_i = 55°$. A spatially overlapped prepulse, created by picking off $\approx 4\%$ of the main pulse through a holey mirror, is focused to a much larger 13 $\mu\mathrm{m}$ FWHM spot (see inset of Fig. 3.10) in order to generate a transversely homogeneous plasma that expands into vacuum. The plasma density profile during the interaction is controlled by varying the delay, Δt, between the prepulse and the main pulse.

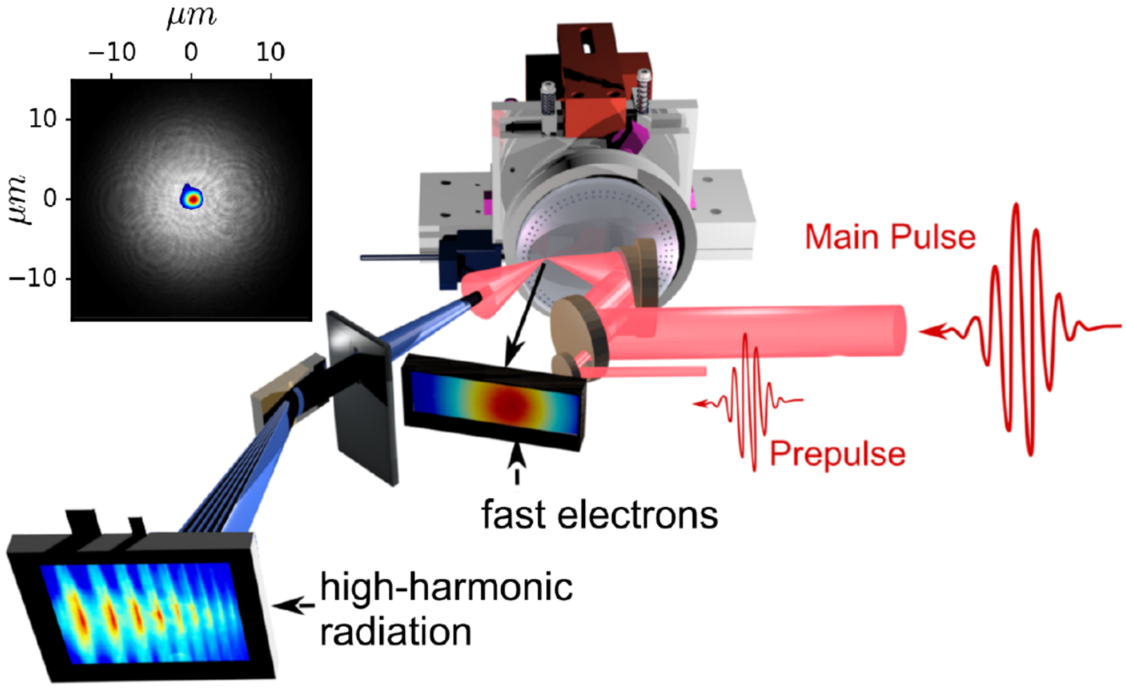

Figure 3.10: Schematic of the experimental setup. The laser pulses interact at 1-kHz repetition rate with a fused silica rotating target. The resulting fast electrons and high-harmonic emission are simultaneously detected. Inset: superimposition of the on-target prepulse (white) and main pulse (color) focal spots. Image taken from [34].

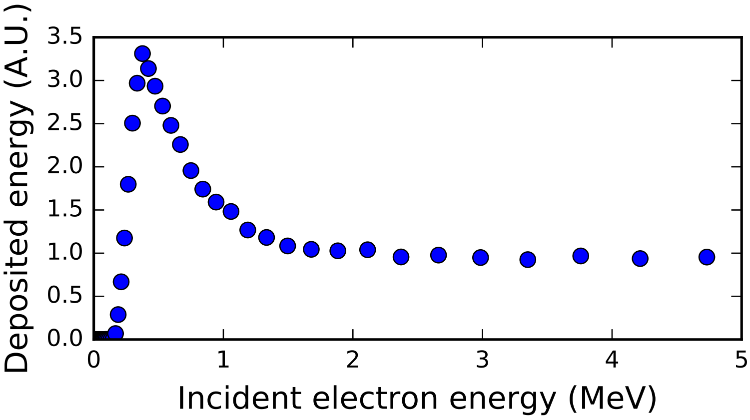

Figure 3.11: Lanex screen spectral response. This data was initially presented in [172].

Backward electron emission is measured using a Lanex screen, protected by a 13 μm thick Al-foil, which detects electrons with energies > 150 keV. The Lanex screen was calibrated prior to the experiment using a 3-MeV RF accelerator. As shown in figure 3.11, the response of the screen depends on the detected electron energy. Therefore, the electron energy spectrum should be known in order to evaluate the absolute detected charge for a given shot. However, electron energy spectra have not been measured in this first experimental campaign. For this reason, the absolute charge is estimated from a spectrum obtained from a PIC simulation described in section 3.4 (see figure 3.21). The resulting uncertainty, of the order of 50%, is mainly due to the fact that the energy spectra are not known. The angular electron distribution in the backward direction is recorded for $-3° < \theta_x < 75°$ and $-15° < \theta_y < 15°$ where θ_x and θ_y are the angles with respect to target normal respectively in the incidence and transverse planes.

Additionally, harmonics emitted in the specular direction can be measured by an XUV spectrometer coupled to a micro-channel plate and a phosphor screen detector. The harmonic spectrum is then measured in the θ_x direction while the harmonic beam divergence is obtained in the θ_y direction. When the high-harmonic signal is measured, the fast electrons can only be detected at angles smaller than the specular direction ($\theta_x < \theta_i$) because the Lanex screen would otherwise block the harmonic beam.

3.2.2 Electron emission

Figure 3.12 shows the measured electron signal as a function of the delay between the prepulse and the main pulse for 5 different laser pulse durations. As expected, we find a strong electron emission for short delays ($\Delta t < 20$ ps), corresponding to a sharp plasma-vacuum interface. This emission, detected for every pulse duration, is optimal for a delay $\Delta t \approx 7$ ps, i.e. $L < \lambda/5$. In this regime, the push-pull mechanism described in section 1.4.2.1 is responsible for the ejection of electrons from the plasma. A typical electron angular distribution obtained with a 5-fs pulse in this case is displayed in figure 3.13(a), showing a broad divergence angle of $\approx 50°$.

As the delay is further increased, the detected charge drops (10 ps $< \Delta t < 30$ ps), and then rises again for longer delays ($\Delta t > 50$ ps). This time however, electrons are only emitted when few-cycle pulses ($\leq$10 fs) are used. Note that chirping a few-cycle pulse to increase its duration results in a similar decline

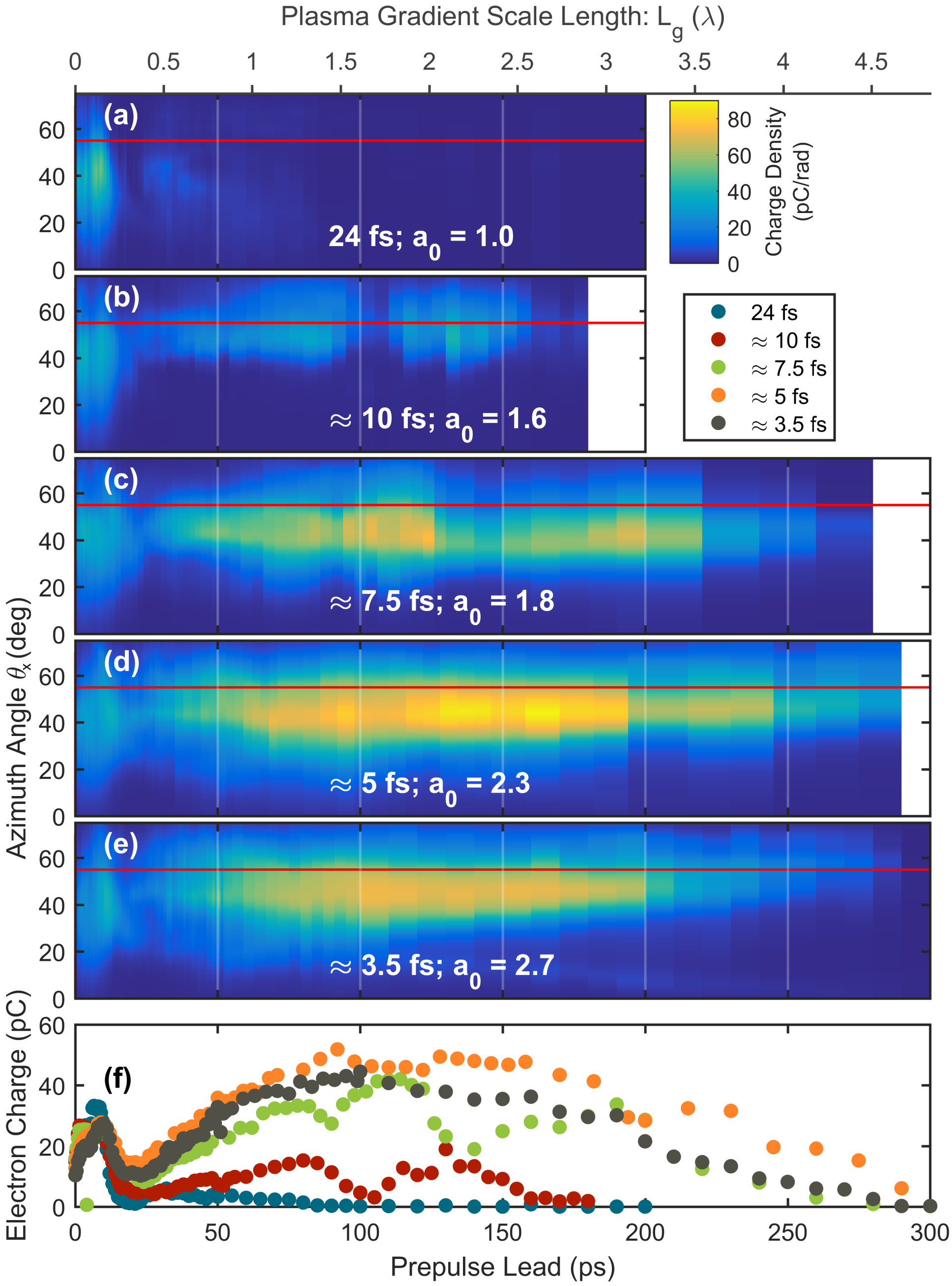

Figure 3.12: (a)-(e) Electron angular distribution integrated over the θ_y angle as a function of the delay between the prepulse and the main pulse for respective pulse durations of 24, 10, 7.5, 5 and 3.5 fs. (f) Total ejected charge as a function of the delay between prepulse and main pulse. The gradient scale lengths given in the top axis are obtained using an expansion velocity of 12.9 nm/ps, as described in section 3.1.2.2. Each data point corresponds to an average over 50 shots (50 ms acquisition time at 1 kHz repetition rate). The red lines mark the specular direction.

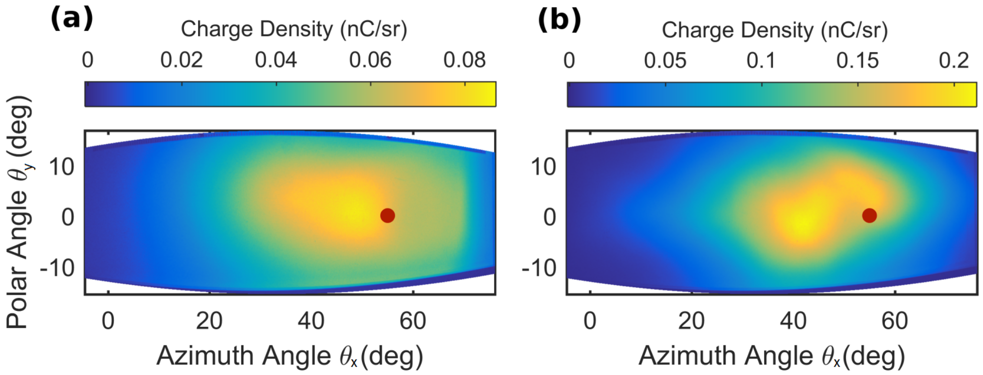

Figure 3.13: Typical electron angular distribution obtained with 5-fs pulses respectively in the short ((a), $\Delta t = 9$ ps) and long ((b), $\Delta t = 140$ ps) plasma scale length regimes. The red dots mark the specular direction.

of the electron signal, as can be seen in figure 3.14. This is thus a very distinct physical regime, in which the gradient length is much larger ($L > \lambda$) and the duration of the laser pulse plays a major role. In this case, the obtained electron beams have more charge and a narrower divergence angle of $\approx 25°$ as is visible in figure 3.13(b). The electrons are emitted near the specular direction, with a slight shift towards the normal direction. The detected signal is very stable over a wide range of delays (50 ps$<\Delta t<$200 ps), indicating that the electron ejection mechanism is not highly sensitive to the exact shape of the plasma density profile. The beam also exhibits good shot-to-shot stability: the fluctuation is on the order of 10% on the charge and 5% on the divergence and the beam pointing fluctuation is on the order of $1°$. These statistics have been computed for the case of a pulse duration $\tau = 3.5$ fs and at a delay $\Delta t = 90$ ps and using either 18 100-ms data acquisitions (corresponding to 100 shots per acquisition at 1 kHz) or 15 shorter acquisitions with a duration ranging between 1 ms and 10 ms.

It should be noted that the electron charge in figure 3.12(f) has been evaluated using the energy spectrum obtained from a 2D PIC simulation in the long gradient regime (combined with the spectral response of the Lanex screen) that will be shown later (see figure 3.21(c)). The values given correspond to an electron energy of $\approx$ 850 keV (i.e. the absolute value of the charge would be correct if all detected electrons had an energy of 850 keV). This results in high uncertainties because the experimental energy spectra may be different from the one originating from the 2D PIC simulation and because they may significantly vary depending on the experimental parameters. For instance, it may seem like the absolute charge in the short gradient regime is highest for 24-fs pulses. However, this might not be the case since we can reasonably expect higher electron energies from lower pulse durations (due to the increase in intensity) which would deposit less energy in the detector and result in an underestimation of the charge. Similarly, we cannot assert with certainty from figure 3.12(f) that the charge in the long gradient regime is significantly higher than the charge in the short gradient regime, because the corresponding energy spectra could considerably differ.

Experiments have also been carried out with intensities reduced to 11% of their original values, ranging from $2.5 \times 10^{17}\,\mathrm{W/cm^2}$ ($a_0 \simeq 0.3$) for 24 fs pulses to $1.8 \times 10^{18}\,\mathrm{W/cm^2}$ ($a_0 \simeq 0.9$) for 3.5 fs pulses. This drop in intensity has been obtained by aperturing the main laser beam. The experimental results in this case are shown in figure 3.15. It appears that, for a given pulse duration, the signal at

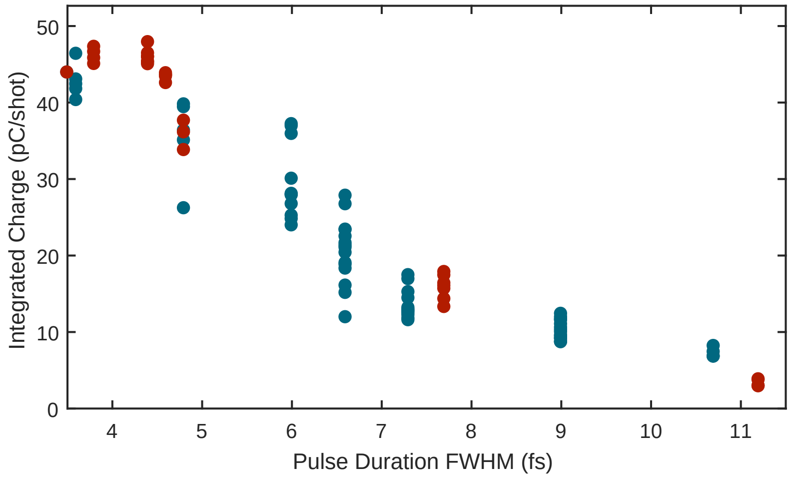

Figure 3.14: Total detected charge as a function of pulse duration for a delay $\Delta t = 90$ ps between the prepulse and the main pulse. The pulse duration is tuned here by chirping positively (red points) or negatively (blue points) the 3.5-fs driving laser.

long gradient drops much faster than the signal at short gradient (coming from the push-pull mechanism) when the intensity is decreased.

3.2.3 High-harmonic generation

In a previous experimental campaign in Salle Noire with longer pulses and lower intensities (30 fs and $a_0 \approx 0.7$), it was observed that the harmonics were emitted for sharper density gradients than the electrons [59]. This is because Coherent Wake Emission (see section 1.4.3.1) is the dominant high-harmonic generation mechanism at this nonrelativistic intensity.

In the new experimental campaign presented here, the reduced pulse duration leads to relativistic field values ($a_0 > 1$) for which the Relativistic Oscillating Mirror (see section 1.4.3.2) mechanism is expected to become predominant, for gradients of the order of $L \sim \lambda/10$. A strong correlation between the harmonic and electron signal should be found in this case. This is indeed what is observed experimentally as can be seen in figure 3.16.

Another interesting result is that for extremely short pulse durations, the measured harmonic signal strongly depends on the laser CEP. Although the CEP was not fully stabilized during these experiments, data could be recorded over short sequences of shots lasting 30 ms (30 pulses per sequence) during which the CEP is approximately stable. Even though the CEP drift is random from one sequence to the next, it could be estimated for each data sequence, thus effectively making it possible to study the effect of CEP on high-harmonic generation. Figure 3.17 shows two extreme cases of measured harmonic signal. In the left image, the spectrum is strongly modulated, indicating that two similarly intense attosecond pulses are generated in this case. On the opposite, the spectrum becomes nearly continuous when the CEP is shifted by π, which corresponds to the emission of a single high-harmonic pulse. In this case, the reflected pulse duration is estimated from 2D PIC simulations to be on the order of 200 as. These results suggest that isolated attosecond pulses could be routinely generated at a kHz repetition rate with a

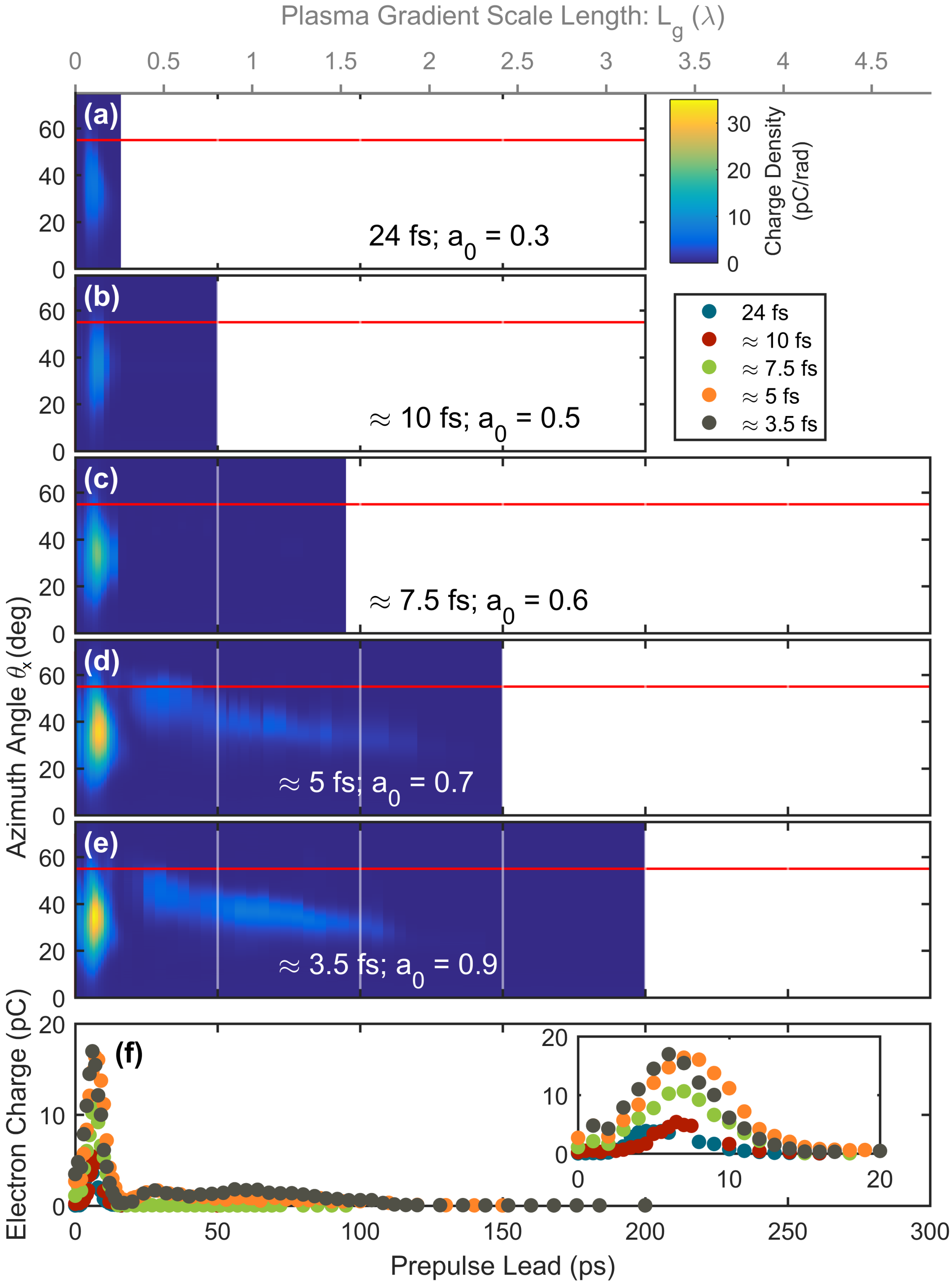

Figure 3.15: (a)-(e) Electron angular distribution integrated over the θ_y angle as a function of the delay between the prepulse and the main pulse for respective pulse durations of 24, 10, 7.5, 5 and 3.5 fs and reduced intensity. (f) Total ejected charge as a function of the delay between prepulse and main pulse.

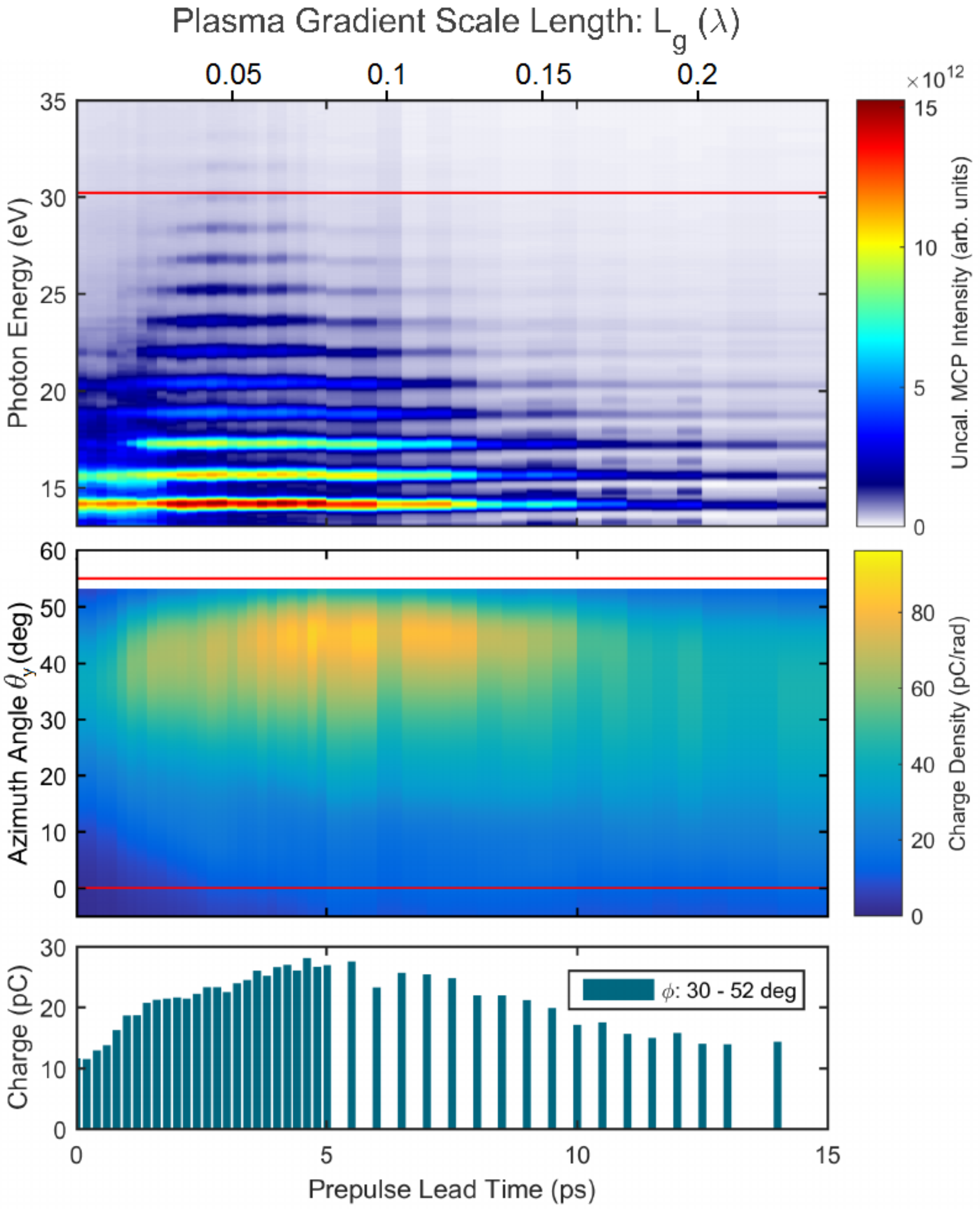

Figure 3.16: Top panel: measured harmonic signal as a function of the delay between the prepulse and the main pulse for a pulse duration of 9 fs and a peak normalized electric field of $a_0 \approx 1.8$. The detected photon energies ranging between ≈ 14 eV and ≈ 35 eV correspond to harmonic orders from ≈ 9 to ≈ 22. The red line shows the maximum plasma frequency for a bulk plasma density of $n_{e0} = 400\ n_c$. The fact that harmonics are detected above this frequency shows that the harmonics are not originating from the CWE mechanism. Middle panel: Simultaneously measured electron angular distribution integrated over the θ_y angle. The bottom red line shows the normal direction while the top red line shows the specular direction. Bottom panel: electron charge integrated between $\theta_x = 30^\circ$ and $\theta_x = 52^\circ$. Image taken from [34].

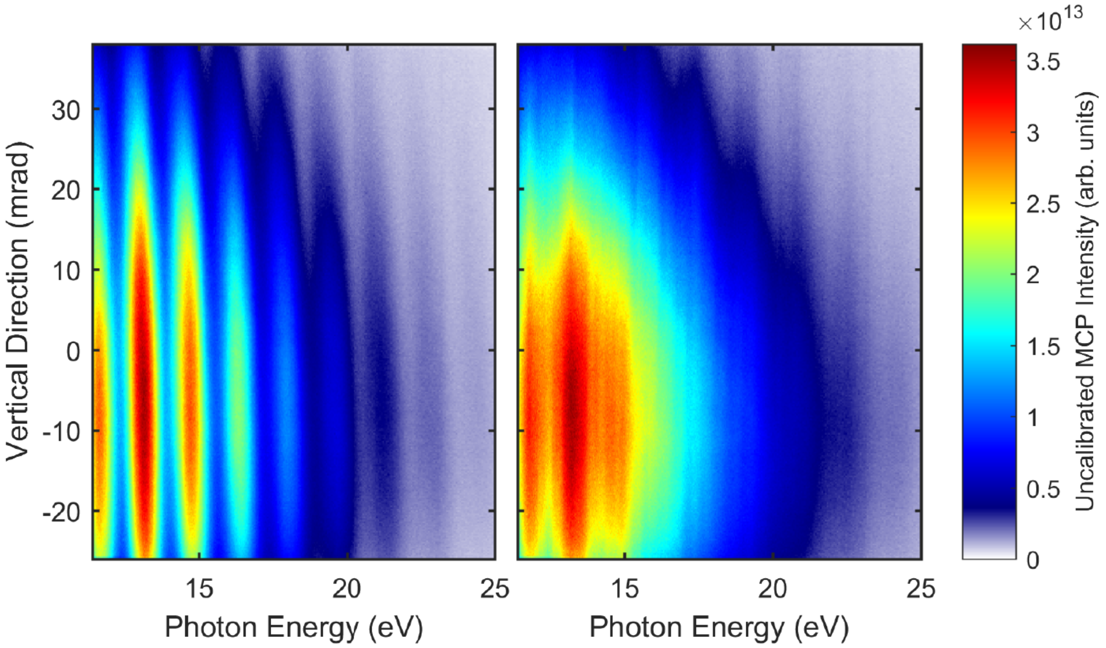

Figure 3.17: Two XUV spectrograms obtained with a 3.6-fs driving laser ($a_0 \approx 2.7$) and two different CEP values, presumably shifted by π.

precise control of the CEP. It can be pointed out that no such strong effect of the CEP has been observed on the electron signal.

Finally, it should be noted that, regardless of pulse duration, no high-harmonic signal is measured at long gradients ($L > \lambda$), even when a strong electron emission is observed. This is a confirmation that electron acceleration at long gradients originates from a different mechanism which is not associated to any high-harmonic generation.

More details regarding the high-harmonic emission during this experimental campaign can be found in [34].

3.2.4 Conclusion

At short gradients ($L \ll \lambda$), the experimental results shown in the previous sections are fully consistent with the theory presented in 1.4 and with previous experimental results [24]. In particular, at relativistic intensities, the simultaneous emission of electrons via the push-pull mechanism and high-harmonics through the ROM mechanism is detected.

At longer gradients, ($L > \lambda$), no harmonics are measured but a strong electron emission is observed when sub-10 fs pulses are used. Understanding the origin of this electron beam is the main objective of section 3.4.

3.3 PIC simulations of electron acceleration in the short gradient regime

Even though the physics at short gradients is well understood, it is still instructive to examine PIC simulations of the interaction. We present in this section two plasma mirror simulations with Salle Noire laser parameters ; one in two-dimensions and one in three-dimensions. On top of the additional physical information, in particular regarding the energy of the emitted electrons which was not measured experimentally, a direct comparison between 2D and 3D PIC simulations of the interaction is obtained.

In both simulations, a 3.5-fs laser pulse with $w_0 = 1.5\,\mu\mathrm{m}$ and $a_0 = 2.92$ impinges at $45°$ incidence on an overdense plasma with an exponential density profile and a gradient scale length $L = \lambda/7$. The maximum plasma density is 200 n_c in the 2D case and 100 n_c in the 3D case but this parameter does not play a significant role. In the 2D simulation, the Yee solver is used with a spatial resolution $\Delta x = \Delta z = \lambda/143$ and 36 macroelectrons per cell while in the 3D simulation the order-100 PSATD solver is used with $\Delta x = \Delta y = \Delta z = \lambda/36$ and 6 macroelectrons per cell. Note that the incidence angle in the simulations ($45°$) is different from the incidence angle in the experiments presented in the previous section ($55°$). This is because the 3D simulation was initially carried out to be compared with a simulation with radial polarization that is presented in appendix A.

Figure 3.18 shows snapshots from the two simulations. The electron density is only displayed in the 2D case because it was not included as a diagnostic in the 3D simulation. The reflected laser field shape is very similar in both cases, meaning that the oscillation of the plasma surface, visible in figure 3.18(b) is well reproduced in two-dimensions. We also observe in figure 3.18(c) that the ejected electron bunches have a rather complex structure, indicating that the push-pull mechanism leading to electron ejection occurs nontrivially in multiple dimensions.

The ejected electrons angular distribution in the 3D simulation is displayed in figure 3.19(b). It can be compared with the experimental distribution of figure 3.13(a), showing a good agreement. The electron beam might be slightly less diverging in the simulation which could be explained by the fact that space charge effect will tend to broaden the distribution as the electron beam propagates towards the detector in experiments. This effect is not included in the simulation since the electron beam propagation is only computed for the first $70\,\mu\mathrm{m}$ while the Lanex screen is located 10 cm away from the target in experiments.

On the other hand, unlike in experiments, a hole is observed in the specular direction in the 2D angular distribution shown in figure 3.19(a), with most electrons accelerated between the specular and grazing directions. As we have seen in section 1.5, this hole can be caused by the ponderomotive force during the interaction of the ejected electrons with the reflected laser pulse in vacuum. The reason this hole is not observed in either the experiments or the 3D simulation is not entirely clear. In previous experiments in Salle Noire with many cycle pulses, it was observed that the presence of this hole depended on the laser focus position [169], meaning that this parameter, whose influence has not been fully studied, might still be at play here. The presence of the hole in the specular direction in the 2D simulation suggests that the acceleration of electrons in vacuum is poorly modeled in two-dimensions, although it could also be partly due to differences in the initial electron injection into the reflected field between the 2D and 3D cases.

The electron energy spectra, visible in figures 3.13(c)-(d), have a similar shape in both cases. The electrons have a typical energy of ~ 1 MeV with a tail in the energy distribution that extends to 3.5 MeV in the 2D simulation and 5 MeV in the 3D simulation. The correlations between the electron energy and the emission angle θ_x, displayed in figures 3.13(e)-(f), reveal that the most energetic electrons are accelerated closer to the specular direction in 3D than in 2D. Finally, the total ejected charge is $\approx 12\mathrm{pC}/\,\mu\mathrm{m}$ in

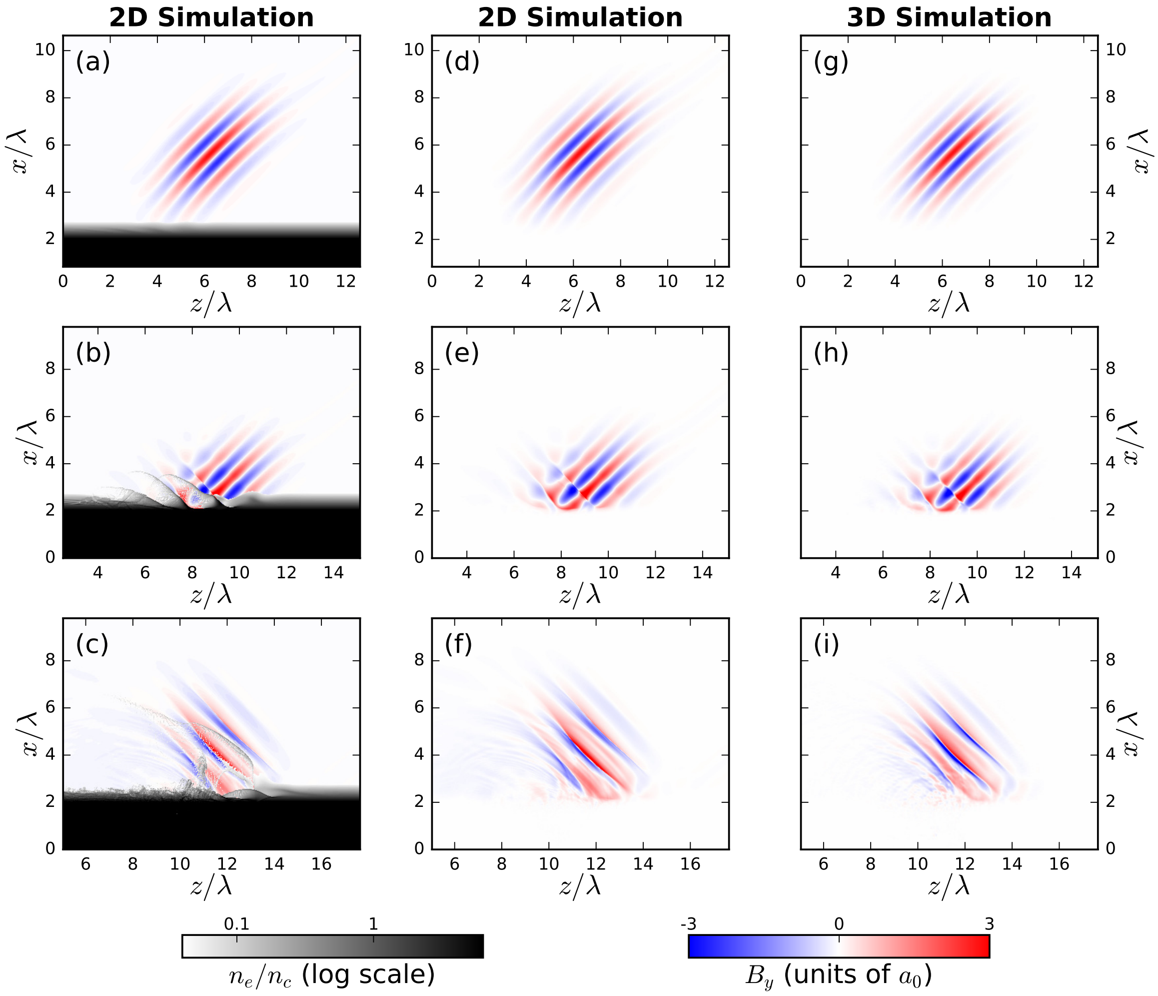

Figure 3.18: Snapshots from the 2D and 3D PIC simulations. In (a)-(c), both the electron density and the laser magnetic field are shown in the 2D case. In (d)-(i), only the laser magnetic field is shown in the 2D case (d)-(f) and in the incidence plane of the 3D simulation (g)-(i). There is approximately 4 laser periods between each snapshot. Detailed simulation parameters are provided in appendix B.

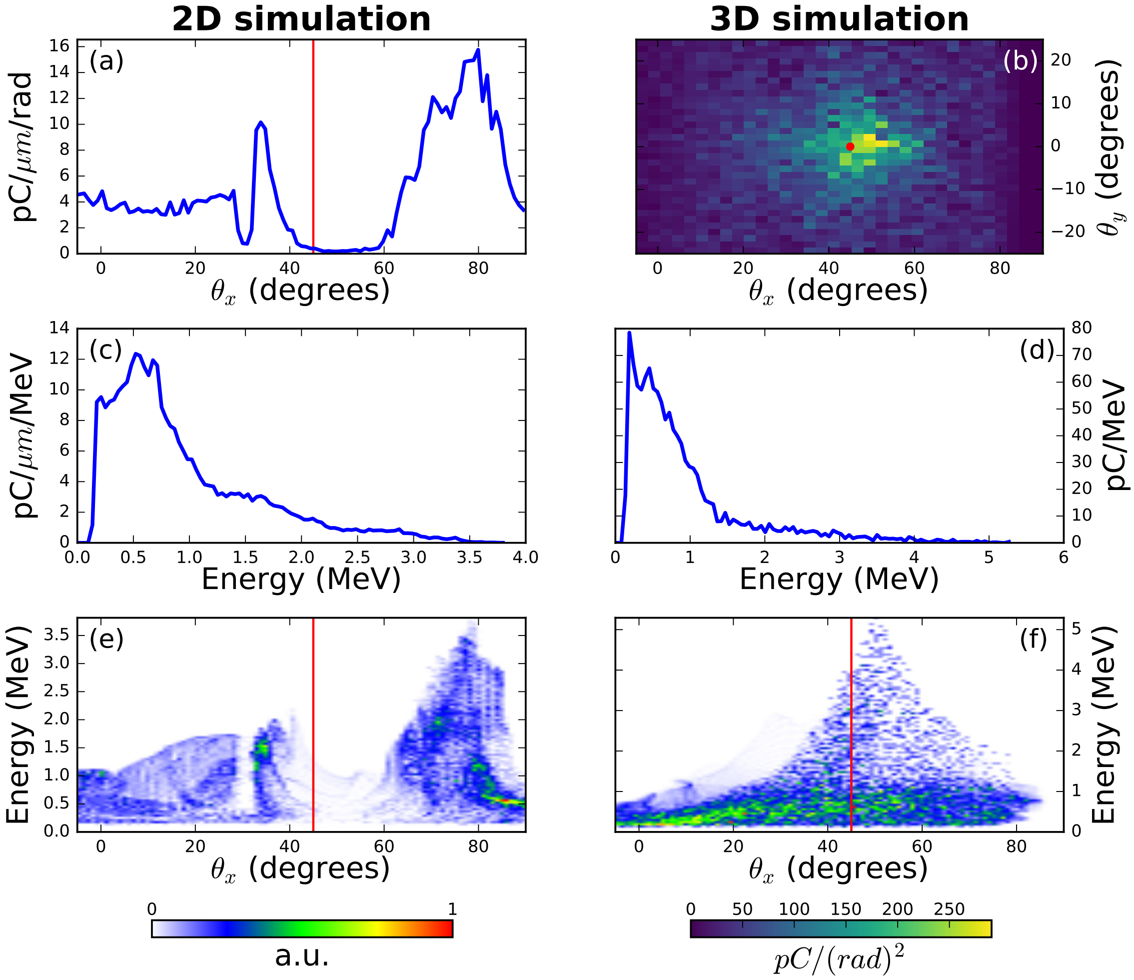

Figure 3.19: Ejected electron distributions. (a)-(b) Angular distribution respectively in 2 and 3 dimensions. (c)-(d) Energy spectrum respectively in 2 and 3 dimensions. (e)-(f) Correlation between energy and θ_x angle with respect to normal direction in the incident plane respectively in 2 and 3 dimensions. Only the electrons with an energy higher than 150 keV are displayed. The red lines and dot mark the specular direction. Detailed simulation parameters are provided in appendix B.

2D and ≈ 63 pC in 3D. These numbers are in good agreement with the estimated experimental ejected charge.

The main findings from these simulations are that:

- ≈ 1 MeV electrons can be expected from the experiments performed with few-cycle pulses in Salle Noire.
- 2D PIC simulations of relativistic plasma mirror interaction correctly reproduce the main qualitative trends regarding the oscillation of the plasma surface and the energy of the emitted electrons, but cannot provide accurate electron distributions.

3.4 Laser wakefield acceleration at long gradients

We present in this section PIC simulations aimed at understanding the origin of the electrons detected at long gradients with few-cycle pulses in experiments. We find that the electrons are accelerated by a laser wakefield formed in the near-critical density part of the preplasma. We then determine the conditions under which this mechanism occurs as well as the effect of the different experimental parameters.

3.4.1 Simulation parameters

Several 2D PIC simulations of the interaction have been performed using the code WARP. We took great care in providing a realistic description of the plasma density gradient. First, field ionization is taken into account in the simulations. Initially, the SiO_2 plasma is partially ionized up to Si^{4+} and O^{2+}. These ionization states are estimated from the prepulse peak intensity ($\sim 10^{15}\,\mathrm{W/cm^2}$) and the intensity thresholds for barrier-suppression ionization in silicon and oxygen. It not entirely clear whether these values are accurate but we have checked that our results remain valid when the initial ionization states are either lowered or raised up to Si^{4+} and O^{6+} (which correspond to the barrier-suppresion ionization states induced by a $10^{17}\,\mathrm{W/cm^2}$ beam). Then, further ionization (either tunnel or barrier-suppression) can be induced by the main pulse in the course of the simulations. Secondly, the initial plasma density profile is obtained from the ESTHER hydrodynamic 1D simulation presented in section 3.1.3. We have indeed seen that the preplasma densities deviate from an exponential at long gradients, and we therefore use the density profiles shown in figure 3.5(b) as inputs for the PIC simulations.

The numerical parameters are the following: spatial steps $\Delta x = \Delta z = \lambda/71$ where λ = 800 nm, 4 particles per cell per species (electrons, Si^{4+} ions and O^{2+} ions) initially. After further ionization by the main pulse, the number of electron per cell ranges from 4 to 60, depending on the final degree of ionization. We use the same laser parameters as in the experiments: $z_R = 8.84\,\mu\mathrm{m}$ (corresponding to $w_0 = 1.5\,\mu\mathrm{m}$), τ ranging between 3.5 fs and 24 fs and a_0 accordingly ranging between 2.57 (3.5-fs pulses) and 0.98 (24-fs pulses). The laser focus point is located at the position of the initial solid-vacuum interface. The laser is thus reflected slightly before focus because of the plasma expansion. Finally, a moving window is started after the interaction in order to follow the accelerated electrons up to tens of microns away from the plasma. We consider that an electron is ejected if it is located more than $8\,\mu\mathrm{m}$ away from the plasma surface with an energy exceeding 150 keV.

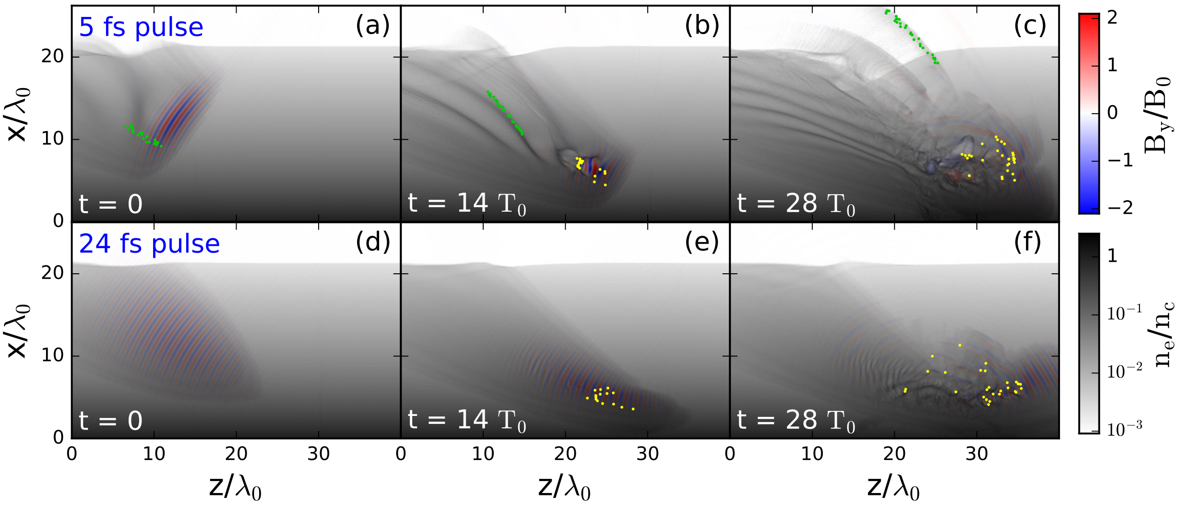

Figure 3.20: Laser magnetic field and electron density from PIC simulations with a large plasma scale length (Δt = 80 ps) and a pulse duration of (a)-(c) 5 fs or (d)-(f) 24 fs. The green and yellow dots show a sample of ejected electrons. T_0 is the laser optical oscillation period. Detailed simulation parameters are provided in appendix B.

3.4.2 Identification of the acceleration mechanism

Snapshots from two different PIC simulations are shown in figure 3.20. Both simulations use the plasma density profile obtained with a delay Δt = 80 ps (i.e. the red curve in figure 3.5(b)), a value for which the electron beam is detected in the experiments. The pulse duration is either 5 fs or 24 fs, resulting in peak intensities of $10^{19}\,\mathrm{W/cm^2}$ ($a_0 = 2.15$) and $2.1\times10^{18}\,\mathrm{W/cm^2}$ ($a_0 = 0.98$) respectively.

The first striking feature is the formation of high amplitude plasma waves in the wake of the 5-fs pulse. Their wavefront is bent by the density gradient, as will be explained in section 3.4.4. Even though these wakefields appear in the whole region where the 5-fs pulse propagates, inside which the density ranges from n_c/100 to $n_\mathrm{c}\cos^2\theta_i \sim 0.3n_\mathrm{c}$, they are completely absent in the 24-fs pulse simulation. This can be easily explained by the fact that wakefield excitation is optimal at the resonance condition, i.e. when the pulse duration is on the order of half the plasma wavelength: $\tau \simeq \lambda_p/2c$. As we have seen in the first chapter, this gives a resonant density of $\approx n_c/12.5$ for 5-fs pulses, versus $\approx n_c/300$ for 24-fs pulses, explaining why large wakefields appear for the few-cycle pulse only. More details will be given in the next section.

Some electrons, represented in green in figure 3.20, are trapped and accelerated by the plasma waves' strong electric fields, that reach up to 1 TV/m. The angular and energy distribution of these LWFA electrons is shown in the green curves of figure 3.21(a) and figure 3.21(c) respectively. Their energy spectrum extends to $\approx$ 2.5 MeV and their total ejected charge is $\approx$ 7 pC/$\mathrm{\mu m}$. These electrons are emitted in the same direction as the electrons detected at long delays in experiments (see the red curve in Fig. 3.21(a)). Moreover, as in experiments, these electrons only appear for few-cycle pulses. We therefore attribute the electron beam detected at long delays in experiments to Laser Wakefield Acceleration (LWFA).

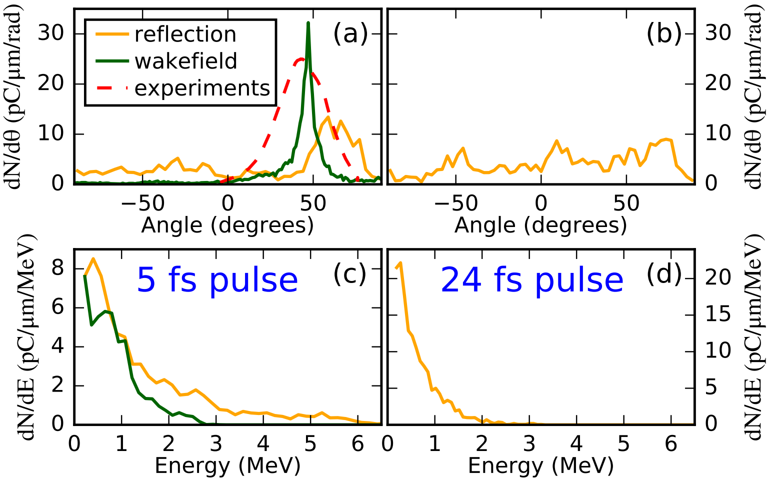

Figure 3.21: (a),(b) Angular and (c),(d) energy distribution of the two families of electrons that are ejected in the (a),(c) 5 fs and (b),(d) 24 fs simulation. The distributions are obtained at the end of the simulation, long after the interaction. The red dashed curve in (a) shows for comparison the experimental angular distribution integrated along the θ_y angle obtained with a 5 fs pulse and an 80 ps prepulse lead, in arbitrary units. Note that the green spectrum in (c) has been used along with the spectral response of the Lanex screen to estimate the absolute charge in experiments. Detailed simulation parameters are provided in appendix B.

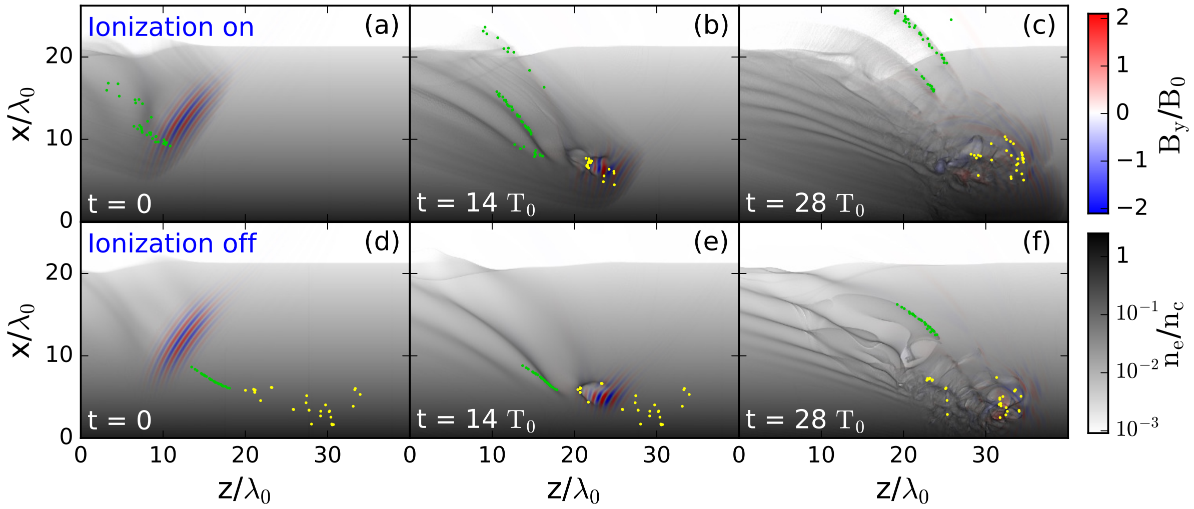

Figure 3.22: Laser magnetic field and electron density from PIC simulations with a large plasma scale length (Δt = 80 ps) and a pulse duration of 5 fs with field ionization turned on (a)-(c) or off (d)-(f). The green and yellow dots show a sample of ejected electrons. Note that the simulation in the top of this image is the same as in figure 3.20, the only difference being that electrons accelerated by different cycles of the wakefield are shown. Detailed simulation parameters are provided in appendix B.

We notice that the angular distribution of the LWFA electrons is significantly narrower in the simulation than in experiments. Once again, this is likely due to space charge effects during the propagation of the electron beam to the detector, which we expect to be important for a sub-MeV beam with tens of pC charge. The electrons are indeed only propagated for tens of microns in the simulation while the Lanex screen is located ≈ 10 cm away from the target in experiments.

In the simulations, the LWFA electrons come from the L-shell of silicon. They have high binding energies (from $\approx$ 150 eV to $\approx$ 500 eV) and can therefore only be ionized by the huge electric fields inside the main laser pulse. The fact that only electrons ionized in the center of the pulse are accelerated suggests that ionization injection, a well-known mechanism in underdense plasmas (see section 1.3.3.1), is responsible for trapping the electrons into the wakefields.

This can be confirmed by rerunning the simulation with field ionization turned off. This is shown in figure 3.22. In the simulation with ionization turned on, electrons are accelerated by 3 consecutive cycles of the wakefield, with most electrons accelerated by the second one (the green electrons displayed in figure 3.20). On the other hand, when field ionization is turned off electrons are only accelerated by the third cycle of the wakefield. In this case, the electrons appear to be self-injected by the wavebreaking of the plasma oscillations. This confirms that most electrons (at least the electrons in the first two cycles) are injected by ionization in the initial simulation. More generally, we observe when varying the interaction parameters that electrons are steadily injected when ionization is turned on whereas the injected charge is unstable with ionization turned off (even though in the best cases it is comparable to the injected charge with ionization turned on). This shows that taking field ionization into account is necessary to properly describe the injection of electrons into the plasma waves in this regime.

Physically, electrons injected by ionization have two advantages in comparison with pre-ionized electrons, which makes them more likely to be trapped by the plasma wave:

- They can be generated at the optimal initial phase of the wakefield. This is similar to the usual case of ionization injection in gas targets.
- They can receive an initial momentum kick in the transverse direction if they are not generated exactly at a maximum of the electric field (this can be seen directly in the one-dimensional case from the conservation of canonical momentum). This effect is not significant in gas targets because electrons are accelerated in this case in the direction of propagation of the laser, implying that electron injection is not aided by a kick in the transverse direction. However, in the LWFA regime identified here, this effect might play a more important role as the electrons are accelerated in the transverse direction.

We may also notice that the laser pulse is reflected deeper into the plasma when ionization is turned off. This shows that the ionization induced by a pulse propagating in a preplasma can affect the position at which it is reflected. As discussed in section 3.1.2, this effect can increase the uncertainty in the interferometric measurement of preplasma expansion.

Another family of electrons, shown in yellow in figure 3.20 and labelled “reflection electrons”, is ejected from the plasma in the simulations. These electrons are accelerated at the reflection point of the laser, where the density is $n_c \cos^2\theta_i$. Their angular and energy distributions are displayed in the yellow curves of figure 3.21. This family of electrons, which appears for both 5-fs and 24-fs pulses and has a very large angular divergence spreading across all directions, is not detected in experiments. The presence of these electrons constitutes the principal discrepancy between simulations and experiments. It will be further discussed in section 3.4.6. Still, the simulations explain the main experimental observations: a well-defined beam of LWFA electrons that appears only for extremely short pulse durations.

Finally, we show for completeness in figure 3.23 the angle-energy distribution of the electrons ejected in the two simulations presented here. The LWFA electrons are isolated in figure 3.23(c). We note in particular that, in the 5-fs simulation, the "yellow electrons" tend to be more energetic than the wakefield accelerated electrons. We also observe an angle-energy correlation in the LWFA electrons distribution, with faster electrons located closer to the specular direction.

3.4.3 Conditions for triggering the mechanism

The aim of this section is to clarify the conditions under which the identified LWFA mechanism occurs. We have previously made the following experimental observations:

- For a constant pulse energy, the electron beam disappears when the pulse duration is increased over 10 fs.
- For a constant few-cycle pulse duration, the electron beam disappears when the intensity is decreased to subrelativistic values ($a_0 < 1$).

The first observation is also found in simulations. Figure 3.24 shows snapshots from PIC simulations performed with all the pulse durations studied experimentally. The transition from a regime without plasma wave formation ($\tau = 24$ fs) to a regime with strong plasma wave formation ($\tau < 10$ fs) is clearly observed. This transition is also visible when plotting the laser wakefield accelerated charge as a function of pulse duration, as shown in figure 3.25.

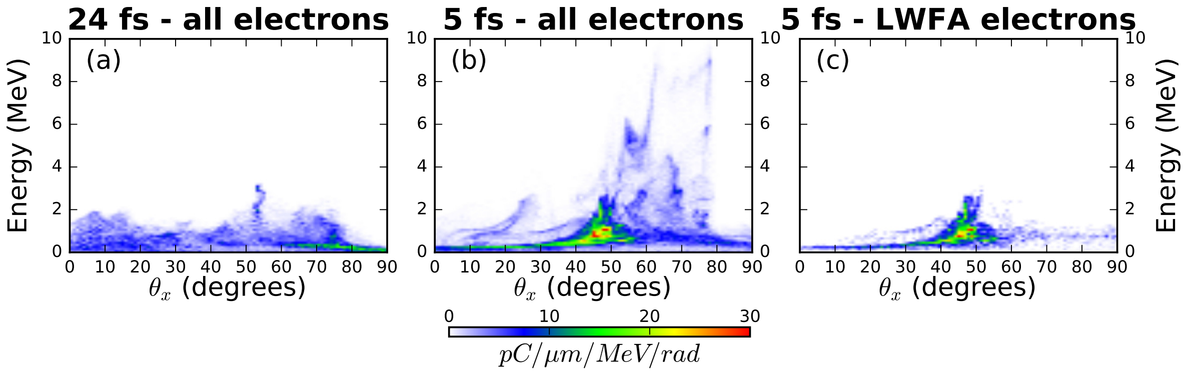

Figure 3.23: Angle-energy distribution of the wakefield accelerated electrons in the 24-fs simulation (a) and the 5-fs simulation (b). The LWFA electrons are isolated in (c). Detailed simulation parameters are provided in appendix B.

At this point, it cannot be concluded that there is an effect of pulse duration. Indeed, in all the experimental and numerical results presented until now, the LWFA electron beam is observed everytime a relativistic driver is used, which in the case of the Salle Noire laser corresponds to sub-10 fs durations. It could therefore be argued that the mechanism might be triggered by a 24-fs pulse with an increased intensity. To explore this possibility, we have carried out simulations with interchanged intensities, i.e. the 5-fs laser pulse has a peak intensity of $2.1\times10^{18}\,\mathrm{W/cm^2}$ ($a_0 = 0.98$) and the 24-fs laser pulse has a peak intensity of $1\times10^{19}\,\mathrm{W/cm^2}$ ($a_0 = 2.15$). Snapshots from these simulations are shown in figure 3.26.

Interestingly, the main results stay the same: a very small amount (≈ 300 fC/μm) of electrons are laser wakefield accelerated in the 5-fs simulation while no plasma wave formation is observed in the 24-fs simulation[4]. This clearly confirms that there is an effect of pulse duration and that the emergence of the electron beam cannot simply be attributed to the increase in intensity when reducing the pulse duration. Note that the 5-fs simulation shown here is consistent with results from experiments at reduced intensity presented in figure 3.15, which were obtained using similar laser parameters. We indeed see in both cases a very strong drop of the wakefield accelerated electron charge when reducing the intensity.

As stated in the previous section, the effect of pulse duration is due to the resonance condition. In layman's terms, the 24-fs pulse is too long to excite a plasma wave in the near-critical density plasma considered here. More quantitatively, we can estimate the amplitude of the wakefields generated in our experiments from the 1D nonlinear theory of wakefield generation presented in section 1.3.2. This can be done in two different ways.

First, we can consider a given plasma density n_e and calculate the amplitude of the plasma waves that a Salle Noire pulse would generate in a plasma with constant density n_e as a function of pulse duration. The result is shown in the blue curve of figure 3.27 for $n_e = n_c/50$, which is a typical density for which wakefields are formed in the simulations. Unsurprisingly, only ultrashort laser pulses ($\tau < 10$ fs) are able to excite high amplitude plasma waves. In particular, the wakefield potential amplitude is $\approx$ 100 times higher with 5-fs pulses than with 24-fs pulses. Note that the laser energy is kept constant in these calculations; the laser electric field amplitude thus scales as $a_0 \propto 1/\sqrt{\tau}$. The red markers in

---

[4] There is however in this case a significant amount of ejected electrons, but none of them are accelerated from a wakefield.

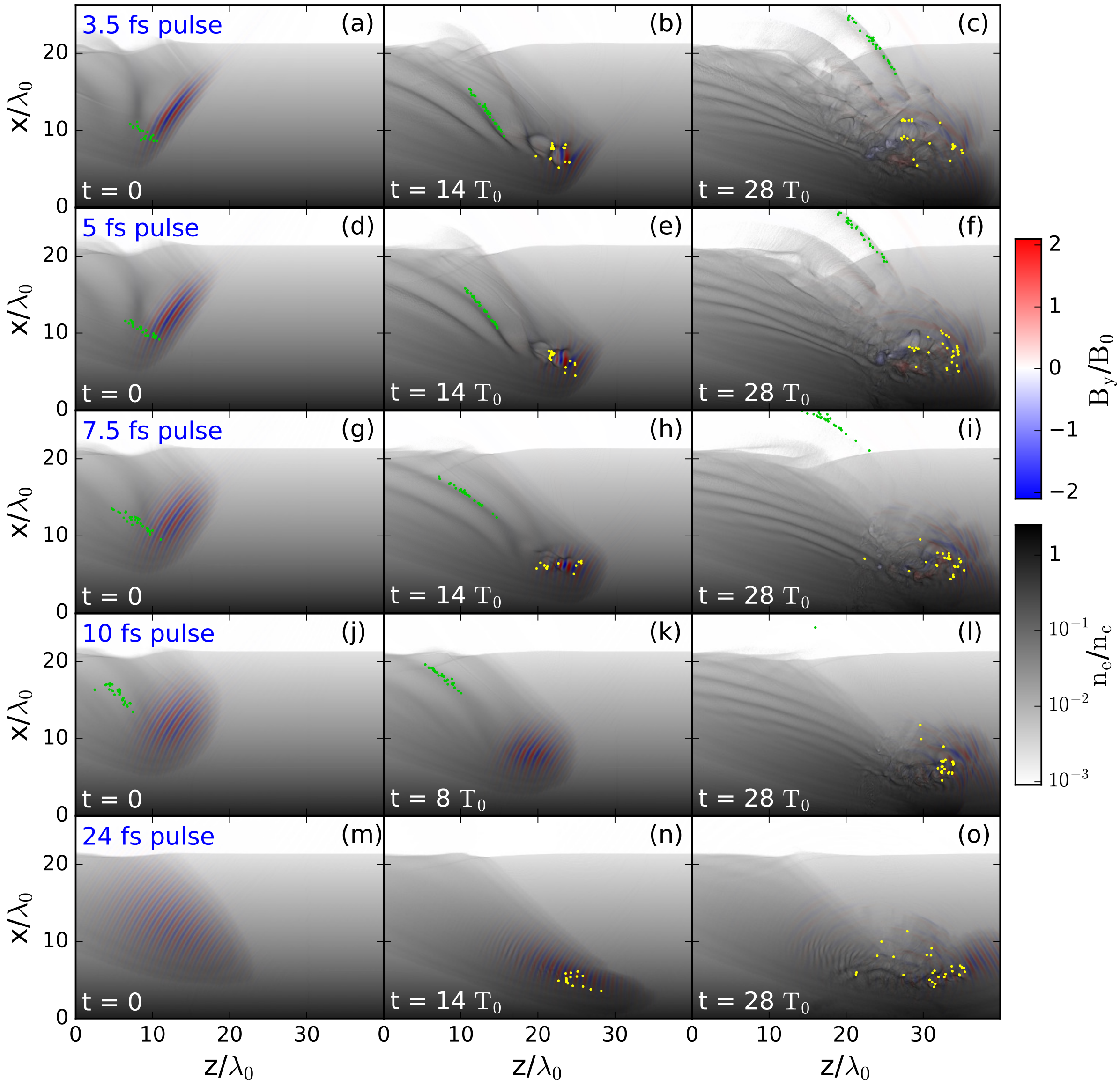

Figure 3.24: Laser magnetic field and electron density from PIC simulations with a large plasma scale length ($\Delta t = 80$ ps) and pulse durations of (a)-(c) 3.5 fs, (d)-(f) 5 fs, (g)-(i) 7.5 fs, (j)-(l) 10 fs or (m)-(o) 24 fs, respectively corresponding to normalized field amplitudes a_0 of 2.57, 2.15, 1.76, 1.52 and 0.98. The green and yellow dots show a sample of ejected electrons that are originating from silicon ions. Detailed simulation parameters are provided in appendix B.

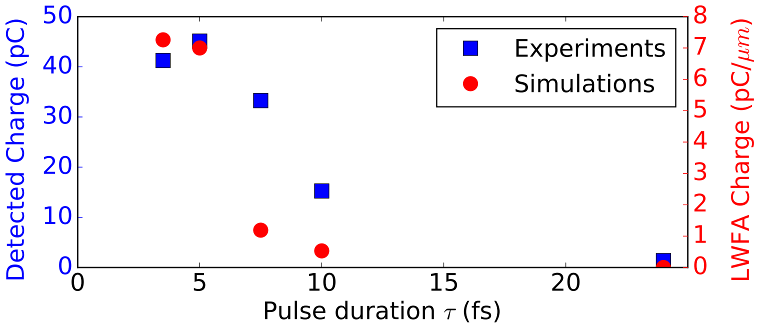

Figure 3.25: Detected electron charge in experiments and laser wakefield accelerated charge in simulations as a function of pulse duration. All points are obtained for a delay Δt = 80 ps between the prepulse and the main pulse. Detailed simulation parameters are provided in appendix B.

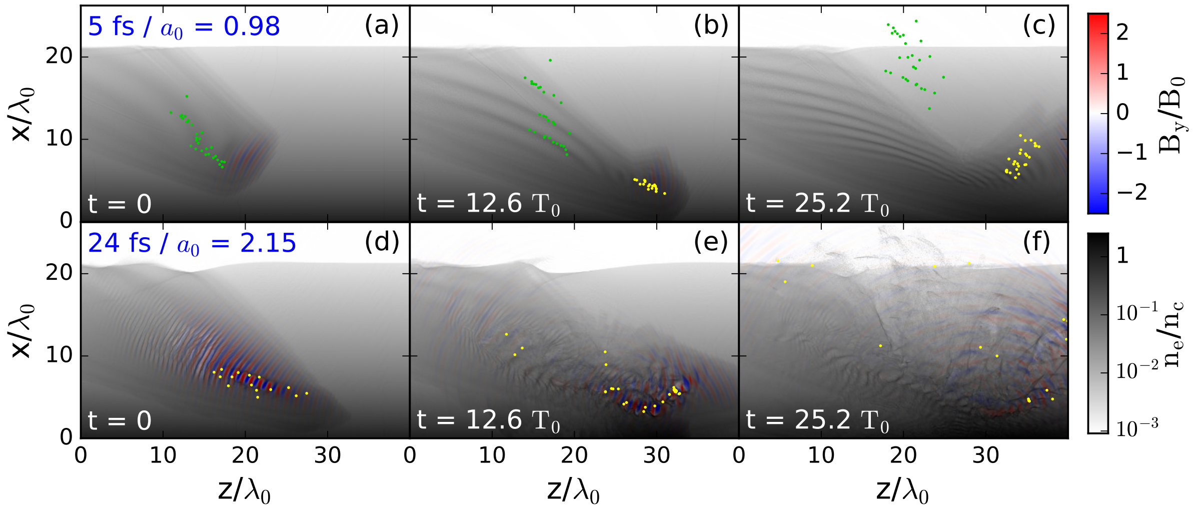

Figure 3.26: Laser magnetic field and electron density from PIC simulations with a large plasma scale length ($\Delta t = 80$ ps), a pulse duration of (a)-(c) 5 fs or (d)-(f) 24 fs and a normalized field amplitude a_0 of (a)-(c) 0.98 or (d)-(f) 2.15. The green and yellow dots show a sample of ejected electrons that are originating from silicon ions. Detailed simulation parameters are provided in appendix B.

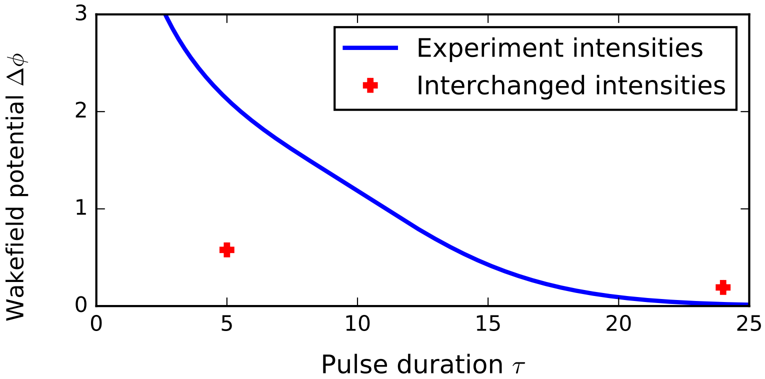

Figure 3.27: Normalized peak-to-peak amplitude $\Delta\phi$ of the electric potential of a laser-driven wakefield in an n_c/50 density plasma as a function of the FWHM pulse duration τ obtained using the 1D nonlinear theory of wakefield generation. The blue curve corresponds to laser parameters that are accessible in experiments (in particular $a_0^2\tau$ is kept constant along the curve). The red markers correspond to the laser parameters used in the simulations with interchanged intensities presented in figure 3.26.

figure 3.27 show the wakefield amplitudes obtained with the laser parameters used in the simulations with interchanged intensities presented in figure 3.26 (5 fs, $a_0 = 0.98$ and 24 fs, $a_0 = 2.15$). Although the laser pulse energy is 25 times higher in the 24-fs pulse, the generated wakefield amplitude is 3 times higher with the 5-fs pulse. This result highlights the necessity of using few-cycle pulses in order to generate plasma waves in near-critical density plasmas.

Alternatively, we can consider given laser parameters and compute the amplitude of the plasma wave they would generate in a homogeneous plasma as a function of the density. This is done in figure 3.28 for laser parameters corresponding to the 5-fs and 24-fs Salle Noire pulses (blue and green curves) as well as the laser parameters used in the simulations with interchanged intensities (orange and red curves). Of course, the same conclusions are drawn: only ultrashort pulse durations lead to substantial plasma waves in the density region of interest. This representation offers the advantage of quantitatively comparing the relative effects of pulse intensity and pulse duration. If both effects are important, the effect of pulse duration appears to be even more critical.

In conclusion, the conditions for which the identified LWFA mechanism is triggered are the following:

- The gradient scale length must be long enough ($L > \lambda$) so that the laser pulse can propagate in the near-critical density part of the preplasma and excite the wakefield.

- Few-cycle pulses (< 10 fs for $\lambda = 800$ nm) are required to efficiently drive plasma waves at such high densities, in accordance with the resonance condition.

- Relativistic intensities ($a_0 > 1$) are required so that the wakefields are strong enough to trap and accelerate a significant amount of electrons to high energies.

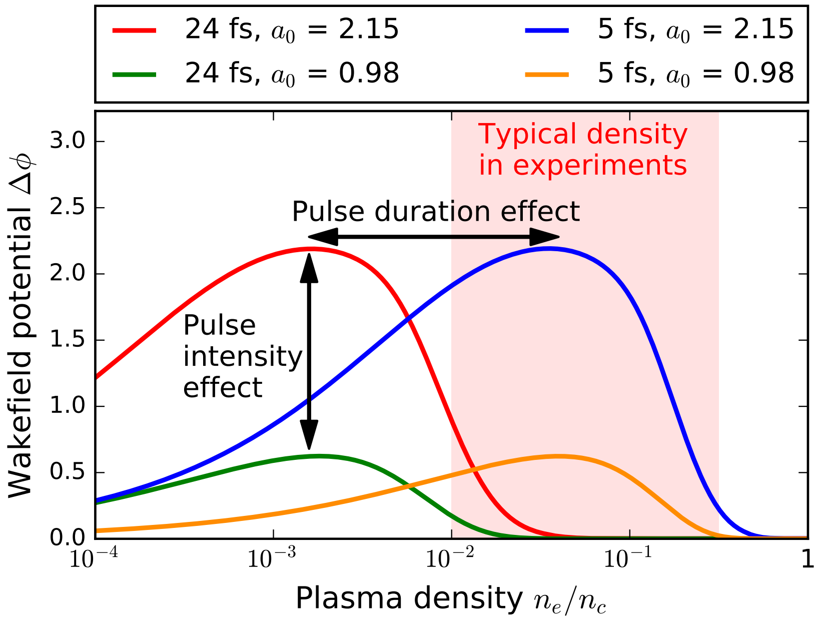

Figure 3.28: Normalized peak-to-peak amplitude $\Delta\phi$ of the electric potential of a laser driven wakefield in a homogeneous plasma as a function of plasma density obtained using the 1D nonlinear theory of wakefield generation for a 24-fs pulse with $a_0 = 0.98$ (green curve), a 24-fs pulse with $a_0 = 2.15$ (red curve), a 5-fs pulse with $a_0 = 0.98$ (orange curve) and a 5-fs pulse with $a_0 = 2.15$ (blue curve). The reddened part correspond to typical densities for which wakefields are generated in the simulations.

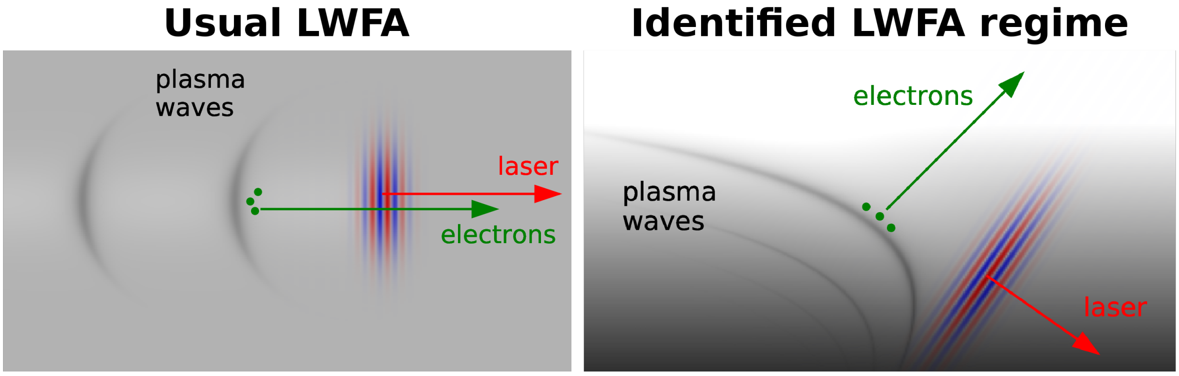

Figure 3.29: Schematic illustration of the standard LWFA regime (left) and the identified LWFA regime (right). The main difference is that, due to the plasma waves wavefront rotation induced by the density gradient, the electrons are not accelerated in the same direction as the driving laser pulse in the identified regime.

3.4.4 Rotation of the wakefield

A unique feature of the identified acceleration regime is that the electrons are not emitted in the same direction as the driving laser pulse, as is usually the case with LWFA. This effect is illustrated schematically in figure 3.29. It is due to the wakefield's wavefront rotation induced by the density gradient. To explain this rotation, we can use a similar approach as that developed in the case of injection in density gradients in conventional LWFA (see 1.3.3.2). The only difference, which does not change the main reasoning, is that in our case the density gradient is not solely in the direction of propagation of the pulse, but also partly transverse.

As we have seen in chapter 1, in the linear regime the laser triggers a sinusoidal response from a homogeneous density plasma. Far behind the laser pulse, the normalized potential ϕ associated to the plasma wave is in this case of the form $\phi_0 \sin(k_p(z - v_g t))$, where we use the same notations as in chapter 1 (in particular $k_p = \omega_p / v_g$, where ω_p is the plasma frequency and v_g is the group velocity of the laser). This can be rewritten as $\phi = \phi_0 \sin(\omega_p(t_0(z) - t))$, where $t_0(z) = z/v_g$ is the time at which the temporal center of the laser pulse excites the plasma wave.

As a first approximation, we can assume that in the presence of a density gradient, the potential is of the form:

$$\phi(\boldsymbol{r}, t) = \phi_0(\boldsymbol{r}) \sin(\omega_p(\boldsymbol{r})(t_0(\boldsymbol{r}) - t)) \tag{3.22}$$

This approximation is reasonable if the plasma density varies smoothly enough: $k_p L \gg 1$. In our case, t_0 can be expressed as a function of the laser incidence angle θ_i:

$$t_0 = \frac{z \sin\theta_i - x \cos\theta_i}{c} \tag{3.23}$$

Additionally, we assume that the plasma density (and thus the plasma frequency ω_p) only depends on x. Then, we can define the phase φ of the plasma wave as:

$$\varphi(x, z, t) = \omega_p(x) \left(\frac{z \sin\theta_i - x \cos\theta_i}{c} - t \right) \tag{3.24}$$

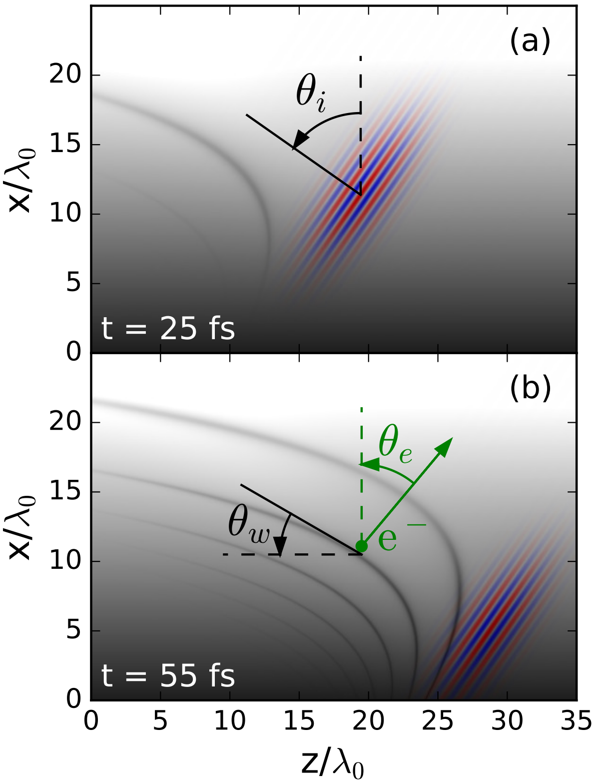

Figure 3.30: Wavefronts (darker lines) obtained using equation 3.24 during the propagation of a laser pulse (represented in blue and red) in a plasma with an exponential density profile ($L = 3\lambda$). Two consecutive wavefronts are separated by a phase of 2π. Panels (a) and (b) correspond to two different values of the time t.

Plasma wavefronts obtained using this equation in an exponential density gradient are shown in figure 3.30. It is a good time to recall that this expression has been obtained relying on multiple approximations (linear regime $a_0 \ll 1$, quasi-static approximation, long pulse durations $\tau \gg 2\pi/\omega$, strongly underdense plasma $\omega_p \ll \omega$, smooth gradient $k_pL \gg 1$), all of which are not valid in our experimental case. We cannot therefore reasonably expect the wavefronts obtained using equation 3.24 to perfectly match those found in the 2D PIC simulation. Still, the qualitative shape of the plasma waves is reproduced and we see in particular a similar rotation of the wavefronts. Physically, this rotation can be explained by the transverse density gradient seen by the laser, i.e. the fact that one side of the laser pulse excites a plasma wave with a higher frequency than the other. A given phase will therefore be reached quicker in the region of higher frequency, which results in rotated wavefronts[5].

We can also use this model to qualitatively explain the measured angular distribution. Let us consider an electron moving with an angle θ_e with respect to the x-axis at a position where the wavefront of the

---

[5] It is worth mentioning that an almost identical expression for the phase φ of the plasma wave has been previously obtained in the same manner in the context of the Coherent Wake Emission (CWE) mechanism of high-harmonic generation [29]. In this case, the plasma waves are generated by Brunel electrons returning to the plasma. Since these electrons are also propagating obliquely with respect to the density gradient, this leads to a similar rotation of the plasma wavefronts.

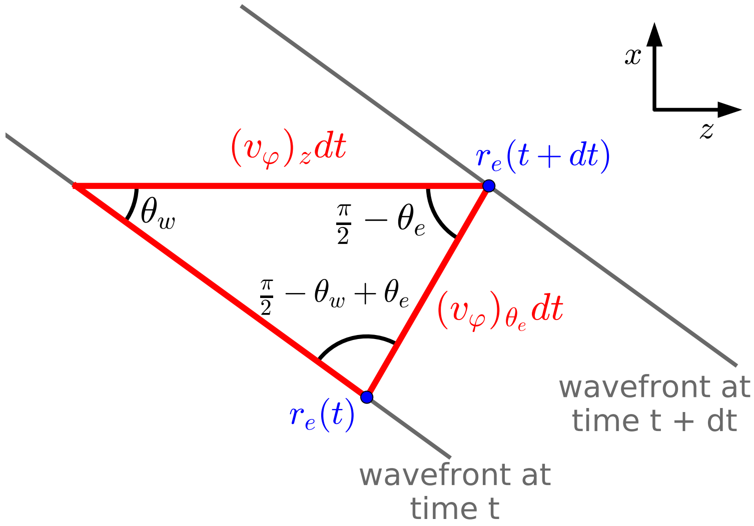

Figure 3.31: Geometric derivation of the plasma wave phase velocity in the direction of electron motion $(v_\varphi)_{\theta_e}$*. We consider an electron moving at* $(v_\varphi)_{\theta_e}$*, which therefore remains at a constant phase of the wakefield. The blue dots show the position* $\boldsymbol{r_e}$ *of the electron at times* t *and* $t+dt$*. The grey lines show, to first order, the wavefronts around the electron position at times* t *and* $t+dt$*. We use the law of sines on the red triangle, which reads* $(v_\varphi)_{\theta_e} dt \sin(\pi/2-\theta_w+\theta_e) = (v_\varphi)_z dt \sin(\theta_w)$*.*

plasma wave makes an angle θ_w with respect to the z-axis (see figure 3.30(b)). We first note that since the plasma frequency only depends on x, the phase velocity of the plasma waves in the z-direction is $(v_\varphi)_z = c/\sin\theta_i$. We can then, using the law of sines (see figure 3.31 for more details), calculate the phase velocity along the direction of electron motion:

$$(v_\varphi)_{\theta_e} = \frac{\sin\theta_w}{\cos(\theta_e-\theta_w)\sin\theta_i}c \tag{3.25}$$

If the electron is trapped in the wakefield, its velocity is mainly colinear with the electric field of the plasma waves, i.e. perpendicular to the wavefronts. In this case, we have $\theta_e \approx \theta_w$ and equation 3.25 is simplified to:

$$(v_\varphi)_{\theta_e} = \frac{\sin\theta_e}{\sin\theta_i}c \tag{3.26}$$

Trapping of electrons by the plasma wave is only possible if the phase velocity of the wakefield is lower than c, meaning in our case that electrons can only be emitted when $\theta_e < \theta_i$. Furthermore, electron acceleration to relativistic energies is efficient when the phase velocity is close to c. Equation (3.26) therefore indicates that the electrons should be emitted close to the specular direction with a slight shift towards the normal direction, in good agreement with experiments and simulations. Electrons directed closer to the grazing direction ($\theta_e > \theta_i$) cannot be trapped as the phase velocity of the plasma waves in their direction is greater than c while electrons emitted close to the normal direction cannot reach high energies as they would quickly dephase from the plasma waves. We can in particular expect an angle-energy colleration in the wakefield accelerated electrons, with the fastest electrons accelerated near the

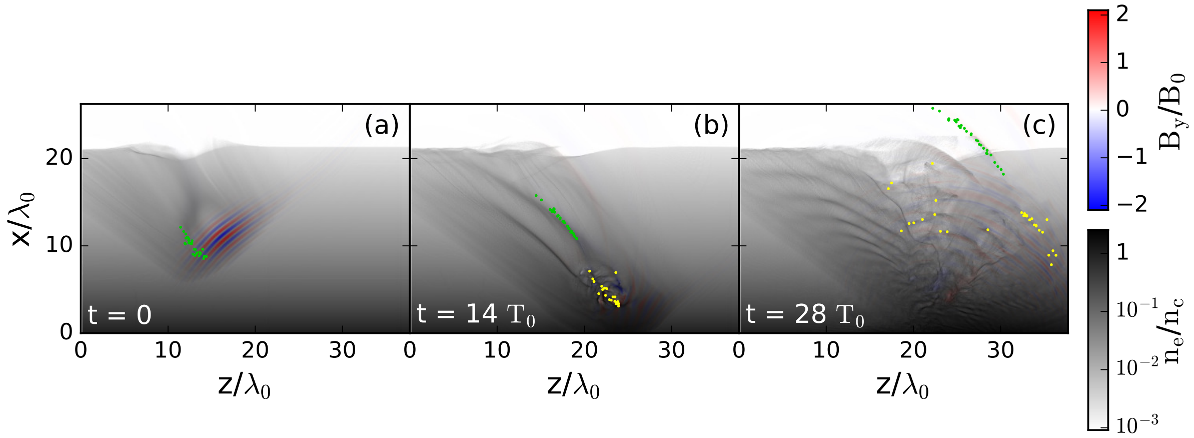

Figure 3.32: Laser magnetic field and electron density from a PIC simulation with a large plasma scale length ($\Delta t = 80$ ps), a pulse duration of 5 fs, a normalized field amplitude a_0 of 2.15 and an incidence angle θ_i of 40°. The green and yellow dots show a sample of ejected electrons that are originating from silicon ions. Detailed simulation parameters are provided in appendix B.

specular direction and the slowest electrons accelerated closer to the normal. Such a correlation is indeed observed in simulations, as can be seen in figure 3.23(c).

3.4.5 Dependence on the interaction parameters

We study in this section the effect of various interaction parameters on the identified LWFA mechanism.

3.4.5.1 Effect of the incidence angle

We first consider the influence of the incidence angle θ_i. According to the model of wakefield rotation developed in the previous section, the LWFA electrons are accelerated close to the specular direction, with a slight shift towards the normal direction. We thus expect that when varying the laser incidence angle, the ejected electron beam will follow the direction of the reflected laser pulse. To test this hypothesis, we have performed simulations with incidence angles of 40° and 70° (in addition to the previously shown simulation at 55° incidence). Snapshots from these simulations are displayed in figures 3.32 and 3.33. We notice that the main physical results are unchanged in these simulations and in particular electrons accelerated by a wakefield (green) and electrons accelerated at the reflection point of the laser (yellow) are still observed.

Figure 3.34 shows the angle-energy correlation of the ejected LWFA electrons in these simulations, while their angular distribution is plotted in the same axes in figure 3.35. The following observations can be made:

- The ejected electrons indeed tend to follow the specular direction. However, the angle of emission of the electron beam appears to "vary more slowly" than the laser incidence angle. This can be

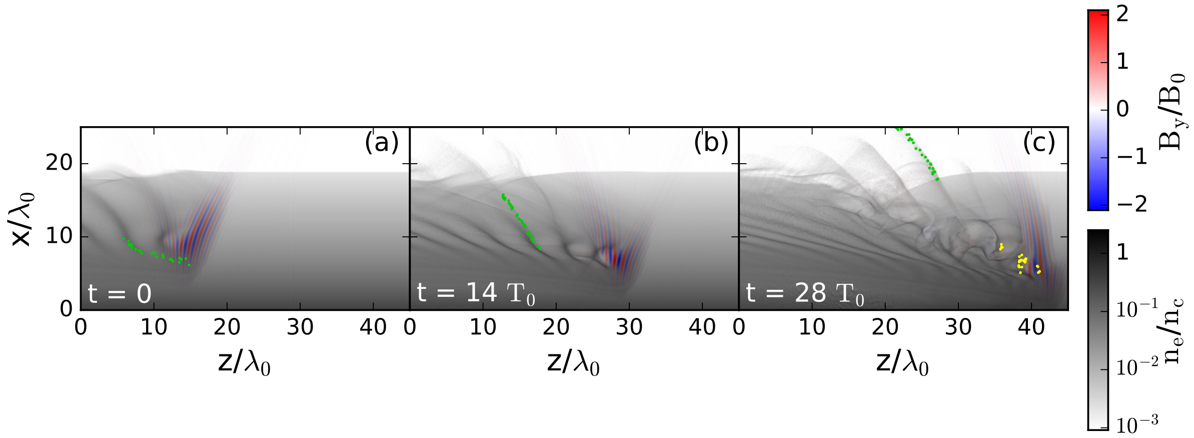

Figure 3.33: Laser magnetic field and electron density from a PIC simulation with a large plasma scale length ($\Delta t = 80$ ps), a pulse duration of 5 fs, a normalized field amplitude a_0 of 2.15 and an incidence angle θ_i of 70°. The green and yellow dots show a sample of ejected electrons that are originating from silicon ions. Detailed simulation parameters are provided in appendix B.

seen by the fact that some electrons are accelerated over the specular direction ($\theta_x > \theta_i$) in the 40° simulation, while electrons tend to be further away from the specular direction in the 70° simulation. Our prediction that the LWFA electrons are ejected close to the specular direction with a slight shift towards the normal direction therefore provides a reasonable trend but cannot be seen as a strict rule. This can be explained by the excessive simplicity of the wakefield rotation model as well as the fact that electrons might still be deflected after being accelerated by the plasma waves (this is particularly true in the 70° simulation) .

- The angle-energy correlation in the electron distribution, with the fastest electrons emitted closer to the specular direction, is still found at other incidence angles.

- The experimental incidence angle of 55° seems to be (roughly) close to optimal. The total LWFA charge is indeed the highest in this case (4.2 pC/μm for $\theta_i = 40°$, 7 pC/μm for $\theta_i = 55°$ and 2.6 pC/μm for $\theta_i = 70°$). Additionally, the highest energies are reached for $\theta_i = 55°$ and the angular distribution is significantly more peaked.

3.4.5.2 Effect of the density gradient

Generally, we find that the LWFA mechanism consistently occurs for long enough gradient scale lengths. For instance, very similar results as those presented in section 3.4.2 are found when an exponential density profile with a gradient scale length $L = 3\lambda$ is chosen. This confirms our previous experimental observation that the identified mechanism is not highly sensitive to the exact shape of the plasma density profile.

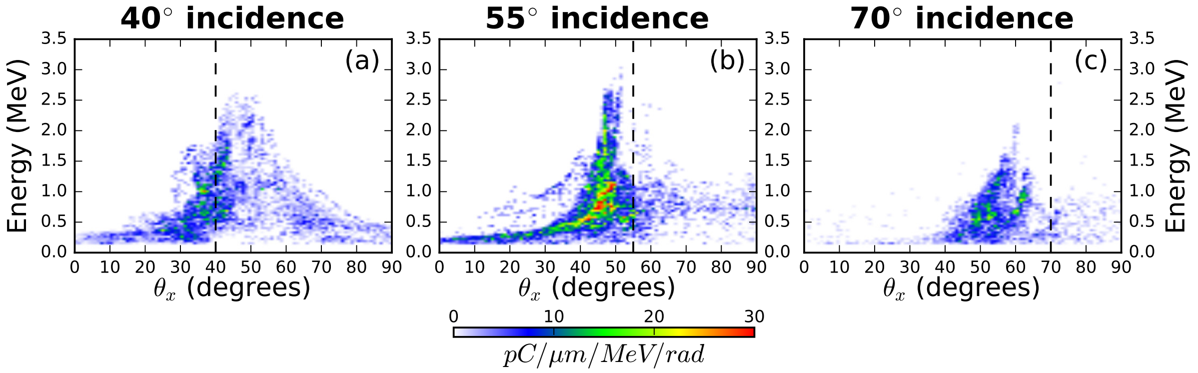

Figure 3.34: Angle-energy distribution of the wakefield accelerated electrons in the simulation with (a) 40° incidence, (b) 55° incidence and (c) 70° incidence. The dashed lines mark the specular direction. Detailed simulation parameters are provided in appendix B.

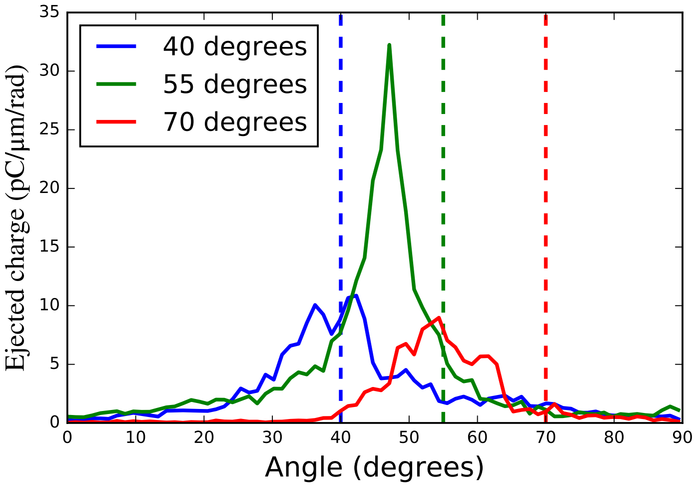

Figure 3.35: Angular distribution of the wakefield accelerated electrons in the simulation with 40° incidence (blue curve), 55° incidence (green curve) and 70° incidence (red curve). The dashed lines mark the specular direction. Detailed simulation parameters are provided in appendix B.

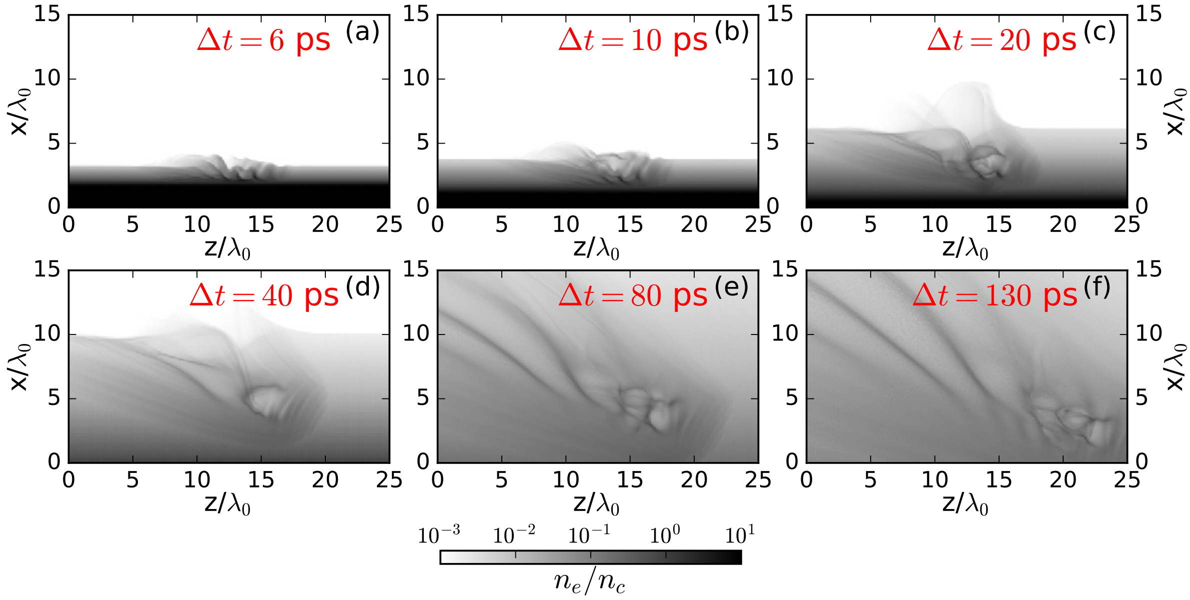

Figure 3.36: Electron density from PIC simulations with a pulse duration of 5 fs, a normalized field amplitude a_0 of 2.15 and a incidence angle θ_i of 55° for varying density profiles corresponding to a prepulse lead Δt of (a) 6 ps, (b) 10 ps, (c) 20 ps, (d) 40 ps, (e) 80 ps and (f) 130 ps. Note that the 80-ps simulation is the same as that presented earlier in figure 3.20. Detailed simulation parameters are provided in appendix B.

To estimate more quantitatively what is meant by "long enough gradient scale lengths", we have performed a series of 6 simulations with varying initial plasma density profiles. The density profiles are all obtained from the same Esther hydrodynamic simulation and the delay Δt between the prepulse and the main pulse is varied between 6 ps (short gradient regime) and 130 ps (long gradient regime). A representative snapshot from each simulation is shown in figure 3.36.

A delay of 6 ps roughly corresponds to a gradient scale length of $\approx \lambda/4$ (see figure 3.8(c)), which is slightly larger than the optimal for electron ejection at short gradients. Nevertheless, the characteristic oscillation of the plasma surface in this regime is visible in figure 3.36(a). For Δt = 10 ps, these oscillations are still visible but become blurred and they are completely absent for Δt = 20 ps. In the latter case, the plasma oscillations in the wake of the laser become visible but there are still no wakefield accelerated electrons. In this simulations, nearly all fast ejected electrons are accelerated at the position of reflection of the laser ("yellow electrons"). This is no longer the case for Δt = 40 ps, where LWFA electrons are observed, albeit in slightly smaller numbers than in the following simulations. Finally, for delays of 80 ps and 130 ps, the LWFA electrons are present in both cases in similar numbers and this corresponds to the regime previously identified.

Overall, the transition from the push-pull mechanism to LWFA is visible in simulations. We observe that the push-pull mechanism starts vanishing for a delay of approximately 10 ps while the wakefield acceleration mechanism starts taking place roughly around $\Delta t \approx$ 40 ps (in term of gradient scale length L, this means that the mechanism roughly starts taking place for $L \sim \lambda$, even though a similar gradient scan has not been performed with exponential density gradients). These values are consistent with the experiments.

However the trend of the total ejected charge as a function of the delay Δt is not reproduced. In experiments, a peak is observed at short gradients ; then the detected charge drops before rising again at longer gradients (see figure 3.12(f)). In simulations, a monotonous increase of the total ejected charge is observed during the transition from the push-pull mechanism to LWFA. This increase is due to the electrons emitted at the position of reflection of the laser pulse which start being significant as soon as the push-pull ejected charge is reduced.

Larger density gradients ($\Delta t > 130$ ps) have not been explored in the course of this thesis.

3.4.5.3 Effect of other parameters

We very succintly describe here the impact of other parameters that we have studied and that do not play a major role on the LWFA mechanism.

- Very similar results are found when switching the laser polarization from p to s. In particular, the two populations of ejected electrons remain present.
- We also find that the CEP has little impact on the LWFA mechanism. The wakefield accelerated electron beam is indeed stable when varying this parameter. The angular distribution of the electrons accelerated at the position of reflection tends to vary in an erratic manner but these electrons are still present regardless of the CEP.

3.4.5.4 Simulation at higher intensity

Finally, we present a simulation carried out with a much higher intensity ($a_0 = 10$ with τ = 5 fs). The objective of this simulation is to see how we can expect the mechanism to behave with the next generation of ultraintense few-cycle laser pulses (the parameters roughly correspond to those targeted by the SYLOS laser system at ELI-ALPS [173]). Electron density maps from this simulation are visible in figure 3.37. We observe in figure 3.37(a) that plasma waves are still formed in the wake of the laser, but are highly distorted. Large cavities nearly void of electrons are also observed. Very rapidly, the plasma waves break and the interaction becomes highly erratic. If a large amount of electrons are accelerated by the charge separation associated with the wakefields (most of them after the wavebreaking), we find that this does not lead to a collimated electron beam, as is the case in the simulation with Salle Noire parameters.

3.4.6 Electrons accelerated at the reflection position

As we have stated previously, in all 2D simulations that we have carried out at moderate or long gradients ($L > \lambda/2$), a significant amount of electrons are accelerated at the reflection point of the laser, where the density is $n_c \cos^2 \theta_i$. They have been labelled in the previous sections "reflection electrons" or "yellow electrons". The corresponding charge is usually higher than the charge accelerated by plasma waves and the "yellow electrons" have the highest energies. Moreover, these electrons are observed for every pulse duration, even for τ = 24 fs, a duration for which virtually no electrons are observed in experiments, which constitutes the main difference between experiments and simulations. Reducing the intensity of the 24-fs pulse by a factor ≈ 2 ($a_0 = 0.98 \rightarrow a_0 = 0.7$) in simulations only leads to a $\approx 25\%$ drop of the ejected charge, meaning that this discrepancy can seemingly not be explained by an overestimation of the experimental intensity.

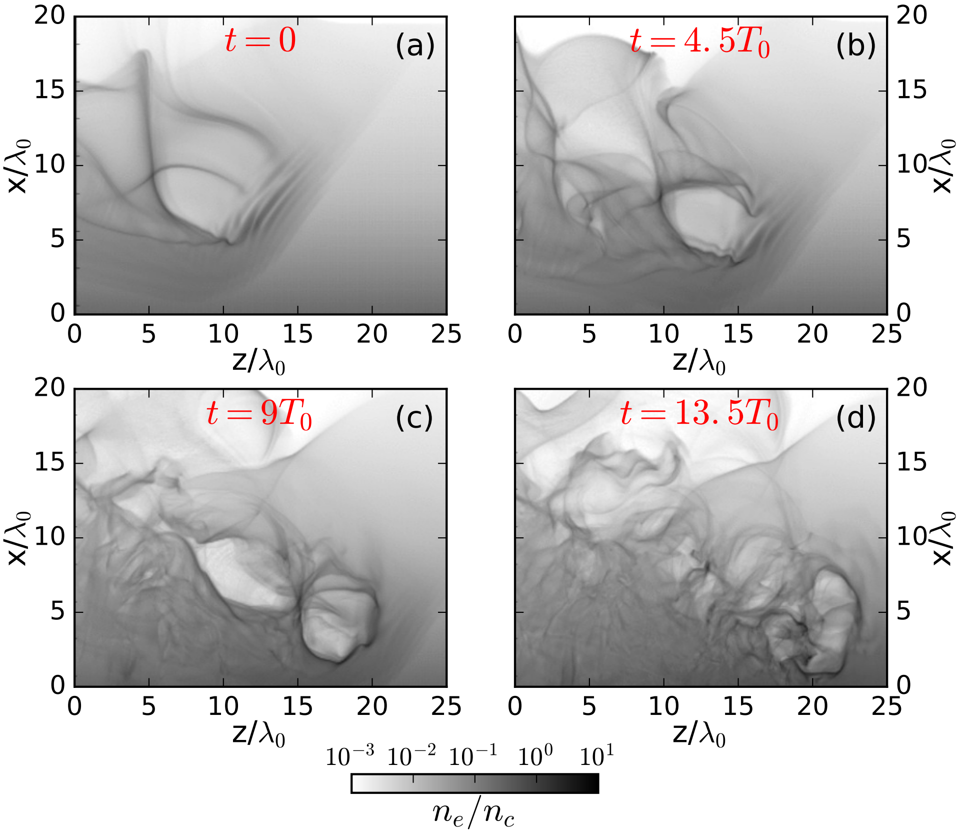

Figure 3.37: Electron density maps from a PIC simulation with a large plasma scale length ($\Delta t = 80$ ps), a pulse duration of 5 fs and a normalized field amplitude a_0 of 10. Each snapshot is separated by 4.5 laser periods. Detailed simulation parameters are provided in appendix B.

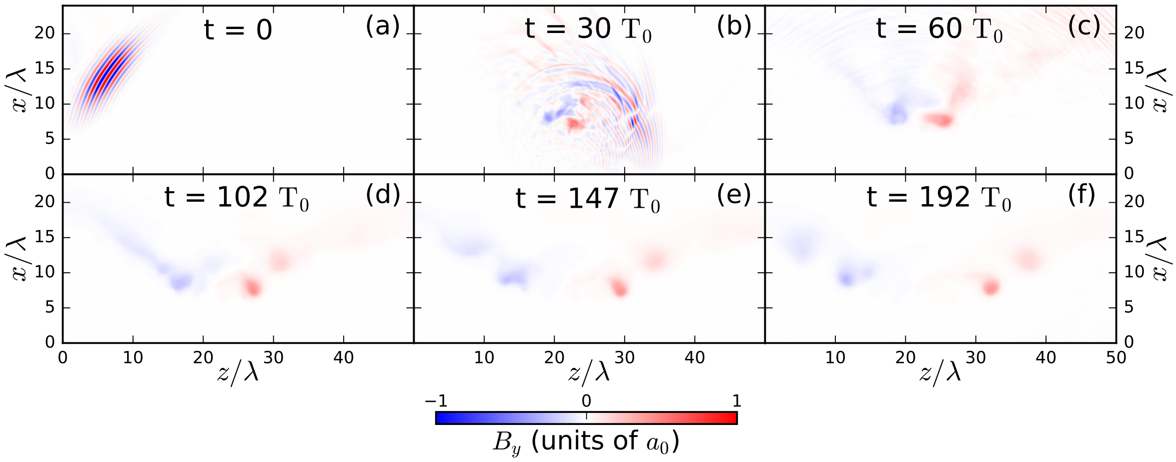

Figure 3.38: Laser magnetic field during and after the interaction from a PIC simulation with a large plasma scale length ($\Delta t = 80$ ps), a pulse duration of 5 fs, a normalized field amplitude a_0 of 2.15 and an incidence angle θ_i of 55°. The observed quasistatic magnetic fields remain long after the interaction and tend to move away from the reflection point of the laser. Detailed simulation parameters are provided in appendix B.

The mechanism leading to the emission of these electrons, observed both in s and p-polarization, has not been studied very thoroughly. Plasma oscillations appear to be triggered by the laser as it is reflected and eventually break, leading to the emission of energetic electrons in an erratic manner. Strong quasistatic magnetic fields are usually observed when the plasma oscillations break and can remain long after the laser pulse is reflected. An example is shown in figure 3.38. Such magnetic fields have been observed in similar simulations with the UHI100 laser and a $L = \lambda/1.5$ gradient scale length [24]. They can also correspond to the magnetic vortices observed in PIC simulations of either the "magnetic vortex acceleration" mechanism of ion acceleration [174] or of the experimentally observed collapse of a laser pulse in a near-critical density gas target [175]. It is not clear whether these magnetic fields directly play a role in the emission of fast electrons, but they at least have an impact on the final angular distribution by deflecting part of the accelerated electrons (in any case, the quasistatic magnetic fields play no part in the dynamics of the LWFA electrons, which are accelerated before the laser is reflected).

Our initial thought was that the relative importance of the "reflected electrons" would be reduced in more accurate 3D simulations. This can happen through changes in the physics of the interaction when taking variations in the y-direction into account. Another possibility is that a significant portion of these electrons are ejected at angles such that they were not detected in experiments. This is motivated by the fact that the "reflection electrons" have a wide angular spread in the θ_x angle in simulations. If there is a similar spread in the transverse θ_y angle, this would make most of these electrons undetectable in experiments since the Lanex screen only covers the $|\theta_y| < 15°$ region. In order to examine these possibilities, low-resolution 3D simulations[6] have been carried out at the very end of this thesis. We have

---

[6] The main changes between the 3D simulations and the previously presented 2D simulations are the following:

- The spatial step is increased to $\lambda/16$.

performed a simulation with a 5-fs pulse duration and a simulation with a 24-fs pulse duration. The laser intensity is slightly lower in these simulations ($a_0 = 2$ for $\tau = 5$ fs and $a_0 = 0.86$ for $\tau = 24$ fs) than in the previous ones.

Overall, we find that performing 3D simulations does not change the main qualitative results. The rotated wakefields, shown in figure 3.39(b), are once again only observed in the 5-fs simulation. We show for comparison in figure 3.39(a) results from a 2D simulation performed with identical laser and numerical parameters. We remark that the plasma waves are more "linear" in the 3D simulations: the density peaks are less pronounced and the amplitude of the oscillations is smaller (notice the change in the color scale). This is due to the facts that the laser is reflected before reaching focus and that diffraction occurs more rapidly in 3D, which results in a lower laser intensity in the 3D simulation at the position where the wakefields are generated. Indeed, because of diffraction, the electric field amplitude of a Gaussian beam on the optical axis scales as $\frac{w_0}{w(z)}$ in 3D but only as $\sqrt{\frac{w_0}{w(z)}}$ in a 2D geometry. More quantitatively, the laser pulse would be focused in the simulations at approximately $x = -0.7\lambda$ in the absence of a plasma, where we have used the axis of figure 3.39 to define to absolute x values. If we use $x = 14\lambda$ as a typical position for which the plasma waves are generated, we find that the laser is ≈ 2.3 Rayleigh lengths away from focus when driving the wakefields, corresponding to $w(z) = 2.5w_0$. This results in a laser electric field of $a_0 \approx 1.26$ in 2D but only $a_0 \approx 0.79$ in the 3D simulation, thus explaining the difference in the plasma waves' shape.

These snapshots show that the exact position at which the laser is focused is an important parameter for the wakefield acceleration mechanism, especially in three-dimensions. In the experiments, the absolute position of focus was not precisely known, but it was kept constant during a given gradient scan at fixed pulse duration. The fact that electrons were detected at short gradients indicates that the focus was located around the initial target-vacuum interface as in the simulations, but we cannot be more accurate than this at the moment.

Ejected electron distributions from the 3D simulations are displayed in figure 3.40. The two electron populations are still observed and we have isolated the wakefield accelerated electrons in panels (c) and (f). The total ejected charge in the 24-fs simulation is ≈ 100 pC, among which ≈ 40 pC are emitted at angles covered by the Lanex screen ($-3° < \theta_x < 75°$ and $-15° < \theta_y < 15°$). In the 5-fs simulations, these numbers become ≈ 200 pC and ≈ 90 pC respectively, with ≈ 30 pC and ≈ 15 pC accelerated by the laser wakefield. Unlike what we expected, the ratio between LWFA electrons and "yellow electrons" appears to be reduced in the 3D simulation. The wakefield electrons also have a lower energy, that does not exceed 1 MeV. We attribute the decrease in the LWFA electrons charge and energy to the faster diffraction in 3D which reduces the amplitude of the plasma waves. We expect that it is possible to obtain a more intense LWFA beam simply by changing the position of focus of the laser pulse.

On the other hand, solely performing 3D simulations is apparently not sufficient to reduce the elec-

---

- The number of particles per cell per species is dropped to 1.
- Oxygen ions are removed. This is because the corresponding electrons tend to either be ionized early in front of the main pulse (up to O^{5+}) or not be ionized at all (O^{6+} and O^{7+}). In both cases, they essentially do not contribute to the dynamics of ionization injection, unlike electrons originating from silicon ions.
- The minimum density at which the plasma is cut is increased from $n_c/450$ to $n_c/140$.
- No moving window is started to follow the electrons after the laser-plasma interaction.

These changes might seem drastic, but we have checked that they do not alter the main conclusions from 2D simulations. In this manner, the presented 3D simulations cost less than 70 000 computation hours.

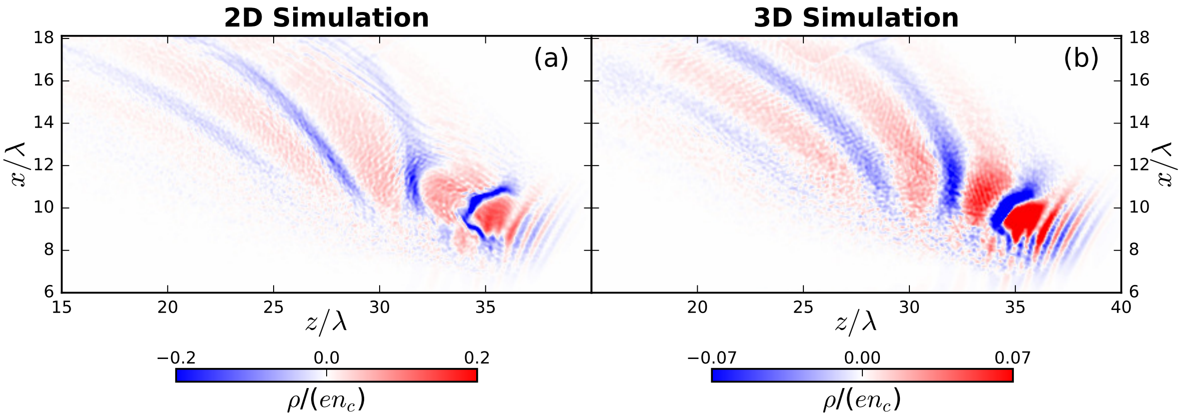

Figure 3.39: Snapshot showing the charge density of the rotated wakefield generated by a 5-fs pulse with $a_0 = 2$ in a large preplasma ($\Delta t = 80$ ps) in a low-resolution simulation ($\Delta x = \lambda/16$) either in a 2D (a) or a 3D (b) geometry. Detailed simulation parameters are provided in appendix B.

trons accelerated at the reflection point of the laser. Even though this result should be confirmed by higher-resolution 3D simulations, it is a non-negligible source of uncertainty in the interpretation of the experiments. For instance, it cannot entirely be excluded that part of the electrons detected at longer gradients with few-cycle pulses in experiments are in fact accelerated at the point of reflection of the laser and not by a wakefield in the underdense part of the plasma.

A better understanding of these ejected electrons, and in particular of the reason why they were not detected in experiments with 24-fs pulses, could be the object of further work. Possible avenues to explain this discrepancy include matching more closely the experimental parameters in the simulations (e.g. by using more accurate 3D preplasma density profile as well as an experimental laser focal spot and an exact position of laser focus), carrying out 3D simulations with better spatial resolution, and gathering new experimental data (e.g. to obtain electron energy spectra and to study the effect of various experimental parameters such as the polarization state, the position of laser focus and the CEP on the emitted electron beam).

3.5 Conclusion

We have presented and analyzed in this chapter experimental results obtained in Salle Noire regarding the acceleration of electrons from solid targets using relativistic intensity few-cycle pulses. We have identified two regimes where an intense electron emission is detected. First, push-pull electrons are ejected at short gradients for every pulse duration. A simultaneous emission of ROM harmonics is observed in this case, consistently with the known theory presented in section 1.4.

When decreasing the pulse duration to sub-10 fs values, another electron acceleration regime is found, this time at long gradients ($L > \lambda$). No simultaneous emission of harmonics is detected this time. Using 2D PIC simulations, we have attributed this unanticipated electron beam to laser wakefield acceleration occuring in the underdense part of the preplasma. This new LWFA regime, which is distinguished by the rotation of the plasma waves behind the laser driver, has been fully characterized in section 3.4.

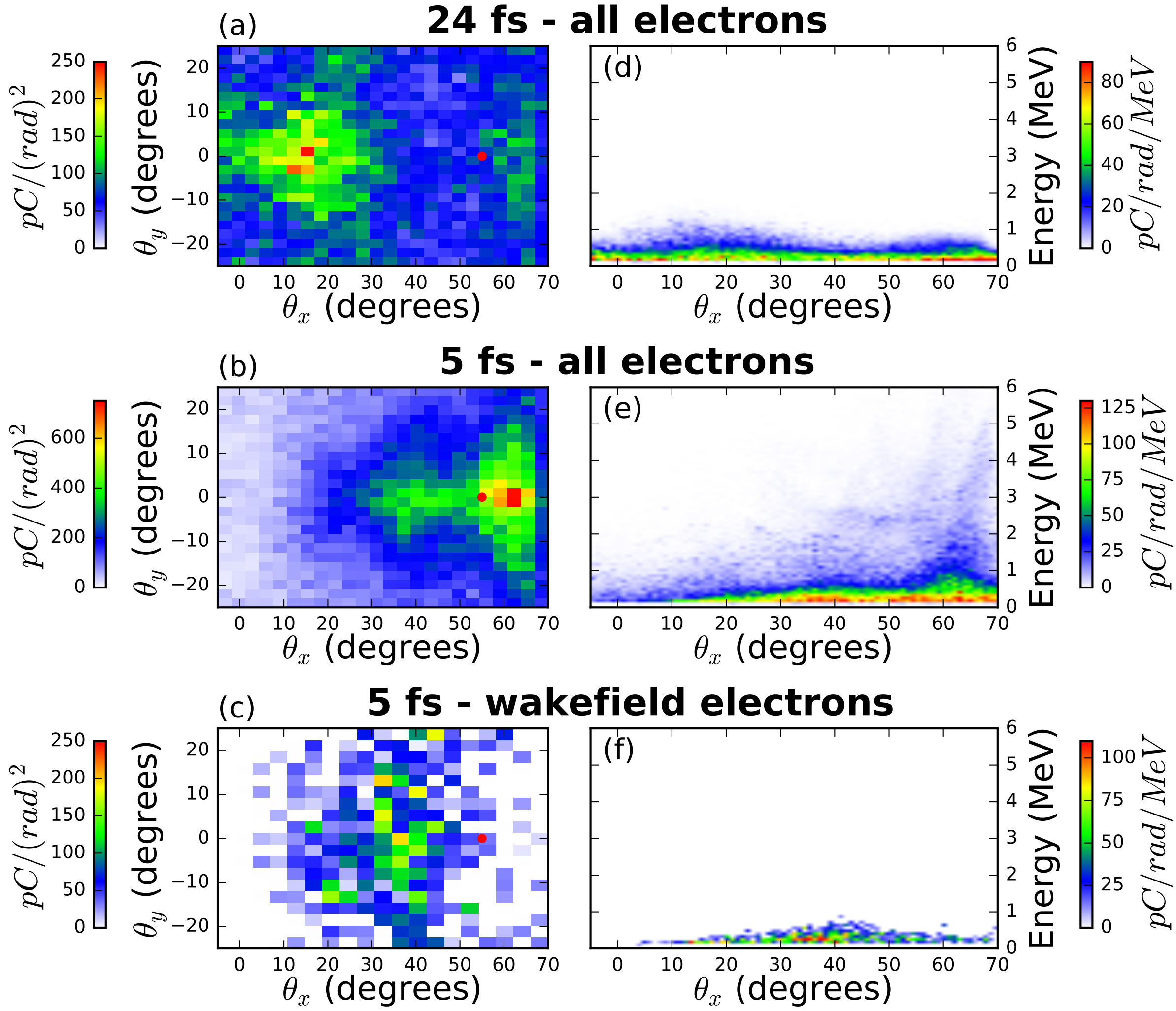

Figure 3.40: (a)-(b) Ejected electron angular distribution in the 3D simulation with (a) $\tau = 24$ fs and (b) $\tau = 5$ fs. The angular distribution of the wakefield accelerated electrons in this case is isolated in (c). (d)-(f) Correlation between the θ_x angle and the electron energy in the same cases. The distributions of the wakefield electrons are particularly noisy because only a small number of test particles have been used to separate the two ejected populations. Detailed simulation parameters are provided in appendix B.

These results were the subject of a publication in Physics of Plasmas [176]. We also observe in the simulations electrons accelerated at the reflection point of the laser, which are not detected in experiments, at least for many-cycle pulses. Further work is required to understand the reason behind this discrepancy.

More generally, the fact that it can be challenging to exactly reproduce experimental results in simulations, even when efforts are made to use a realistic description of the preplasma, illustrates the complexity of laser-overdense plasma interactions, which depend nontrivially on the difficult to control plasma density profile. Because of this intricacy, extra care must be taken when analyzing experimental data. In particular, not much information can be extracted from experiments performed without very high temporal contrast, without a prepulse or without varying the gradient scale length because the preplasma density profile remains uncertain in these cases. Yet, many experimental results are still obtained and published in this manner.

Overall, these experiments offer a better understanding of the interaction between ultraintense laser pulses and solid targets and confirms that extremely short pulse durations provide access to new acceleration regimes.

CHAPTER 4

Numerical study with radially polarized pulses at normal incidence

Contents

We have seen in the first chapter that when a relativistic intensity laser pulse is focused with oblique incidence on a plasma mirror, electrons are periodically ejected from the plasma at every optical cycle of the laser with a strong enough electric field. These electrons are ideally injected into the reflected laser pulse where they can receive a substantial energy gain from VLA. When linear polarization is used, the accelerating fields are transverse, which tends to result in large angular spreads. This may no longer be the case with radially polarized beams, which, as we have seen in section 1.5.2, possess a strong on-axis E_z field that can directly accelerate electrons in the longitudinal direction. We therefore study in the following chapters the acceleration of electrons from the interaction between an overdense plasma and a relativistic intensity radially polarized pulse. In this chapter, we study the interaction numerically and focus on the case of normal incidence. We will present in chapter 5 recent experiments performed at oblique incidence with the UHI100 laser.

This chapter is organized as follows. In section 4.1, we start by presenting the initial conditions that lead to efficient acceleration in vacuum by a radially polarized beam. We then show, by performing a PIC simulation at normal incidence, that electrons ejected from a plasma mirror satisfy these conditions and are accelerated to higher energies than with other injection methods. Using test-particle simulations, we next investigate in section 4.2 the requirements for generating highly collimated electrons beams. The simulations indicate in particular that increasing the longitudinal field amplitude can result in a significant decrease in the beam angular divergence. This is confirmed in section 4.3, in which we perform PIC simulations of the interaction at normal incidence for various laser parameters.

4.1 Conditions for optimal injection into a radially polarized pulse

4.1.1 The optimal conditions

We have seen in section 1.5.1.4 that VLA with linear polarization is efficient when the electrons are injected inside the laser pulse, close to a zero of the electric field, and with a relativistic velocity in the laser propagation direction. Here, we show that the optimum injection conditions into a radially polarized beam are very similar. To this end, we perform on-axis test-particle simulations of an electron accelerated by a radially polarized pulse. On the optical axis, the transverse fields vanish and the electrons is only subject to the E_z field. It will therefore remain on the axis throughout the simulation. We recall that, within the framework of the paraxial approximation, this longitudinal field reads, at $r = 0$:

$$E_z(z,t) = -E_{0,z}\left(\frac{w_0}{w(z)}\right)^2 \sin\phi \, \exp\left(-2\log(2)\frac{\left(t-\frac{z}{c}\right)^2}{\tau^2}\right) \tag{4.1}$$

Where $\phi = kz - \omega t - 2\arctan(z/z_R) + \phi_{CEP}$ is the laser phase, $w(z) = w_0\sqrt{1+\frac{z^2}{z_R^2}}$ is the beam radius at position z, w_0 the beam waist, $z_R = kw_0^2/2$ is the Rayleigh length, τ is the pulse duration in FWHM of the intensity and ϕ_{CEP} is the CEP. We have here assumed a Gaussian temporal envelope.

We start by studying the motion of an electron, initially at rest at $r = z = 0$, in the field given by equation 4.1. We have stated in chapter 2 that the paraxial approximation should not be used in test-particle simulations. However, it has been shown that paraxial fields are sufficient to describe the *on-axis* motion of an electron accelerated by a radially polarized field [123, 177]. We use parameters corresponding to the Salle Noire laser: $\lambda = 800$ nm, $a_{0,z} = 0.7$, $w_0 = 1.5\,\mu\text{m}$, $\tau = 3.5$ fs and $\phi_{CEP} = \pi/2$. We consider three different initial phases for the electron, which are represented in figure 4.1(a). Figures 4.1(b) and (c) show trajectories for non optimal initial phases, where the electron starts respectively in front of the laser pulse and inside the pulse at a maximum of the electric field. This is similar to the case of the ionization of a gas with respectively a low ionization energy and a high ionization energy. In each of these cases, the electron quickly dephases, resulting in negligible energy gains (respectively 9.3 eV and 0.81 eV). On the opposite, figure 4.1(d) shows more efficient acceleration when the electron is initially at a zero of the electric field. This is because the electron starts with a whole accelerating half-cycle and stays in it much longer than in the previous cases, resulting in a final energy of 1.3 MeV.

We can note that this optimal phase corresponds to a maximum of the initial longitudinal canonical momentum. We can indeed write, in the Coulomb Gauge, $E_z = -\dfrac{\partial A_z}{\partial t}$. We see that a zero of the electric field corresponds to an extremum of the magnetic potential A_z and thus to an extremum of the canonical momentum $-eA_z$ (in the absence of initial velocity). Of course the longitudinal canonical momentum is not a conserved quantity, since there is no invariance in the z direction. However, it can still be understood

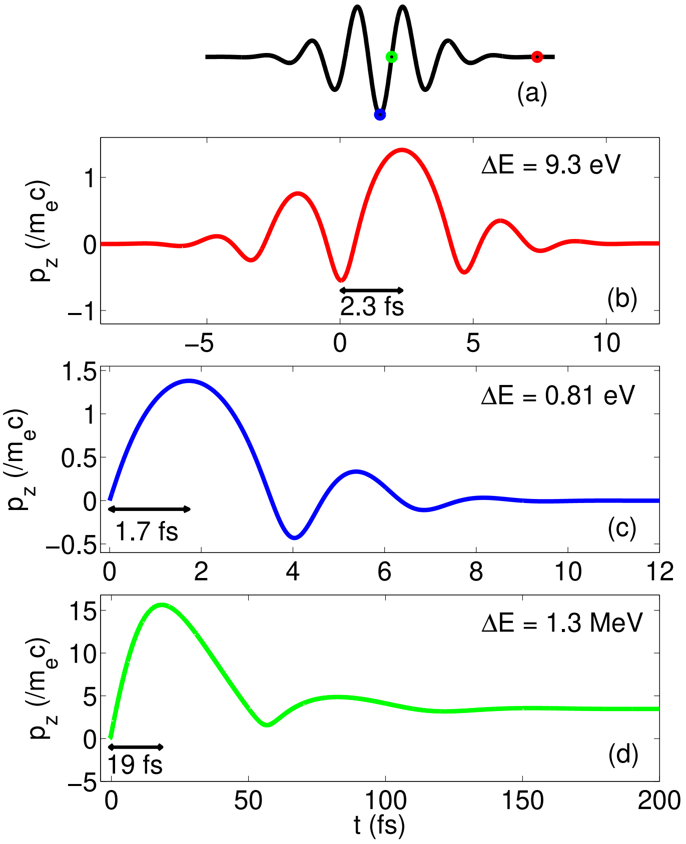

Figure 4.1: Results from test particle simulations with on-axis electrons. (a) Waveform of the few-cycle longitudinal electric field. The colored dots represent the initial positions of the electron in (b)-(d). (b)-(d) Longitudinal momentum p_z *along the electron trajectory for various cases: the electron is initially at rest either (b) in front of the pulse, (c) inside the pulse at a maximum of the field, (d) inside the pulse at a zero of the field. The double headed arrows show the time spent inside the main accelerating half-cycle.*

by noting that:

$$-eA_z(z,t) = \int_{-\infty}^{t} eE_z(z,t')dt' = \int_{t}^{+\infty} -eE_z(z,t')dt' \tag{4.2}$$

Where we have used the fact that $A_z(z,t=-\infty) = A_z(z,t=+\infty) = 0$, since $\int_{-\infty}^{+\infty} E_z(z,t)dt$ must be zero for a laser pulse that has no static component. We can see that the canonical momentum corresponds to the longitudinal momentum that an electron initially at (z,t) would get if it were to remain at the same position z until $t=+\infty$. This is of course not the case in practice (except in the limit $a_{0,z} \ll 1$) but it can help us understand why the optimal phase corresponds to a maximum of the canonical momentum. In reality, we can expect the final momentum of an electron at the optimal phase to exceed its initial canonical momentum because the decelerating half-cycles following the initial accelerating half-cycle will be diminished due to diffraction. This is for example the case of the electron of figure 4.1(d), which has an initial canonical momentum of the order of $0.7\ m_ec$ and a final momentum of $\approx 3.4\ m_ec$.

We can remark that, so far, the optimal conditions are very similar for linear and radial polarization: the electrons should initially be inside the laser pulse close to a zero of the accelerating electric field. We can however already notice a slight difference between the optimal conditions for the two polarization states. In the case of linear polarization, all the zeros of the electric field (two per optical cycle) are optimal initial phases for electron acceleration. On the other hand, for radial polarization only one of the zeros of the E_z field is optimal at every cycle (corresponding to $\phi = \pi$). The other zero ($\phi = 0$) corresponds in fact to the worst initial case for which the electron starts with a decelerating half-cycle (or alternately has a canonical momentum which is maximum and directed opposite to the laser propagation direction).

We next study the effect of having a relativistic initial velocity. Figure 4.2(a) shows the trajectory of an electron at the optimal initial phase with no initial velocity. This is in fact the same trajectory as in figure 4.1(d), which results in a 1.3 MeV energy gain. In figure 4.2(b), the electron starts at the same phase but with an initial velocity of 200 keV in the direction of propagation of the laser. This initial velocity allows the electron to remain for a much longer time in the first accelerating half-cycle, which eventually results in an energy gain increased by one order of magnitude (10.2 MeV compared to 1.3 MeV). In this case the electron appears to experience in total less than an optical cycle (one accelerating half-cycle and one decelerating half-cycle). We can also note that even a moderately relativistic initial energy can result in large changes in the energy gain.

In conclusion, we observe that the conditions leading to an efficient acceleration with radial polarization are very similar to that of linear polarization:

- The electron should start its interaction near the spatial and temporal maxima of the laser pulse and close to a zero of the E_z field, so that it begins with a strong accelerating half-cycle.
- The electron should have an initially relativistic velocity in the laser propagation direction, so that it can remain for a long time in the first accelerating half-cycle.

4.1.2 On-axis parameter study

Here, we examine the effect of various parameters on the acceleration of an electron fulfilling the optimal conditions identified in the previous section. To simplify the analysis, we consider throughout this section an electron on the optical axis. This parameter study is performed in the following manner:

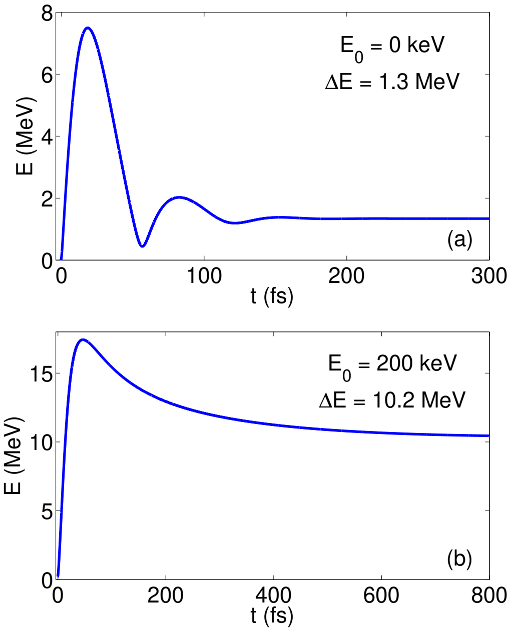

Figure 4.2: Result from test particle simulations with on-axis electrons. Energy of single electrons along their trajectories. The electrons are initially inside the laser pulse at a zero of the longitudinal electric field with either (a) no initial velocity or (b) an initial velocity of 200 keV in the direction of propagation of the laser.

- The standard case corresponds to an electron initially at $t = 0$ and $z = r = 0$ with an initial kinetic energy of 200 keV at the optimal phase of the laser. The laser parameters are: $\lambda = 800$ nm, $a_{0,z} = 0.7$, $w_0 = 1.5\,\mu\text{m}$, $\tau = 3.5$ fs and $\phi_{CEP} = \pi$. This standard case corresponds to the electron of figure 4.2(b) except that the CEP has been changed from $\pi/2$ to π (note that in both cases the electrons starts at the optimal phase of the laser, i.e. at $E_z = 0$).

- We then consecutively vary the parameters one at a time, while keeping the value of the other parameters equal to that of the standard case.

As in the previous section, we use the expression of the E_z field given by the paraxial approximation combined with a Gaussian temporal envelope.

This study also serves as a test-bed for the threshold between the ponderomotive and VLA regimes that we have derived in section 1.5.2.3, and which reads:

$$a_{0,z} \geq a_{0,zc} = \frac{1}{1-\cos\phi_i}\sqrt{\frac{1-\beta_{e,zi}}{1+\beta_{e,zi}}} \tag{4.3}$$

Where ϕ_i is the initial phase seen by the electron and $c\beta_{e,zi}$ is the initial velocity of the electron. Whenever applicable, we indicate in the figures the values for which this threshold is attained.

The first simulations that we perform will allow us to analyze more precisely the optimal conditions presented in the previous section. In a second part, we will study the effect of varying the laser parameters.

4.1.2.1 Detailed study of the optimal initial conditions

Effect of initial phase

We start by studying the influence of the initial phase seen by an electron initially inside the pulse. In this scan, the electron is initially at $t = z = 0$ and the initial phase is varied by changing the CEP of the laser. The resulting final electron energy as a function of the initial phase is plotted in figure 4.3. We observe, as stated in the previous section, that the optimal phase is π, which corresponds to an electron starting its interaction with an accelerating half-cycle. The green line shows the theoretical threshold between the VLA and ponderomotive regimes. We find that it indeed provides a good estimation of the phase after which the energy gain is negligible.

Effect of initial velocity

In this scan, we vary the initial kinetic energy of the electron. The result is plotted in figure 4.4. The red dashed line shows the final energy corresponding to the maximum theoretical energy gain derived in section 1.5.2.3 ($\Delta W_{MAX}[\text{MeV}] \approx 31\sqrt{P[\text{TW}]}$). With our choice of laser parameters, the maximum energy gain is ≈ 24.86 MeV. We observe that the kinetic energy gained by the electron first increases rapidly with its initial velocity and then saturates at the maximum theoretical value. This result was expected because this theoretical value has precisely been obtained for an ultrarelativsitic electron interacting with the laser from $z = 0$ to $z = +\infty$. We can note that the energy gain always increases with the electron initial velocity. This is different from the linear polarization case, for which an initial velocity that is too high results in the electron being barely deflected and consequently receiving a low energy gain.

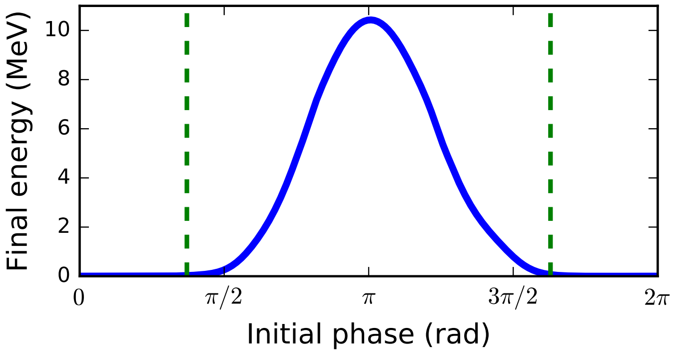

Figure 4.3: Final energy of an electron initially at $t = z = 0$ with an initial energy of 200 keV as a function of the initial phase in a radially polarized pulse with $\lambda = 800$ nm, $a_{0,z} = 0.7$, $w_0 = 1.5\,\mu\text{m}$, $\tau = 3.5$ fs. The green lines show the threshold between the ponderomotive and VLA regime as estimated by equation 4.3.

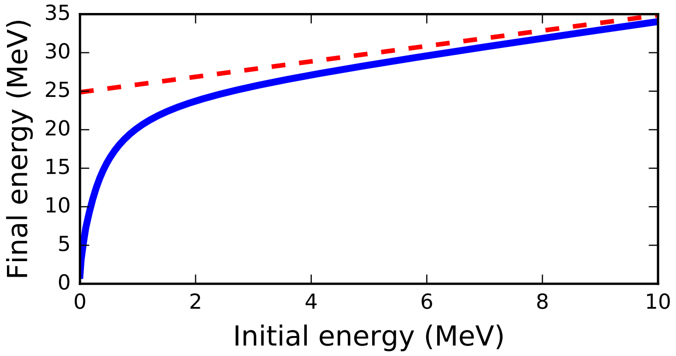

Figure 4.4: Final energy of an electron initially at $t = z = 0$ as a function of its initial velocity in a radially polarized pulse with $\lambda = 800$ nm, $a_{0,z} = 0.7$, $w_0 = 1.5\,\mu\text{m}$, $\tau = 3.5$ fs and $\phi_{CEP} = \pi$. The red dashed line shows the final energy corresponding to the maximum theoretical energy gain.

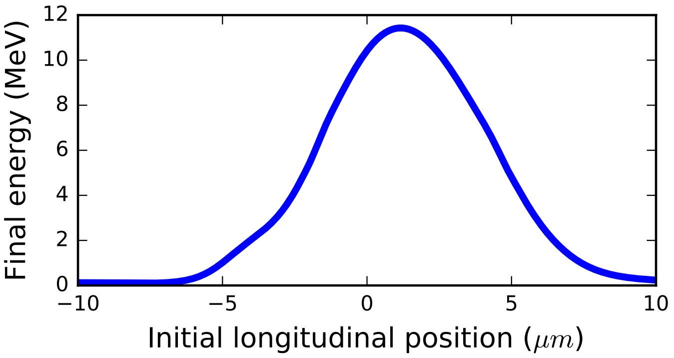

Figure 4.5: Final energy of an electron with an initial energy of 200 keV as a function of its initial longitudinal position in a radially polarized pulse with $\lambda = 800$ *nm,* $a_{0,z} = 0.7$*,* $w_0 = 1.5\,\mu\text{m}$*,* $\tau = 3.5$ *fs and* $\phi_{CEP} = \pi$*.*

Effect of initial longitudinal position

We have stated in the previous section that acceleration is efficient when the electron is initially close to the spatial maxima of the laser field (i.e. at focus). Here, we verify this assertion by varying the initial longitudinal position of the electron. The initial time is adjusted so that the electron is always at the optimal phase and at the center of the temporal envelope. The results are displayed in figure 4.5. We observe that the optimal initial position is in fact slightly after focus, although the distance from focus is smaller than a Rayleigh length. At the optimal initial position, electrons gain less energy in the first accelerating half-cycle than if they were initially at focus, but then lose less energy in the following decelerating phase, resulting in a higher energy gain. On the opposite, too far from focus, the E_z field amplitude is not strong enough to trap electrons in an accelerating cycle, which leads to low energy gains. We can also note that the optimal value depends on the other laser parameters, but is very often either slightly after focus (as is the case here) or exactly at focus (most notably in the ultrarelativistic limit).

Overall, these simulations confirm the well-foundedness of the optimal conditions evidenced in the previous section.

4.1.2.2 Laser parameter scan

Effect of beam waist

Here, we vary the laser beam waist w_0 while keeping the laser power constant. This means that the longitudinal field amplitude varies as $a_{0,z} \propto \dfrac{1}{w_0^2}$. Decreasing the beam waist thus strongly increases the E_z field but also decreases the Rayleigh length and increases the phase velocity around focus (because of the quicker variation of the Gouy phase $2\arctan(z/z_R)$). We plot in figure 4.6 the final electron energy as a function of w_0. We observe that decreasing the beam waist always results in more efficient acceleration in this regime. This indicates that the tighest possible focusing should be used in experiments. We note that the energy gain approaches the maximum theoretical value as w_0 is decreased. This is because $a_{0,z}$ acquires very high values in this case, meaning that the electron will almost instantaneously

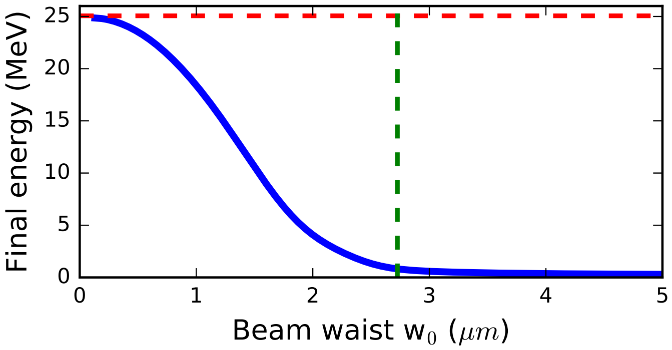

Figure 4.6: Final energy of an electron initially at $t = z = 0$ *with an initial energy of 200 keV as a function of the laser beam waist in a radially polarized pulse with* $\lambda = 800$ *nm,* $\tau = 3.5$ *fs and* $\phi_{CEP} = \pi$. *The laser peak power is kept constant as the beam waist is varied and the field amplitude is chosen such that* $a_{0,z} = 0.7$ *when* $w_0 = 1.5\,\mu\text{m}$. *The green line shows the threshold between the ponderomotive and VLA regime as estimated by equation 4.3. The red dashed line shows the final energy corresponding to the maximum theoretical energy gain.*

be ultrarelativistic. It should however be kept in mind that the energy gains for $w_0 < \lambda$ are probably not entirely meaningful (because the paraxial approximation is still used and because diffraction will anyways always limit w_0 to $\approx \lambda$). Finally, we also remark that the theoretical threshold between the VLA and ponderomotive regime once again provides a good estimation of the beam waist above which the gained energy becomes negligible.

Effect of electric field amplitude $a_{0,z}$

We now vary the longitudinal field amplitude $a_{0,z}$. We first note that, since all other parameters are kept constant, the laser power scales as $P \propto a_{0,z}^2$. This means in particular that the maximum theoretical energy gain is proportional to $a_{0,z}$. The results of the scan are shown in figure 4.7. Unsurprisingly, we find that increasing the amplitude of the E_z field increases the energy gain. We note that, once the amplitude is high enough, the final energy scales almost linearly with $a_{0,z}$ and that the ratio between the effective energy gain and the theoretical maximum energy gain approaches 1. This is once again because the electron becomes almost instantaneously ultrarelativistic when $a_{0,z}$ is significantly greater than 1. Finally, we once gain remark that the theoretical threshold between the VLA and ponderomotive regime provides a good estimation of the field amplitude below which the energy gain is negligible.

Effect of pulse duration

Here, we vary the pulse duration τ while keeping $a_{0,z} = 0.7$. This means that the pulse energy increases as τ increases. Figure 4.8 indicates that the pulse duration does not have a significant effect on the acceleration as long as τ is larger than an optical period. This is because the electron only sees approximately one optical cycle during its interaction (see figure 4.2(b)), so that adding other optical cycles does not affect the electron trajectory. This result suggests that, at a fixed laser energy, the pulse duration should be chosen as small as possible in order to increase the peak power and the final electron

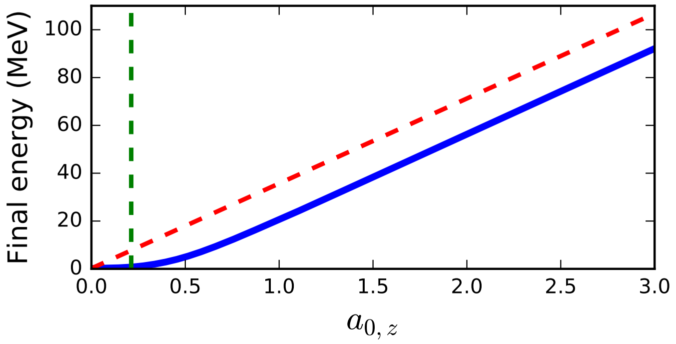

Figure 4.7: Final energy of an electron initially at $t = z = 0$ *with an initial energy of 200 keV as a function of* $a_{0,z}$ *in a radially polarized pulse with* $\lambda = 800$ *nm,* $w_0 = 1.5\,\mu\mathrm{m}$*,* $\tau = 3.5$ *fs and* $\phi_{CEP} = \pi$*. The green line shows the threshold between the ponderomotive and VLA regime as estimated by equation 4.3. The red dashed line shows the final energy corresponding to the maximum theoretical energy gain.*

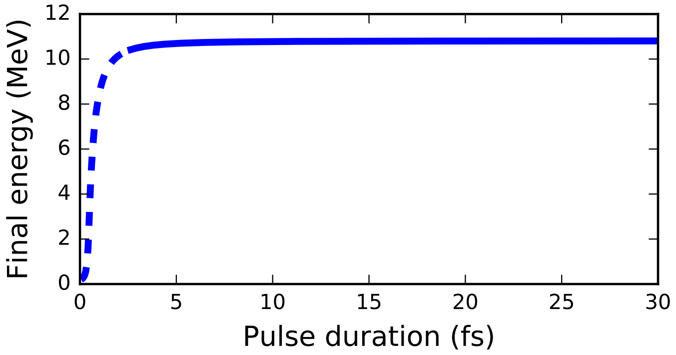

Figure 4.8: Final energy of an electron initially at $t = z = 0$ *with an initial energy of 200 keV as a function of* τ *in a radially polarized pulse with* $\lambda = 800$ *nm,* $w_0 = 1.5\,\mu\mathrm{m}$*,* $a_{0,z} = 0.7$ *and* $\phi_{CEP} = \pi$*. The dashed part of the curve shows the region where* τ *is smaller than a laser period, for which the results are not entirely meaningful.*

energy. Once again, the results are probably not entirely meaningful when the pulse duration is lower than the laser period, because using a Gaussian temporal envelope is not completely valid in this case (and more generally because a laser pulse shorter than its period is not entirely meaningful in itself). In particular, since the CEP is such that E_z is zero at the maximum of the temporal envelope, the amplitude of the longitudinal field never actually approaches 0.7 for very short pulse durations because it is already substantially reduced by the temporal envelope at the position where it is maximum. This explains the drop in the energy gain as τ approaches zero.

Effect of CEP

Finally, we examine the effect of varying the laser CEP. As the CEP is varied, the electron is always

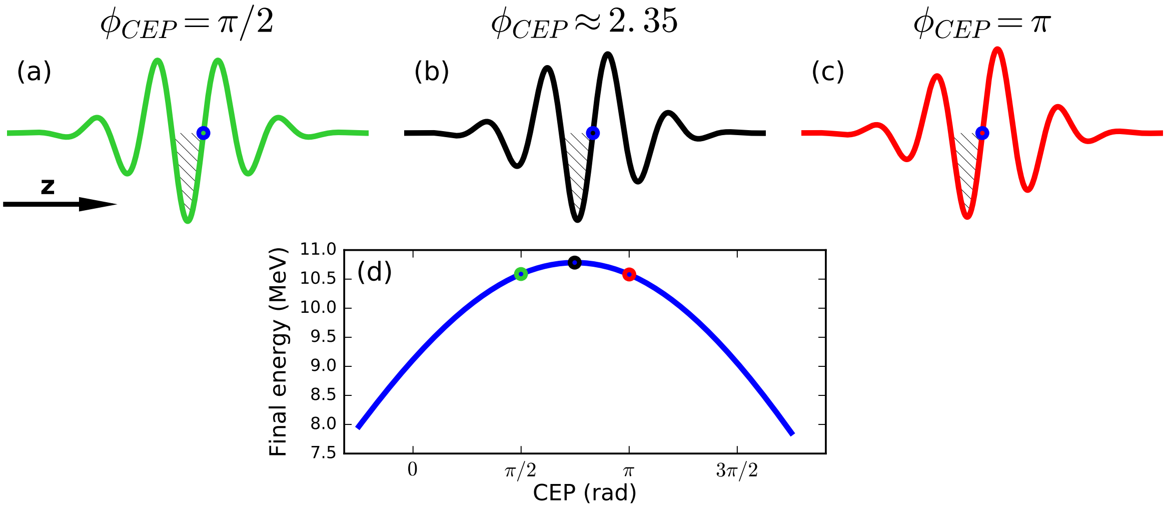

Figure 4.9: (a)-(c) Waveform of the longitudinal electric field of a 3.5-fs pulse with (a) $\phi_{CEP} = \pi/2$, (b) $\phi_{CEP} \approx 2.35$ and (c) $\phi_{CEP} = \pi$. The blue dots show the initial electron position in the test-particle simulations while the hatched areas show the first accelerating half-cycle seen by the electron in blue. (d) Final energy of an electron initially at $t = z = 0$ with an initial energy of 200 keV as a function of the CEP in a radially polarized pulse with $\lambda = 800$ nm, $w_0 = 1.5\,\mu\text{m}$, $a_{0,z} = 0.7$ and $\tau = 3.5$ fs. The coloured dots show the positions of the CEP values of (a)-(c).

at $z = 0$ initially, but the initial time is continuously changed so that the electron always starts with an accelerating half-cycle. This means that in this case the electron does not always start at the temporal maximum of the pulse envelope. Beforehand, we could expect that two different values for the CEP could be optimal. The first one is $\phi_{CEP} = \pi$, which we have considered throughout this section and which corresponds to the maximum value for the initial canonical momentum. The waveform of the longitudinal electric field with this choice of CEP is shown in figure 4.9(c). The second value is $\phi_{CEP} = \pi/2$, which corresponds to the maximum value for the accelerating field and which was used in the previous section. The waveform of the longitudinal electric field with this choice of CEP is shown in figure 4.9(a). We find that, with our choice of parameters, the optimal CEP is actually approximately halfway between the two previously cited values, as can be seen in figure 4.9(d). The waveform of the longitudinal electric field at the optimal CEP value is shown in figure 4.9(b). It should be noted that the exact value for which the CEP is optimal depends on the electron initial velocity and on the other laser parameters. We heuristically find that it is almost always between $\phi_{CEP} = \pi/2$ and $\phi_{CEP} = \pi$. Finally, we remark that using the worst CEP only results in a 25% drop in the electron final energy, even with a pulse duration as short as 3.5 fs. This suggests that, while the CEP can influence the acceleration, this parameter is not as crucial as the laser peak power or beam waist.

In conclusion, this section has allowed us to identify the key laser parameters of the interaction in vacuum. We first note that the theoretical threshold between the ponderomotive and VLA regime appears to provide a good estimation of the required longitudinal field to obtain a significant energy gain. $a_{0,z}$ is therefore the key first laser parameter and should be chosen as high as possible. This can be achieved by using tight focusing and high peak powers. Once $a_{0,z}$ is substantially over the threshold, the energy gain is mainly dictated by the laser peak power, with the expected scaling $\Delta W \propto \sqrt{P}$.

4.1.3 Plasma mirror as ideal injector

In this section, we show that, as in the case of linear polarization, the conditions leading to efficient vacuum laser acceleration with radial polarization can be attained by using a plasma mirror to inject the electrons into the reflected pulse. To demonstrate this, we perform a PIC simulation of the interaction between a relativistic intensity radially polarized pulse and an overdense plasma with a sharp density gradient. The simulation is performed at normal incidence, for two principal reasons:

- As we have explained in the first chapter, electron ejection by the push-pull mechanism requires a strong electric field component in the direction of the density gradient. This makes normal incidence inefficient with linear polarization because in this case the electric field is parallel to the plasma surface. For radial polarization however, the longitudinal E_z field is directed towards the density gradient at normal incidence. We can thus expect the electrons to be ejected close to the optical axis, where the E_z field is maximum, which would be ideal for acceleration in the longitudinal direction by the reflected pulse.

- The interaction at normal incidence is axisymmetric. This means that it can be simulated in cylindrical coordinates (see section 2.2.3) with the cost of a 2D simulation. We use the code CALDER-CIRC for this purpose. On the other hand, oblique incidence requires full 3D simulations which are much more demanding computationally[1].

In the PIC simulation, we once again use parameters corresponding to the Salle Noire laser: $\lambda = 800$ nm, $a_{0,z} = 0.7$, $w_0 = 1.5\,\mu\text{m}$ and $\tau = 3.5$ fs. The CEP is $\phi_{CEP} = \pi/2$ for the incident field, which becomes $\phi_{CEP} = -\pi/2$ for the reflected field. The laser is focused on the plasma, which has a maximum density of $200 n_c$ and an exponential density gradient with $L = \lambda/7$ (we find that the results are for the most part unchanged when the gradient scale length is lowered to $L = \lambda/10$). The numerical parameters are the following: space steps $\Delta x \approx \lambda/882$ and $\Delta r \approx \lambda/205$, timestep $\Delta t \approx T/1045$ (where T is the laser period), 50 electrons per cell, box size $N_z \times N_r = 5624 \times 6552$, 2 orders for the Fourier expansion along the poloidal direction. A moving window is started after the interaction, making it possible to follow the ejected electrons far from the plasma.

Figure 4.10 displays three different snapshots from the PIC simulation, showing the interaction between the laser and the plasma. The push-pull mechanism, which is responsible for the ejection of

---

[1] In principle we could perform 2D simulations at oblique incidence with a laser that has a transverse electric field of the form $E_x \propto x \exp\left(-\left(\frac{x}{w_0}\right)^2\right)$ at focus. Such a laser would indeed exhibit a longitudinal field and could be used to mimic radial polarization in two-dimensions. However, we do not expect this 2D field to accurately model the acceleration in vacuum by a radially polarized beam. There are several reasons for this. On the one hand, the ratio between the longitudinal and the transverse field would likely be smaller because there is no variation of the E_y field to contribute to building the E_z field. This would make the acceleration less efficient. On the other hand, the Gouy phase shift would likely be decreased by a factor 2 and the amplitude of the E_z field would probably decrease as $\left(\frac{w_0}{w(z)}\right)^{3/2}$ rather than $\left(\frac{w_0}{w(z)}\right)^2$, since in 2D the beam only diffracts in one direction. This would greatly improve the efficiency of the acceleration. This shows once again that 2D simulations are inadequate for studying VLA, this time mainly because diffraction, which can only be correctly modeled in a 3D geometry, is a crucial element of the interaction and the main limit to the energy gain.

electron in the short gradient regime (see section 1.4.2.1), is clearly visible. We recall that it consists of the following two steps. (1): The normal component of the electric field of the laser pushes electrons inside the plasma, resulting in a density peak, which can be seen in the yellow dots of figure 4.10 and in the red curve of figure 4.11. As the electron density peak is pushed deeper into the density gradient, the immobile ions create a large restoring static field, resembling a plasma capacitor. (2): When the density peak reaches its maximum depth (figure 4.10(b)), the sign of the electric field switches and both the laser and the static field work together to pull the electrons out of the plasma. A small fraction of the electrons inside the density peak can gain enough energy from the plasma capacitor to be ejected from the plasma. These electrons are ideally injected into the reflected pulse since they start with an initial velocity at the optimal phase, where the sign of the longitudinal field changes, and thus begin their interaction with an accelerating half cycle, represented in blue in figure 4.10(c). This simulation therefore shows that the push-pull mechanism can be triggered by the E_z field of a radially polarized beam at normal incidence, which results in optimal electron injection into the reflected pulse.

We observe that the laser is partly distorted by the reflection on the plasma mirror, as is illustrated in figure 4.12. However, we note that the high-harmonic content of the reflected pulse remains small, as no harmonics are visible beyond order 10, even in log scale. This comes from the fact that the normalized electric field in the gradient direction is relatively weak ($a_{0,z} = 0.7$). For comparison, at oblique incidence with linear polarization and similar laser parameters, the normalized electric field in the gradient direction is ≈ 2 and harmonics up to order 60 are visible in 2D simulations. We also remark in figure 4.12(b) that the transverse fields of the reflected pulse vanish on the optical axis, which is expected because the interaction is cylindrically symmetric. We can thus anticipate that the generated harmonics have an overall small impact on the acceleration of electrons by the reflected beam. This will be confirmed in the following paragraphs.

Figures 4.13(a) and 4.13(c) show the energy-angle and the angular distributions of the electrons ejected from the plasma mirror. The total ejected charge is about 60 pC and the divergence of the electron beam is of the order of 30°. This value is slightly lower but comparable to the divergence obtained in 3D simulations with the Salle Noire laser and linear polarization ($\approx 40^\circ$, see figure 3.19). Furthermore, because they are injected into the laser with optimal initial conditions, a group of electrons representing several pC is accelerated to relativistic energies, typically from 1 to 8 MeV. Once again, this value is higher than in simulations with linear polarization, where the maximum observed energy is ≈ 5 MeV. This shows that radial polarization can result in a sensible improvement of the acceleration compared to linear polarization. The highly energetic electrons in the radial polarization simulation form a ring-shaped beam with a typical angle of 150 mrad with respect to the optical axis. We also note that there is a correlation between the energy and the emission angle among the MeV electrons, with the fastest ones emitted closer to the specular direction.

Figures 4.14(a) and 4.14(c) show the energy spectrum and time distribution of the electrons with $\theta < 200$ mrad and $E > 1$ MeV, after $145\,\mu\mathrm{m}$ of propagation. Such filtering can typically be achieved using a pinhole and a magnet to select only certain angles and energies. These electrons represent 3.3 pC. Thanks to its high energy, this fast electron bunch is kept ultrashort, with a duration of around 12 fs. It would be possible to diminish the duration of the bunch by reducing the acceptance angle of the selected electrons, at the cost of also diminishing the selected charge. The transverse normalized emittance of this electron beam is $\varepsilon_{n,x} = 3.18\,\mu\mathrm{m}$, which is too high for electron diffraction experiments. However, filtering this electron bunch can result in lower emittance values. For instance, selecting electrons with an energy between 4.06 MeV and 4.14 MeV results in a 2% energy spread, a charge of 100 fC and

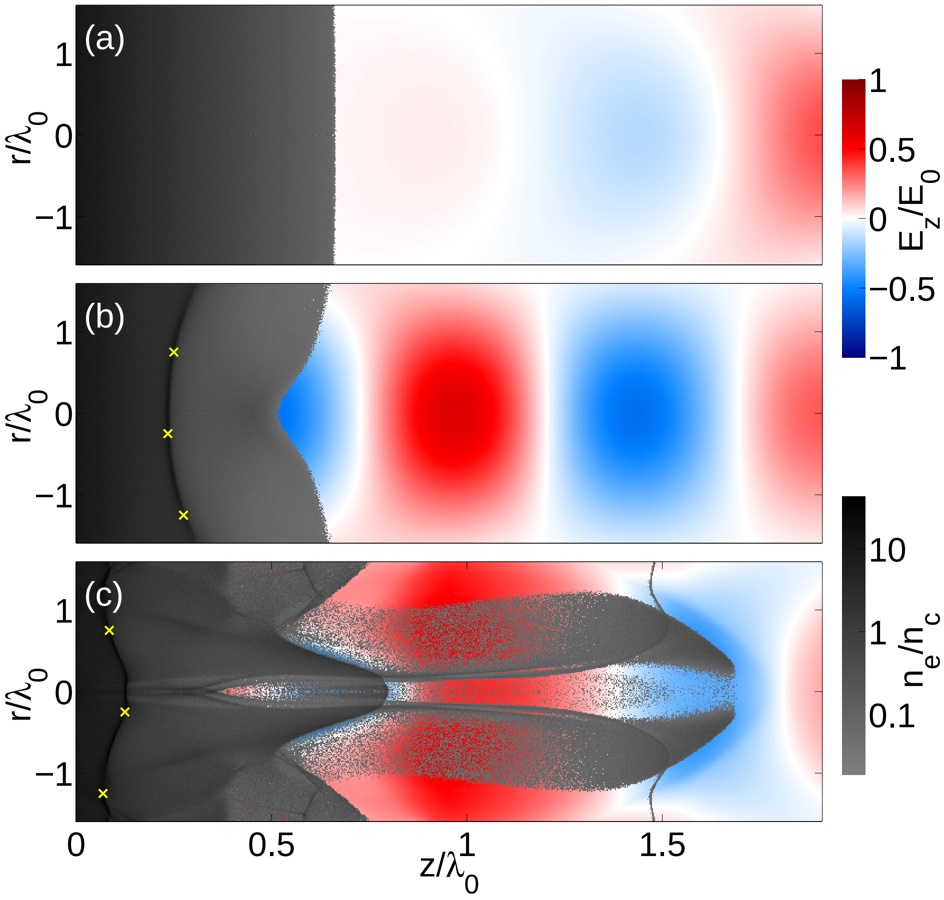

Figure 4.10: Snapshots from the CALDER-CIRC *PIC simulation showing the longitudinal electric field and electron density extracted at three different timesteps. (a) The plasma is still unperturbed by the incoming laser. (b) The electrons are pushed into the plasma by the laser, resulting in a density peak indicated by the yellows markers. (c) Electrons that were in the density peak are now pulled away from the plasma, between $z = 1.2\ \lambda$ and $z = 1.7\ \lambda$. A second electron bunch is also being ejected one wavelength behind, between $z = 0.3\ \lambda$ and $z = 0.8\ \lambda$, whereas a new density peak is visible two wavelengths behind, at $z = 0.1\ \lambda$. Detailed simulation parameters are provided in appendix B.*

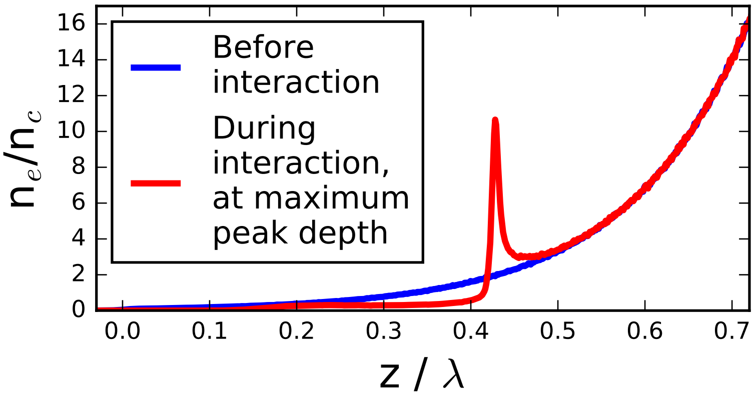

Figure 4.11: Results from the Calder-Circ *PIC simulation. Plasma electronic density averaged between $r = 0.05\ \lambda$ and $r = 0.3\ \lambda$ as a function of longitudinal position z either before the interaction (blue curve) or during the interaction, at the time where the density peak reaches its maximum depth (red curve). Detailed simulation parameters are provided in appendix B.*

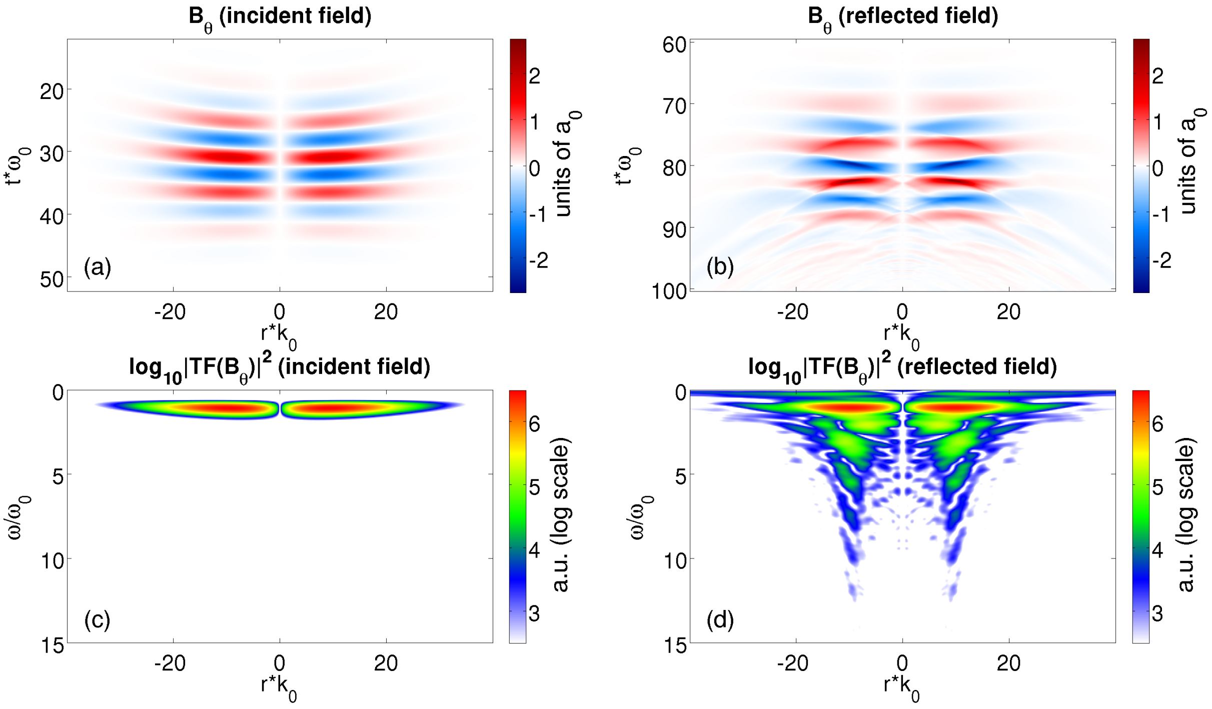

Figure 4.12: Results from the Calder-Circ *PIC simulation. (a) Incident B_θ field as a function of r and t obtained $\approx 4\ \lambda$ away from the plasma surface. (b) Reflected B_θ field as a function of r and t obtained $\approx 4\ \lambda$ away from the plasma surface. (c) Amplitude of the Fourier transform of the incident B_θ field with respect to time performed for every transverse position r. (d) Same for the reflected B_θ field. Detailed simulation parameters are provided in appendix B.*

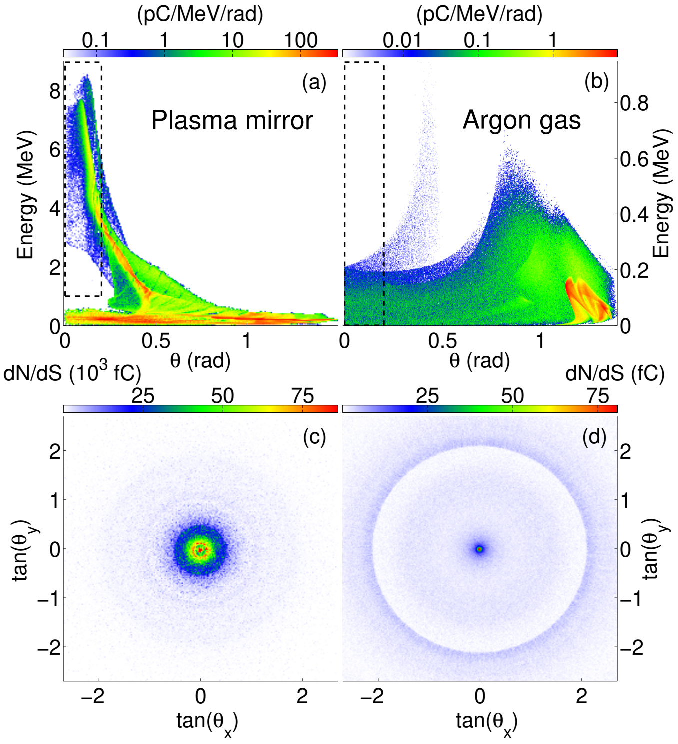

Figure 4.13: (a)-(b) Energy-angle distributions and (c)-(d) angular distributions of the obtained electron beam after interaction of the pulse with (a),(c) a plasma mirror or (b),(d) argon gas. On the top images, the electrons inside the black rectangles are the one represented in figure 4.14. On the bottom images, the angular distribution is represented in the form dN/dS, with $dS = d\tan\theta_x \times d\tan\theta_y = d(p_x/p_z) \times d(p_y/p_z)$. Detailed simulation parameters are provided in appendix B.

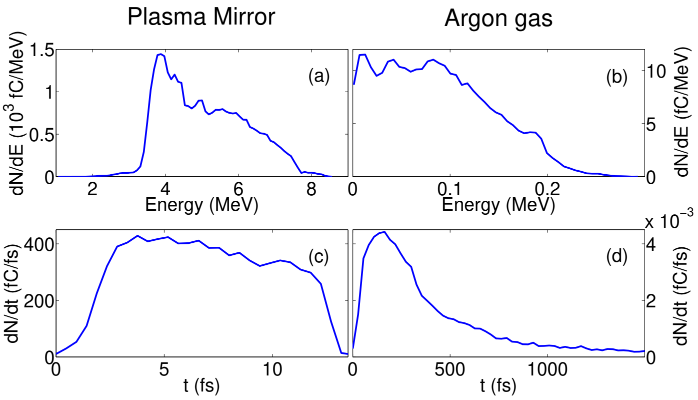

Figure 4.14: (a)-(b) Energy spectrum and (c)-(d) time distribution of a chosen subset of electrons after $145\,\mu\mathrm{m}$ *of propagation for (a),(c) the plasma mirror simulation and (b),(d) the argon gas simulation. Detailed simulation parameters are provided in appendix B.*

a normalized emittance of $\varepsilon_{n,x} = 0.18\,\mu\mathrm{m}$. Emittance in the nm range can even be obtained by further filtering the beam while still maintaining the charge at the fC level. The characteristics of this electron beam would make it useful for applications in ultrafast science. Note that to obtain the time distribution plots, electrons leaving the simulation box are assumed to travel with constant speed afterwards.

Figure 4.15(a) shows the energy of representative fast electrons along their trajectories outside the plasma. The electrons are randomly chosen among the electrons with $\theta < 0.1$ rad and $E > 1$ MeV. These electrons leave the plasma with an energy of a few hundreds of keV. Most of their final energy is thus gained by VLA in the reflected pulse. Figure 4.15(b) shows the work done by the longitudinal field, defined by $WE_z = -e\int \vec{v}.\vec{E_z}dt$, for the same electrons. Figures 4.15(a) and 4.15(b) are very similar, which proves that electrons are mainly accelerated by the longitudinal electric field of the laser, taking full advantage of the radial polarization. We can remark that the trajectories of the fastest electrons in the PIC simulation closely resemble that of the electron in figure 4.2(b), obtained with a test-particle simulation. This confirms that the high-harmonic content of the reflected pulse, which is not taken into account in the test-particle simulation, does not play a major role on the acceleration in vacuum. This result also indicates that the initial velocity given by the plasma in the push-pull mechanism is crucial for reaching high energies. Indeed, the test-particle simulations performed in section 4.1.1 have shown that the maximum attainable energy without initial velocity was ≈ 1.3 MeV.

In order to demonstrate the benefits of using a plasma mirror, we also perform PIC simulations of the acceleration of electrons injected by ionization of a low density gas target. The same laser parameters are used, except for the CEP, which is set to π so as to have the same value as in [89]. The gas target is either made of hydrogen or argon. It is infinite in the transverse direction and is $10\,\mu\mathrm{m}$ long in the longitudinal direction. The maximum electron density is chosen to be $3 \times 10^{16}\,\mathrm{cm}^{-3}$, a value for which space-charge and plasma effects are negligible [89].

In the case of hydrogen, we did not observe significant on-axis electron acceleration. This is because hydrogen has a low ionization energy, resulting in the electrons being ionized early in front of the laser pulse. Because, the normalized amplitude of the longitudinal field ($a_{0,z} = 0.7$) is smaller than the threshold value $a_{0,zc} = 1$, this leads to a case very similar to that of figure 4.1(a) and to a low final energy. In [89],

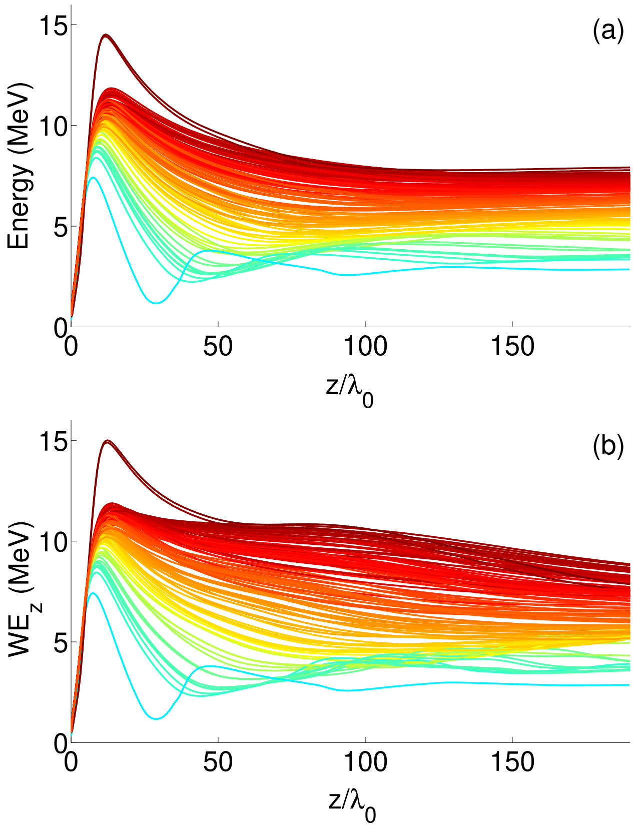

Figure 4.15: (a) Energy of representative ejected electrons as a function of their distance z from the plasma. (b) Work done by the longitudinal electric field as a function of the distance from the plasma, for these same electrons. The color of the different plots is given by the final energy of the electrons. Detailed simulation parameters are provided in appendix B.

it was reported that electrons could be accelerated by ionizing a hydrogen target, but a much tighter focusing, $w_0 = 785$ nm, that is harder to obtain in practice, was used in the simulations, resulting in a higher value for $a_{0,z}$ of ≈ 1.6.

With argon however, some deep shell electrons are generated inside the laser pulse, making it possible to accelerate on-axis electrons. Figures 4.13(b) and 4.13(d) show the energy-angle and the angular distributions of the obtained electrons. The total ejected charge is about 70 fC, three orders of magnitude lower than with the plasma mirror, and a few fC stay near the axis. The charge can nonetheless be increased by raising the initial gas density, at the cost of decreasing the electron beam quality [89]. The on-axis electrons are very well collimated but have an energy ranging from 0 to 200 keV, one to two orders of magnitude lower than with the plasma mirror. The energy spectrum and time distribution of the electrons with $\theta < 0.2$ rad after $145\,\mu\mathrm{m}$ of propagation is shown in figures 4.14(b) and (d). This corresponds to a selected charge of 1.7 fC. As can be expected from its low energy and high energy spread, the time duration of this electron bunch is already over 300 fs after $145\,\mu\mathrm{m}$ of propagation.

The main conclusion from these simulations is therefore that plasma mirrors can be used to inject electrons with ideal conditions into a radially polarized pulse, which results in a more efficient acceleration than with other proposed acceleration schemes. These results were the subject of a publication in Physical Review Letters [178].

4.2 Acceleration of an electron bunch in test-particle simulations

We have studied in the previous section the conditions leading to the efficient acceleration of an on-axis electron. We have then shown using a PIC simulation that plasma mirrors could be used to attain these ideal conditions. The longitudinal dynamics of the accelerated electrons in the PIC simulation matches that of test-particle simulations and is encouraging because it shows that high energy gains are achievable. On the other hand, the transverse electron dynamics is not as satisfactory because the final angular divergence is only marginally reduced compared to linear polarization. Yet, obtaining narrower angular distributions was one of the initial objectives of using radial polarization. In section 4.2.1, we therefore analyze using test-particle simulations electron trajectories in a 3D geometry and provide insights explaining why the electron beam is not well collimated in the previous PIC simulation. While it is often stated in the literature that the transverse fields of a radially polarized beam can help confine the electrons near the optical axis [101, 91, 113, 103], we find that it is actually the opposite in our case: the transverse fields tend to increase the electron transverse momenta and are the principal reason the electrons are deflected away from the optical axis. We then discuss in the following sections several scenarios for which narrow divergences can be obtained. In particular, using stronger longitudinal fields appears to be a promising solution.

4.2.1 Analysis of the transverse electron dynamics

We start by showing that single particle simulations can appropriately reproduce the transverse dynamics of the accelerated electron beam in the previously shown PIC simulation. We use in all test-particle simulations presented in the remainder of this chapter an exact solution to Maxwell's equations for the electromagnetic field, as described in section 2.3.3. The laser parameters correspond to the Salle Noire

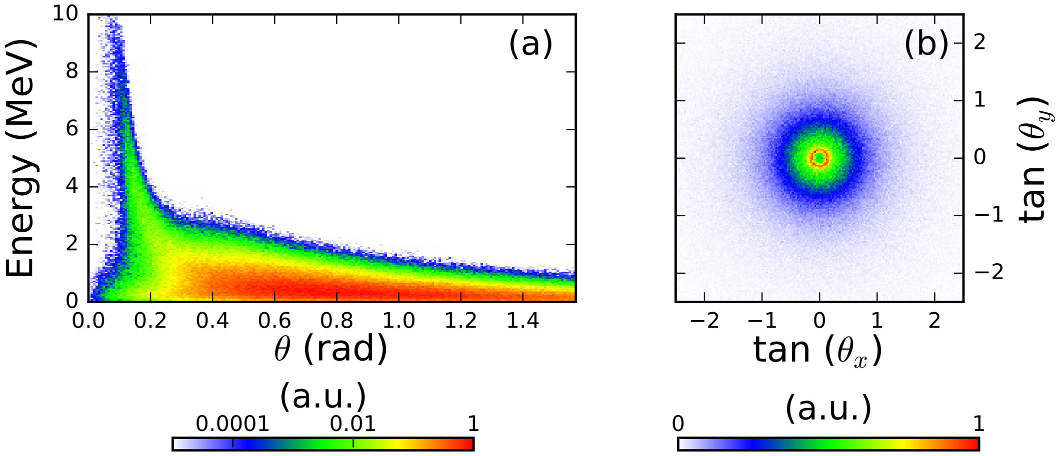

Figure 4.16: (a) Energy-angle distribution and (b) angular distribution of the electron bunch at the end of the test-particle simulation.

laser ($\lambda = 800$ nm, $w_0 = 1.5\,\mu\mathrm{m}$, $\tau = 3.5$ fs), except that the longitudinal electric field has been lowered from $a_{0,z} = 0.7$ to $a_{0,z} = 0.59$ to take into account the energy absorbed by the plasma mirror when generating the fast electrons. The value of $a_{0,z}$ for the reflected beam corresponds to a reflectivity of the plasma mirror of $\approx 70\%$, which is consistent with the typical fraction of incident laser energy used to acceleration electrons ($\approx 30\%$ [24]). The laser CEP is $\phi_{CEP} = \pi$. For simplicity, we consider a single electron bunch initially inside the laser pulse close to a zero of the electric field. The electron beam initially has a Gaussian distribution both in real and momentum space, with an adaptable mean and variance. These initial parameters are then adjusted so as to match the PIC simulation results. The test-particle simulations themselves consist in solving the motion of one million electrons with the previously described initial conditions in a radially polarized field.

Figure 4.16 shows the energy-angle and angular distribution of an electron beam with a mean initial momentum of $0.7\ m_e c$ in the longitudinal direction (corresponding to ≈ 113 keV). The initial standard deviations of the Gaussian distributions are $\sigma_z = 0.15\,\mu\mathrm{m}$ and $\sigma_{pz} = 0.7\ m_e c$ in the longitudinal direction and $\sigma_\perp = 1\,\mu\mathrm{m}$ and $\sigma_{p\perp} = 0.7\ m_e c$ in the transverse directions. These initial values are consistent with those obtained $\approx 2\,\mu\mathrm{m}$ away from the plasma surface in the PIC simulation. We observe that figure 4.16 is very similar to figures 4.13(a) and (c). This shows that test-particle simulations are able to reproduce the electron dynamics in vacuum observed in the PIC simulation. This also confirms that the generated high-harmonics do not play in significant part in the vacuum laser acceleration process at normal incidence. The fact that single particle simulations can provide accurate results is valuable because such simulations are computationally cheap, which allows us to easily vary the parameters and thus obtain useful information regarding the interaction.

We start by examining the electron transverse dynamics and collimating properties of radially polarized beams. Figures 4.17(a) and (b) show the initial and final angular distributions of the simulated electron bunch. Figure 4.17(b) is in fact the same as figure 4.16(b) except that the axes have been changed. We first note that the overall electron beam angular spread is not significantly reduced by the interaction with the radially polarized pulse. In fact, we can observe from the distributions of figures 4.17(c) and (d) that most electrons do not see a significant change in both their transverse and longitudinal momenta from the interaction. Of course, these electrons, whose kinetic energies remain low, could be filtered out in practice if the electron beam were to be used in pump-probe experiments for ultrafast science.

This is what we do in figures 4.17(e) to (h), which show the same distributions, but only considering the electrons whose final energy exceeds 1.5 MeV. This allows us to focus on the dynamics of the electrons which are actually accelerated by the radially polarized beam. For these fast electrons, the interaction leads this time to a decrease in the angular spread, by a factor ~ 2. We remark from figures 4.17(g) and (h) that both the longitudinal momentum p_z and the transverse momentum $p_\perp$ of these electrons increase during the acceleration in vacuum. This means that the reduction of the angular divergence comes from an increase in p_z (which is stronger than the increase in $p_\perp$) rather than a decrease in $p_\perp$. Still, the fast electrons are not very well collimated and, as noted in the previous section, form a ring-shaped beam with a typical angle of 150 mrad with respect to the optical axis.

We can further separate the fast electrons depending on whether they are accelerated mostly by the longitudinal field or by the transverse fields. We have indeed seen in the first chapter that electrons could be accelerated by the E_r/B_θ fields with radial polarization in the same way that electrons could be accelerated by the E_x/B_y fields with linear polarization. To achieve this separation, we calculate the work done by the E_z and E_r field in the test-particle simulation and sort the fast electrons in two populations: (i) electrons for which the work done by the E_z field is greater than that done by the E_r field and (ii) electrons for which the work done by the E_r field is higher. We find that both populations have approximately the same number of test electrons ($\sim$ 50 000 out of the 1 000 000 initial electrons in each population). The resulting distributions are shown in figure 4.18. Unsurprisingly, electrons accelerated by the E_z are emitted at much smaller angles than electrons accelerated by the E_r. Moreover, we remark that E_z accelerated electrons reach much higher energies (although this is not directly visible in figure 4.18, we can clearly observe that the highest momentum attained in figure 4.18(d) is much higher than the highest momentum attained in figure 4.18(h)). This is mainly because the initial electron distribution is optimal for acceleration by the E_z field but not for acceleration by the E_r field (the electrons are initially around a zero of the longitudinal field, which corresponds to a maximum of the transverse fields). Still, these results validate the whole idea of using radial polarization as it shows that acceleration by longitudinal field can lead to high energy electrons emitted much closer to the optical axis.

An interesting result is that the final electron beam becomes well-collimated if the simulation is performed with the fields given by the paraxial approximation, as is visible in figure 4.19. Of course, this first shows that, as explained in chapter 2, great care must be taken when choosing the electromagnetic field in single particle simulations. In particular, the paraxial approximation leads to heavily inaccurate results. Nevertheless, this simulation remains useful because it can help us understand why the electron is not well-collimated when nonparaxial fields are used.

A first hint can be obtained by looking at the correlation between the work done by the electric field and the variation in the electron momentum, both in the longitudinal and transverse directions. The corresponding distributions are plotted in figure 4.20, in the paraxial and the nonparaxial cases, for the E_z accelerated electrons with a final energy exceeding 1.5 MeV. We observe in both cases that electrons for which the work done by the E_z field is high receive a large momentum kick in the longitudinal direction, which is reasonable. On the other hand, the results in the transverse direction are more surprising. First, we observe substantial differences between the paraxial and nonparaxial simulations. Secondly, we remark that in the nonparaxial case the electrons which lose the most energy from the transverse fields

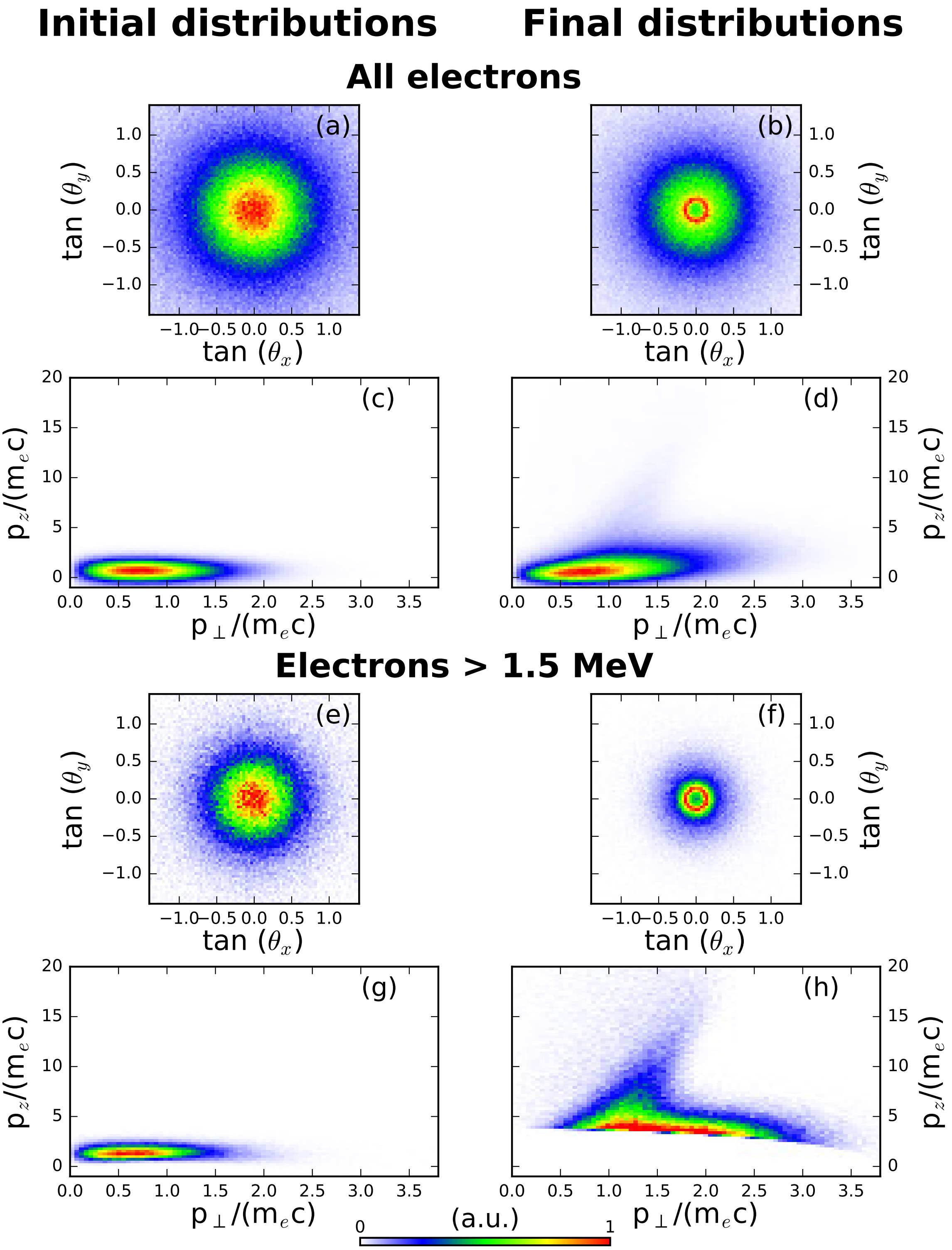

Figure 4.17: Results from a test-particle simulation reproducing the PIC simulation. (a)-(b) Electron beam angular distribution respectively before and after the interaction. (c)-(d) Electron beam momentum distribution respectively before and after the interaction. (e)-(f) Angular distribution of the electrons with a final energy greater than 1.5 MeV respectively before and after the interaction. (g)-(h) Momentum distribution of the electrons with a final energy greater than 1.5 MeV respectively before and after the interaction.

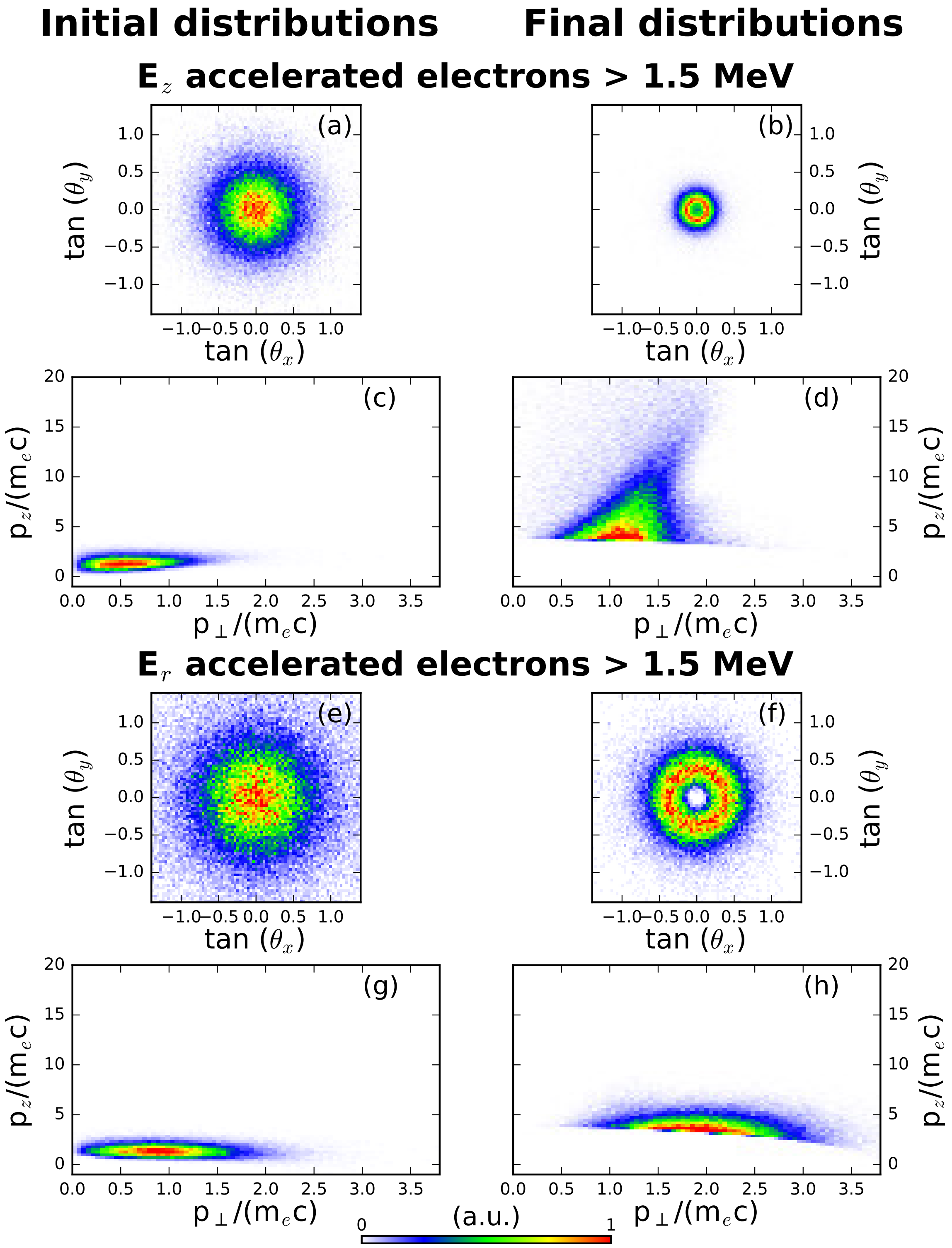

Figure 4.18: Results from a test-particle simulation reproducing the PIC simulation. (a)-(b) Angular distribution of the E_z accelerated electrons with a final energy greater than 1.5 MeV respectively before and after the interaction. (c)-(d) Momentum distribution of the E_z accelerated electrons with a final energy greater than 1.5 MeV respectively before and after the interaction. (e)-(f) Angular distribution of the E_r accelerated electrons with a final energy greater than 1.5 MeV respectively before and after the interaction. (g)-(h) Momentum distribution of the E_r accelerated electrons with a final energy greater than 1.5 MeV respectively before and after the interaction.

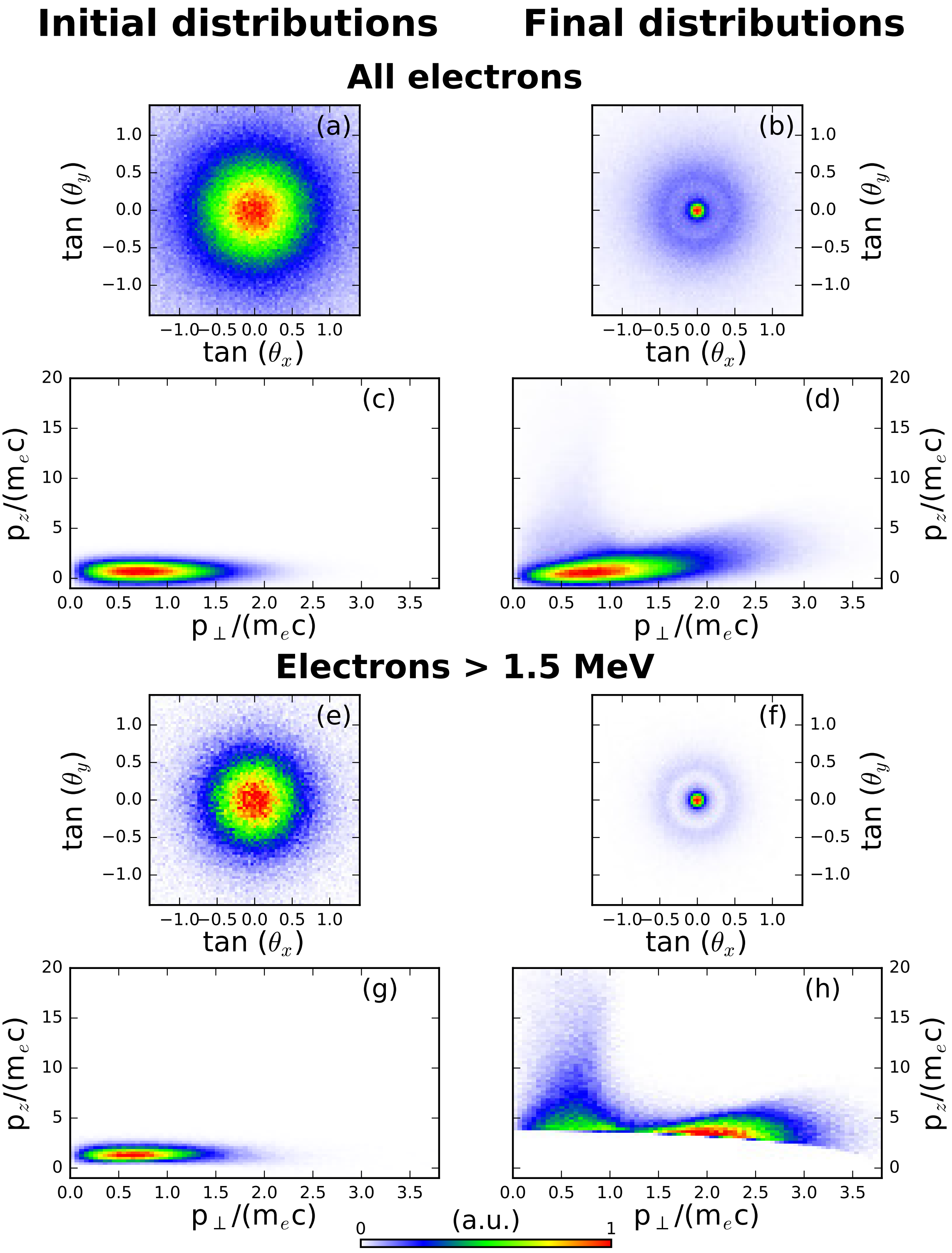

Figure 4.19: Results from a test-particle simulation using the fields given by the paraxial approximation. (a)-(b) Electron beam angular distribution respectively before and after the interaction. (c)-(d) Electron beam momentum distribution respectively before and after the interaction. (e)-(f) Angular distribution of the electrons with a final energy greater than 1.5 MeV respectively before and after the interaction. (g)-(h) Momentum distribution of the electrons with a final energy greater than 1.5 MeV respectively before and after the interaction.

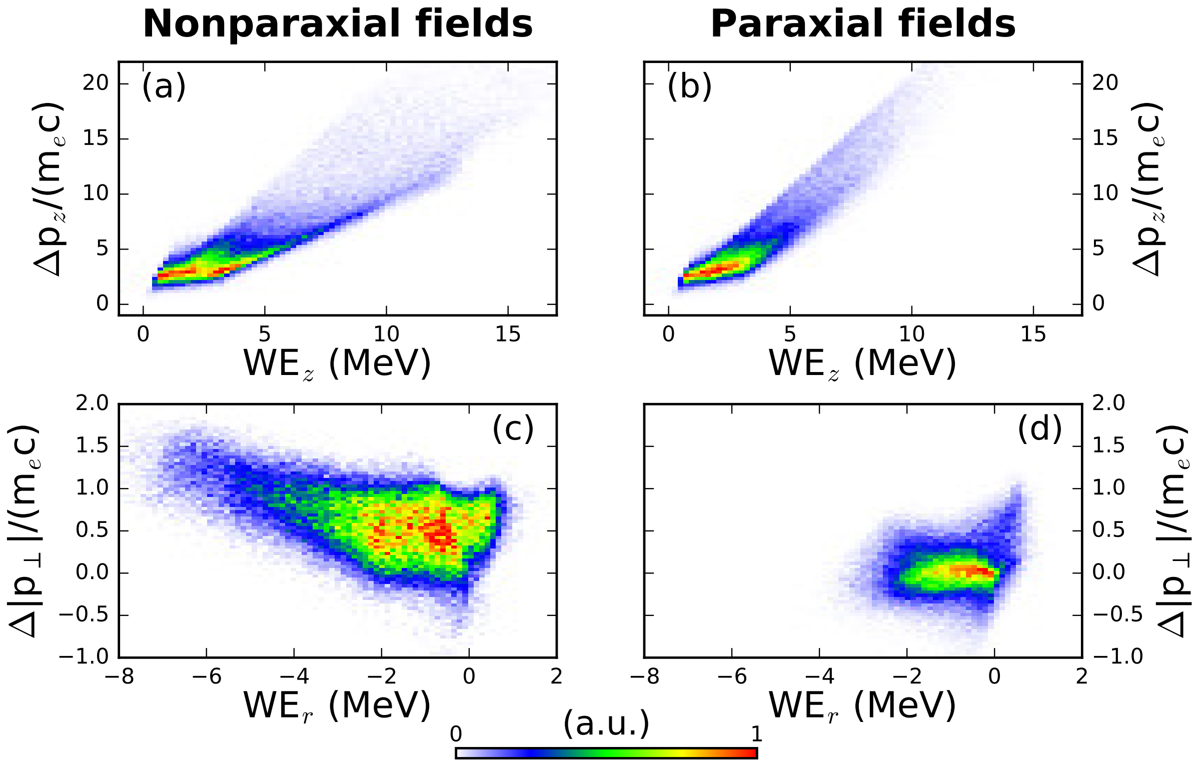

Figure 4.20: (a)-(b) Correlation between the work done by the E_z field and the variation in the electron longitudinal momentum Δp_z in a test-particle simulation using either an exact solution to Maxwell's equations (a) or the fields given by the paraxial approximation (b). (c)-(d) Correlation between the work done by the E_r field and the variation in the electron absolute transverse momentum $\Delta|p_\perp|$ in a test-particle simulation using either an exact solution to Maxwell's equations (c) or the fields given by the paraxial approximation (d). We have only considered the E_z accelerated electrons with a final energy exceeding 1.5 MeV in the distributions.

are in fact the electrons which receive the highest transverse momentum kick. This unanticipated result appears to be inconsistent with the acceleration principle with transverse fields that we have presented in section 1.5.1.1. We have indeed stated that, as illustrated in figure 4.21(a), when the transverse fields decelerate the electrons, they should also induce a decrease in the transverse momentum, which is exactly the opposite of what we observe in figure 4.20(c).

This discrepancy can be explained by the fact that figure 4.21(a) has been obtained by assuming that the transverse E_r and B_θ fields have the same amplitude ($cB_\perp = E_\perp$). This is indeed the case in the paraxial approximation, but for a nonparaxial radially polarized field, the E_r and B_θ fields do not have the same amplitude everywhere. For an ultrarelativistic electron with no transverse momentum, this means that the $\boldsymbol{v_e} \times \boldsymbol{B_\theta}$ force does not always compensate the E_r force. This results in a deflection of the fast electrons that does not exist with the paraxial fields and tends to widen the electron angular distributions [123]. For an electron with a nonzero transverse momentum, the fact that the E_r and B_θ fields do not have the same amplitude can significantly alter the result of figure 4.21(a). For instance, figure 4.21(b)

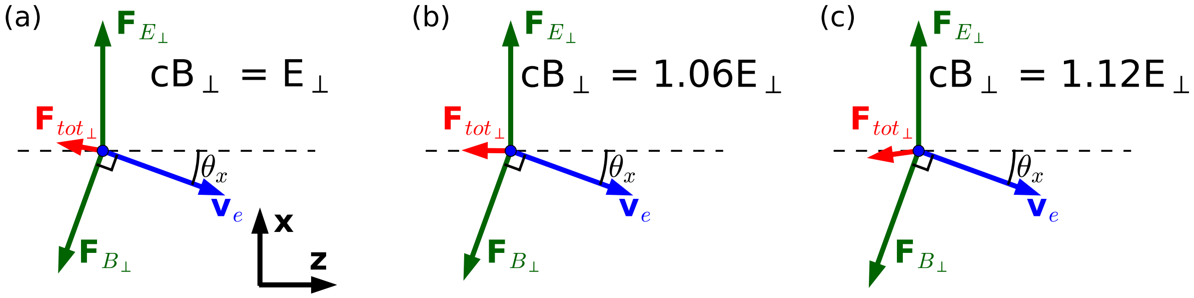

Figure 4.21: Schematic illustration of the transverse field forces acting on a relativistic electron interacting with a laser. The blue dot represents an electron moving with a velocity $\boldsymbol{v}_e$ in the direction indicated by the blue arrow. The green arrows represent either the transverse electric force $\boldsymbol{F}_{E_\perp}$ or the transverse magnetic force $\boldsymbol{F}_{B_\perp}$ acting on the electron while the red arrows represent the total transverse force $\boldsymbol{F}_{tot_\perp}$ acting on the electron. The dashed black lines show the z-axis. The electron is ultrarelativistic ($\beta_e \approx 1$) and is moving with an angle $\theta_x = 20°$ with respect to the z-axis such that it is decelerated by the transverse fields. In (a), the transverse E and B fields have the same amplitude. In (b), the B field has an amplitude which is 1.06 times that of the E field. In (c), the B field has an amplitude which is 1.12 times that of the E field.

shows a scenario in which, because the B_θ field has a larger amplitude than the E_r field, the transverse forces are decelerating the electron while leaving its transverse momentum unchanged. Similarly, figure 4.21(c) shows a scenario in which, as the B_θ field is even larger, the transverse forces are decelerating and at the same time increasing the electron transverse momentum. This worst-case scenario, which is forbidden with the fields given by the paraxial approximation, explains the unexpected correlation between the work done by the E_r field and the change in transverse momentum of figure 4.20(c) and is in fact the principal reason why the electron beam is well collimated in the paraxial simulation but not in the nonparaxial simulation (and thus in the PIC simulation). Before continuing, two relevant points can be noted:

- In figure 4.21, rather large differences between the transverse E and B fields (on the order of 10%) are necessary to obtain a case where the transverse forces are both decelerating and defocusing. This is because a large angle of $20°$ was chosen for θ_x for illustration purposes. In reality this angle can be much smaller, in which case lesser differences between the transverse E and B fields can result in the same situation.

- In principle we could also have the ideal case where the transverse fields are both accelerating the electron and reducing its transverse momentum. However, we observe that this scenario very rarely occurs in practice in the typical trajectories of the simulations presented here.

To illustrate the difference between the paraxial and the nonparaxial cases, we now study the trajectory of a typical E_z accelerated electron. To simplify the analysis, we consider a plane trajectory for which $y = 0$ at all times. At $t = 0$ (i.e. at the focus of the laser pulse), the electron is initially at $x \approx 228$ nm, $y = 0$ and $z \approx 6.46$ nm with an initial momentum $p_x \approx 0.48 m_e c$, $p_y = 0$ and $p_z \approx 1.05 m_e c$. This corresponds to an initial kinetic energy of ≈ 270 keV and an initial angle θ_x of $\approx 24.5°$ with respect to the x-axis.

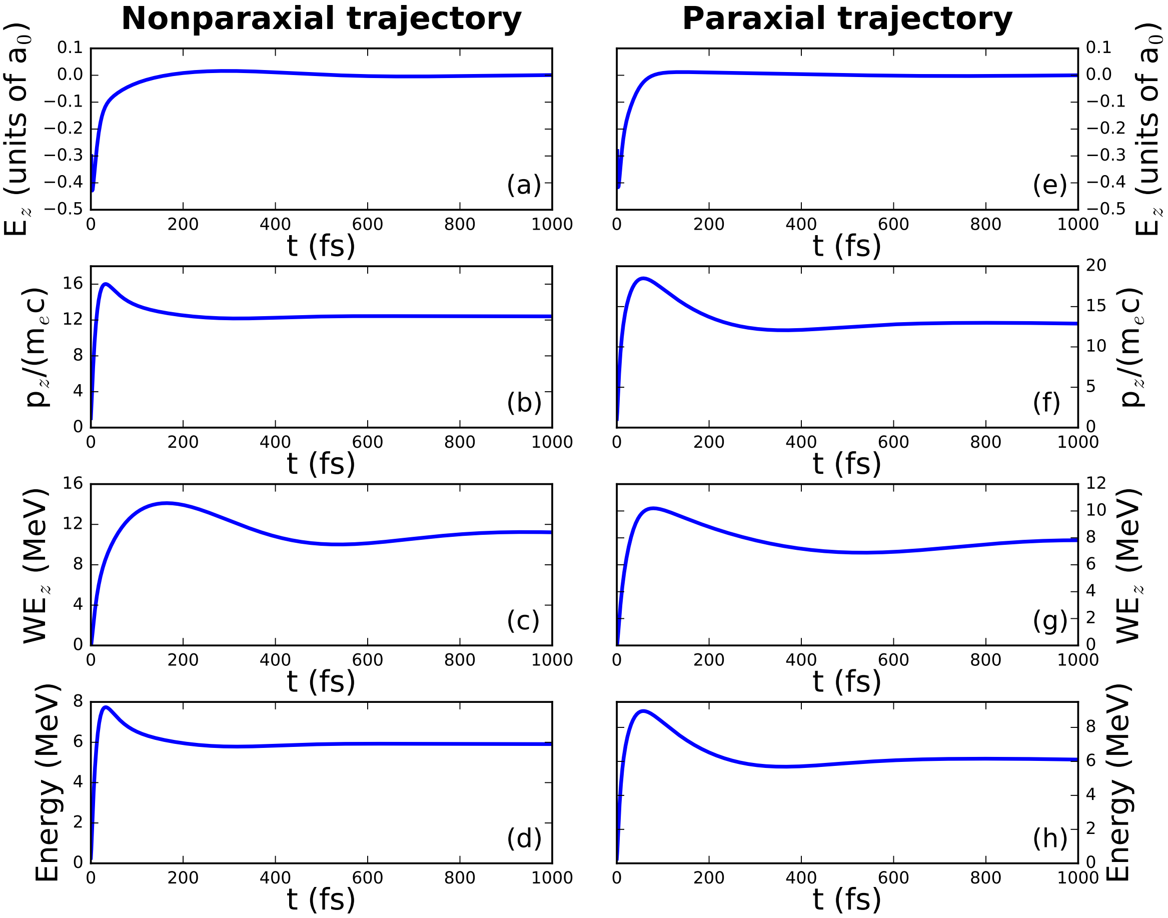

Figure 4.22: Longitudinal dynamics of a typical E_z accelerated electron in a radially polarized pulse. (a),(e) E_z field seen by the electron as a function of time. (b),(f) Longitudinal electron momentum as a function of time. (c),(g) Work done by the E_z field on the electron as a function of time. (d),(h) Electron kinetic energy as a function of time. Panels (a)-(d) have been obtained with an exact solution to Maxwell's equation. Panels (e)-(h) have been obtained with fields given by the paraxial approximation.

The motion of this electron is then solved either with the fields which are an exact solution to Maxwell's equations or with the paraxial fields. We use the same laser parameters as in the previously presented simulations (corresponding to the Salle Noire laser).

Figure 4.22 shows the longitudinal dynamics of the electron. It is very similar in both cases. The electron is initially accelerated by the E_z field up to ≈ 8 MeV before entering a decelerating phase. The exact time at which the electron begins its deceleration is different in the paraxial and the nonparaxial simulations, but the electron has in both cases a final energy of ≈ 6 MeV. We remark in particular that the curves for the longitudinal momentum, the kinetic energy and the work done by the E_z field are all very much alike, which shows that, for this electron, the interaction is dominated by the longitudinal field.

Figure 4.23 shows the transverse dynamics of the electron. There are in this image significant differences between the nonparaxial and paraxial trajectories. At first sight, the plots of E_x (E_r) and B_y (B_θ) as a function of time are all very similar. However, we observe that in the nonparaxial case the normalized amplitude of the transverse magnetic field seen by the electron tends to be higher than that of the transverse electric field by up to ≈ 0.02 (in units of a_0). Of course this is not the case in the paraxial simulation where we have by construction $E_r = cB_\theta$.

In the two trajectories, the transverse fields are initially negative and, consequently, the transverse electron momentum rapidly increases in the first few femtoseconds from $\sim 0.5m_ec$ to $\sim m_ec$. During these first instants, the electron is not yet fully relativistic and the E_x force dominates to $\boldsymbol{v}_e \times B_y$ force. In this case the transverse forces are both accelerating (the work done by the E_x field is positive) and defocusing (the transverse momentum increases), which is an expected situation.

Then, the sign of the transverse fields changes and they therefore become decelerating (the work done by the E_x field decreases). At this point, the evolution of the transverse momentum is radically different in the two trajectories. In the nonparaxial trajectory, the B_y field is stronger than the E_x field and the scenario represented in figure 4.21(c) occurs: even though the transverse fields are decelerating, they increase the electron transverse momentum, which rises almost up to $\sim 2m_ec$. This scenario is forbidden in the paraxial trajectory, and only the case depicted in figure 4.21(a) can occur: as soon as the sign of the transverse field changes, they become decelerating and at the same time decrease the electron momentum. The transverse momentum in the nonparaxial trajectory eventually stabilizes around $\sim 1.7\, m_ec$ while in the paraxial trajectory it stabilized around $\sim 0.75\, m_ec$. This results in an emission angle with respect to the optical axis $\theta_x \approx 7.9^\circ$ in the nonparaxial case and $\theta_x \approx 3.4^\circ$ in the paraxial case.

This example illustrates the fundamental differences between the two simulations presented in this section. It also sheds light on the reason why the fast electrons are not very well collimated as they are accelerated by a radially polarized beam: at phases where we could naively expect the transverse fields to be focusing, we find that they can in fact be defocusing due to the amplitude difference between the E_r and B_θ fields, which leads to larger than expected transverse electron momenta. We discuss in the following sections several possibilities for obtaining narrow divergence electron beams with radial polarization.

4.2.2 Narrow divergence from better initial beam quality

We study in this section the effect of varying the initial electron beam properties, namely its transverse extent in real space and in momentum space, with the following question in mind: does improving the initial electron beam quality also result in an improvement of the accelerated beam properties?

We can first notice that the longitudinal field is responsible for the longitudinal momentum gained by the electron, while the transverse fields are responsible for the transverse momentum gained by the electron. Thus, one way to increase the ratio between p_z and $p_\perp$ (which corresponds to the emission angle) is to reduce the effect of the transverse fields. This can be achieved by having the electrons initially located closer to the optical axis, where the E_z field is maximum and the E_r/B_θ fields are weak. To illustrate this, we perform the same simulation as in the previous section, except that the initial transverse positions are all divided by 10. This corresponds to an initial standard deviation in the transverse direction of $\sigma_\perp = 100$ nm, which is now much smaller than the beam waist ($1.5\,\mu$m).

The results of this simulation are displayed in figure 4.24. We indeed find in this case that the transverse momentum gained by the fast electrons is smaller, which results in an electron beam with a narrow angular spread. Once again, the collimation of the electron beam does not come from a decrease in its transverse momentum, but from a stronger increase in its longitudinal momentum than in its transverse

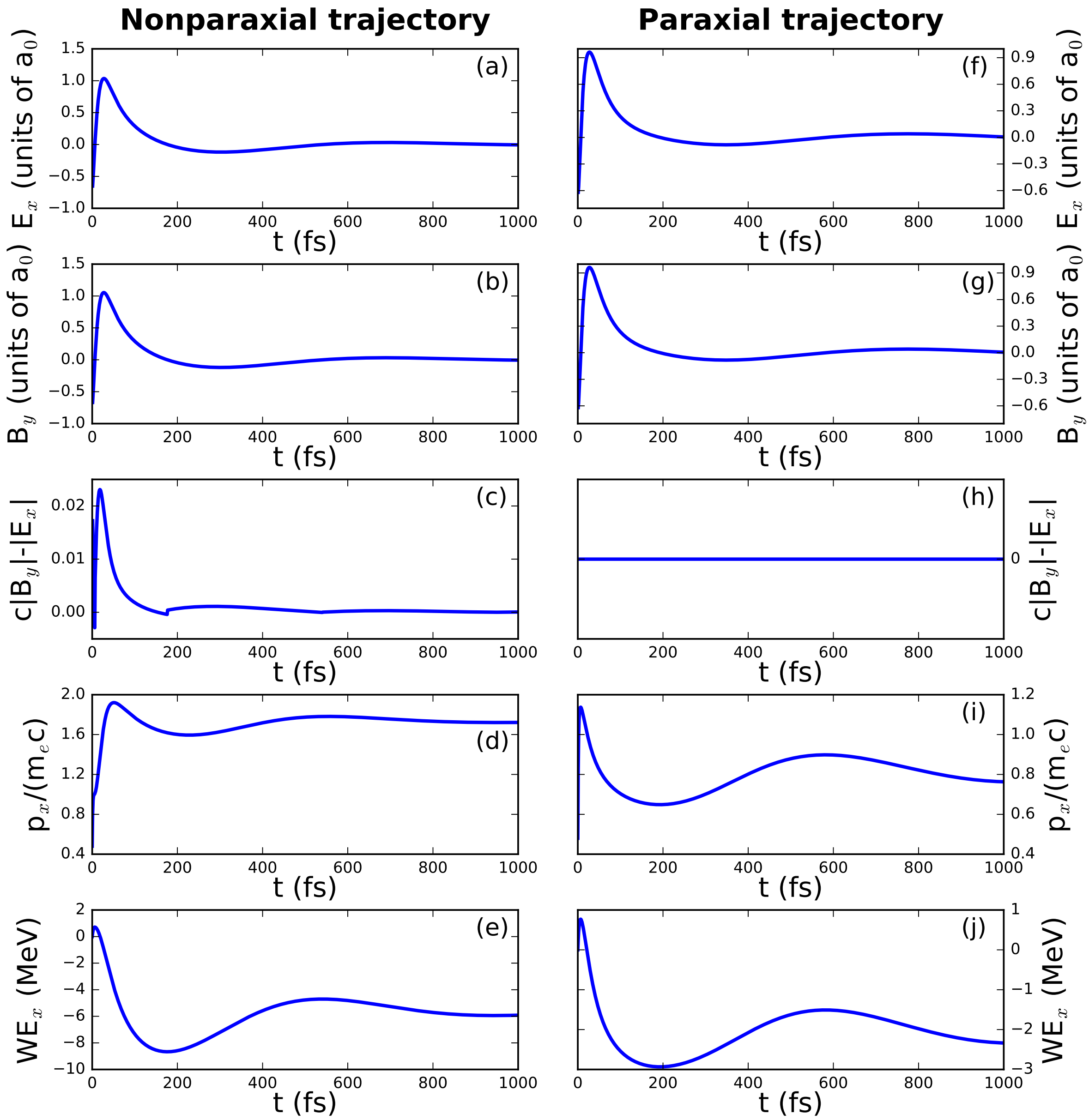

Figure 4.23: Transverse dynamics of a typical E_z accelerated electron in a radially polarized pulse. (a),(f) E_x (E_r) field seen by the electron as a function of time. (b),(g) B_y (B_θ) field seen by the electron as a function of time. (c),(h) Difference between the absolute values of the B_y and E_x fields seen by the electron as a function of time. (d),(i) Transverse electron momentum as a function of time. (e),(j) Work done by the E_x (E_r) field on the electron as a function of time. Panels (a)-(e) have been obtained with an exact solution to Maxwell's equation. Panels (f)-(j) have been obtained with fields given by the paraxial approximation.

momentum. This confirms that the transverse fields of a radially polarized beam tend to be defocusing, even for electrons located very close to the optical axis. This simulation nevertheless shows that it is in principle possible to obtain few-MeV electron beams with good quality from VLA with radial polarization, provided that the electron beam is initially very close to the optical axis, with a transverse extent that is much smaller than the laser beam waist. However, such small widths cannot be obtained with the plasma mirror injection method described in section 4.1.3, precisely since in this case the electrons are ejected with a transverse extent that is on the order of the beam waist.

We also perform a simulation with an initially well-collimated electron beam. We use the same parameters as in the previous section except that the transverse momenta are all divided by 10. This corresponds to an initial standard deviation in the transverse direction of $\sigma_{p\perp} = 0.07\ m_e c$, which is now much smaller than the average momentum in the longitudinal direction ($0.7\ m_e c$). Results from this simulation are shown in figure 4.25. We find that reducing the transverse momenta indeed results in an overall narrower angular spread. However:

- The final beam is more divergent than the initial beam. This is because the transverse fields increase the initially very small transverse momenta.
- The angular spread of the fast electrons is only marginally reduced compared to the simulation of the previous section. They in particular still form a ring-shaped beam with a typical angle of 150 mrad with respect to the optical axis.

Overall, we find that improving the initial beam quality can indeed result in better final beam properties. Of course, these parameters cannot directly be controlled when plasma mirror injectors are used and so this does not provide a practical way to reduce the electron beam divergence with this injection method.

More generally, we can remember from this section that the final distributions of an electron bunch accelerated by a radially polarized field can be quite sensitive to the initial injection conditions. This means that test-particles simulations cannot be used to predict the result of experiments (or of PIC simulations) because the exact initial injection conditions with plasma mirrors, which result from intricate laser-plasma interaction processes and depend on the experimental parameters in a nontrivial way, cannot be easily forecast.

4.2.3 Narrow divergence from more energetic electrons

Another way to obtain collimated beams is to exploit the correlation between the energy and emission angle of VLA accelerated electrons. We have indeed observed in the PIC simulation that the fastest electrons tend to be emitted closer to the optical axis, because they acquire a larger longitudinal momentum. We could thus expect that using laser parameters such that electrons are accelerated to much larger energies would result in narrower angular spreads. We find that it is indeed the case in test-particle simulations.

For instance, we show in figure 4.26 results from a simulation performed with a much more intense radially polarized laser. The parameters are the same as in section 4.2.1, expect that the normalized amplitude of the E_z field is increased from $a_{0,z} = 0.59$ to $a_{0,z} = 5.9$ ($a_{0,r}$ is accordingly increased from 1.49 to 14.9). This corresponds to increasing the pulse energy by a factor 100. Note that, unlike in the previous figures, the bottom panels in figure 4.26 ((e) to (h)) do not show the electrons with a final energy greater than 1.5 MeV because virtually all electrons reach MeV energies with such a high intensity laser.

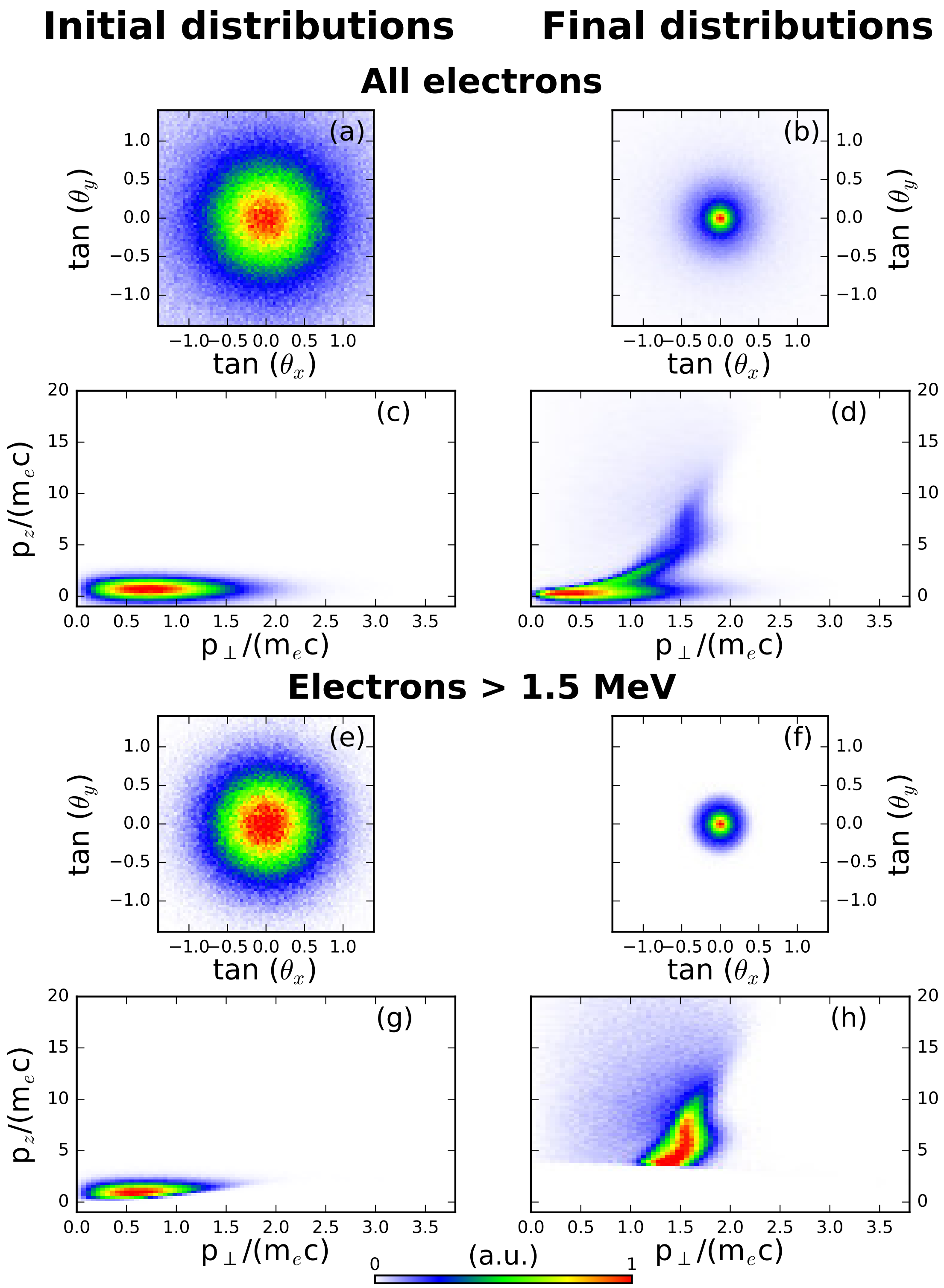

Figure 4.24: Results from a test-particle simulation with the electrons initially located very close to the optical axis. (a)-(b) Electron beam angular distribution respectively before and after the interaction. (c)-(d) Electron beam momentum distribution respectively before and after the interaction. (e)-(f) Angular distribution of the electrons with a final energy greater than 1.5 MeV respectively before and after the interaction. (g)-(h) Momentum distribution of the electrons with a final energy greater than 1.5 MeV respectively before and after the interaction.

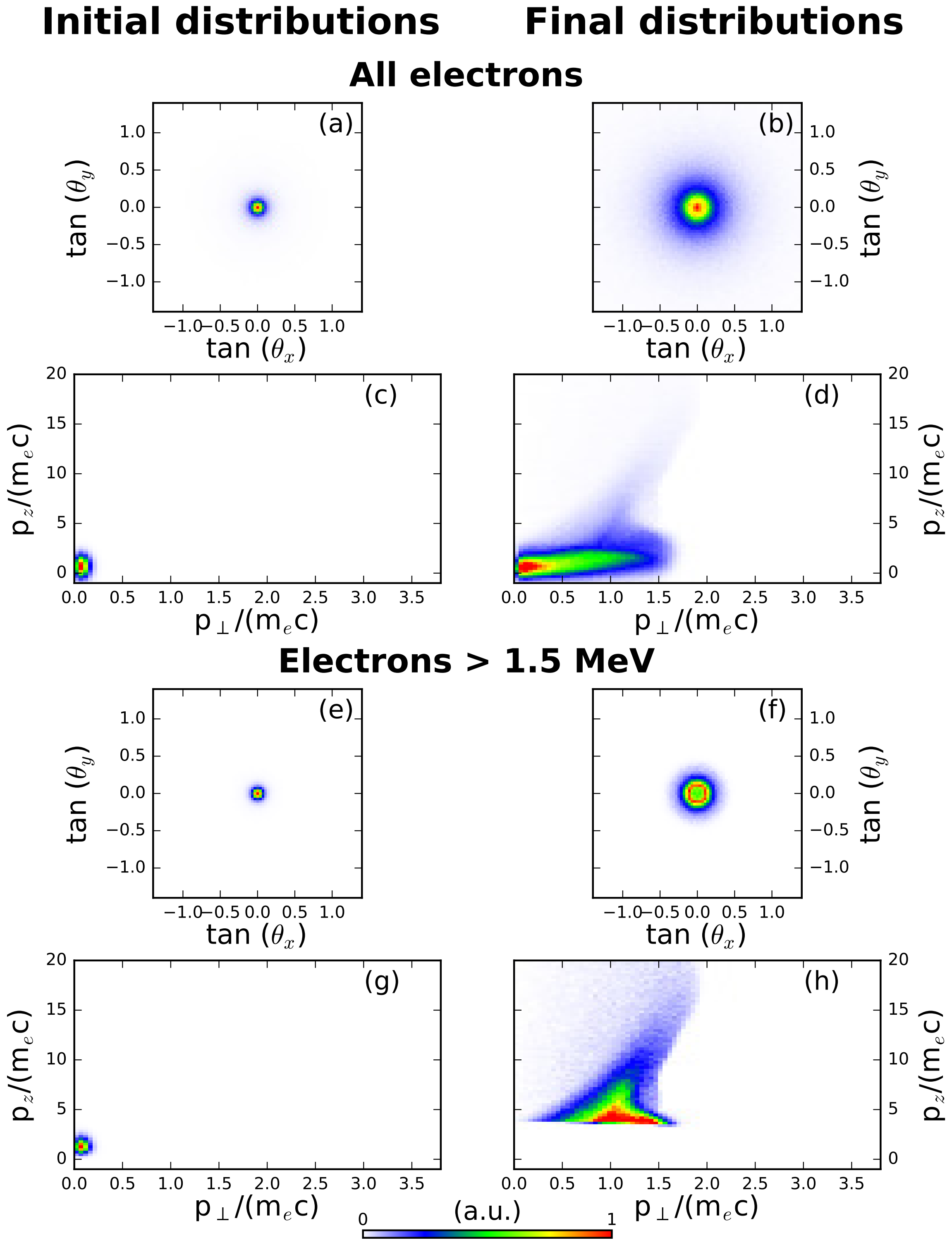

Figure 4.25: Results from a test-particle simulation with an initially well-collimated electron beam. (a)-(b) Electron beam angular distribution respectively before and after the interaction. (c)-(d) Electron beam momentum distribution respectively before and after the interaction. (e)-(f) Angular distribution of the electrons with a final energy greater than 1.5 MeV respectively before and after the interaction. (g)-(h) Momentum distribution of the electrons with a final energy greater than 1.5 MeV respectively before and after the interaction.

Instead, we show in figures 4.26(e) to (h) the electrons for which the work done by the E_z field is greater than the work done by the E_r field.

We find that the angular divergence is greatly reduced when the laser intensity is increased. We generally observe that both the transverse and longitudinal momenta tend to be increased when $a_{0,z}$ is raised from 0.59 to 5.9. However, the ratio between p_z and $p_\perp$ at the end of the simulation for the E_z accelerated electrons is greatly improved when increasing the laser intensity, explaining why we obtain in this case an electron beam with a very narrow divergence.

In contrast to the previous section, this method for reducing the angular spread can be applied to plasma mirror injectors. We just need in principle to focus an ultraintense laser pulse at normal incidence on an overdense plasma with a sharp density gradient. We will see in section 4.3.3 that such high laser intensities can indeed lead to extremely peaked electron angular distributions in PIC simulations.

This acceleration regime was in fact previously observed in PIC simulations with the ionization of a low-density gas injection method [102]. In this article (which was already mentioned in the first chapter), the authors focus a radially polarized laser with $w_0 = 3\lambda$ and a peak power ranging between 2 PW and 100 PW ($a_{0,z}$ between $\approx$ 15 and $\approx$ 100) onto a low-density nanosphere with a radius of $\lambda/4$ to generate high quality GeV electron beams. We can remark that these PIC simulations combine two of the methods that we have presented to obtain collimated electrons: the use of high intensity lasers to increase the longitudinal electron momenta and the use of small initial transverse sizes to reduce the defocusing effect of the transverse fields. Even though these parameters are probably difficult to attain experimentally, they lead in the best cases to angular divergences of the order of 2°.

4.2.4 Narrow divergence from ponderomotive electrons

Finally, we point out in this section that peaked angular distributions can also originate from low-energy electrons. Here, "low-energy" refers to electrons whose final energy is much lower than the theoretical maximum energy gain for given laser parameters. This corresponds for example to the electrons forming a sharp peak in the specular direction in the PIC simulation with injection by ionization of argon gas presented in section 4.1.3 (see figure 4.13(d)). The energy of these electrons (at most ≈ 200 keV) is indeed much lower than the maximum possible energy gain with the Salle Noire laser (≈ 29 MeV).

It is also possible to obtain collimated MeV electron beams in this manner. As an illustration, we show in figure 4.27 results from a simulation performed with parameters corresponding to the UHI100 laser: $\lambda = 800$ nm, $w_0 = 3.1\,\mu\text{m}$, $\tau = 24$ fs and $a_{0,z} = 0.75$. The initial electron distribution is the same as in the previous sections except that the standard deviation in the transverse spatial direction has been raised from $1\,\mu\text{m}$ to $2\,\mu\text{m}$: the mean initial momentum is $0.7\ m_e c$ in the z-direction, the standard deviations are $\sigma_z = 0.15\,\mu\text{m}$, $\sigma_{pz} = 0.7\ m_e c$, $\sigma_\perp = 2\,\mu\text{m}$ and $\sigma_{p\perp} = 0.7\ m_e c$. In this test-particle simulation, the electron bunch is as previously initially at focus ($z = 0$) and at the optimal phase of the laser. However, it is this time located 4 optical cycles in front of the temporal center of the pulse envelope.

We find that the final electron beam is well-collimated. Looking at the angle-energy distribution of figure 4.27(a), we remark that the electrons emitted with very small angles (visible on the bottom left corner of this image) have an energy ranging between ≈ 1 MeV and ≈ 5 MeV, which is much lower than the maximum final energy reached in the simulation (≈ 50 MeV) and the theoretical maximum energy gain (≈ 114 MeV for the ≈ 13.5 TW laser considered here).

Figure 4.28 allows us to compare the initial and final distributions in this simulation. We observe that the angular spread is indeed reduced during the acceleration. We can note from figures 4.28(c) and

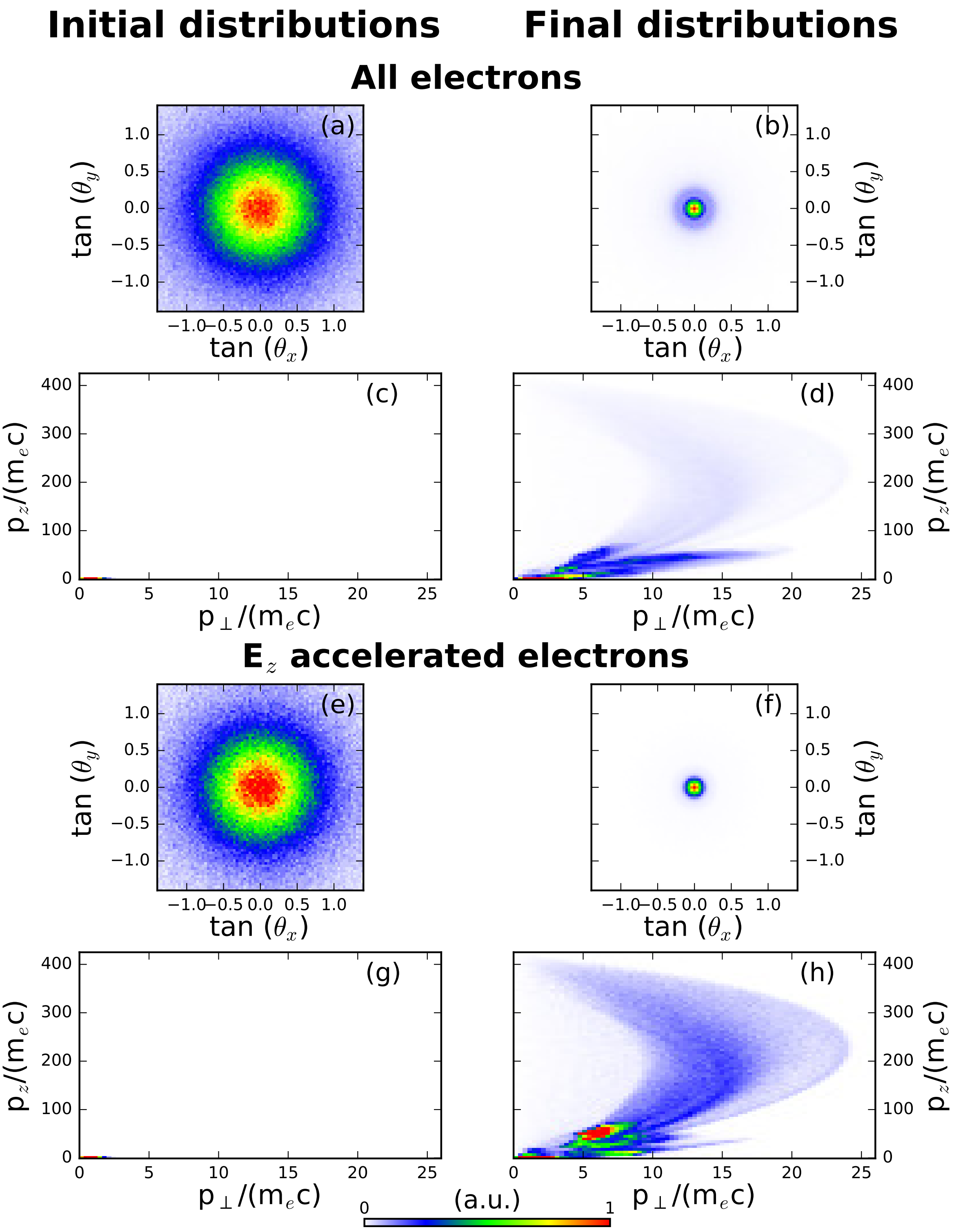

Figure 4.26: Results from a test-particle simulation with a more intense radially polarized pulse. (a)-(b) Electron beam angular distribution respectively before and after the interaction. (c)-(d) Electron beam momentum distribution respectively before and after the interaction. (e)-(f) Angular distribution of the electrons with a final energy greater than 1.5 MeV respectively before and after the interaction. (g)-(h) Momentum distribution of the electrons with a final energy greater than 1.5 MeV respectively before and after the interaction.

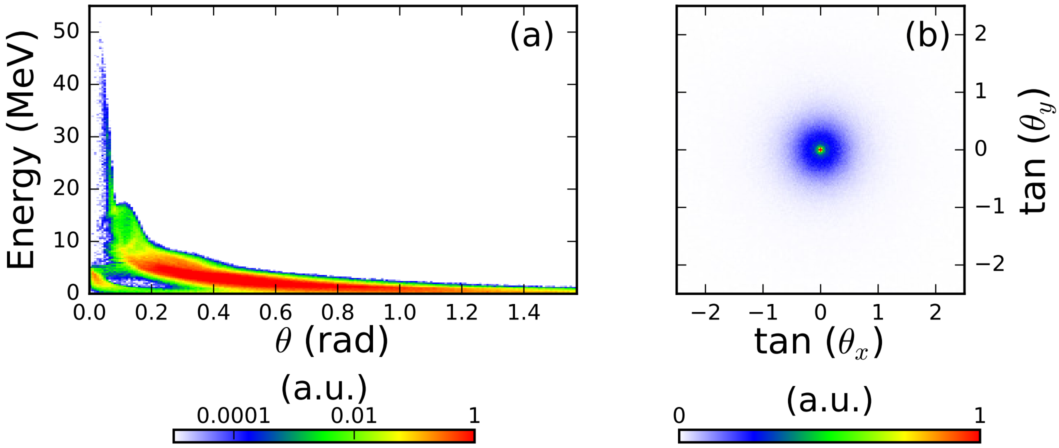

Figure 4.27: (a) Energy-angle distribution and (b) angular distribution of the electron bunch at the end of a test-particle simulation with parameters corresponding to the UHI100 laser.

(d) that most electrons will see an increase in both their transverse and longitudinal momentum during their interaction with the radially polarized pulse. However, we observe that the electrons emitted less than 50 mrad from the specular direction, which are isolated in figures 4.28(e) to (h), see a significant decrease in their transverse momentum as well as a modest increase in their longitudinal momentum. This is the only scenario in which we observe that the transverse fields of a radially polarized beam can reduce the electron transverse momenta. If a sufficient number of electrons are collimated in this manner, the angular distribution becomes peaked around the laser propagation direction, which is what occurs in this simulation.

By analyzing electron trajectories, we can remark that these collimated low-energy electrons tend to explore many optical cycles of the laser and therefore correspond to ponderomotively accelerated electrons. With linear polarization, we have previously seen that electrons subject to the ponderomotive force tend to be isotropically scattered in the transverse direction, which leads to angular distributions containing a hole in the laser propagation direction. With radial polarization, there is an intensity minimum around $r = 0$, which means that the ponderomotive force can also push the electrons towards the optical axis. This could explain why the lower energy electrons can form a sharp peak in the angular distribution. Several points can be noted.

- This method for obtaining narrow divergences is not very efficient. Indeed, attaining a desired energy level requires a laser capable of accelerating electrons to much larger energies.
- It is possible for an electron to see many laser oscillations without being emitted in the direction of laser propagation. Likewise, it is possible for an electron bunch to be accelerated to low energies without resulting in a narrow divergence beam. The exact initial conditions leading to peaked angular distributions in this regime appear to be nontrivial and have not been studied thoroughly in this thesis. They could be the subject of future work.
- This regime (in which the lower energy electrons give rise to low angular spreads) can also occur

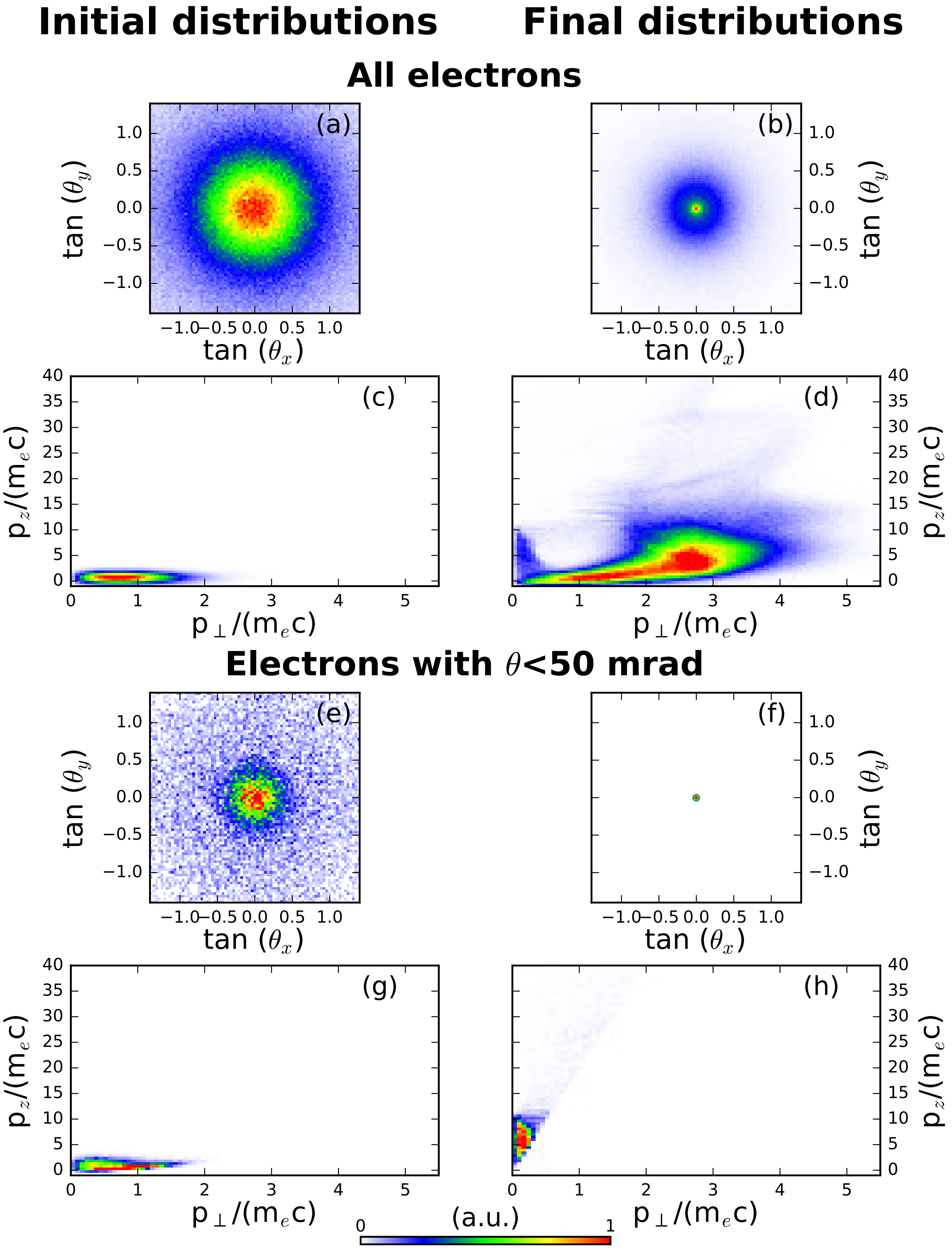

Figure 4.28: Results from a test-particle simulation with parameters corresponding to the UHI100 laser. (a)-(b) Electron beam angular distribution respectively before and after the interaction. (c)-(d) Electron beam momentum distribution respectively before and after the interaction. (e)-(f) Angular distribution of the electrons with a final angle with respect to the optical axis smaller than 50 mrad respectively before and after the interaction. (g)-(h) Momentum distribution of the electrons with a final angle with respect to the optical axis smaller than 50 mrad respectively before and after the interaction.

with few-cycle lasers. This is not inconsistent with the presence of a ponderomotive force which, as we have seen in section 1.5.1.6, still has relevance for extremely short pulse durations.

- These lower energy electrons accelerated in the laser propagation direction gain most of their energy from the E_z field, which therefore seems to play a role in this regime.
- This regime can also be observed with azimuthally polarized beams, which also possess a minimum in the intensity distribution around $r = 0$. In this case of course the electrons cannot be accelerated by the E_z field (which is zero everywhere), which means that there are differences between the lower energy electron trajectories in radial and azimuthal polarization.

4.2.5 Conclusion

We have studied in this section the transverse dynamics of vacuum laser accelerated electrons in a radially polarized laser. We have noted that the transverse fields have an overall negative effect on the acceleration as they tend to deflect the electrons and widen the resulting angular distributions. We have then presented several scenarios in which narrow divergences can be obtained. This can occur when electrons are accelerated to large energies using very intense lasers or, oppositely, can also result from the lower energy electrons which do not experience the VLA regime. We have also pointed out that the acceleration process, and in particular its transverse dynamics, is sensitive to the initial injection conditions.

4.3 PIC simulations with other laser parameters

We have presented in section 4.1.3 a PIC simulation showing that electrons are ideally injected in the reflected pulse when an intense radially polarized laser is focused at normal incidence on a plasma mirror. In this section, we present results from similar PIC simulations at normal incidence performed with different laser parameters. We first study the influence of the CEP in section 4.3.1. Then we present in section 4.3.2 results from a simulation with a many-cycle pulse, using parameters corresponding to the UHI100 laser. Finally, we examine in section 4.3.3 results from simulations performed with higher intensity lasers, which demonstrate that peaked angular distributions can be obtained in this regime.

4.3.1 Effect of the CEP

We show in this section results from 4 PIC simulations performed with different values of the CEP. We use in the simulations a gradient scale length $L = \lambda/7$ and laser parameters corresponding to the Salle Noire laser: $\lambda = 800$ nm, $a_{0,z} = 0.7$, $w_0 = 1.5\,\mu\mathrm{m}$ and $\tau = 3.5$ fs. The values of the CEP of the reflected pulse are $-\pi/2$, 0, $\pi/2$ and π. The corresponding waveforms of the longitudinal field are shown in figures 4.29(c), (f), (i) and (l). We can note that the simulation with $\phi_{CEP} = -\pi/2$ is the simulation that was presented in section 4.1.3. Final angle-energy and angular distributions from these simulations are displayed in figure 4.29.

We first find that changing the laser CEP does not alter the main qualitative results: electrons are still ejected from the plasma and ideally injected into the reflected laser pulse where they can receive energy gains up to several MeV from the E_z field. We also always observe the correlation between the energy of the fast electrons and their emission angle, with the fastest electrons emitted closer to the

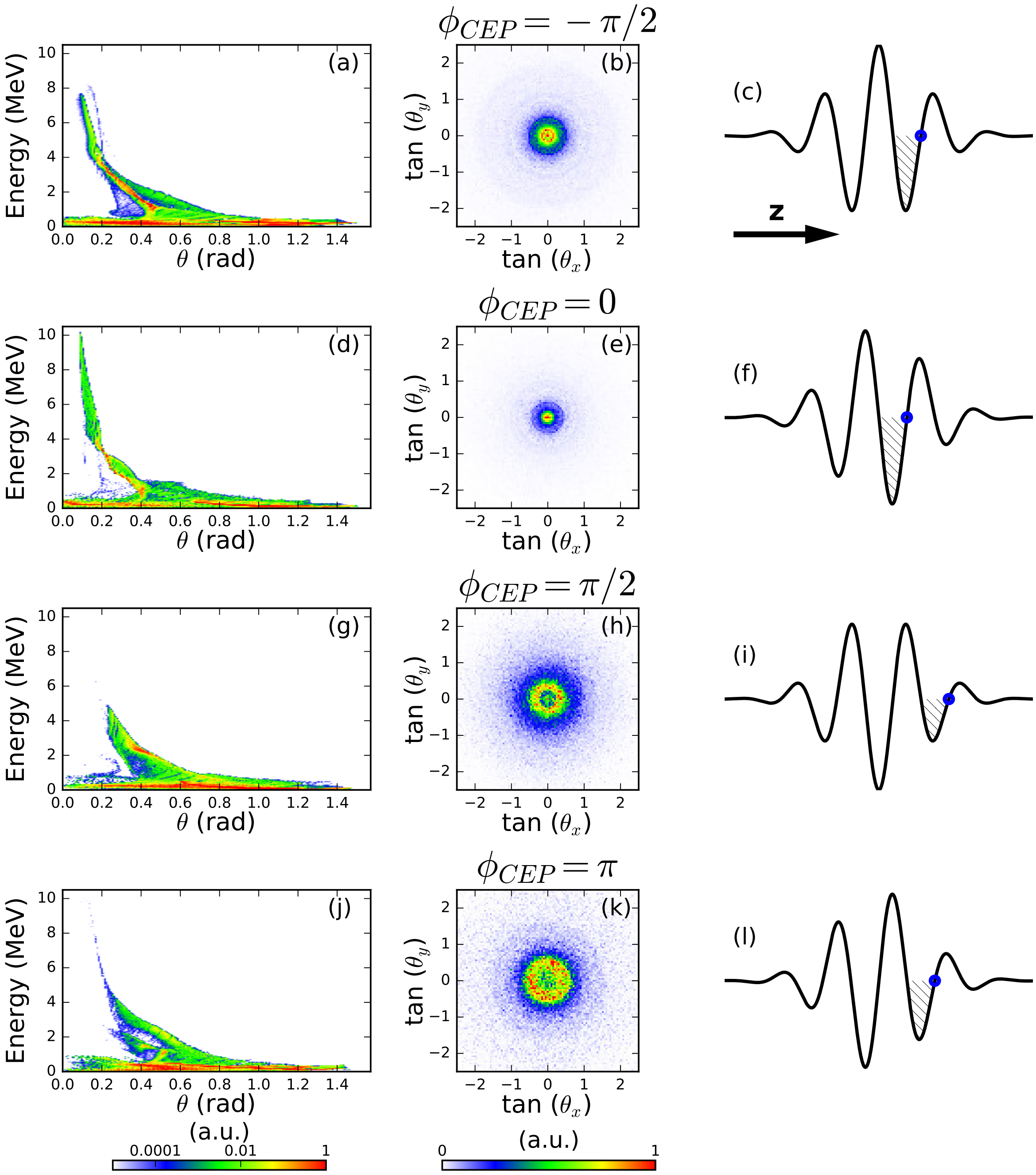

Figure 4.29: Results from PIC simulations at normal incidence for 4 different values of the CEP. (a),(d),(g),(j) Final angle-energy distribution respectively for $\phi_{CEP} = -\pi/2$, $\phi_{CEP} = 0$, $\phi_{CEP} = \pi/2$ and $\phi_{CEP} = \pi$. (b),(e),(h),(k) Final angular distribution respectively for $\phi_{CEP} = -\pi/2$, $\phi_{CEP} = 0$, $\phi_{CEP} = \pi/2$ and $\phi_{CEP} = \pi$. (c),(f),(i),(l) Waveform of the reflected E_z field (excluding its high-harmonic content) respectively for $\phi_{CEP} = -\pi/2$, $\phi_{CEP} = 0$, $\phi_{CEP} = \pi/2$ and $\phi_{CEP} = \pi$. The blue dots show the the first position at which a significant amount of electrons are ejected from the plasma in the simulations. The hatched area shows the corresponding initial accelerating half-cycle. Detailed simulation parameters are provided in appendix B.

specular direction. However, we also note that there are substantial quantitative differences in the final distributions depending on the value of the CEP. For instance, the maximum reached energy varies from ≈ 5 MeV for $\phi_{CEP} = \pi/2$ to ≈ 10 MeV for $\phi_{CEP} = 0$. The simulations where higher energies are attained also correspond to simulations where the final angular divergence is narrower, consistently with the fact that the fastest electrons are accelerated closer to the specular direction. Consequently, while the total ejected charge is similar in all simulations (from ≈ 45 pC for $\phi_{CEP} = \pi/2$ to ≈ 60 pC for $\phi_{CEP} = -\pi/2$), there are very large variations in the number of MeV electrons emitted at an angle smaller than 200 mrad, which are the electrons that would be most useful for applications: ≈ 3.3 pC for $\phi_{CEP} = -\pi/2$, ≈ 5.5 pC for $\phi_{CEP} = 0$, ≈ 11 fC for $\phi_{CEP} = \pi/2$ and ≈ 100 fC for $\phi_{CEP} = \pi$.

We can remark that the values of the CEP that we had identified as being close to optimal using on-axis test-particle simulations ($\phi_{CEP} = \pi/2$ and $\phi_{CEP} = \pi$, see section 4.1.2.2) lead in this case to the least efficient acceleration. This can be explained by differences in the ejection from the plasma as the CEP is varied. In particular, the blue dots in figures 4.29(c), (f), (i) and (l) show the first position at which a significant amount of electrons are ejected from the plasma. For $\phi_{CEP} = \pi$ and $\phi_{CEP} = \pi/2$, this first ejected electron bunch is not emitted at the temporal center of the laser and does not take advantage of the most intense accelerating half-cycle. Although electrons are also injected in the following cycle, where the accelerating E_z field is stronger, they do not reach very high energies. This may be because the charge separation created by the ejection of the first electron bunch negatively impacts the initial injection conditions of the electrons in the second electron bunch[2]. We more generally note that the simulations where the highest energies are reached correspond to the simulations where the first ejected electrons are initially the closest to the temporal center of the laser pulse. This can provide a reasonable explanation as to why the best values of the CEP are not necesarily the ones with the strongest accelerating half-cycle.

This strong effect of the CEP should probably be observable in experiments with few-cycle pulses. These results thus indicate that this parameter should be taken into account in such experiments. They also illustrate that electron ejection from the plasma can depend nontrivially on the interaction parameters. Combined with the fact that the subsequent acceleration in the reflected radially polarized pulse is also quite sensitive to the initial injection conditions, this means that accurately predicting experimental results is not simple.

4.3.2 Simulation with multi-cycle pulses

Here, we present a simulation performed with parameters corresponding to the UHI100 laser: $\lambda = 800$ nm, $w_0 = 3.1\,\mu\text{m}$, $\tau = 24$ fs, $a_{0,r} = 4.9$ and $a_{0,z} = 0.94$. We still use a plasma with a gradient scale length $L = \lambda/7$. One of the objectives from this simulation is to study whether there are fundamental changes in the interaction when multi-cycle pulses are used. We find that the results are in fact quite similar: electrons are still ejected from the plasma at every optical cycle of the laser and accelerated to relativistic energies by the E_z field. Final electron distributions are shown in figure 4.30. Electron energies reach up to ≈ 25 MeV but we note that the final electron beam is not well collimated, with an angular divergence that is approximately twice as large as in the best simulations with Salle Noire laser parameters. Out of the ≈ 550 pC ejected from the plasma, approximately 30 pC are eventually emitted with an angle smaller than 200 mrad.

---

[2] For $\phi_{CEP} = \pi/2$, the first ejected electron bunch actually returns to the plasma and is not accelerated by the reflected pulse. This however does not prevent it from negatively affecting the initial injection conditions of the following electron bunch.

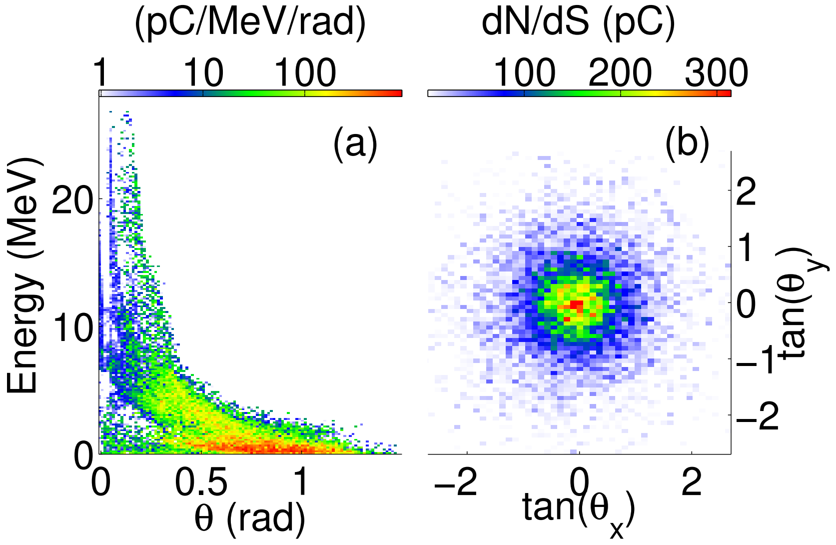

Figure 4.30: Results from a PIC simulation at normal incidence using UHI100 laser parameters. (a) Final electron angle-energy distribution and (b) final electron angular distribution. Detailed simulation parameters are provided in appendix B.

We can also observe in the simulation that only electrons in the first ejected bunches tend to remain close to the optical axis as they are accelerated by the reflected pulse. The reasons why the following bunches are more strongly deflected are not entirely clear but this explains why the final angular distribution is broader in this simulation. This would mean that using few-cycle pulses, for which only one or two electron bunches are emitted from the plasma, is more favorable than using multi-cycle pulses in the objective of obtaining narrow divergences.

4.3.3 Simulations with more intense pulses

We have observed in test-particle simulations that electrons accelerated to ultrarelativistic energies tend to be emitted very close to the laser propagation direction, leading to narrow angular spreads. In order to test whether high-quality electron beams could be obtained in this manner using plasma mirror injection, we have carried out simulations with much higher laser intensities, which we present in this section. We use for all these simulations a gradient scale length $L = \lambda/7$.

We first show results from a simulation performed with a few-cycle pulse, using the parameters targeted by the SYLOS laser system [173]: a pulse energy of 100 mJ, a beam waist of $w_0 = 1.5\,\mu\mathrm{m}$ and a pulse duration of 5 fs in FWHM of intensity. This leads to $a_{0,z} = 3.78$ and $a_{0,r} = 9.55$. Final electron distributions are shown in figure 4.31. As expected, we observe that the electron beam is now very well collimated. In fact, we find that the charge ejected within an angle θ of the specular direction scales almost linearly with θ (this approximation is valid for small values of θ, typically when $\theta < 200$ mrad). For instance, there is an ejected charge of 23.7 pC within 100 mrad of the specular direction, 9.84 pC within 50 mrad and 1.45 pC within 10 mrad (for comparison, the total ejected charge is ≈ 668 pC). This means that the ejected charge per solid angle scales as $1/\theta$ and thus that the angular distribution remains nar-

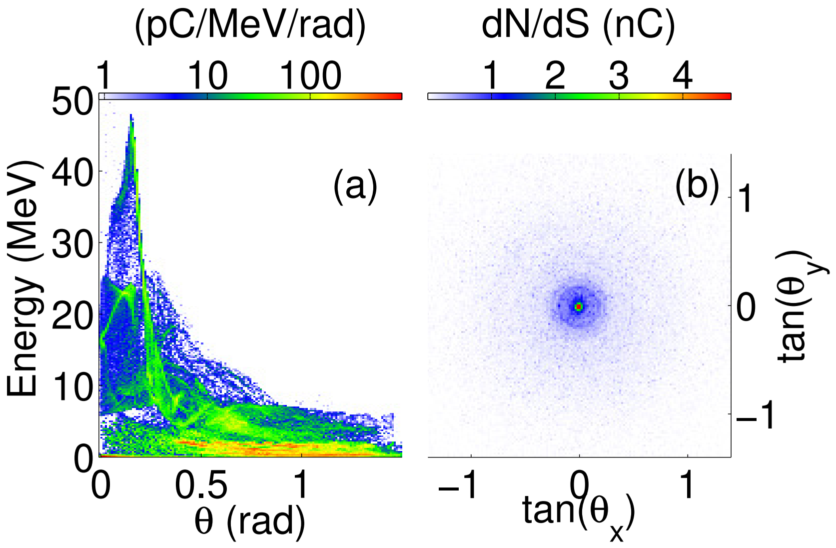

Figure 4.31: Results from a PIC simulation at normal incidence using parameters targeted by the SYLOS laser system. (a) Final electron angle-energy distribution and (b) final electron angular distribution. Detailed simulation parameters are provided in appendix B.

row even for very small values of θ. For instance, figure 4.32(a) shows the same angular distribution as in figure 4.31(b) but zoomed on the angles $\theta < 35$ mrad. We observe that this distribution is indeed still peaked. The energy spectrum of the electrons accelerated within 5 mrad of the specular direction, visible in figure 4.32(b), also presents a narrow peak around 16 MeV. These electrons represent a charge of ≈ 635 fC and have a transverse emittance of ≈ 650 nm. The emittance can be reduced to ≈ 10 nm while maintaining the charge to ≈ 80 fC by selecting the electrons within 16.2 MeV and 16.5 MeV ($\approx 2\%$ energy spread). Such a small divergence ultrashort relativistic beam with monoenergetic energy could be particularly useful for applications such as ultrafast electron diffraction. This simulation probably corresponds to the best regime of acceleration by a radially polarized pulse that we have observed in this thesis.

We also show for completeness in figure 4.33 results from a simulation performed with Salle Noire parameters except that the electric field amplitude has been multiplied by 10. This corresponds to a pulse energy of 250 mJ, a beam waist of $w_0 = 1.5\,\mu\mathrm{m}$ and a pulse duration of 3.5 fs in FWHM of intensity, which leads to $a_{0,z} = 7$ and $a_{0,r} = 17.7$. We once again observe that the charge ejected within an angle θ of the specular direction scales quasi-linearly with θ (≈ 64 pC within 100 mrad of the specular direction, ≈ 7.2 pC within 10 mrad and ≈ 540 fC within 1 mrad out of ≈ 1 nC ejected in total), which results in an even narrower angular distribution. This time the energy spectrum of the electrons accelerated within 5 mrad of the specular direction presents two marked peaks, around 25 MeV and 60 MeV. Although such parameters are probably unachievable with current laser technology, this simulation shows the robustness of this method for generating high-quality electron beams.

Finally, we show in figure 4.34 results from a simulation carried out with a multi-cycle pulse with very high intensity. The aim of this simulation is to check whether high-quality electron beams can also be obtained in this case. For this purpose, we use the following laser parameters: $\lambda = 800$ nm, $w_0 = 1.5\,\mu\mathrm{m}$,

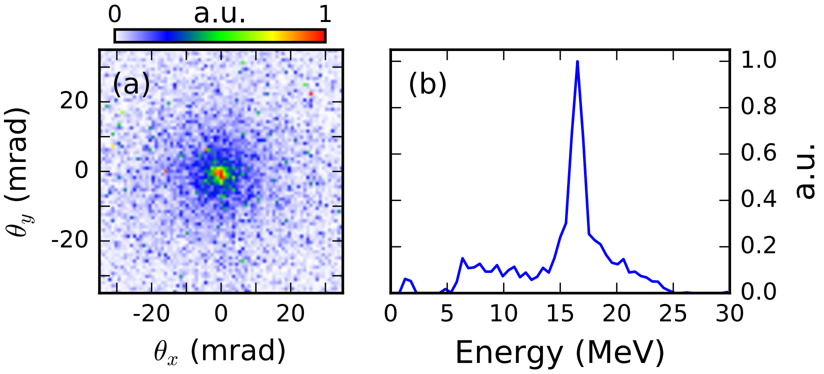

Figure 4.32: Results from a PIC simulation at normal incidence using parameters targeted by the SYLOS laser system. (a) Angular distribution of the electrons with an energy greater than 1 MeV around the specular direction. (b) Energy spectrum of the electrons accelerated within 5 mrad of the specular direction. Detailed simulation parameters are provided in appendix B.

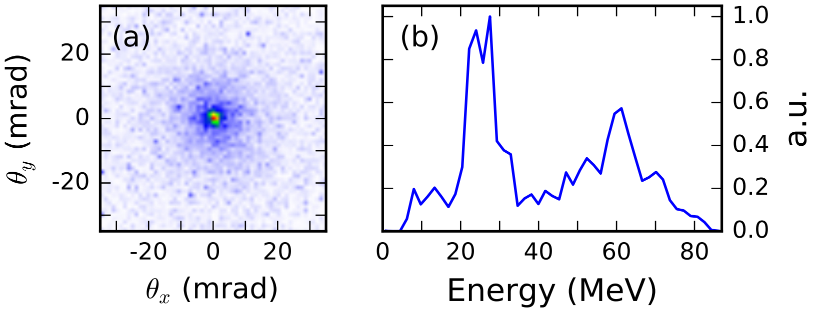

Figure 4.33: Results from a PIC simulation at normal incidence using Salle Noire laser parameters with the electromagnetic field amplitude multiplied by 10. (a) Angular distribution of the electrons with an energy greater than 1 MeV around the specular direction. (b) Energy spectrum of the electrons accelerated within 5 mrad of the specular direction. Detailed simulation parameters are provided in appendix B.

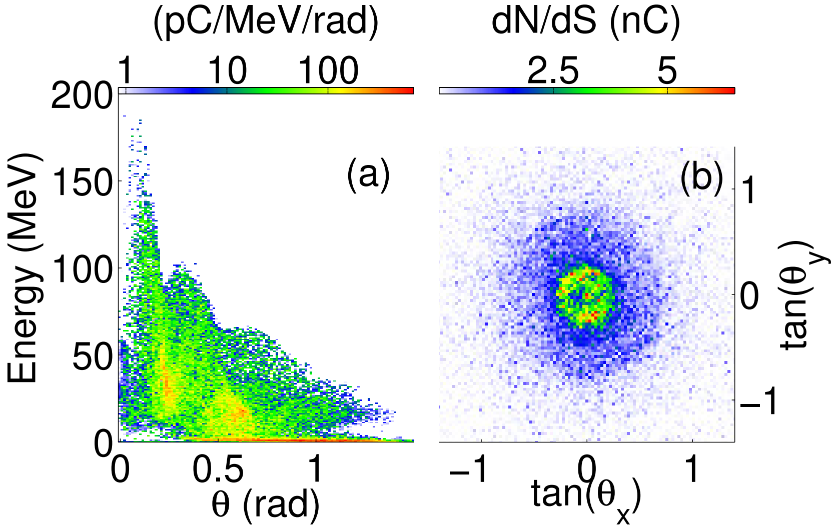

Figure 4.34: Results from a PIC simulation at normal incidence using a very intense multi-cycle radially polarized pulse. (a) Final electron angle-energy distribution and (b) final electron angular distribution. Detailed simulation parameters are provided in appendix B.

$\tau = 24$ fs, $a_{0,r} = 32$ and $a_{0,z} = 12.7$. This corresponds to a pulse energy of ≈ 5 J and a peak power of ≈ 200 TW. As in the previous section, we find that only the electrons emitted during the first optical cycles remain close to the optical axis throughout the simulation. This leads to an angular distribution that is much broader than in the previous simulations performed with shorter pulse durations. As a result, from the ≈ 3.3 nC ejected in the simulations, only ≈ 93 pC are ejected within 100 mrad of the specular direction and ≈ 2.3 pC within 10 mrad. This result once again indicates that few-cycle pulses are better-suited for accelerating electrons with radial polarization when using plasma mirrors at normal incidence as an injection method.

CHAPTER 5

Experiments at oblique incidence with radial polarization

Contents

In the previous chapter, we have examined the acceleration of electrons injected by focusing an ultraintense laser pulse at **normal incidence** on an overdense plasma. The choice of studying the interaction at normal incidence was made for two principal reasons:

1. At normal incidence, only the E_z component of the electric field is directed towards the density gradient. This means that electrons are injected close to the optical axis of the reflected pulse, which is ideal.

2. At normal incidence, the interaction is axisymmetric. This has allowed us to perform PIC simulations in cylindrical coordinates at a reasonable cost.

However, from an experimental point of view, the interaction is easier to study at oblique incidence. Once again, there are two main reasons for this:

1. Electron acceleration experiments with linear polarization already exist and are carried out at oblique incidence. Thus, experiments with radial polarization at oblique incidence can be readily performed simply by converting the laser polarization state with an appropriate waveplate, without any further change in the experimental setup.

2. At normal incidence, the laser pulse might be reflected back into the laser system, which could cause damage to optics and amplifying media.

We therefore investigate in this chapter the possibility of accelerating electrons injected by focusing a laser pulse at **oblique incidence** on a plasma mirror. This study is based on recent experiments performed

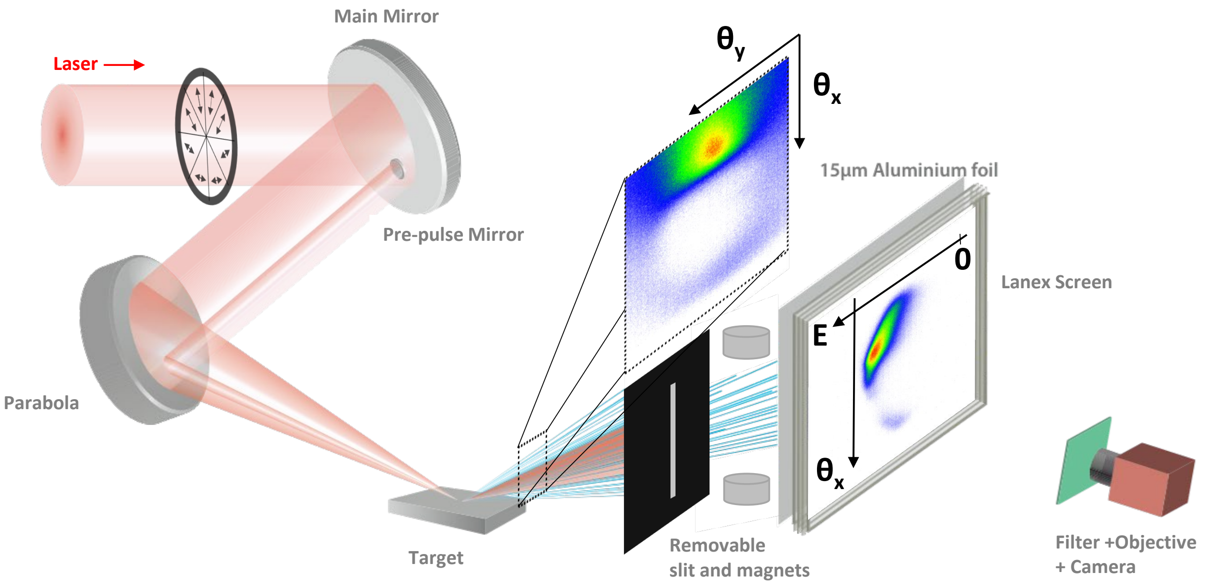

Figure 5.1: Experimental setup. The images on the screens show the electron beam angular distribution after the interaction (left screen) and its angularly resolved spectrum (right screen).

by Diego Guenot, Ludovic Chopineau, Adrien Denoeud and Jérôme Faure with the UHI100 laser at CEA Saclay, which demonstrate for the first time electron acceleration to relativistic energies with radial polarization. The experimental results are displayed in section 5.1 and analyzed in section 5.2 using full-3D PIC simulations. We also mention that results from 3D PIC simulations carried out at oblique incidence with Salle Noire laser parameters are presented in the appendix.

5.1 Experimental results

5.1.1 Experimental setup

The experimental setup is represented in figure 5.1. The UHI100 laser at CEA Saclay is a 100-TW class system which provides 800-nm, 24-fs laser pulses with an ultrahigh temporal contrast ($> 10^{12}$) thanks to a double plasma mirror system [179] located before the experimental chamber. We use a deformable mirror to correct the laser wavefront. A phase mask consisting of eight half-wave plates with different optical axes, as shown in figure 5.2(a), can be inserted in order to convert the laser polarization from linear to radial or azimuthal. Each octant of the phase mask is made of a 80-μm thick piece of mica, which is thin enough to result in a low B-integral of 0.15 rad. By rotating the entire waveplate, the polarization can be continuously varied from radial to azimuthal. A circular aperture, not depicted in figure 5.1, is used to remove the edges of the beam and improve the focal spot. In the case of linear polarization, a $50\,$mm aperture is used, thus reducing the energy on target to $460\,$mJ. When the radial polarization waveplate is introduced in the beam, a $65\,$mm aperture is used such that the energy on target is $675\,$mJ. The beam is focused with a 60° incidence angle onto a fused silica target by a parabola with a focal length $f = 200$ mm. Resulting focal spots are shown in figures 5.2(b) and (c). For linear polarization, the beam

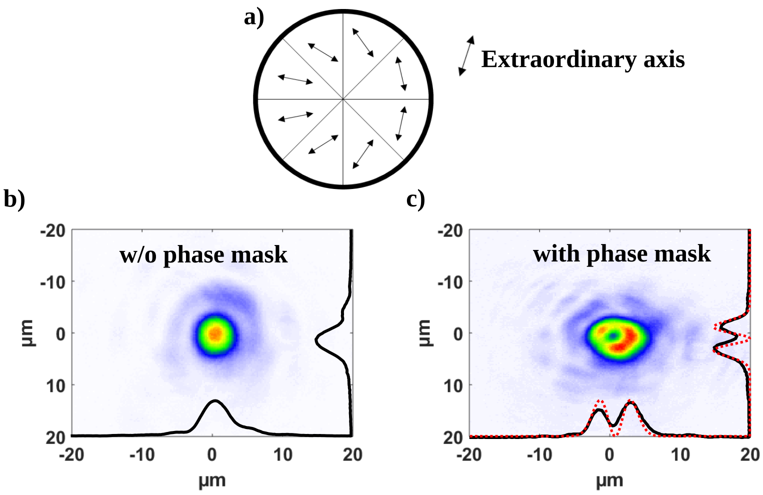

Figure 5.2: Generation of radial polarization. a) Sketch of the waveplate used and extraordinary axes of the eight octants. b) Focal spot for linear polarization, i.e. without the waveplate. c) Focal spot for radial polarization.

waist is measured to be $3 \times 3.4\,\mu$m, which results in an estimated peak intensity of $I = 5.8 \times 10^{19}\,\mathrm{W/cm^2}$ ($a_0 = 5.2$). For radial polarization, the characteristic doughnut shape is clearly observed. The slight asymmetry of the spot is probably due to imperfections in the wavefront and/or imperfect centering of the beam on the waveplate. The beam waist is obtained by fitting $r^2 \exp\left(-2r^2/w_0^2\right)$ to the spatial profile, which gives $3.05 \times 3.2\,\mu$m. The resulting peak intensity is $I = 4.8 \times 10^{19}\,\mathrm{W/cm^2}$ ($a_{0,r} = 4.7$). Using these parameters we estimate the longitudinal normalized field to be:

$$a_{0,z} = 0.742 a_{0,r} \left(\frac{\lambda}{w_0}\right) = 0.9. \tag{5.1}$$

This value is probably somewhat overestimated because of the asymmetry in the focal spot but it indicates that the longitudinal component of the electric field approaches relativistic intensities, making the laser suitable for electron acceleration in the longitudinal direction.

A small mirror is inserted before the parabola in order to create a weak prepulse from the main laser beam [26]. This prepulse is used to ionize the target and initiate a plasma expansion at an adjustable delay before the main pulse, therefore creating a transversely homogeneous preplasma with an accurately controlled density gradient.

A calibrated phosphor screen [172] (KODAK LANEX fine) is used in combination with a camera to observe the electron angular distribution around the specular direction. The screen is covered by a 1.63 mm aluminium plate to provide shielding against the laser light and remove the electrons with an energy lower than ~900 keV. A pair of magnets in combination with a slit can be added in front of the screen to measure angularly resolved electron energy spectrum in the incidence plane ($\theta_y = 0$, where θ_y is as defined in figure 5.1).

In parallel to the electron distributions, high order harmonics emitted in the specular direction can be measured by replacing the electron spectrometer with an XUV spectrometer. The spectrometer uses a 1200 lines per mm varied line spacing concave extreme ultraviolet grating (Shimadzu 30-002) coupled

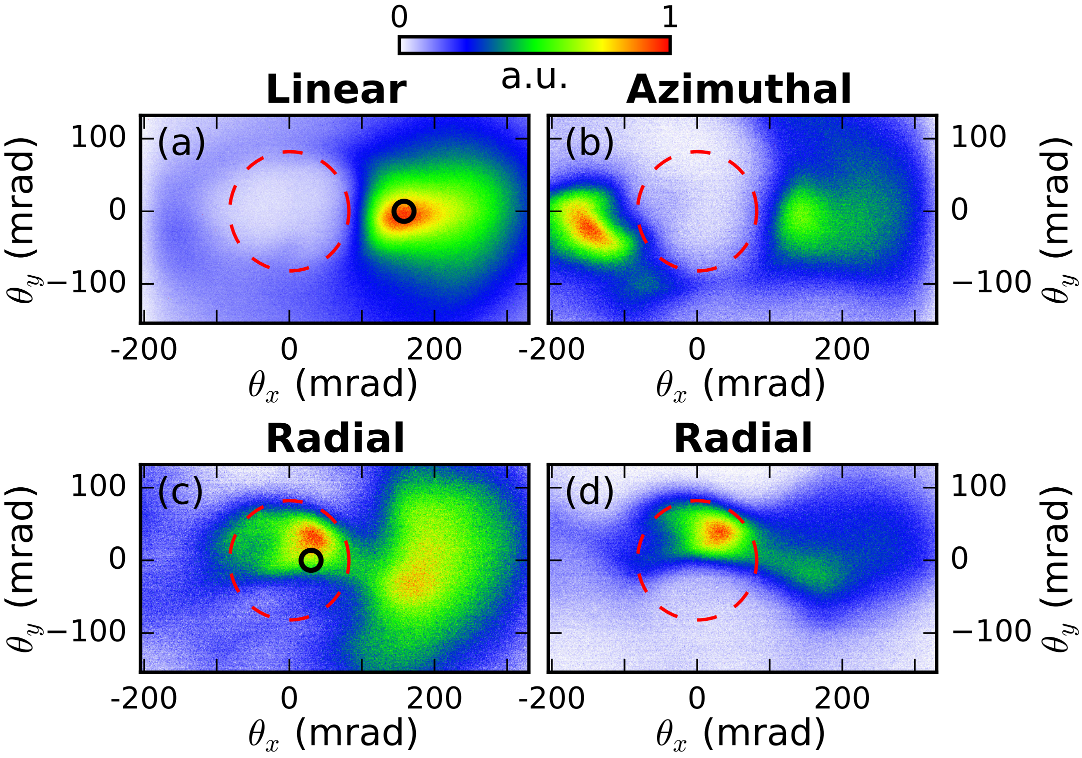

Figure 5.3: Typical experimental angular electron distributions. The specular direction corresponds to $\theta_x = \theta_y = 0$. *(a) linear polarization: the electron beam is located between the specular and normal directions. (b) azimuthal polarization: electrons are located on both sides of the specular direction (c) radial polarization. (d) Angular distribution obtained in the best shots with radial polarization. Both (c) and (d) display an on-axis electron beam in the specular direction. The dashed red lines show the angular extent of the reflected laser beam.*

to a large 69×88 mm rectangular microchannel plate and a phosphor screen. This provides harmonic spectra which are angularly resolved in the transverse θ_y direction. With linear polarization, it is possible to observe up to the 45^{th} harmonic order.

5.1.2 Electron emission

A typical electron angular distribution obtained with linear polarization is displayed in figure 5.3(a). The main features of this distribution are the presence of a hole in the specular direction and of a bright peak between the specular and the normal directions, in good agreement with previous experiments [27, 24]. This bright spot is located approximately 150 mrad from the specular direction and contains a charge of ≈ 700 pC. The electron signal in this regime is optimal when the gradient scale length is on the order of $\lambda/10$ (see [24]).

While the electron signal exhibits good stability in linear polarization, we observe significant shot-to-shot fluctuations in the electron charge and angular distribution when the phase mask is introduced to generate radial polarization, which we attribute to shot-to-shot fluctuations in the laser focal spot.

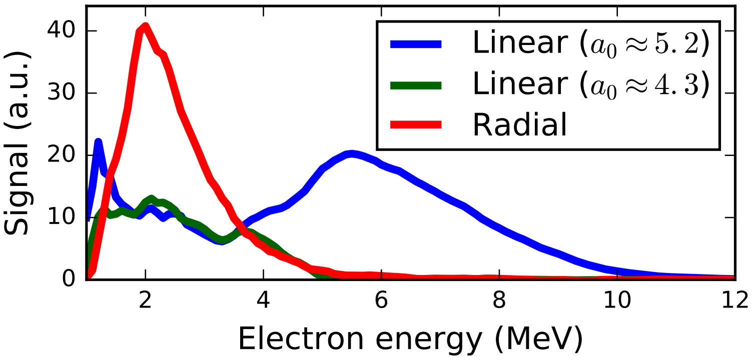

Figure 5.4: Experimental electron spectra obtained with radial polarization (red curve), linear polarization (blue curve) and linear polarization at reduced energy (green curve).

We nonetheless consistently observe an electron beam emitted very close the specular direction, while another spot remains visible between the normal and specular directions, as can be seen in figure 5.3(c). This peak has a narrower divergence, typically in the $50\,$mrad range, and can contain up to $200\,$pC ($100\,$pC on average). In the best shots, the spot in the specular direction can even contain more charge than the spot located between specular and normal, which results in an electron beam with a divergence halved compared to the electron beam accelerated with linear polarization. An example of such shot is shown in figure 5.3(d). It can be noted that the shot-to-shot fluctuations have prevented us from clearly establishing the precise influence of the gradient scale length in this regime.

When rotating the waveplate to generate azimuthal polarization, the electron peak in the center fades away, as shown in figure 5.3(b). In this case, a significant amount of electrons tend to be located on the other side of the hole, between the specular and the grazing directions.

Overall, we remark that electrons are only emitted in the specular direction when radially polarized pulses, which possess a considerable longitudinal electric field, are used. This strongly suggests that these electron are, as initially desired, accelerated by the E_z field.

Figure 5.4 shows the electron energy spectra recorded at the position of the bright spot for linear polarization and at the position of the specular spot for radial polarization. With linear polarization, the maximum reached energy is $11\,$MeV with a peak at $6\,$MeV while with radial polarization the maximum energy is $6\,$MeV with a peak around $2\,$MeV. In order to obtain a similar spectrum with linear polarization it is necessary to reduce the laser energy by 30% (we have in this case 320 mJ on target and $a_0 \approx 4.3$).

5.1.3 High-harmonic generation

With the purpose of gaining additional insight on the interaction, we also study the generation of high-harmonics, which is closely related to the generation of fast electrons in the relativistic regime [23, 24]. Figure 5.5 shows typical angularly resolved harmonic spectra for linear, radial and azimuthal polarization between harmonic orders 9 and 18. When the waveplate is introduced in the beam the total harmonic yield decreases. Each spectrum is therefore renormalized separately in figure 5.5. In the case of azimuthal polarization, we observe interference fringes on each harmonics in the θ_y angle. These fringes correspond to the interference pattern that would be generated by two sources separated by $4.8 \pm 0.1\,\mu\mathrm{m}$

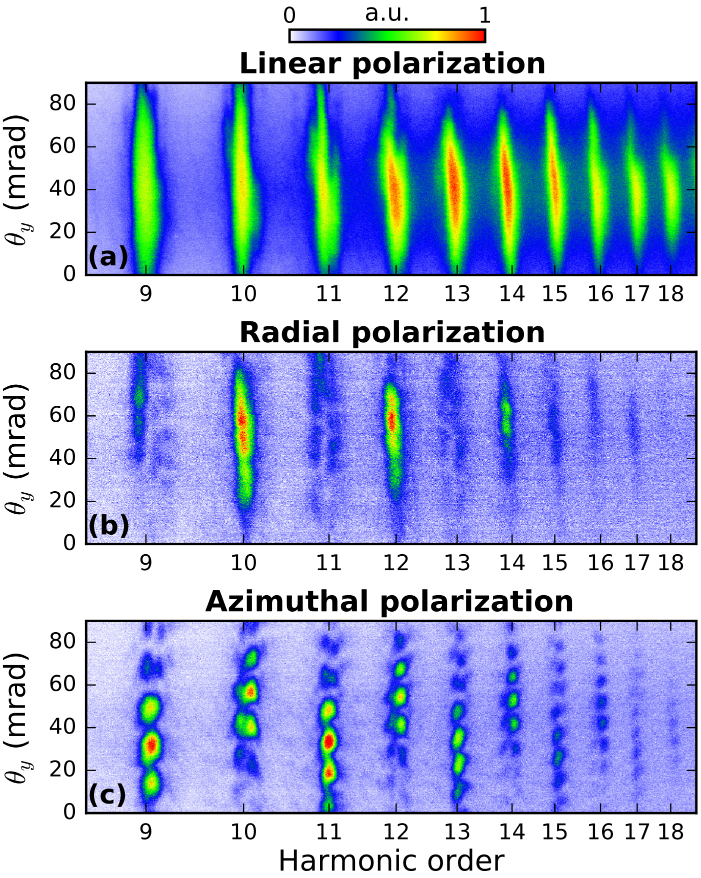

Figure 5.5: Experimental angularly resolved harmonic spectra in the case of (a) linear polarization, (b) radial polarization and (c) azimuthal polarization.

in the transverse y-direction. The interference patterns for consecutive harmonic orders appear to be shifted by π. In other words, if the signal is close to 0 at a given angle for harmonic order n, it will be close to maximum at the same angle for harmonic order $n+1$. In the case of radial polarization, we observe no interference pattern but we notice that the harmonic intensity can substantially vary between even and odd harmonics (in figure 5.5(b) the even harmonics are stronger but in some other shots the odd harmonics can become stronger).

5.2 Analysis of the experiments

5.2.1 Electron ejection and high-harmonic generation at oblique incidence

The fact that the harmonic signal in azimuthal polarization seems to originate from two sources from either side of the incidence plane strongly suggests that only the parts of the laser for which the electric field is directed in the incidence plane (p-polarization) contribute to high-harmonic emission, while no harmonics are emitted from the positions where the electric field is perpendicular to the incidence plane

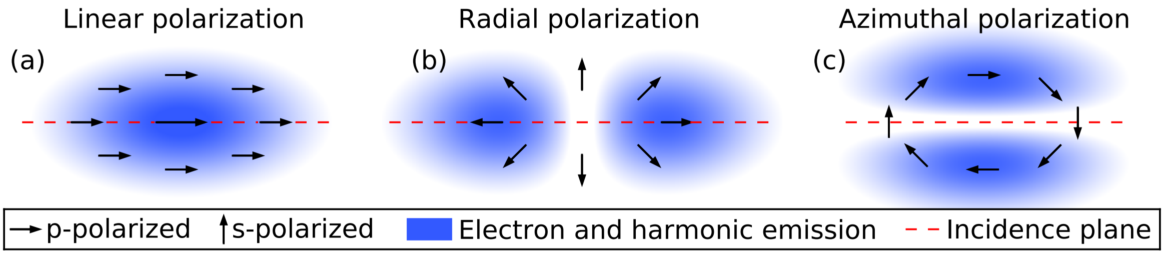

Figure 5.6: Schematic view of the laser field footprint on the plasma surface for (a) linear, (b) radial or (c) azimuthal polarization. Electrons and harmonics are only emitted when the laser is p-polarized, which results in two distinct sources in the case of radial and azimuthal polarization.

(s-polarization). This is illustrated in figure 5.6. It has indeed been shown that, at the laser intensities considered here, the harmonics signal is suppressed when the polarization is switched from p to s (see [24]). For linear polarization, the whole beam can be p-polarized, which leads to a single harmonic source. On the other hand, for radial or azimuthal polarization, the locally p-polarized parts of the beam form two separate spots which can result in two separate harmonic sources. This is supported by the fact that the distance between the two sources obtained from the interference pattern ($4.8 \pm 0.1\ \mu$m) matches the distance between the two maxima in the focal spot ($4.3 \pm 0.2\,\mu$m, see figure 5.2(c)).

This physical interpretation can also be used to explain why interference patterns for consecutive harmonic orders appear to be shifted by π. We indeed know that the harmonic signal is emitted periodically at a precise phase of the incident laser field. Since, for either radial or azimuthal polarization, the electric field in the two separate sources have opposite sign, the harmonic emission is delayed by half a laser cycle from one source to the other. This leads, for harmonic n, to a phase shift of $n\pi$ between the two sources, which results in a phase shift of π in the interference patterns for consecutive harmonics.

For radial polarization, we also expect to see an interference pattern but this time in the θ_x angle. However, the fringes cannot be seen in the experiment as our spectrometer samples the harmonic beam at a given θ_x. Therefore, the spectrometer only sees one position in the interference pattern for each harmonic. Since there is a π phase difference between consecutive harmonic patterns, this means that the harmonic intensity may strongly vary between odd and even harmonics, which is precisely what we observe in figure 5.5(b).

In order to confirm this physical explanation, we turn to 3D PIC simulations using the code Warp combined with the high-performance library PICSAR. We use the high-order Pseudo-Spectral Analytical Time Domain (PSATD) Maxwell solver which strongly reduces numerical dispersion, with a stencil spatial order of 100 and 8 guard cells (see section 2.2.4). Each of the simulations presented here costs around 3 million computation hours on supercomputer Mira at the Argonne Leadership Computing Facility. We use in the simulations a spatial resolution of $\Delta x = \Delta y = \Delta z = \lambda/57$, a temporal resolution of $\Delta t = T/57$ (where T is the laser period) and 6 particles per cell per specie. The laser impinges the plasma with a 60° incidence angle, a central wavelength $\lambda = 800$ nm, a beam waist of $w_0 = 3.1\ \mu\mathrm{m}$ and a pulse duration of 24 fs in FWHM of intensity. The peak normalized amplitude of the transverse field is $a_0 = 5.4$ for linear polarization and $a_{0,r} = 4.9$ (corresponding to $a_{0,z} = 0.94$) for radial and azimuthal polarization. A cosine temporal envelope is used. The plasma density profile is exponential with a minimum density of $n_c/20$, a maximum density of $100\,n_c$ and a gradient scale length of either $L = \lambda/10$ or $L = \lambda/7$. Finally, a moving window is used in order to follow the trajectory of the electrons in the reflected pulse up to 80 μm away from the plasma (approximately 2 Rayleigh lengths).

Angularly resolved harmonic spectra obtained from the simulations are displayed in figure 5.7. In panels (a) to (c), the harmonics are resolved in the θ_y direction so that they can be directly compared with the experimental measurements shown in figure 5.5. A very good agreement is found: in azimuthal polarization, we observe interferences with a phase shift of π between consecutive harmonics while in radial polarization we notice that the harmonic intensity considerably differs between even and odd harmonics. In figure 5.7(d), the angular dependence is shown with respect to the θ_x angle in the radially polarized case, allowing us to uncover the interference pattern which is not visible in experiments. Both the experimental and simulation harmonic spectra show clear evidence that using either radial or azimuthal polarization results in two separate harmonic sources that correspond to positions where the laser is locally p-polarized. This is once again supported by the fact that the distance between the two sources obtained from the simulation harmonic signal is $\approx 4.7\,\mu\mathrm{m}$, which is consistent with the theoretical distance between the two maxima in the focal spot ($\sqrt{2}w_0 \approx 4.4\,\mu\mathrm{m}$).

As we have stated in the first chapter, the harmonics are emitted via the Relativistic Oscillating Mirror (ROM) mechanism, which occurs as the reflecting plasma surface oscillates nonlinearly following the laser field (see section 1.4.3.2). At the moments when the oscillating electrons are pulled towards vacuum, the incident field is strongly Doppler upshifted, leading to the high-harmonic generation. At the same time, part of the oscillating electrons acquire a high enough energy to escape from the plasma, leading to the ejection of electrons. Since both electron and high-harmonic emissions are originating from the same oscillation of the plasma surface, they happen simultaneously and are efficient for the same laser and plasma parameters. Such a correlation between ROM harmonics and electron ejection has indeed been observed experimentally [24]. In the case of radial or azimuthal polarization, we have just seen that harmonics are only generated at the positions where the laser is locally p-polarized. We can therefore expect a similar behaviour for electron ejection, which would mean that the electrons are emitted from two separate sources.

In order to confirm this prediction, we plot in figure 5.8 the initial position of the electrons that are ejected from the plasma in the simulations. As anticipated, only the p-polarized parts of the laser contribute to electron ejection, which results in two distinct electron sources in radial and azimuthal polarization. The fact that electron emission only occurs at specific parts of the focal spot can partly explain the significant shot-to-shot fluctuations observed in experiments with radial and azimuthal polarization. We have indeed seen that the focal spot possesses an asymmetry (see figure 5.2(c)) which can vary depending on the shots. Shots with a higher intensity in the p-polarized parts of the beam will result in a much higher detected charge than shots with a higher intensity in the s-polarized parts of the beam.

From a VLA point of view, the fact that the E_z field in radial polarization does not contribute to electron injection and that the interaction is still dominated by the transverse fields is not ideal. Indeed, the initial purpose of using radial polarization was to accelerate the electrons close to the optical axis where the transverse fields are negligible whereas in our case the electrons are injected on the side of the beam where the transverse fields are the highest. Nevertheless, the fact that we have detected experimentally electrons in the longitudinal direction suggests that it is possible for some electrons to reach the optical axis after being injected on the side of the beam.

Another important result of the simulations is that the laser partially loses its spatial structure upon reflection. Indeed, high-harmonic generation is more efficient in the p-polarized parts of the pulse whereas

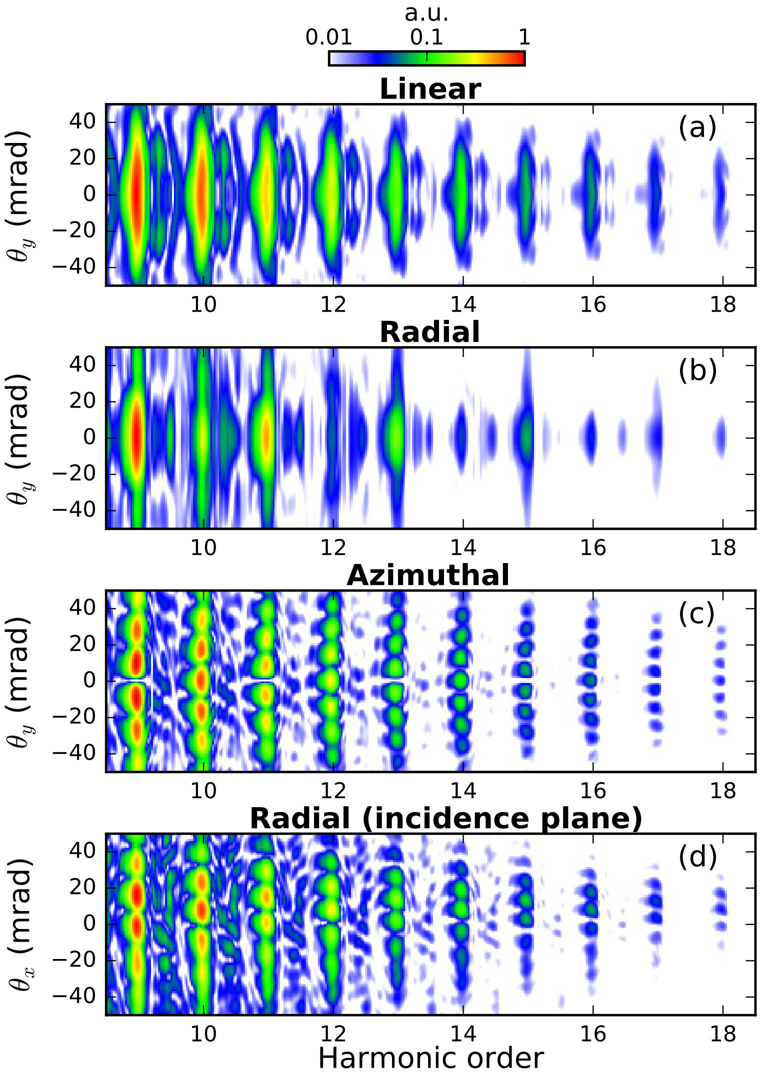

Figure 5.7: Results from 3D PIC simulations. Angularly resolved harmonic spectra for (a) linear, (b),(d) radial or (c) azimuthal polarization. The angular dependence is shown with respect to the θ_y angle in panels (a) to (c), which corresponds to the experimental case, and with respect to the θ_x angle in panel (d), so that the interference pattern becomes apparent. These images have been obtained with $a_0 = 5.4$ for linear polarization and $a_{0,r} = 4.9$ for radial and azimuthal polarization and a gradient scale length $L = \lambda/10$. Detailed simulation parameters are provided in appendix B.

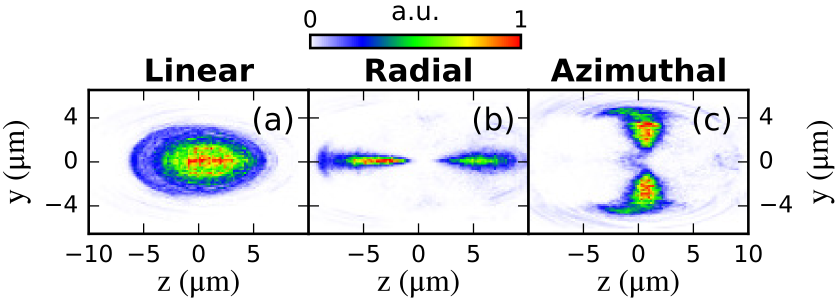

Figure 5.8: Results from 3D PIC simulations. Initial position of the electrons that are ejected $4\,\mu\mathrm{m}$ *away from the plasma in the case of (a) linear, (b) radial or (c) azimuthal polarization. These images have been obtained with* $a_0 = 5.4$ *for linear polarization and* $a_{0,r} = 4.9$ *for radial and azimuthal polarization and a gradient scale length* $L = \lambda/10$*. Detailed simulation parameters are provided in appendix B.*

the reflectivity of the fundamental frequency is higher in the s-polarized parts of the pulse, since the laser spends in this case less energy in the generation of harmonics and fast electrons. Consequently, the reflected laser field no longer has cylindrical symmetry. Figure 5.9 displays snapshots from the PIC simulation with radial polarization showing the laser pulse in the incidence plane before and after reflection. We most notably observe that the hole in the intensity distribution at the center of the laser is suppressed after the interaction. This may make the VLA process in the reflected pulse more complex. In particular, we remark that high-amplitude harmonic fields, which have a much longer Rayleigh length than the fundamental pulse, remain present on the optical axis far from the plasma. Such harmonic fields could cause an unwanted deflection of electrons accelerated by the longitudinal field close to the optical axis, where transverse fields are usually negligible.

5.2.2 Electron distributions

If the harmonic spectra obtained in PIC simulations showed excellent agreement with experiments, we find that it is more difficult to reproduce the electron angular and energy distributions in the 3D PIC simulations with radial and azimuthal polarization. In particular, we have observed, as will be seen hereafter, that a better agreement could be found in radial polarization by reducing the laser intensity. Consequently, the electron distributions shown here have been obtained with a lower value of a_0 compared to the previous images. Figures 5.10(a) and (b) show typical electron angular distributions obtained in simulations with respectively radial and linear polarization. Before commenting these distributions, it must be noted that they have been obtained after propagating the reflected pulse $80\,\mu\mathrm{m}$ away from the plasma. Even though this value exceeds two Rayleigh lengths for the fundamental frequency, some electrons are still interacting with the laser and these distributions are therefore susceptible to evolve. In the linearly polarized case, we nevertheless find that the main features of the experimental angular distribution are well reproduced: most electrons are accelerated between the specular and normal directions ($\theta_x > 0$) and there is virtually no electron emitted in the specular direction. This is in good agreement with previous 3D PIC simulations performed with similar laser and plasma parameters [133, 24]. When the polarization is switched to radial, we observe as in experiments more electrons located around the specular direction, which could correspond to electrons accelerated by the E_z field. However, we find that this does not lead

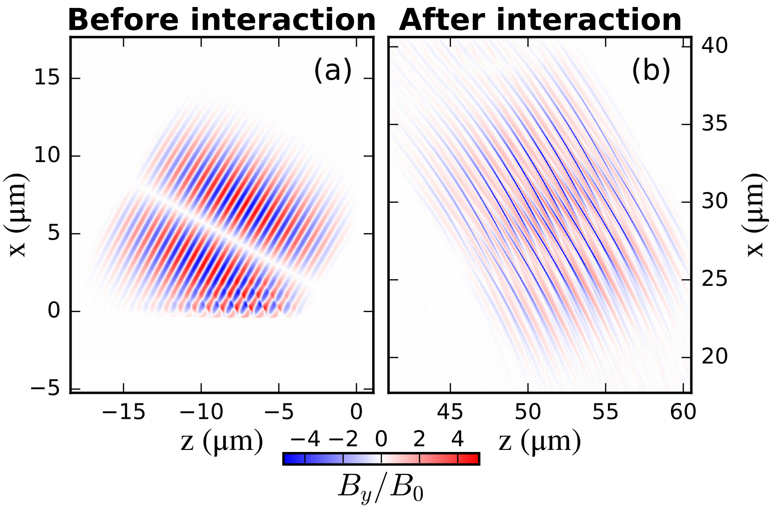

Figure 5.9: Results from a 3D PIC simulation. Laser magnetic field in the incidence plane with radial polarization, either (a) before or (b) after the interaction. Here, the magnetic field is given in units of a_0 *(*$B_0 = m_e\omega/e$*). These images have been obtained with* $a_{0,r} = 4.9$ *and a gradient scale length* $L = \lambda/10$*. Detailed simulation parameters are provided in appendix B.*

to a reduction of the electron beam angular spread.

The energy spectra obtained at the angles indicated by the black circles in figure 5.10 are shown in figures 5.11(a) and (b). We first point out that these distributions have been obtained with an intensity about two times lower than the experimental value estimated in section 5.1.1. Even with this decrease in the field amplitude, we observe that electrons in the simulation with radial polarization acquire an energy that is approximately twice as high as detected experimentally. This suggests that imperfections appearing in the laser focal spot (such as intensity inhomogeneities and phase aberrations) when the waveplate is introduced may degrade the acceleration process compared to the ideal case that is considered in the simulations. This would be consistent with the facts that electron ejection from the plasma depends nontrivially on the laser parameters and that VLA is sensitive to the initial injection conditions as well as to the exact shape of the laser [104]. As an illustration of the effect that imperfections can have on the interaction, we can mention that it was recently shown that longitudinal chromatism can have a considerable impact on VLA with radially polarized beams [180]. Moreover, we remark in figure 5.11 that, unlike in the experiments, using radially polarized pulses with similar parameters does not lead to a decrease in the electron energy compared to linear polarization, which tends to corroborate our interpretation.

To obtain an electron energy spectrum matching the experimental one, we have performed another simulation with radial polarization with an intensity even further decreased to approximately a tenth of the experimental value given in section 5.1.1. Although this is a large difference, we find that it leads to a good agreement with experiments, as can be seen in figure 5.11(c). This shows the extent to which the acceleration process seems to be negatively affected by the imperfections introduced by the waveplate. Interestingly, we find that reducing the laser intensity leads to a much more collimated electron beam, whose angular distribution is shown in figure 5.10(c). This distribution resembles that of the best experimental shots with radial polarization (see figure 5.3(d)), which confirms that a better agreement

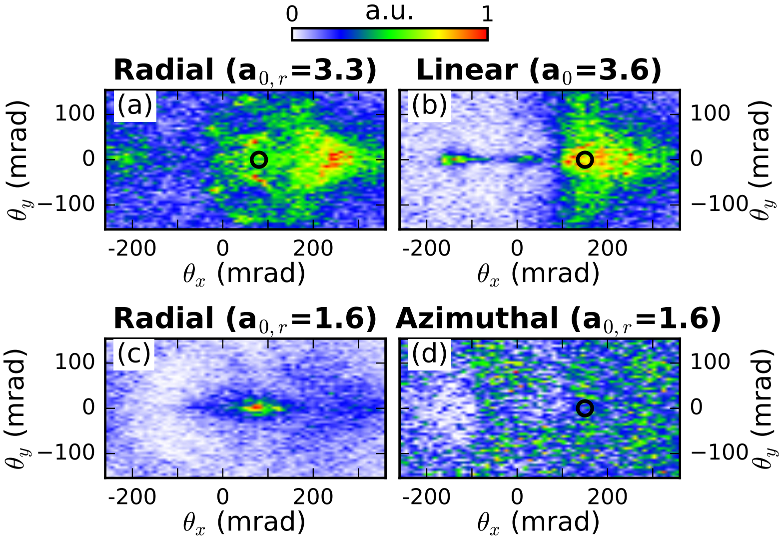

Figure 5.10: Results from 3D PIC simulations. (a)-(b) Angular distributions of the electrons with an energy greater than 1 MeV obtained at the end of the simulations with (a) radial polarization and $a_{0,r} \approx 3.3$, (b) linear polarization and $a_0 \approx 3.6$, (c) radial polarization and $a_{0,r} \approx 1.6$ and (d) azimuthal polarization and $a_{0,r} \approx 1.6$. Panel (b) has been obtained with $L = \lambda/10$ while the other panels have been obtained with $L = \lambda/7$. Detailed simulation parameters are provided in appendix B.

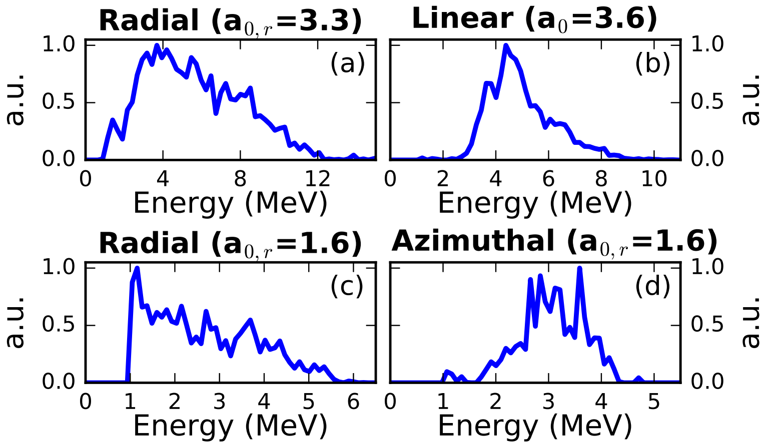

Figure 5.11: Results from 3D PIC simulations. Energy spectra of the electrons located within 30 mrad of the black circles shown in figure 5.10. Panel (b) has been obtained with $L = \lambda/10$ while the other panels have been obtained with $L = \lambda/7$. Detailed simulation parameters are provided in appendix B.

with experiment is found by reducing the intensity. We also once again find that using radial polarization can result in a significant decrease in the electron beam divergence. However, the simulations are not entirely satisfactory as they indicate that increasing the energy of the laser, and thus of the resulting electron beam, leads to a broadening of the angular distribution.

We can point out that we do not obtain a similarly narrow electron beam in the specular direction with azimuthal polarization. For example, we show in figure 5.10(d) the angular distribution obtained with the same parameters as in figure 5.10(c), except that the polarization is changed from radial to azimuthal. We find in this case that the electrons are emitted with a very wide divergence of the order of 600 mrad (which is not entirely visible in figure 5.10(d), for direct comparison with the other numerical and experimental distributions).

In the remainder of this section, we investigate the reasons why we obtain a narrow divergence with radial polarization when $a_{0,r} = 1.6$, but not when $a_{0,r} = 3.3$, with the ultimate purpose of understanding the conditions leading to a high-quality electron beam. We can first note that the electrons forming the sharp peak in figure 5.10(c) have a final energy (up to ≈ 5 MeV) that is much lower than the theoretical maximum energy gain (≈ 47.5 MeV for a peak power of ≈ 2.4 TW). This could mean that the peak in the angular distribution originates from electrons having ponderomotive trajectories, as in the test-particle simulation presented in section 4.2.4. This would be consistent with the fact that the electrons forming this peak tend to explore multiple optical cycle of the laser in the PIC simulation. However, this is not a sufficient explanation of why the electron beam is only well-collimated in the simulation with $a_{0,r} = 1.6$. Indeed, the electrons accelerated near the specular direction in figure 5.10(a) also have an energy that is much lower than the theoretical maximum energy gain (≈ 95.1 MeV for a peak power of ≈ 9.4 TW) and also tend to explore multiple optical cycle of the laser in the PIC simulation.

In order to understand the fundamental differences between the angular distributions of figures 5.10(a) and (c), we have further analyzed the trajectories of the corresponding electrons in the PIC simulations. We first find that, if electrons are ejected in two spatially-separated bunches (corresponding to positions where the laser is locally p-polarized, as previously seen), only the electrons initially in the bunch located on the right (such that $z > 0$) in figure 5.8(b) contribute to the collimated spot in the specular direction in figure 5.10(c). This can be understood fairly easily and is illustrated in figure 5.12. The main reason is that the electrons are ejected from the plasma at a phase which is such that they tend to be deflected towards the normal direction by the transverse fields. This explains why the electrons are detected between the specular and normal directions ($\theta_x > 0$) with linear polarization, rather than between the specular and grazing directions. In the case of radial polarization, electrons initially in the bunch such that $z < 0$, labeled "bunch A" in figure 5.12, tend to directly escape on the side of the beam and thus never interact with the E_z field. On the other hand, electrons initially in the bunch such that $z > 0$, labeled "bunch B" in figure 5.12, tend to be shifted towards the center of the pulse, where they may be accelerated by the E_z field. The fact that electrons have different trajectories depending on their initial location will also further increase the fluctuations in the experimental angular distributions when the focal spot possesses an asymmetry that varies from shot to shot, as was the case in the experiments.

In the following, we focus on the electrons initially in "bunch B", both in the simulation with $a_{0,r} = 1.6$ and the simulation with $a_{0,r} = 3.3$. As we have just explained, these electrons are initially on the side of the reflected laser pulse but a significant fraction of them are shifted towards the center of the beam and subsequently spend a long time close to the optical axis where the longitudinal field has a high amplitude. This is another indication that the electrons emitted in the specular direction are, at least partly, accelerated by the E_z field. We show in figures 5.13(a) to (d) the angular distribution of the electrons such

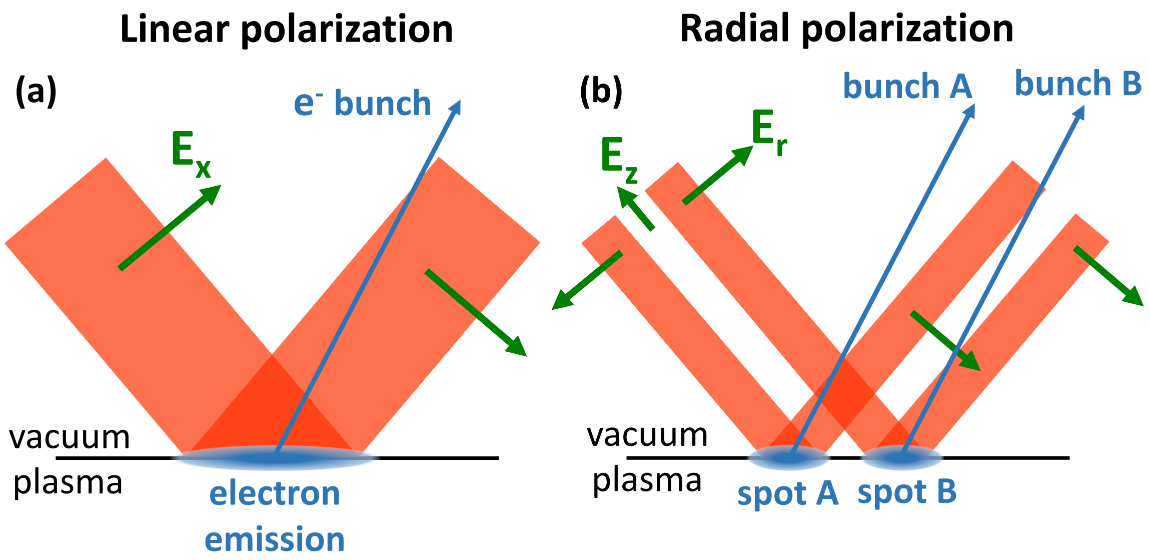

Figure 5.12: Schematic illustration of electron emission from the plasma in the incident plane for linear (a) and radial (b) polarization. The green arrows in the reflected field indicate the direction of the transverse electric field seen by the electrons immediatly after they are ejected. The electrons are always emitted at a phase such that they tend to be deviated towards the normal direction (this implies in particular that the phase at which electrons are ejected is shifted by π between spot A and spot B). For radial polarization, the electrons originating from spot B are more likely to interact with the E_z field than those coming from spot A. Detailed simulation parameters are provided in appendix B.

that $z > 0$ initially, either ≈ 80 fs after reflection or at the end of the simulation, ≈ 270 fs after reflection. At the beginning of their interaction, the electrons have a very narrow angular spread in the θ_y direction in both simulations. In the lower intensity case ($a_{0,r} = 1.6$), this angular divergence remains small until the end, and we eventually observe a collimated beam in the specular direction. On the opposite, when the intensity is increased, a considerable widening of the angular distribution in the θ_y direction is visible. This means that electrons initially accelerated in the longitudinal direction are deflected in the transverse direction during their interaction with the reflected beam. This deflection, occuring far from the plasma, could be due to the harmonic fields which, as previously stated, have a longer Rayleigh length and remain for a long time close to the optical axis. The harmonic fields are much more intense in the simulation with $a_{0,r} = 3.3$ because the high-harmonic generation efficiency increases nonlinearly with the intensity [29], which would explain why the electrons are not deflected in the simulation with $a_{0,r} = 1.6$.

In order to test this possibilty, we perform inexpensive 3D test particle simulations of the acceleration of an electron bunch by an ideal radially polarized pulse, which has no high-harmonic content. To simplify the interaction, we only consider a single attosecond electron bunch which is, as in experiments, initially located off the optical axis where the transverse fields are the most intense. The electrons start their interaction at a zero of the E_r field and the initial phase is chosen such that the electrons are pushed by the transverse fields towards the optical axis, which corresponds to the electron bunch B in the simulations. The electrons are initially at the focus of the laser, around 4 optical cycles before the temporal center of the pulse and have a Gaussian distribution both in real and momentum space, with an adjustable mean and variance. We use in the simulations a laser with a central wavelength of $\lambda = 800$ nm, a beam waist of $w_0 = 3.1\,\mu\mathrm{m}$, a pulse duration of 24 fs in FWHM of intensity and a peak normalized amplitude of the radial electric field of $a_{0,r} = 2.6$ or $a_{0,r} = 1.3$. These values are slightly lower than in the PIC simulations to take into account the fact that the reflectivity of the plasma mirror is smaller than unity.

We find that, with an approriate choice of parameters for the initial electron bunch, it is possible to obtain similar trajectories as in the PIC simulation with the lowest intensity. For example, we show in figures 5.13(e) and (f) the angular distributions obtained either ≈ 80 fs after focus or ≈ 270 fs after focus for an electron beam initially located $2\,\mu\mathrm{m}$ from the optical axis with an initial mean kinetic energy of 1 MeV and an average angle of 10° away from the specular direction, oriented towards the grazing direction. The initial standard deviations of the Gaussian distributions are $\sigma_z = 0.17\,\mu\mathrm{m}$ and $\sigma_{pz} = 0.9\ m_e c$ in the longitudinal direction and $\sigma_x = 0.5\,\mu\mathrm{m}$, $\sigma_y = 1.2\,\mu\mathrm{m}$, $\sigma_{px} = m_e c$ and $\sigma_{py} = 0$ in the transverse directions. We observe as in the PIC simulations the formation of a collimated spot in the specular direction. The test particle simulation additionally allows us to calculate the work done by the different components of the electric field. We find that the electrons emitted in the collimated spot gain most of their energy from the work done by the E_z field, which provides further evidence that the electrons detected in the specular direction in experiments are indeed accelerated by the longitudinal field.

When increasing the intensity in the test-particule simulations, we are unable to reproduce the large broadening of the angular spread in the θ_y direction that was observed in the PIC simulation. For instance, we show in figures 5.13(g) and (h) the angular distributions obtained for an electron beam initially located $3.1\,\mu\mathrm{m}$ from the optical axis with an initial mean kinetic energy of 2 MeV oriented towards the specular direction. The initial standard deviations of the Gaussian distributions are $\sigma_z = 0.19\,\mu\mathrm{m}$ and $\sigma_{pz} = m_e c$ in the longitudinal direction and $\sigma_x = 0.8\,\mu\mathrm{m}$, $\sigma_y = 0.8\,\mu\mathrm{m}$, $\sigma_{px} = 3.2\ m_e c$ and $\sigma_{py} = 0$ in the transverse directions. We observe that the electron beam remains collimated in the y-direction, which strongly differs from the PIC simulation. **This is an indication that the high-harmonics fields, which are not included in the test-particle simulations, are indeed deflecting the electrons off the optical axis.**

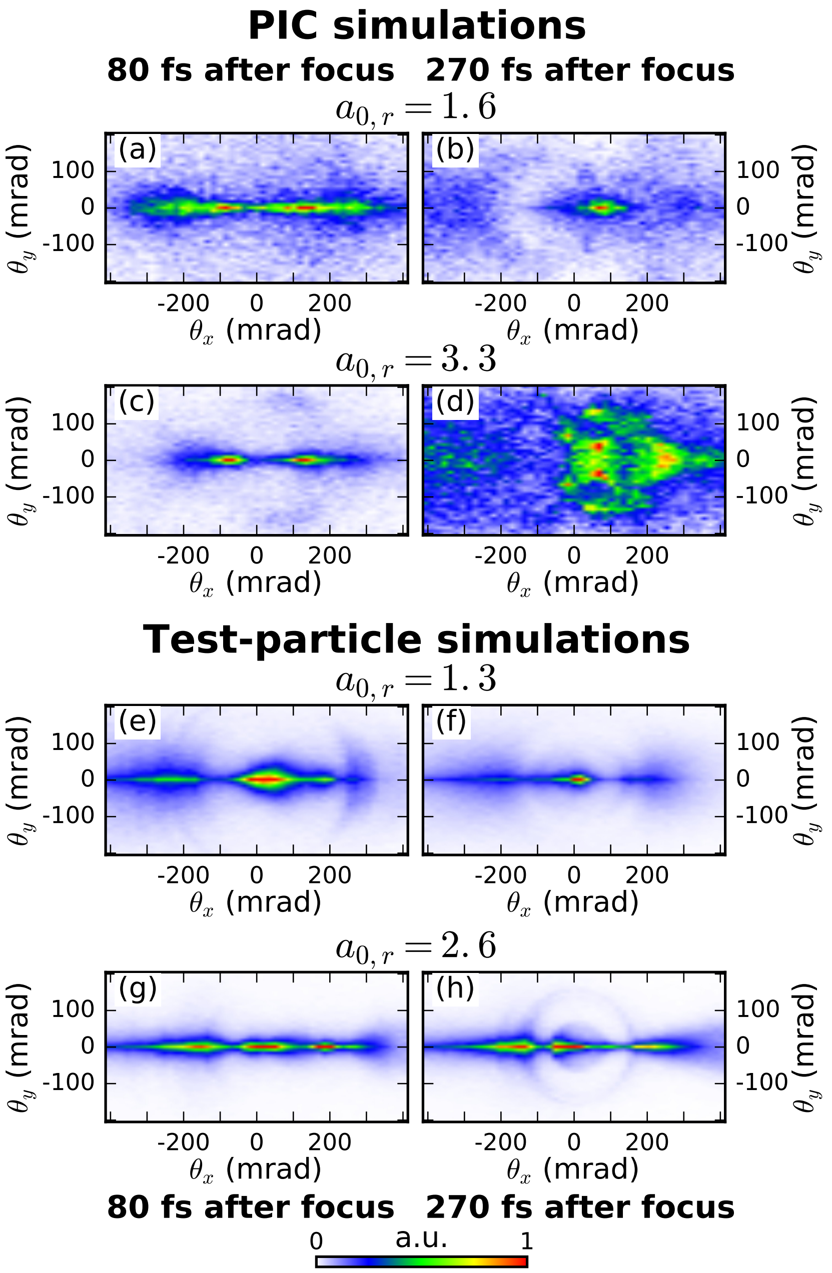

Figure 5.13: (a)-(d) Angular distribution of the electrons such that $z > 0$ initially in the 3D PIC simulation with (a)-(b) $a_{0,r} = 1.6$ or (c)-(d) $a_{0,r} = 3.3$. The distributions are shown either ≈ 80 fs after reflection or ≈ 270 fs after reflection, which corresponds to the end of the simulation. (e)-(h) Similar angular distributions reproduced in test-particle simulations. The laser intensity is slightly reduced in the test-particle simulations to take into account the energy absorption by the plasma mirror. Detailed simulation parameters are provided in appendix B.

5.3 Conclusion

These experiments have demonstrated for the first time the possibility to accelerate electrons to relativistic energies with a radially polarized laser pulse. This provides a clear validation of the effectiveness of the plasma mirror injection method studied in the previous two chapters. It was shown that radial polarization can lead to acceleration in the longitudinal direction and reduce the divergence of the electron beam compared to linear polarization. We have also noted some interesting differences in the physics of the laser-plasma interaction at oblique incidence, as using either radial or azimuthal polarization leads to two distinct sources of electrons and high-harmonics. This is not ideal for electron acceleration as the electrons are mainly injected by the E_r field at a position of the beam where the longitudinal field is negligible. Moreover, the radially polarized structure is partially lost upon reflection, which results in particular in strong harmonic fields which may deviate the electrons located on the optical axis if the laser is intense enough. While these limitations have not prevented us from obtaining a narrow divergence electron beam, PIC simulations indicate that they will make this acceleration method at oblique incidence difficult to scale to larger laser (and electron) energies because we expect in this case an increase in the electron beam angular spread. This result indicates that normal incidence should be favoured in future experiments with radial polarization.

Conclusion and perspectives

In this thesis, the interaction between an overdense plasma and a femtosecond relativistic intensity laser pulse has been investigated in two rather unusual regimes.

First, we have considered the case of few-cycle pulses. For short gradient scale lengths ($L \ll \lambda$), reducing the pulse duration does not fundamentally change the interaction. We nonetheless observe that, for a given pulse energy, shorter durations result in higher electron energies because of the increased intensity. For longer gradient scale lengths ($L > \lambda$), extremely short pulse durations can on the opposite drastically change the interaction. In this case, the laser now satisfies the resonance condition as it propagates in the underdense part of the preplasma and is therefore able to trigger high amplitude plasma waves. Electrons can be injected by ionization into these rotated wakefields and accelerated to relativistic energies towards vacuum.

This result confirms that few-cycle pulses may provide access to new acceleration regimes. It more generally shows that new electron emission mechanisms can still be identified from the interaction of an ultraintense laser pulse with an overdense plasma. This is especially true for long gradient scale lengths. Indeed, although many experiments have been performed in this case, clearly establishing the existing acceleration mechanisms and the precise conditions for which they occur remains challenging. Fully understanding the physics of the interaction at these long gradients will require more experiments with diverse parameters and precisely controled conditions. We anticipate that this field will profit from future progress in the control and diagnostic of the plasma density profile, since we have seen that uncertainties associated with the preplasma expansion could result in uncertainties on the analysis of experimental results. The current development and increase in accessibility of high-resolution 3D PIC simulations will likely also be highly beneficial to the accurate modeling of coming experiments.

Secondly, we have considered the case where the incident laser has radial polarization. We have first seen that plasma mirrors can ideally inject electrons into the reflected pulse, where they can be accelerated to high energies. This has been confirmed for normal incidence in PIC simulations and for oblique incidence both in PIC simulations and in experiments. The ejected electrons can be directly accelerated in the longitudinal direction by the E_z field, which can, under adequate conditions, result in a smaller angular spread than with linear polarization. This precisely corresponds to the initial objective of using radially polarized pulses, which confirms that such beams have an excellent structure for vacuum laser acceleration.

Nonetheless, while relativistic energies can be obtained in a robust manner with this acceleration scheme, the simulations indicate that the conditions leading to very narrow angular spreads are more difficult to predict. This is largely due to the inherent intricacy of the laser plasma interaction and of the subsequent acceleration in vacuum, which is sensitive to the exact initial electron distributions. At oblique incidence, the interaction in vacuum is made even more complex by the partial loss of the radially polarized structure which is caused by the difference in the reflectivity between the *s* and *p*-polarized parts of the beam. We anticipate that this phenomenon, which leads to the emergence of strong transverse fields on the optical axis, could be the main limit preventing the obtention of high-quality electron beams with large energies at oblique incidence.

Overall, the range of parameters for which acceleration is optimal is quite narrow. First, the electrons should be accelerated to high energies (> 10 MeV) so that they are emitted close to the specular direction. This mandates to use of lasers with high peak powers and tight focusings. Next, the interaction should be perfomed at normal incidence so that the radially polarized structure is preserved, ensuring that the deflecting transverse fields remain weak close to the optical axis. Finally, few-cycle pulses are preferred because we have observed that only electrons injected in the first few bunches tend to be well-collimated. With such short pulse durations, the CEP of the laser should be stabilized since we have seen that it can have a considerable impact on the injection of electrons from the plasma. In these optimal conditions, which correspond to parameters targeted by the SYLOS laser at the ELI-ALPS institute in Hungary, the obtained electron beam is expected to have peaked angular and energy distributions. This could make VLA with radial polarization a credible alternative to laser wakefield acceleration in the quest for ultrafast electron diffraction experiments with sub-10 fs resolution. This therefore clearly calls for experiments to be carried out in this promising scenario. Such experiments would also be the occasion to confirm the predicted large effect of the CEP on the interaction. In order to attain these objectives, two challenges should be overcome:

- Existing experiments should be adapted so that they can be performed at normal incidence and that an electron beam backpropagating towards the employed focusing optical element can be detected. In the case where this would be too difficult to achieve, experiments at quasi-normal incidence could be considered. An interesting follow-up study would therefore be to investigate whether results at small incidence angles would be significantly different from results at normal incidence.
- Efforts should be made to generate high-quality radially polarized pulses with relativistic intensity. We have indeed seen that the waveplate used to generate radial polarization in the experiments with the UHI100 laser could bring about imperfections in the incident laser pulse. We suspect that these imperfections have in turn deteriorated the acceleration process to the point that (i) we had to reduce the intensity by nearly an order of magnitude in the PIC simulations so that a good agreement with the experimental results could be found and (ii) electrons were accelerated in experiments to significantly higher energies with linear polarization than with radial polarization. This shows in particular that VLA with radial polarization can only be competitive with other acceleration methods if the laser beam has a very good quality, which should probably be as close as possible to the ideal case that is considered in the simulations. Furthermore, we have also observed that introducing the waveplate has led to a substantial increase in the shot-to-shot fluctuations, which have prevented the study of the influence of crucial parameters, such as the gradient scale length. Drastically improving the stability of the radially polarized beam is also a necessary step so that the optimal acceleration regimes can be identified experimentally and so that the generated electron beams can eventually be used in applications in ultrafast science.

All in all, we can remark that the experimental requirements for achieving high-quality acceleration appear to be much more stringent for VLA with radial polarization than for laser-wakefield accelerators. Experiments should be performed at normal incidence, using ≈ 100 mJ few-cycle pulses with a high temporal contrast, and even with a precise control of the CEP. However, this does not necesarily mean that there is no benefit from this acceleration scheme. For instance, since the interaction with the plasma only occurs on the surface and is only used for injection, we could expect the acceleration in vacuum to be less subject to nonlinear phenomena than laser wakefield acceleration, which relies on the propagation of an ultraintense laser pulse inside a plasma. This could result in improved stability, which might in the end be a decisive advantage for applications.

On a broader level, this study with radially polarized pulses illustrates the potential for tunability of plasma mirrors as a source of synchronized electrons and high-harmonics or as a test-bed for studying laser-plasma interactions. Here, simply by changing the laser polarization state, we have been able to trigger the acceleration of electrons in the specular direction and the emission of high-harmonics in two separate interfering sources. We have examined the case of radial polarization, due to its attractive capacity as an electron accelerator, but many other exotic beam structures can also in principle be used. We can mention for example laser beams carrying orbital angular momentum, which have been previously studied in the case of plasma mirrors [181] and also in the case of underdense targets [182] as a way to further control the interaction (in the latter case for instance to obtain donut-shaped wakefields that can be useful for positron acceleration).

Shaping the laser in order to study new physical processes can now be considered as an established technique, as is demonstrated by the recent experimental results obtained on plasma mirrors with beams carrying orbital angular momentum and with radially polarized beams. Nevertheless, using exotic pulses to generate high-quality electron beams might prove more challenging. In our case for example, we have just stated that converting the polarization from linear to radial has resulted in an overall deterioration of the plasma mirror as a source of energetic particles due to imperfections in the radially polarized pulse. This may be a more general feature of ultrahigh intensity exotic beams: in order to obtain improved results compared to a standard Gaussian beam, not only should the new beam structure be able to enhance the interaction *in principle* (e.g. in simulations), but it should also have *in practice* (i.e. in experiments) a high enough quality so that the degradations induced by the beam imperfections do not outweigh the benefits of the chosen structure. The latter point could be critical for the tunability of plasma mirrors as source of particles and radiations and strongly motivate further research towards the generation of high-quality relativistic intensity exotic beams.

It is also worth mentioning that the adaptability of plasma mirrors comes not only from the possibility of shaping the incident laser pulse but also from the possibility of shaping the plasma density profile. This can be achieved either by using preformed targets [183] or spatially shaped prepulses [184]. This could also open up new possibilities and provide an even high degree of control over the interaction. We could for instance consider adjusting the density profile in order to optimize the injection process into a radially polarized beam.

Of course, plasma mirrors are currently not competitive with gas targets as a source of ultrashort electrons and high-harmonics. This could however change in the future due to continuing progress in laser technology and in the control of the interaction. We should in particular keep in mind that high-harmonic generation and electron emission mechanisms at short gradients have only been understood fairly recently and offer an interesting potential for tunability and optimization (the promising interaction at normal incidence with radial polarization is a good illustration). At longer gradients, we can even expect to find new processes for accelerating electrons, whose potential as a source is by definition unknown. In any case, there are still interesting physics to explore in the field of laser-overdense plasma interaction.

Appendix A: 3D PIC simulations with Salle Noire laser parameters

We present in this appendix a 3D PIC simulation performed at oblique incidence with radial polarization and parameters corresponding to the Salle Noire laser. This simulation is compared to the simulation with linear polarization that was presented in section 3.3 and which was carried out with similar laser parameters. We use in both simulations the order-100 PSATD solver with $\Delta x = \Delta y = \Delta z = \lambda/36$ and 6 macroelectrons per cell. These values might not be sufficient to attain full convergence of the simulations, but we have observed that increasing the resolution to $\lambda/48$ in the radial polarization simulation did not significantly change the results. We use a gradient scale length $L = \lambda/7$ and the following laser parameters: a central wavelength $\lambda = 800$ nm, an incidence angle $\theta_i = 45°$, a pulse energy of 2.5 mJ, a beam waist $w_0 = 1.5\,\mu\mathrm{m}$, a pulse duration $\tau = 3.5$ fs, a CEP for the reflected pulse $\phi_{CEP} = -\pi/2$ for radial polarization and $\phi_{CEP} = 0$ for linear polarization (with the notations of equation 1.1). This leads to $a_0 = 2.92$ for linear polarization and $a_{0,r} = 1.77$ and $a_{0,z} = 0.7$ for radial polarization. We note that, since the laser is more tightly focused, the ratio between $a_{0,z}$ and $a_{0,r}$ is higher than in the previous simulations carried out at oblique incidence with parameters corresponding to the UHI100 laser. We could expect that this more important contribution from the E_z field will lead to better results with radial polarization.

We show in figure A.1 the initial position of the electrons that are ejected from the plasma in the simulation. We first notice that the shapes of these distributions become quite complex when using few-cycle pulses. This illustrates the intricacy of the processes leading to electron ejection from the plasma. We nonetheless still observe that electrons tend to be ejected at positions where the E_r field is strong with radial polarization. This is once again not an ideal scenario as the interaction is still dominated by the transverse fields.

We also observe that, as previously, the radially polarized beam partially loses its stucture upon reflection. This is visible in figure A.2 where we can see in particular that there is no longer a clear hole on the optical axis in the transverse field distribution of the reflected pulse.

Ejected electron distributions are displayed in figure A.3. The total ejected charge is similar in both simulations: ≈ 63 pC with linear polarization and ≈ 58 pC with radial polarization. However, we find in this case that using radial polarization actually worsens the results compared to linear polarization. First, the angular divergence is broader, as can be seen in figure A.3(b). Secondly, if the low energy part of the spectrum is similar in both simulations, we observe a high energy tail that extends up to ≈ 5 MeV with linear polarization and which is not present with radial polarization. The maximum reached energy in the latter case in only ≈ 2 MeV. This means that with the chosen parameters, the structure of the radially polarized beam is not sufficient to compensate the lower intensity coming from the conversion from linear to radial polarization. We can note that in the simulation with radial polarization, the electron beam already has a wide angular spread very close from the plasma surface, which is probably because the longitudinal electron momenta remain small. This is different from the higher intensity simulation with UHI100 parameters (see figure 5.10(a)) in which the electrons were initially well collimated before being deflected in the θ_y direction by the harmonic fields.

These simulations confirm that it can be difficult to predict experimental results when plasma mirrors are used with radial polarization. Indeed, although we had hoped that the tighter focusing associated

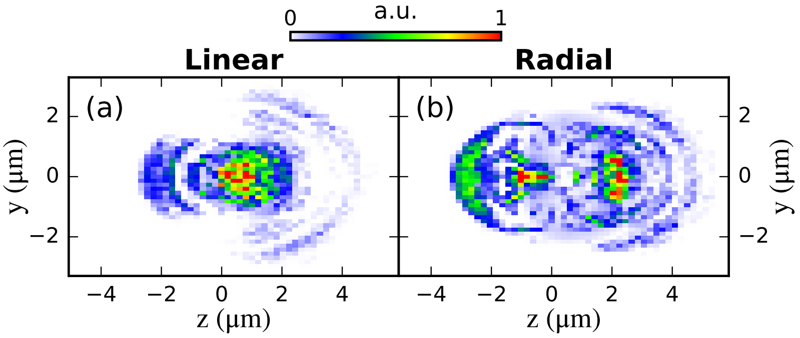

Figure A.1: Results from 3D PIC simulations with Salle Noire laser parameters. Initial position of the electrons that are ejected $4\,\mu\mathrm{m}$ *away from the plasma in the case of (a) linear and (b) radial polarization. Detailed simulation parameters are provided in appendix B.*

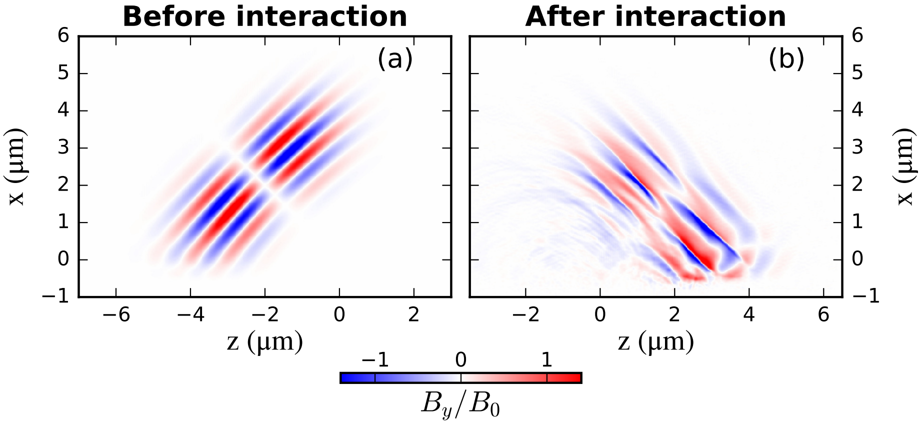

Figure A.2: Results from a 3D PIC simulation with Salle Noire laser parameters. Laser magnetic field in the incidence plane with radial polarization, either (a) before or (b) after the interaction. Here, the magnetic field is given in units of a_0 $(B_0 = m_e\omega/e)$*. Detailed simulation parameters are provided in appendix B.*

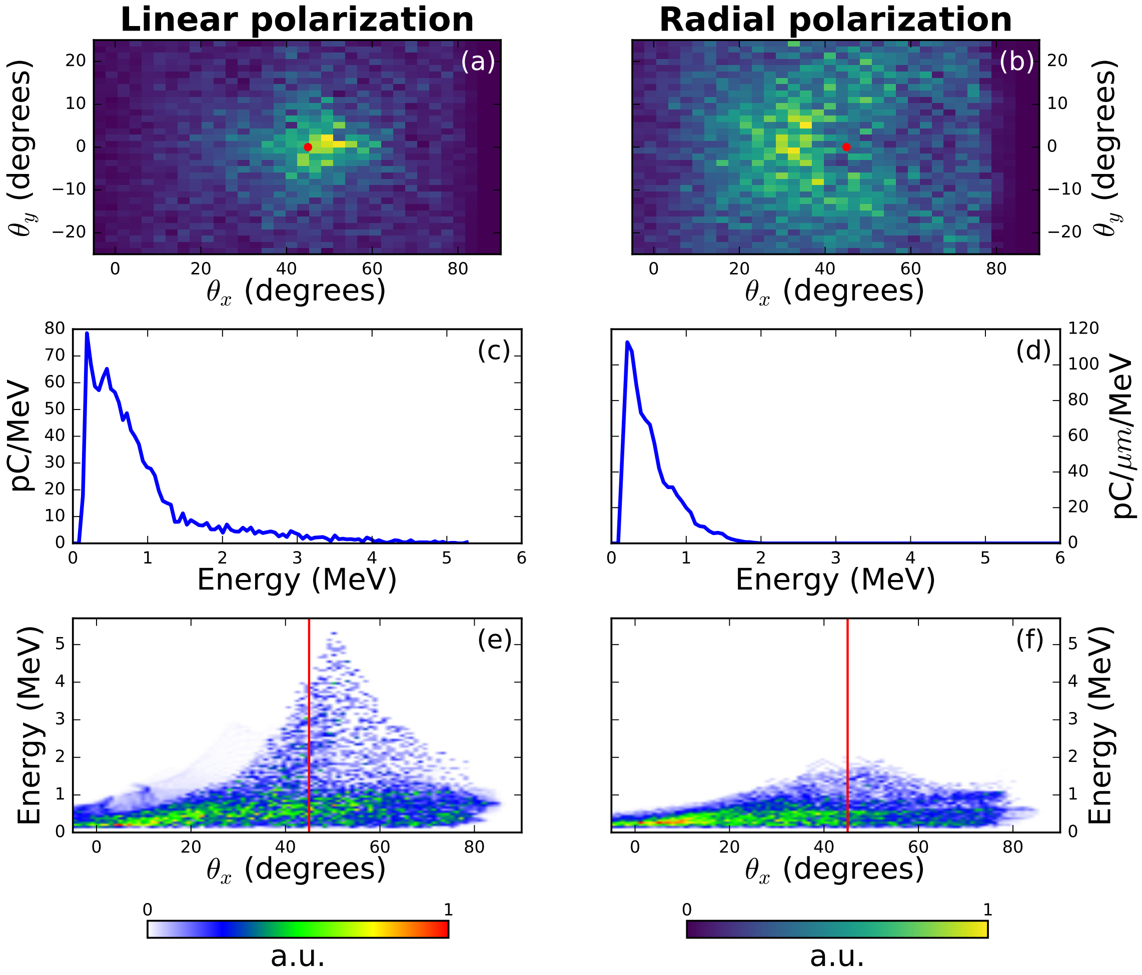

Figure A.3: Ejected electron distributions in the 3D PIC simulations with Salle Noire laser parameters. (a)-(b) Angular distribution respectively for linear and radial polarization. (c)-(d) Energy spectrum respectively for linear and radial polarization. (e)-(f) Correlation between energy and θ_x angle with respect to normal direction in the incident plane respectively for linear and radial polarization. Only the electrons with an energy higher than 150 keV are displayed. The red lines and dot mark the specular direction. Detailed simulation parameters are provided in appendix B.

with the Salle Noire laser could improve the results thanks to a stronger E_z field (relative to the E_r field), we have found that radial polarization actually deteriorates the acceleration process in this case. We can however recall that, using the same laser parameters, we have obtained at normal incidence more collimated electron beams with energies reaching up to ≈ 10 MeV (see for instance figures 4.29(d) and (e)) from radial polarization. The latter case corresponds to the best VLA scenario that we have observed with Salle Noire laser parameters.

Appendix B: Parameters for PIC simulations

Detailed PIC simulation parameters are provided in this appendix. In all simulations the plasma density gradient is parallel to one of the grid directions and we use λ = 800 nm.

Figures	Geometry	Spatial step	ppc	Solver	interp	azim	moving window
1.12	2D	$\lambda/30$	25	Yee	3	-	no
2.6	2D	$\lambda/9.5$-$\lambda/19$-$\lambda/28.5$	0	Yee	3	-	yes
2.9	2D	$\lambda/9.5$-$\lambda/4.8$-$\lambda/3.2$	0	PSATD-100	3	-	yes
2.10	3D	$\lambda/12.5$	0	PSATD-100	3	-	yes
3.18(a)-(f)-3.19(a)-(e)	2D	$\lambda/143$	36	Yee	3	-	yes, 100 μm propagation
3.18(g)-(i)-3.19(b)-(f)	3D	$\lambda/36$	6	PSATD-100	3	-	yes, 70 μm propagation
3.20-3.38	2D	$\lambda/71$	4	Yee	3	-	yes, 100 μm propagation
3.39(a)	2D	$\lambda/16$	1	Yee	3	-	no
3.39(b)-3.40	3D	$\lambda/16$	1	Yee	3	-	no
4.10-4.15	r-z	$\Delta x \approx \lambda/882$; $\Delta r \approx \lambda/205$	50	Yee	3	1	yes, 150 μm propagation
4.29	r-z	$\Delta x \approx \lambda/294$; $\Delta r \approx \lambda/68$	200	Yee	3	1	yes, 150 μm propagation
4.30	r-z	$\Delta x \approx \lambda/294$; $\Delta r \approx \lambda/68$	30	Yee	3	1	yes, 800 μm propagation
4.31-4.32	r-z	$\Delta x \approx \lambda/294$; $\Delta r \approx \lambda/68$	250	Yee	3	1	yes, 150 μm propagation
4.33	r-z	$\Delta x \approx \lambda/294$; $\Delta r \approx \lambda/68$	200	Yee	3	1	yes, 150 μm propagation
4.34	r-z	$\Delta x \approx \lambda/294$; $\Delta r \approx \lambda/68$	50	Yee	3	1	yes, 800 μm propagation
5.7-5.13	3D	$\lambda/57$	6	PSATD-100	3	-	yes, 80 μm propagation
A.1-A.3	3D	$\lambda/36$	6	PSATD-100	3	-	yes, 70 μm propagation

Table 1: Numerical parameters for the PIC simulations presented in this manuscript. ppc: particles per cell per species before ionization, interp: interpolation order, azim: azimuthal decomposition order in cylindrical coordinates (azim = 1 corresponds to orders 0 and 1).

Figures	a_0	w_0 (μm)	τ **(fs)**	**Incidence**	**Envelope**
1.12	2.15	1.5	5	45°	eqs. 2.82-2.87
2.6	1	6	3.14	0°	eqs. 2.47-2.48
2.9	1	6	3.14	0°	eqs. 2.47-2.48
2.10	1	1.5	3.5	0°	eqs. 2.82-2.87 + eqs. 2.47-2.48
3.18(a)-(f)-3.19(a)-(e)	2.92	1.5	3.5	45°	eqs. 2.65-2.66
3.18(g)-(i)-3.19(b)-(f)	2.92	1.5	3.5	45°	eqs. 2.82-2.87
3.20-3.26	2.57-0.98	1.5	3.5-24	55°	eqs. 2.65-2.66
3.32-3.35	2.15	1.5	5	40°-70°	eqs. 2.65-2.66
3.36	2.15	1.5	5	55°	eqs. 2.65-2.66
3.37	10	1.5	5	55°	eqs. 2.65-2.66
3.38	2.15	1.5	5	55°	eqs. 2.65-2.66
3.39-3.40	2-0.86	1.5	5-24	55°	eqs. 2.82-2.87
4.10-4.15 + 4.29	$a_{0,z} = 0.7$; $a_{0,r} = 1.77$	1.5	3.5	0°	eqs. 2.89-2.91
4.30	$a_{0,z} = 0.94$; $a_{0,r} = 4.9$	3.1	24	0°	cosine + paraxial
4.31-4.32	$a_{0,z} = 3.78$; $a_{0,r} = 9.55$	1.5	5	0°	eqs. 2.89-2.91
4.33	$a_{0,z} = 7$; $a_{0,r} = 17.7$	1.5	3.5	0°	eqs. 2.89-2.91
4.34	$a_{0,z} = 12.7$; $a_{0,r} = 32$	1.5	24	0°	cosine + paraxial
5.7-5.8	5.4	3.1	24	60°	cosine + paraxial
5.7-5.9	$a_{0,z} = 0.94$; $a_{0,r} = 4.9$	3.1	24	60°	cosine + paraxial
5.10(b)-5.11(b)	3.6	3.1	24	60°	cosine + paraxial
5.10(a)-5.11(a)-5.13(c),(d)	$a_{0,z} = 0.63$; $a_{0,r} = 3.3$	3.1	24	60°	cosine + paraxial
5.10(c),(d)-5.11(c),(d)-5.13(a),(b)	$a_{0,z} = 0.31$; $a_{0,r} = 1.6$	3.1	24	60°	cosine + paraxial
A.1(a)-A.3(a)-(e)	2.92	1.5	3.5	45°	eqs. 2.82-2.87
A.1(b)-A.2-A.3(b)-(f)	$a_{0,z} = 0.7$; $a_{0,r} = 1.77$	1.5	3.5	45°	eqs. 2.89-2.91

Table 2: Laser parameters for the PIC simulations presented in this manuscript. cosine + paraxial: cosine temporal envelope with paraxial approximation fields.

Figures	**L ($/\lambda$)**	n_{MAX} ($/n_c$)	n_{MIN} ($/n_c$)	T_e **(eV)**	T_i **(eV)**	**Ions**
1.12	0-1/7-2	100	1/20	0	0	C^{6+}
3.18(a)-(f)-3.19(a)-(e)	1/7	200	1/20	0	0	O^{8+}
3.18(g)-(i)-3.19(b)-(f)	1/7	100	1/20	0	0	C^{6+}
3.20-3.35	Hydro (80 ps)	-	1/450	0	0	Si^{4+} + O^{2+}
3.36	Hydro (6-130 ps)	-	1/450	0	0	Si^{4+} + O^{2+}
3.37-3.38	Hydro (80 ps)	-	1/450	0	0	Si^{4+} + O^{2+}
3.39-3.40	Hydro (80 ps)	-	1/140	0	0	Si^{4+}
4.10-4.15 + 4.29	1/7	200	1/10	50	10	$\sim O^{8+}$
4.30	1/7	20	1/5	50	10	$\sim O^{8+}$
4.31-4.34	1/7	200	1/10	50	10	$\sim O^{8+}$
5.7-5.9-5.10(b)-5.11(b)	1/10	100	1/20	0	0	C^{6+}
5.10(a),(c),(d)-5.11(a),(c),(d)-5.13	1/7	100	1/20	0	0	C^{6+}
A.1-A.3	1/7	100	1/20	0	0	C^{6+}

Table 3: Plasma parameters for the PIC simulations presented in this manuscript. L: plasma gradient scale length, T_e: electron temperature, T_i: ion temperature. Simulations with initially fully ionized ions correspond to simulations with ionization turned off.

Bibliography

[1] W. Hittorf. Ueber die Elektricitätsleitung der Gase. Annalen der physik 136, 1 (1869).

[2] Y. Jiang, Z. Chen, Y. Han, P. Deb, H. Gao, S. Xie, P. Purohit, M. W. Tate, J. Park, S. M. Gruner et al. Electron ptychography of 2D materials to deep sub-ångström resolution. Nature 559, 343 (2018).

[3] J. A. Valdmanis, R. L. Fork and J. P. Gordon. Generation of optical pulses as short as 27 femtoseconds directly from a laser balancing self-phase modulation, group-velocity dispersion, saturable absorption, and saturable gain. Opt. Lett. 10, 131 (1985).

[4] A. H. Zewail and J. M. Thomas. *4D electron microscopy: imaging in space and time* (World Scientific, 2010).

[5] G. Sciaini and R. J. D. Miller. Femtosecond electron diffraction: heralding the era of atomically resolved dynamics. Rep. Prog. Phys. 74, 096101 (2011).

[6] J. Maxson, D. Cesar, G. Calmasini, A. Ody, P. Musumeci and D. Alesini. Direct Measurement of Sub-10 fs Relativistic Electron Beams with Ultralow Emittance. Phys. Rev. Lett. 118, 154802 (2017).

[7] R. P. Chatelain, V. R. Morrison, C. Godbout and B. J. Siwick. Ultrafast electron diffraction with radio-frequency compressed electron pulses. Applied Physics Letters 101, 081901 (2012).

[8] A. Gliserin, M. Walbran and P. Baum. Passive optical enhancement of laser-microwave synchronization. Applied Physics Letters 103, 031113 (2013).

[9] M. Gao, Y. Jiang, G. H. Kassier and R. J. Dwayne Miller. Single shot time stamping of ultrabright radio frequency compressed electron pulses. Applied Physics Letters 103, 033503 (2013).

[10] J. A. Fülöp, L. Pálfalvi, S. Klingebiel, G. Almási, F. Krausz, S. Karsch and J. Hebling. Generation of sub-mJ terahertz pulses by optical rectification. Opt. Lett. 37, 557 (2012).

[11] A. Fallahi, M. Fakhari, A. Yahaghi, M. Arrieta and F. X. Kärtner. Short electron bunch generation using single-cycle ultrafast electron guns. Phys. Rev. Accel. Beams 19, 081302 (2016).

[12] R. K. Li, M. C. Hoffmann, E. A. Nanni, S. H. Glenzer, M. E. Kozina, A. M. Lindenberg, B. K. Ofori-Okai, A. H. Reid, X. Shen, S. P. Weathersby, J. Yang, M. Zajac and X. J. Wang. Terahertz-based subfemtosecond metrology of relativistic electron beams. Phys. Rev. Accel. Beams 22, 012803 (2019).

[13] D. Strickland and G. Mourou. Compression of amplified chirped optical pulses. Optics Communications 55, 447 (1985).

[14] T. Tajima and J. M. Dawson. Laser Electron Accelerator. Phys. Rev. Lett. 43, 267 (1979).

[15] E. Esarey, C. B. Schroeder and W. P. Leemans. Physics of laser-driven plasma-based electron accelerators. Rev. Mod. Phys. 81, 1229 (2009).

[16] S. P. D. Mangles, C. D. Murphy, Z. Najmudin, A. G. R. Thomas, J. L. Collier, A. E. Dangor, E. J. Divall, P. S. Foster, J. G. Gallacher, C. J. Hooker, D. A. Jaroszynski, A. J. Langley, W. B. Mori, P. A. Norreys, F. S. Tsung, B. R. Walton and K. Krushelnick. Monoenergetic beams of relativistic electrons from intense laser-plasma interactions. Nature 431, 535 (2004).

[17] C. G. R. Geddes, C. Tóth, J. van Tilborg, E. Esarey, C. B. Schroeder, D. Bruhwiler, C. Nieter, J. Cary and W. P. Leemans. High quality electron beams from a laser wakefield accelerator using plasma-channel guiding. Nature 431, 538 (2004).

[18] J. Faure, Y. Glinec, A. Pukhov, S. Kiselev, S. Gordienko, E. Lefebvre, J.-P. Rousseau, F. Burgy and V. Malka. A laser-plasma accelerator producing monoenergetic electron beams. Nature 431, 541 (2004).

[19] A. J. Gonsalves, K. Nakamura, J. Daniels, C. Benedetti, C. Pieronek, T. C. H. de Raadt, S. Steinke, J. H. Bin, S. S. Bulanov, J. van Tilborg, C. G. R. Geddes, C. B. Schroeder, C. Tóth, E. Esarey, K. Swanson, L. Fan-Chiang, G. Bagdasarov, N. Bobrova, V. Gasilov, G. Korn, P. Sasorov and W. P. Leemans. Petawatt Laser Guiding and Electron Beam Acceleration to 8 GeV in a Laser-Heated Capillary Discharge Waveguide. Phys. Rev. Lett. 122, 084801 (2019).

[20] O. Lundh, J. Lim, C. Rechatin, L. Ammoura, A. Ben-Ismail, X. Davoine, G. Gallot, J.-P. Goddet, E. Lefebvre, V. Malka and J. Faure. Few femtosecond, few kiloampere electron bunch produced by a laser-plasma accelerator. Nat. Phys. 7, 219 (2011).

[21] J. Faure, B. van der Geer, B. Beaurepaire, G. Gallé, A. Vernier and A. Lifschitz. Concept of a laser-plasma-based electron source for sub-10-fs electron diffraction. Phys. Rev. Accel. Beams 19, 021302 (2016).

[22] Z.-H. He, B. Beaurepaire, J. A. Nees, G. Gallé, S. A. Scott, J. R. S. Pérez, M. G. Lagally, K. Krushelnick, A. G. R. Thomas and J. Faure. Capturing Structural Dynamics in Crystalline Silicon Using Chirped Electrons from a Laser Wakefield Accelerator. Sci. Rep. 6, 36224 (2016).

[23] M. Thévenet, H. Vincenti and J. Faure. On the physics of electron ejection from laser-irradiated overdense plasmas. Physics of Plasmas 23, 063119 (2016).

[24] L. Chopineau, A. Leblanc, G. Blaclard, A. Denoeud, M. Thévenet, J.-L. Vay, G. Bonnaud, P. Martin, H. Vincenti and F. Quéré. Identification of Coupling Mechanisms between Ultraintense Laser Light and Dense Plasmas. Phys. Rev. X 9, 011050 (2019).

[25] C. Thaury, F. Quéré, J.-P. Geindre, A. Levy, T. Ceccotti, P. Monot, M. Bougeard, F. Réau, P. d'Oliveira, P. Audebert, R. Marjoribanks and P. Martin. Plasma mirrors for ultrahigh-intensity optics. Nature Physics 3, 424 (2007).

[26] S. Kahaly, S. Monchocé, H. Vincenti, T. Dzelzainis, B. Dromey, M. Zepf, P. Martin and F. Quéré. Direct Observation of Density-Gradient Effects in Harmonic Generation from Plasma Mirrors. Phys. Rev. Lett. 110, 175001 (2013).

[27] M. Thévenet, A. Leblanc, S. Kahaly, H. Vincenti, A. Vernier, F. Quéré and J. Faure. Vacuum laser acceleration of relativistic electrons using plasma mirror injectors. Nature Physics 12, 355 EP (2015). Article.

[28] A. Macchi, M. Borghesi and M. Passoni. Ion acceleration by superintense laser-plasma interaction. Rev. Mod. Phys. 85, 751 (2013).

[29] C. Thaury and F. Quéré. High-order harmonic and attosecond pulse generation on plasma mirrors: basic mechanisms. Journal of Physics B: Atomic, Molecular and Optical Physics 43, 213001 (2010).

[30] A. Kemp, F. Fiuza, A. Debayle, T. Johzaki, W. Mori, P. Patel, Y. Sentoku and L. Silva. Laser–plasma interactions for fast ignition. Nuclear Fusion 54, 054002 (2014).

[31] A. E. Siegman. Lasers. Mill Valley, CA: Univ. Science pp. 298–301 (1986).

[32] A. Jullien, A. Ricci, F. Böhle, J.-P. Rousseau, S. Grabielle, N. Forget, H. Jacqmin, B. Mercier and R. Lopez-Martens. Carrier-envelope-phase stable, high-contrast, double chirped-pulse-amplification laser system. Opt. Lett. 39, 3774 (2014).

[33] F. Böhle, M. Kretschmar, A. Jullien, M. Kovacs, M. Miranda, R. Romero, H. Crespo, U. Morgner, P. Simon, R. Lopez-Martens and T. Nagy. Compression of CEP-stable multi-mJ laser pulses down to 4 fs in long hollow fibers. Laser Physics Letters 11, 095401 (2014).

[34] F. Böhle. Near-single-cycle laser for driving relativistic plasma mirrors at kHz repetition rate-development and application. Ph.D. thesis (2017).

[35] M. Ouillé, A. Vernier, F. Boehle, M. Bocoum, M. Lozano, J.-P. Rousseau, Z. Cheng, D. Gustas, A. Blumenstein, P. Simon, S. Haessler, J. Faure, T. Nagy and R. Lopez-Martens. Relativistic near-single-cycle optics at 1 kHz (2019).

[36] P. Gibbon. *Short pulse laser interactions with matter* (World Scientific Publishing Company Singapore, 2004).

[37] J.-M. Rax. *Physique des plasmas: cours et applications* (Dunod, 2005).

[38] J. Delcroix and A. Bers. Physique des plasmas, 2 volumes. InterEditions/CNRS (1994).

[39] R. O. Dendy. *Plasma physics: an introductory course* (Cambridge University Press, 1995).

[40] E. Lefebvre and G. Bonnaud. Transparency/Opacity of a Solid Target Illuminated by an Ultrahigh-Intensity Laser Pulse. Phys. Rev. Lett. 74, 2002 (1995).

[41] S. Guérin, P. Mora, J. C. Adam, A. Héron and G. Laval. Propagation of ultraintense laser pulses through overdense plasma layers. Physics of Plasmas 3, 2693 (1996).

[42] N. E. Andreev, L. M. Gorbunov, A. A. Pogasova, R. R. Ramazashvili and V. I. Kirsanov. Resonant excitation of wake fields by a laser pulse in a plasma. JETP Lett. 55, 571 (1992). [Pisma Zh. Eksp. Teor. Fiz.55,551(1992)].

[43] V. I. Berezhiani and I. G. Murusidze. Interaction of highly relativistic short laser pulses with plasmas and nonlinear wake-field generation. Physica Scripta 45, 87 (1992).

[44] E. Esarey, A. Ting, P. Sprangle, D. Umstadter and X. Liu. Nonlinear analysis of relativistic harmonic generation by intense lasers in plasmas. IEEE Transactions on Plasma Science 21, 95 (1993).

[45] W. Lu, M. Tzoufras, C. Joshi, F. S. Tsung, W. B. Mori, J. Vieira, R. A. Fonseca and L. O. Silva. Generating multi-GeV electron bunches using single stage laser wakefield acceleration in a 3D nonlinear regime. Phys. Rev. ST Accel. Beams 10, 061301 (2007).

[46] J. Faure. Accélération de faisceaux d'électrons par interaction laser-plasma .

[47] J. Faure. Plasma Injection Schemes for Laser-Plasma Accelerators. CERN Yellow Report pp. 143–157. 15 p (2017). 15 pages, contribution to the CAS - CERN Accelerator School: Plasma Wake Acceleration, CERN, Geneva, Switzerland, 23 - 29 Nov 2014.

[48] J. Faure, C. Rechatin, A. Norlin, A. Lifschitz, Y. Glinec and V. Malka. Controlled injection and acceleration of electrons in plasma wakefields by colliding laser pulses. Nature 444, 737 (2006).

[49] W. L. Jianfei Hua, Yipeng Wu. External injection from a Linac into a LWFA with $\sim$100% capture efficiency (Conference Presentation) (2019).

[50] C. McGuffey, A. G. R. Thomas, W. Schumaker, T. Matsuoka, V. Chvykov, F. J. Dollar, G. Kalintchenko, V. Yanovsky, A. Maksimchuk, K. Krushelnick, V. Y. Bychenkov, I. V. Glazyrin and A. V. Karpeev. Ionization Induced Trapping in a Laser Wakefield Accelerator. Phys. Rev. Lett. 104, 025004 (2010).

[51] A. Pak, K. A. Marsh, S. F. Martins, W. Lu, W. B. Mori and C. Joshi. Injection and Trapping of Tunnel-Ionized Electrons into Laser-Produced Wakes. Phys. Rev. Lett. 104, 025003 (2010).

[52] M. Chen, E. Esarey, C. B. Schroeder, C. G. R. Geddes and W. P. Leemans. Theory of ionization-induced trapping in laser-plasma accelerators. Physics of Plasmas 19, 033101 (2012).

[53] A. V. Brantov, T. Z. Esirkepov, M. Kando, H. Kotaki, V. Y. Bychenkov and S. V. Bulanov. Controlled electron injection into the wake wave using plasma density inhomogeneity. Phys. Plasmas 15, 073111 (2008).

[54] M. C. Downer, R. Zgadzaj, A. Debus, U. Schramm and M. C. Kaluza. Diagnostics for plasma-based electron accelerators. Rev. Mod. Phys. 90, 035002 (2018).

[55] S. Corde, K. Ta Phuoc, G. Lambert, R. Fitour, V. Malka, A. Rousse, A. Beck and E. Lefebvre. Femtosecond x rays from laser-plasma accelerators. Rev. Mod. Phys. 85, 1 (2013).

[56] D. Guénot, D. Gustas, A. Vernier, B. Beaurepaire, F. Böhle, M. Bocoum, M. Lozano, A. Jullien, R. Lopez-Martens, A. Lifschitz and J. Faure. Relativistic electron beams driven by kHz single-cycle light pulses. Nat. Photon. 11, 293 (2017). Letter.

[57] D. Gustas, D. Guénot, A. Vernier, S. Dutt, F. Böhle, R. Lopez-Martens, A. Lifschitz and J. Faure. High-charge relativistic electron bunches from a kHz laser-plasma accelerator. Phys. Rev. Accel. Beams 21, 013401 (2018).

[58] G. G. Scott, V. Bagnoud, C. Brabetz, R. J. Clarke, J. S. Green, R. I. Heathcote, H. W. Powell, B. Zielbauer, T. D. Arber, P. McKenna and D. Neely. Optimization of plasma mirror reflectivity and optical quality using double laser pulses. New Journal of Physics 17, 033027 (2015).

[59] M. Bocoum, M. Thévenet, F. Böhle, B. Beaurepaire, A. Vernier, A. Jullien, J. Faure and R. Lopez-Martens. Anticorrelated Emission of High Harmonics and Fast Electron Beams From Plasma Mirrors. Phys. Rev. Lett. 116, 185001 (2016).

[60] P. McKenna, D. Carroll, O. Lundh, F. Nürnberg, K. Markey, S. Bandyopadhyay, D. Batani, R. Evans, R. Jafer, S. Kar and et al. Effects of front surface plasma expansion on proton acceleration in ultraintense laser irradiation of foil targets. Laser and Particle Beams 26, 591–596 (2008).

[61] M. Thévenet. Modeling the interaction between a few-cycle relativistic laser pulse and a plasma mirror: from electron acceleration to harmonic generation. Ph.D. thesis, Université Paris-Saclay (2016).

[62] J. P. Geindre, P. Audebert, A. Rousse, F. Falliès, J. C. Gauthier, A. Mysyrowicz, A. D. Santos, G. Hamoniaux and A. Antonetti. Frequency-domain interferometer for measuring the phase and amplitude of a femtosecond pulse probing a laser-produced plasma. Opt. Lett. 19, 1997 (1994).

[63] M. Bocoum, F. Böhle, A. Vernier, A. Jullien, J. Faure and R. Lopez-Martens. Spatial-domain interferometer for measuring plasma mirror expansion. Optics Letters 40, 3009 (2015).

[64] F. Brunel. Not-so-resonant, resonant absorption. Phys. Rev. Lett. 59, 52 (1987).

[65] W. L. Kruer and K. Estabrook. J×B heating by very intense laser light. The Physics of Fluids 28, 430 (1985).

[66] D. W. Forslund, J. M. Kindel, K. Lee, E. L. Lindman and R. L. Morse. Theory and simulation of resonant absorption in a hot plasma. Phys. Rev. A 11, 679 (1975).

[67] J. Zhang, J. Zhang, Z. M. Sheng, Y. T. Li, Y. Qiu, Z. Jin and H. Teng. Emission direction of fast electrons in laser-solid interactions at intensities from the nonrelativistic to the relativistic. Phys. Rev. E 69, 046408 (2004).

[68] J. P. Geindre, P. Audebert and R. S. Marjoribanks. Relativistic AC Gyromagnetic Effects in Ultraintense Laser-Matter Interaction. Phys. Rev. Lett. 97, 085001 (2006).

[69] Y. T. Li, J. Zhang, L. M. Chen, Y. F. Mu, T. J. Liang, Z. Y. Wei, Q. L. Dong, Z. L. Chen, H. Teng, S. T. Chun-Yu, W. M. Jiang, Z. J. Zheng and X. W. Tang. Hot electrons in the interaction of femtosecond laser pulses with foil targets at a moderate laser intensity. Phys. Rev. E 64, 046407 (2001).

[70] D. F. Cai, Y. Q. Gu, Z. J. Zheng, W. M. Zhou, X. D. Yang, C. Y. Jiao, H. Chen, T. S. Wen and S. T. Chunyu. Double-peak emission of hot electrons generated by femtosecond laser interaction with solid targets. Phys. Rev. E 70, 066410 (2004).

[71] Y. T. Li, X. H. Yuan, M. H. Xu, Z. Y. Zheng, Z. M. Sheng, M. Chen, Y. Y. Ma, W. X. Liang, Q. Z. Yu, Y. Zhang, F. Liu, Z. H. Wang, Z. Y. Wei, W. Zhao, Z. Jin and J. Zhang. Observation of a Fast Electron Beam Emitted along the Surface of a Target Irradiated by Intense Femtosecond Laser Pulses. Phys. Rev. Lett. 96, 165003 (2006).

[72] J. Y. Mao, L. M. Chen, K. Huang, Y. Ma, J. R. Zhao, D. Z. Li, W. C. Yan, J. L. Ma, M. Aeschlimann, Z. Y. Wei and J. Zhang. Highly collimated monoenergetic target-surface electron acceleration in near-critical-density plasmas. Applied Physics Letters 106, 131105 (2015).

[73] A. Pukhov, Z.-M. Sheng and J. Meyer-ter Vehn. Particle acceleration in relativistic laser channels. Physics of Plasmas 6, 2847 (1999).

[74] T. Toncian, C. Wang, E. McCary, A. Meadows, A. Arefiev, J. Blakeney, K. Serratto, D. Kuk, C. Chester, R. Roycroft, L. Gao, H. Fu, X. Yan, J. Schreiber, I. Pomerantz, A. Bernstein, H. Quevedo, G. Dyer, T. Ditmire and B. Hegelich. Non-Maxwellian electron distributions resulting from direct laser acceleration in near-critical plasmas. Matter and Radiation at Extremes 1, 82 (2016).

[75] Y. Ma, J. Zhao, Y. Li, D. Li, L. Chen, J. Liu, S. J. D. Dann, Y. Ma, X. Yang, Z. Ge, Z. Sheng and J. Zhang. Ultrahigh-charge electron beams from laser-irradiated solid surface. Proceedings of the National Academy of Sciences (2018).

[76] I. Tsymbalov, D. Gorlova, S. Shulyapov, V. Prokudin, A. Zavorotny, K. Ivanov, R. Volkov, V. Bychenkov, V. Nedorezov, A. Paskhalov, N. Eremin and A. Savel'ev. Well collimated MeV electron beam generation in the plasma channel from relativistic laser-solid interaction. Plasma Physics and Controlled Fusion 61, 075016 (2019).

[77] F. V. Hartemann, S. N. Fochs, G. P. L. Sage, J. N. C. Luhmann, J. G. Woodworth, M. D. Perry, Y. J. Chen and A. K. Kerman. Nonlinear ponderomotive scattering of relativistic electrons by an intense laser field at focus. Phys. Rev. E 51, 4833 (1995).

[78] E. Esarey, P. Sprangle and J. Krall. Laser acceleration of electrons in vacuum. Phys. Rev. E 52, 5443 (1995).

[79] W. B. Mori and T. Katsouleas. Laser acceleration. AIP Conference Proceedings 335, 112 (1995).

[80] B. Quesnel and P. Mora. Theory and simulation of the interaction of ultraintense laser pulses with electrons in vacuum. Phys. Rev. E 58, 3719 (1998).

[81] W. Yu, M. Y. Yu, J. X. Ma, Z. M. Sheng, J. Zhang, H. Daido, S. B. Liu, Z. Z. Xu and R. X. Li. Ponderomotive acceleration of electrons at the focus of high intensity lasers. Phys. Rev. E 61, R2220 (2000).

[82] I. Y. Dodin and N. J. Fisch. Relativistic electron acceleration in focused laser fields after above-threshold ionization. Phys. Rev. E 68, 056402 (2003).

[83] G. V. Stupakov and M. S. Zolotorev. Ponderomotive Laser Acceleration and Focusing in Vacuum for Generation of Attosecond Electron Bunches. Phys. Rev. Lett. 86, 5274 (2001).

[84] Y. I. Salamin and C. H. Keitel. Electron Acceleration by a Tightly Focused Laser Beam. Phys. Rev. Lett. 88, 095005 (2002).

[85] J. Pang, Y. K. Ho, X. Q. Yuan, N. Cao, Q. Kong, P. X. Wang, L. Shao, E. H. Esarey and A. M. Sessler. Subluminous phase velocity of a focused laser beam and vacuum laser acceleration. Phys. Rev. E 66, 066501 (2002).

[86] A. Maltsev and T. Ditmire. Above Threshold Ionization in Tightly Focused, Strongly Relativistic Laser Fields. Phys. Rev. Lett. 90, 053002 (2003).

[87] D. Cline. First Observation of Acceleration of Electrons by a Laser in a Vacuum. Journal of Modern Physics 4, 1 (2013).

[88] C. Varin, S. Payeur, V. Marceau, S. Fourmaux, A. April, B. Schmidt, P. L. Fortin, N. Thiré, T. Brabec, F. Légaré, J. C. Kieffer and M. Piché. Direct Electron Acceleration with Radially Polarized Laser Beams. Applied Sciences 3, 70 (2013).

[89] V. Marceau, C. Varin, T. Brabec and M. Piché. Femtosecond 240-keV electron pulses from direct laser acceleration in a low-density gas. Phys. Rev. Lett. 111, 224801 (2013).

[90] P. L. Fortin, M. Piché and C. Varin. Direct-field electron acceleration with ultrafast radially polarized laser beams: scaling laws and optimization. Journal of Physics B: Atomic, Molecular and Optical Physics 43, 025401 (2009).

[91] L. J. Wong and F. X. Kärtner. Direct acceleration of an electron in infinite vacuum by a pulsed radially-polarized laser beam. Opt. Express 18, 25035 (2010).

[92] S. J. McNaught, J. P. Knauer and D. D. Meyerhofer. Photoelectron initial conditions for tunneling ionization in a linearly polarized laser. Phys. Rev. A 58, 1399 (1998).

[93] C. I. Moore, A. Ting, S. J. McNaught, J. Qiu, H. R. Burris and P. Sprangle. A Laser-Accelerator Injector Based on Laser Ionization and Ponderomotive Acceleration of Electrons. Phys. Rev. Lett. 82, 1688 (1999).

[94] G. Malka, E. Lefebvre and J. L. Miquel. Experimental Observation of Electrons Accelerated in Vacuum to Relativistic Energies by a High-Intensity Laser. Phys. Rev. Lett. 78, 3314 (1997).

[95] K. T. McDonald. Comment on “Experimental Observation of Electrons Accelerated in Vacuum to Relativistic Energies by a High-Intensity Laser”. Phys. Rev. Lett. 80, 1350 (1998).

[96] P. Mora and B. Quesnel. Comment on “Experimental Observation of Electrons Accelerated in Vacuum to Relativistic Energies by a High-Intensity Laser”. Phys. Rev. Lett. 80, 1351 (1998).

[97] C. Varin and M. Piché. Acceleration of ultra-relativistic electrons using high-intensity TM01 laser beams. Applied Physics B 74, s83 (2002).

[98] C. Varin, M. Piché and M. A. Porras. Acceleration of electrons from rest to GeV energies by ultrashort transverse magnetic laser pulses in free space. Phys. Rev. E 71, 026603 (2005).

[99] C. Varin and M. Piché. Relativistic attosecond electron pulses from a free-space laser-acceleration scheme. Phys. Rev. E 74, 045602 (2006).

[100] Y. I. Salamin. Electron acceleration from rest in vacuum by an axicon Gaussian laser beam. Phys. Rev. A 73, 043402 (2006).

[101] Y. I. Salamin. Mono-energetic GeV electrons from ionization in a radially polarized laser beam. Opt. Lett. 32, 90 (2007).

[102] A. Karmakar and A. Pukhov. Collimated attosecond GeV electron bunches from ionization of high-Z material by radially polarized ultra-relativistic laser pulses. Laser and Part. Beams 25, 371 (2007).

[103] A. Sell and F. X. Kärtner. Attosecond electron bunches accelerated and compressed by radially polarized laser pulses and soft-x-ray pulses from optical undulators. Journal of Physics B: Atomic, Molecular and Optical Physics 47, 015601 (2013).

[104] A. Martens, K. Dupraz, K. Cassou, N. Delerue, A. Variola and F. Zomer. Direct electron acceleration with tightly focused TM0,1 beams: boundary conditions and non-paraxial corrections. Opt. Lett. 39, 981 (2014).

[105] V. Marceau, P. Hogan-Lamarre, T. Brabec, M. Piché and C. Varin. Tunable high-repetition-rate femtosecond few-hundred keV electron source. Journal of Physics B: Atomic, Molecular and Optical Physics 48, 045601 (2015).

[106] C. Varin, V. Marceau, P. Hogan-Lamarre, T. Fennel, M. Piché and T. Brabec. MeV femtosecond electron pulses from direct-field acceleration in low density atomic gases. Journal of Physics B: Atomic, Molecular and Optical Physics 49, 024001 (2015).

[107] L. J. Wong, K.-H. Hong, S. Carbajo, A. Fallahi, P. Piot, M. Soljacic, J. D. Joannopoulos, F. X. Kärtner and I. Kaminer. Laser-Induced Linear-Field Particle Acceleration in Free Space. Scientific Reports 7, 11159 (2017).

[108] D. Pohl. Operation of a Ruby Laser in the Purely Transverse Electric Mode TE01. Applied Physics Letters 20, 266 (1972).

[109] F. P. Schäfer. On some properties of axicons. Applied Physics B 39, 1 (1986).

[110] S. C. Tidwell, D. H. Ford and W. D. Kimura. Generating radially polarized beams interferometrically. Appl. Opt. 29, 2234 (1990).

[111] E. Churin, J. Hossfeld and T. Tschudi. Polarization configurations with singular point formed by computer generated holograms. Optics Communications 99, 13 (1993).

[112] A. V. Nesterov, V. G. Niziev and V. P. Yakunin. Generation of high-power radially polarized beam. Journal of Physics D: Applied Physics 32, 2871 (1999).

[113] S. Payeur, S. Fourmaux, B. E. Schmidt, J. P. MacLean, C. Tchervenkov, F. Légaré, M. Piché and J. C. Kieffer. Generation of a beam of fast electrons by tightly focusing a radially polarized ultrashort laser pulse. Applied Physics Letters 101, 041105 (2012).

[114] S. Carbajo, E. Granados, D. Schimpf, A. Sell, K.-H. Hong, J. Moses and F. X. Kärtner. Efficient generation of ultra-intense few-cycle radially polarized laser pulses. Opt. Lett. 39, 2487 (2014).

[115] N. Nakanii, T. Hosokai, N. C. Pathak, S. Masuda, A. G. Zhidkov, H. Nakahara, K. Iwasa, Y. Mizuta, N. Takeguchi, T. P. Otsuka, K. Sueda, J. Ogino, H. Nakamura, M. Mori, M. Kando and R. Kodama. Decomposition of powerful axisymmetrically polarized laser pulses in underdense plasma. Phys. Rev. E 94, 063205 (2016).

[116] A. V. Nesterov and V. G. Niziev. Laser beams with axially symmetric polarization. Journal of Physics D: Applied Physics 33, 1817 (2000).

[117] T. P. Wangler. *RF Linear accelerators* (John Wiley & Sons, 2008).

[118] A. April. Nonparaxial TM and TE beams in free space. Opt. Lett. 33, 1563 (2008).

[119] S. Carbajo, E. A. Nanni, L. J. Wong, G. Moriena, P. D. Keathley, G. Laurent, R. J. D. Miller and F. X. Kärtner. Direct longitudinal laser acceleration of electrons in free space. Phys. Rev. Accel. Beams 19, 021303 (2016).

[120] R. Palmer. An introduction to acceleration mechanisms. In *Frontiers of Particle Beams* (Springer, 1988), pp. 607–635.

[121] J. P. BORIS. Relativistic plasma simulation-optimization of a hybrid code. Proc. 4th Conf. Num. Sim. Plasmas pp. 3–67 (1970).

[122] J.-L. Vay. Simulation of beams or plasmas crossing at relativistic velocity. Physics of Plasmas 15, 056701 (2008).

[123] V. Marceau, C. Varin and M. Piché. Validity of the paraxial approximation for electron acceleration with radially polarized laser beams. Opt. Lett. 38, 821 (2013).

[124] A. Grassi, L. Fedeli, A. Sgattoni and A. Macchi. Vlasov simulation of laser-driven shock acceleration and ion turbulence. Plasma Physics and Controlled Fusion 58, 034021 (2016).

[125] R. W. Hockney and J. W. Eastwood. *Computer simulation using particles* (crc Press, 1988).

[126] C. K. Birdsall and A. B. Langdon. *Plasma physics via computer simulation* (CRC press, 2004).

[127] R. Lehe, C. Thaury, E. Guillaume, A. Lifschitz and V. Malka. Laser-plasma lens for laser-wakefield accelerators. Phys. Rev. ST Accel. Beams 17, 121301 (2014).

[128] T. Esirkepov. Exact charge conservation scheme for Particle-in-Cell simulation with an arbitrary form-factor. Computer Physics Communications 135, 144 (2001).

[129] Kane Yee. Numerical solution of initial boundary value problems involving maxwell's equations in isotropic media. IEEE Transactions on Antennas and Propagation 14, 302 (1966).

[130] T. D. Arber, K. Bennett, C. S. Brady, A. Lawrence-Douglas, M. G. Ramsay, N. J. Sircombe, P. Gillies, R. G. Evans, H. Schmitz, A. R. Bell and C. P. Ridgers. Contemporary particle-in-cell approach to laser-plasma modelling. Plasma Physics and Controlled Fusion 57, 113001 (2015).

[131] M. Ammosov, N. Delone and V. Krainov. Tunnel ionization of complex atoms and of atomic ions in an alternating electric field. Sov. Phys. JETP 64, 1191 (1986).

[132] G. Blaclard, H. Vincenti, R. Lehe and J. L. Vay. Pseudospectral Maxwell solvers for an accurate modeling of Doppler harmonic generation on plasma mirrors with particle-in-cell codes. Phys. Rev. E 96, 033305 (2017).

[133] H. Vincenti and J.-L. Vay. Ultrahigh-order Maxwell solver with extreme scalability for electromagnetic PIC simulations of plasmas. Computer Physics Communications 228, 22 (2018).

[134] A. Lifschitz, X. Davoine, E. Lefebvre, J. Faure, C. Rechatin and V. Malka. Particle-in-Cell modelling of laser–plasma interaction using Fourier decomposition. Journal of Computational Physics 228, 1803 (2009).

[135] A. Taflove and S. C. Hagness. *Computational electrodynamics: the finite-difference time-domain method* (Artech house, 2005).

[136] S. Jalas, I. Dornmair, R. Lehe, H. Vincenti, J.-L. Vay, M. Kirchen and A. R. Maier. Accurate modeling of plasma acceleration with arbitrary order pseudo-spectral particle-in-cell methods. Physics of Plasmas 24, 033115 (2017).

[137] B. Fornberg. Generation of finite difference formulas on arbitrarily spaced grids. Mathematics of computation 51, 699 (1988).

[138] Q. H. Liu. The PSTD algorithm: A time-domain method requiring only two cells per wavelength. Microwave and Optical Technology Letters 15, 158 (1997).

[139] I. Haber, R. Lee, H. Klein and J. Boris. Advances in electromagnetic simulation techniques. In *Proc. Sixth Conf. Num. Sim. Plasmas, Berkeley, CA* (1973), pp. 46–48.

[140] J.-L. Vay, I. Haber and B. B. Godfrey. A domain decomposition method for pseudo-spectral electromagnetic simulations of plasmas. Journal of Computational Physics 243, 260 (2013).

[141] Y. Ohmura and Y. Okamura. Staggered grid pseudo-spectral time-domain method for light scattering analysis. Piers Online 6, 632 (2010).

[142] R. Lehé and J.-L. Vay. Review of Spectral Maxwell Solvers for Electromagnetic Particle-in-Cell: Algorithms and Advantages. In *Proceedings, 13th International Computational Accelerator Physics Conference, ICAP2018: Key West, FL, USA, 20-24 October 2018* (2019), p. WEPLG05.

[143] B. Fornberg. High-Order Finite Differences and the Pseudospectral Method on Staggered Grids. SIAM Journal on Numerical Analysis 27, 904 (1990).

[144] H. Vincenti and J.-L. Vay. Detailed analysis of the effects of stencil spatial variations with arbitrary high-order finite-difference Maxwell solver. Computer Physics Communications 200, 147 (2016).

[145] H. Vincenti. Achieving Extreme Light Intensities using Optically Curved Relativistic Plasma Mirrors. Phys. Rev. Lett. 123, 105001 (2019).

[146] P. Yu, X. Xu, V. K. Decyk, W. An, J. Vieira, F. S. Tsung, R. A. Fonseca, W. Lu, L. O. Silva and W. B. Mori. Modeling of laser wakefield acceleration in Lorentz boosted frame using EM-PIC code with spectral solver. Journal of Computational Physics 266, 124 (2014).

[147] B. B. Godfrey, J.-L. Vay and I. Haber. Numerical stability analysis of the pseudo-spectral analytical time-domain PIC algorithm. Journal of Computational Physics 258, 689 (2014).

[148] R. Lehe, M. Kirchen, B. B. Godfrey, A. R. Maier and J.-L. Vay. Elimination of numerical Cherenkov instability in flowing-plasma particle-in-cell simulations by using Galilean coordinates. Phys. Rev. E 94, 053305 (2016).

[149] J.-L. Vay, D. P. Grote, R. H. Cohen and A. Friedman. Novel methods in the Particle-In-Cell accelerator Code-Framework Warp. Computational Science & Discovery 5, 014019 (2012).

[150] H. Vincenti, M. Lobet, R. Lehe, R. Sasanka and J.-L. Vay. An efficient and portable SIMD algorithm for charge/current deposition in Particle-In-Cell codes. Computer Physics Communications 210, 145 (2017).

[151] A. April. *Ultrashort, strongly focused laser pulses in free space* (InTech Rijeka, Croatia, 2010).

[152] A. April. Impulsions laser ultrabrèves et fortement focalisées dans le vide. Ph.D. thesis (2012).

[153] G. Deschamps. Gaussian beam as a bundle of complex rays. Electronics Letters 7, 684 (1971).

[154] R. W. Ziolkowski and J. B. Judkins. Propagation characteristics of ultrawide-bandwidth pulsed Gaussian beams. J. Opt. Soc. Am. A 9, 2021 (1992).

[155] Y. I. Salamin and S. Carbajo. A Simple Model for the Fields of a Chirped Laser Pulse With Application to Electron Laser Acceleration. Frontiers in Physics 7, 2 (2019).

[156] M. A. Porras. Ultrashort pulsed Gaussian light beams. Phys. Rev. E 58, 1086 (1998).

[157] D. an der Brügge and A. Pukhov. Ultrashort focused electromagnetic pulses. Phys. Rev. E 79, 016603 (2009).

[158] C. F. R. Caron and R. M. Potvliege. Free-space propagation of ultrashort pulses: Space-time couplings in Gaussian pulse beams. Journal of Modern Optics 46, 1881 (1999).

[159] M. Lax, W. H. Louisell and W. B. McKnight. From Maxwell to paraxial wave optics. Phys. Rev. A 11, 1365 (1975).

[160] G. P. Agrawal and D. N. Pattanayak. Gaussian beam propagation beyond the paraxial approximation. J. Opt. Soc. Am. 69, 575 (1979).

[161] L. W. Davis. Theory of electromagnetic beams. Phys. Rev. A 19, 1177 (1979).

[162] L. W. Davis and G. Patsakos. TM and TE electromagnetic beams in free space. Opt. Lett. 6, 22 (1981).

[163] M. Born and E. Wolf. *Principles of optics: electromagnetic theory of propagation, interference and diffraction of light* (Elsevier, 2013).

[164] J. D. Jackson. Classical electrodynamics (1999).

[165] C. J. R. Sheppard and S. Saghafi. Beam modes beyond the paraxial approximation: A scalar treatment. Phys. Rev. A 57, 2971 (1998).

[166] P. Mora. Plasma Expansion into a Vacuum. Phys. Rev. Lett. 90, 185002 (2003).

[167] W. Kruer. *The physics of laser plasma interactions* (CRC Press, 2018).

[168] P. Mora. Thin-foil expansion into a vacuum. Phys. Rev. E 72, 056401 (2005).

[169] M. Bocoum. Harmonic and electron generation from laser-driven plasma mirrors. Ph.D. thesis, Paris Saclay (2016).

[170] J. P. Colombier, P. Combis, A. Rosenfeld, I. V. Hertel, E. Audouard and R. Stoian. Optimized energy coupling at ultrafast laser-irradiated metal surfaces by tailoring intensity envelopes: Consequences for material removal from Al samples. Phys. Rev. B 74, 224106 (2006).

[171] P. Grua, D. Hébert, L. Lamaignère and J.-L. Rullier. Role of suprathermal electrons during nanosecond laser energy deposit in fused silica. Applied Physics Letters 105, 081902 (2014).

[172] Y. Glinec, J. Faure, A. Guemnie-Tafo, V. M. H. Monard, J. P. Larbre, V. D. Waele, J. L. Marignier and M. Mostafavi. Absolute calibration for a broad range single shot electron spectrometer. Rev. Sci. Instrum. 77, 103301 (2006).

[173] S. Kühn, M. Dumergue, S. Kahaly, S. Mondal, M. Füle, T. Csizmadia, B. Farkas, B. Major, Z. Várallyay, E. Cormier, M. Kalashnikov, F. Calegari, M. Devetta, F. Frassetto, E. Månsson, L. Poletto, S. Stagira, C. Vozzi, M. Nisoli, P. Rudawski, S. Maclot, F. Campi, H. Wikmark, C. L. Arnold, C. M. Heyl, P. Johnsson, A. L'Huillier, R. Lopez-Martens, S. Haessler, M. Bocoum, F. Boehle, A. Vernier, G. Iaquaniello, E. Skantzakis, N. Papadakis, C. Kalpouzos, P. Tzallas, F. Lépine, D. Charalambidis, K. Varjú, K. Osvay and G. Sansone. The ELI-ALPS facility: the next generation of attosecond sources. Journal of Physics B: Atomic, Molecular and Optical Physics 50, 132002 (2017).

[174] T. Nakamura, S. V. Bulanov, T. Z. Esirkepov and M. Kando. High-Energy Ions from Near-Critical Density Plasmas via Magnetic Vortex Acceleration. Phys. Rev. Lett. 105, 135002 (2010).

[175] F. Sylla, A. Flacco, S. Kahaly, M. Veltcheva, A. Lifschitz, V. Malka, E. d'Humières, I. Andriyash and V. Tikhonchuk. Short Intense Laser Pulse Collapse in Near-Critical Plasma. Phys. Rev. Lett. 110, 085001 (2013).

[176] N. Zaïm, F. Böhle, M. Bocoum, A. Vernier, S. Haessler, X. Davoine, L. Videau, J. Faure and R. Lopez-Martens. Few-cycle laser wakefield acceleration on solid targets with controlled plasma scale length. Physics of Plasmas 26, 033112 (2019).

[177] V. Marceau. Accélération d'électrons à l'aide d'impulsions laser ultrabrèves et fortement focalisées. Ph.D. thesis (2015).

[178] N. Zaïm, M. Thévenet, A. Lifschitz and J. Faure. Relativistic Acceleration of Electrons Injected by a Plasma Mirror into a Radially Polarized Laser Beam. Phys. Rev. Lett. 119, 094801 (2017).

[179] A. Lévy, T. Ceccotti, P. D'Oliveira, F. Réau, M. Perdrix, F. Quéré, P. Monot, M. Bougeard, H. Lagadec, P. Martin, J. P. Geindre and P. Audebert. Double plasma mirror for ultrahigh temporal contrast ultraintense laser pulses. Opt. Lett. 32, 310 (2007).

[180] S. W. Jolly. Influence of longitudinal chromatism on vacuum acceleration by intense radially polarized laser beams. Opt. Lett. 44, 1833 (2019).

[181] A. Denoeud, L. Chopineau, A. Leblanc and F. Quéré. Interaction of Ultraintense Laser Vortices with Plasma Mirrors. Phys. Rev. Lett. 118, 033902 (2017).

[182] J. Vieira and J. T. Mendonça. Nonlinear Laser Driven Donut Wakefields for Positron and Electron Acceleration. Phys. Rev. Lett. 112, 215001 (2014).

[183] A. Macchi. Surface plasmons in superintense laser-solid interactions. Physics of Plasmas 25, 031906 (2018).

[184] S. Monchocé, S. Kahaly, A. Leblanc, L. Videau, P. Combis, F. Réau, D. Garzella, P. D'Oliveira, P. Martin and F. Quéré. Optically Controlled Solid-Density Transient Plasma Gratings. Phys. Rev. Lett. 112, 145008 (2014).

List of publications and conference contributions

Publications

Relativistic Acceleration of Electrons Injected by a Plasma Mirror into a Radially Polarized Laser Beam
N. Zaïm, M. Thévenet, A. Lifschitz, and J. Faure
Physical Review Letters 119, 094801 (2017)

Few-cycle laser wakefield acceleration on solid targets with controlled plasma scale length
N. Zaïm, F. Böhle, M. Bocoum, A. Vernier, S. Haessler, X. Davoine, L. Videau, J. Faure, and R. Lopez-Martens
Physics of Plasmas 26, 033112 (2019)

Interaction of ultraintense radially-polarized laser pulses with plasma mirrors
D. Guénot, N. Zaïm, L. Chopineau, A. Denoeud, O. Lundh, H. Vincenti, F. Quéré, and J. Faure
To be submitted

Conference contributions

Relativistic acceleration of ultrahosrt electron bunches injected by a plasma mirror into a radially polarized laser
N. Zaïm, M. Thévenet, A. Lifschitz, and J. Faure
Poster - 2ème Réunion plénière du GDR Ultrafast Phenomena, 9-10 November 2017, Paris, France

Interaction relativiste entre lasers de quelques cycles optiques et plasmas surdenses
N. Zaïm, F. Böhle, M. Bocoum, M. Thévenet, S. Haessler, R. Lopez-Martens, and J. Faure
Oral presentation - 9ème Forum Lasers et Plasmas, 10-15 June 2018, Oléron, France

Relativistic interaction between few-cycle laser pulses and overdense plasmas
N. Zaïm, F. Böhle, M. Bocoum, M. Thévenet, A. Vernier, S. Haessler, X. Davoine, L. Videau, R. Lopez-Martens, and J. Faure
Oral presentation - ICUIL 2018, 9-14 September 2018, Lindau, Germany

Relativistic interaction between few-cycle laser pulses and overdense plasmas
N. Zaïm, F. Böhle, M. Bocoum, A. Vernier, S. Haessler, X. Davoine, L. Videau, R. Lopez-Martens, and J. Faure
Oral presentation - 3ème Réunion plénière du GDR Ultrafast Phenomena, 10-11 December 2018, Paris,

France

Laser wakefield acceleration driven by few-cycle pulses on plasma mirrors
N. Zaïm, F. Böhle, M. Bocoum, A. Vernier, S. Haessler, X. Davoine, L. Videau, R. Lopez-Martens, and J. Faure
Oral presentation - SPIE Optics and Electronics 2019, 1-4 April 2019, Prague, Czech Republic
Best Student Paper Award recipient

Few-cycle laser wakefield acceleration on solid targets with controlled plasma scale length
N. Zaïm, F. Böhle, M. Bocoum, A. Vernier, S. Haessler, X. Davoine, L. Videau, R. Lopez-Martens, and J. Faure
Oral presentation - Laser-Plasma Accelerator Workshop 2019, 5-10 May 2019, Split, Croatia

PRL **119,** 094801 (2017) PHYSICAL REVIEW LETTERS week ending
1 SEPTEMBER 2017

Relativistic Acceleration of Electrons Injected by a Plasma Mirror into a Radially Polarized Laser Beam

N. Zaïm,[*] M. Thévenet, A. Lifschitz, and J. Faure
LOA, ENSTA ParisTech, CNRS, Ecole polytechnique, Université Paris-Saclay, 828 bd des Maréchaux, 91762 Palaiseau cedex, France

(Received 9 May 2017; published 31 August 2017)

We propose a method to generate femtosecond, relativistic, and high-charge electron bunches using few-cycle and tightly focused radially polarized laser pulses. In this scheme, the incident laser pulse reflects off an overdense plasma that injects electrons into the reflected pulse. Particle-in-cell simulations show that the plasma injects electrons ideally, resulting in a dramatic increase of charge and energy of the accelerated electron bunch in comparison to previous methods. This method can be used to generate femtosecond pC bunches with energies in the 1–10 MeV range using realistic laser parameters corresponding to current kHz laser systems.

DOI: 10.1103/PhysRevLett.119.094801

The advent of femtosecond lasers that can reach enormous intensities, well beyond 10^{18} W/cm^2 [1], brings about new possibilities. Among these, the acceleration of electrons to relativistic energies in very short distances is particularly promising. One of the many advantages of using lasers to accelerate electrons is the possibility to create ultrashort relativistic electron beams, with durations of a few femtoseconds [2]. As they are perfectly synchronized with the driving laser, these electron beams could drastically reduce the time resolution in various experiments such as ultrafast imaging and diffraction [3,4] or femtosecond pulse radiolysis [5]. As of today, laser wakefield accelerators [6] have paved the way to electron acceleration in the 100 MeV to multi-GeV range using 100 TW to PW laser drivers [2,7], with low repetition rates. However, these beams are inappropriate for the aforementioned applications as lower energy electrons but high reliability and statistics, and thus higher repetition rates are required. There is therefore a strong need for electron sources with MeV energies and high-repetition rates. Despite recent progress of kHz laser wakefield accelerators in the MeV range [8–11], vacuum laser acceleration (VLA) is a very good candidate for producing MeV electrons at high-repetition rates. Indeed, in VLA, electrons are directly accelerated using the laser fields and the energy gain scales as $\Delta W[\mathrm{MeV}] = 30\sqrt{P[\mathrm{TW}]}$ [12], showing that MeV acceleration is possible with sub-TW laser systems. This is of great interest because TW peak powers have been demonstrated in milliJoule and kiloHertz laser systems, by postcompressing laser pulses to few cycle, sub-5-fs duration [13,14]. VLA using such lasers could enable the development of kHz femtosecond electron sources.

VLA with radially polarized laser beams (rather than with linearly polarized beams) was proposed as a way to improve the electron beam quality [12,15–23]. Indeed, such beams contain both features of an efficient accelerator: an accelerating field in the longitudinal direction E_z as well as a radial field E_r that can confine electrons close to the optical axis. The longitudinal field E_z becomes more significant as the beam is tightly focused. Numerical simulations have shown that VLA with radial polarization resulted in more energetic and more collimated electron beams than VLA with linear polarization [16]. Two schemes are commonly proposed for injecting and accelerating electrons into radially polarized laser pulses: (i) ionization injection, where electrons are released near a maximum of the laser electric field by ionizing a low density gas [21] and (ii) external beam injection, where a preaccelerated electron beam is injected into the laser fields [23]. At present only two experimental results have been published, in which energy gains ranging from a few keV to tens of keV have been obtained [18,23]. In this Letter, we show that these modest energy gains are due to nonoptimal injection conditions. We propose a simple method based on the use of an overdense plasma for optimally injecting and accelerating electrons into radially polarized laser pulses. We show that high-charge (several pC), relativistic (1–10 MeV) beams with femtosecond durations can be obtained with current mJ lasers operating at a kHz repetition rate.

We start by explaining how the initial injection condition affects the subsequent acceleration of electrons. For simplicity, we first consider the linear polarization case, with a laser electric field $E_L \propto \sin\phi$, where $\phi = \omega_0 t - k_0 z$ is the electron phase in a field with wave vector k_0 and angular frequency ω_0. In a plane wave, it is straightforward to show [24] that the maximum energy gain is $\Delta W_{\max} = m_e c^2 \gamma_0 a_0^2 (1 + |\cos\phi_i|)^2$. Here, γ_0 is the initial Lorentz factor of the electron, a_0 is the normalized amplitude of the field, given by $a_0 = E_{L,\max}/E_0$ with $E_0 = m_e c \omega_0 / e$, and ϕ_i is the initial phase of the electron in the laser. This formula shows that the energy gain is highest when (i) using high amplitude laser fields, (ii) injecting electrons inside the laser pulse at the optimal phase, $\phi_i = 0$, i.e., at a zero of the electric field, and

(iii) injecting electrons with a high initial energy γ_0. These specific initial conditions are difficult to achieve experimentally, explaining why the observation of VLA has been a challenge. For radially polarized laser pulses, the problem is intrinsically 3-dimensional and obtaining simple analytical estimates is quite difficult. Therefore, in the following, we use numerical calculations to show that the optimum injection conditions are the same as in the linear polarization case.

Within the framework of the paraxial approximation and assuming a Gaussian temporal envelope, the on-axis longitudinal electric field of the lowest order radially polarized laser beam is [15]

$$E_z(z,t) = E_{z0}\frac{w_0}{w(z)}\sin\phi \exp\left(-2\log(2)\frac{(t-\frac{z}{c})^2}{\tau_0^2}\right). \qquad (1)$$

With $\phi = \omega_0 t - k_0 z + 2\arctan(z/z_0) - \phi_0$, $w(z) = w_0\sqrt{1+(z^2/z_0^2)}$ is the beam waist, w_0 the minimum beam waist, $z_0 = k_0 w_0^2/2$ is the Rayleigh length, τ_0 is the pulse duration in FWHM of the intensity, and ϕ_0 is the initial phase. We also define a_{0z} as the normalized amplitude of the longitudinal field: $a_{0z} = E_{z0}/E_0$ with E_0 defined earlier. Because of the Gouy phase $2\arctan(z/z_0)$, the axial phase velocity of the beam is superluminous [19]. If the interaction between the electron and the laser is limited between $z = 0$ (i.e., the beam waist) and $z = +\infty$, as is the case for most proposed accelerating schemes, the phase difference due to the Gouy phase is π. As a consequence, electrons cannot stay indefinitely in an accelerating phase of the laser (where E_z is negative). An electron can reach high energies if it remains in an accelerating half-cycle for a long time and net energy gains can be obtained if the subsequent decelerating half-cycle is diminished due to diffraction or the temporal shape of the pulse. An electron can stay in an accelerating phase longer if it has a velocity close to the speed of light, explaining why it is advantageous to inject electrons with a high initial energy or to use high laser amplitudes.

The efficiency of the acceleration can also be greatly improved by carefully choosing the initial phase of the electron. To illustrate this, we perform on-axis test particle simulations of an electron initially at rest at $r = z = 0$ that is accelerated by the field in Eq. (1), for three different initial phases. To model current kHz laser systems [14], we use the following parameters: $\lambda_0 = 800$ nm, $a_{0z} = 0.7$, $w_0 = 1.5$ μm, $\tau_0 = 3.5$ fs, and $\phi_0 = \pi/2$. With these values, using the paraxial approximation and a Gaussian envelope is not perfectly valid but can nonetheless lead to decent estimates for the on-axis energy gain [20]. Figures 1(b) and 1(c) show trajectories for nonoptimal initial phases, where the electron starts respectively in front of the laser pulse and inside the pulse at a maximum of the electric field. This is similar to the case of the ionization of a gas with, respectively, a low ionization energy and a high ionization energy. In each of these cases, the electron quickly dephases, resulting in negligible energy gains (respectively, 9.3 eV and 0.81 eV). On the opposite, Fig. 1(d) shows more efficient acceleration when the electron is initially at a zero of the electric field. This is because the electron starts with a whole accelerating half-cycle and stays in it much longer than in the previous cases, resulting in a final energy of 1.3 MeV. The above considerations show that VLA with radial polarization can lead to strong acceleration if electrons are injected (i) inside the laser pulse (ii) at a zero of the longitudinal field and (iii) with a high velocity in the propagation direction. While no current experimental setup allows such subwavelength precision, we show that these condition can be naturally satisfied using a plasma mirror injector.

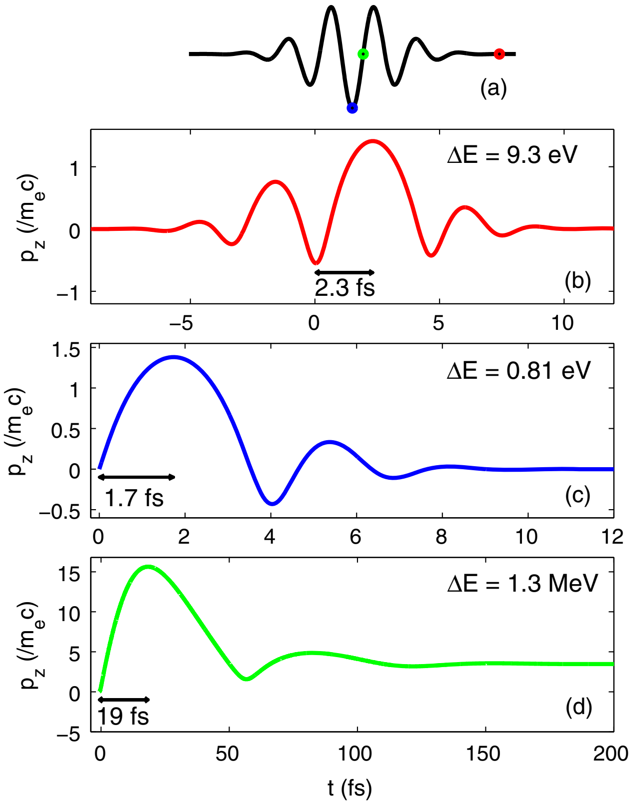

FIG. 1. Results from test particle simulations. (a) Waveform of the few-cycle longitudinal electric field. The colored dots represent the initial positions of the electron in (b)-(d). (b)-(d) Longitudinal momentum p_z along the electron trajectory for various cases: the electron is initially at rest either (b) in front of the pulse, (c) inside the pulse at a maximum of the field, (d) inside the pulse at a zero of the field. The double headed arrows show the time spent inside the main accelerating half-cycle.

A plasma mirror is an overdense plasma with a short density gradient, with a typical scale length of $< \lambda_0/10$. When an ultraintense laser pulse is focused on such an overdense plasma, it reflects off the plasma which behaves like a nearly perfect mirror (hence the term *plasma mirror*). Nevertheless, while the laser pulse interacts with the plasma density gradient, it is able to pull out electrons and inject them into the reflected pulse with ideal initial conditions, allowing them to be efficiently accelerated. Recent experiments using Gaussian lasers with linear polarization led to a clear observation of electron acceleration to energies in the MeV range [25], but with rather large divergence angles of tens of degrees [25,26]. We demonstrate in the following that the concept of plasma mirror injection can also be applied to radially polarized laser pulses, potentially leading to more efficient acceleration and better beam quality.

We used PIC simulations with the quasi-3D code CALDER-CIRC [27] to confirm that plasma mirrors fittingly allow us to inject a highly charged bunch of electrons near the zero of the electric field and with an initial velocity of a few hundreds of keV. Thanks to these optimal initial conditions, the electrons are then accelerated to relativistic energies by the reflected pulse. In our simulation, the plasma has a maximum electron density of $200n_c$, with $n_c = 1.7 \times 10^{21}$ cm^{-3}. The density decays exponentially with a gradient length of $\lambda_0/7$. The laser beam is focused on the plasma at normal incidence, and a moving window is started after the interaction, making it possible to follow the ejected electrons far from the plasma. Following [21], we use an exact closed-form solution with a Poisson-like spectrum to model the radially polarized pulse (more details can be found in the Supplemental Material [28]). We take the same laser parameters as for the single particle simulations: $\lambda_0 = 800$ nm, $a_{0z} = 0.7$, $\phi_0 = \pi/2$, $w_0 = 1.5$ μm, and $\tau_0 = 3.5$ fs. Numerical parameters can be found in the Supplemental Material [28].

Figure 2 displays three different snapshots from the PIC simulation, showing the interaction between the laser and the plasma. The electrons are ejected via the push-pull mechanism that was identified and fully described for linearly polarized beams in [31]. It consists of the following two steps. (1) The normal component of the electric field of the laser E_z pushes electrons inside the plasma, resulting in a density peak. As the electron density peak is pushed deeper into the density gradient, the immobile ions create a large restoring static field, resembling a plasma capacitor. (2) When the density peak reaches its maximum depth [Fig. 2(b)], the sign of the electric field switches and both the laser and the static field work together to pull the electrons out of the plasma. A small fraction of the electrons inside the density peak can gain enough energy from the plasma capacitor to be ejected from the plasma. These electrons are ideally injected into the reflected pulse since they start with an initial velocity at the optimal phase, where the sign of the longitudinal field changes, and thus start with an accelerating half cycle, represented in blue in Fig. 2(c). This push-pull mechanism is repeated for every cycle of the laser with a strong enough electric field in the density gradient direction, and is optimal when the gradient length is on the order of $\lambda_0/10$ [31].

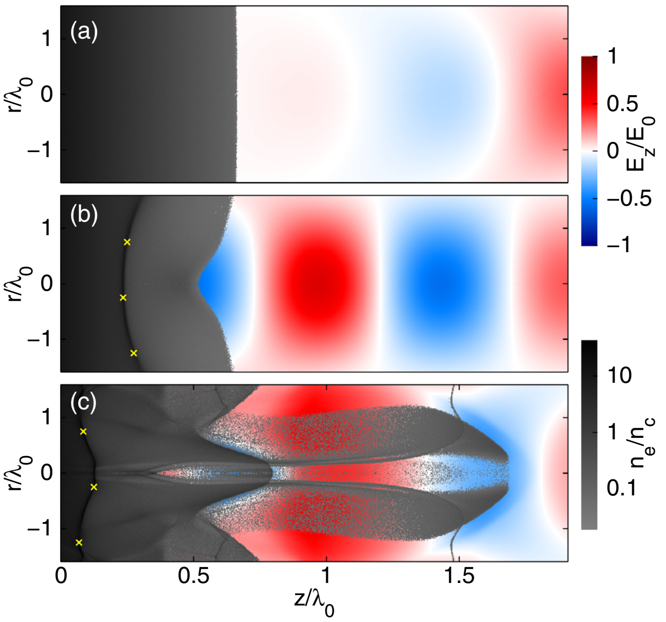

FIG. 2. PIC simulations showing the longitudinal electric field and electron density extracted at three different timesteps. (a) The plasma is still unperturbed by the incoming laser. (b) The electrons are pushed into the plasma by the laser, resulting in a density peak indicated by the yellows markers. (c) Electrons that were in the density peak are now pulled away from the plasma, between $z = 1.2\lambda_0$ and $z = 1.7\lambda_0$. (See also Supplemental Material movie [28] for more insight on the electron ejection.)

Figures 3(a) and 3(c) show the energy-angle and the angular distributions of the electrons ejected from the plasma mirror. The total ejected charge is about 60 pC. Furthermore, because they are injected into the laser with optimal initial conditions, a group of electrons representing several pC is accelerated to relativistic energies, typically from 1 to 8 MeV. At such relativistic speeds, the magnetic force $v_z \times B_\theta$ opposes the radial force E_r [20], mitigating the collimating effect of the radial polarization. These highly energetic electrons consequently form a ring-shaped beam with a typical angle of 200 mrad with respect to the optical axis. This divergence angle is nonetheless significantly lower than what is achieved experimentally with linearly polarized lasers [25,26]. Analysis of the work done by the different forces shows that these electrons are accelerated by VLA in the reflected pulse by the longitudinal component of the electric field E_z, taking full advantage of the radial polarization. See Supplemental Material [28] for more details.

Figures 4(a) and 4(c) show the energy spectrum and time distribution of the electrons with $\theta < 200$ mrad and $E > 1$ MeV, after 145 μm of propagation. Such filtering can typically be achieved using a pinhole and a magnet to select only certain angles and energies. These electrons represent 3.3 pC. Thanks to its high energy, this fast electron bunch is kept ultrashort, with a duration of around 12 fs. It is possible to diminish the duration of the pulse by

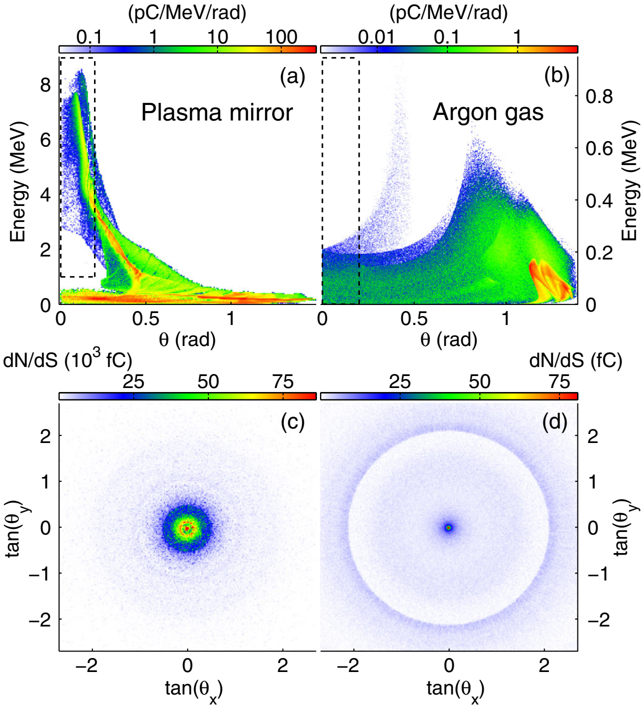

FIG. 3. (a), (b) Energy-angle distribution and (c), (d) angular distributions of the obtained electron beam after interaction of the pulse with (a), (c) a plasma mirror or (b), (d) argon gas. On the top images, the electrons inside the black rectangles are the one represented in Fig. 4. On the bottom images, the angular distribution is represented in the form dN/dS, with $dS = d\tan\theta_x \times d\tan\theta_y = d(p_x/p_z) \times d(p_y/p_z)$.

reducing the acceptance angle of the selected electrons, at the cost of also diminishing the selected charge. To obtain the time distribution plots, electrons leaving the simulation are assumed to travel with constant speed afterwards.

In order to demonstrate the benefits of using a plasma mirror, we also perform PIC simulations of the ionization scheme. The same laser parameters are used, except for the absolute phase ϕ_0, which is set to π so as to have the same value as in [21]. The gas target is either hydrogen or argon. It is infinite in the transverse direction and is 10 μm long in the longitudinal direction. The maximum electron density is chosen to be 3×10^{16} cm^{-3}, a value for which space-charge and plasma effects are negligible [21].

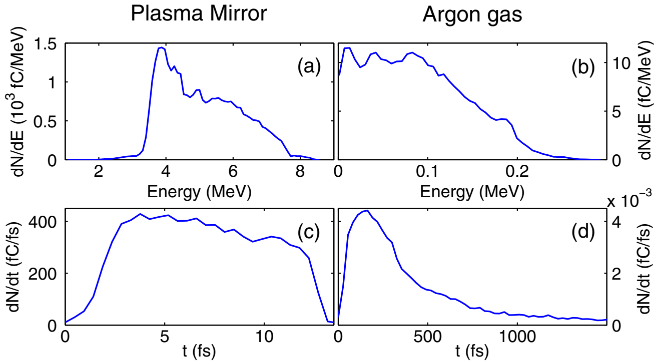

FIG. 4. (a), (b) Energy spectrum and (c), (d) time distribution of a chosen subset of electrons after 145 μm of propagation for (a), (c) the plasma mirror simulation and (b), (d) the argon gas simulation.

In the case of hydrogen, we did not observe significant on-axis electron acceleration. This is because hydrogen has a low ionization energy, resulting in the electrons being ionized early in front of the laser pulse. This leads to a case very similar to that of Fig. 1(a) and to a low final energy. In [21], it was reported that electrons could be accelerated by ionizing a hydrogen target, but a much tighter focusing, $w_0 = 785$ nm, that is harder to obtain in practice, was used in the simulations, resulting in a higher value for a_{0z}.

With argon, however, some deeper shells electrons are generated inside the laser pulse, making it possible to accelerate on-axis electrons. Figures 3(b) and 3(d) show the energy-angle and the angular distributions of the obtained electrons. The total ejected charge is about 70 fC, 3 orders of magnitude lower than with the plasma mirror, and a few fC stay near the axis. The charge can nonetheless be increased by raising the initial gas density, at the cost of decreasing the electron beam quality [21]. The on-axis electrons are rather well focused and have an energy ranging from 0 to 200 keV, 1–2 orders of magnitude lower than with the plasma mirror. The energy spectrum and time distribution of the electrons with $\theta < 0.2$ rad after 145 μm of propagation is shown in Figs. 4(b) and 4(d). This corresponds to a selected charge of 1.7 fC. As can be expected from its low energy and high energy spread, the time duration of this electron bunch is already over 300 fs after 145 μm of propagation.

To conclude, plasma mirrors can inject high-charge electron beams with optimal conditions in the reflected pulse, making it possible to study experimentally VLA with radially polarized beams. Femtosecond, pC bunches of electrons with an energy between 3 and 7 MeV could be readily obtained with current kHz lasers. Moreover, we can take advantage of the high ejected charge to improve the quality of the electron beam, characterized by its transverse normalized emittance $\varepsilon_{n,x}$, by selecting only a subset of the ejected electrons. Depending on the application, a compromise between the charge, the energy spread, and the normalized emittance of the beam can be found by filtering the electron beam, which could be achieved experimentally with an appropriate transport beam line. For instance, selecting electrons with an energy between 4.06 and 4.14 MeV results in a 2% energy spread, a charge of 100 fC, and a normalized emittance of $\varepsilon_{n,x} = \varepsilon_{n,y} = 0.18$ μm. Emittance in the nm range can even be obtained by further filtering the beam while still maintaining the charge at the fC level. Such a low emittance ultrashort beam could be of great interest for ultrafast electron diffraction experiments.

This work was funded by the European Research Council under Contract No. 306708, ERC Starting Grant FEMTOELEC, and by the Agence Nationale pour la Recherche (ANR-14-CE32-0011-03 APERO). This work was granted access to the HPC resources of CINES under the allocation 2017-A0020506057 made by GENCI.

---

[*] Corresponding author.
neil.zaim@ensta-paristech.fr

[1] T. J. Yu, S. K. Lee, J. H. Sung, J. W. Yoon, T. M. Jeong, and J. Lee, Opt. Express **20**, 10807 (2012).
[2] O. Lundh, J. Lim, C. Rechatin, L. Ammoura, A. Ben-Ismail, X. Davoine, G. Gallot, J.-P. Goddet, E. Lefebvre, V. Malka *et al.*, Nat. Phys. **7**, 219 (2011).
[3] A. H. Zewail, Annu. Rev. Phys. Chem. **57**, 65 (2006).
[4] G. Sciaini and R. J. D. Miller, Rep. Prog. Phys. **74**, 096101 (2011).
[5] T. Kozawa, Y. Mizutani, M. Miki, T. Yamamoto, S. Suemine, Y. Yoshida, and S. Tagawa, Nucl. Instrum. Methods Phys. Res., Sect. A **440**, 251 (2000).
[6] E. Esarey, C. B. Schroeder, and W. P. Leemans, Rev. Mod. Phys. **81**, 1229 (2009).
[7] W. P. Leemans, A. J. Gonsalves, H.-S. Mao, K. Nakamura, C. Benedetti, C. B. Schroeder, C. Tóth, J. Daniels, D. E. Mittelberger, S. S. Bulanov *et al.*, Phys. Rev. Lett. **113**, 245002 (2014).
[8] Z.-H. He, B. Hou, J. H. Easter, J. Faure, K. Krushelnick, J. A. Nees, and A. G. R. Thomas, New J. Phys. **15**, 053016 (2013).
[9] B. Beaurepaire, A. Vernier, M. Bocoum, F. Böhle, A. Jullien, J.-P. Rousseau, T. Lefrou, D. Douillet, G. Iaquaniello, R. Lopez-Martens *et al.*, Phys. Rev. X **5**, 031012 (2015).
[10] F. Salehi, A. J. Goers, G. A. Hine, L. Feder, D. Kuk, B. Miao, D. Woodbury, K. Y. Kim, and H. M. Milchberg, Opt. Lett. **42**, 215 (2017).
[11] D. Guénot, D. Gustas, A. Vernier, B. Beaurepaire, F. Böhle, M. Bocoum, M. Lozano, A. Jullien, R. Lopez-Martens, A. Lifschitz *et al.*, Nat. Photonics **11**, 293 (2017).
[12] E. Esarey, P. Sprangle, and J. Krall, Phys. Rev. E **52**, 5443 (1995).
[13] S. Bohman, A. Suda, T. Kanai, S. Yamaguchi, and K. Midorikawa, Opt. Lett. **35**, 1887 (2010).
[14] F. Böhle, M. Kretschmar, A. Jullien, M. Kovacs, M. Miranda, R. Romero, H. Crespo, U. Morgner, P. Simon, R. Lopez-Martens *et al.*, Laser Phys. Lett. **11**, 095401 (2014).
[15] Y. I. Salamin, Phys. Rev. A **73**, 043402 (2006).
[16] A. Karmakar and A. Pukhov, Laser Part. Beams **25**, 371 (2007).
[17] L. J. Wong and F. X. Kärtner, Opt. Express **18**, 25035 (2010).
[18] S. Payeur, S. Fourmaux, B. E. Schmidt, J. P. MacLean, C. Tchervenkov, F. Légaré, M. Piché, and J. C. Kieffer, Appl. Phys. Lett. **101**, 041105 (2012).
[19] C. Varin, S. Payeur, V. Marceau, S. Fourmaux, A. April, B. Schmidt, P. L. Fortin, N. Thiré, T. Brabec, F. Légaré *et al.* Appl. Sci. Res. **3**, 70 (2013).
[20] V. Marceau, C. Varin, and M. Piché, Opt. Lett. **38**, 821 (2013).
[21] V. Marceau, C. Varin, T. Brabec, and M. Piché, Phys. Rev. Lett. **111**, 224801 (2013).
[22] V. Marceau, P. Hogan-Lamarre, T. Brabec, M. Piché, and C. Varin, J. Phys. B **48**, 045601 (2015).
[23] S. Carbajo, E. A. Nanni, L. J. Wong, G. Moriena, P. D. Keathley, G. Laurent, R. J. D. Miller, and F. X. Kärtner, Phys. Rev. Accel. Beams **19**, 021303 (2016).
[24] F. V. Hartemann, S. N. Fochs, G. P. LeSage, J. N. C. Luhmann, J. G. Woodworth, M. D. Perry, Y. J. Chen, and A. K. Kerman, Phys. Rev. E **51**, 4833 (1995).
[25] M. Thévenet, A. Leblanc, S. Kahaly, H. Vincenti, A. Vernier, F. Quéré, and J. Faure, Nat. Phys. **12**, 355 (2015).
[26] M. Bocoum, M. Thévenet, F. Böhle, B. Beaurepaire, A. Vernier, A. Jullien, J. Faure, and R. Lopez-Martens, Phys. Rev. Lett. **116**, 185001 (2016).
[27] A. Lifschitz, X. Davoine, E. Lefebvre, J. Faure, C. Rechatin, and V. Malka, J. Comput. Phys. **228**, 1803 (2009).
[28] See Supplemental Material at http://link.aps.org/supplemental/10.1103/PhysRevLett.119.094801, which includes Refs. [29,30], for more details.
[29] A. April, *Coherence and Ultrashort Pulse Laser Emission*, edited by F. J. Duarte (InTech, Rijeka, Croatia, 2010), pp. 355–382.
[30] C. F. R. Caron and R. M. Potvliege, J. Mod. Opt. **46**, 1881 (1999).
[31] M. Thévenet, H. Vincenti, and J. Faure, Phys. Plasmas **23**, 063119 (2016).

Physics of Plasmas ARTICLE scitation.org/journal/php

Few-cycle laser wakefield acceleration on solid targets with controlled plasma scale length

Cite as: Phys. Plasmas **26**, 033112 (2019); doi: 10.1063/1.5084783
Submitted: 7 December 2018 · Accepted: 26 February 2019 ·
Published Online: 15 March 2019

N. Zaïm,[1,a)] F. Böhle,[1] M. Bocoum,[1] A. Vernier,[1] S. Haessler,[1] X. Davoine,[2] L. Videau,[2] J. Faure,[1] and R. Lopez-Martens[1]

AFFILIATIONS

[1]Laboratoire d'Optique Appliquée (LOA), ENSTA ParisTech, CNRS, Ecole Polytechnique, Institut Polytechnique de Paris, 181 Chemin de la Hunière et des Joncherettes, 91762 Palaiseau Cedex, France
[2]CEA, DAM, DIF, F-91297 Arpajon, France

[a)]Electronic mail: neil.zaim@ensta-paristech.fr

ABSTRACT

We measure the emission of energetic electrons from the interaction between relativistic-intensity ultrashort laser pulses and a solid density plasma with a tunable density gradient scale length. We detect an electron beam that only appears with few-cycle pulses (<10 fs) and large plasma scale lengths ($L > \lambda_0$). Numerical simulations, in agreement with the experiments, reveal that these electrons are accelerated by a laser wakefield. Plasma waves are indeed resonantly excited by the few-cycle laser pulses in the near-critical density region of the plasma. Electrons are then injected by ionization into the plasma waves and accelerated to relativistic energies. In this laser wakefield acceleration regime, the plasma waves are rotated by the plasma density gradient, which results in the electrons not being emitted in the same direction as the driving laser pulse.

I. INTRODUCTION

Since the recent advent of ultrahigh intensity lasers, bright particle and radiation sources with a femtosecond duration have been developed from relativistic laser-plasma interactions. These new sources are expected to find applications in various fields including medicine, imaging, and ultrafast probing of matter.[1,2] Laser wakefield acceleration (LWFA) is an efficient process for driving relativistic electron beams with few femtosecond durations[3] and energies in the 100 MeV to multi-GeV range[4–6] or more recently in the few-MeV range with kHz lasers.[7–9] In this scheme, the laser pulse ponderomotive force drives a high amplitude plasma wave that is able to trap and accelerate electrons over very short distances.[10] Usually, LWFA takes place in mm-scale underdense plasmas (gas jets) but is quite inefficient with solid targets. Indeed, for solid-density plasmas, the processes responsible for transferring the laser energy to particles and radiation are radically different. Understanding the pathways and mechanisms of energy transfer to the plasma electrons is a complex and fundamental question that has implications for ion acceleration[11] and high harmonic generation.[12]

It is well known that the plasma density profile at the front surface is a key parameter that can dramatically transform the nature of the interaction.[13–18] When the plasma scale length is short compared to the laser wavelength ($L < \lambda_0/10$), the physics is now fairly well understood. At moderate intensity, vacuum heating[19] is the dominant mechanism for energy transfer to the electrons. At relativistic intensities, the physics becomes more complex: the laser field triggers a periodic push-pull motion of the front surface that follows the sign of the laser field.[20,21] This nonlinear periodic motion leads to high harmonic generation via the relativistic oscillating mirror mechanism[22,23] and also results in electron ejection from the front surface.[21,24,25] These electrons are subsequently injected into the reflected laser field where they can directly gain large amounts of energy.[24] In this regime, electron emission has been reported to be optimal when the gradient scale length is on the order of $\sim\lambda_0/10$, with electron energies ranging from 100 keV to multi-MeV, depending on laser intensity.[24–29]

For longer gradient scale lengths, interaction in the near-critical density part of the plasma, which has also been investigated in the context of ion acceleration,[30–33] becomes significant. The physics gets extremely complex, and there is no unified description of energy transfer and electron acceleration. There is a wide disparity of experimental results, and various mechanisms have been proposed, including resonant absorption,[34,35] $J \times B$ heating,[36] ponderomotive acceleration,[37] stochastic heating,[38,39] acceleration by surface quasistatic fields,[40] or direct laser acceleration.[41,42] However, it is still unclear what mechanisms actually arise in experiments and the precise experimental conditions under which they appear are not known. This may be due to the lack of control and measurement of the density gradients, which makes the interpretations difficult. In this article, we show that by using few-cycle laser pulses with durations as short as 3.5 fs, we find a regime where LWFA occurs in the near-critical density region of the plasma. Even though this mechanism was previously suggested to explain experimental results with thick solid targets,[35,43] LWFA is here clearly identified by varying and precisely controlling the key parameters of the interaction, namely, the gradient length and the pulse duration, and by performing Particle-In-Cell (PIC) simulations with realistic plasma density profiles. We find that this regime, which results in the emission of an $\approx 25°$-wide stable electron beam, only occurs with few-cycle laser pulses.

II. EXPERIMENTAL SETUP AND RESULTS

The experiments are performed with the Salle Noire laser system at the Laboratoire d'Optique Appliquée (LOA). The laser delivers 2.6-mJ pulses at a 1-kHz repetition rate with an extremely high temporal contrast ($>10^{10}$).[44] The 800 nm, 24 fs laser pulses are post-compressed in a helium-filled stretched hollow-core fiber.[45,46] The pulse duration can be tuned by changing the pressure in the fiber, thereby providing near Fourier transform limited pulses from 3.5 fs to 24 fs. The laser beam is focused down to a 1.75 μm FWHM spot, resulting in peak intensities ranging from 2.3×10^{18} W/cm^2 ($a_0 \simeq 1$) for 24 fs pulses to 1.6×10^{19} W/cm^2 ($a_0 \simeq 2.7$) for 3.5 fs pulses. Here, a_0 is defined as the normalized amplitude of the peak laser field: $a_0 = E_{MAX}/E_0$ with $E_0 = m_e c\omega_0/e$, where ω_0 is the laser frequency, c is the speed of light in vacuum, and m_e and e are the electron mass and charge, respectively. In this experiment, as shown in Fig. 1, p-polarized pulses impinge on an optically flat fused silica (SiO$_2$) target with an incidence angle of $\theta_i = 55°$. A spatially overlapped prepulse, created by picking off $\approx 4\%$ of the main pulse through a holey mirror, is focused to a much larger 13 μm FWHM spot (see the inset of Fig. 1) in order to generate a transversely homogeneous plasma that expands into vacuum. The plasma density profile during the interaction is controlled by varying the delay, Δt, between the prepulse and the main pulse. The density scale length is estimated experimentally using spatial domain interferometry (SDI) and by assuming isothermal expansion.[47] Backward electron emission is measured using a Lanex screen, protected by a 13 μm thick Al-foil, which detects electrons with energies >150 keV. The Lanex screen was calibrated prior to the experiment using a 3-MeV RF accelerator. The absolute charge is estimated from the electron energy spectrum obtained from the PIC simulations described below, combined with the known spectral response of the Lanex screen. The resulting uncertainty, of the order of 50%, is mainly due to the fact that the exact shape of the energy spectra was not measured. The angular electron distribution in the backward direction is recorded for $-3° < \theta < 75°$ and $-15° < \phi < 15°$, where θ and ϕ are the angles with respect to the target normal in the incidence and transverse planes, respectively.

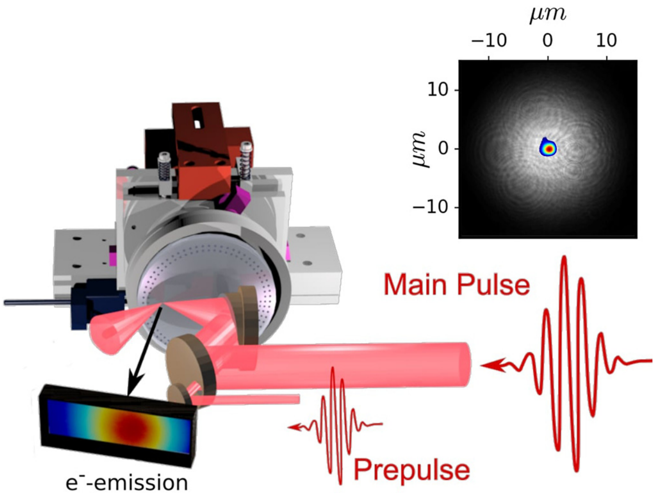

FIG. 1. Schematic of the experimental setup. The laser pulses interact at a 1-kHz repetition rate with a fused silica rotating target. Inset: superimposition of the on-target prepulse (white) and main pulse focal spots.

Figures 2(a)–2(f) show the measured electron signal as a function of the delay between the prepulse and the main pulse for 5 different laser pulse durations. We first find a strong electron emission for short delays ($\Delta t < 20$ ps), corresponding to a sharp plasma-vacuum interface. This emission, detected for every pulse duration, is optimal for a delay of $\Delta t \approx 9$ ps, i.e., $L < \lambda_0/5$. In this regime, the push-pull mechanism mentioned in the introduction is responsible for the ejection of electrons from the plasma.[21,24,29] A typical electron angular distribution in this case is displayed in Fig. 2(g), showing a broad divergence angle of $\approx 50°$.

As the delay is further increased, the detected charge drops (10 ps $< \Delta t <$ 30 ps) and then rises again for longer delays ($\Delta t >$ 50 ps). This time, however, electrons are only emitted when few-cycle pulses (≤ 10 fs) are used. Note that chirping a few-cycle pulse to increase its duration results in a similar decline of the electron signal, as can be seen in Fig. 3. This is thus a very distinct physical regime, in which the gradient length is much larger ($L > \lambda_0$) and the duration of the laser pulse plays a major role. In this case, the obtained electron beams have more charge and a narrower divergence angle of $\approx 25°$ as is visible in Fig. 2(h). The electrons are emitted near the specular direction, with a slight shift towards the normal direction. The detected signal is very stable over a wide range of delays (50 ps $< \Delta t <$ 200 ps), indicating that the electron ejection mechanism is not highly sensitive to the exact shape of the plasma density profile. In contrast to the emission of electrons for short delays ($\Delta t <$ 20 ps) which is strongly correlated with high-harmonics generation,[25] we measure no high-harmonics signal at these longer delays ($\Delta t >$ 30 ps).

III. PIC SIMULATIONS

To understand the origin of this new electron emission process, we turn to 2D PIC simulations using the code WARP[48,49] coupled to the high performance PICSAR library.[50–53] We use the same laser parameters as in the experiments (more details are given in the supplementary material). A moving window is started after the interaction in order to follow the accelerated electrons far from the plasma. We took great care in providing a realistic description of the plasma density gradient. First, the plasma is initially partially ionized (up to Si^{4+} and O^{2+}) in order to model ionization by the prepulse. The initial ionization states are estimated from the prepulse peak intensity ($\sim 10^{15}$ W/cm^2) and the intensity thresholds for barrier-suppression ionization[54] in silicon and oxygen. Further ionization by the main pulse is

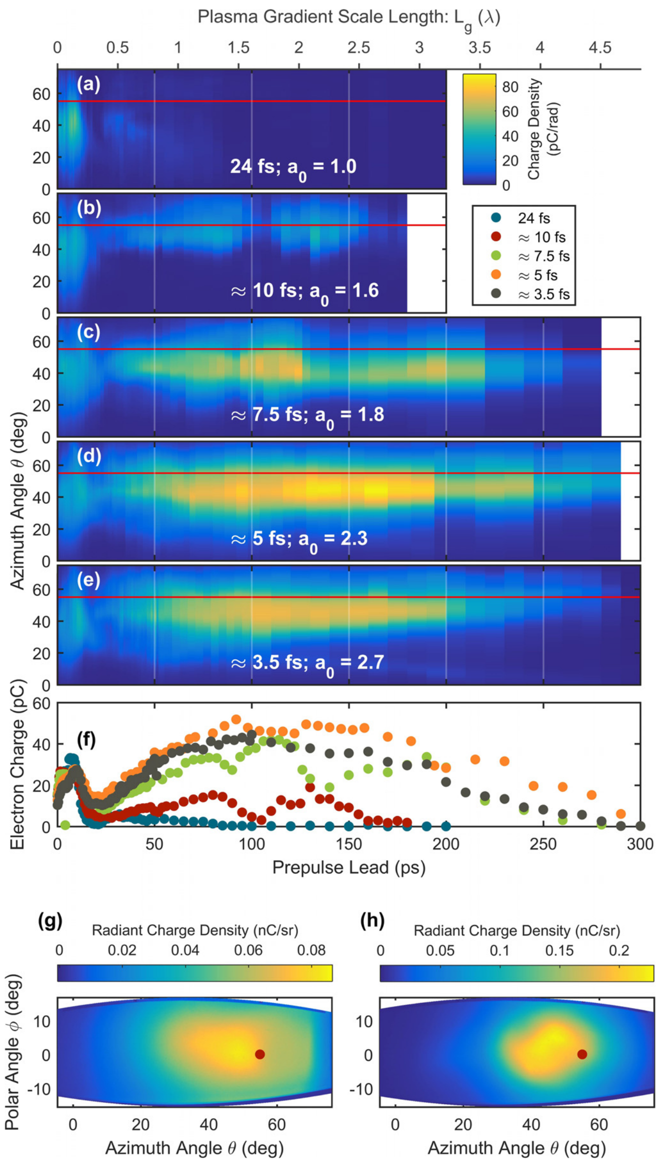

FIG. 2. (a)–(e) Electron angular distribution integrated over the ϕ angle as a function of the delay between the prepulse and the main pulse for respective pulse durations of 24, 10, 7.5, 5, and 3.5 fs. (f) Total ejected charge as a function of the delay between the prepulse and the main pulse. (g) and (h) Typical electron angular distribution obtained with 5-fs pulses in the short ($\Delta t = 9$ ps) and long ($\Delta t = 140$ ps) plasma scale length regimes, respectively. The gradient scale lengths given in the top axis are obtained from SDI measurements.[47] The white lines in (a)–(e) represent the prepulse leads corresponding to the ticks in (f). The red lines and dots mark the specular direction.

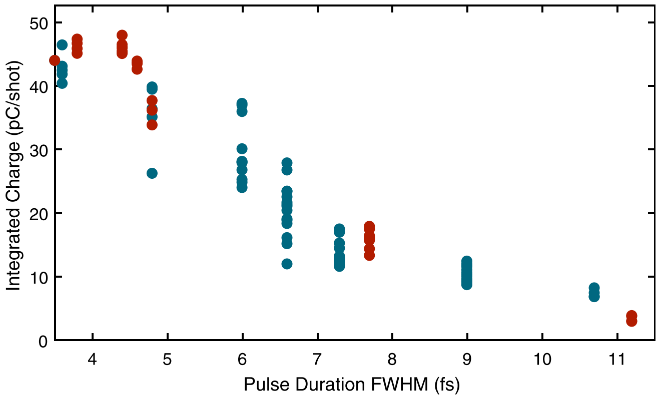

FIG. 3. Total detected charge as a function of pulse duration for a delay of $\Delta t = 90$ ps between the prepulse and the main pulse. The pulse duration is tuned here by chirping positively (red points) or negatively (blue points) the 3.5-fs driving laser.

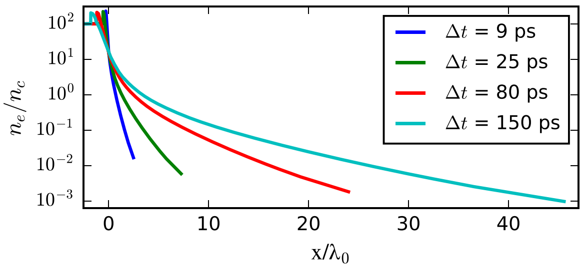

FIG. 4. Results from 1D hydrodynamic simulations. Normalized electron density n_e/n_c as a function of position x for different delays after a prepulse with a fluence of 50 J/cm^2 ionizes a solid fused-silica target. $x = 0$ is the initial solid-vacuum interface position. $n_c = m_e\varepsilon_0\omega_0^2/e^2$ is the critical density above which the laser cannot propagate. ε_0 is the vacuum permittivity.

also taken into account in the simulations. Second, the plasma density profile is obtained by performing hydrodynamic 1D simulations with the code ESTHER.[55] Figure 4 shows the resulting profiles for 4 different values of the delay between the prepulse and the main pulse. Note that the density profiles are not always exponential in Fig. 4, in contrast to the results from models assuming isothermal expansion. The gradient appears to have an exponential shape only for short delays (i.e., for sharp plasma-vacuum interfaces) but not for longer delays. The isothermal hypothesis, used to estimate the gradient scale length in the previously mentioned SDI measurements,[47] likely fails due to radiation and convection losses on these longer timescales. In our case, the electron beam appears for long delays Δt, and we therefore use the density profiles shown in Fig. 4 as inputs for the PIC simulations.

Snapshots from two different PIC simulations are shown in Fig. 5. Both simulations use the plasma density profile obtained with a delay of $\Delta t = 80$ ps (i.e., the red curve in Fig. 4), a value for which the electron beam is detected in the experiments. The pulse duration is either 5 fs or 24 fs, resulting in peak intensities of 10^{19} W/cm^2 ($a_0 = 2.15$) and 2.1×10^{18} W/cm^2 ($a_0 = 0.98$), respectively.

The first striking feature is the formation of high amplitude plasma waves in the wake of the 5-fs pulse. Their wavefront is bent by the density gradient, akin to the plasma waves generated by Brunel electrons in the coherent wake emission mechanism of high-harmonic generation.[12] Even though these wakefields appear in the whole region where the 5-fs pulse propagates, inside which the density ranges from $n_c/1000$ to $n_c \cos^2\theta_i \sim 0.3n_c$,[56] they are completely absent in the 24-fs pulse simulation. This can be easily explained by the fact that wakefield

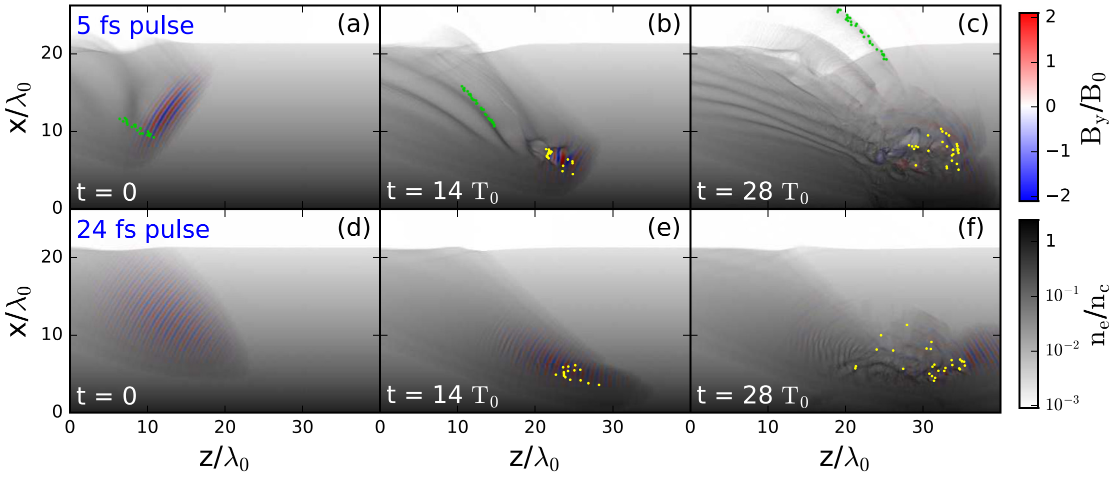

FIG. 5. Laser magnetic field and electron density from PIC simulations with a large plasma scale length ($\Delta t = 80$ ps) and a pulse duration of (a)–(c) 5 fs or (d)–(f) 24 fs. The green and yellow dots show a sample of ejected electrons. T_0 is the laser optical oscillation period, and $B_0 = E_0/c$ with E_0 defined earlier. Multimedia views: https://doi.org/10.1063/1.5084783.1; https://doi.org/10.1063/1.5084783.2

excitation is optimal at the resonance condition, i.e., when the pulse duration is on the order of half the plasma wavelength:[10] $\tau \simeq \lambda_p/2c$. This gives a resonant density of $n_c/14$ for 5-fs pulses, versus $n_c/300$ for 24-fs pulses, explaining why large wakefields appear for the few-cycle pulse only (see also supplementary material).

Some electrons, presented in green in Fig. 5, are trapped and accelerated by the plasma waves' strong electric fields that reach up to 1 TV/m. The angular and energy distributions of these LWFA electrons are shown in the green curves of Figs. 6(a) and 6(c), respectively. Their energy spectrum extends to ≈2.5 MeV, and their total ejected charge is ≈7 pC/μm. These electrons are emitted in the same direction as the electrons detected at long delays in experiments [see the red curve in Fig. 6(a)]. Moreover, as in experiments, these electrons only appear for few-cycle pulses. We therefore conclude that the electron beam detected at long delays in experiments originates from LWFA. We notice that the angular distribution of these electrons is significantly narrower in the simulation than in experiments. This is likely due to space charge effects during the propagation of the electron beam to the detector, which we expect to be important for a sub-MeV beam with tens of pC charge. The electrons are indeed only propagated for tens of microns in the simulation, while the Lanex screen is located ≈10 cm away from the target in experiments.

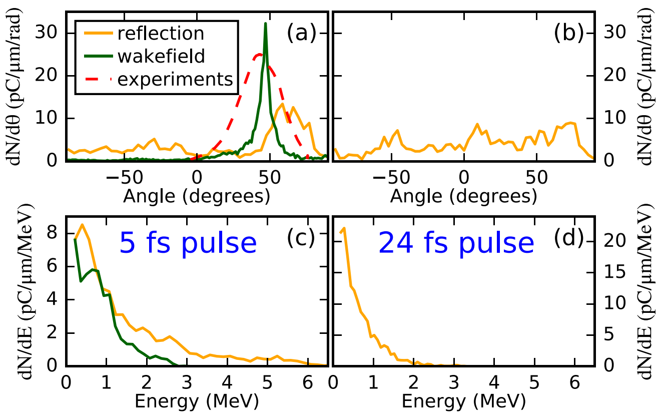

FIG. 6. (a) and (b) Angular and (c) and (d) energy distribution of the two families of electrons that are ejected in the (a) and (c) 5 fs and (b) and (d) 24 fs simulation. The distributions are obtained at the end of the simulation, long after the interaction. The red dashed curve in (a) shows for comparison the experimental angular distribution integrated along the ϕ angle obtained with a 5 fs pulse and an 80 ps prepulse lead, in arbitrary units.

In the simulations, the LWFA electrons come from the L-shell of silicon. They have high binding energies (from ≈150 eV to ≈500 eV) and can therefore only be ionized by the huge electric fields inside the main laser pulse. The fact that only electrons ionized in the center of the pulse are accelerated suggests that injection by ionization, a well-known mechanism in underdense plasmas,[57,58] is responsible for trapping the electrons into the wakefields. Taking field ionization into account is therefore needed to properly describe the injection of electrons into the plasma waves and more generally to correctly model laser interactions with overdense plasmas when the plasma scale length is large.

Another family of electrons, shown in yellow in Fig. 5 and labelled "reflection electrons," is ejected from the plasma in the simulations. These electrons are accelerated at the reflection point of the laser, where the density is $n_c \cos^2\theta_i$. Their angular and energy distributions are displayed by the yellow curves of Fig. 6. This family of electrons, which appears for both 5-fs and 24-fs pulses and has a very large angular divergence spreading across all directions, is not detected in experiments. This fact shows that our 2D PIC simulations do not accurately reproduce the ratio between the two populations. This second family of electrons would likely be attenuated in more accurate but more costly 3D simulations. However, this is not a major concern because the simulations explain the main experimental observations, i.e., a well-defined beam of LWFA electrons which appears only for an extremely short pulse duration.

It is also worth noting that the same qualitative results are found when the simulations are performed with an exponential density profile with $L = 3\lambda_0$, thus confirming our previous observation that the electron ejection mechanism is not highly sensitive to the exact shape of the plasma density profile. Another interesting point is that a similar trend can be found when the intensities are interchanged in the simulations (i.e., when the 5-fs simulation is carried out with a peak intensity of 2.1×10^{18} W/cm^2, while the 24-fs simulation is performed with a 1×10^{19} W/cm^2 peak intensity). In this case, even though the laser pulse energy is 25 times lower in the 5-fs simulation, a very small number of electrons remain laser wakefield accelerated, while there is still no plasma wave formation in the 24-fs simulation (see supplementary material). These simulations show a clear effect of the pulse duration and confirm that the emergence of the electron beam is not simply due to the increase in intensity when reducing the pulse duration.

IV. PLASMA WAVE FORMATION AND ELECTRON ACCELERATION IN A TRANSVERSE GRADIENT

A unique feature of this acceleration regime is that the electrons are not emitted in the same direction as the driving laser pulse, as is usually the case with LWFA, even with similar laser parameters and plasma densities.[7,8] This is because the wakefields' wavefronts are rotated by the density gradient. To explain this rotation, we use a simple heuristic model based on the following assumptions: (i) the plasma wave is initiated at the temporal center of the laser pulse. This is formally equivalent to an infinitely short driving pulse and is reasonable if the pulse duration is much shorter than a plasma period. (ii) The plasma wave is longitudinal, i.e., the electrons forming it oscillate in the direction of laser propagation. This assumption is equivalent to an infinitely wide (1D) driving laser pulse and is valid when the laser transverse size is larger than a plasma wavelength. (iii) The center of the laser pulse travels at c, neglecting the decrease in group velocity. (iv) The phase of the plasma wave varies at each point at the local plasma frequency. This is valid if the gradient scale length is much larger than the plasma wavelength.[12] With these assumptions, the phase φ of the plasma wave is

$$\varphi(x, z, t) = \omega_p(x)(t - t_0(x, z)). \tag{1}$$

Here, ω_p is the local plasma frequency and $t_0 = (z \sin\theta_i - x\cos\theta_i)/c$ is the time at which the temporal center of the laser pulse excites the plasma wave. Plasma wavefronts obtained using Eq. (1) in an exponential density gradient are shown in Fig. 7. Even though this simple model is not perfectly valid for the considered experimental case, it can qualitatively reproduce the shape of the plasma waves. Physically, the rotation of the wavefronts can be explained by the transverse density gradient seen by the laser, i.e., the fact that one side of the laser pulse excites a plasma wave with a higher frequency than the other. A given phase will therefore be reached quicker in the region of higher frequency, which results in rotated wavefronts.

We can also use this model to qualitatively explain the measured angular distribution. Let us consider an electron moving with an angle θ_e with respect to the x-axis at a position where the wavefront of the plasma wave makes an angle θ_w with respect to the z-axis [see Fig. 7(b)]. We first note that since the plasma frequency only depends on x, the phase velocity of the plasma waves in the z-direction is $(v_\varphi)_z = c/\sin\theta_i$. We can then, using the law of sines, calculate the phase velocity along the direction of electron motion

$$(v_\varphi)_{\theta_e} = \frac{\sin\theta_w}{\cos(\theta_e - \theta_w)\sin\theta_i} c. \tag{2}$$

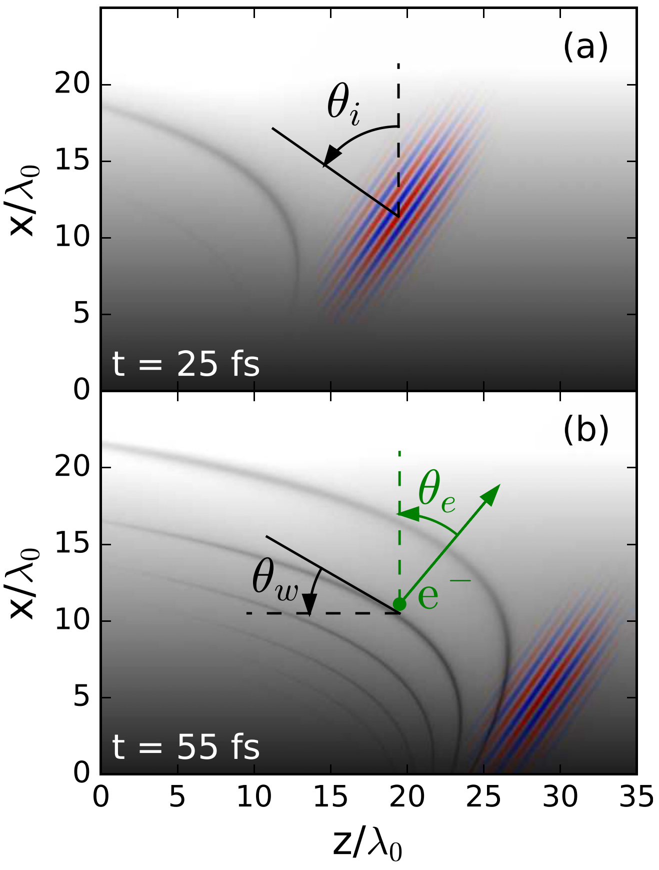

FIG. 7. Wavefronts (darker lines) obtained using Eq. (1) during the propagation of a laser pulse (represented in blue and red) in a plasma with an exponential density profile ($L = 3\lambda_0$). Two consecutive wavefronts are separated by a phase of 2π.

If the electron is trapped in the wakefield, its velocity is mainly collinear with the electric field of the plasma waves, i.e., perpendicular to the wavefronts. In this case, we have $\theta_e \approx \theta_w$ and Eq. (2) is simplified to

$$(v_\varphi)_{\theta_e} = \frac{\sin\theta_e}{\sin\theta_i} c. \tag{3}$$

Trapping of electrons by the plasma wave is only possible if the phase velocity of the wakefield is lower than c, meaning in our case that electrons can only be emitted when $\theta_e < \theta_i$. Furthermore, electron acceleration to relativistic energies is efficient when the phase velocity is close to c. Equation (3) therefore indicates that the electrons should be emitted close to the specular direction with a slight shift towards the normal direction, in good agreement with experiments and simulations. Electrons directed closer to the grazing direction ($\theta_e > \theta_i$) cannot be trapped as the phase velocity of the plasma waves in their direction is greater than c, while electrons emitted close to the normal direction cannot reach high energies as they would quickly dephase from the plasma waves.

V. CONCLUSION

In conclusion, we detect an electron beam that only appears for few-cycle pulses and large plasma scale lengths. Particle-In-Cell simulations successfully explain the experimental results: the detected electrons are injected by ionization into wakefields formed behind the pulse. These plasma waves can only be efficiently excited by few-cycle pulses at these near-critical densities, explaining why this new electron emission mechanism is only observed with extremely short pulses. A singular trait of this acceleration regime is that, due to the rotation of the wakefields induced by the density gradient, the electron beam is not emitted in the same direction as the driving laser pulse. This work offers a better understanding of the interaction between ultraintense laser pulses and solid targets and confirms that extremely short pulse durations and controlled plasma conditions provide access to new acceleration regimes.

SUPPLEMENTARY MATERIAL

See supplementary material for the experimental results obtained when reducing the main laser pulse intensity (first section). In the second section, we provide detailed explanations regarding how few-cycle laser pulses are modeled in our Particle-In-Cell simulations. In the third section, we give more information concerning the numerical parameters of the Particle-In-Cell simulations presented in the main text. In the fourth section, we present simulations performed with the other pulse durations studied experimentally. In the fifth section, we present more exhaustively the simulations with interchanged intensities that are mentioned in the main text. In the sixth section, we estimate the amplitude of the plasma waves generated in our experiments using the 1D nonlinear theory of wakefield generation.

ACKNOWLEDGMENTS

We would like to thank H. Vincenti for his help and expertise with PIC simulations and for insightful discussions. This work was funded by the European Research Council under Contract No. 306708 (ERC Starting Grant No. FEMTOELEC), the Région Île-de-France (under Contract No. SESAME-2012-ATTOLITE), the Agence Nationale pour la Recherche (under Contracts No. ANR-11-EQPX-005-ATTOLAB and ANR-14-CE32-0011-03), the Extreme Light Infrastructure-Hungary Non-Profit Ltd (under Contract No. NLO3.6LOA), and the LabEx PALM (ANR-10-LABX-0039). This work was granted access to the HPC resources of CINES under the Allocation No. A0020506057 made by GENCI.

REFERENCES

[1] V. Malka, J. Faure, Y. A. Gauduel, E. Lefebvre, A. Rousse, and K. Ta Phuoc, "Principles and applications of compact laser–plasma accelerators," Nat. Phys. **4**, 447–453 (2008).

[2] F. Albert and A. G. R. Thomas, "Applications of laser wakefield accelerator-based light sources," Plasma Phys. Controlled Fusion **58**, 103001 (2016).

[3] O. Lundh, J. Lim, C. Rechatin, L. Ammoura, A. Ben-Ismail, X. Davoine, G. Gallot, J.-P. Goddet, E. Lefebvre, V. Malka, and J. Faure, "Few femtosecond, few kiloampere electron bunch produced by a laser-plasma accelerator," Nat. Phys. **7**, 219 (2011).

[4] J. Faure, Y. Glinec, A. Pukhov, S. Kiselev, S. Gordienko, E. Lefebvre, J.-P. Rousseau, F. Burgy, and V. Malka, "A laser-plasma accelerator producing monoenergetic electron beams," Nature **431**, 541–544 (2004).

[5] X. Wang, R. Zgadzaj, N. Fazel, Z. Li, S. A. Yi, X. Zhang, W. Henderson, Y. Y. Chang, R. Korzekwa, H. E. Tsai, C. H. Pai, H. Quevedo, G. Dyer, E. Gaul, M. Martinez, A. C. Bernstein, T. Borger, M. Spinks, M. Donovan, V. Khudik, G. Shvets, T. Ditmire, and M. C. Downer, "Quasi-monoenergetic laser-plasma acceleration of electrons to 2 GeV," Nat. Commun. **4**, 1988 (2013).

[6] W. P. Leemans, A. J. Gonsalves, H.-S. Mao, K. Nakamura, C. Benedetti, C. B. Schroeder, C. Tóth, J. Daniels, D. E. Mittelberger, S. S. Bulanov, J.-L. Vay, C. G. R. Geddes, and E. Esarey, "Multi-GeV electron beams from capillary-discharge-guided subpetawatt laser pulses in the self-trapping regime," Phys. Rev. Lett. **113**, 245002 (2014).

[7] D. Guénot, D. Gustas, A. Vernier, B. Beaurepaire, F. Böhle, M. Bocoum, M. Lozano, A. Jullien, R. Lopez-Martens, A. Lifschitz, and J. Faure, "Relativistic electron beams driven by khz single-cycle light pulses," Nat. Photonics **11**, 293–296 (2017).

[8] D. Gustas, D. Guénot, A. Vernier, S. Dutt, F. Böhle, R. Lopez-Martens, A. Lifschitz, and J. Faure, "High-charge relativistic electron bunches from a kHz laser-plasma accelerator," Phys. Rev. Accel. Beams **21**, 013401 (2018).

[9] F. Salehi, A. J. Goers, G. A. Hine, L. Feder, D. Kuk, B. Miao, D. Woodbury, K. Y. Kim, and H. M. Milchberg, "MeV electron acceleration at 1 kHz with <10 MJ laser pulses," Opt. Lett. **42**, 215–218 (2017).

[10] E. Esarey, C. B. Schroeder, and W. P. Leemans, "Physics of laser-driven plasma-based electron accelerators," Rev. Mod. Phys. **81**, 1229–1285 (2009).

[11] A. Macchi, M. Borghesi, and M. Passoni, "Ion acceleration by superintense laser-plasma interaction," Rev. Mod. Phys. **85**, 751–793 (2013).

[12] C. Thaury and F. Quéré, "High-order harmonic and attosecond pulse generation on plasma mirrors: Basic mechanisms," J. Phys. B: At., Mol. Opt. Phys. **43**, 213001 (2010).

[13] S. C. Wilks and W. L. Kruer, "Absorption of ultrashort, ultra-intense laser light by solids and overdense plasmas," IEEE J. Quantum Electron. **33**, 1954–1968 (1997).

[14] Y. Sentoku, V. Bychenkov, K. Flippo, A. Maksimchuk, K. Mima, G. Mourou, Z. Sheng, and D. Umstadter, "High-energy ion generation in interaction. of short laser pulse with high-density plasma," Appl. Phys. B **74**, 207–215 (2002).

[15] P. McKenna, D. Carroll, O. Lundh, F. Nürnberg, K. Markey, S. Bandyopadhyay, D. Batani, R. Evans, R. Jafer, S. Kar *et al.*, "Effects of front surface plasma expansion on proton acceleration in ultraintense laser irradiation of foil targets," Laser Part. Beams **26**, 591–596 (2008).

[16] A. J. Kemp, Y. Sentoku, and M. Tabak, "Hot-electron energy coupling in ultraintense laser-matter interaction," Phys. Rev. E **79**, 066406 (2009).

[17] S. Kahaly, S. Monchocé, H. Vincenti, T. Dzelzainis, B. Dromey, M. Zepf, P. Martin, and F. Quéré, "Direct observation of density-gradient effects in harmonic generation from plasma mirrors," Phys. Rev. Lett. **110**, 175001 (2013).

[18] G. G. Scott, V. Bagnoud, C. Brabetz, R. J. Clarke, J. S. Green, R. I. Heathcote, H. W. Powell, B. Zielbauer, T. D. Arber, P. McKenna, and D. Neely, "Optimization of plasma mirror reflectivity and optical quality using double laser pulses," New J. Phys. **17**, 033027 (2015).

[19] F. Brunel, "Not-so-resonant, resonant absorption," Phys. Rev. Lett. **59**, 52–55 (1987).

[20] A. A. Gonoskov, A. V. Korzhimanov, A. V. Kim, M. Marklund, and A. M. Sergeev, "Ultrarelativistic nanoplasmonics as a route towards extreme-intensity attosecond pulses," Phys. Rev. E **84**, 046403 (2011).

[21] M. Thévenet, H. Vincenti, and J. Faure, "On the physics of electron ejection from laser-irradiated overdense plasmas," Phys. Plasmas **23**, 063119 (2016).

[22] R. Lichters, J. Meyer-ter Vehn, and A. Pukhov, "Short-pulse laser harmonics from oscillating plasma surfaces driven at relativistic intensity," Phys. Plasmas **3**, 3425–3437 (1996).

[23] T. Baeva, S. Gordienko, and A. Pukhov, "Theory of high-order harmonic generation in relativistic laser interaction with overdense plasma," Phys. Rev. E **74**, 046404 (2006).

[24] M. Thévenet, A. Leblanc, S. Kahaly, H. Vincenti, A. Vernier, F. Quéré, and J. Faure, "Vacuum laser acceleration of relativistic electrons using plasma mirror injectors," Nat. Phys. **12**, 355 (2016).

[25] L. Chopineau, A. Leblanc, G. Blaclard, A. Denoeud, M. Thévenet, J.-L. Vay, G. Bonnaud, P. Martin, H. Vincenti, and F. Quéré, "Identification of coupling mechanisms between ultraintense laser light and dense plasmas," preprint arXiv:1809.03903 (2018); Phys. Rev. X (to be published).

[26] S. Bastiani, A. Rousse, C. Q. J.-P. Geindre, P. Audebert, G. Harmoniaux, A. Antonetti, and J.-C. Gauthier, "Experimental study of the interaction of subpicosecond laser pulses with solid targets of varying initial scalelengths," Phys. Rev. E **56**, 7179–7185 (1997).

[27] A. G. Mordovanakis, J. Easter, N. Naumova, K. Popov, P.-E. Masson-Laborde, B. Hou, I. Sokolov, G. Mourou, I. V. Glazyrin, W. Rozmus, V. Bychenkov, J. Nees, and K. Krushelnick, "Quasimonoenergetic electron beams with relativistic energies and ultrashort duration from laser-solid interactions at 0.5 kHz," Phys. Rev. Lett. **103**, 235001 (2009).

[28] Y. Tian, J. Liu, W. Wang, C. Wang, A. Deng, C. Xia, W. Li, L. Cao, H. Lu, H. Zhang, Y. Xu, Y. Leng, R. Li, and Z. Xu, "Electron emission at locked phases from the laser-driven surface plasma wave," Phys. Rev. Lett. **109**, 115002 (2012).

[29] M. Bocoum, M. Thévenet, F. Böhle, B. Beaurepaire, A. Vernier, A. Jullien, J. Faure, and R. Lopez-Martens, "Anticorrelated emission of high harmonics and fast electron beams from plasma mirrors," Phys. Rev. Lett. **116**, 185001 (2016).

[30] A. Yogo, H. Daido, S. V. Bulanov, K. Nemoto, Y. Oishi, T. Nayuki, T. Fujii, K. Ogura, S. Orimo, A. Sagisaka, J.-L. Ma, T. Z. Esirkepov, M. Mori, M. Nishiuchi, A. S. Pirozhkov, S. Nakamura, A. Noda, H. Nagatomo, T. Kimura, and T. Tajima, "Laser ion acceleration via control of the near-critical density target," Phys. Rev. E **77**, 016401 (2008).

[31] A. Henig, D. Kiefer, K. Markey, D. C. Gautier, K. A. Flippo, S. Letzring, R. P. Johnson, T. Shimada, L. Yin, B. J. Albright, K. J. Bowers, J. C. Fernández, S. G. Rykovanov, H.-C. Wu, M. Zepf, D. Jung, V. K. Liechtenstein, J. Schreiber, D. Habs, and B. M. Hegelich, "Enhanced laser-driven ion acceleration in the relativistic transparency regime," Phys. Rev. Lett. **103**, 045002 (2009).

[32] J. H. Bin, W. J. Ma, H. Y. Wang, M. J. V. Streeter, C. Kreuzer, D. Kiefer, M. Yeung, S. Cousens, P. S. Foster, B. Dromey, X. Q. Yan, R. Ramis, J. Meyer-ter Vehn, M. Zepf, and J. Schreiber, "Ion acceleration using relativistic pulse shaping in near-critical-density plasmas," Phys. Rev. Lett. **115**, 064801 (2015).

[33] H. W. Powell, M. King, R. J. Gray, D. A. MacLellan, B. Gonzalez-Izquierdo, L. C. Stockhausen, G. Hicks, N. P. Dover, D. R. Rusby, D. C. Carroll, H. Padda, R. Torres, S. Kar, R. J. Clarke, I. O. Musgrave, Z. Najmudin, M. Borghesi, D. Neely, and P. McKenna, "Proton acceleration enhanced by a plasma jet in expanding foils undergoing relativistic transparency," New J. Phys. **17**, 103033 (2015).

[34] Y. T. Li, J. Zhang, L. M. Chen, Y. F. Mu, T. J. Liang, Z. Y. Wei, Q. L. Dong, Z. L. Chen, H. Teng, S. T. Chun-Yu, W. M. Jiang, Z. J. Zheng, and X. W. Tang, "Hot electrons in the interaction of femtosecond laser pulses with foil targets at a moderate laser intensity," Phys. Rev. E **64**, 046407 (2001).

[35] D. F. Cai, Y. Q. Gu, Z. J. Zheng, W. M. Zhou, X. D. Yang, C. Y. Jiao, H. Chen, T. S. Wen, and S. T. Chunyu, "Double-peak emission of hot electrons generated by femtosecond laser interaction with solid targets," Phys. Rev. E **70**, 066410 (2004).

[36] G. Malka and J. L. Miquel, "Experimental confirmation of ponderomotive-force electrons produced by an ultrarelativistic laser pulse on a solid target," Phys. Rev. Lett. **77**, 75–78 (1996).

[37] J. Zhang, J. Zhang, Z. M. Sheng, Y. T. Li, Y. Qiu, Z. Jin, and H. Teng, "Emission direction of fast electrons in laser-solid interactions at intensities from the nonrelativistic to the relativistic," Phys. Rev. E **69**, 046408 (2004).

[38] R. Tommasini, E. Fill, R. Bruch, and G. Pretzler, "Generation of monoenergetic ultrashort electron pulses from a fs laser plasma," Appl. Phys. B **79**, 923–926 (2004).

[39] S. Feister, D. R. Austin, J. T. Morrison, K. D. Frische, C. Orban, G. Ngirmang, A. Handler, J. R. H. Smith, M. Schillaci, J. A. LaVerne, E. A. Chowdhury, R. R. Freeman, and W. M. Roquemore, "Relativistic electron acceleration by MJ-class kHz lasers normally incident on liquid targets," Opt. Express **25**, 18736–18750 (2017).

[40] Y. T. Li, X. H. Yuan, M. H. Xu, Z. Y. Zheng, Z. M. Sheng, M. Chen, Y. Y. Ma, W. X. Liang, Q. Z. Yu, Y. Zhang, F. Liu, Z. H. Wang, Z. Y. Wei, W. Zhao, Z. Jin, and J. Zhang, "Observation of a fast electron beam emitted along the surface of a target irradiated by intense femtosecond laser pulses," Phys. Rev. Lett. **96**, 165003 (2006).

[41] T. Toncian, C. Wang, E. McCary, A. Meadows, A. Arefiev, J. Blakeney, K. Serratto, D. Kuk, C. Chester, R. Roycroft, L. Gao, H. Fu, X. Yan, J. Schreiber, I. Pomerantz, A. Bernstein, H. Quevedo, G. Dyer, T. Ditmire, and B. Hegelich, "Non-maxwellian electron distributions resulting from direct laser acceleration in near-critical plasmas," Matter Radiat. Extremes **1**, 82– 87 (2016).

[42] Y. Ma, J. Zhao, Y. Li, D. Li, L. Chen, J. Liu, S. J. D. Dann, Y. Ma, X. Yang, Z. Ge, Z. Sheng, and J. Zhang, "Ultrahigh-charge electron beams from laser-irradiated solid surface," Proc. Natl. Acad. Sci. **115**, 6980 (2018).

[43] J. Y. Mao, L. M. Chen, K. Huang, Y. Ma, J. R. Zhao, D. Z. Li, W. C. Yan, J. L. Ma, M. Aeschlimann, Z. Y. Wei, and J. Zhang, "Highly collimated monoenergetic target-surface electron acceleration in near-critical-density plasmas," Appl. Phys. Lett. **106**, 131105 (2015).

[44] A. Jullien, A. Ricci, F. Böhle, J.-P. Rousseau, S. Grabielle, N. Forget, H. Jacqmin, B. Mercier, and R. Lopez-Martens, "Carrier-envelope-phase stable, high-contrast, double chirped-pulse-amplification laser system," Opt. Lett. **39**, 3774–3777 (2014).

[45] F. Böhle, M. Kretschmar, A. Jullien, M. Kovacs, M. Miranda, R. Romero, H. Crespo, U. Morgner, P. Simon, R. Lopez-Martens, and T. Nagy, "Compression of CEP-stable multi-mJ laser pulses down to 4 fs in long hollow fibers," Laser Phys. Lett. **11**, 095401 (2014).

[46] M. Ouillé, F. Böhle, A. Vernier, M. Bocoum, A. Jullien, M. Lozano, J.-P. Rousseau, D. Gustas, D. Guénot, M. Kovacs, A. Blumenstein, P. Simon, J. Faure, S. Haessler, T. Nagy, and R. Lopez-Martens, "Relativistic near-single-cycle light waves at 1 kHz" (unpublished).

[47] M. Bocoum, F. Böhle, A. Vernier, A. Jullien, J. Faure, and R. Lopez-Martens, "Spatial-domain interferometer for measuring plasma mirror expansion," Opt. Lett. **40**, 3009–3012 (2015).

[48] See http://warp.lbl.gov for more information concerning the code WARP.

[49] J.-L. Vay, D. P. Grote, R. H. Cohen, and A. Friedman, "Novel methods in the particle-in-cell accelerator code-framework Warp," Comput. Sci. Discovery **5**, 014019 (2012).

[50] See https://www.picsar.net for more information concerning the high performance PICSAR library.

[51] H. Vincenti and J.-L. Vay, "Detailed analysis of the effects of stencil spatial variations with arbitrary high-order finite-difference Maxwell solver," Comput. Phys. Commun. **200**, 147–167 (2016).

[52] H. Vincenti, M. Lobet, R. Lehe, R. Sasanka, and J.-L. Vay, "An efficient and portable simd algorithm for charge/current deposition in particle-in-cell codes," Comput. Phys. Commun. **210**, 145–154 (2017).

[53] H. Vincenti and J.-L. Vay, "Ultrahigh-order maxwell solver with extreme scalability for electromagnetic PIC simulations of plasmas," Comput. Phys. Commun. **228**, 22–29 (2018).

[54] P. Gibbon, *Short Pulse Laser Interactions with Matter* (World Scientific Publishing Company, 2004).

[55] J. P. Colombier, P. Combis, A. Rosenfeld, I. V. Hertel, E. Audouard, and R. Stoian, "Optimized energy coupling at ultrafast laser-irradiated metal surfaces by tailoring intensity envelopes: Consequences for material removal from Al samples," Phys. Rev. B **74**, 224106 (2006).

[56] W. L. Kruer, *The Physics of Laser Plasma Interactions* (Addison-Wesley, New York, 1988).

[57] C. McGuffey, A. G. R. Thomas, W. Schumaker, T. Matsuoka, V. Chvykov, F. J. Dollar, G. Kalintchenko, V. Yanovsky, A. Maksimchuk, K. Krushelnick, V. Y. Bychenkov, I. V. Glazyrin, and A. V. Karpeev, "Ionization induced trapping in a laser wakefield accelerator," Phys. Rev. Lett. **104**, 025004 (2010).

[58] A. Pak, K. A. Marsh, S. F. Martins, W. Lu, W. B. Mori, and C. Joshi, "Injection and trapping of tunnel-ionized electrons into laser-produced wakes," Phys. Rev. Lett. **104**, 025003 (2010).

Interaction of ultraintense radially-polarized laser pulses with plasma mirrors

N. Zaïm,[1, a)] D. Guénot,[1, 2, a)] L. Chopineau,[3, a)] A. Denoeud,[3] O. Lundh,[2] H. Vincenti,[3] F. Quéré,[3] J. Faure[1, b)]
[1)]*LOA, CNRS, École Polytechnique, ENSTA Paris, Institut Polytechnique de Paris, 181 Chemin de la Hunière et des Joncherettes, 91120 Palaiseau, France*
[2)]*Department of physics, Lund University, SE-22100 Lund, Sweden.*
[3)]*Lasers, Interactions and Dynamics Laboratory (LIDyL), Commissariat à l'Énergie Atomique, Université Paris-Saclay, DSM/IRAMIS, CEN Saclay, 91191 Gif sur Yvette, France*

(Dated: 28 January 2020)

We present experimental results of the vacuum laser acceleration (VLA) of electrons using radially polarized laser pulses interacting with a plasma mirror. Tightly focused radially polarized laser pulses were proposed for electron acceleration because of their strong longitudinal electric field, making them ideal for VLA. However, experimental results have been limited until now because injecting electrons into the laser field has remained a considerable challenge. Here, we demonstrate experimentally that using a plasma mirror as an injector solves this problem and permits to inject electrons at the ideal phase of the laser, which results in the acceleration of electrons along the laser propagation while reducing the electron beam divergence compared to the linear polarization case. We obtain electron beams with few-MeV energies and a 200 pC charge, thus demonstrating for the first time electron acceleration to relativistic energies using a radially polarized laser. High-harmonic generation from the plasma surface is also measured and provides additional insight into the physics of the interaction. Detailed comparisons between the experimental results and full 3D simulations unravels the complex physics of electron injection and acceleration in this new regime: we find that electrons are ejected into the radially polarized pulse in the form of two spatially-separated bunches emitted p-polarized regions of the focus. Finally, we propose an experimental configuration in which this process is further optimized, leading to extremely peaked electron angular distributions and higher energy beams.

I. INTRODUCTION

Owing to the progress of intense femtosecond lasers[1], new methods for accelerating particles have been developed in the last two decades. Most notably, laser wakefield accelerators[2,3] take advantage of extremely high accelerating gradients, on the order of 100 GV/m, to generate ultrashort[4] electron bunches with high beam quality and energies ranging from few-MeV[5] to multi-GeV[6]. Vacuum Laser Acceleration (VLA), in which the electrons are directly accelerated by the laser field, is another method for accelerating electrons that has also drawn significant attention. Many theoretical[7–11] and numerical[12–15] studies of VLA have been carried out with the prospects of understanding this fundamental interaction and profiting from the immense accelerating fields involved, that can exceed 10 TV/m. However, experimental observation of high energy gains from VLA has proven difficult to achieve[16–19]. This is due to the fact that acceleration is efficient when electrons are injected with a high initial velocity at a precise phase of the laser pulse, close to a zero of the electric field, so that they remain in an accelerating phase of the laser for a long time. Since the accelerating structure has superluminal phase velocity[8] and usually sub-micron wavelength, these stringent injection conditions are not attained with conventional injection methods. Indeed, two methods have been tried so far to inject electrons into an intense laser field: the ionization of a low density gas target or the use of a pre-accelerated electron beam. In the first case, electrons are injected with no initial velocity at a phase of the laser that is not optimal for electron acceleration (close to a maximum of the electric field), which leads to inefficient acceleration. In the second case it is particularly challenging to inject the electrons at a precise phase of the accelerating structure, as it would require electron bunches with attosecond duration and synchronization with the laser. For this reason, experimental attempts at VLA with this method tend to result in a widening of the energy spread rather than a net acceleration.

It was recently observed that plasma mirrors could solve this issue and act as ideal injectors for VLA[20]. A plasma mirror is an overdense plasma with a sharp density gradient on its front surface ($L \ll \lambda_0$, where L is the gradient scale length and λ_0 the laser wavelength). The term "plasma mirror" comes from the fact that they reflect light specularly. When a p-polarized laser pulse with ultrahigh intensity is focused on such target, nonlinear oscillations of the plasma surface occur following the sign of the laser pulse. These oscillations lead to the periodic emission of high-harmonics, via the Relativistic Oscillating Mirror (ROM) mechanism[21], and ejection of electrons at a precise phase of the laser pulse[22]. These electrons are ideally injected in the reflected laser field: they begin their interaction close to a zero of the electric field with a relativistic velocity directed towards the specular direction, which allows them to gain large amounts of energy from the reflected pulse. Using 20 TW laser pulses on-target, it was demonstrated that 3 nC, 5-10 MeV electron bunches with 150 mrad divergence could be produced[20,23].

When VLA is carried out with linearly polarized pulses, the accelerating fields are transverse. This means that the electrons are pushed off the optical axis as they are accelerated, which tends to widen the angular distribution. For this rea-

---

[a)] These three authors contributed equally

[b)] Electronic mail: jerome.faure@ensta-paris.fr son, the possibility of accelerating electrons with longitudinal electric fields has frequently been studied[8,24–29]. Radially polarized beams are ideal candidates for achieving this[24–29]. A laser is radially polarized if at every position the polarization vector points towards its center. In this case, the magnetic field only has an azimuthal component B_θ. The relevance of this polarization state comes from the presence of a strong longitudinal field at focus, located on the optical axis, where the transverse fields vanish. The main components of a paraxial radially polarized pulse at focus can be written in cylindrical coordinates as:

$$E_r = E_{0,z}\frac{k_0 r}{2}\exp\left(-\frac{r^2}{w_0^2}\right)\cos\omega_0 t \times f(t) \tag{1}$$

$$B_\theta = E_r/c \tag{2}$$

$$E_z = E_{0,z}\exp\left(-\frac{r^2}{w_0^2}\right)\left(1-\frac{r^2}{w_0^2}\right)\sin\omega_0 t \times f(t). \tag{3}$$

where $E_{0,z}$ is the peak amplitude of the longitudinal electric field, c is the speed of light in vacuum, $k_0 = 2\pi/\lambda_0$ is the laser central wavenumber, ω_0 its central frequency, w_0 its beam waist and $f(t)$ a normalized temporal envelope. It is common to define $a_{0,z} = E_{0,z}/E_0$ as the normalized amplitude of the longitudinal field. Here $E_0 = m_e c\omega_0/e$ where m_e and e are the electron mass and charge respectively. The normalized peak amplitude of the radial field, noted $a_{0,r}$, is given by $a_{0,r} = \frac{\exp(-0.5)k_0 w_0}{\sqrt{2}}a_{0,z}$. It can be noted that $\frac{a_{0,z}}{a_{0,r}} \propto \frac{1}{w_0}$. Therefore, the longitudinal field is predominant only in the case of very tight focusing. If the E_z field is strong enough, it can be used to directly accelerate electrons in the longitudinal direction. This requires the electrons to be located very close to the optical axis, where the longitudinal field is maximum and the deflecting E_r and B_θ fields are negligible. In such a case, the electrons can remain for a long time in the center of the laser beam, which can in principle result in an electron beam with higher energy and smaller divergence than with linear polarization[25]. In the past, there have been two experimental attempts at VLA using radial polarization, but modest energy gains, of at most tens of keV, have been achieved[17,19]. This is due to the fact that relatively small laser energies were used, and, as explained earlier, that electron injection into the laser pulse was not optimal. However, numerical simulations have recently demonstrated that, as in the case of linear polarization, plasma mirrors could be used to inject electrons with ideal initial conditions into radially polarized beams, resulting in relativistic and low divergence electron beams[30].

This paper presents experimental results of electron acceleration to relativistic energies using radially polarized pulses combined to a plasma mirror injector. We observe that using radial polarization leads to electron acceleration in the longitudinal direction, thereby reducing the angular spread. Electron beams with a charge exceeding 100 pC and an energy spectrum peaking at 2 MeV have been obtained. In order to gain further insight from the interaction and the electron injection process, we also study the case of azimuthal polarization. Azimuthally polarized beams are similar to radially polarized beams but have the electric and magnetic fields "exchanged", meaning that the main components of such pulses are E_θ, B_r and B_z. They do not exhibit an E_z field and therefore cannot directly accelerate electrons in the longitudinal direction, which we verify experimentally. While the propagation of ultraintense radially or azimuthally polarized pulses in underdense plasmas has been previously studied[31], this is the first time that the interaction of such pulses with overdense plasmas is investigated experimentally.

The paper is organized as follows. In Sec. II, we describe our experimental setup. The experimental results are presented in Sec. III and analyzed in Sec. IV with the help of full-3D Particle-In-Cell (PIC) simulations. Finally, the ideal experimental parameters that would be required to optimize the acceleration with radially polarized beams are discussed in Sec. V.

II. EXPERIMENTAL SETUP

The experimental setup is represented in Fig. 1. The UHI100 laser at CEA Saclay is a 100-TW class system which provides 800-nm, 24-fs laser pulses with an ultrahigh temporal contrast ($> 10^{12}$) thanks to a double plasma mirror system[32] located before the experimental chamber. We use a deformable mirror to correct the laser wavefront. A phase mask consisting of eight half-wave plates with different optical axes, as shown in Fig. 2(a), can be inserted in order to convert the laser polarization from linear to radial or azimuthal. Each octant of the phase mask is made of a 80-μm thick piece of mica, which is thin enough to result in a low B-integral of 0.15 rad. By rotating the entire phase mask, the polarization can be continuously varied from radial to azimuthal. A circular aperture, not depicted in Fig. 1, is used to remove the edges of the beam and improve the focal spot. In the case of linear polarization, a 50 mm aperture is used, thus reducing the energy on target to 460 mJ. When the radial polarization phase mask is introduced in the beam, a 65 mm aperture is used such that the energy on target is 675 mJ. The beam is focused with a 60° incidence angle onto a fused silica target by a parabola with a focal length $f = 200$ mm. Resulting focal spots are shown in Figs. 2(b) and 2(c). For linear polarization, the beam waist is measured to be $3 \times 3.4\,\mu$m, which results in an estimated peak intensity of $I = 5.8 \times 10^{19}\,\mathrm{W/cm^2}$ ($a_0 = 5.2$). For radial polarization, the characteristic doughnut shape is clearly observed. The slight asymmetry of the spot is probably due to imperfections in the wavefront and/or imperfect centering of the beam on the phase mask. The beam waist is obtained by fitting $r^2\exp\left(-2r^2/w_0^2\right)$ to the spatial profile, which gives $3.05 \times 3.2\,\mu$m. The resulting peak intensity is $I = 4.8 \times 10^{19}\,\mathrm{W/cm^2}$ ($a_{0,r} = 4.7$). Using these parameters we estimate the longitudinal normalized field to be:

$$a_{0,z} = 0.742 a_{0,r}\left(\frac{\lambda_0}{w_0}\right) = 0.9. \tag{4}$$

This value is probably somewhat overestimated because of the asymmetry in the focal spot but it indicates that the longitudinal component of the electric field approaches relativistic intensities, making the laser suitable for electron acceleration in the longitudinal direction.

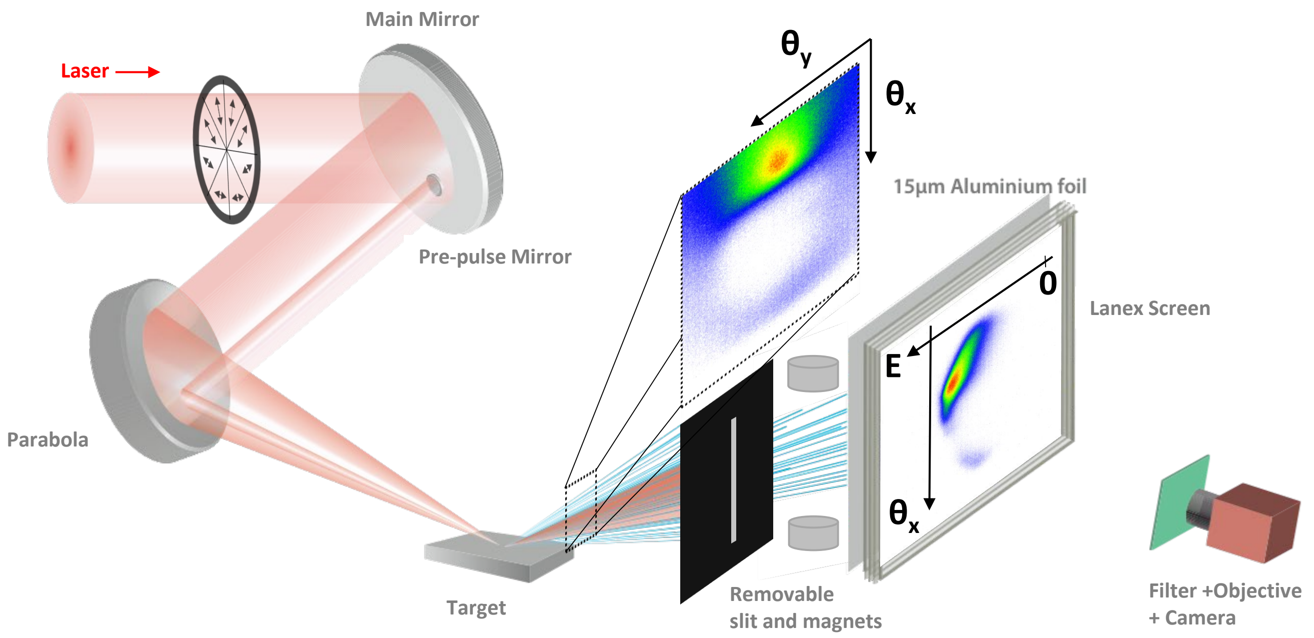

FIG. 1. Experimental setup. The images on the screens show the electron beam angular distribution after the interaction (left screen) and its angularly resolved spectrum (right screen).

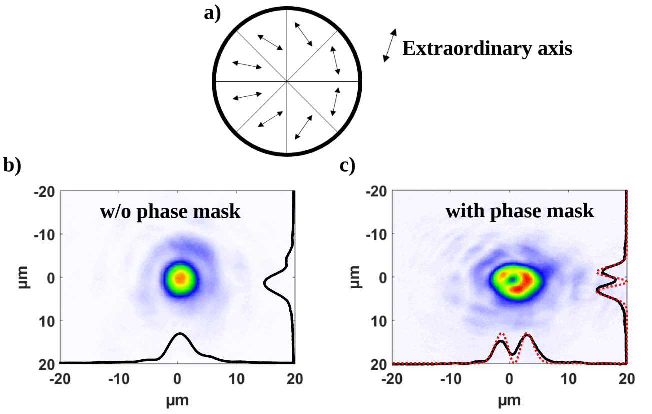

FIG. 2. Generation of radial polarization. a) Sketch of the phase mask and extraordinary axes of the eight octants. b) Focal spot for linear polarization, i.e. without the phase mask. c) Focal spot for radial polarization.

A small mirror is inserted before the parabola in order to create a weak pre-pulse from the main laser beam[33]. This pre-pulse is used to ionize the target and initiate a plasma expansion at an adjustable delay before the main pulse, therefore creating a transversely homogeneous preplasma with an accurately controlled density gradient.

A calibrated phosphor screen[34] (KODAK LANEX fine) is used in combination with a camera to observe the electron angular distribution around the specular direction. The screen is covered by a 1.63 mm aluminium plate to provide shielding against the laser light and remove the electrons with an energy lower than ~900 keV. A pair of magnets in combination with a slit can be added in front of the screen to measure angularly resolved electron energy spectrum in the incidence plane ($\theta_y = 0$, with θ_y defined in Fig. 1).

In parallel to the electron distributions, high order harmonics emitted in the specular direction can be measured by replacing the electron spectrometer with an XUV spectrometer. The spectrometer uses a 1200 lines per mm varied line spacing concave extreme ultraviolet grating (Shimadzu 30-002) coupled to a large 69×88 mm rectangular microchannel plate and a phosphor screen. This provides harmonic spectra which are angularly resolved in the transverse θ_y direction. With linear polarization, it is possible to observe up to the 45^{th} harmonic order.

III. EXPERIMENTAL RESULTS

A typical electron angular distribution obtained with linear polarization is displayed in Fig. 3(a). The main features of this distribution are the presence of a hole in the specular direction and of a bright peak between the specular and the normal directions, in good agreement with previous experiments[20,23]. This bright spot is located approximately 150 mrad from the specular direction and contains a charge of ≈ 700 pC. The electron signal in this regime is optimal when the gradient scale length is on the order of $\lambda_0/10$ (see Ref.[23]).

While the electron signal exhibits good stability in linear polarization, we observe significant shot-to-shot fluctuations in the radial polarization case, which we attribute to shot-to-shot fluctuations in the laser focal spot that appear when the phase mask is inserted in the laser beam. We nonetheless consistently observe an electron beam emitted very close the specular direction, while another spot remains visible between the normal and specular directions, as can be seen in

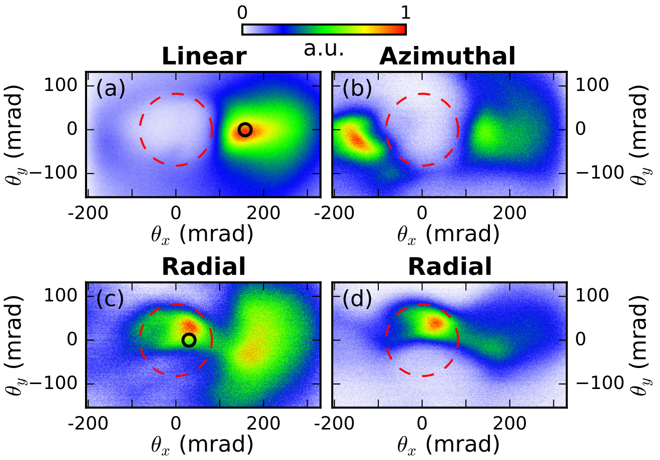

FIG. 3. Typical experimental angular electron distributions. The specular direction corresponds to $\theta_x = \theta_y = 0$. (a) linear polarization: the electron beam is located between the specular and normal directions. (b) azimuthal polarization: electrons are located on both sides of the specular direction (c) radial polarization. (d) Angular distribution obtained in the best shots with radial polarization. Both (c) and (d) display an on-axis electron beam in the specular direction. The dashed red lines show the angular extent of the reflected laser beam.

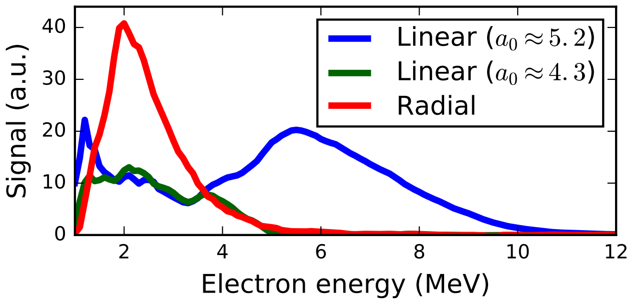

FIG. 4. Experimental electron spectra obtained with radial polarization (red curve), linear polarization (blue curve) and linear polarization at reduced energy (green curve).

Fig. 3(c). This peak in the specular direction has a narrower divergence, typically in the 50 mrad range, and can contain up to 200 pC (100 pC on average). For the best shots, the spot in the specular direction can even contain more charge than the spot located between specular and normal, and the electron beam divergence is reduced by a factor of two compared to the linear polarization case. An example of such shot is shown in Fig. 3(d).

When rotating the phase mask to generate azimuthal polarization, the electron peak in the center fades away, as shown in Fig. 3(b). In this case, a significant amount of electrons are located on the other side of the hole, between the specular and the grazing directions. Overall, we remark that electrons are only emitted in the specular direction when radially polarized pulses, which possess a considerable longitudinal electric field, are used. This strongly suggests that these electron are, as initially desired, accelerated by the E_z field.

Figure 4 shows the electron energy spectra recorded at the position of the bright spot for linear polarization and at the position of the specular spot for radial polarization. With linear polarization, the maximum reached energy is 11 MeV with a peak at 6 MeV while with radial polarization the maximum energy is 6 MeV with a peak around 2 MeV. In order to obtain a similar spectrum with linear polarization it is necessary to reduce the laser energy by 30% (we have in this case 320 mJ on target and $a_0 \approx 4.3$).

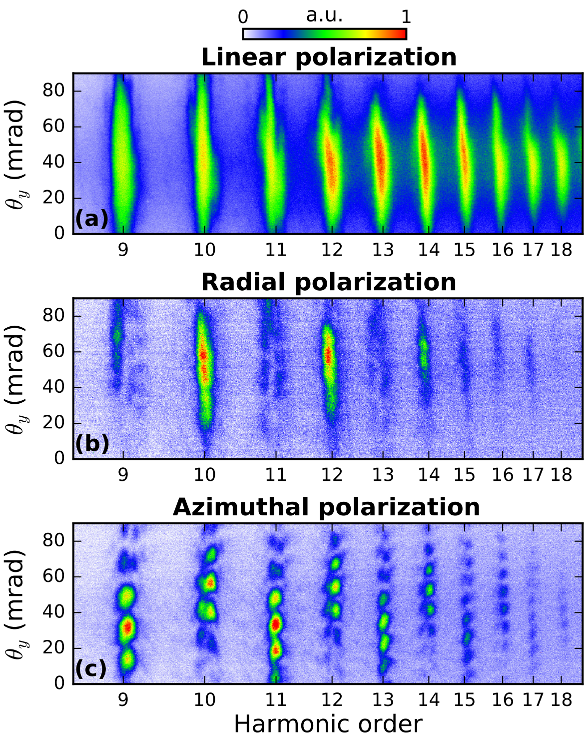

FIG. 5. Experimental angularly resolved harmonic spectra in the case of (a) linear polarization, (b) radial polarization and (c) azimuthal polarization.

With the purpose of gaining additional insight on the interaction, we also study high-harmonic generation (HHG), which is closely related to the generation of fast electrons in the relativistic regime[22,23]. Figure 5 shows typical angularly resolved harmonic spectra for linear, radial and azimuthal polarization between harmonic orders 9 and 18. When the phase mask is introduced in the beam, the total harmonic yield decreases. Each spectrum is therefore renormalized separately in Fig. 5. In the case of azimuthal polarization, we observe interference fringes on each harmonics in the θ_y angle. These fringes correspond to the interference pattern that would be generated by two sources separated by 4.8 ± 0.1 µm in the transverse y-direction. The interference patterns for consecutive harmonic orders appear to be shifted by π. In other words, if the signal is close to 0 at a given angle for harmonic order n, it will be close to maximum at the same angle for harmonic order $n+1$. In the case of radial polarization, we observe no interference pattern but we notice that the harmonic intensity can substantially vary between even and odd harmonics (in Fig. 5(b) the even harmonics are stronger but in some other shots the odd harmonics can become stronger).

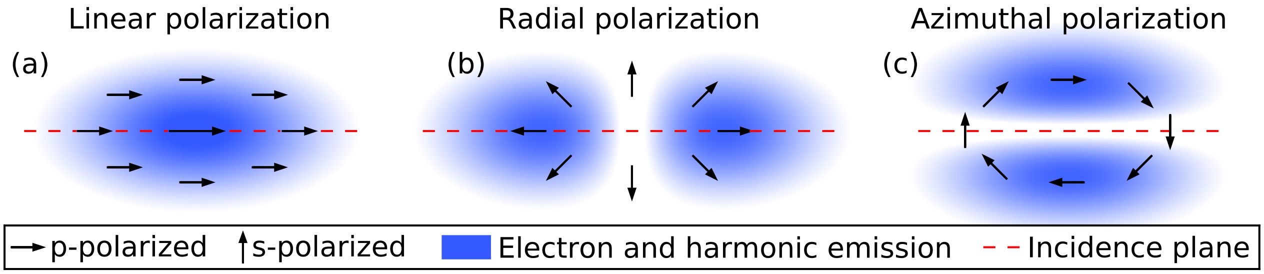

FIG. 6. Schematic view of the laser field footprint on the plasma surface for (a) linear, (b) radial or (c) azimuthal polarization. Electrons and harmonics are only emitted when the laser is p-polarized, which results in two distinct sources in the case of radial and azimuthal polarization.

IV. INTERPRETATION AND DISCUSSION

A. Harmonic generation

1. *Physical interpretation for the two sources of HHG*

The fact that the harmonic signal with azimuthal polarization seems to originate from two sources from either side of the incidence plane strongly suggests that only the parts of the laser that are p-polarized contribute to high-harmonic emission, while no harmonics are emitted in the regions where the laser is s-polarized. It has indeed been shown that, at the laser intensities considered here, the harmonics signal is suppressed when the polarization is switched from p to s (see Ref.[23]). These ideas are illustrated in Fig. 6: for linear polarization, the whole beam can be p-polarized, which leads to a single harmonic source. On the other hand, for radial or azimuthal polarization, the locally p-polarized parts of the beam form two separate spots which can result in two separate harmonic sources. This is supported by the fact that the distance between the two sources obtained from the interference pattern ($4.8 \pm 0.1\,\mu$m) matches the distance between the two maxima in the focal spot ($4.3 \pm 0.2\,\mu$m, see Fig. 2(c)).

This physical interpretation can also be used to explain why interference patterns for consecutive harmonic orders appear to be shifted by π. We indeed know that the harmonic signal is emitted periodically at a precise phase of the incident laser field. Since the electric field in the two separate sources have opposite sign for radial or azimuthal polarization, the harmonic emission is delayed by half a laser cycle from one source to the other, i.e. a π phase delay. This leads, for harmonic n, to a phase shift of $n\pi$ between the two sources, which results in a phase shift of π in the interference patterns for consecutive harmonics.

For radial polarization, we also expect to see an interference pattern but this time in the θ_x angle. However, the fringes cannot be seen in the experiment as our spectrometer samples the harmonic beam at a given θ_x. Therefore, the spectrometer only sees one position in the interference pattern for each harmonic. Since there is a π phase difference between consecutive harmonic patterns, the harmonic intensity strongly varies between odd and even harmonics, which is precisely what we observe in Fig. 5(b).

2. *3D PIC simulations of harmonic generation*

In order to confirm this physical explanation, we turn to 3D PIC simulations using the code WARP[35,36] combined with the high-performance library PICSAR[37,38]. We use the high-order Pseudo-Spectral Analytical Time Domain (PSATD) Maxwell solver which strongly reduces numerical dispersion[39,40]. As a result, convergence of the simulations is attained with larger spatial and temporal steps, which makes full 3D PIC simulations at solid density feasible using current petascale machines[41,42]. Each of the simulations presented here costs around 3 million computation hours on supercomputer Mira[43]. The gradient scale length is either $\lambda_0/10$ or $\lambda_0/7$ and the laser parameters are the same as as in experiments. A moving window is used in order to follow the trajectory of the electrons in the reflected pulse up to 80 µm away from the plasma (approximately 2 Rayleigh lengths). More details regarding the simulations are given in appendix A.

Angularly resolved harmonic spectra obtained from the simulations are displayed in Fig. 7. In panels (a) to (c), the harmonics are resolved in the θ_y direction so that they can be directly compared with the experimental measurements shown in Fig. 5. A very good agreement is found: in azimuthal polarization, we observe interferences with a phase shift of π between consecutive harmonics while in radial polarization, we notice that the harmonic intensity considerably differs between even and odd harmonics. In Fig. 7(d), the angular dependence is shown with respect to the θ_x angle in the radially polarized case, allowing us to uncover the interference pattern which is not visible in experiments. Both the experimental and simulated harmonic spectra show clear evidence that radial or azimuthal polarizations result in two separate harmonic sources that correspond to positions where the laser is locally p-polarized. This, again, is supported by the $\approx 4.7\,\mu$m distance between the two sources obtained from the simulated harmonic signal, which is consistent with the theoretical distance between the two maxima in the focal spot ($\sqrt{2}w_0 \approx 4.4\,\mu$m).

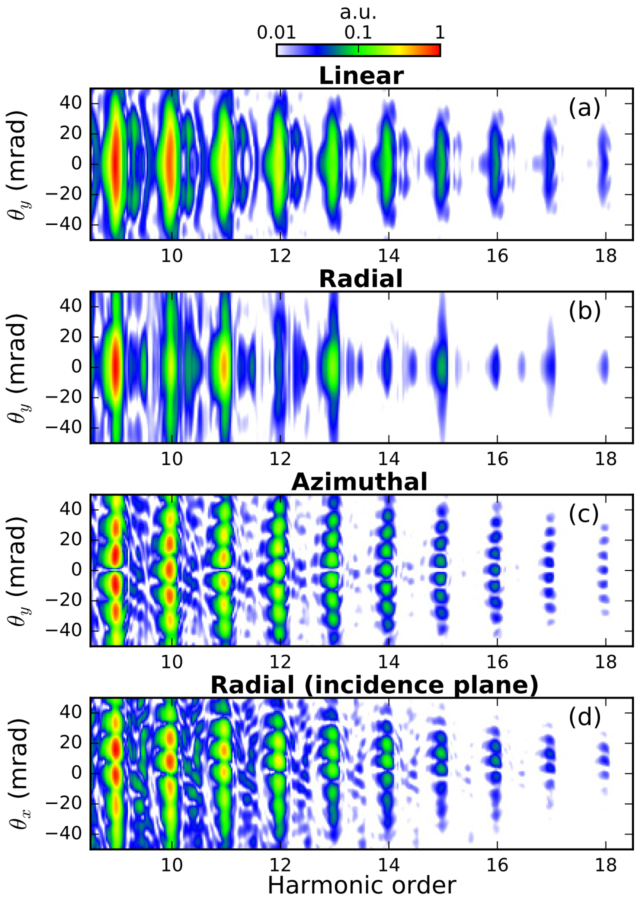

FIG. 7. Results from 3D PIC simulations. Angularly resolved harmonic spectra for (a) linear, (b),(d) radial or (c) azimuthal polarization. The angular dependence is shown with respect to the θ_y angle in panels (a) to (c), which corresponds to the experimental case, and with respect to the θ_x angle in panel (d), so that the interference pattern becomes apparent.

3. *Two sources of electron injection*

As we have stated in the introduction, the harmonics are emitted via the Relativistic Oscillating Mirror (ROM) mechanism, which occurs as the reflecting plasma surface oscillates nonlinearly following the laser field. At the moments when the oscillating electrons are pulled towards vacuum, the incident field is strongly Doppler upshifted, leading to the high-harmonic generation. At the same time, part of the oscillating electrons acquire a high enough energy to escape the plasma, leading to the ejection of electrons. Since both electron and high-harmonic emissions are originating from the same oscillation of the plasma surface, they happen simultaneously and are optimized for the same laser and plasma parameters. Such a correlation between ROM harmonics and electron ejection has indeed been observed experimentally[23]. In the case of radial or azimuthal polarization, we have just seen that harmonics are only generated at the positions where the laser is locally p-polarized. We can therefore expect a similar behavior for electron ejection, which would mean that electrons are also emitted from two separate sources.

In order to confirm this prediction, we plot in Fig. 8 the initial position of the electrons that are ejected from the plasma in the simulations. As anticipated, only the p-polarized parts of the laser contribute to electron ejection, which results in two distinct electron sources in radial and azimuthal polarization. The fact that electron emission only occurs at specific parts of the focal spot can partly explain the significant shot-to-shot fluctuations observed in experiments with radial and azimuthal polarization. We have indeed seen that the focal spot possesses an asymmetry (see Fig. 2(c)) which can vary depending on the shots. Shots with a higher intensity in the p-polarized parts of the beam will result in a much higher detected charge than shots with a higher intensity in the s-polarized parts of the beam.

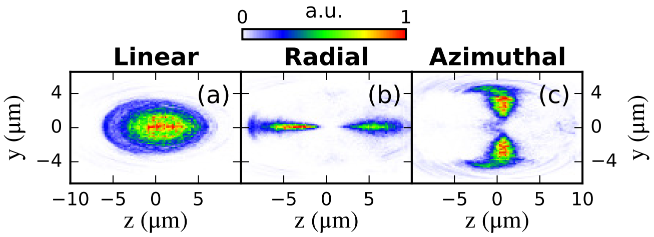

FIG. 8. Results from 3D PIC simulations. Initial position of the electrons that are ejected 4 μm away from the plasma in the case of (a) linear, (b) radial or (c) azimuthal polarization.

From a VLA point of view, the fact that the E_z field in radial polarization does not contribute to electron injection and that the interaction is still dominated by the transverse fields is not ideal. Indeed, the initial purpose of using radial polarization was to accelerate the electrons close to the optical axis where the transverse fields are negligible whereas in our case the electrons are injected on the side of the beam where the transverse fields are the highest. Nevertheless, the fact that we have detected experimentally electrons in the longitudinal direction suggests that it is possible for some electrons to reach the optical axis after being injected on the side of the beam.

4. *Loss of radial symmetry of the reflected pulse*

Another important result of the simulations is that the laser partially loses its spatial structure upon reflection. This is due to the fact that that laser absorption is higher in the p-polarized parts of the focal spot, and lower in the s-polarized parts of the spot (this can be understood by the fact that electron emission and harmonic generation are stronger for the p-polarized components of the field). Consequently, the reflected laser field no longer has cylindrical symmetry. Figure 9 displays snapshots from the PIC simulation with radial polarization showing the laser pulse in the incidence plane before and after reflection. We most notably observe that the hole in the intensity distribution at the center of the laser is suppressed after the interaction. This may make the VLA process in the reflected pulse more complex. In particular, we remark that high-amplitude harmonic fields, which have a much longer Rayleigh length than the fundamental pulse, remain present on the optical axis far from the plasma. Such on-axis harmonic fields could cause an unwanted deflection of electrons accelerated by the longitudinal field close to the optical axis, where transverse fields are supposed to be negligible in a perfect radially polarized pulse.

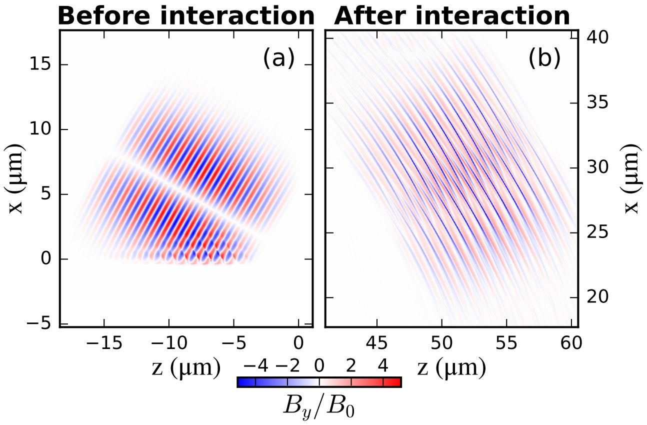

FIG. 9. Results from a 3D PIC simulation. Laser magnetic field in the incidence plane with radial polarization, either (a) before or (b) after the interaction. Here, $B_0 = E_0/c$ with E_0 defined earlier.

B. Electron acceleration

1. 3D PIC simulations of electron acceleration

The harmonic spectra obtained in PIC simulations show excellent agreement with experiments, but we find that it is more difficult to reproduce the electron angular and energy distributions in the 3D PIC simulations with radial and azimuthal polarization. First, it must be noted that in order to obtain accurate results, the simulations should be run until electrons completely exit the laser field, which is a considerable computational challenge. In our simulations, the reflected pulse propagates 80 μm away from the plasma, i.e. more than two Rayleigh lengths; nevertheless, some electrons are still interacting with the laser, indicating that their angular and energy distributions might still evolve. Secondly, as we have seen in the experiment, results obtained with the phase mask for radial polarization give lower performance in terms of electron acceleration (energy and charge) and harmonic yield, compared to the linear polarization case. This suggests that imperfections of the focal spot (such as intensity inhomogeneities and phase aberrations) might affect the interaction more severely in the case of radial polarization, probably because the radial symmetry can easily be broken when imperfections are present in the focal region.

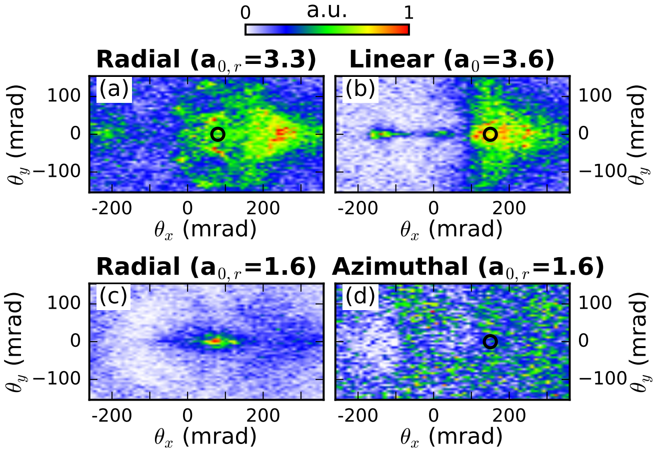

FIG. 10. Results from 3D PIC simulations. (a)-(b) Angular distributions of the electrons with an energy greater than 1 MeV obtained at the end of the simulations with (a) radial polarization and $a_{0,r} = 3.3$, (b) linear polarization and $a_0 = 3.6$, (c) radial polarization and $a_{0,r} = 1.6$ and (d) azimuthal polarization and $a_{0,r} = 1.6$.

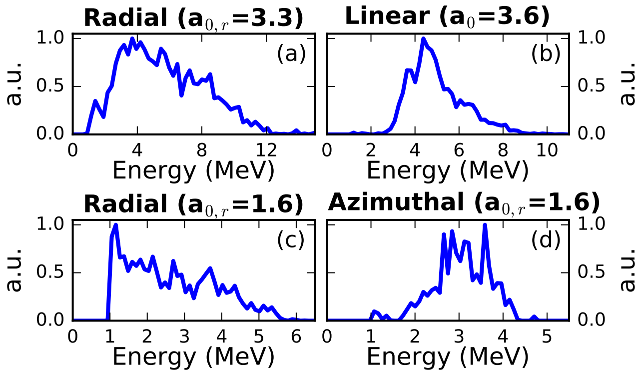

FIG. 11. Results from 3D PIC simulations. Electron energy distributions are computed in a 30 mrad cone angle defined by the black circles shown in Fig. 10.

Therefore, we find that in order to obtain a quantitative agreement with the experiment, it is necessary to reduce the laser intensity substantially, and even more so in the case of radial polarization. Figures 10(a) and 10(b) show typical electron angular distributions obtained in simulations with lower intensity for, respectively, radial and linear polarization. Here, $a_0 = 3.6$ for the linear case and $a_{0r} = 3.3$ for the radial case, corresponding to a factor of two lower intensity compared to the experiment described in Sec. II. In the linearly polarized case, we find that the main features of the experimental angular distribution are well reproduced: most electrons are accelerated between the specular and normal directions ($\theta_x > 0$) and there is virtually no electron emitted in the specular direction. This is in good agreement with previous 3D PIC simulations performed with similar laser and plasma parameters[23,42]. When the polarization is switched to radial, there are more electrons located around the specular direction, as in experiments. However, we find that contrary to the experiment, this does not lead to a reduction of the electron beam angular spread and the overall simulated beam does not completely match the experimental results.

The corresponding energy spectra are computed at the angles indicated by the black circles and are shown in Figs. 11(a) and 11(b). Even with this lower intensity level, the simulation with radial polarization yields electrons with an energy that is approximately twice as high as detected experimentally. This, again, suggests that imperfections of the laser focal spot degrade substantially the acceleration process compared to the ideal case that is considered in the simulations. This is consistent with the fact that both electron ejection from the plasma and subsequent VLA are sensitive to the exact spatio-temporal shape of the laser pulse[28,44].

To obtain an electron energy spectrum matching the experimental one, we have performed another simulation with radial polarization with an intensity even further decreased to approximately a tenth of the experimental value given in Sec. II. Although this is a large difference, we find that it leads to a good agreement with experiments, as can be seen in Fig. 11(c). This shows the extent to which the acceleration process seems to be negatively affected by the imperfections introduced by the phase mask. Interestingly, we find that reducing the laser intensity leads to a much more collimated electron beam, whose angular distribution is shown in Fig. 10(c). This distribution resembles that of the best experimental shots with radial polarization (see Fig. 3(d)), which confirms that a better agreement with experiment is found by reducing the intensity. We also once again find that using radial polarization can result in a significant decrease in the electron beam divergence.

Finally, simulations confirm that azimuthal polarization does not yield a collimated electron beam in the specular direction, in agreement with experiments. For example, in Fig. 10(d), we show the angular distribution obtained with the same parameters as in Fig. 10(c), except that the polarization is changed from radial to azimuthal. We find in this case that the electrons are emitted with a very wide divergence of the order of 600 mrad (which is not entirely visible in Fig. 10(d), for direct comparison with the other numerical and experimental distributions).

2. *Physical explanation for the narrow divergence e-beam*

In this section, we investigate the reasons why we obtain a narrow divergence with radial polarization when $a_{0,r} = 1.6$, but not when $a_{0,r} = 3.3$, with the ultimate purpose of understanding the conditions leading to a high-quality electron beam. In order to understand the fundamental differences between the two cases, we have analyzed the trajectories of the corresponding electrons in the PIC simulations. Recalling that electrons are ejected in two spatially-separated bunches (corresponding to regions where the laser is locally p-polarized, as previously seen), we find that only the electrons originating from the bunch located on the right (such that $z > 0$) in Fig. 8(b) contribute to the collimated spot in the specular direction in Fig. 10(c). This can be understood fairly easily and is illustrated in Fig. 12. First, we stress a general feature of this plasma mirror injection mechanism: most electrons are ejected from the plasma at a phase which is such that they tend to be deflected by the transverse fields towards the normal direction, see Fig. 12(a). This explains why, in the linear polarization case, the electron beam is located between the specular and normal directions ($\theta_x > 0$). In the case of radial polarization, electrons initially in the bunch such that $z < 0$, labeled "bunch A" in Fig. 12, tend to directly escape on the side of the beam and thus never interact with the E_z field. On the other hand, electrons initially in the bunch such that $z > 0$, labeled "bunch B" in Fig. 12, are shifted towards the center of the pulse, where they can be accelerated by the E_z field. The fact that electrons have different trajectories depending on their initial location will also further increase the fluctuations in the experimental angular distributions when the focal spot possesses an asymmetry that varies from shot to shot, as was the case in the experiments.

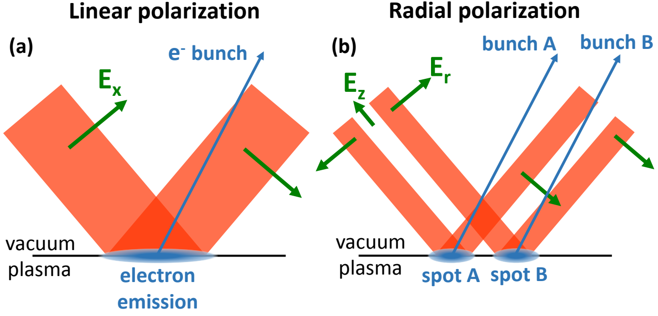

FIG. 12. Schematic illustration of electron emission from the plasma in the incident plane for linear (a) and radial (b) polarization. The green arrows in the reflected field indicate the direction of the transverse electric field seen by the electrons immediately after they are ejected. The electrons are always emitted at a phase such that they tend to be deviated towards the normal direction (this implies in particular that the phase at which electrons are ejected is shifted by π between spot A and spot B). For radial polarization, the electrons originating from spot B are more likely to interact with the E_z field than those coming from spot A.

We now focus on the electrons initially in "bunch B", both in the simulation with $a_{0,r} = 1.6$ and the simulation with $a_{0,r} = 3.3$. These electrons, initially on the side of the reflected laser pulse, propagate towards the center of the beam and subsequently spend a long time close to the optical axis where the longitudinal field has a high amplitude. This is another indication that electrons emitted in the specular direction are, at least partly, accelerated by the E_z field. We show in Figs. 13(a) to (d) the angular distribution of the electrons such that $z > 0$ initially, either ≈ 80 fs after reflection or at the end of the simulation, ≈ 270 fs after reflection. At the beginning of their interaction, these electrons have a very narrow angular spread in the θ_y direction in both simulations. In the lower intensity case ($a_{0,r} = 1.6$), this angular divergence remains small until the end, and we eventually observe a collimated beam in the specular direction. On the opposite, when the intensity is increased, a considerable widening of the angular distribution in the θ_y direction is visible. This means that electrons initially accelerated in the longitudinal direction are deflected in the transverse direction during their interaction with the reflected beam. This deflection, occurring far from the plasma, could be due to the harmonic fields which, as previously stated, have a longer Rayleigh length and remain for a long time close to the optical axis. The harmonic fields are much more intense in the simulation with $a_{0,r} = 3.3$ because the high-harmonic generation efficiency increases nonlinearly with the intensity[21], which would explain why the electrons are not deflected in the simulation with $a_{0,r} = 1.6$.

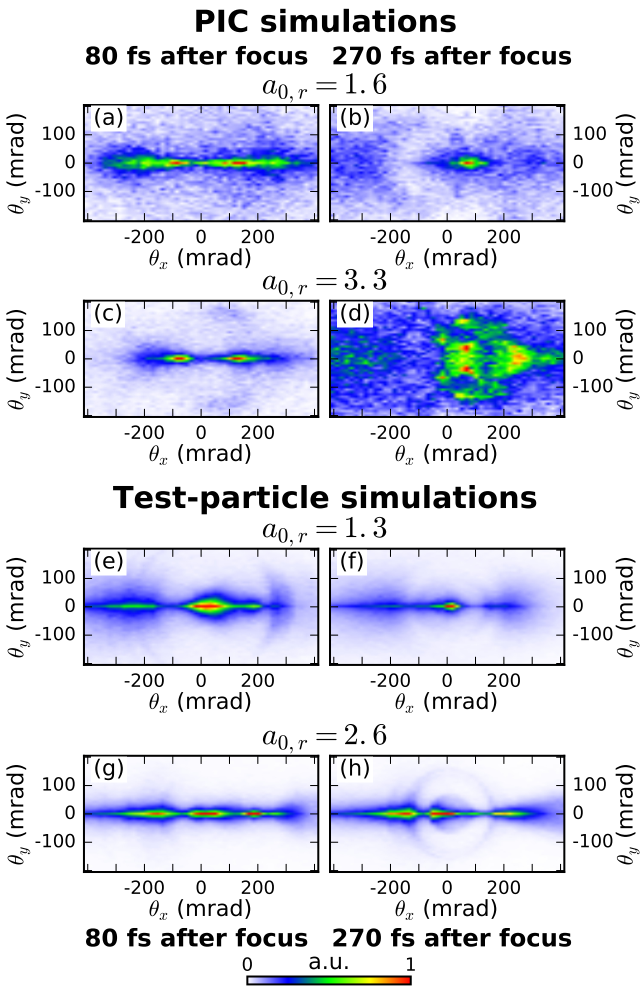

FIG. 13. 3D-PIC simulations. (a)-(d) Angular distribution of electrons with $z > 0$ initially, with (a)-(b) $a_{0,r} = 1.6$ or (c)-(d) $a_{0,r} = 3.3$. The distributions are shown either ≈ 80 fs after reflection or ≈ 270 fs after reflection, which corresponds to the end of the simulation. (e)-(h) Similar angular distributions reproduced in test-particle simulations. The laser intensity is slightly reduced in the test-particle simulations to take into account the energy absorption by the plasma mirror.

3. Test particle simulation of electron acceleration

In order to confirm the deleterious role of high-harmonic fields, we have performed a series of fast 3D test particle simulations of the acceleration of an electron bunch by an ideal radially polarized pulse, without high-harmonic fields. To simplify the interaction, we only consider a single attosecond electron bunch which is, as in experiments, initially located off the optical axis where the transverse fields are the most intense. The electrons start their interaction at a zero of the E_r field and the initial phase is chosen such that the electrons are pushed by the transverse fields towards the optical axis, which corresponds to the electron bunch B in the simulations. Electrons are initially placed at the focus of the laser, around four optical cycles before the temporal center of the pulse and have a Gaussian distribution both in real and momentum space, with an adjustable mean and variance. More details concerning these simulations can be obtained in appendix B.

By choosing the adequate initial electron distribution, we find that it is possible to obtain similar trajectories as in the PIC simulation with the lowest intensity. For example, we show in Figs. 13(e) and (f) the angular distributions obtained either ≈ 80 fs after focus or ≈ 270 fs after focus for an electron beam initially located 2 µm from the optical axis with an initial mean kinetic energy of 1 MeV and an average angle of 10° away from the specular direction, oriented towards the grazing direction. The initial standard deviations of the Gaussian distributions are $\sigma_z = 0.17\,\mu\text{m}$ and $\sigma_{pz} = 0.9\, m_e c$ in the longitudinal direction and $\sigma_x = 0.5\,\mu\text{m}$, $\sigma_y = 1.2\,\mu\text{m}$, $\sigma_{px} = m_e c$ and $\sigma_{py} = 0$ in the transverse directions. We observe as in the PIC simulations the formation of a collimated spot in the specular direction. The test particle simulation additionally allows us to calculate the work done by the different components of the electric field. We find that the electrons emitted in the collimated spot gain most of their energy from the work done by the E_z field, which provides further evidence that the electrons detected in the specular direction in experiments are indeed accelerated by the longitudinal field.

When increasing the intensity in the test-particule simulations, we do not obtain the large broadening of the angular spread in the θ_y direction that was observed in the PIC simulation. For instance, we show in Figs. 13(g) and (h) the angular distributions obtained for an electron beam initially located 3.1 µm from the optical axis with an initial mean kinetic energy of 2 MeV oriented towards the specular direction. The initial standard deviations of the Gaussian distributions are $\sigma_z = 0.19\,\mu\text{m}$ and $\sigma_{pz} = m_e c$ in the longitudinal direction and $\sigma_x = 0.8\,\mu\text{m}$, $\sigma_y = 0.8\,\mu\text{m}$, $\sigma_{px} = 3.2\, m_e c$ and $\sigma_{py} = 0$ in the transverse directions. We observe that the electron beam remains collimated in the y-direction, which strongly differs from the PIC simulation. This is an indication that the high-harmonics fields, which are not included in the test-particle simulations, are indeed deflecting the electrons off the optical axis and are detrimental to the electron beam quality.

Overall, the 3D simulations confirm that radial polarization can lead to acceleration in the longitudinal direction, most likely driven by the E_z field. This can lead to a decrease in the divergence of the accelerated electrons compared to linear polarization. However, the simulations also indicate that the experiments were not performed with ideal interaction conditions. First, the electrons are mainly injected by the E_r field at a position of the beam where the longitudinal field is negligible. Secondly, the radially polarized structure is partially lost upon reflection. This results in particular in strong harmonic fields which may deviate the electrons located on the optical axis if the laser is intense enough. These limitations make this acceleration method difficult to scale to larger energies because we expect in this case an increase in the electron beam angular spread.

V. IDEAL CONDITIONS FOR VLA WITH RADIAL POLARIZATION

In this section, we explain how to overcome the previously mentioned limitations. To this end, we describe the interaction parameters that should be used to take full advantage of radial polarization while using similar laser pulse energies. In particular, two key elements can be changed in order to drastically improve the results.

The first one is the use of normal incidence rather than oblique incidence. With normal incidence, the E_r field is parallel to the plasma surface so that only the E_z field contribute to electron ejection. Electrons are therefore injected close to the optical axis where the longitudinal field can accelerate them efficiently. This is a considerable enhancement compared with oblique incidence where the electrons are ejected in regions with intense radial fields. Moreover, since the axisymmetry of the reflected pulse is preserved at normal incidence, the transverse fields will always vanish on axis so that electrons will not be deflected from the region with strong accelerating fields.

The second key element is the increase of the amplitude of the longitudinal field $a_{0,z}$. This can be done both by focusing the laser pulse more tightly, as $a_{0,z}$ scales as $1/w_0^2$, and by reducing the pulse duration in order to increase the laser power. Using shorter pulses has other advantages: it leads to shorter electron beams and limits the interaction in the interference pattern formed by the incident and reflected beam.

Figure 14 presents results from a PIC simulation carried out in these conditions. Since the interaction at normal incidence has axial symmetry, the simulation is performed in cylindrical coordinates with the code CALDER-CIRC[45], thus hugely reducing its numerical cost. We use parameters targeted by the SYLOS laser system[46]: a pulse energy of 100 mJ, a beam waist of $w_0 = 1.5\,\mu\text{m}$ and a pulse duration of 5 fs in FWHM of intensity. This leads to $a_{0,z} = 3.78$ and $a_{0,r} = 9.55$. See also appendix C for more information regarding this simulation. We observe that the charge ejected within an angle θ of the specular direction scales quasi-linearly with θ. For instance, there is an ejected charge of 23.7 pC within 100 mrad of the specular direction, 9.84 pC within 50 mrad and 1.45 pC within 10 mrad. This means that the ejected charge per solid angle scales as $1/\theta$, which results in the peaked angular distribution shown in Fig. 14(a). The energy spectrum of the electrons accelerated in the specular direction, visible in Fig. 14(b), presents a narrow peak around 16 MeV. Such a narrow divergence ultrashort relativistic beam with quasi-monoenergetic energy could be particularly useful for applications such as ultrafast electron diffraction and femtosecond X-ray generation via inverse Compton scattering.

VI. CONCLUSION

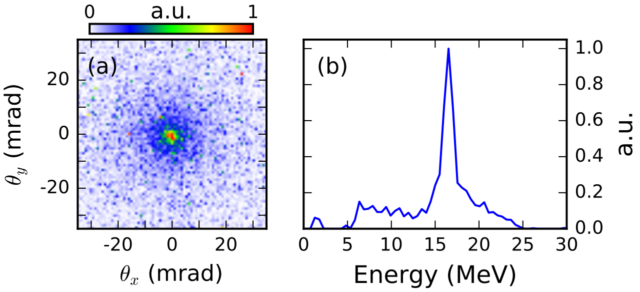

FIG. 14. Results from the PIC simulation at normal incidence. (a) Angular distribution of the electrons with an energy greater than 1 MeV around the specular direction. (b) Energy spectrum of the electrons accelerated within 5 mrad of the specular direction.

We have demonstrated for the first time the possibility to accelerate electrons to relativistic energies with a radially polarized laser pulse. It was shown that radial polarization can lead to acceleration in the longitudinal direction and reduce the divergence of the electron beam. However, while this work clearly demonstrates that the relativistic regime is reached for radially polarized laser pulses, the data shows that the performance is still degraded when compared to linear polarization. This suggest that more work is still required to generate higher purity radially polarized pulses at ultrahigh intensity. We have also unveiled the details of the physics of the laser-plasma interaction, and found that the use of radial or azimuthal polarization at oblique incidence leads to two spatially separated sources of electrons and high-harmonics. We conclude that harmonic generation is detrimental to the acceleration process so that these experiments were not performed in ideal conditions because of the use of oblique incidence. We expect that the accelerated electron beams can be greatly improved at normal incidence and with stronger longitudinal fields. These results refine our understanding of the interaction between exotic ultra-intense laser pulses and plasma mirrors and may provide a new path for generating high quality ultra-short relativistic electron bunches.

ACKNOWLEDGMENTS

The authors thank Dr. Götz Zinner from Bernard Halle (Germany) for producing the phase mask and Guillaume Blaclard for fruitful discussions. The research leading to these results has received funding from LASERLAB-EUROPE (grant agreement No. 654148, European Union's Horizon 2020 research and innovation programme), the Agence Nationale pour la Recherche (Contract No. ANR-14-CE32-0011-03 APERO) and the European Research Council (Contracts No. 306708, ERC Starting Grant FEMTOELEC and No. 694596, Grant ExCoMet). An award of computer time (PlasmInSilico) was provided by the Innovative and Novel Computational Impact on Theory and Experiment (INCITE) program. This research used resources of the Argonne Leadership Computing Facility (MIRA), which is a U.S. DOE Office of Science User Facility supported under Contract No. DE-AC02-06CH11357.

Appendix A: Parameters for the 3D PIC simulations

We use a spatial resolution of $\Delta x = \Delta y = \Delta z = \lambda_0/57$, a temporal resolution of $\Delta t = T_0/57$ and 6 particles per cell per specie. The PSATD Maxwell solver is used with a stencil spatial order of 100 and 8 guard cells. The laser impinges the plasma with a 60° incidence angle, a central wavelength of $\lambda_0 = 800$ nm, a beam waist of $w_0 = 3.1\,\mu$m and a pulse duration of 24 fs in FWHM of intensity. The peak normalized amplitude of the transverse field is $a_0 = 5.4$ for linear polarization and $a_{0,r} = 4.9$ for radial and azimuthal polarization. The intensity was reduced to obtain the accelerated electron distributions, as indicated in Figs. 10, 11 and 13. A cosine temporal envelope is used. The plasma density profile is exponential with a minimum density of $n_c/20$ and a maximum density of 100 n_c. The gradient scale length is $L = \lambda_0/10$, except in the simulations at reduced intensity in radial and azimuthal polarization, where it is $L = \lambda_0/7$.

Appendix B: Parameters for the test particle simulation

We use in the test particle simulation a laser pulse with the same spatio-temporal profile as in Ref.[27]. We use a central wavelength of $\lambda_0 = 800$ nm, a beam waist of $w_0 = 3.1\,\mu$m, a pulse duration of 24 fs in FWHM of intensity and a peak normalized amplitude of the radial electric field of $a_{0,r} = 2.6$ or $a_{0,r} = 1.3$. These values are slightly lower than in the PIC simulations to take into account the fact that the reflectivity of the plasma mirror is smaller than unity.

The initial electron distributions are as indicated in the main text.

Appendix C: Parameters for the PIC simulation in cylindrical coordinates

We use a spatial resolution of $\Delta x = \lambda_0/279$ and $\Delta r = \lambda_0/65$, a temporal resolution of $\Delta t = T_0/331$, 250 particles per cell per specie and 2 orders for the Fourier expansion along the azimuthal direction. The plasma density profile is exponential with a gradient scale length of $L = \lambda_0/7$, a minimum density of $n_c/10$ and a maximum density of 200 n_c. The laser has a central wavelength of $\lambda_0 = 800$ nm, a beam waist of $w_0 = 1.5\,\mu$m and a pulse duration of 5 fs in FWHM of intensity. The peak normalized amplitude of the longitudinal field is $a_{0,z} = 3.78$ and the peak amplitude of the radial field is $a_{0,r} = 9.55$ for radial and azimuthal polarization. We use the same laser spatio-temporal profile as in Ref.[27].

[1] T. J. Yu, S. K. Lee, J. H. Sung, J. W. Yoon, T. M. Jeong, , and J. Lee. Generation of high-contrast, 30 fs, 1.5 PW laser pulses from chirped-pulse amplification ti:sapphire laser. *Optics Express*, 20:10807–10815, 2012.

[2] T. Tajima and J. M. Dawson. Laser electron accelerator. *Physical Review Letters*, 43:267–270, 1979.

[3] E. Esarey, C. B. Schroeder, and W. P. Leemans. Physics of laser-driven plasma-based electron accelerators. *Review of Mordern Physics*, 81:4833–4843, 2009.

[4] O. Lundh, J. Lim, C. Rechatin, L. Ammoura, A. Ben-Ismail, X. Davoine, G. Gallot, J.-P. Goddet, E. Lefebvre, V. Malka, and J. Faure. Few femtosecond, few kiloampere electron bunch produced by a laser-plasma accelerator. *Nat. Phys.*, 7:219, 2011.

[5] D. Guénot, D. Gustas, A. Vernier, B. Beaurepaire, F. Böhle, M. Bocoum, M. Lozano, A. Jullien, R. Lopez-Martens, A. Lifschitz, and J. Faure. Relativistic electron beams driven by kHz single-cycle light pulses. *Nat. Photon.*, 11(5):293–296, May 2017. Letter.

[6] A. J. Gonsalves, K. Nakamura, J. Daniels, C. Benedetti, C. Pieronek, T. C. H. de Raadt, S. Steinke, J. H. Bin, S. S. Bulanov, J. van Tilborg, C. G. R. Geddes, C. B. Schroeder, Cs. Tóth, E. Esarey, K. Swanson, L. Fan-Chiang, G. Bagdasarov, N. Bobrova, V. Gasilov, G. Korn, P. Sasorov, and W. P. Leemans. Petawatt laser guiding and electron beam acceleration to 8 GeV in a laser-heated capillary discharge waveguide. *Phys. Rev. Lett.*, 122:084801, Feb 2019.

[7] F. V. Hartemann, S. N. Fochs, G. P. Le Sage, Jr. N. C. Luhmann, J. G. Woodworth, M. D. Perry, Y. J. Chen, and A. K. Kerman. Nonlinear ponderomotive scattering of relativistic electrons by an intense laser field at focus. *Phys. Rev. E*, 51(5):4833–4843, 1995.

[8] E. Esarey, P. Sprangle, and J. Krall. Laser acceleration of electrons in vacuum. *Phys. Rev. E*, 52:5443–5453, 1995.

[9] B. Quesnel and P. Mora. Theory and simulation of the interaction of ultraintense laser pulses with electrons in vacuum. *Phys. Rev. E*, 58:3719–3732, 1998.

[10] Wei Yu, M. Y. Yu, J. X. Ma, Z. M. Sheng, J. Zhang, H. Daido, S. B. Liu, Z. Z. Xu, and R. X. Li. Ponderomotive acceleration of electrons at the focus of high intensity lasers. *Phys. Rev. E*, 61:R2220–R2223, Mar 2000.

[11] I. Y. Dodin and N. J. Fisch. Relativistic electron acceleration in focused laser fields after above-threshold ionization. *Phys. Rev. E*, 68:056402, Nov 2003.

[12] G. V. Stupakov and M. S. Zolotorev. Ponderomotive laser acceleration and focusing in vacuum for generation of attosecond electron bunches. *Phys. Rev. Lett.*, 86:5274–5277, Jun 2001.

[13] Yousef I. Salamin and Christoph H. Keitel. Electron acceleration by a tightly focused laser beam. *Phys. Rev. Lett.*, 88:095005, Feb 2002.

[14] J. Pang, Y. K. Ho, X. Q. Yuan, N. Cao, Q. Kong, P. X. Wang, L. Shao, E. H. Esarey, and A. M. Sessler. Subluminous phase velocity of a focused laser beam and vacuum laser acceleration. *Phys. Rev. E*, 66:066501, Dec 2002.

[15] A. Maltsev and T. Ditmire. Above threshold ionization in tightly focused, strongly relativistic laser fields. *Phys. Rev. Lett.*, 90:053002, Feb 2003.

[16] C. I. Moore, A. Ting, S. J. McNaught, J. Qiu, H. R. Burris, and P. Sprangle. A laser-accelerator injector based on laser ionization and ponderomotive acceleration of electrons. *Phys. Rev. Lett.*, 82:1688–1691, Feb 1999.

[17] S. Payeur, S. Fourmaux, B. E. Schmidt, J. P. MacLean, C. Tchervenkov, F. Légaré, M. Piché, and J. C. Kieffer. Generation of a beam of fast electrons by tightly focusing a radially polarized ultrashort laser pulse. *Applied Physics Letters*, 101(4):041105, 2012.

[18] D. Cline. First Observation of Acceleration of Electrons by a Laser in a Vacuum. *Journal of Modern Physics*, 4:1–6, 2013.

[19] S. Carbajo, E. A. Nanni, L. J. Wong, G. Moriena, P. D. Keathley, G. Laurent, R. J. D. Miller, and F. X. Kärtner. Direct longitudinal laser acceleration of electrons in free space. *Phys. Rev. Accel. Beams*, 19:021303, 2016.

[20] M. Thévenet, A. Leblanc, S. Kahaly, H. Vincenti, A. Vernier, F. Quéré, and J. Faure. Vacuum laser acceleration of relativistic electrons using plasma mirror injectors. *Nature physics*, 12:355–360, 2016.

[21] C. Thaury and F. Quéré. High-order harmonic and attosecond pulse generation on plasma mirrors: basic mechanisms. *Journal of Physics B: Atomic, Molecular and Optical Physics*, 43:213001, 2010.

[22] M. Thévenet, H. Vincenti, and J. Faure. On the physics of electron ejection from laser-irradiated overdense plasmas. *Physics of plasmas*, 23:063119, 2016.

[23] L. Chopineau, A. Leblanc, G. Blaclard, A. Denoeud, M. Thévenet, J-L. Vay, G. Bonnaud, Ph. Martin, H. Vincenti, and F. Quéré. Identification of coupling mechanisms between ultraintense laser light and dense plasmas. *Phys. Rev. X*, 9:011050, Mar 2019.

[24] Y. I. Salamin. Electron acceleration from rest in vacuum by an axicon gaussian laser beam. *Phys. Rev. A*, 73(4):043402, 2006.

[25] A. Karmakar and A. Pukhov. Collimated attosecond GeV electron bunches from ionization of high-Z material by radially polarized ultra-relativistic laser pulses. *Laser and Part. Beams*, 25(3):371–377, 2007.

[26] C. Varin, S. Payeur, V. Marceau, S. Fourmaux, A. April, B. Schmidt, P. L. Fortin, N. Thiré, T. Brabec, F. Légaré, J. C. Kieffer, and M. Piché. Direct

electron acceleration with radially polarized laser beams. *Applied Sciences*, 3(1):70–93, 2013.

[27] V. Marceau, C. Varin, T. Brabec, and M. Piché. Femtosecond 240-keV electron pulses from direct laser acceleration in a low-density gas. *Phys. Rev. Lett.*, 111(22):224801, 2013.

[28] Aurélien Martens, Kevin Dupraz, Kevin Cassou, Nicolas Delerue, Alessandro Variola, and Fabian Zomer. Direct electron acceleration with tightly focused TM01 beams: boundary conditions and non-paraxial corrections. *Opt. Lett.*, 39(4):981–984, Feb 2014.

[29] Liang Jie Wong, Kyung-Han Hong, Sergio Carbajo, Arya Fallahi, Philippe Piot, Marin Soljacic, John D. Joannopoulos, Franz X. Kärtner, and Ido Kaminer. Laser-induced linear-field particle acceleration in free space. *Scientific Reports*, 7(1):11159, 2017.

[30] N. Zaim, M. Thévenet, A. Lifschitz, and J. Faure. Relativistic acceleration of electrons injected by a plasma mirror into a radially polarized laser beam. *Physical review Letters*, 119:094801, 2017.

[31] Nobuhiko Nakanii, Tomonao Hosokai, Naveen C. Pathak, Shinichi Masuda, Alexei G. Zhidkov, Hiroki Nakahara, Kenta Iwasa, Yoshio Mizuta, Naoki Takeguchi, Takamitsu P. Otsuka, Keiichi Sueda, Jumpei Ogino, Hirotaka Nakamura, Michiaki Mori, Masaki Kando, and Ryosuke Kodama. Decomposition of powerful axisymmetrically polarized laser pulses in underdense plasma. *Phys. Rev. E*, 94:063205, Dec 2016.

[32] A. Lévy, T. Ceccotti, P. D'Oliveira, F. Réau, M. Perdrix, F. Quéré, P. Monot, M. Bougeard, H. Lagadec, P. Martin, J. P. Geindre, and P. Audebert. Double plasma mirror for ultrahigh temporal contrast ultraintense laser pulses. *Opt. Lett.*, 32:310–312, 2007.

[33] S. Kahaly, S. Monchocé, H. Vincenti, T. Dzelzainis, B. Dromey, M. Zepf, Ph. Martin, and F.Quéré. Direct observation of density-gradient effects in harmonic generation from plasma mirrors. *Physical Review Letters*, 110:175001, 2013.

[34] Y. Glinec, J. Faure, A. Guemnie Tafo, V. Malka, H. Monard, J. P. Larbre, V. De Waele, J. L. Marignier, and M. Mostafavi. Absolute calibration for a broad range single shot electron spectrometer. *Review of Scientific Instruments*, 77:103301, 2006.

[35] J-L Vay, D P Grote, R H Cohen, and A Friedman. Novel methods in the particle-in-cell accelerator code-framework WARP. *Computational Science & Discovery*, 5(1):014019, dec 2012.

[36] See `http://warp.lbl.gov` for more information concerning the code WARP.

[37] H. Vincenti, M. Lobet, R. Lehe, R. Sasanka, and J.-L. Vay. An efficient and portable SIMD algorithm for charge/current deposition in particle-in-cell codes. *Computer Physics Communications*, 210:145 – 154, 2017.

[38] See `https://www.picsar.net` for more information concerning the high-performance PICSAR library.

[39] Jean-Luc Vay, Irving Haber, and Brendan B. Godfrey. A domain decomposition method for pseudo-spectral electromagnetic simulations of plasmas. *Journal of Computational Physics*, 243:260 – 268, 2013.

[40] H. Vincenti and J.-L. Vay. Detailed analysis of the effects of stencil spatial variations with arbitrary high-order finite-difference maxwell solver. *Computer Physics Communications*, 200:147 – 167, 2016.

[41] G. Blaclard, H. Vincenti, R. Lehe, and J. L. Vay. Pseudospectral maxwell solvers for an accurate modeling of doppler harmonic generation on plasma mirrors with particle-in-cell codes. *Phys. Rev. E*, 96:033305, Sep 2017.

[42] Henri Vincenti and Jean-Luc Vay. Ultrahigh-order maxwell solver with extreme scalability for electromagnetic PIC simulations of plasmas. *Computer Physics Communications*, 228:22 – 29, 2018.

[43] See `https://www.alcf.anl.gov/mira` for more information regarding supercomputer Mira.

[44] Spencer W. Jolly. Influence of longitudinal chromatism on vacuum acceleration by intense radially polarized laser beams. *Opt. Lett.*, 44(7):1833–1836, Apr 2019.

[45] A.F. Lifschitz, X. Davoine, E. Lefebvre, J. Faure, C. Rechatin, and V. Malka. Particle-in-cell modelling of laser–plasma interaction using Fourier decomposition. *Journal of Computational Physics*, 228(5):1803 – 1814, 2009.

[46] Sergei Kühn, Mathieu Dumergue, Subhendu Kahaly, Sudipta Mondal, Miklós Füle, Tamás Csizmadia, Balázs Farkas, Balázs Major, Zoltán Várallyay, Eric Cormier, Mikhail Kalashnikov, Francesca Calegari, Michele Devetta, Fabio Frassetto, Erik Månsson, Luca Poletto, Salvatore Stagira, Caterina Vozzi, Mauro Nisoli, Piotr Rudawski, Sylvain Maclot, Filippo Campi, Hampus Wikmark, Cord L Arnold, Christoph M Heyl, Per Johnsson, Anne L'Huillier, Rodrigo Lopez-Martens, Stefan Haessler, Maïmona Bocoum, Frederik Boehle, Aline Vernier, Gregory Iaquaniello, Emmanuel Skantzakis, Nikos Papadakis, Constantinos Kalpouzos, Paraskevas Tzallas, Franck Lépine, Dimitris Charalambidis, Katalin Varjú, Károly Osvay, and Giuseppe Sansone. The ELI-ALPS facility: the next generation of attosecond sources. *Journal of Physics B: Atomic, Molecular and Optical Physics*, 50(13):132002, jun 2017.

université
PARIS-SACLAY

ÉCOLE DOCTORALE
Ondes et Matière
(EDOM)

Titre : Modélisation de l'accélération d'électrons par des impulsions lasers relativistes de quelques cycles optiques sur des plasmas surdenses

Mots clés : accélération d'électrons, lasers de quelques cycles optiques, plasmas surdenses, polarisation radiale

Résumé : Cette thèse de doctorat est consacrée à l'accélération d'électrons lors de l'interaction entre un laser d'intensité relativiste et un plasma surdense. Deux scénarios d'interaction précédemment inexplorés y sont étudiés. Premièrement, nous considérons le cas où l'impulsion laser n'est composée que de quelques cycles optiques. En utilisant des résultats expérimentaux et numériques, nous identifions un nouveau régime d'accélération par sillage laser caractérisé par la rotation des ondes plasmas qui est induite par le gradient de densité plasma. Ce mécanisme requiert des gradients de densité étendus ($> \lambda$) et ne peut être déclenché que par des impulsions de quelques cycles optiques, en vertu de la condition de résonance pour les hautes densités plasma considérées. Deuxièmement, nous considérons le cas où l'impulsion laser est polarisée radialement. Cette polarisation a été fréquemment considérée pour l'accélération d'électrons dans le vide car elle possède d'un champ électrique longitudinal très intense. Cependant, les résultats expérimentaux sont restés jusqu'alors limités parce qu'il est particulièrement difficile d'injecter efficacement les électrons dans le laser. Nous montrons que ce problème peut être résolu en utilisant des plasmas surdenses pour injecter les électrons. Ce résultat est confirmé par des expériences récentes réalisées au CEA Saclay, dans lesquelles l'accélération d'électrons dans la direction longitudinale est clairement observée. Nous identifions finalement les conditions pour lesquelles ce mécanisme est optimal et peut mener à des distributions angulaires extrêmement piquées.

Title : Modeling electron acceleration driven by relativistic intensity few-cycle laser pulses on overdense plasmas

Keywords : electron acceleration, few-cycle lasers, overdense plasmas, radial polarization

Abstract : This PhD thesis is devoted to electron acceleration from the interaction between a relativistic intensity laser pulse and an overdense plasma. Two previously unexplored interaction scenarios are studied. First, we consider the case where the laser pulse only consists of a few optical oscillations. Using experimental and numerical results, we identify a new laser wakefield acceleration regime characterized by the rotation of the plasma waves induced by the plasma density gradient. This process requires large gradient scale lengths ($> \lambda$) and can only be driven by few-cycle pulses, by virtue of the resonant condition at such high densities. Secondly, we study the case where the laser pulse has radial polarization. This polarization state has been frequently proposed for accelerating electrons in vacuum because of its strong longitudinal electric field. However, experimental results remained limited because injecting electrons into the laser is a considerable challenge. We show that this issue can be solved using overdense plasmas as an injection method. This result is confirmed by recent experiments performed at CEA Saclay, in which electron acceleration in the longitudinal direction is demonstrated. Finally, we identify the conditions for which this process is optimal and can lead to extremely peaked angular distributions.

Université Paris-Saclay
Espace Technologique / Immeuble Discovery
Route de l'Orme aux Merisiers RD 128 / 91190 Saint-Aubin, France